The Loma Prieta, California, Earthquake of October 17, 1989—Aftershocks and Postseismic Effects

PAUL A. REASENBERG, *Editor*

EARTHQUAKE OCCURRENCE
WILLIAM H. BAKUN and WILLIAM H. PRESCOTT, *Coordinators*

U.S. GEOLOGICAL SURVEY PROFESSIONAL PAPER 1550–D

Prepared in cooperation with the National Science Foundation

UNITED STATES GOVERNMENT PRINTING OFFICE, WASHINGTON : 1997

DEPARTMENT OF THE INTERIOR

BRUCE BABBITT, *Secretary*

U.S. GEOLOGICAL SURVEY

Gordon P. Eaton, *Director*

Manuscript approved for publication, January 2, 1997

Library of Congress catalog-card No. 92–32287

For sale by the
U.S. Geological Survey
Information Services
Box 25286
Denver Federal Center
Denver, CO 80225

CONTENTS

THE LOMA PRIETA, CALIFORNIA, EARTHQUAKE OF OCTOBER 17, 1989:
EARTHQUAKE OCCURRENCE

AFTERSHOCKS AND POSTSEISMIC EFFECTS

INTRODUCTION

By Paul A. Reasenberg,
U.S. Geological Survey

CONTENTS

INTRODUCTION

While the damaging effects of the earthquake represent a significant social setback and economic loss, the geophysical effects have produced a wealth of data that have provided important insights into the structure and mechanics of the San Andreas fault system. Generally, the period after a large earthquake is vitally important to monitor. During this part of the seismic cycle, the primary fault and the surrounding faults, rock bodies, and crustal fluids rapidly readjust in response to the earthquake's sudden movement. Geophysical measurements made at this time can provide unique information about fundamental properties of the fault zone, including its state of stress and the geometry and frictional/rheological properties of the faults within it. Because postseismic readjustments are rapid compared with corresponding changes occurring in the preseismic period, the amount and rate of information that is available during the postseismic period is relatively high. From a geophysical viewpoint, the occurrence of the Loma Prieta earthquake in a section of the San Andreas fault zone that is surrounded by multiple and extensive geophysical monitoring networks has produced nothing less than a scientific bonanza.

The reports assembled in this chapter collectively examine available geophysical observations made before and after the earthquake and model the earthquake's principal postseismic effects. The chapter covers four broad categories of postseismic effect: (1) aftershocks; (2) postseismic fault movements; (3) postseismic surface deformation; and (4) changes in electrical conductivity and crustal fluids.

SEISMOLOGICAL STUDIES

The earthquake occurred inside the U.S. Geological Survey's Northern California Seismographic Network (NCSN) and is the largest earthquake within the network to be recorded by it. More than 75 high-gain seismographs recorded the main shock and nearly 11,000 aftershocks during the first 2 years of the earthquake sequence. Many of these instruments had been recording for 20 years before the earthquake. The approximately 5,600 earthquakes that they recorded in the region before the earthquake allow detailed comparisons of the pre- and post-earthquake activity. In addition, some 170 records were obtained from strong-motion instruments within 200 km of the epicenter. After the earthquake, 38 temporary seismographs (mostly strong motion instruments) were deployed to record the aftershock sequence. The first three papers in this chapter analyze the seismological data and focus their analyses on the structure of the San Andreas fault, its interaction with the major nearby faults, and the contemporary tectonics of the greater Pacific-North American plate boundary in the San Francisco Bay area.

Dietz and Ellsworth provide a comprehensive survey of the aftershock locations and magnitudes, the focal mechanisms for the main shock and the larger aftershocks, and the time-evolution of the aftershock sequence. From these observations they infer possible geometries of the faulting structures active in the earthquake and their possible kinematic and geometric relationship to the San Andreas fault. The aftershock focal mechanisms were highly diverse in orientation and unlike those of the pre-earthquake seismicity, leading Dietz and Ellsworth to conclude that the stress drop in the main shock may have been nearly complete.

At greater distances from the earthquake, Reasenberg and Simpson examine the post-earthquake seismicity changes in central California. They compare the 20 years of seismicity recorded in central California before the earthquake to the activity during the 20-month postseismic period. They find that some regions (for example, the San Francisco peninsula) sustained an increase in seismic activity after the earthquake, while at least one other area (the Hayward fault) sustained a decrease in activity. These

changes are consistent with the stress changes calculated for simple elastic dislocation models of the earthquake when the effective coefficient of friction on the faults is assumed to be low (less than 0.3). A surprisingly small amount of stress change (0.1 bar) was apparently sufficient to affect the seismicity on these nearby faults.

Another view of the stress changes produced by the earthquake is provided by the aftershock focal mechanisms. Gephart uses fault plane solutions for the first 6 weeks of the aftershock sequence to map the spatial variations in stress in the vicinity of the main shock rupture. Near and northwest of the main shock hypocenter, he finds low shear stress remaining on the main shock fault plane after the earthquake, again consistent with the inference of a nearly complete stress drop in the earthquake. Southeast of the hypocenter, near Pajaro Gap and the creeping segment of the fault, significant right lateral shear apparently remained on the fault.

Aftershock observations also were used to hone seismological technique. Schwartz and Nelson use synthetic calculations and data from portable (PASSCAL) three-component seismographs in order to compare earthquake hypocenter location methods based on various combinations of P, S, and S-P arrival times. They find that the unsynchronized S-P arrival times observed with a sparse, portable array provided remarkably good locations relative to those obtained from the more extensive, permanent NCSN array. The PASSCAL data also were used by Guo and others to estimate source characteristics of the aftershocks. Using an empirical Green's function technique, they estimate Brune-model stress drops from the corner frequencies and moments of the aftershocks. They report an apparent dependence of stress drop on earthquake moment.

Other portable seismic instruments, in addition to the PASSCAL instruments, were deployed after the earthquake to record aftershocks. Altogether, 38 digital seismographs were deployed at 195 sites during the 3-month period after the earthquake. Wennerberg documents these deployments and the massive and disparate data sets they produced. He provides us with detailed maps, instrument descriptions, and data logs for the aftershock deployments. He also provides a table of references to studies utilizing these data and published elsewhere. In so doing, he assures that future seismological investigations of the earthquake will be able to proceed efficiently with a map of these essential, recorded seismological data sets.

POSTSEISMIC MOVEMENT ON THE SAN ANDREAS AND NEARBY FAULTS

At the time of the earthquake, 27 creepmeters were recording surface movements at points on the San Andreas and Calaveras faults within about 200 km of the epicenter. These instruments had been recording fault movement for periods up to 25 years before the earthquake. In addition, small-scale (50-200 m) triangulation networks at about two dozen sites in the San Francisco Bay Area on the San Andreas, Calaveras, Hayward, and Concord-Green Valley faults had been observed regularly to measure surface fault displacements for up to 13 years before the earthquake. These observations form the basis for three papers describing and modeling the surface movements of the major faults in the Bay Area after the earthquake.

In a detailed study of surface fault displacements (creep) at the eight nearest creepmeter sites on the San Andreas and Calaveras faults, Breckenridge and Simpson find that both the sense (right-lateral or left-lateral) and magnitude of long-term creep rate changes on nearby faults agree with coseismic changes in horizontal shear stress calculated for elastic dislocation models of the earthquake. In contrast, the amplitudes of coseismic steps in fault displacement measured at the same sites apparently bear little similarity to the calculated static stress changes; they propose that dynamic stresses (shaking) likely account for these coseismic steps. The correlation between the regional creep rate changes and the earthquake-induced static stress changes parallels changes observed in the regional seismicity rates (Reasenberg and Simpson) and suggests that over a period of a few years a dominant effect of the earthquake on the major Bay area faults was the sympathetic advancement and retardation of ongoing processes of seismicity and creep, driven by the static stress changes.

Behr and others also investigate the increases in creep rate at the five USGS creepmeter sites on the San Andreas fault studied by Breckenridge and Simpson, and at three additional sites between San Juan Bautista and Pajaro Gap. In contrast to the ephemerally enhanced fault creep observed after some earthquakes, they find a sustained level of elevated creep rate during the first 3 years after the Loma Prieta earthquake. Their two-dimensional elastic boundary models of the San Andreas and Calaveras faults can qualitatively explain the observed decrease in postseismic slip with distance from the earthquake.

Triangulation measurements over small (50-200 m) aperture arrays spanning Bay area faults tell a similar story. Galehouse reports that the creep rate on the San Francisco peninsula section of the San Andreas fault was nil both before and after the earthquake, while creep rates approximately doubled on the San Andreas fault southeast of the rupture. At the same time, creep on the Hayward and southern Calaveras faults decreased and, at some stations along the southern Hayward fault, creep may have stopped or become left lateral. Galehouse's findings are consistent with the seismicity and other creep observations presented in this chapter and with static stress change calculations (Breckenridge and Simpson), suggesting that the East Bay faults were at least temporarily relaxed by the earthquake.

How long this relaxation will last before being overtaken by continuing tectonic and additional seismogenic loading will surely be the subject of continuing measurements and modeling efforts.

POSTSEISMIC DEFORMATION OF THE CRUST

Prior to the earthquake, horizontal deformation in the epicentral region had been monitored for about 20 years by land-based trilateration measurements, and for several years by Global Positioning System (GPS) measurements. Thus, from a geodetic monitoring point of view, the earthquake's location was indeed advantageous. Resurveying of these sites and the rapid and repeated survey of new sites by several campaigns launched after the earthquake has provided an extensive and varied data set for constraining the surface deformation and inferring the deformation at depth associated with the earthquake. The data and conclusions of these studies compliment the seismological and fault slip studies; together they provide one of the most extensive sets of geophysical observations of the crustal response to a large earthquake.

Bürgmann and others investigate the deformation of the crust after the earthquake using data from repeated GPS measurements in two fault-crossing networks and compare it to the deformation inferred from preseismic observations. They find that horizontal displacement rates northwest of the epicenter did not change significantly at the time of the earthquake, while the fault-parallel station velocities in the epicentral region increased significantly over pre-earthquake rates. They also find evidence for San Andreas fault-normal shortening near the epicenter and within the Foothills thrust. Using linear, elastic dislocation models, they find that a two-plane slip model with maximum depth of about 16 km best explains these data. They suggest that the inferred reverse slip on the Foothills thrust fault appears to have been triggered by stress changes produced by the earthquake.

At the northwest end of the main shock rupture, just northwest of the study region of Bürgmann and others, a 10-km aperture trilateration network was repeatedly measured by Langbein in the 2-year period after the earthquake. Although no preseismic observations of these lines had been made, comparisons are made to preseismic measurements of the Black Mountain geodetic net 15 km to the northwest. Langbein's analysis of these data finds that the rapid temporal decay in the postseismic deformation rate in the network is typical for a postseismic geodetic response. It fails to find evidence for the fault-normal horizontal contraction inferred by Bürgmann and others from the regional GPS data.

Linker and Rice use the geodetic observations to explore viscoelastic, time-dependent models of the postseismic deformation. Their models contrast with those of Bürgmann and others in that they allow for transient, postseismic slip in the deep, aseismic region of the fault zone, well below the maximum depth of slip in the elastic dislocation models. While the deep, viscoelastic models are compatible with most of the strike-slip deformation observed in the epicentral region, they do not explain the fault-normal contraction observed there and may overpredict strike-slip deformation near Black Mountain to the northwest of the earthquake. The paper explores a wide range of alternative assumptions about fault zone rheology and slip distribution in the crust.

Near the southeast end of the main shock rupture, a borehole strainmeter recorded the tensor strain during and after the earthquake. This instrument had been recording changes in tensor strain for 10 years before the earthquake. Gladwin and others compare the pre- and post-earthquake strain rates at this site and find an apparent increase in fault-parallel shear strain rate. The timing of this strain anomaly relative to the Loma Prieta earthquake and its regional extent are addressed in detail through comparisons with surface creep and geodetic measurements. The occurrence of the Chittenden earthquake sequence in April 1990, located near the southeast end of the main shock rupture and only 10 km from the borehole, apparently increased the shear strain rate at this site. To explain these strain observations, Gladwin and others propose that a shallow asperity southeast of the main shock rupture initially resisted the increased shear load on the San Andreas fault, and then yielded in the April 1990 sequence, thereby unpinning the San Andreas fault and resulting in even higher shear strain rates.

CRUSTAL FLUIDS AND ELECTRICAL CONDUCTIVITY

Finally, Mackie and others present the results of a magnetotelluric survey of the epicentral area. Working with observations made one year after the earthquake, they find evidence for a vertical tabular zone of anomalously high electrical conductance in the lower crust below the earthquake. Unfortunately, no corresponding measurements were made before the earthquake, so their interpretation of these data cannot conclusively associate the anomaly with the earthquake; it might instead be a permanent feature of the San Andreas fault. However, they suggest an intriguing scenario in which fluids (water) that were already present in the crust experienced increased flow due to an increase in porosity and fluid connectivity in the fault zone caused by fracturing during the earthquake.

THE LOMA PRIETA, CALIFORNIA, EARTHQUAKE OF OCTOBER 17, 1989:
EARTHQUAKE OCCURRENCE

AFTERSHOCKS AND POSTSEISMIC EFFECTS

AFTERSHOCKS OF THE LOMA PRIETA EARTHQUAKE AND THEIR TECTONIC IMPLICATIONS

By Lynn D. Dietz and William L. Ellsworth,
U.S. Geological Survey

CONTENTS

ABSTRACT

The Loma Prieta earthquake and its aftershocks ruptured faults within a broad zone along the San Andreas fault in the southern Santa Cruz Mountains. The main body of aftershocks forms a southwest-dipping zone, rising from the main shock hypocenter at 15.9 km depth to the San Andreas fault, and extending bilaterally along strike for a distance of 42 km. This zone, however, does not mark a simple fault plane, as it has a width of 1 to 2 km. Aftershocks also occur on faults well removed from the main zone on both sides of the San Andreas fault. The aftershock zone assumed essentially its final form within less than 1 day and only showed apparent growth to the southeast, where aftershock activity occurred on the normally active part of the San Andreas and Castro faults. Aside from these two faults, the aftershocks occurred on structures that were essentially aseismic in the 20 years preceding the earthquake. Focal mechanisms of the aftershocks bear little resemblance to the main shock or preceding seismicity. The mechanisms tend to have fault-normal *P*-axes, although a very wide range of mechanism types is observed. The diversity and orientation of the aftershock mechanisms and the lack of spatial correlation with the preshocks argue for a major reorientation of the stress field by the main shock and are consistent with a complete stress drop on the main shock fault.

The main shock nucleated with a foreshock 1.6 s before the start of large-amplitude high-frequency seismic radiation. Although the foreshock was too feeble to trigger many of the strong-motion stations in the epicentral region (vertical acceleration$\leq$0.01 *g*), it had an amplitude magnitude of 5. Nearfield displacement seismograms indicate significantly larger moment release at long periods, equivalent to M_W=5 1/2. The foreshock thus appears to mark the beginning of a continuous and relatively smooth process of moment release that only began to propagate away from the initial hypocenter after 1.6 s. The aftershock sequence has no distinct beginning, with the earliest locatable events emerging from the main shock coda.

The Loma Prieta fault, as mapped by the main zone of aftershocks, exists as a structure distinct from the San Andreas fault along most of its length. Along its southern end, where the sense of displacement changes from reverse to strike slip, it merges seamlessly with the San Andreas fault near Pajaro Gap. We speculate that the fault represents a former part of the San Andreas that has been abandoned as a strike slip fault and has evolved into a right-reverse fault to accommodate motion around the compressional bend in the San Andreas fault through the southern Santa Cruz Mountains.

INTRODUCTION

The Loma Prieta earthquake presents an unparalleled opportunity to study the source process of a major earthquake using multiple and complementary data provided by geology, geodesy, and seismology. Our objectives in this paper are to describe the spatial distribution and temporal characteristics of the sequence, the connection between the earthquake and the San Andreas fault, and the relationship between the preshocks, the main shock, and the aftershocks from the vantage point of short-period network seismology.

The Loma Prieta earthquake occurred within a portion of the San Andreas fault system in one of the most densely instrumented regions for the observation of microearthquake activity. Systematic cataloging of accurately located hypocenters, magnitude ≥1.5, as recorded by the U.S. Geological Survey's telemetered seismic network (CALNET), began in this area over two decades before the 1989 earthquake. The CALNET thus provides a wealth of information on not only the complete aftershock sequence of a major event, but also on its relationship to background seismicity over an extended period of time.

This study builds on the work of many of our colleagues who have analyzed various aspects of the CALNET data to determine the crustal structure, hypocentral locations, focal mechanisms, and state of stress as reported in this chapter and other chapters in this volume [also Eberhart-Phillips and others (1990), Michael and others (1990), Foxall and others (1993), Olson (1990), Oppenheimer (1990), Schwartz and others (1990), and Zoback and Beroza (1993)]. In this paper we extend the results of our earlier paper (Dietz and Ellsworth, 1990) to present a comprehensive picture of the earthquake and attendant seismicity through the first two years of the aftershock period, and we compare the patterns of hypocenters and focal mechanisms with those observed during the preceding 20 years using uniform analysis methods.

DATA AND METHODS

The primary data sets examined in this study are the locations, magnitudes, and focal mechanisms of earthquakes that occurred in the vicinity of the Loma Prieta earthquake. These data are derived from the analysis of seismograms recorded by CALNET, and are based on the measured arrival times and polarities of *P*-wave onsets and the duration of coda waves, recorded as the time from the *P*-wave onset to the time when the average absolute amplitude (2-second window) falls below a threshold value of 60 millivolts (Eaton, 1992).

Earthquakes within the dashed box in figure 1 from January 1, 1969, through October 17, 1991, are considered in this study. About 5,600 events were recorded in this region before the Loma Prieta earthquake and nearly 11,000 were processed in the first 2 years of the sequence. The region completely encompasses the primary aftershock sequence and is approximately twice as long and twice as wide as the extent of main shock rupture determined by geodetic and seismic means.

HYPOCENTER ANALYSIS PROCEDURES

Earthquake magnitude, denoted M_d, is determined using the formulation of Eaton (1992). Supplementary magnitudes, principally M_L, are used for the largest events. During the 1970's, the CALNET's detection capability increased to lower magnitudes as the network was enlarged and densified. Also, a change in network amplification in 1977 is thought to have introduced an artificial shift in catalog magnitudes (Marks and Lester, 1980; Habermann and Craig, 1988). Since 1980 the detection threshold in the study area has remained relatively constant and no network change affecting magnitudes is known to have occurred. Figure 2 shows the frequency-magnitude density distribution, binned by 0.1 magnitude units, of the

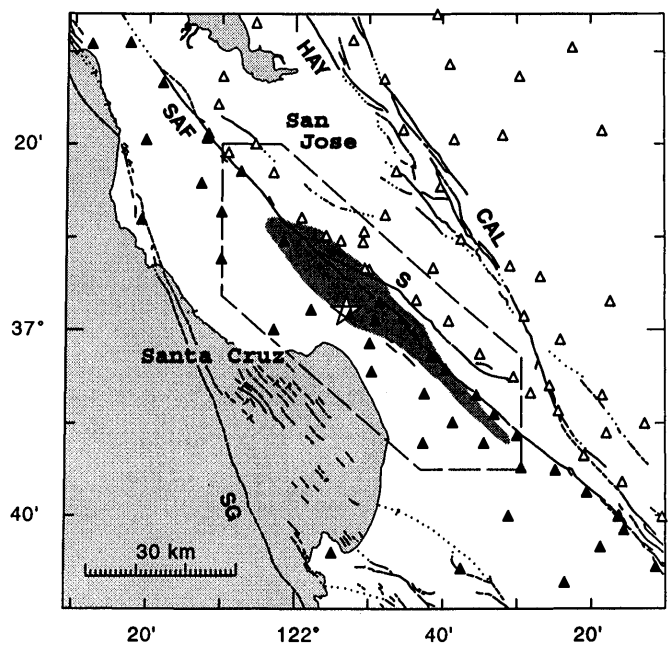

Figure 1.—Map showing study region (dashed line) and locations of CALNET seismic stations (triangles) within ~60 km of the Loma Prieta main shock (star). Solid triangles are assigned to velocity model 1; open triangles to model 2 (see table 1). Shaded area represents the extent of the aftershock zone. Labeled faults are the San Andreas, SAF; Sargent, S; Calaveras, CAL; Hayward, HAY; and San Gregorio, SG.

pre-Loma Prieta earthquake catalog. Due to the network changes mentioned above, we make no estimate of catalog completeness or *b*-value for the early time range (fig. 2*A*). From 1980 through the end of the study, the catalog appears to be complete to magnitude 1.0 (fig. 2*B*). It should be understood, however, that a small percentage of the earthquakes with magnitudes above these thresholds are missing because their seismograms are obscured by larger events, such as in the coda of the main shock. The *b*-value of the preshocks is 0.64±0.02 calculated from $M \geq 1.0$ events (0.74±0.04 from $M \geq 2.0$ events). The aftershock *b*-value, omitting the incomplete record of the first day's activity, is 0.83±0.01 calculated from $M \geq 1.0$ events (0.74±0.03 from $M \geq 2.0$ events).

Event locations were derived from a merged set of hand- and machine-picked *P*-wave arrivals at CALNET stations (fig. 1) using the location program HYPOINVERSE (Klein, 1989), with the station corrections and *P*-wave velocity model described below. In locating events, the data are weighted as the product of a function of their quality (inversely proportional to the variance of the pick uncertainty), and a function of the epicentral distance of the station. The distance weight is unity out to an epicentral distance of 52.5 km, and decreases to zero at a distance of 105 km.

When examining the spatial distribution of hypocenters, we restrict our attention to the most accurate locations (fig. 3). The selected hypocenters have root mean square residual (rms) <0.15 s, horizontal standard error <1.0 km, vertical standard error <2.0 km, number of stations ≥8, and magnitude ≥1.0. The 3,085 selected preshocks include 78 percent of all $M_d \geq 1.0$ and 82 percent of all $M_d \geq 2.0$ events. The 4,998 selected aftershocks include 79 percent of the total number of events with $M_d \geq 1.0$ and 86 percent of those $M_d \geq 2.0$. The mean rms is 0.07 s.

CRUSTAL MODEL AND LOCATION ACCURACY

In developing a traveltime model for locating the events, our objective was to find a simple model that accounted for the pronounced near-surface variations in velocity known to exist in the region (Wesson and others, 1973a) without introducing biases in the overall distribution due to incorrect modeling of the true three-dimensional earth structure. In the main shock, for example, traveltimes depart from a laterally homogeneous model by up to 2 s (fig. 4). Fortunately, the fact that traveltime residuals at individual stations change slowly as a function of event location within the sequence implies that near-station structure and path-averaged delays account for most of the observed variance in traveltime. Accordingly, we model the traveltimes using a one-dimensional velocity model with station corrections. Obviously, locations made with these assumptions will contain biases due to unmodeled three-dimensional effects, but these appear to be both predictable and of minor importance in light of similar locations from the three-dimensional studies of Michael and Eberhart-Phillips (1991), and Foxall and others (1993).

Using *P*-wave traveltimes from the main shock and 107 aftershocks distributed evenly throughout the aftershock zone, we calculated station traveltime corrections and one-dimensional velocity models with the joint hypocenter-velocity inversion program VELEST (Roecker, 1981; Kradolfer, 1989). To account for the obvious differences in crustal geology across the San Andreas fault, we partitioned the stations into two sets corresponding to the northeast (Franciscan basement) and southwest (Salinian basement) sides of the San Andreas fault (fig. 1). Then we simultaneously derived station corrections and a separate velocity model (seven layers over halfspace)

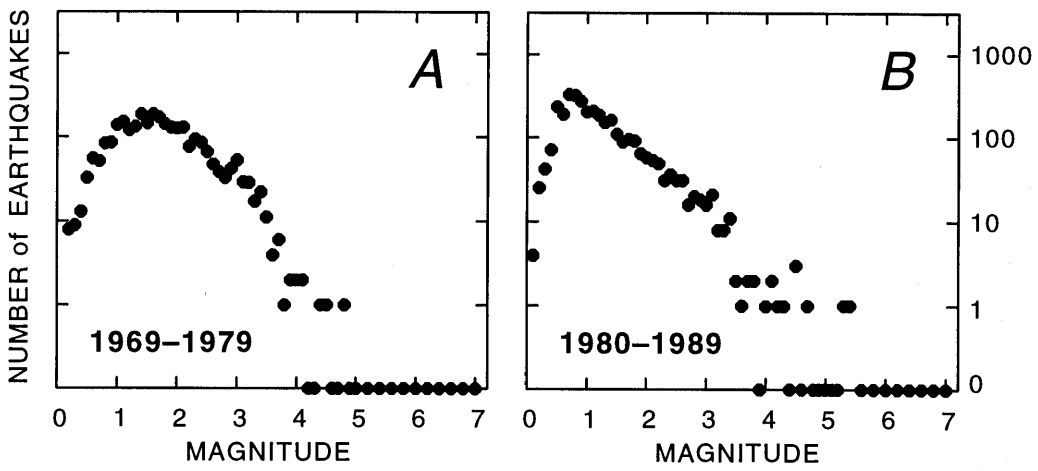

Figure 2.—Pre-Loma Prieta seismicity catalog. Number of earthquakes in each 0.1 magnitude-unit bin (*A*) from 1969 through 1979 and (*B*) from 1980 through October 17, 1989.

for each side of the fault. Following the recipe to calculate a minimum one-dimensional velocity model (Kissling and others, 1994), we initially considered several candidate models; our preferred velocity model (table 1) is used to locate all events in this study. Velocities below 18 km are poorly resolved, principally due to inadequate sampling. As a consequence, a tradeoff exists between focal depth and velocity for the deepest events in the sequence. In particular, the depth of the main shock could be in error by about 1 km.

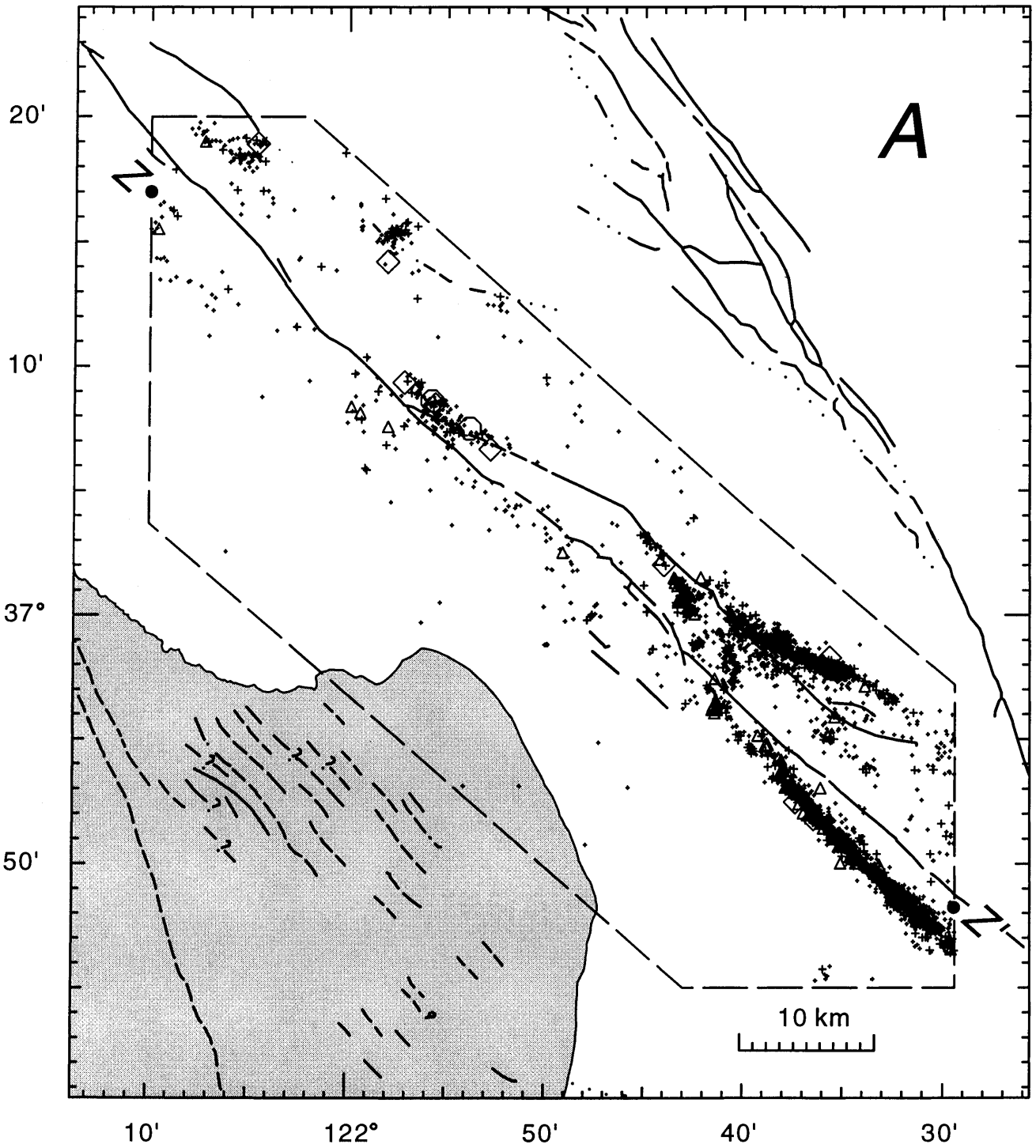

Figure 3.—Best located events within the study region (dashed line). (*A*) January 1, 1969, through October 17, 1989, and (*B*) October 18, 1989, through October 17, 1991. Symbols vary by magnitude: star = $M \geq 7.0$, circle = $M \geq 5.0$, diamond = $M \geq 4.0$, triangle = $M \geq 3.0$, and + = $M \geq 1.0$. Dots labeled *Z* and *Z'* are depth section endpoints.

When considering the location results, two types of errors need to be distinguished: relative location error, which measures the precision of the location in the reference frame of other locations; and absolute location error. The relative error is estimated from the standard error, or confidence ellipse, of the hypocenter location and averages ±0.3 km in epicenter and ±0.6 km in depth for our catalog. This means that internal structures with dimensions of about 1 km may be reliably interpreted in most cases. Figure 5 illustrates the distribution of standard error for

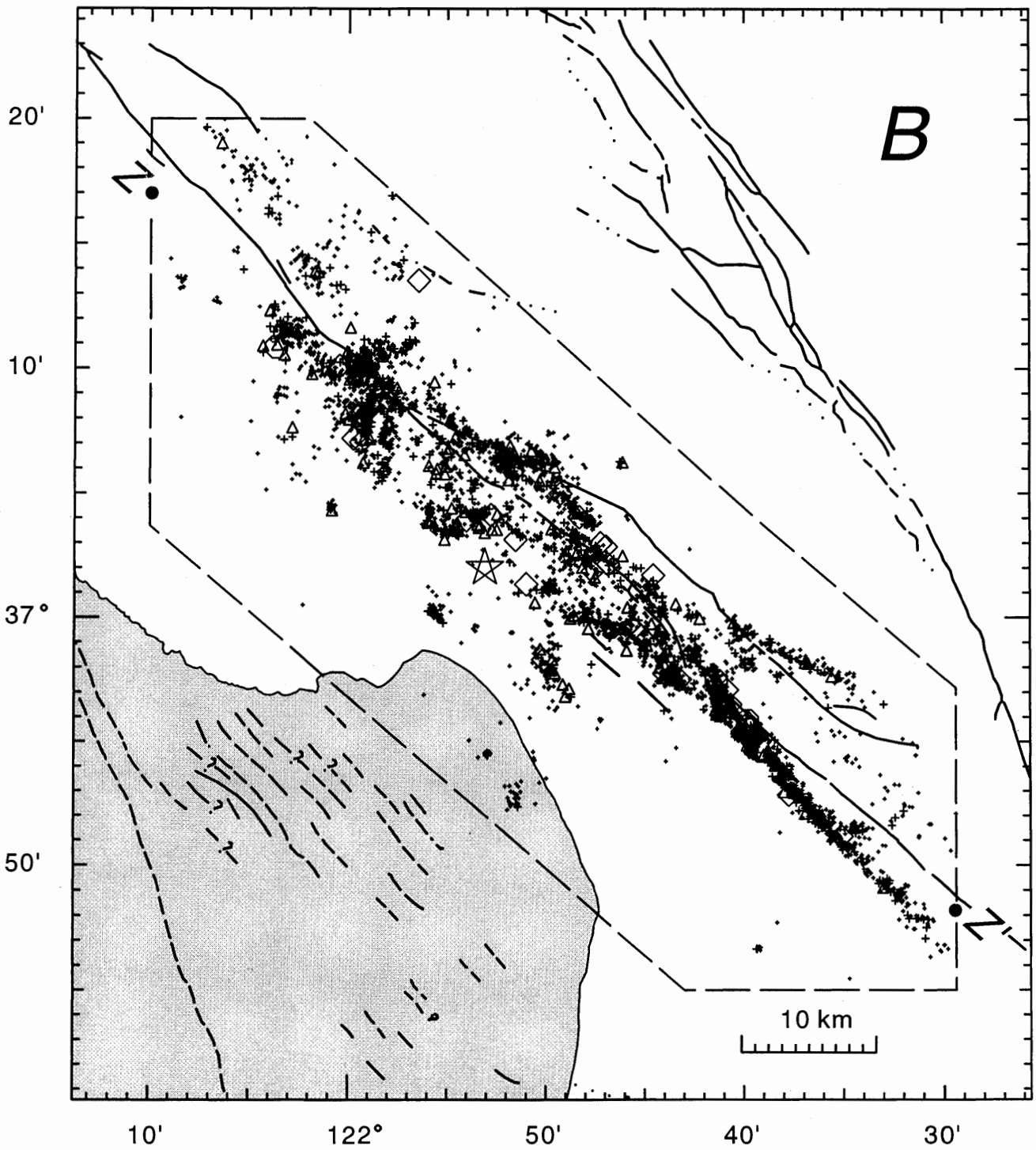

Figure 3.—Continued.

two portions of the aftershock zone, shown in transverse cross section. In figure 5*A*, the central portion of the aftershock zone has an apparent width of about 2 km, which is supported by the confidence ellipsoids. In contrast, the San Andreas fault at the southern end of the zone may have zero width (fig. 5*B*).

Absolute location errors are more difficult to assess. It is well known (for example, Reasenberg and Ellsworth, 1982) that many velocity models may be constructed which produce equivalent patterns of relative event locations that differ in absolute location by up to several kilometers. We found this to be true of the Loma Prieta data in deriving our final velocity model. Using the method to calculate a minimum one-dimensional velocity model (Kissling and others, 1994), we constructed several models that fit the data equally well and have the same pattern of relative locations but have significantly different absolute locations. The absolute locations vary in a northeast-southwest direction, normal to the fault and the geologic fabric of the region. To choose among candidate models, we selected the one that best reproduces the locations of surface explosions in the center of the aftershock zone (fig. 6). This model relocates the explosion nearest the main shock epicenter to within 0.3 km, and the nearby shots to within 1 km or better (table 2).

A dense network of portable instruments deployed shortly after the main shock in the center of the aftershock zone recorded several events with sufficient spatial resolution to permit a direct contouring of their traveltimes. The event shown in figure 7 exhibits clear evidence for slower velocities southwest of the San Andreas fault as demonstrated by the more closely spaced isochrons to the southwest of the fault and by the suggestion of a refraction angle at the fault. Locations produced by the three-dimensional model of Michael and Eberhart-Phillips (1991) and by our model agree well with each other, but both are systematically displaced ~1 km southwest from the apparent center of the isochrons. We expect the isochron center to be displaced to the northeast of the true epicenter when higher velocities exist to the northwest of the fault, as appears to be the case here. Thus, this qualitative evidence supports the absolute accuracy (~0.5 km) of both our location and the three-dimensional location.

The performance of the model at the southeastern end of the area is substantially poorer. The southernmost shot, in the San Andreas fault zone near San Juan Bautista, locates almost 3 km west of its actual position (fig. 6, table 2). Earthquake hypocenters in this vicinity also locate about 3 km west of the San Andreas surface trace. The shot's mislocation suggests that our model does not account for velocity variations in the southernmost portion of the aftershock zone. This segment of the fault is known to have a very strong velocity contrast across it (Wesson and others, 1973a; Michael and Eberhart-Phillips, 1991), with very low velocity material located to the northeast of the fault. Traveltime contours for the main shock (fig. 8) show a refraction angle in the isochrons along the fault at San Juan Bautista, strong evidence for low velocities to the northeast of the San Andreas in this region. This velocity contrast is of the opposite sense than the smaller contrast observed along the main body of the aftershock zone (Lees, 1990; Mooney and Colburn, 1985; fig. 7). We infer that the seismicity near San Juan Bautista occurs on the San Andreas fault and that the westward mislocation is an artifact of improperly modeled velocity perturbations in this region.

FOCAL MECHANISM DETERMINATION

Focal mechanisms were calculated for the best-recorded aftershocks from *P*-wave first motions using FPFIT (Reasenberg and Oppenheimer, 1985), a grid-search algorithm that finds acceptable double-couple mechanisms. A minimum of 15 hand-picked first motions and a misfit value ≤0.15 were required. For the mechanisms studied

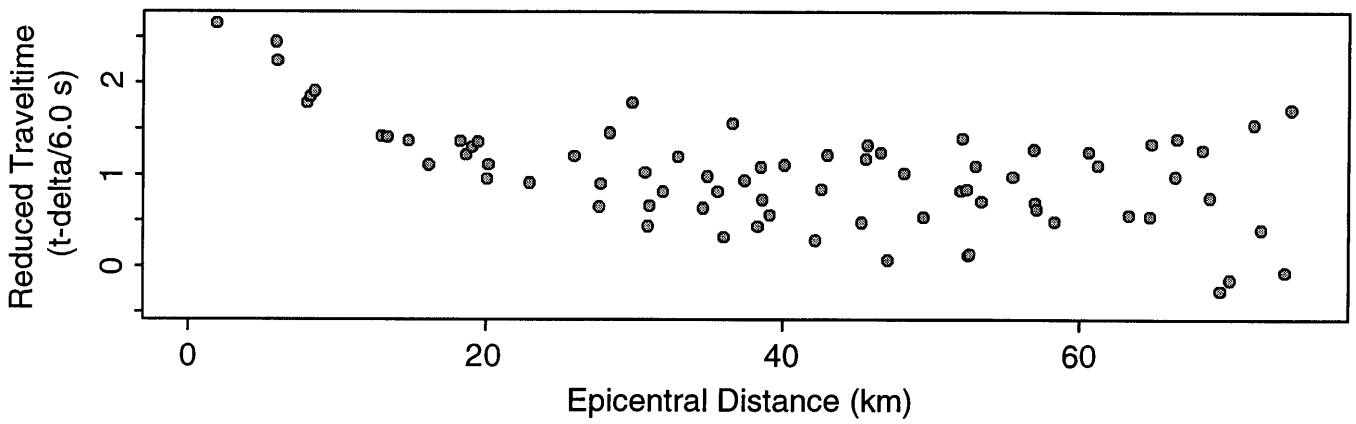

Figure 4.—Main shock traveltimes to CALNET seismic stations versus epicentral distance. Times are reduced by 6 km/s.

Table 1.—*Seismic velocity models (P-wave)*

Depth to Top of Layer km	Model 1 SW of San Andreas km/s	Model 2 NE of San Andreas km/s
0.0	3.35	2.99
1.0	4.58	3.99
2.0	5.26	5.57
5.0	5.96	5.98
8.0	6.16	6.26
13.0	6.22	6.44
18.0	6.52	6.58
25.0	8.00	7.98

here, the average uncertainties in strike, dip, and rake are 16°, 21°, and 30°, from an average of 57 first motions per event. In addition to determining the most probable mechanism for a particular earthquake, we also use FPFIT to test the hypothesis that a particular mechanism or class of mechanisms will fit the first motion data of an event within the confidence limits of its unconstrained (most probable) solution. For example, we can search for all earthquakes that have mechanisms that resemble the main shock.

In almost all parts of the study area, we find that the FPFIT focal mechanisms for our HYPOINVERSE-located events explain the first-motion data as accurately as mechanisms of the same events located by three-dimensional methods. However, minor first-motion discrepancies exist for most mechanisms, whether computed using one-dimensional or three-dimensional models. The main shock, for example, has discrepant motions at a number of stations (fig. 9). The three-dimensional models of Michael and Eberhart-Phillips (1991) and Foxall and others (1993) do not account for these discrepancies. Discrepant first-motions at stations to the northwest of the epicenter cannot be explained by a lateral refraction, which would be apparent in the main shock isochrons of figure 8. These discrepancies suggest that significant lateral variations in structure may be present near the hypocenter.

The one area where unmodeled effects of lateral structure appear to significantly bias the focal mechanisms is the southeastern part of the study region. For events on the San Andreas fault near San Juan Bautista, the velocity contrast across the San Andreas fault is so strong that first *P*-arrivals to all stations on the northeast side undergo significant lateral refraction (Spieth, 1981). Because this refraction is not accounted for in the one-dimensional velocity model, the calculated take-off angles are incorrect, and the resulting focal mechanisms for these San Andreas events have an apparent shallow dip on their northwest-trending fault plane, whereas the northeast-trending auxiliary plane is vertical and strikes normal to the fault. We believe that these events actually have nearly vertical nodal planes and represent horizontal strike slip movement along the San Andreas fault proper. The apparent dip of the San Andreas fault as defined by the hypo-

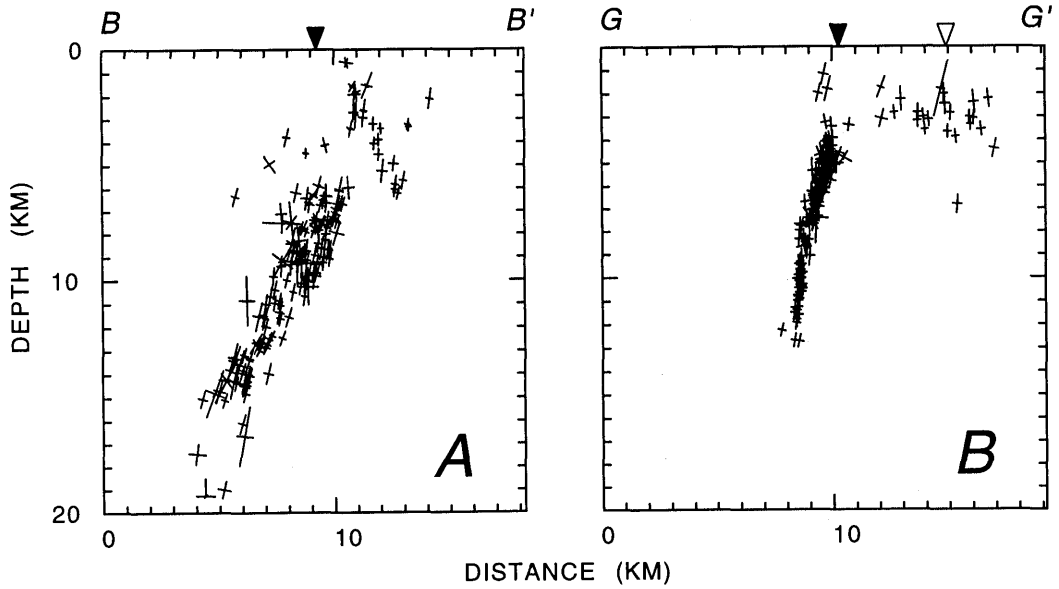

Figure 5.—HYPOINVERSE error ellipse axes of well-located $M_d \geq 2.0$ aftershocks projected in cross section for (*A*) the region just north of the main shock (section *B-B´* of figure 21*A*) and (*B*) the creeping section of the San Andreas fault (section *G-G´* of figure 21*A*). Solid inverted triangle marks the surface trace of the San Andreas fault; open triangle marks the Sargent fault.

centers (fig. 5*B*) may also be an artifact of the unmodeled strong velocity contrast across the fault.

DISPLAY OF EARTHQUAKES

Many cross sections of hypocenters in this paper portray each earthquake as a circular area with its dimension scaled to correspond to the rupture area of a constant stress drop circular crack. By displaying earthquakes as rupture areas, cross sections in the plane of the earthquake display the approximate faulting area of the events. For our figures, we assume a 30 bar (3 MPa) stress drop ($\Delta\sigma$) and use M_d to determine seismic moment (M_0), and thereby radius (r), using the formulas

$$\log_{10} M_0 = 1.5 M_d + 16.0$$

and

$$r = \left(\frac{7M_0}{16\Delta\sigma}\right)^{\frac{1}{3}}$$

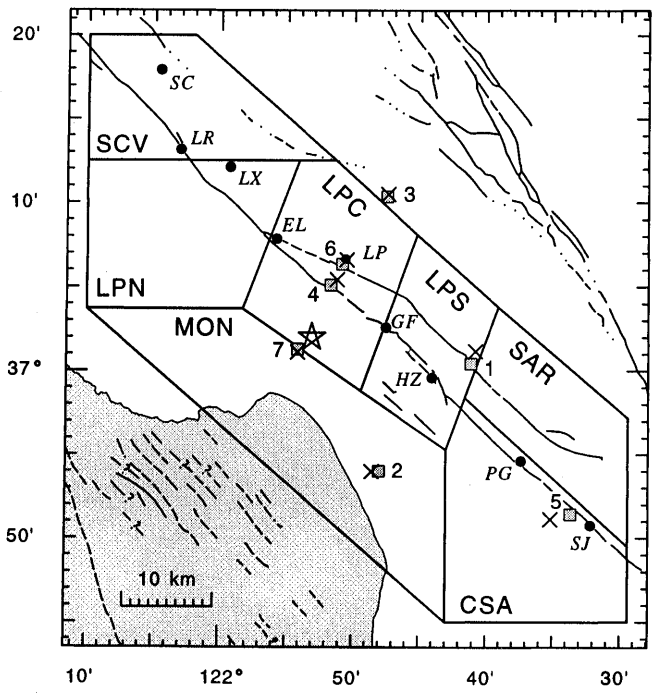

Figure 6.—Map of study region shows the main shock (star), actual shot locations (numbered squares, listed by shot number in table 2) and shot locations using our velocity model (×). Dots show landmarks: SC, Stevens Creek reservoir dam; LR, Lake Ranch reservoir; LX, Lexington dam; EL, Lake Elsman; LP, Loma Prieta peak; GF, Grizzly Flat; HZ, Hazell Dell and Mt Madonna Rd. intersection; PG, Pajaro Gap; SJ, San Juan Bautista. The study area is divided into 7 subregions: SCV, Santa Clara Valley; LPN, Loma Prieta North; LPC, Loma Prieta Central; LPS, Loma Prieta South; CSA, Creeping San Andreas; SAR, Sargent and Castro faults; MON, Monterey Bay area.

Note that r scales as $\Delta\sigma^{-1/3}$. Because a change in $\Delta\sigma$ of a factor of 3 translates into a change in r of only a factor of 0.7, the plotted symbols only weakly depend on the assumed value of $\Delta\sigma$. The analysis of small subsets of aftershocks by Hough and others (1991) and Fletcher and Boatwright (1991) suggest that the mean $\Delta\sigma$ value for the sequence may be greater than our assumed value by as much as a factor of 3. Thus our rupture areas may overestimate the area involved in faulting up to a factor of 2.

Earthquake focal mechanisms appear in back-hemisphere projection on cross sections and as lower-hemisphere projections in map view, with compressional quadrants shaded. Strain axes for the equivalent double couple appear as correctly proportioned horizontal projections of the three-dimensional axes.

OVERVIEW OF SEQUENCE

Hypocenters of the main shock and its aftershocks activated a 45- to 60-km-long and 10- to 20-km-wide volume of the crust along the San Andreas fault in the southern Santa Cruz Mountains. The events occur over the entire depth range of the seismogenic crust. The main body of aftershocks defines a tabular, southwest-dipping zone, with the main shock near the base and center of the distribution (fig. 10). Aftershocks deeper than 10 km define a plane dipping 65°±5°SW and striking N51°W±2°, consistent with the main shock focal mechanism. Rupture in the main shock evidently spread upward and bilaterally along the strike of this tabular zone. Most aftershocks cluster around the perimeter of the distribution and surround a relatively aseismic interior (fig. 10) which generally corresponds to the extent of main shock rupture, as described in detail in Spudich (1996). The less-seismic interior is somewhat obscured in figures 10*C* and 10*D* by off-fault activity projected onto the main aftershock surface; later figures offer a clearer view. At its southeastern end, the aftershock zone warps into a near-vertical surface and merges with the San Andreas fault.

The diversity of focal mechanisms in the aftershock series is particularly great, with few events possessing mechanisms similar to the main shock. The larger events have mechanisms that span the full range of possibilities: right-lateral, left-lateral, reverse, and normal. Analysis of the state of stress implied by the aftershock mechanisms suggest near-total shear-stress release in the main shock (Michael and others, 1990; Beroza and Zoback, 1993).

In addition to the main dipping zone, aftershocks define numerous other clusters, many of which are well removed from the primary rupture surface of the earthquake. Hypocenters within these clusters align with the nodal planes of their focal mechanisms, providing strong support for the argument that they represent coherent faults

Table 2.—*Actual shot locations and misfits of their relocations using our velocity model*

Shot	Ref	Shot Location: Time yrmoda	hrmn	s	Latitude N	Longitude W	Misfit (Actual → Relocation): Δt s	Epicentral azm	Error km	Depth km
1	SP2*	810612	730	0.00	37° 0.42′	121° 41.15′	0.22	20°	1.46	1.50
2	SP3*		800	0.02	36° 54.01′	121° 48.02′	0.08	267°	0.79	0.17
3	SP3†	910522	604	0.00	37° 10.37′	121° 47.49′	0.09	23°	0.26	1.10
4	SP5†	910524	700	0.00	37° 5.10′	121° 51.68′	0.11	48°	0.94	0.99
5	SP6†		702	0.00	36° 51.43′	121° 33.68′	0.49	256°	2.62	3.52
6	SP2†		704	0.00	37° 6.34′	121° 50.83′	0.15	46°	0.69	1.30
7	SP1†		804	0.00	37° 1.28′	121° 54.17′	-0.01	178°	0.31	0.44

*Mooney and Colburn (1985)
†Murphy and others (1992)

(L. Seeber, written commun., 1992). While some of the secondary faults activated in the aftershock sequence were also active in the two decades preceding the main shock, most were not; thus they represent a triggered response to the stress redistribution of the main shock.

The complexity of the sequence, in particular the large component of vertical displacement in the earthquake, while surprising at first appearance, can be understood in terms of the local geometry of the San Andreas fault (Dietz and Ellsworth, 1990). Within the southern Santa Cruz Mountains, the San Andreas fault makes a prominent left

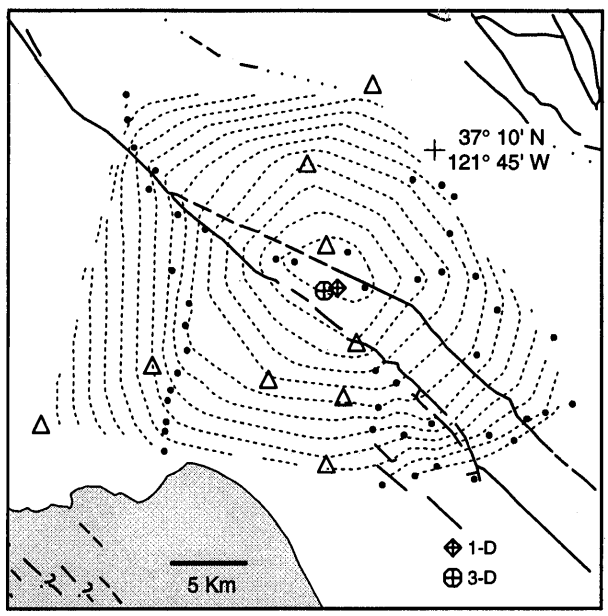

Figure 7.—Map showing the epicenter of an aftershock (October 19, 1989, at 0634 UTC) as determined from one-dimensional velocity model (diamond) and three-dimensional model (hexagon); positions of CALNET seismographic stations (triangles) and portable seismic instruments (dots); and contours of relative *P*-wave traveltimes of the event (dotted lines, contour interval 0.2 s).

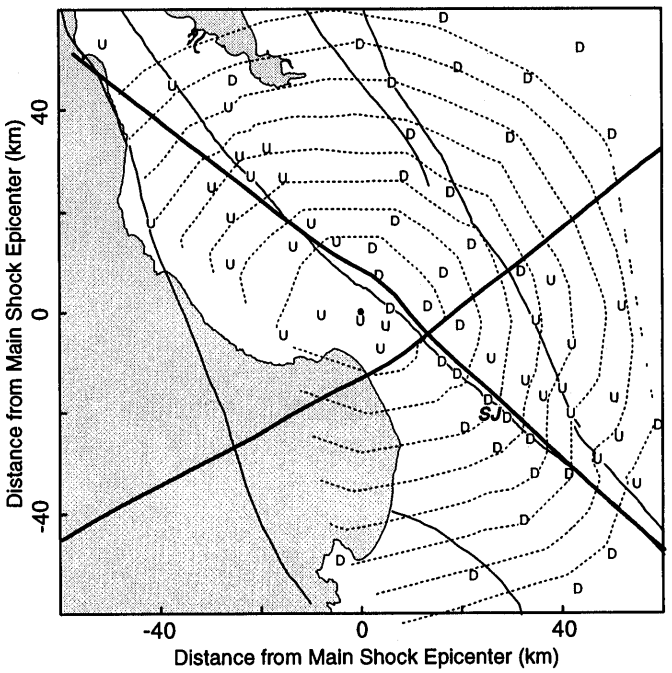

Figure 8.—Map of epicentral region showing epicenter of the Loma Prieta earthquake (dot), first motions at CALNET seismographic stations (U or D), contours of relative *P*-wave traveltimes of main shock (dotted lines, contour interval 1 s), and surface projection of main shock focal mechanism nodal lines from figure 9 (heavy lines). Note the field of compressional first-motions (U) in the dilatational quadrant to the north of the epicenter. Discrepant dilatational first-motions (D) may also be seen to the east of the epicenter. SJ, San Juan Bautista.

(compressional) bend, connecting straighter subparallel segments to the north and south. Over geologic time, the compression within the bend must be relieved as the plates move either by lateral flow, subduction or mountain-building. This event contributed to the uplift of the mountain range (although Loma Prieta peak was downdropped about 10 cm), and the ratio of horizontal to vertical slip on the fault is predicted well by simple kinematic arguments (Dietz and Ellsworth, 1990).

MAIN SHOCK

The Loma Prieta M_S=7.1 earthquake initiated at 00:04 15.28 UTC on October 18, 1989, at 37° 2.01′ N 121° 53.08′W and 15.9 km depth. The 95-percent confidence ellipsoid for this hypocenter has semi-major axes with azimuth, plunge, and length (km) of 133°, 0°, 0.29; 43°, 15°, 0.58; and 226°, 74°, 0.89. Our preferred hypocenter is slightly southwest and significantly shallower than our previously published estimate (Dietz and Ellsworth, 1990). It is also slightly shallower than several other recent estimates (table 3). The revised depth results from slight changes in the crustal structure and station corrections. We prefer the present value principally because our revised velocity model fits the explosion traveltime data significantly better than our previous model for stations with epicentral distances of less than the main shock focal depth.

The focal mechanism of the earthquake, or more properly, of the initial slip at the hypocenter, corresponds to a fault plane striking N50°W and dipping 70°SW, with a rake of 140° (Oppenheimer, 1990). This regional first-motion solution agrees well with teleseismic solutions (Choy and Boatwright, 1990; Kanamori and Satake, 1990; Romanowicz and Lyon-Caen, 1990), and simple geodetic models of the static displacement field (Arnadottir and others, 1992; Marshall and others, 1991; Lisowski and others, 1990).

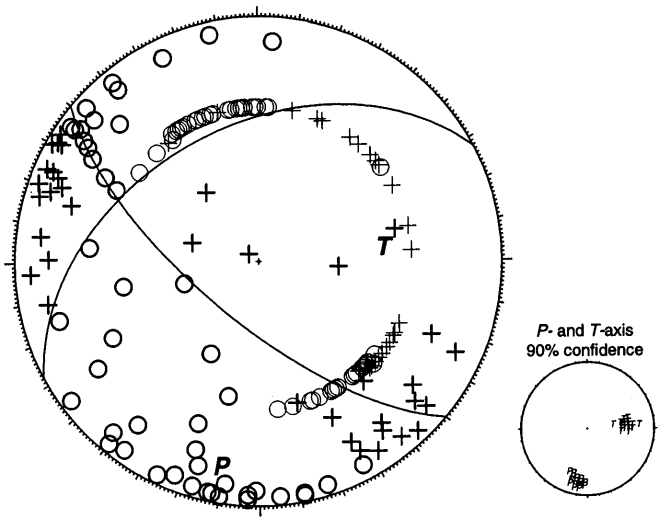

Figure 9.—Lower hemisphere projection of main shock focal mechanism showing dilatational (open circle) and compressional (+) first arrivals at CALNET stations.

FOCAL DEPTH

A trade-off exists between origin time, earthquake depth, and model parameters for the deepest events in our catalog due to poor resolution of the deep velocity structure. Therefore, we conducted a series of experiments to test the stability of the main shock hypocenter. In one experiment, a range of starting depths between 1 and 22 km was used to test the convergence of the HYPOINVERSE soluton. All runs yielded main shock depths between 15.6 and 15.9 km. When the depth of the shock was held fixed at the trial starting depth (again varying from 1 to 22 km), the hypocenter at 16.5 km depth had the lowest rms (0.09 s; fig. 11). Fixed-depth solutions outside of the range from 15 to 17.5 km had significantly higher rms. Finally, we examined the performance of a suite of velocity models computed using the same 108 events used to develop the final model. Here we fixed the depth of the main shock and simultaneously solved for the aftershock hypocenters and station corrections that minimized the overall data misfit. The lowest overall data variances were obtained when the initial slip of the main shock was fixed between 15 and 17 km; the minimum data variance was obtained with the main shock depth fixed at 16 km (fig. 12).

NUCLEATION PROCESS

The process by which the earthquake started is of interest, as it did not simply propagate uniformly away from the hypocenter beginning at the above origin time. As noted by Wald and others (1991, 1996), the CALNET origin time precedes the initiation of strong motion from the hypocenter by about 2 s, suggesting that our origin time corresponds either to a foreshock or to a more complex initiation process. Amplitudes of the high-frequency waves radiated in the first 1.5 s of the event were generally too weak to trigger strong-motion instruments (typically a vertical acceleration of 0.01 *g*), indicating relatively small slip at the initiation of rupture. Most strong-motion recorders, however, did trigger before the arrival of the shear waves radiated by the initial slip, and thus recorded them. Peak velocities of the shear waves corresponding to the *S* waves of the initial rupture were compared to peak velocities predicted in the frequency band from 2 to 5 Hz for events of various magnitudes using the relation of Joyner and Boore (1988):

$$\log y = a + b(M - 6) + c(M - 6)^2 + d \log r + kr + s$$

$$5.0 \leq M\text{-}7.7$$

$$r = (r_0^2 + h^2)^{1/2},$$

where y is the ground motion parameter to be predicted, M is the earthquake magnitude, r_0 is the shortest distance from the recording site to the vertical projection of the fault rupture on the surface, h is the depth of the earthquake, and the parameters for predicting peak velocity are: $a = 2.17$, $b = 0.49$, $c = 0$, $d = -1.0$, $k = -0.0026$, and $s = 0.17$. The observed peak velocities of the initial rupture generally fall within one standard deviation of the values predicted for a M=5.0 event at 16 km depth (fig. 13).

Large-amplitude, high-frequency motions, corresponding to the start of the "main shock" as inferred from strong motion modeling studies (Beroza, 1991, 1996; Wald and others, 1991, 1996; Steidl and others, 1991, 1996) began 1.6 s after the initial event, or at 00:04 16.9 UTC. *P*- and *S*-arrival times for both the foreshock and the main shock could be read at a number of stations (table 4). *P* arrivals were picked from vertical components and *S* arrivals were picked from horizontal components of acceleration after integration to velocity. Using the program VELEST to determine the separation between their hypocenters, we find the main shock locates 0.3 km to the southeast, 1.1 km above the initial event, and 1.61 s later. However, the uncertainty in this location due to the uncertainty in the identification and timing of the phases and in the shear velocity structure precludes us from rejecting the hypothesis that the two events nucleated at the same point.

While it is possible to interpret the initial event as an immediate M=5 foreshock, examination of digital strong-motion records from instruments in the near-field of the event suggest otherwise. Integration of the observed accelerograms to displacement shows a continuous growth in displacement from the moment of initiation (fig. 14). To model the displacement seismograms, we use the complete synthetic seismogram for a point dislocation in a half-space (Johnson, 1974) and assume the fault orientation determined from the first-motion data. The seismograms are modeled by determining the seismic moment release as a function of time, a well-posed linear inverse problem. The best fit to the observed displacement seismograms shows a continuous growth in seismic moment beginning at the high-frequency origin time of 15.28 s (fig. 15*A*). The total moment release by 1.6 s into the event, just up to the time of the main shock, is equivalent to a M=5 1/2 earthquake (fig. 15*B*), significantly larger than the magnitude determined from 2 to 5 Hz waves (fig. 13). Thus, the initial event appears to mark the beginning of a continuous and relatively smooth process of moment release that only began to propagate away from the hypocenter after 1.6 s.

DEVELOPMENT OF THE AFTERSHOCK ZONE

INITIATION

The divide separating the main shock from its aftershocks is no less ambiguous than the boundary between the foreshock and the main shock. Modeling studies of the main shock, summarized by Spudich (1996) suggest a duration of at least 6 s and not more than 15 s, with most of the slip occurring in the first 10 s of the event. If aftershocks are defined as distinct earthquakes removed in time but not necessarily in space from faulting during the propagation of the main shock, the earliest recognizable aftershock, $M_L = 4.7$, occurred 32 s after the start of the main shock (Simila and others, 1990). Earlier aftershocks of similar or larger magnitude, however, might have occurred but might have been obscured by the arrival of scattered (coda) waves from the main shock, as this first aftershock just emerges from them (see fig. 2-6 of McNally and others, 1996).

During the first 10 minutes of the sequence about 20 aftershocks ($M_d \approx 4$) can be identified in the CALNET seismograms. Locations could be determined for eight of these aftershocks. McNally and others (1996) used records from their digital accelerometers to locate these and seven additional events. After 10 minutes, our catalog appears to be complete to M_d=4.0. Using the frequency-magnitude density distribution (for example, in fig. 16) to estimate completeness at later times, hours 1 to 6 appear complete to $M_d \approx 3.0$, and hours 6 to 13 complete to $M_d \approx 1.5$. After hour 13 of the aftershock sequence, our catalog appears complete to $M_d \approx 1.0$.

A cautionary note is in order, however, as systematic underreporting of earthquakes of all sizes will occur when smaller events are buried in the codas of larger events. At the end of the first day, the aftershock rate was down to one event ($M_d \geq 1.0$) every 2 minutes, with an average event duration of ~10 s. Missing events after the first day should, therefore, be few in number, which agrees with the frequency-magnitude evidence for completeness discussed above.

FORMATION

The aftershock zone formed extremely rapidly, assuming essentially its final shape by the end of the first day (fig. 10). Even the incompletely recovered first 46 minutes of activity conforms well with the later activity, clearly mapping out the main dipping zone as extending approximately 45 km along strike. Some of the early aftershocks fall outside of the main zone and are associated with

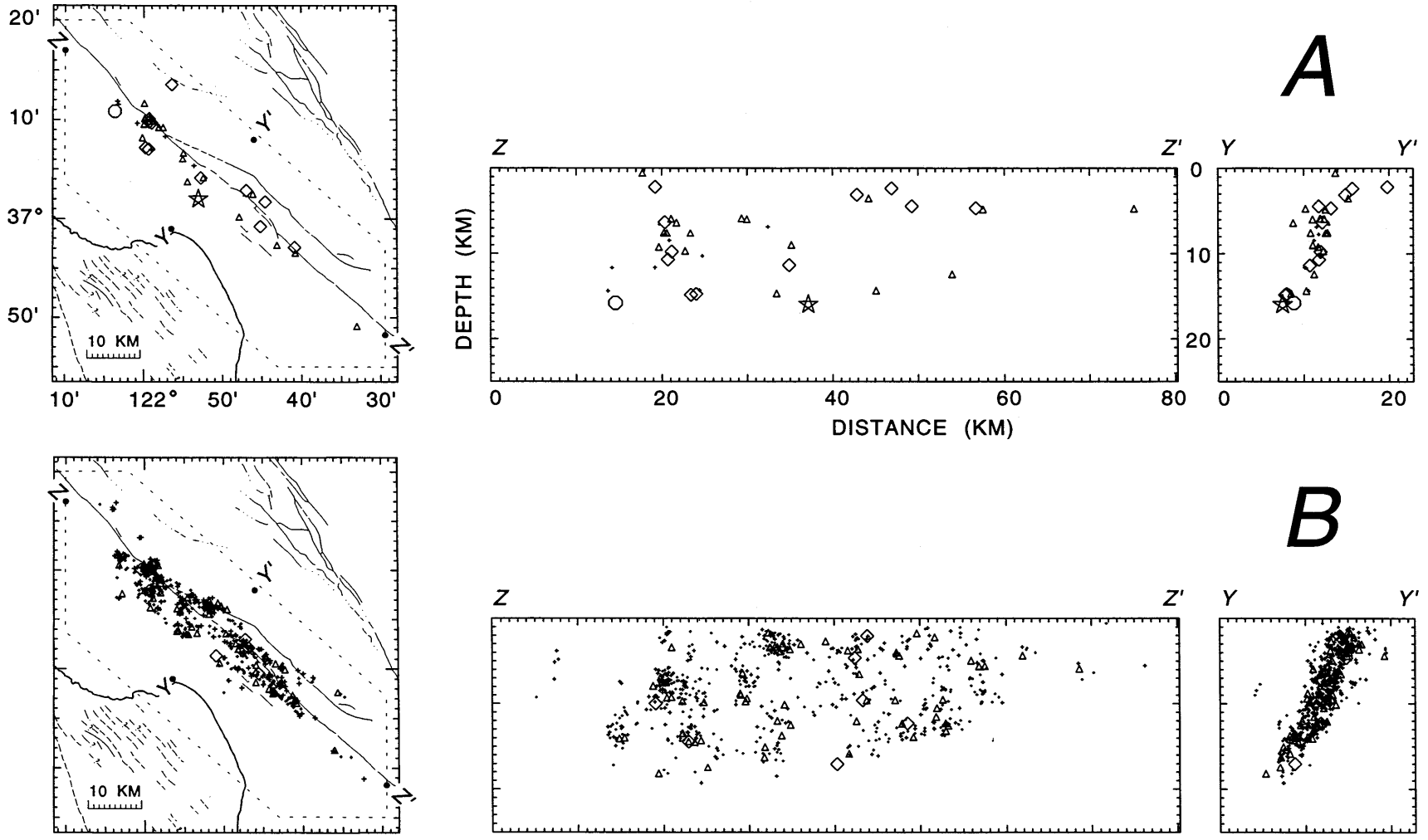

Figure 10.—Spatial and temporal development of the sequence. Earthquakes within (*A*) 0.001 to 0.032 days, (*B*) 0.032 to 1.0 days, (*C*) 1.0 to 31.6 days, and (*D*) 31.6 to 730 days after the main shock. Maps, and longitudinal (*Z-Z'*) and transverse (*Y-Y'*) cross sections correspond to equal logarithmic time intervals which would contain equal numbers of events if the aftershock rate decayed with time as $dN/dt = t^{-1}$. Earthquake symbols are the same as in figure 3.

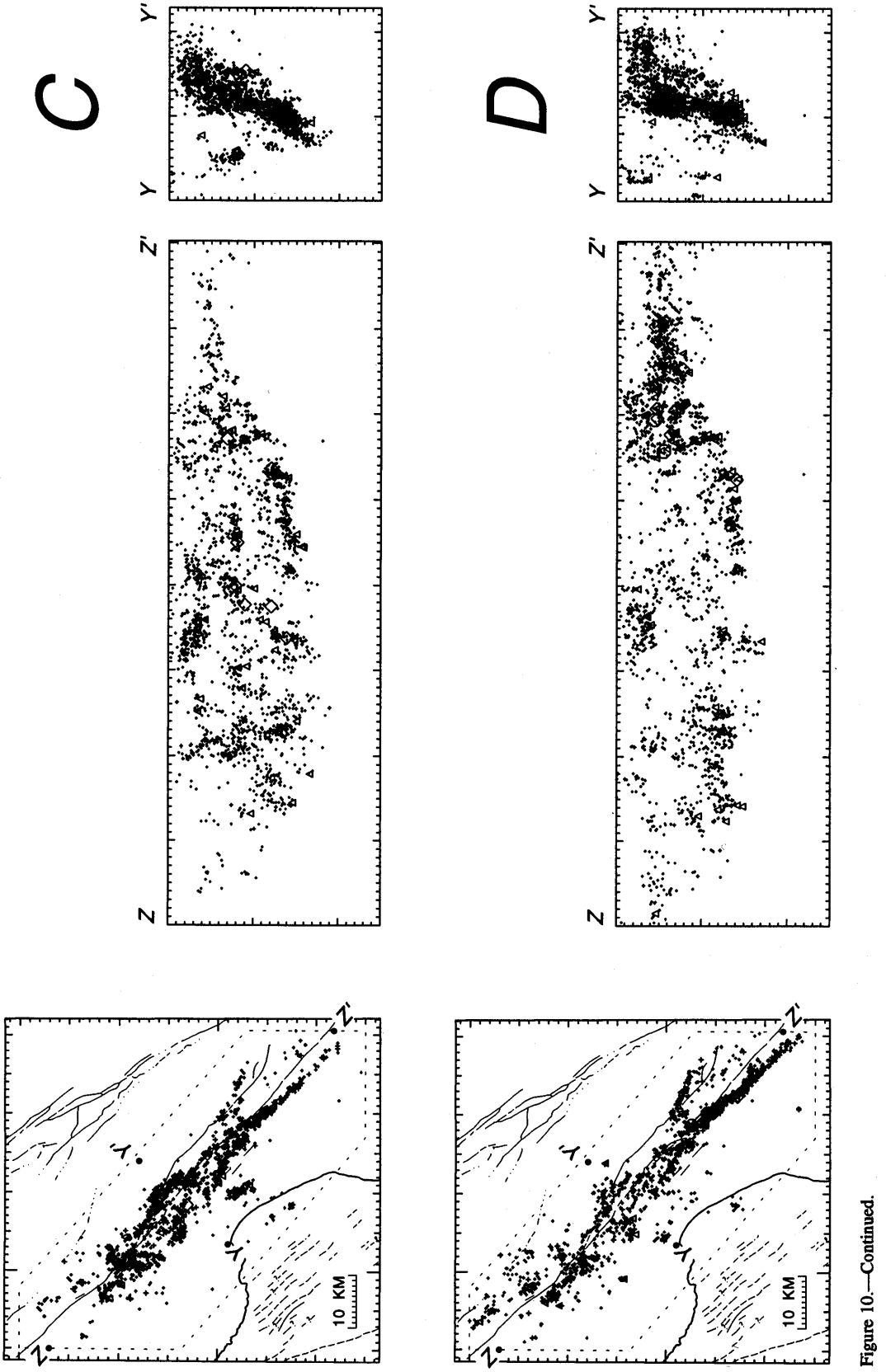

Figure 10.—Continued.

Table 3.—*Main shock hypocentral estimates*

Source	Origin Time yrmoda hrmn	s	Latitude N	Longitude W	Depth km
This study	891018 0004	15.28	37° 2.01′	121° 53.08′	15.94
Dietz and Ellsworth (1990)		15.21	37° 2.37′	121° 52.81′	17.85
U.S. Geological Survey Staff (1990)		15.25	37° 2.19′	121° 52.98′	17.6
Eberhart-Phillips and Stuart (1992)		15.34	37° 2.02′	121° 52.85′	17.16
Pujol (1995)		15.26	37° 1.92′	121° 52.98′	16.3
Roecker and Gupta (this volume)		15.45	37° 2.22′	121° 53.46′	15.60

aftershock activity on secondary faults, principally to the northeast of the San Andreas fault.

The aftershock zone apparently lengthens with time to the southeast where it overlaps the seismically active central segment of the San Andreas fault (figs. 3, 10). While some of this extension reflects the occurrence of earthquakes normally expected to occur along this part of the San Andreas fault, the analysis of Reasenberg and Simpson (1992, and this chapter) shows that these events occurred at a higher rate after the mainshock and decayed in an aftershock-like manner. Including them in the definition of the aftershock zone would increase its length to about 60 km.

In general, the aftershocks are highly clustered and tend to populate the periphery of the main shock rupture as determined from studies of the main shock seismograms (Beroza, 1991, 1996; Wald and others, 1991, 1996). In nearly every case, these clusters contain at least one large aftershock (M_d>4) from the first few hours' activity. The persistence of activity in these clusters is particularly striking (figs. 10, 17) and clearly cannot be explained as secondary aftershock activity spawned by a large aftershock from early in the sequence. One secondary aftershock sequence, however, can be recognized following the April 18, 1990, M_L=5.4 Chittenden earthquake (north of PG, fig. 17), which was also the largest event in the entire aftershock sequence. Note the rapid decay of its aftershocks, compared to the overall decline in activity (figs. 17, 18).

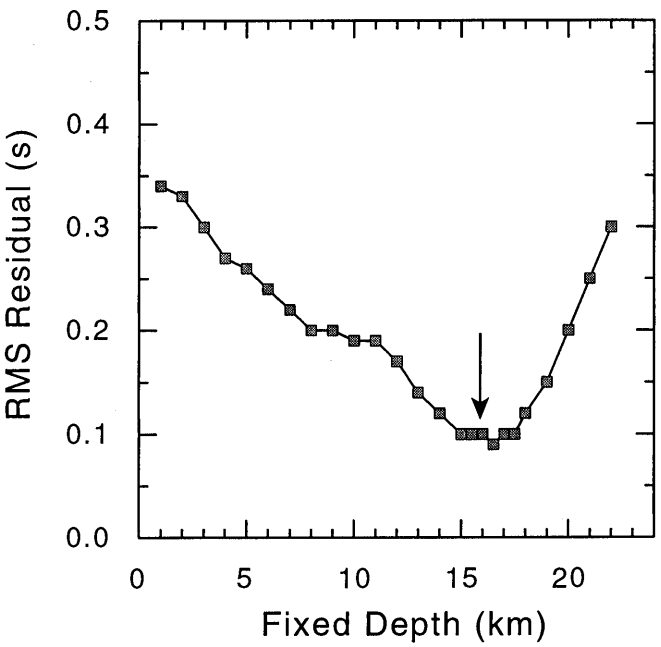

Figure 11.—Final traveltime rms-residual versus depth for the Loma Prieta main shock location. In these HYPOINVERSE tests the epicenter was free to move, but the depth was fixed. The main shock's depth of 15.9 km from an unconstrained relocation (arrow) falls within the fixed-depth range (15.0-17.5 km) yielding the lowest rms values.

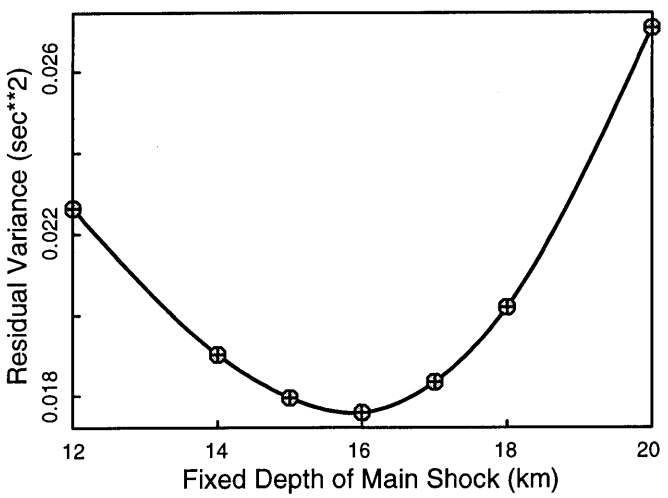

Figure 12.—Residual variance of traveltimes for 108 earthquakes used to develop final velocity model for models computed with the main shock depth held fixed. Each data point corresponds to the residual variance obtained by inverting the traveltime observations for optimum earthquake hypocenters and station delays, with the constraint that the main shock depth has the value shown. Results show a clear preference for the unconstrained model solution that places the main shock at a depth of 15.9 km.

DECAY

As a whole, the decay of the aftershock sequence conforms with the modified Omori's law (Utsu, 1969; Reasenberg and Simpson, this chapter). We determine a best-fit to Omori's law, $dN/dt = K/(t + c)^p$, by binning the aftershocks into equal log time intervals, starting 11.5 minutes after the main shock (fig. 19). Using all events $M_d \geq 1.0$ for the entire two-year catalog, we find: $p = 0.94 \pm 0.01$, $c = 0.34 \pm 0.04$, and $K = 670 \pm 25$. Observed rates during the first 13 hours of the sequence (first 6 intervals, figure 19) undoubtedly underestimate the true rate of $M_d \geq 1.0$ events, due to grossly incomplete reporting at this magnitude threshold. When only events $M_d \geq 3$ are considered, $p = 1.07 \pm 0.04$, $c = 0.04 \pm 0.03$, and $K = 26 \pm 3.4$.

The end of aftershock activity may be defined as the intersection of the Omori rate dN/dt with the rate preceding the earthquake. Reasenberg and Simpson (this chapter) estimate this time as 2.3±0.3 years, based on activity ($M_d \geq 1.5$) within the broadly defined aftershock zone through April 17, 1990. In this study we define the "main aftershock zone" with a series of polygons and depth ranges (fig. 21*B*). Because the pre-earthquake rate varies widely throughout the aftershock zone, we compare the aftershock decay to the background rate (average number of $M_d \geq 1.0$ events per day from 1980 to October 17, 1989) in three different areas: the main, dipping part of the aftershock zone (portion of the main zone which lies in regions LPS, LPC, and LPN of figure 6; generally north of 36° 58′); the part of the main zone along the microseismically active part of the San Andreas fault at the south end of the sequence (portion of the main zone in region CSA of figure 6); and the previously active part of the Castro fault (commonly thought to be the Sargent fault—see below) to the southeast of the main shock hypocenter (region SAR in figure 6). Within the main dipping zone, aftershock activity will not reach the very low pre-Loma Prieta rate of 0.02 events/day until over 25 years have passed, or until 2015. This long time reflects the very low level of pre-Loma Prieta seismicity in this zone. Activity along the San Andreas fault immediately southeast of the earthquake would be expected to intersect the background rate of 0.16 events/day after t=1.5 years if we model only the aftershocks prior to the April 18, 1990, Chittenden earthquake. However, this event further boosted the seismicity rate in this region with its own aftershock sequence, lengthening the actual time to decay to background rate. Activity along the Castro fault met the background rate after just one year.

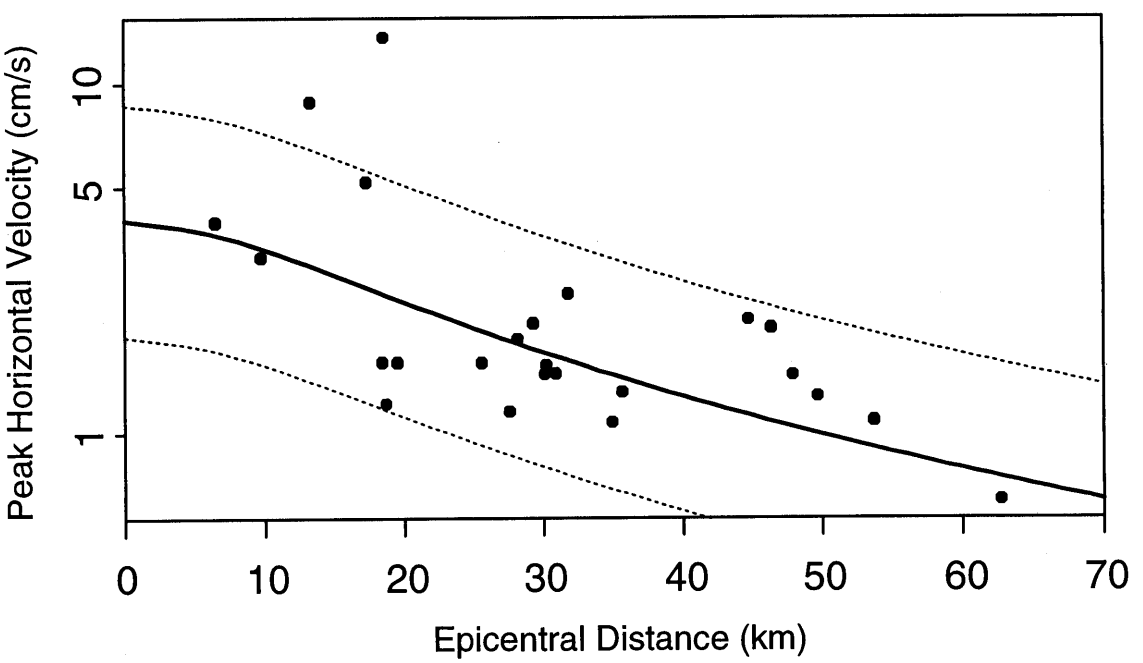

Figure 13.—Peak horizontal velocity of *S*-waves recorded by strong-motion accelerographs from the first 1.0 s of rupture. Amplitudes were measured from accelerograms after integration to velocity. Measurement window restricted to direct arrivals from the foreshock and excludes arrivals from the main shock. Curves are predicted mean (solid) and ±1σ (dashed) peak horizontal velocity from Joyner and Boore (1988) for M=5 earthquake at 16 km depth.

Table 4.—*Foreshock and main shock arrival times (seconds after 891018 0004 15.35)*

Station	Latitude	Longitude	Foreshock				Main Shock			
	N	W	*P*	wt	*S*	wt	*P*	wt	*S*	wt
C563	37 12.60	121 48.18	4.51	0	7.73	2	6.13	0	9.65	2
SAOC	36 45.9	121 26.7	8.60	0			10.23	0		
C007	37 2.76	121 48.18			5.75	0			7.05	0
BSRZ	36 39.99	121 31.12	8.90	0			10.38	0		
WAHO	36 58.38	121 59.76	3.87	0	6.01	3	5.25	0	7.72	3
LGPC	37 10.32	122 0.60	4.35	0	6.95	0	5.85	0	8.45	0
BRAN	37 2.82	121 59.10	3.25	0	5.40	0	4.95	0	6.65	0
BKSB	37 56.2	122 14.1	15.80	0			17.55	0		
HBTM	36 51.01	121 33.04	6.62	0			7.97	0		
HSFM	36 48.72	121 29.97	7.32	0			8.77	0		
JBLM	37 7.69	122 10.08	5.25	0			6.90	0		
JMPM	37 27.33	122 9.93	9.57	0			11.12	0		
HPLM	37 3.13	121 17.40	9.49	0			10.94	0		
HQRM	36 50.02	121 12.76	11.11	0			12.66	0		

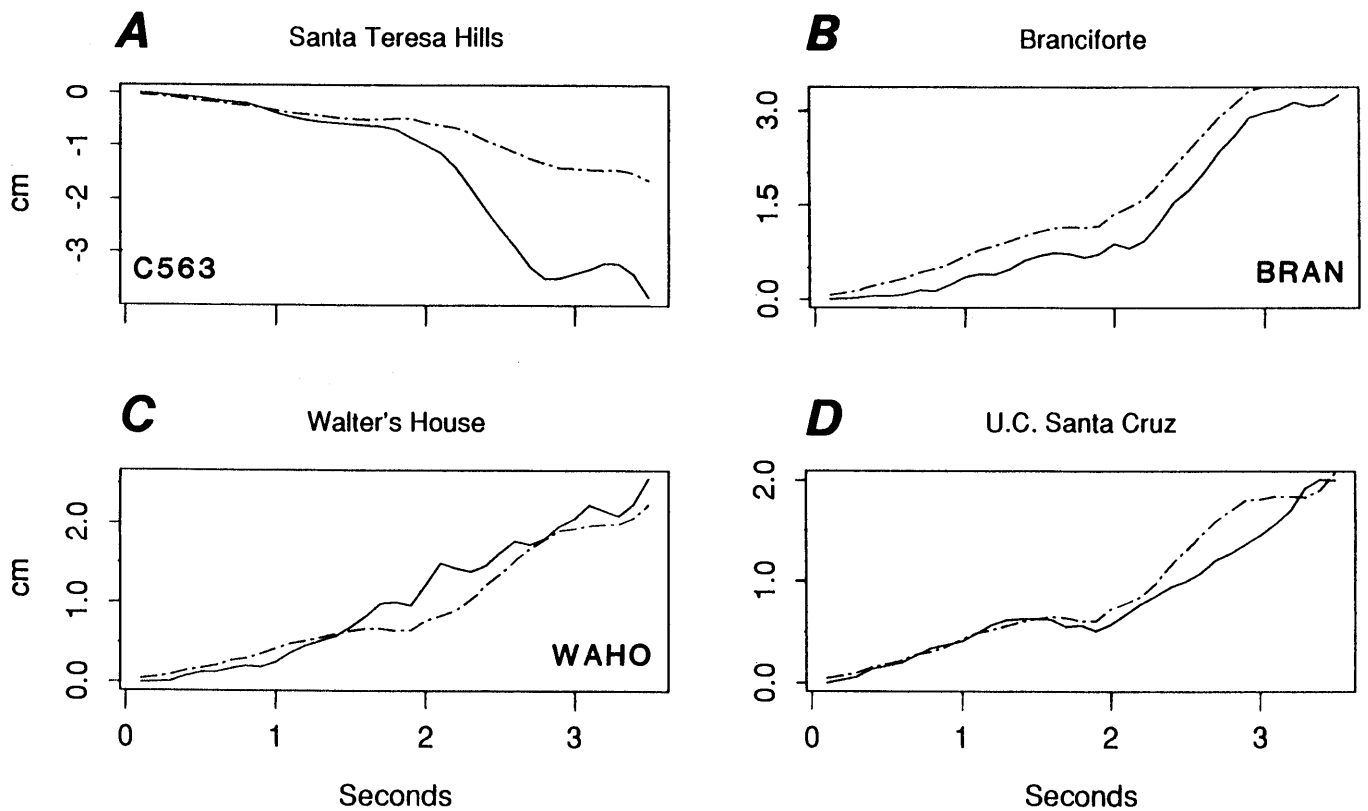

Figure 14.—Displacement seismograms of vertical component of motion from broad-band integration of digital accelerogaph stations located in the near-field of the earthquake (solid line) and synthetic seismograms (dot-dash line). Bandpass of displacement filtered with 1-pole Butterworth filter at 0.01 Hz. Origin time for each seismogram is *P*-wave arrival time of the foreshock. Synthetic seismograms determined by inverting observed displacements for seismic moment release rate of point source double couple with orientation of main shock focal mechanism. Divergence of fit after 2 s reflects breakdown of point source approximation and may reflect change in radiation pattern.

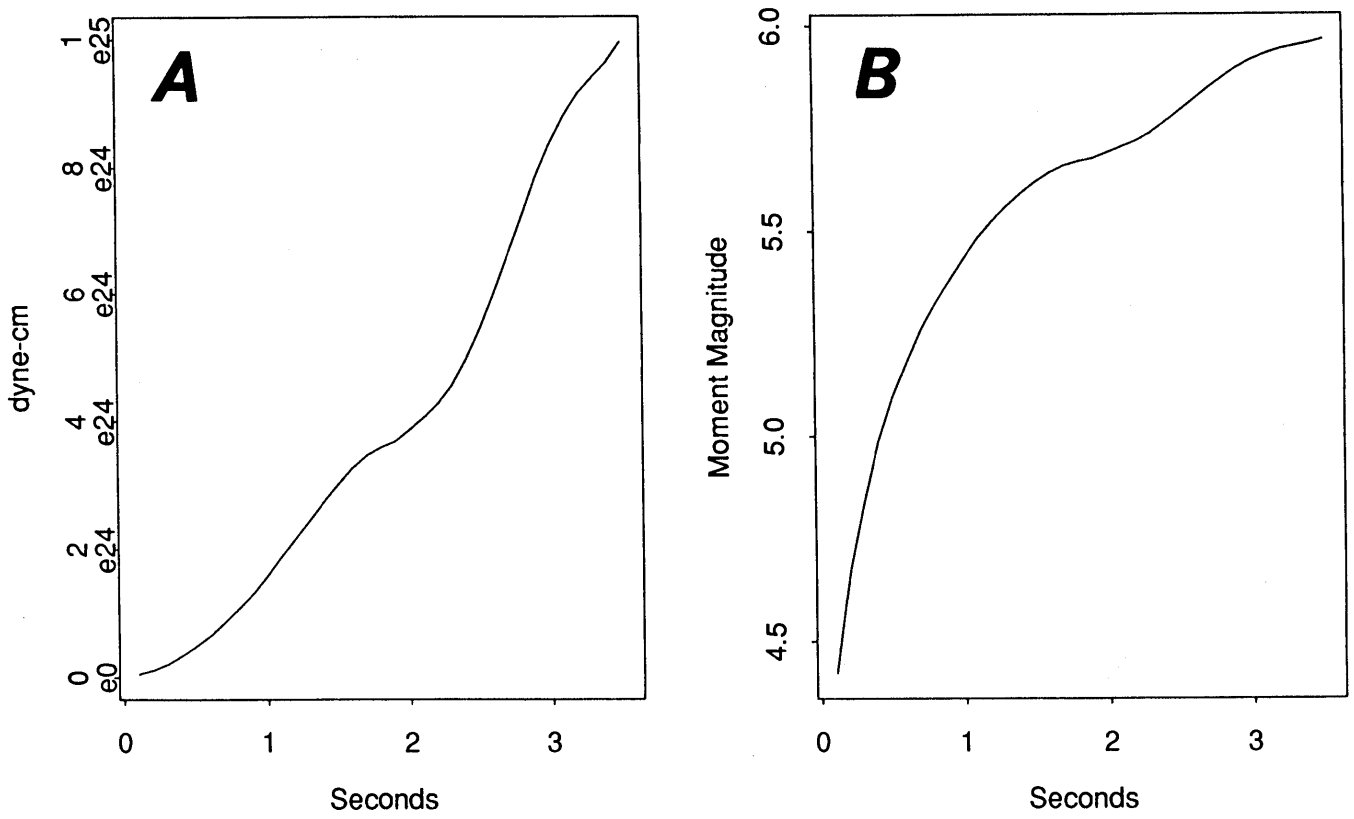

Figure 15.—Cumulative seismic moment release versus time determined by inversion of near-field displacement seismograms (figure 14). Both the total seismic moment (*A*) and equivalent moment magnitude (*B*) are shown. Results indicate that the foreshock released more moment than would be predicted by either its amplitude magnitude of 5 (figure 13) or its triggering of strong-motion stations.

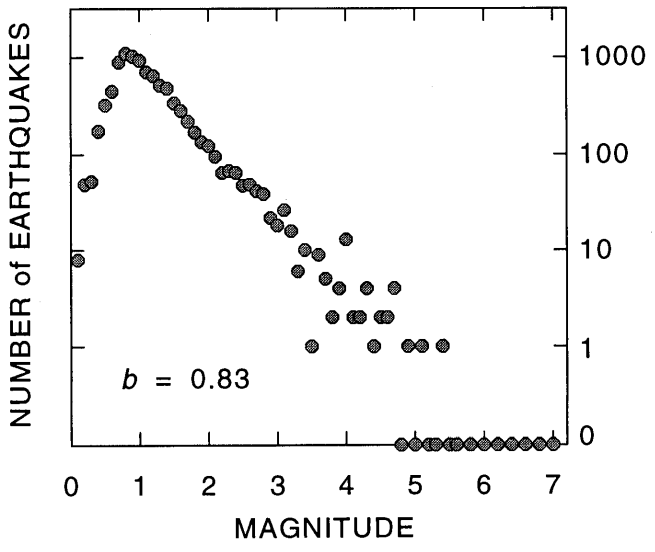

Figure 16.—Number of earthquakes in each 0.1 magnitude-unit bin for aftershocks (excluding activity on October 18, 1989) in our catalog. The aftershock catalog is complete at $M_d \geq 1.0$ and the *b*-value for the sequence is 0.83±0.01.

STRUCTURE OF THE AFTERSHOCK ZONE

The overall form of the aftershock zone is dominated by the central dipping zone, or main zone, that rises from the main shock hypocenter toward the San Andreas fault to the northeast. About 75 percent of the aftershocks fall in this zone which extends from 2 to 18 km depth. The coincidence between the N51°W±2° strike and 65°±5°SW dip of the zone and the main shock fault plane leaves little doubt about the existence of a primary, causal relationship between these events and the main shock.

There is much more to the sequence, however, than continuing faulting in the style of the main shock dislocation. Both the occurrence of aftershocks within a much larger crustal volume, and the wide range of aftershock focal mechanism types demonstrate that numerous faults participated in the post-main shock process of crustal adjustment. As first noted by Oppenheimer (1990), almost none of the aftershock focal mechanisms resemble the main shock. Indeed, with the exception of aftershocks at the base of the zone near the main shock, it can be fairly

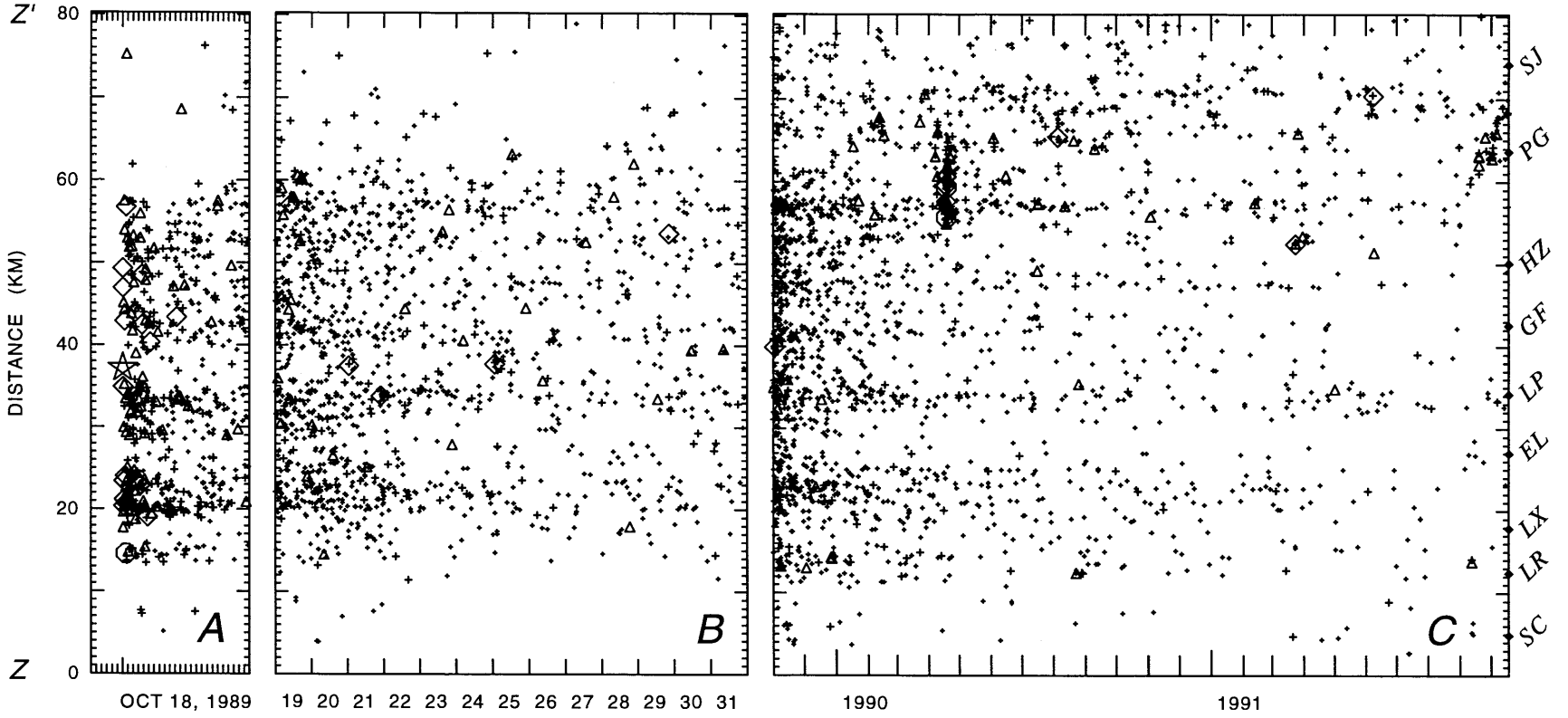

Figure 17.—Distance versus time plots of aftershock seismicity from northwest (*Z*) to southeast (*Z'*) along the San Andreas fault for (*A*) day 1; (*B*) days 2-14; and (*C*) days 15-730. Labeled dots show positions of landmarks from figure 6. Earthquake symbols are the same as in figure 3.

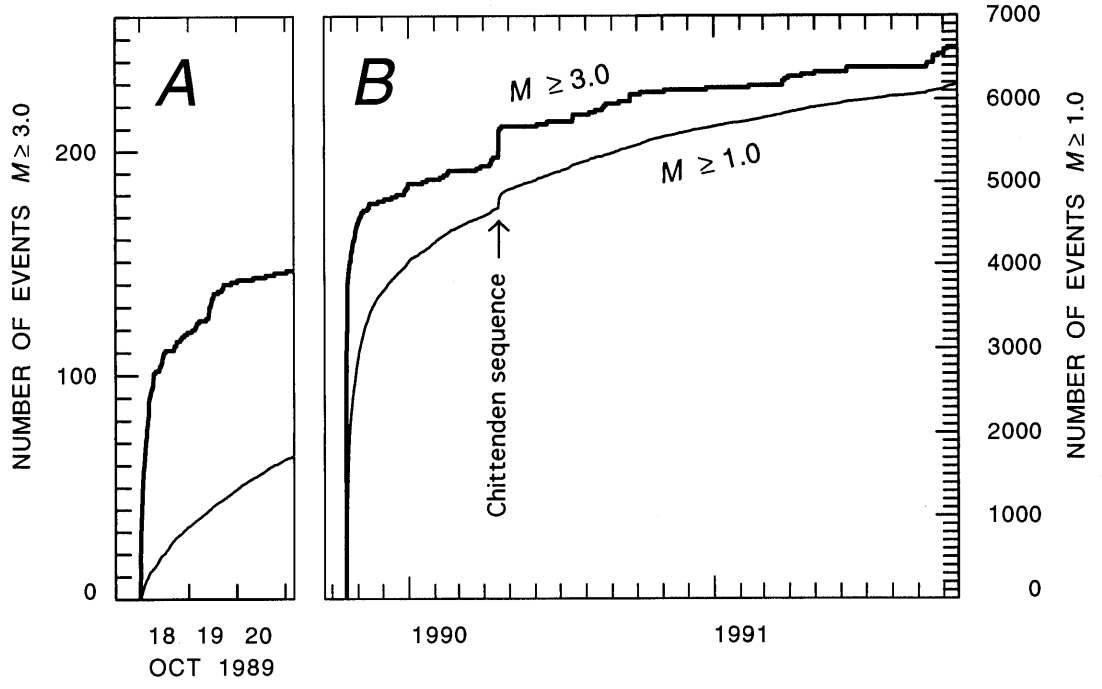

Figure 18.—Cumulative number of events versus time for (*A*) the first 3 days of the sequence and (*B*) 2 years of the sequence. Heavy line shows all $M_d \geq 3.0$ events in our catalog and thin line shows all $M_d \geq 1.0$ events.

stated that no seismic displacements took place on the main shock fault once its dynamic motions stopped. Thus, the central dipping zone and the more removed parts of the sequence both speak to a complex process of adjustment that bears little resemblance to the typical San Andreas earthquake sequence in which the aftershocks continue the main shock faulting process (for example, Eaton and others, 1970).

To facilitate the examination of the aftershock zone we subdivide our discussion into five parts corresponding to the main dipping zone and four geographically distinct areas surrounding it.

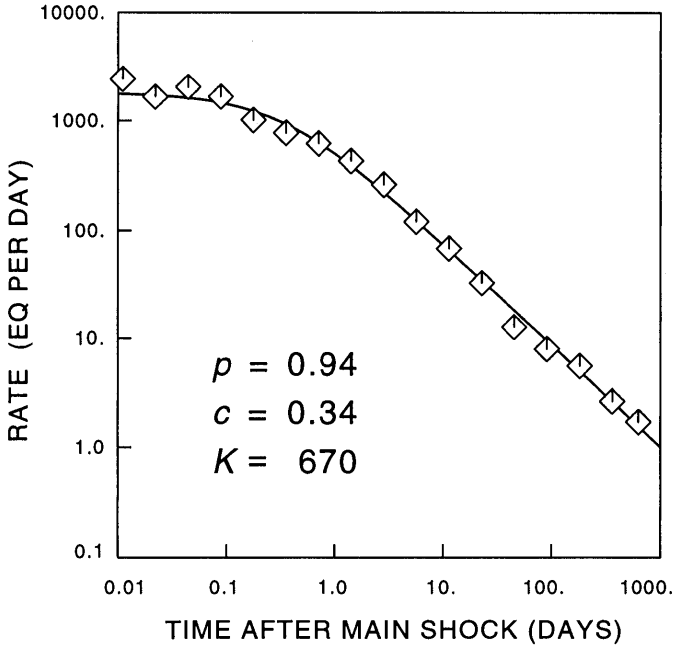

Figure 19.—Seismicity rate (number of earthquakes per day) versus time after the main shock (in days) for all $M_d \geq 1.0$ aftershocks in our catalog (diamonds). The line shows the best fit to Omori's Law, $dN/dt = K/(t + c)^p$, with parameter values given above.

MAIN ZONE

The main zone consists of a tabular volume of aftershock hypocenters that maintains a nearly-constant dip of 60° to 65° for a distance of 42 km, centered approximately on the main shock (figs. 10, 20, 22, 23). The depth at the base of the zone averages about 18 km to the northwest of the main shock and shoals to about 8 km to the southeast at the point where it joins the San Andreas fault. The top of the dipping zone lies about 6 km below the surface, on average, and locates directly beneath the surface trace of the San Andreas fault. Seismicity shallower than 6 km primarily locates northeast of the San Andreas trace and defines no single large-scale structure. Specifically, the main zone does not appear to cross the San Andreas fault as a continuous body.

Viewed in longitudinal cross section (figs. 10, 23), the main zone is seen to be composed of numerous clusters of

activity, generally located on the periphery of the zone. The interior of the zone is relatively devoid of activity. As has been noted by numerous authors, the less seismic interior of the zone correlates well with the regions that slipped during the main shock (see Spudich, 1996). The absence of aftershocks on the portions of the fault that slipped during the main shock is a general feature of the main shock/aftershock process, at least for California earthquakes (Mendoza and Hartzell, 1988).

Transverse cross-sections show that the main zone has an average width of 1 to 2 km (fig. 22). Because the width is resolved by the hypocentral locations (fig. 5) and has relatively sharply defined edges, it implies that these aftershocks map out a volume of relatively weak rock triggered into activity by the main shock. We cannot tell, however, on the basis of these data, where the main shock rupture passes in relation to the main zone. It could locate equally well within or on either edge of the body.

Aftershock focal mechanisms in the dipping zone do little to clarify this picture. With the exception of a few focal mechanisms located at the base of the zone just northwest of the main shock, none of the aftershock focal mechanisms in the main zone show right-lateral, oblique-thrust motion on the main shock plane. Rather, they display a very wide range of mechanism types and orientations (fig. 20), with the only unifying trend being a tendency for the *P*-axes to orient approximately normal to the fault plane (fig. 24). This fault-normal coordination of the *P*-axes is consistent with an approximately uniaxial stress field acting perpendicular to the main shock fault plane (Zoback and Beroza, 1993) and thus is incompatible with the stresses that drove the main shock faulting.

It is possible that some aftershock mechanisms may have closely resembled the main shock mechanism while the grid search method of FPFIT selected a different mechanism as the optimal solution. To test this hypothesis, we re-examined each aftershock through December 1989 to determine if the main shock focal mechanism (initial slip) could provide a reasonable explanation of the aftershock's observed first-motion polarities. Using FPFIT, we constrained the solution to be the main shock mechanism and compared the resulting misfit to the confidence region of each

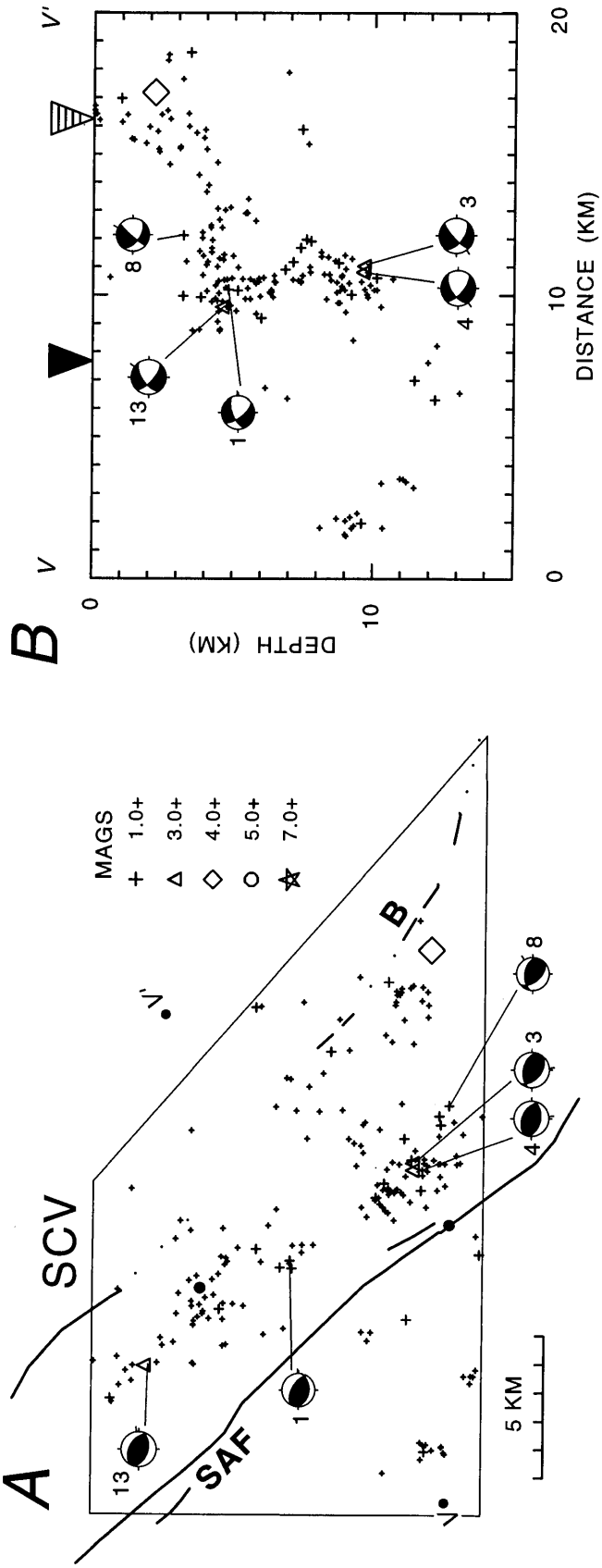

Figure 20.—Enlargements of aftershock seismicity and selected focal mechanisms (lower hemisphere projections) in map view and depth section for the seven subregions shown in figure 6. Earthquake symbols are the same as in figure 3. For map views: lettered dots show depth section endpoints, and unlabeled dots are the landmarks from figure 6. Faults are labeled in map view and denoted by symbols at 0 km depth on cross sections: San Andreas fault (SAF, solid triangle), Sargent fault (S, open triangle), Berrocal fault (B, hatched triangle), and coastline (arrow). Subregions SCV (*A,B*); LPN (*C,D,E*); LPC (*F,G,H*); LPS (*I,J,K*); CSA (*L,M*); SAR (*N,O*); and MON (*P,Q*). For all plotted mechanisms: number and letter labels refer to entries for the same event in appendix A (first motion data) and in table 6 (event locations and nodal planes).

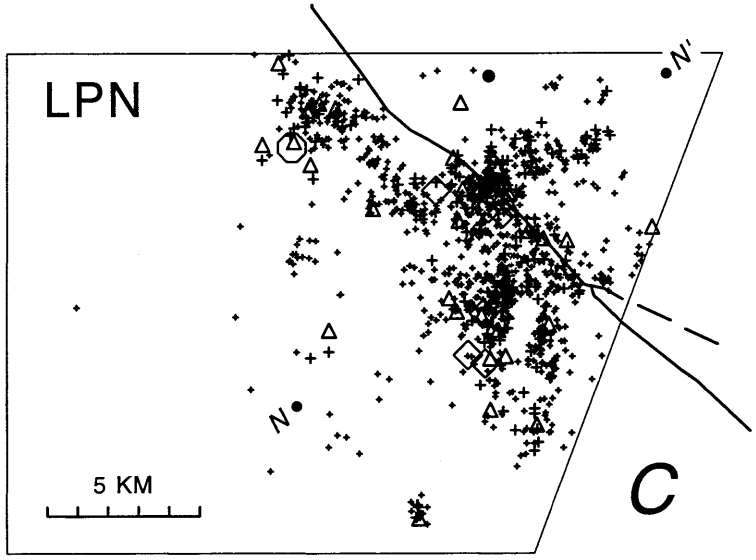

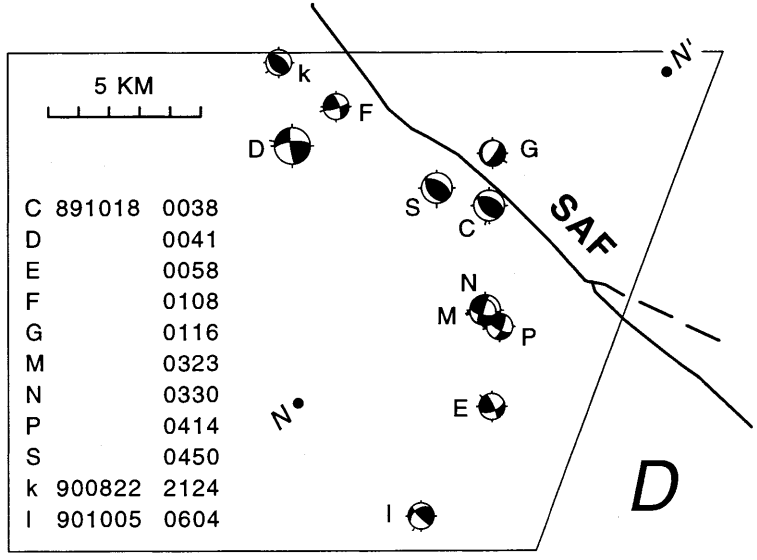

Figure 20.—Continued

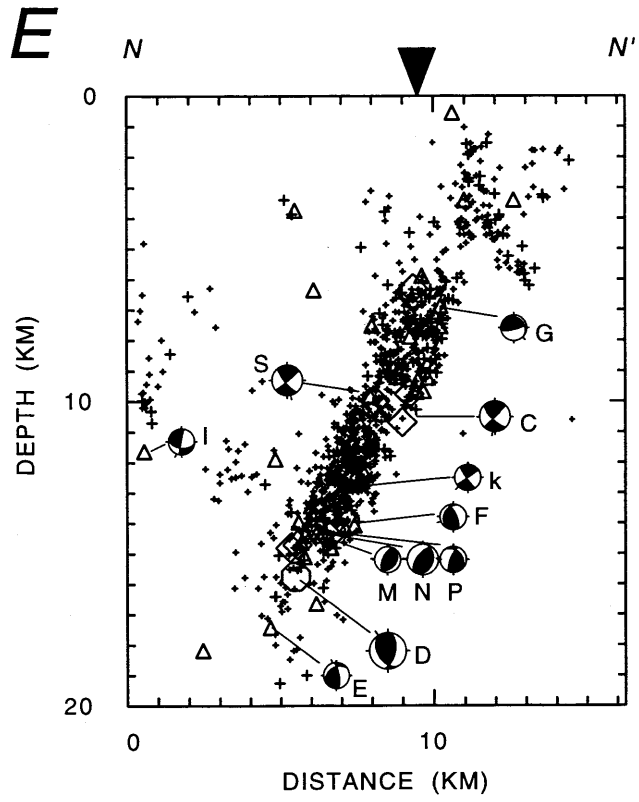

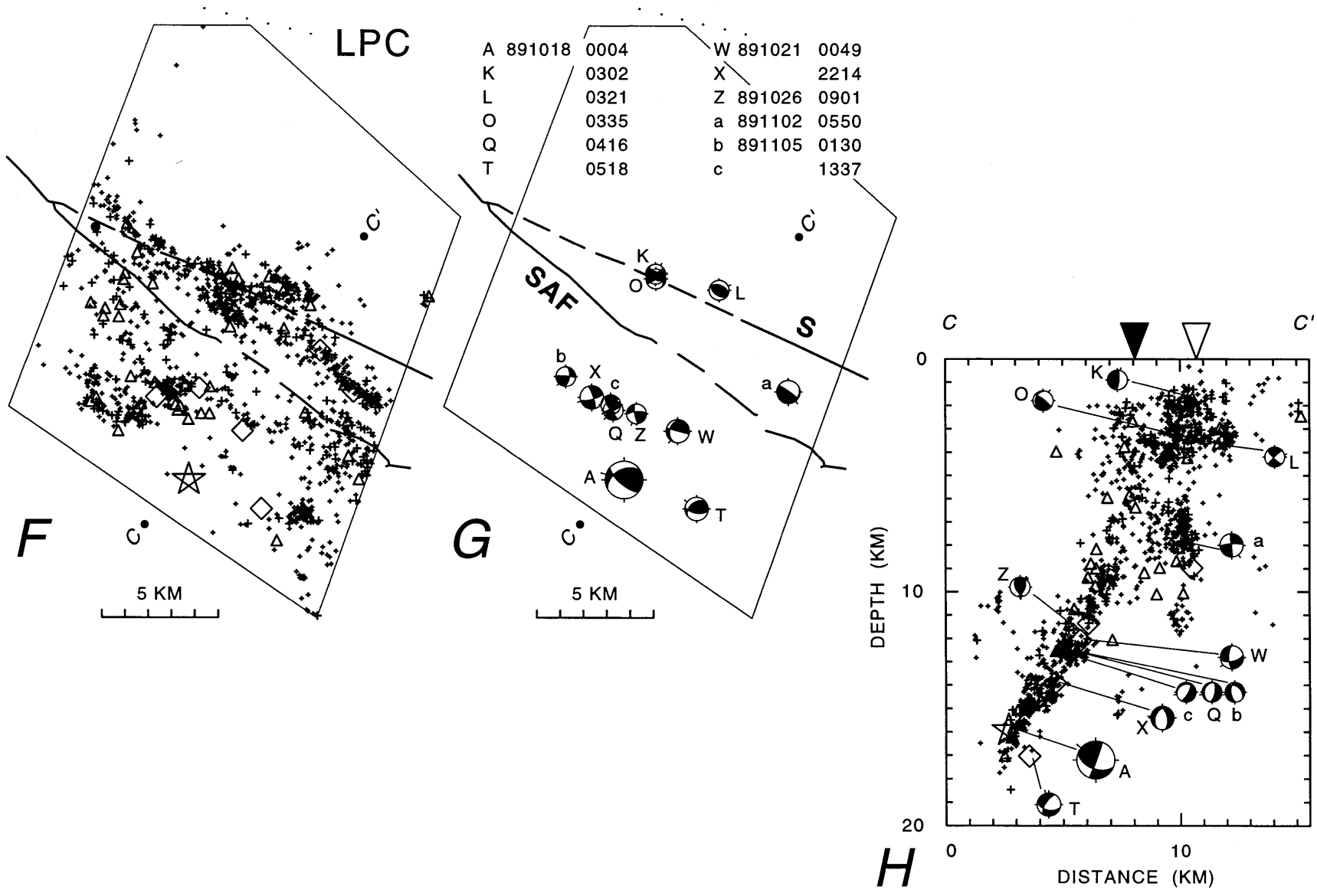

Figure 20.—Continued

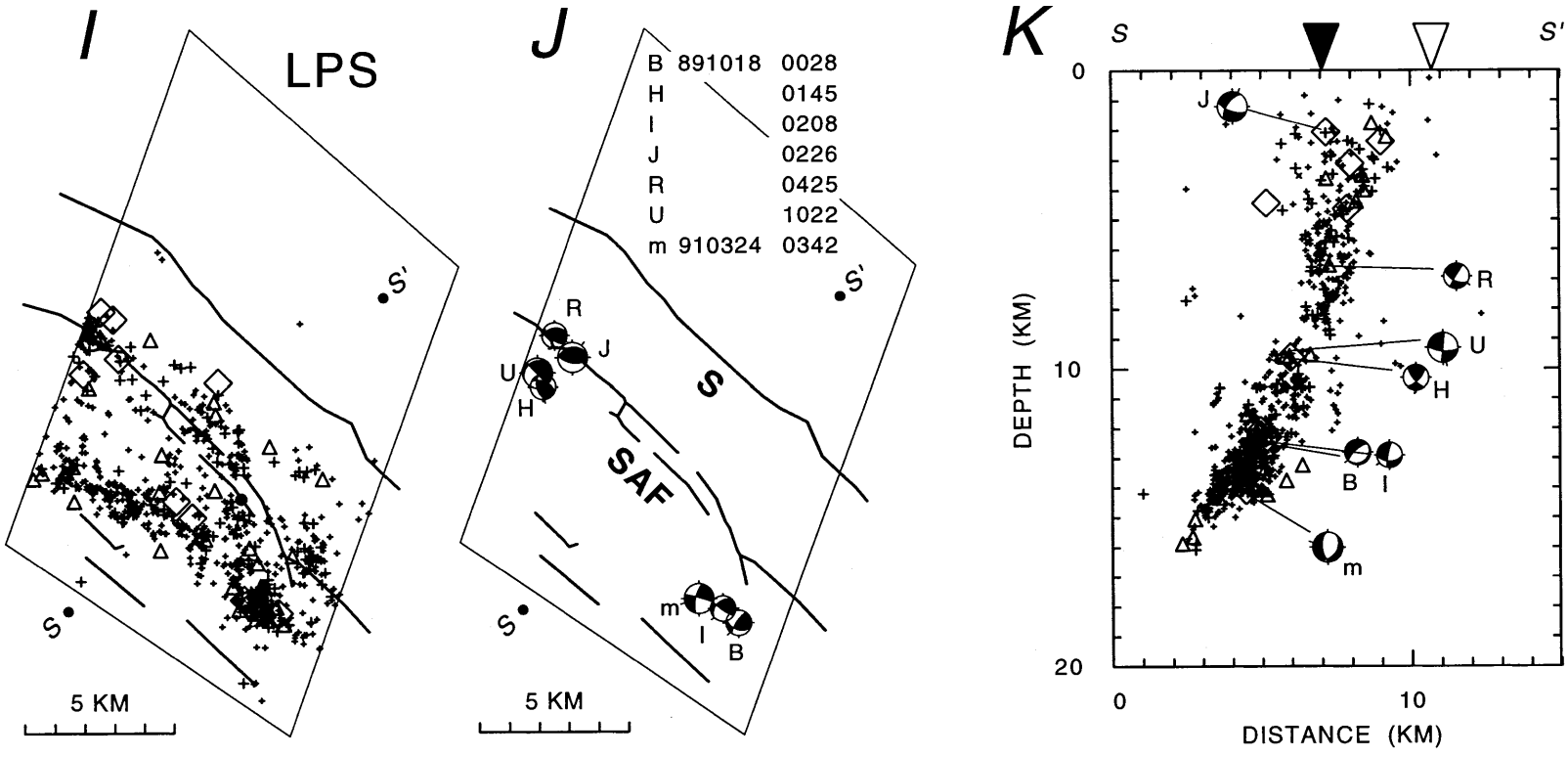

Figure 20.—Continued

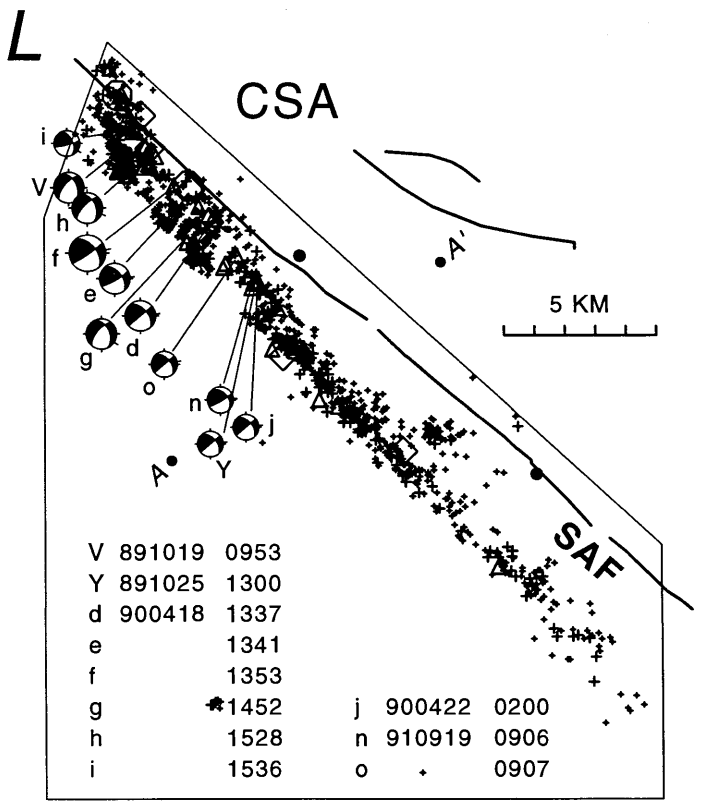

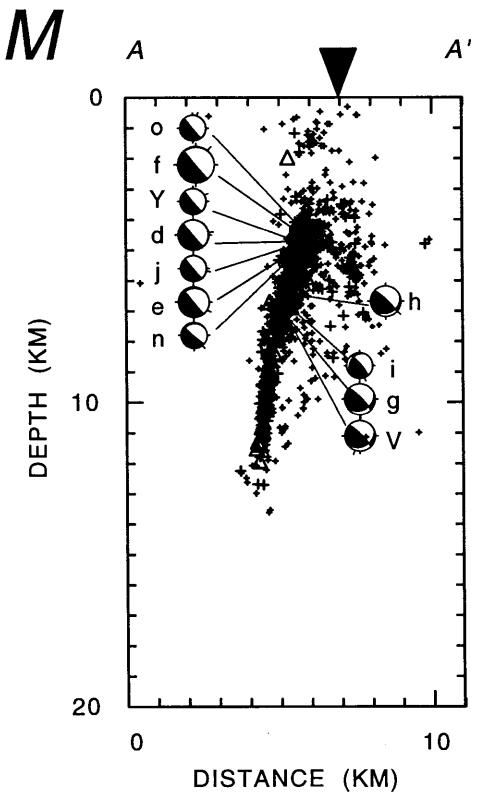

Figure 20.—Continued

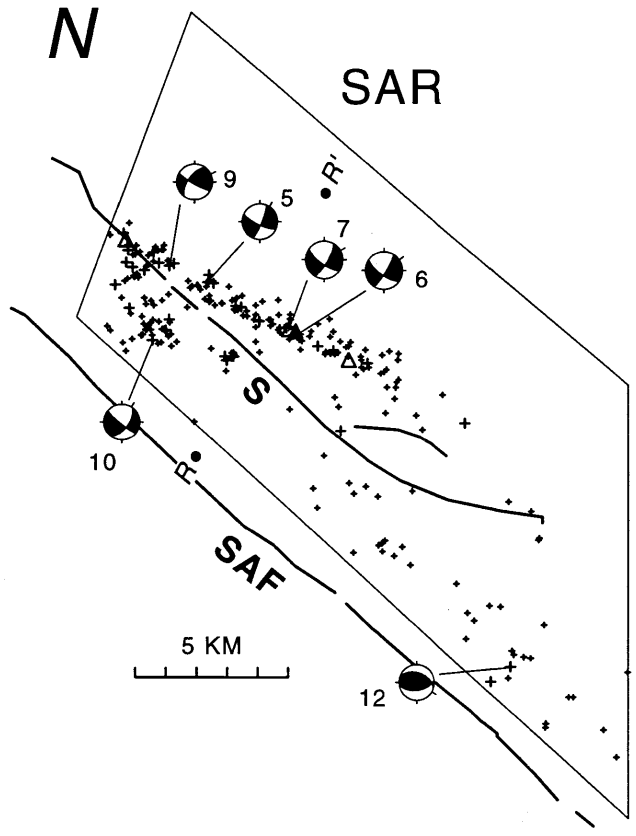

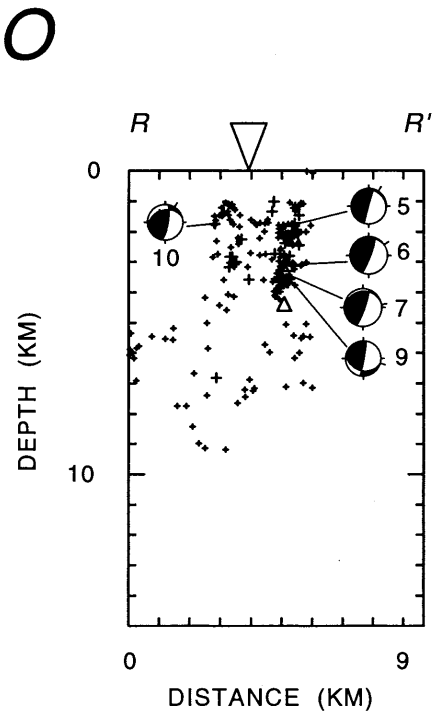

Figure 20.—Continued

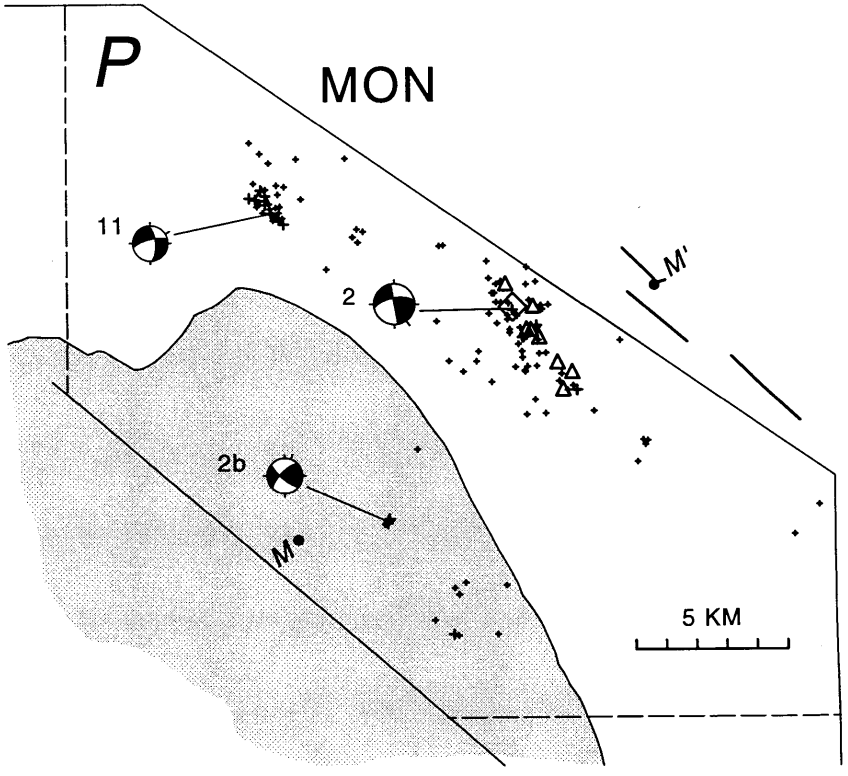

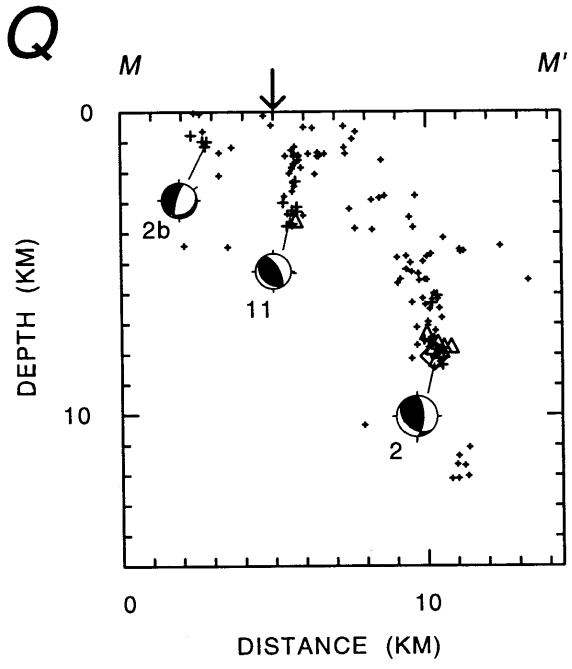

Figure 20.—Continued

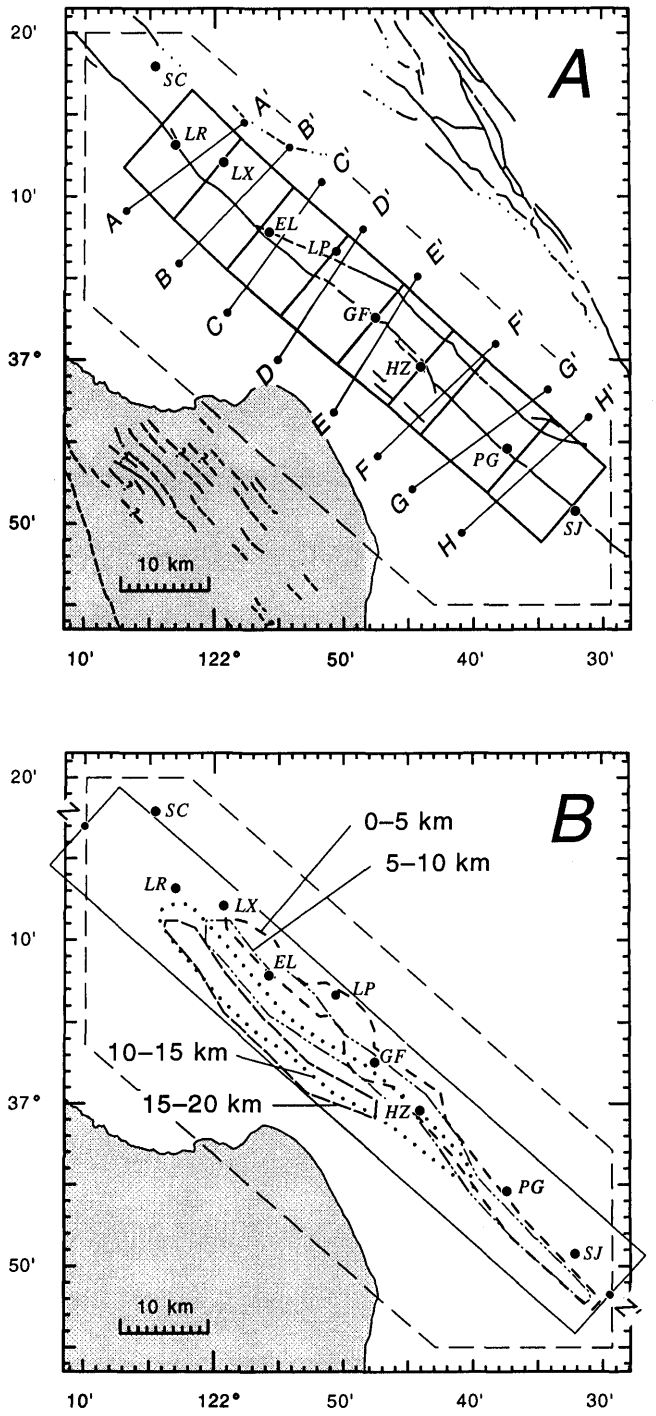

Figure 21.—Key maps showing selection criteria used in following figures. Labeled dots show landmarks from figure 6. Dashed line is the perimeter of the study region. (*A*) Selection boxes (solid outlines) and corresponding cross sections (labeled lines) for the series of transverse depth sections in figure 22. (*B*) Selection polygons and corresponding depth ranges used to define "main zone" seismicity for figure 23*A,B*. Events which are outside of the "main zone" regions but inside the *Z-Z'* box (solid line) are plotted as "outside-main zone" events in figure 23*C,D*.

unconstrained mechanism, only considering constrained solutions having misfits ≤0.15. We found that at the 80-percent confidence level only 6 percent of the aftershock mechanisms (47 of 730) matched the main shock. Next we freed the rake on the northwest-trending plane and found only 10 percent more events (74 of 730 within the 80-percent limit) which fit any kind of motion on the main shock rupture plane. These results strongly imply that the post-main shock stress field fundamentally differs from the pre-main shock stress field.

Although there is great diversity and heterogeneity in the distribution of aftershock focal mechanisms, several large-scale trends are noteworthy. Right-lateral strike-slip and right-lateral oblique-thrust events tend to cluster around the perimeter of the aftershock distribution, principally to the southeast of the main shock (figs. 20, 25). The line of events at the base of the zone to the southeast of the main shock display nearly uniform slip on planes slightly steeper than the main shock and with a slightly more horizontal rake. These mechanisms are consistent with the greater component of strike-slip displacement in the main shock to the southeast of the epicenter inferred from waveform modeling (see Spudich, 1996), and geodetic modeling (Lisowski and others, 1990; and Arnadottir and others, 1992).

Strike-slip mechanisms also occur at the northwest end of the zone. These mechanisms, however, are rotated about 45° to the trend of the zone, and have fault-normal *P*-axes. The largest aftershock in the early part of the sequence, the *M*=5.3 event of October 18 at 00:41 (event D, fig. 20 *D, E*) has this mechanism. Strike-slip events with the same fault plane orientations, but the opposite sense of slip (fault-normal *T*-axes) are also observed, such as the *M*=4.7 event within the interior of the main zone a few kilometers to the northwest and above the main shock (event X, fig. 20 *G, H*). Thus, the pattern of fault-normal compression is not universal, even within the interior of the zone.

Normal faulting mechanisms principally occur below 7 km depth and within the interior of the main zone (fig. 25). These events also have fault-normal coordinated *T*-axes. Thrust mechanisms are scattered through the entire aftershock zone. Most of them occur northwest of the main shock, and many occur at depths above 6 km. Most thrust mechanisms strike sub-parallel to the main zone (and San Andreas surface trace) and have fault-normal *P*-axes. Some of the events toward the northern end of the zone, however, (events S and C, fig. 20 *D, E*) could represent pure reverse slip on the main fault plane. Nodal planes of the thrust events more commonly have too shallow a dip (~45°) to match the more steeply dipping main shock fault plane and thus most probably occur on secondary structures.

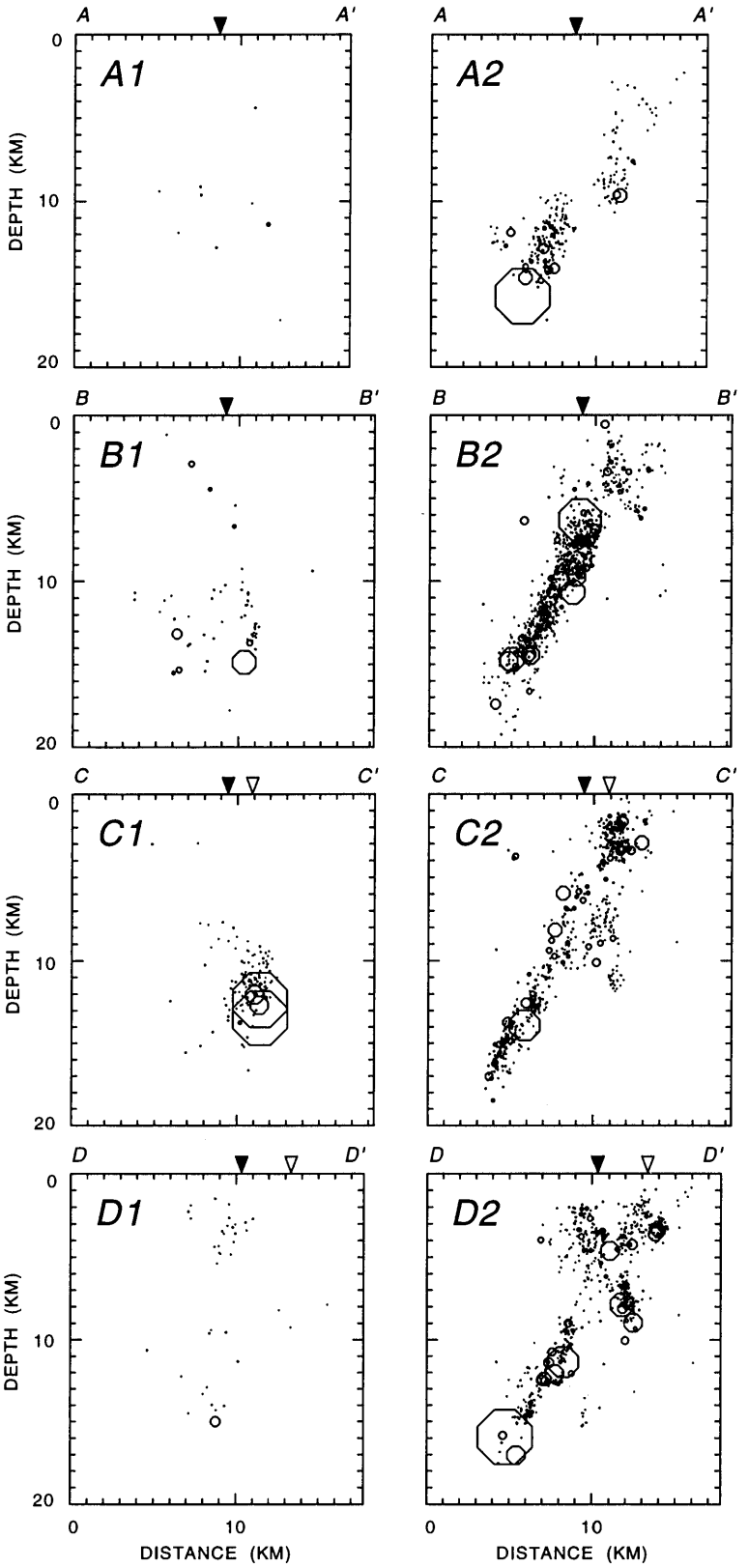

Figure 22.—Series of transverse cross sections from northwest (*A*) to southeast (*H*) along the San Andreas fault. Well-located $M_d \geq 1.0$ events from (*A1-H1*) January 1, 1969, to October 17, 1989; and (*A2-H2*) October 18, 1989, to October 17, 1991. Symbol sizes are scaled to rupture area assuming a 30-bar stress drop. Inverted solid triangle represents the surface trace of the San Andreas fault, open triangle shows the Sargent fault. See figure 21*A* for selection boxes and section endpoints chosen to minimize the projected width of the aftershock zone.

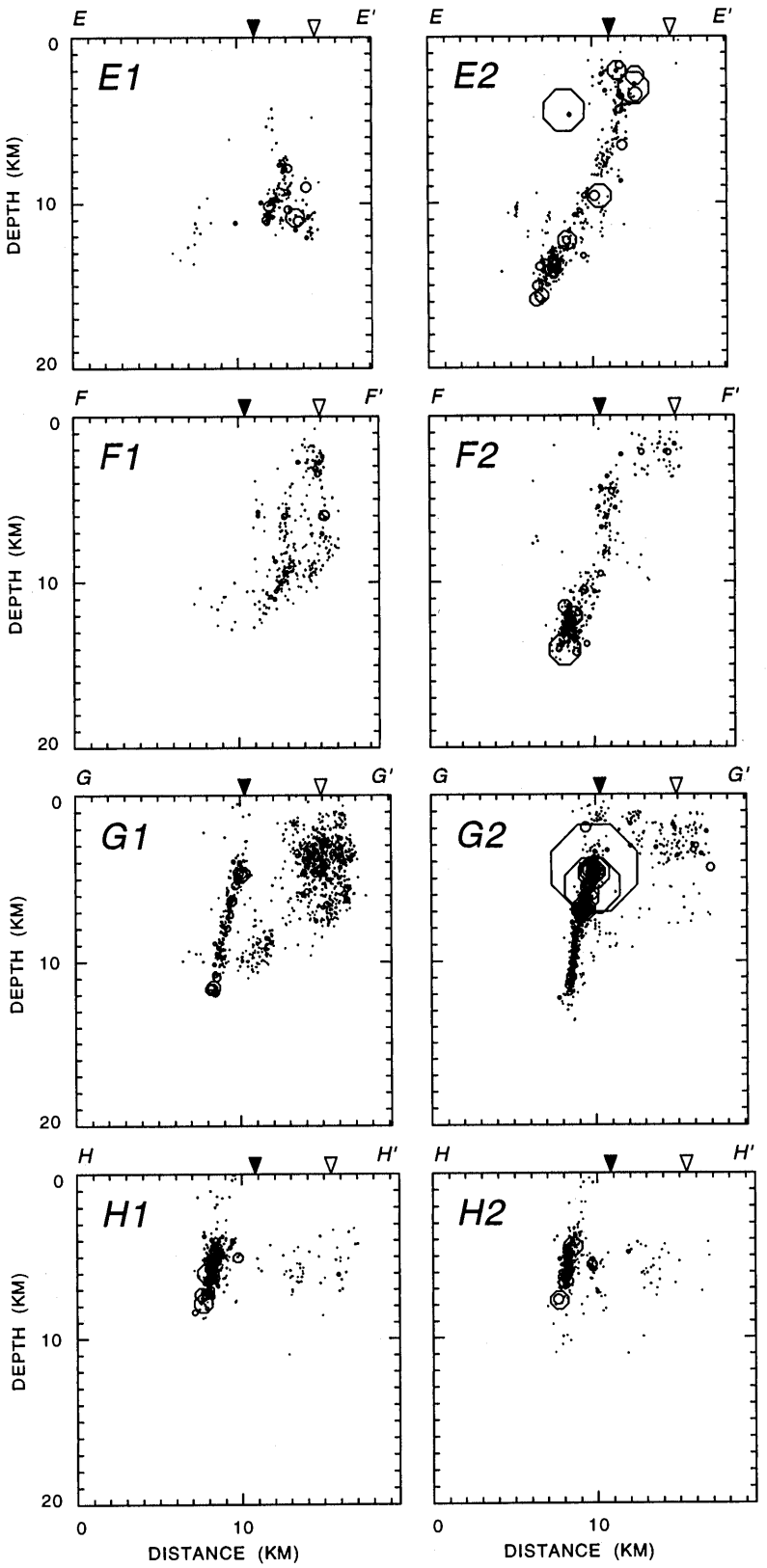

Figure 22.—Continued

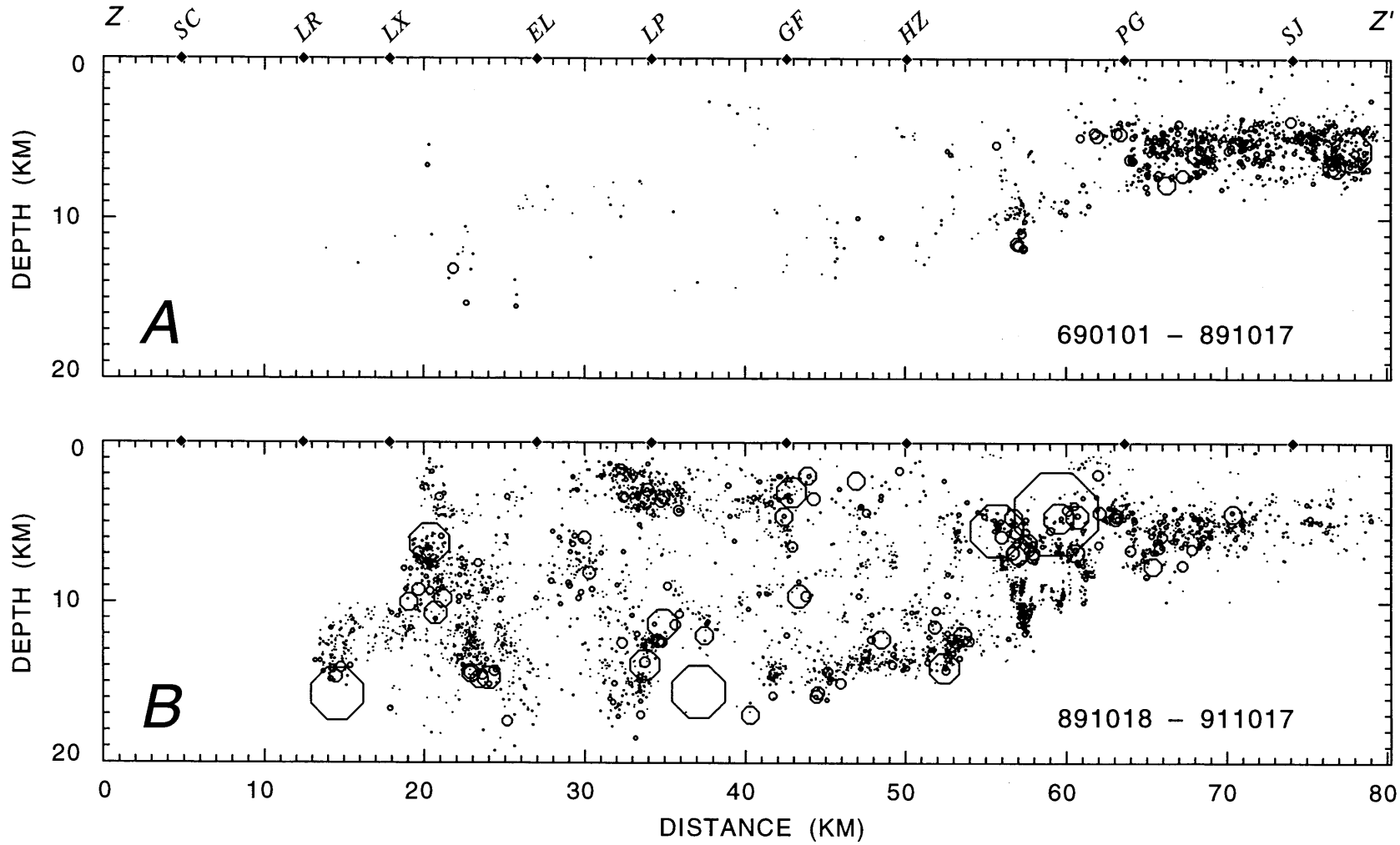

Figure 23.—Depth sections of the best-located earthquakes from NW (*Z*) to SE (*Z'*) along the San Andreas fault. "Main zone" seismicity (*A*) January 1, 1969, through October 17, 1989, and (*B*) October 18, 1989, through October 17, 1991. "Outside-main zone" seismicity (*C*) January 1, 1969, through October 17, 1989, and (*D*) October 18, 1989, through October 17, 1991. Symbol sizes are scaled to rupture area assuming a 30-bar stress drop. See figure 21*B* for event selection criteria used here.

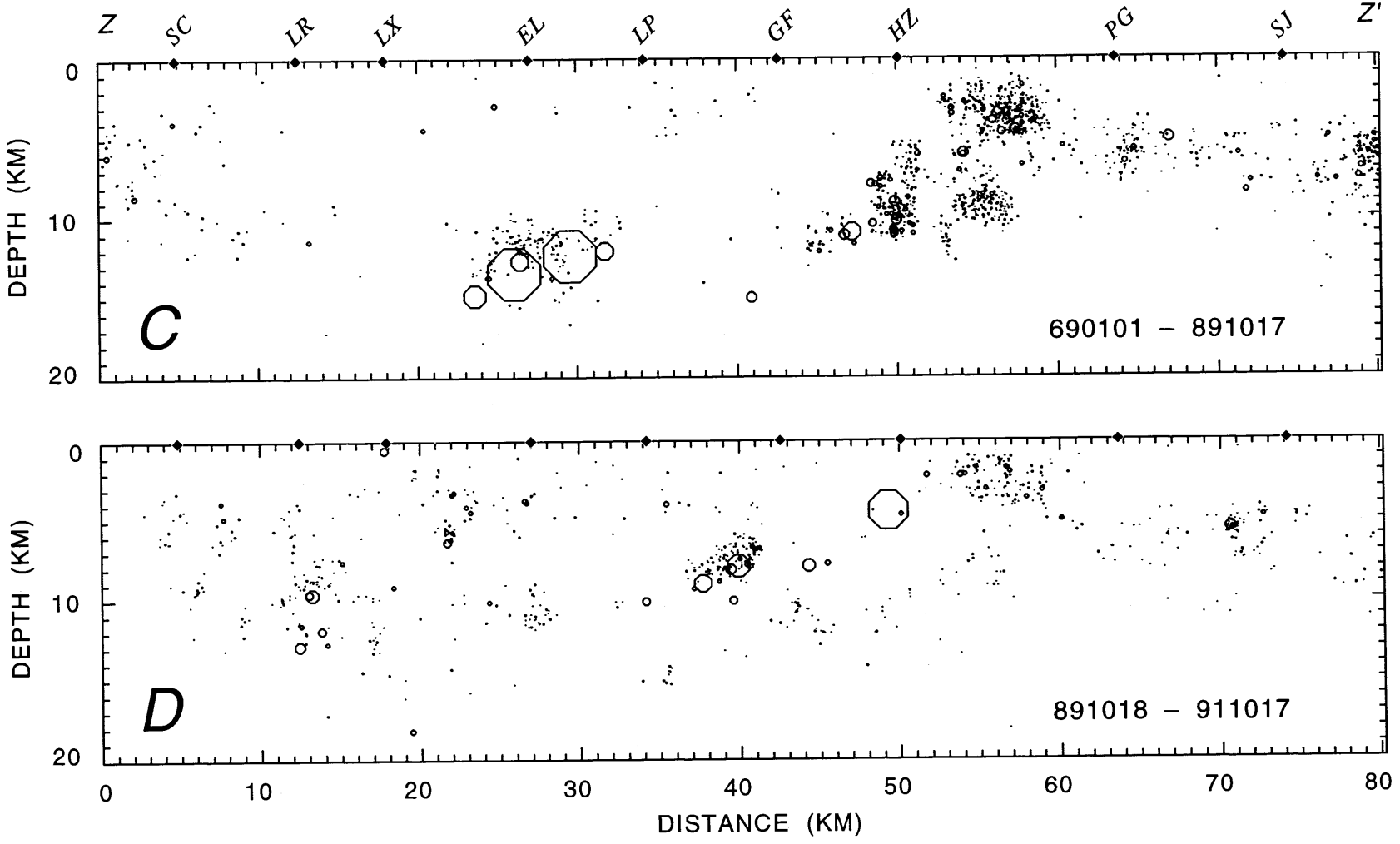

Figure 23.—Continued

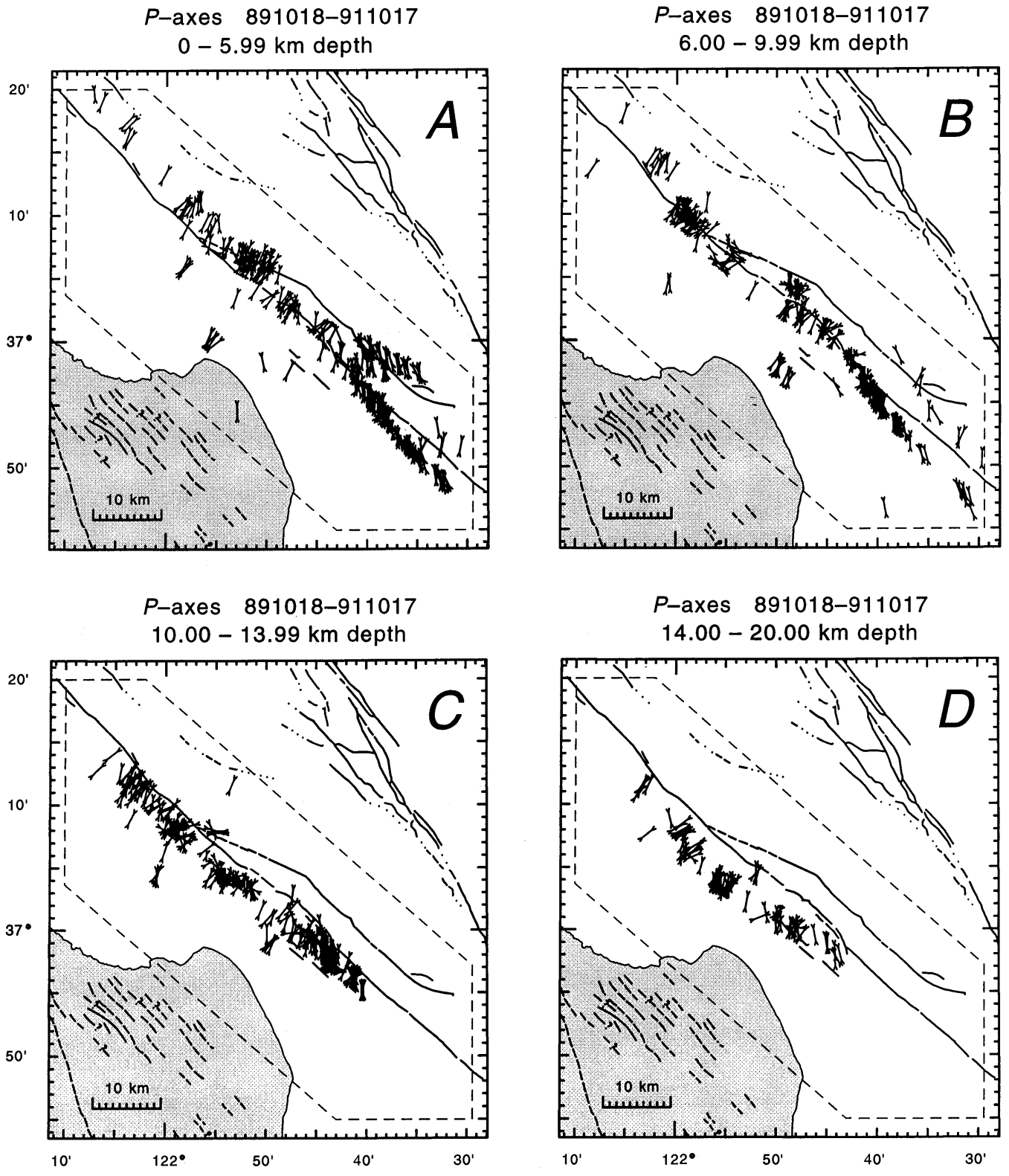

Figure 24.—Map view projections of *P*-axes from well-determined mechanisms of $M_d \geq 1.5$ earthquakes. Events from October 18, 1989, to October 17, 1991, at (*A*) 0-6 km depth, (*B*) 6-10 km depth, (*C*) 10-14 km depth, and (*D*) 14-20 km depth; and (*E*) January 1, 1969, to October 17, 1989, 0-20 km depth. (*F*) a few focal mechanisms of small events near the San Andreas fault, 1969 to 1989.

SAN ANDREAS FAULT

At its southern end, the aftershock zone merges seamlessly into the activity of the creeping central segment of the San Andreas fault where fault slip occurs as a mix of earthquakes and fault creep (Wesson and others, 1973b). Focal mechanisms of earthquakes on this section of the San Andreas fault are homogeneous and reflect dextral slip on the San Andreas fault. Slip in the main shock, as determined from both dynamic (Beroza, 1991; Steidl and others, 1991; Wald and others, 1991) and static models (Lisowski and others, 1990; Snay and others, 1991; and Marshall and others, 1991), extended for no more than 15 to 20 km to the southeast of the hypocenter. The seismicity rate in the southernmost section decays differently from the rate in the dipping portion of the aftershock zone (Reasenberg and Simpson, this chapter). Thus, activity along the southeastern 25 km of the aftershock zone probably reflects stress transfer to it from slip in the main shock.

About 10 km southeast of the main shock epicenter, the main zone begins to steepen in dip and it warps toward a slightly more northerly strike. It continues to steepen until it merges with the San Andreas fault at a point about 8 km northwest of Pajaro Gap (PG in figs. 6, 21, 23). As the zone steepens, it also narrows in width, until it has no measurable width (≤0.7 km) after merging with the San Andreas fault.

The southern terminus of rupture in the main shock coincides with the point where the aftershock zone reaches the San Andreas fault. The end of the rupture may be marked by the clusters of aftershocks located 20 to 21 km southeast of the main shock hypocenter. The largest aftershock, the M=5.4 Chittenden earthquake of April 18, 1990, locates immediately to the southeast of this point at the top of the aftershock zone. This earthquake triggered a major secondary aftershock sequence that extended for 10 km to the southeast along the San Andreas fault (fig. 17). This sequence filled a 7-km-long gap on the fault between 3 and 8 km depth that was visible in the pre-Loma Prieta seismicity (fig. 23*A*). The mechanisms of these events show predominantly right-lateral strike-slip motion on northwest-trending planes. Any dip to these fault planes is believed to be an artifact caused by lateral refractions from unmodeled local velocity changes, as previously stated.

CASTRO AND SOUTHERN SARGENT FAULTS

Directly to the northeast of the San Andreas fault along the southeastern part of the aftershock zone (region SAR, fig. 20 *N*, *O*), aftershock activity defines a shallow (1-4 km), near-vertical, right-lateral strike-slip fault. This fault also stands out as a prominent feature in the pre-Loma Prieta seismicity (fig. 3; Olson and Hill, 1993). This activity has been commonly assumed to be on the Sargent

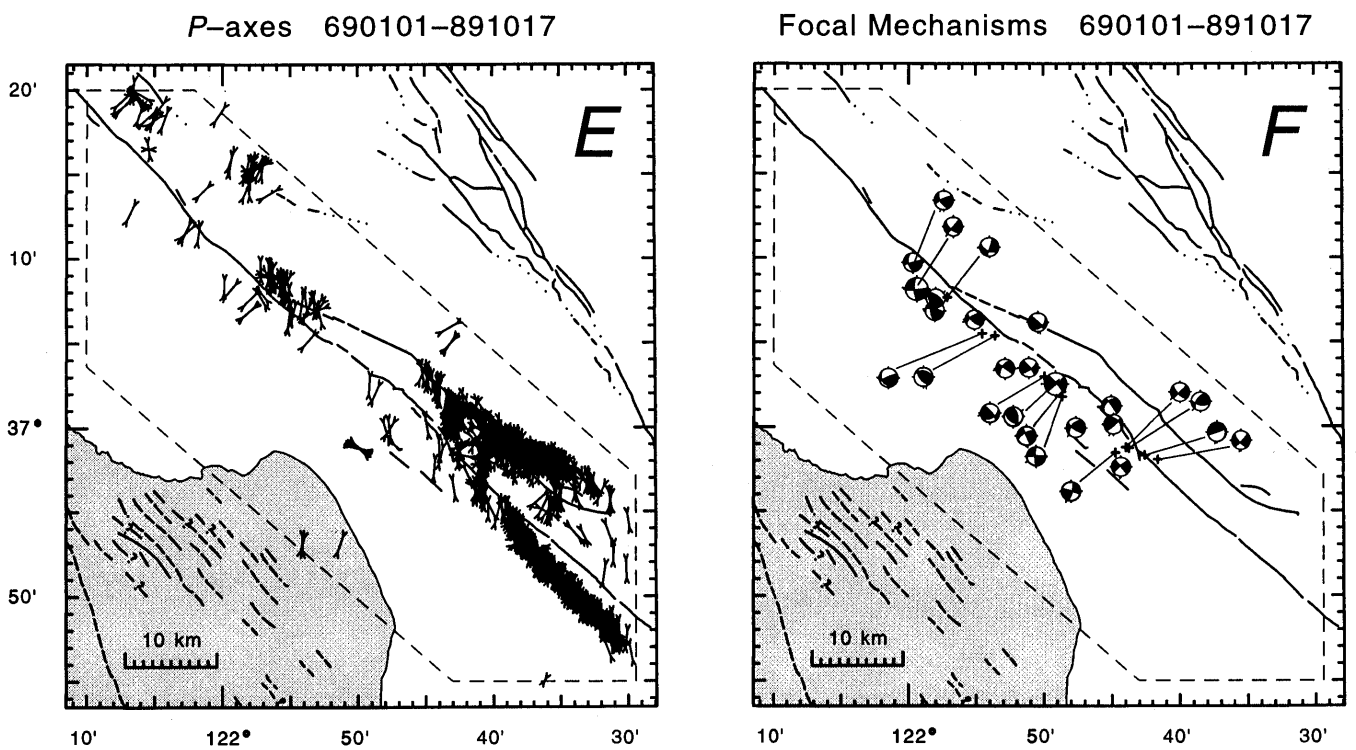

Figure 24.—Continued

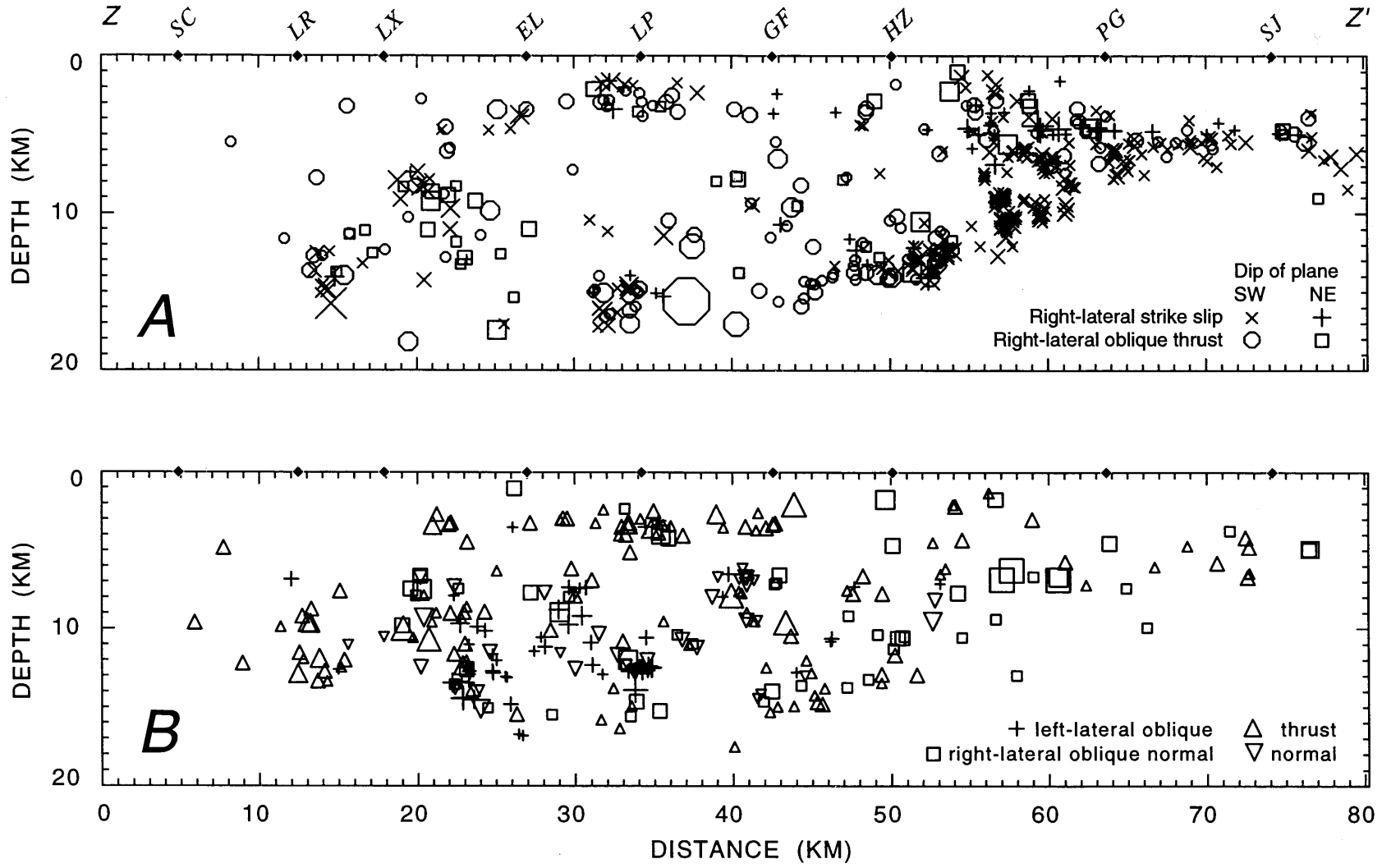

Depth sections of aftershocks within the Z-Z′ box (see figure 21*B*) having ...al mechanisms with one nodal plane sub-parallel (130°±45°) to the ...Symbol type depends on rake, symbol size is proportional to ...eral strike-slip events (| rake | ≥ 155°) on SW-dipping (×) and ...planes; Right-lateral oblique-thrust events (115° ≤ rake ≤ 154°) on SW-dipping (open circle) and NE-dipping (square) planes. (*B*) Right-lateral oblique-normal events (-154° ≤ rake ≤ -115°, square); thrust events (65° ≤ rake ≤ 114°, triangle-point-up); normal events (-114° ≤ rake ≤ -65°, triangle-point-down); and left-lateral and oblique events (-64° ≤ rake ≤ 64°, +).

fault (for example, Eaton and others, 1970). Our locations, as well as those of Olson and Hill, however, lie distinctly east of and at an acute angle to the southern Sargent fault. They coincide, however, with the Castro fault, first described by Allen (1946). We believe that this seismically defined fault is most probably the subsurface expression of the Castro fault and is not associated with the Sargent fault.

A few aftershocks are also scattered between the traces of the Sargent and San Andreas faults. Most of these events also show right-lateral strike-slip on northwest planes, but a few shallow thrust events occur as well. Only 4 of the events in this region are $M_d \geq 3.0$, the largest a M_d=3.2 on December 31, 1989. As noted previously, the rate of activity along the Castro fault underwent a step-like increase at the time of the Loma Prieta earthquake, then declined to the pre-event rate within about one year.

FAULTS NORTH OF THE MAIN ZONE AND EAST OF THE SAN ANDREAS

The Loma Prieta earthquake triggered activity within a plexus of faults in the footwall block, principally within the southern Santa Cruz Mountains to the east of the San Andreas fault. Aside from the activity along the Castro fault (described above) the aftershock activity in this region occurred on faults that were virtually aseismic during the two decades before the earthquake (figs. 3, 22, 23). Areas that had been active before the main shock were stilled by the earthquake.

The overall pattern of aftershocks in this region reflects release of fault-normal compression, principally on reverse faults. These events are generally deepest adjacent to the San Andreas fault, shallow to the northeast, and are consistent with movement on the Shannon, Monte Vista, and Berrocal faults (fig. 22). Within this general framework, however, the case can be made for reverse faulting on steeply northeast-dipping planes, in addition to the named northwest-dipping faults.

Strike-slip events, although rare, are also observed. These occur at shallow depth (1-2 km), and directly underlie the northern part of the Sargent fault (fig. 20 *F*, *H*). At only slightly greater depth, reverse faulting predominates within the same area.

One of the clearest examples of a distinct secondary fault outlined by aftershock activity appears updip of the main shock hypocenter. This activity clusters in a near-vertical plane between 6 and 9 km depth lying between the surface traces of the San Andreas and Sargent faults. This cluster was initiated by a M=4.3 aftershock on October 25, 1989, at 0127 UTC. The focal mechanism implies pure reverse motion (SW side down) on a vertical plane parallel to the San Andreas (event a, fig. 20 *G*, *H*; appendix A).

The total amount of aftershock activity in the northernmost portion of the foot wall of the Loma Prieta earthquake was relatively modest, with only four well-located aftershocks $M_d \geq 3$ (region SCV, fig. 20 *A*, *B*). The largest of these, M_d=4.7, occurred 3 minutes after the main shock along the northeastern perimeter of the entire sequence, just to the west of the Shannon fault. Because *P*-wave arrivals for this event were obscured by the main shock coda waves, a reliable focal mechanism could not be determined. We strongly suspect, however, that this event was a shallow reverse-faulting event associated with the Shannon fault.

Field investigations along the Monte Vista and Shannon faults revealed systematic evidence of tectonic shortening caused by the Loma Prieta earthquake (Schmidt and others, 1996). The events along this northernmost extension of the aftershock zone (fig. 20 *A*, *B*) are consistent with minor displacement along these faults during the main shock or in the earliest moments of the aftershock sequence. The prompt occurrence of the M_d=4.7 event at shallow depth just west of the trace of the Shannon fault supports this interpretation.

HANGING WALL ACTIVITY

Although the majority of all aftershocks locate southwest of the San Andreas fault, almost all of these lie within the main zone, and comparatively few locate in the hanging-wall block of the earthquake. The aftershock activity in the hanging wall (region MON, fig. 20 *P*, *Q*) concentrate in one large and several smaller clusters. The large cluster contains the M_d=4.5 event of October 19, 1989, at 1014 UTC (event 2, fig. 20 *P*, *Q*; appendix A) and its aftershocks. This sub-vertical cluster trends 143° and is centered about 10 km south-southeast of the main shock. It is about 5 km long and lies between 5 and 8.5 km depth. The focal mechanism indicates right-lateral strike-slip on a 170° trending vertical plane, with the *P*-axis in fault-normal coordination with the main zone. This secondary fault lies near the projected position of the Zayante fault (R. Jachens and A. Griscom, written commun., 1992), but has focal mechanisms and fault plane strikes that are incompatible with their occurrence on this reverse fault.

A second cluster locates 9 km northwest of the first, at a depth between 1 and 4 km. The largest event in this group also has a north-striking, right-slip fault plane solution (event 11, fig. 20 *P*, *Q*; appendix A). Ten kilometers further to the northwest, strike-slip faulting in the hanging-wall activity appears again, this time with a northwest strike and reverse component (event I, fig. 20 *D*, *E*; appendix A). The fourth minor cluster locates in Monterey Bay, a few km seaward of the shoreline and directly south of the main shock epicenter. The largest event in this cluster (event 2b, fig. 20 *P*, *Q*; appendix A) shows right

slip on a N50°W, near-vertical plane. No young faults have been identified at the surface in the vicinity of these other clusters.

RELATIONSHIP OF PRESHOCKS TO THE MAIN SHOCK AND AFTERSHOCKS

The detailed record of seismic activity afforded by the CALNET during the 20+ years before the Loma Prieta earthquake bears little resemblance to the distribution of aftershocks (fig. 3; Olson and Hill, 1993). In only three peripheral areas does it appear that the aftershocks occurred on the same faults displaying activity in the two decades before the shock. These are the San Andreas fault southeast of the main shock, the Castro fault to the south and east of the earthquake, and the zone of reverse faulting at the extreme northwestern end of the zone, generally in the area near Stevens Creek Reservior (SC, fig. 6). As noted above, all of these areas continued to be active after the Loma Prieta earthquake and each experienced an accelerated rate of earthquake production following the main shock (Reasenberg and Simpson, 1992, and this chapter).

As discussed by Olson and Hill (1993), the main zone had very little activity for at least the 20 years leading to the main shock (figs. 3, 22, 23). While the deep activity forming the prominent "U-shaped" band of activity that was subsequently filled by the main shock (U.S. Geological Survey Staff, 1990) included the sparse main zone activity, it was principally constructed from activity to the northeast of the main zone. These northeastern areas, however, were virtually silent during the aftershock sequence, as can be seen by comparing the pre- and post-earthquake event distributions (fig. 23). In general, the pre-earthquake seismicity reflects the release of a north-south compressive stress, as would be expected for the San Andreas fault system (fig. 24 *E*, *F*).

Several important sequences of M_L=4-5 earthquakes preceded the main shock. The two events near Lake Elsman in 1988 and 1989, M_L=5.0 and M_L=5.2 respectively, are well-known to be the largest events near the Loma Prieta earthquake in over 20 years (Olson and Hill, 1993; Sykes and Jaumé, 1990). These events ruptured adjacent parts of deep fault at the intersection of the Sargent fault with the San Andreas fault near what was to become the northwest end of the Loma Prieta rupture. As with the other zones noted above, seismicity in the Lake Elsman zone was not activated by the main shock.

In addition to the 1988 and 1989 events, several notable sequences of M=4-5 events also occurred near the main zone in the 1960's. These include the events of November 16, 1964 (M_L=5.0), October 14, 1966 (M_L=4.0), September 7, 1967 (M_L=4.7), December 18, 1967 (M_L=5.3), and March 21, 1968 (M_L=4.3). Although the catalog locations of these events place them in the general region, they lack the precision to draw any firm conclusions regarding their association to the Loma Prieta earthquake. Using the method of joint hypocentral determination (Dewey, 1972), we can accurately locate these events with respect to the modern data. Furthermore, the 1967 and 1968 events were recorded by the CALNET and can be accurately located without resort to JHD.

Relocation of these events using both JHD and absolute methods shows that they are significantly more tightly clustered than the catalog locations would suggest (fig. 26, table 5). The 1964 and 1966 events locate quite near the San Andreas fault, and are plausibly on it. The activity in 1967 and 1968, however, form a clear northwest trending lineation, subparallel to and removed 2 km to the northeast of the San Andreas fault at the latitude of the main shock hypocenter. This trend also contains the M_L=4.5 event of August 19, 1982. A reliable focal mechanism was determined for the largest event (December 18, 1967), and it shows right-lateral strike slip on a N50°W-striking fault. We conclude that these events do indeed fall on a single fault, possibly the Sargent fault, but probably not the San Andreas fault. As with most of the other significant concentrations of pre-Loma Prieta seismicity, activity along this zone was curtailed by the main shock.

Finally, we address the question of whether or not the San Andreas fault was active adjacent to the Loma Prieta

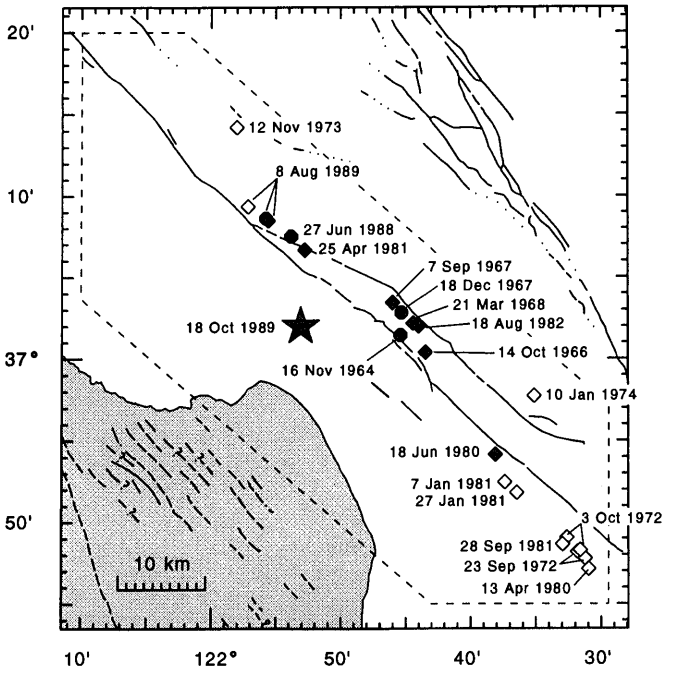

Figure 26.—Map of M_L≥4.0 events from 1964 through October 17, 1989; star = main shock, circle = M_L≥5.0, diamond = M_L≥4.0. Earthquakes occurring in the 1960's were located relative to a subset of later events (solid symbols, table 5) by a joint hypocentral determination (JHD). In the JHD, events after 1970 were fixed at their locations from this study, but their origin times were free to move.

Table 5.—*Earthquakes $M_L \geq 4.0$ located by joint hypocentral determination*

Origin Time yrmoda	hrmn	s	Latitude N	Longitude W	Depth km	M_L
641116	0246	41.94	37° 1.46′	121° 45.39′	9.81	5.0
661014	2034	28.65	37° 0.41′	121° 43.46′	5.57	4.2
670907	1239	17.12	37° 3.46′	121° 46.00′	10.41	4.7
671218	1724	31.83	37° 2.85′	121° 45.32′	9.98	5.3
680321	2154	59.92	37° 2.20′	121° 44.42′	10.69	4.3
800618	0452	26.34	36° 54.16′	121° 38.08′	4.69	4.2
810425	1941	37.22	37° 6.67′	121° 52.78′	12.04	4.1
820818	0843	49.65	37° 2.02′	121° 44.00′	10.88	4.5
880627	1843	22.44	37° 7.50′	121° 53.83′	12.36	5.3
890808	0813	27.57	37° 8.62′	121° 55.76′	13.46	5.4
891018	0004	15.42	37° 2.01′	121° 53.08′	15.94	7.0

rupture and main zone of aftershocks between 1969 and the earthquake. A critical examination of the pre-Loma Prieta activity shows that there are a few events in the central part of the zone that lie vertically below the trace of the San Andreas fault (fig. 22 *D*1; fig. 3*A*). They suggest the possibility of some activity on a vertical San Andreas fault. Although focal mechanisms for these small events are difficult to obtain, a number of them indicate right-lateral slip on planes parallel to the San Andreas fault (fig. 24*F*). If these events locate on the primary fault that moved in the 1906 earthquake, they represent only very minor subsequent movement.

DISCUSSION

Perhaps the most intriguing feature of the Loma Prieta aftershock sequence is its almost complete disassociation from the preceding seismicity. Only at the extreme ends of the sequence, well removed in space from the main shock slip surface, do we observe aftershock activity of the same style and at the same location as the preshocks. Nearer the source, the aftershocks activated numerous faults not seen before the earthquake, and their focal mechanisms reflect a first-order change from release of north-south compression expected for the San Andreas system to release of fault-normal compression. Indeed, it appears probable that the main shock effectively released all of the shear stress acting across its fault plane (Michael and others, 1990), leaving a residual stress field in an average state of uniaxial compression (Zoback and Beroza, 1993).

Activation of the full aftershock zone proceeded very rapidly. In fact, we detected no significant change in the form of the zone from its earliest observable moments (fig. 10). A high degree of spatial clustering of aftershocks, particularly within the main zone and nearby areas northeast of the San Andreas fault, is a primary feature of the distribution. Many of these clusters represent individual faults and have been studied in detail by Seeber (written commun., 1992). These clusters commonly produced their largest locatable event very early in the sequence and thus may be related to short-wavelength variations in main shock displacements such as at the ends of the rupture.

The rapid spatial variations in the style and orientation of aftershock focal mechanisms between the interior clusters, such as changes over short distances from fault-normal compression to fault-normal extension (fig. 25), further suggest a causal association with localized stresses created by the main shock. The general lack of correlation of the aftershock clusters with the main shock slip zones (see Spudich, 1996) thus supports Oppenheimer's assertion (1990) that abrupt spatial variations in main shock displacement is required to account for the observed short distance mechanism variability, particularly within the interior of the main zone.

THE EARTHQUAKE AND THE SAN ANDREAS FAULT

Finally, we examine the question of the relationship between the Loma Prieta rupture and the San Andreas fault in the southern Santa Cruz Mountains. The geologic investigations of Prentice and Schwartz (1991) and detailed trenching studies by Schwartz and others (1991) leave little doubt that the 1906 earthquake ruptured the main trace of the San Andreas fault adjacent to the 1989 earthquake. Furthermore, both geodetic and strong-motion analyses of the Loma Prieta main shock (Spudich, 1996) require a large component of right-lateral strike-slip motion in the earthquake to the southeast of the main shock

epicenter. However, the upper extent of this slip did not reach the surface. We also know that the main zone of aftershocks merges seamlessly with the San Andreas fault near Pajaro Gap, virtually at the southern terminus of the 1906 fault break.

If the main zone of aftershocks faithfully maps the main shock rupture, as we hypothesize, then the association between it and the San Andreas fault could have several resolutions. In one, the Loma Prieta fault truncates a vertical San Andreas fault at ~9 km depth. Alternatively, Olson (1990) suggests that the San Andreas truncates the Loma Prieta rupture plane. A third possibility is that they are one in the same, with the San Andreas fault following the main zone below 10 km and steepening to vertical above that depth.

Neither the aftershocks nor the geodetic models of the earthquake (Lisowski and others, 1990; Snay and others, 1991; Marshall and others, 1991; Horton and others, 1996) imply that main shock faulting continued to the northeast of the San Andreas surface trace. The main zone, like the geodetic models, terminates updip below the trace of the San Andreas fault (sections *B*2 through *F*2, fig. 22). Thus, evidence for the San Andreas being cut by the Loma Prieta fault is lacking. The opposite case of the San Andreas truncating the Loma Prieta fault is at least consistent with these data. Extending the San Andreas to depths below the hypothesized truncation point at ~9 km depth, however, has little to recommend it. A deep extension of the fault might be argued for on the basis of a single earthquake with a right-lateral strike-slip focal mechanism seen before the earthquake (fig. 22 *D*1, deepest event). Regarding the third possibility, slip on both the deeper, inclined part of the fault in the Loma Prieta earthquake and on the vertical part in the 1906 earthquake is kinematically possible only along the southeastern part of the 1989 rupture. North of the epicenter, the 1989 slip vector for the inclined part of the fault (predominately reverse), and the 1906 slip vector for the shallower vertical part (horizontal) are incompatible for a single structure and cannot be sustained in ongoing movement.

Indeed, a common shortcoming of all three of these possibilities is that they fail to address the kinematics of the crust traversing the prominent left (compressional) bend in the San Andreas fault within the southern Santa Cruz Mountains. Over geologic time, flow of the crust around the bend must be accommodated by either lateral flow, subduction or mountain-building (Anderson, 1990). The simple kinematic model of Dietz and Ellsworth (1990) for the present-day geometry successfully predicts the ratio of horizontal to vertical slip on the Loma Prieta fault (fig. 27). While this model is not unique, it suggests that we are observing a rapidly evolving fault geometry which must continually adjust as new crust enters the compressional bend.

The smooth connection between the Loma Prieta rupture and the San Andreas fault to the southeast of the bend raises the possibility that the Loma Prieta earthquake followed what was once the main strand of the fault, but which is now in the process of being abandoned. Along the southern half of the earthquake where motion was predominately strike slip, the strand continues to carry some of the San Andreas motion. Farther to the north, where motion was dominantly reverse, it has been abandoned as a transform fault, but it still released the compressional component of the kinematically prescribed slip, with the translational part presumably being accommodated on the San Andreas.

Ultimately, the resolution of this problem must await a more complete understanding of the faults within the southern Santa Cruz Mountains. The complete absence of seismicity on the fault that ruptured in this M_S=7.1 earthquake over at least the 20 years preceding the event and the absence of an obvious imprint left by its rupture in the geologic record should remind us that other large active faults, including the San Andreas itself, may be "hidden" within the southern Santa Cruz Mountains and will only be fully revealed when they slip in major earthquakes.

ACKNOWLEDGEMENTS

We thank L. Jones and R. Page for their helpful reviews of this manuscript.

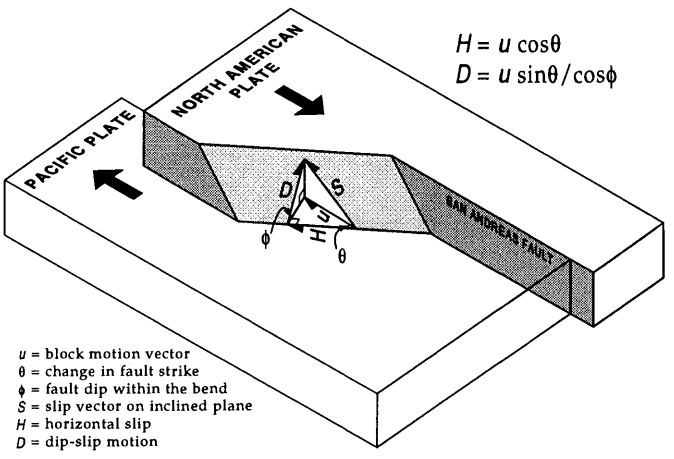

Figure 27.—Simple block model to describe the slip vector (*S*) on a dipping fault segment within a bend of a vertical strike-slip fault. This model successfully predicts the ratio of horizontal (*H*) to vertical (*D*) slip observed on the Loma Prieta fault.

Table 6.—*Event locations and nodal planes from focal mechanisms in figure 20 and appendix A*

EQ	Origin Time		Latitude	Longitude	Depth	M_L	Nodal Plane 1			Nodal Plane 2		
	yrmoda	hrmn	N	W	km		dip-azm	dip	rake	dip-azm	dip	rake
A	891018	4	37° 2.01′	121° 53.08′	15.94	7.1	220	70	130	332	44	30
B		28	36° 57.32′	121° 43.11′	12.39	3.7	200	45	160	304	76	47
C		38	37° 9.78′	121° 59.30′	10.68	4.3	230	45	110	23	48	71
D		41	37° 10.85′	122° 3.67′	15.75	5.2	262	81	160	355	70	10
E		58	37° 6.23′	121° 59.26′	17.43	3.7	65	81	150	160	60	10
F		108	37° 11.54′	122° 2.69′	14.07	3.6	71	70	169	165	80	20
G		116	37° 10.71′	121° 59.22′	6.88	3.6	271	18	-123	125	75	-80
H		145	37° 1.62′	121° 47.52′	9.60	3.7	255	50	130	22	54	53
I		208	36° 57.58′	121° 43.46′	12.55	3.5	215	80	130	317	41	15
J		226	37° 2.15′	121° 46.84′	2.06	4.0	190	60	100	351	31	73
K		302	37° 6.78′	121° 52.16′	1.67	3.5	230	85	-180	140	90	-5
L		321	37° 6.41′	121° 50.32′	3.62	3.8	215	45	100	21	46	80
M		323	37° 7.90′	121° 59.45′	14.40	3.9	195	70	-20	292	71	-159
N		330	37° 7.93′	121° 59.40′	14.43	4.1	190	60	-10	285	81	-150
O		335	37° 6.67′	121° 52.15′	3.39	3.5	54	40	172	150	85	50
P		414	37° 7.64′	121° 59.08′	14.51	3.6	210	70	20	113	71	159
Q		416	37° 3.62′	121° 53.39′	12.48	3.7	241	80	5	150	85	170
R		425	37° 2.55′	121° 47.25′	6.52	3.6	220	60	120	351	41	49
S		450	37° 10.09′	122° 0.45′	9.99	4.2	235	40	110	30	53	74
T		518	37° 1.34′	121° 50.99′	17.04	4.2	190	60	120	321	41	49
U		1022	37° 1.87′	121° 47.64′	9.61	4.3	225	85	110	328	21	14
V	891019	953	36° 56.64′	121° 41.08′	6.88	4.3	67	46	-144	310	65	-50
W	891021	49	37° 3.14′	121° 51.53′	12.08	4.2	195	90	-120	105	30	0
X		2214	37° 3.92′	121° 54.01′	13.91	4.7	72	80	-15	165	75	-170
Y	891025	1300	36° 54.05′	121° 38.43′	4.55	3.8	50	50	180	140	90	40
Z	891026	901	37° 3.54′	121° 52.72′	11.40	3.7	260	75	160	355	71	16
a	891102	550	37° 4.05′	121° 48.32′	7.89	4.3	35	85	100	151	11	27
b	891105	130	37° 4.40′	121° 54.76′	12.54	3.7	98	60	6	5	85	150
c		1337	37° 3.75′	121° 53.46′	12.40	3.9	236	62	23	135	70	150
d	900418	1337	36° 55.22′	121° 39.35′	4.61	4.3	50	50	180	140	90	40
e		1341	36° 55.78′	121° 39.77′	4.70	4.5	52	51	167	150	80	40
f		1353	36° 55.86′	121° 39.82′	4.42	5.4	51	50	173	145	85	40
g		1452	36° 55.06′	121° 39.63′	6.88	4.2	67	46	-144	310	65	-50
h		1528	36° 56.51′	121° 40.67′	6.27	4.2	67	44	-150	315	70	-50
i		1536	36° 56.88′	121° 41.14′	6.87	3.9	67	51	167	165	80	40
j	900422	200	36° 54.13′	121° 38.32′	4.67	3.6	50	50	180	140	90	40
k		2124	37° 12.33′	122° 3.97′	12.86	3.7	230	35	100	38	56	83
l	901005	604	37° 4.31′	122° 0.83′	11.63	3.6	225	80	130	327	41	15
m	910324	342	36° 57.76′	121° 44.00′	14.08	4.5	15	85	-160	283	70	-5
n	910919	906	36° 54.17′	121° 38.36′	4.76	3.9	48	41	165	150	80	50
o		907	36° 54.63′	121° 38.76′	4.36	3.9	50	50	180	140	90	40

REFERENCES CITED

Allen, J.E., 1946, Geology of the San Juan Bautista quadrangle, California: California Division of Mines and Geology Bulletin 133, 111 p.

Anderson, R.S., 1990, Evolution of the northern Santa Cruz Mountains by advection of crust past a San Andreas fault bend: Science, v. 249, p. 397-401.

Arnadottir, T., Segall, P., and Matthews, M., 1992, Resolving the discrepancy between geodetic and seismic fault models for the 1989 Loma Prieta, California, earthquake: Seismological Society of America Bulletin, v. 82, p. 2248-2255.

Beroza, G.C., 1996, Rupture history of the earthquake from high-frequency strong-motion data, *in* Spudich, P., The Loma Prieta, Cali-

Table 6.—*Continued*

EQ	Origin Time		Latitude	Longitude	Depth	M_L	Nodal Plane 1			Nodal Plane 2		
	yrmoda	hrmn	N	W	km		dip-azm	dip	rake	dip-azm	dip	rake
1	891018	330	37° 16.21′	122° 3.90′	4.82	2.8	185	35	70	29	57	103
2	891019	1014	36° 58.30′	121° 50.13′	8.07	4.5	260	90	155	350	65	0
2b	891025	1630	36° 54.50′	121° 52.93′	1.13	2.8	220	75	160	315	71	16
3	891107	2342	37° 13.87′	122° 1.54′	9.65	3.9	220	45	110	13	48	71
4	891202	2002	37° 13.87′	122° 1.71′	9.61	3.4	190	45	80	24	46	100
5	891215	543	36° 59.02′	121° 38.71′	1.80	2.6	205	75	-170	112	80	-15
6	891231	648	36° 58.15′	121° 36.77′	3.07	3.1	215	70	-170	122	81	-20
7		813	36° 58.19′	121° 36.92′	3.33	3.2	215	71	-164	120	75	-20
8	900216	736	37° 13.17′	122° 0.17′	3.21	2.3	230	50	120	8	48	59
9	900417	2126	36° 59.31′	121° 39.56′	3.56	2.4	210	80	150	306	60	12
10	900425	802	36° 57.99′	121° 39.93′	1.74	2.8	220	81	-150	125	60	-10
11	900529	1343	36° 59.98′	121° 55.48′	3.25	2.1	85	65	-160	346	72	-26
12	900910	1701	36° 52.19′	121° 31.99′	6.72	2.0	20	44	112	170	50	70
13	910416	56	37° 19.00′	122° 6.43′	4.60	3.1	195	45	80	29	46	100

fornia, earthquake of October 17, 1989—Earthquake occurrence: U.S. Geological Survey Professional Paper 1550-A, p. A9-A32.

Beroza, G.C., 1991, Near-source modeling of the Loma Prieta earthquake: evidence for heterogeneous slip and implications for earthquake hazard: Seismological Society of America Bulletin, v. 81, p. 1603-1621.

Beroza, G.C., and Zoback, M.D., 1993, Mechanism diversity of the Loma Prieta aftershock sequence: implications for the mechanics of mainshock-aftershock interaction: Science, v. 259, p. 210-213.

Choy, G.L., and Boatwright, J., 1990, Source characteristics of the Loma Prieta, California, earthquake of October 18, 1989 from global digital seismic data: Geophysical Research Letters, v. 17, p. 1183-1186.

Dewey, J.W., 1972, Seismicity and tectonics of western Venezuela: Seismological Society of America Bulletin, v. 62, p. 1711-1751.

Dietz, L.D., and Ellsworth, W.L., 1990, The October 17, 1989 Loma Prieta, California, eathquake and its aftershocks: Geometry of the sequence from high-resolution locations: Geophysical Research Letters, v. 17, p. 1417-1420.

Eaton, J.P., 1992, Determination of amplitude and duration magnitudes and site residuals from short-period seismographs in northern California: Seismological Society of America Bulletin, v. 82, p. 533-579.

Eaton, J.P., Lee, W.H.K., and Pakiser, L.C., 1970, Use of microearthquakes in the study of the mechanics of earthquake generation along the San Andreas fault in central California: Tectonophysics, v. 9, p. 259-282.

Eberhart-Phillips, D., Labson, V.F., Stanley, W.D., and Michael, A.J., 1990, Preliminary velocity and resistivity models of the Loma Prieta earthquake region: Geophyiscal Research Letters, v. 17, p. 1235-1238.

Eberhart-Phillips, D., and Stuart, W.D., 1992, Material heterogeneity simplifies the picture: Loma Prieta: Seismological Society of America Bulletin, v. 82, p. 1964-1968.

Fletcher, J.B., and Boatwright, J., 1991, Source parameters of Loma Prieta aftershocks and wave propagation characteristics along the San Francisco peninsula from a joint inversion of digital seismograms: Seismological Society of America Bulletin, v. 81, p. 1783-1812.

Foxall, W., Michelini, A., and McEvilly, T.V., 1993, Earthquake travel time tomography of the southern Santa Cruz Mountains: Control of fault rupture by lithological heteogeneity of the San Andreas fault zone: Journal of Geophysical Research, v. 98, p. 17691-17710.

Habermann, R.E., and Craig, M.S., 1988, Comparison of Berkeley and Calnet magnitude estimates as a means of evaluating temporal consistency of magnitudes in California: Seismological Society of America Bulletin, v. 78, p. 1255-1267.

Horton, Stephen, Anderson, J.G., and Mendez, A.J., 1996, Frequency-domain inversion for the rupture characteristics during the earthquake, using strong-motion data and geodetic observations, *in* Spudich, P., ed., The Loma Prieta, California, earthquake of October 17, 1989—Earthquake occurrence: U.S. Geological Survey Professional Paper 1550-A, p. A59-A73.

Hough, S.E., Seeber, L., Lerner-Lam, A., Armbruster, J.G., and Guo, H., 1991, Empirical Green's function analysis of Loma Prieta aftershocks: Seismological Society of America Bulletin, v. 81, p. 1737-1753.

Johnson, L.R., 1974, Green's function for Lamb's problem: Geophysical Journal of the Royal Astronomical Society, v. 37, p. 99-131.

Joyner, W.B., and Boore, D.M., 1988, Measurement, characterization, and prediction of strong ground motion: Proceedings of Earthquake Engineering and Soil Dynamics II, GT Div/ASCE, Park City, Utah, June 27-30, 1988, p. 43-102.

Kanamori, H., and Satake, K., 1990, Broadband study of the 1989 Loma Prieta earthquake: Geophysical Research Letters, v. 17, p. 1179-1182.

Kissling, E., Ellsworth, W.L., Eberhart-Phillips, D., and Kradolfer, U., 1994, Initial reference models in local earthquake tomography: Journal of Geophysical Research, v. 99, p. 19635-19646.

Klein, F.W., 1989, User's guide to HYPOINVERSE, a program for VAX computers to solve for earthquake locations and magnitudes: U.S. Geological Survey Open-File Report 89-314, 58 p.

Kradolfer, U., 1989, Seismische tomographie in der Schweiz mittels lokaler erdbeben: Doktor der Naturwissenschaften, Eidgenössischen Technischen Hochschule Zürich, 109 p.

Lees, J.M., 1990, Tomographic P-wave velocity images of the Loma Prieta earthquake asperity: Geophyiscal Research Letters, v. 17, p. 1433-1436.

Lisowski, M.J., Prescott, W.H., Savage, J.C., and Johnston, M.J.,

1990, Geodetic estimate of coseismic slip during the 1989 Loma Prieta, California, earthquake: Geophysical Research Letters, v. 17, p. 1437-1440.

Marks, S.M., and Lester, F.W., 1980, Catalog of earthquakes along the San Andreas fault system in central California, April-June 1977: U.S. Geological Survey Open-File Report 80-1264, 43 p.

Marshall, G.A., Stein, R.S., and Thatcher, W., 1991, Faulting geometry and slip from co-seismic elevation changes: The 18 October 1989, Loma Prieta, California, earthquake: Seismological Society of America Bulletin, v. 81, p. 1660-1693.

McNally, K.C., Simila, G.W., and Brown, J.G., 1996, Main-shock and very early aftershock activity, *in* Spudich, P., ed., The Loma Prieta, California, earthquake of October 17, 1989—Earthquake occurrence: U.S. Geological Survey Professional Paper 1550-A, p. A147-A170.

Mendoza, C., and Hartzell, S.H., 1988, Aftershock patterns and main shock faulting: Seismological Society of America Bulletin, v. 78, p. 1438-1449.

Michael, A.M., Ellsworth, W.L., and Oppenheimer, D.H., 1990, Coseismic stress changes induced by the Loma Prieta, California, earthquake: Geophysical Research Letters, v. 17, p. 1441-1444.

Michael, A.J., and Eberhart-Phillips, D., 1991, Relations among fault behavior, subsurface geology, and three-dimensional velocity models: Science, v. 253, p. 651-654.

Mooney, W.D., and Colburn, R., 1985, A seismic-refraction profile across the San Andreas, Sargent, and Calaveras faults, West-central California: Seismological Society of America Bulletin, v. 75, p. 175-191.

Murphy, J.M., Catchings, R.D., Kohler, W.M., Fuis, G.S., and Eberhart-Phillips, D., 1992, Data report for 1991 active-source seismic profiles in the San Francisco Bay area, California: U.S. Geological Survey Open-File Report 92-570, 45 p.

Olson, J.A., 1990, Seismicity preceding the 1989 Loma Prieta earthquake: Geophysical Research Letters, v. 17, p. 1429-1432.

Olson, J.A., and Hill, D.P., 1993, Seismicity in the southern Santa Cruz Mountains during the 20-year period before the earthquake, *in* Johnston, M.J.S., ed., The Loma Prieta, California, earthquake of October 17, 1989—Preseismic observations: U.S. Geological Survey Professional Paper 1550-C, p. C3-C16.

Oppenheimer, D.H., 1990, Aftershock slip behavior of the 1989 Loma Prieta, California earthquake: Geophysical Research Letters, v. 17, p. 1199-1202.

Prentice, C.S., and Schwartz, D.P., 1991, Re-evaluation of 1906 surface faulting, geomorphic expression, and seismic hazard along the San Andreas fault in the southern Santa Cruz Mountains: Seismological Society of America Bulletin, v. 81, p. 1424-1479.

Pujol, J., 1995, Application of the JHD technique to the Loma Prieta, California, mainshock-aftershock sequence and implications for earthquake location: Seismological Society of America Bulletin, v. 85, p. 129-150.

Reasenberg, P.A., and Ellsworth, W.L., 1982, Aftershocks of the Coyote Lake, California, earthquake of August 6, 1979: a detailed study: Journal of Geophysical Research, v. 87, p. 10637-10655.

Reasenberg, P.A., and Oppenheimer, D., 1985, FPFIT, FPPLOT and FPPAGE: Fortran computer programs for calculating and displaying earthquake fault-plane solutions: U.S. Geological Survey Open-File Report 85-739, 109 p.

Reasenberg, P.A., and Simpson, R.W., 1992, Response of regional seismicity to the static stress change produced by the Loma Prieta earthquake: Science, v. 255, p. 1687-1690.

Romanowicz, B., and Lyon-Caen, H., 1990, The Loma Prieta earthquake of October 18, 1989: results of teleseismic mantle and body wave inversion: Geophysical Research Letters, v. 17, p. 1191-1194.

Schmidt, K.M., Langenheim, V.E., Ellen, S.D., and Jachens, R.C., 1996, Damage patterns from the 1989 Loma Prieta earthquake along the frontal thrust-fault system, Santa Clara Valley, California: implications for strain partitioning along the San Andreas fault: EOS, American Geophysical Union Transactions, v. 77, no. 46, p F742.

Schwartz, D.P., Okumura, K., Pantosti, D., Powers, T.J., and Fuentes, J.M., 1991, Paleoseismic constraints on earthquake recurrence, San Andreas fault, Santa Cruz Mountains, California: Geological Society of America, Abstracts with Programs, v. 23, p. A98.

Schwartz, S.Y., Orange, D.L., and Anderson, R.S., 1990, Complex fault interactions in a restraining bend on the San Andreas fault, southern Santa Cruz Mountains, California: Geophyiscal Research Letters, v. 17, p. 1207-1210.

Simila, G.W., McNally, K.C., Nava, E., Protti-Quesada, M., and Yellin, J., 1990, Evidence of very early aftershock activity along the northwest portion of the 18 October 1989 earthquake rupture zone: Geophysical Research Letters, v. 17, p. 1785-1788.

Snay, R.A., Neugebauer, H.C., and Prescott, W.H., 1991, Horizontal deformation associated with the Loma Prieta earthquake: Seismological Society of America Bulletin, v. 81, p. 1647-1659.

Spieth, M.A., 1981, Two detailed seismic studies in central California, part 1: earthquake clustering and crustal structure studies of the San Andreas fault near San Juan Bautista: Ph.D. Dissertation, Stanford University, 138 p.

Spudich, Paul, 1996, The Loma Prieta, California, earthquake of October 17, 1989—Main-shock characteristics: U.S. Geological Survey Professional Paper 1550-A, 297 p.

Steidl, J.H., and Archuleta, R.J., 1996, Are rupture models consistent with geodetic measurements?, *in* Spudich, P., ed., The Loma Prieta, California, earthquake of October 17, 1989—Earthquake occurrence: U.S. Geological Survey Professional Paper 1550-A, p. A195-A207.

Steidl, J.H., Archuleta, R.J., and Hartzell, S.H., 1991, Rupture history of the 1989 Loma Prieta, California, earthquake: Seismological Society of America Bulletin, v. 81, p. 1573-1602.

Sykes, L.R., and Jaumé, S.C., 1990, Seismic activity on neighbouring faults as a long-term precursor to large earthquakes in the San Francisco Bay area: Nature, v. 348, p. 595-599.

U.S. Geological Survey Staff, 1990, The Loma Prieta, California earthquake: an anticipated event: Science, v. 247, p. 286-293.

Utsu, T., 1969, Aftershocks and earthquake statistics (I): Journal of the Faculty of Science, Hokkaido University, Japan, Ser. VII, Vol. III, no. 3, p. 129-195.

Wald, D.J., Helmberger, D.V., and Heaton, T.H., 1991, Rupture model of the 1989 Loma Prieta earthquake from the inversion of strong-motion and broadband teleseismic data: Seismological Society of America Bulletin, v. 81, p. 1540-1572.

———1996, Strong-motion and broadband teleseismic analysis of the earthquake for rupture-process modeling and hazard assessment, *in* Spudich, P., ed., The Loma Prieta, California, earthquake of October 17, 1989—Earthquake occurrence: U.S. Geological Survey Professional Paper 1550-A, p. A235-A262.

Wesson, R.L., Roller, J.C., and Lee, W.H.K., 1973a, Time-term analysis and geologic interpretation of seismic traveltime data from the Coast Ranges of central California: Seismological Society of America Bulletin, v. 63, p. 1447-1471.

Wesson, R.L., Burford, R.O., and Ellsworth, W.L., 1973b, Relationship between seismicity, fault creep and crustal loading along the central San Andreas fault: Stanford University Publications in Geological Sciences, v. 13, p. 303-321.

Zoback, M.D., and Beroza, G.C., 1993, Evidence for near-frictionless faulting in the 1989 (M6.9) Loma Prieta, California, earthquake and its aftershocks: Geology, v. 21, p. 181-185.

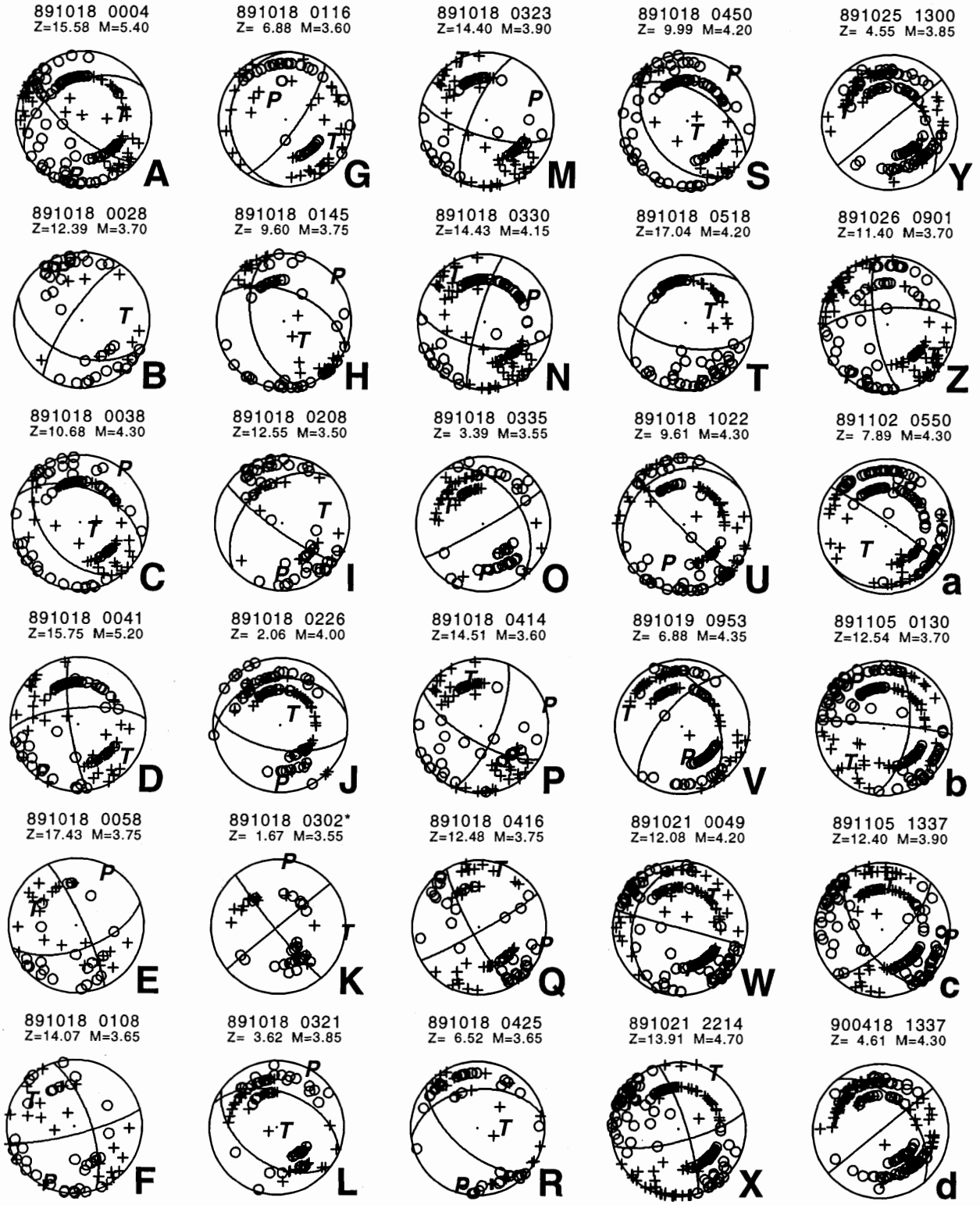

Appendix A.—Focal mechanisms (lower hemisphere projections) from figure 20 showing compressional (+) and dilatational (open circle) first arrivals. Lettered events locate in regions LPN, LPC, LPS, and CSA while numbered events locate in SAR, SCV, and MON. Event locations and nodal planes are listed in table 6.

900418 1341
Z= 4.70 M=4.50

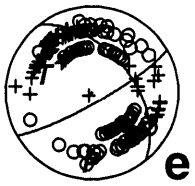

900822 2124
Z=12.86 M=3.70

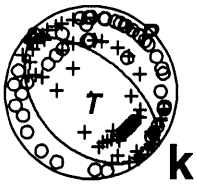

891019 1014
Z= 8.07 M=4.50

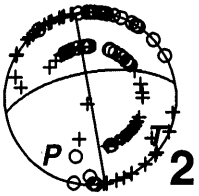

891231 0813
Z= 3.33 M= 3.20

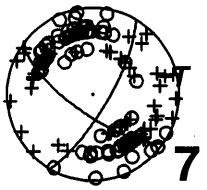

910416 0056
Z= 4.60 M=3.10

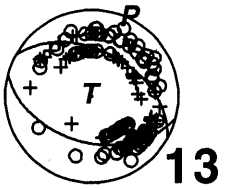

900418 1353
Z= 4.42 M=5.40

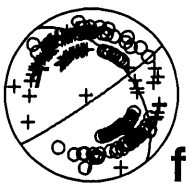

901005 0604
Z=11.63 M=3.60

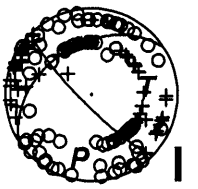

891025 1630
Z= 1.13 M=2.80

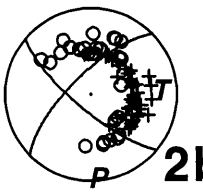

900216 0736
Z= 3.21 M=2.30

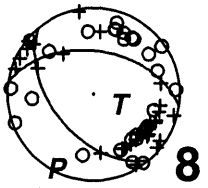

900418 1452
Z= 6.88 M=4.20

910324 0342
Z=14.08 M=4.55

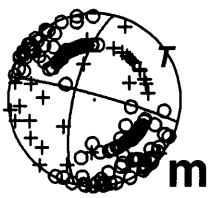

891107 2342
Z= 9.65 M=3.90

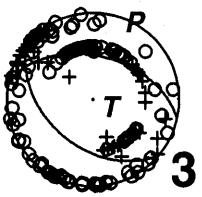

900417 2126
Z= 3.56 M=2.40

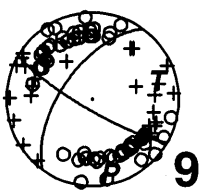

900418 1528
Z= 6.27 M=4.20

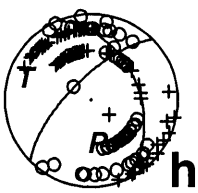

910919 0906
Z= 4.76 M=3.95

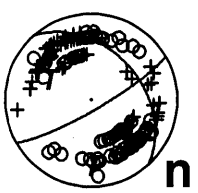

891202 2002
Z= 9.61 M=3.40

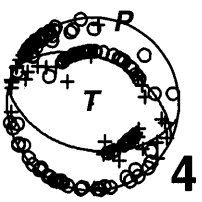

900425 0802
Z= 1.74 M=2.80

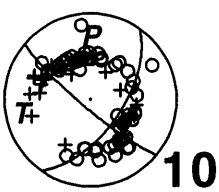

900418 1536
Z= 6.87 M=3.90

910919 0907
Z= 4.36 M=3.95

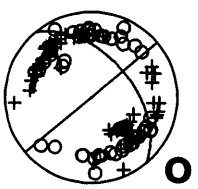

891215 0543
Z= 1.80 M=2.60

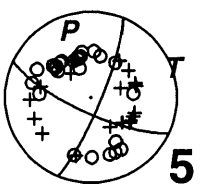

900529 1343
Z= 3.25 M=2.10

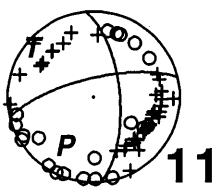

900422 0200
Z= 4.67 M=3.60

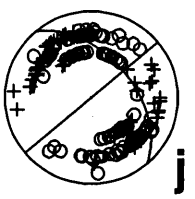

891018 0330
Z= 4.82 M=2.85

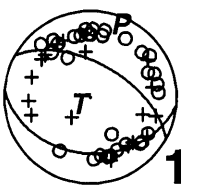

891231 0648
Z= 3.07 M=3.10

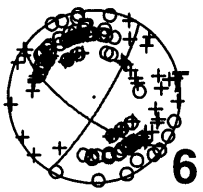

910910 1701
Z= 6.72 M=2.00

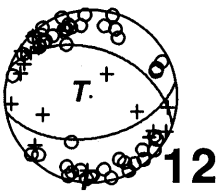

Appendix A.—Continued

THE LOMA PRIETA, CALIFORNIA, EARTHQUAKE OF OCTOBER 17, 1989:
EARTHQUAKE OCCURRENCE

AFTERSHOCKS AND POSTSEISMIC EFFECTS

RESPONSE OF REGIONAL SEISMICITY TO THE STATIC STRESS CHANGE PRODUCED BY THE LOMA PRIETA EARTHQUAKE

By Paul A. Reasenberg and Robert W. Simpson,
U.S. Geological Survey

CONTENTS

ABSTRACT

The Loma Prieta earthquake perturbed the static stress field over a large area of central California and greatly altered the levels of regional microseismicity. We have calculated the static stress changes produced on central California faults using elastic dislocation models of the Loma Prieta rupture. We used a Coulomb failure function (*CFF*) to describe the proximity of these faults to failure, and compared the calculated changes in *CFF* after the earthquake to observed changes in microseismicity rates on these faults. The pattern of stress changes on the major faults in the region that were predicted by our models of the earthquake agree closely with the pattern of changes in the regional seismicity rate observed after the earthquake. The agreement between stress change and seismicity change was detected at epicentral distances of up to 100 km. The agreement is best for models with low assumed values of apparent coefficient of friction ($0.1 \leq \mu' \leq 0.3$) on San Francisco Bay area faults. Both the stress models and the microseismicity observations suggest that stresses were increased on the San Francisco peninsula segments of the San Andreas fault northwest of the Loma Prieta rupture and on the creeping segments of the San Andreas fault southeast of the rupture. These results are consistent with an increase in the long-term probability of a large earthquake on the San Francisco peninsula segments of the San Andreas fault and with geodetic and surface creep-rate observations suggesting accelerated slip on the creeping section of the San Andreas fault southeast of the Loma Prieta earthquake.

The microseismicity observations suggest that the Hayward fault relaxed slightly after the Loma Prieta earthquake. The onset of the observed decrease in seismicity rate on the Hayward fault is poorly resolved, however, because the overall seismicity rate on the Hayward fault is low. In our stress models, the Hayward fault relaxes after the Loma Prieta earthquake because of the addition of small amounts of left-lateral shear to this right-lateral fault. This relaxation is small (a few bars or tenths of bars) and may already have been eroded by continuing tectonic loading. In our models, this relaxation could be countered at the southern end of the Hayward fault by the calculated increase in extensional normal stress that would tend to unclamp this part of the fault if friction is important. In one scenario, the inferred low values of apparent coefficient of friction and calculated stress changes could be the result of pore-fluid pressure changes in the fault zone that would work to diminish the effective normal stress changes initially. With time, as the pore fluids have a chance to re-equilibrate, these normal stress changes may become more effective, and the south end of the Hayward fault could be brought closer to failure. This scenario does provide a mechanism for the cross-bay triggering of a large earthquake on the Hayward fault. However, given the small magnitude of the calculated stress changes, such an earthquake on the Hayward fault would need to be nearly ready to happen in any event, and the changes in the already high long-term probability of a large earthquake on the Hayward fault have probably not been altered greatly.

INTRODUCTION

The Loma Prieta earthquake (M=7.1) was the largest earthquake to strike the Bay Area since the 1906 San

Francisco (M=8.3) earthquake (U.S. Geological Survey Staff, 1990). With an average slip of 2 meters over a 40-km-long rupture surface, the Loma Prieta earthquake profoundly altered the stresses in the crust throughout the Bay Area. An immediate concern after the earthquake was the possible effect this stress perturbation might have on other major faults in the Bay Area. Seventeen days after the Loma Prieta main shock, a magnitude 3.7 earthquake occurred on the Hayward fault about 85 km from the Loma Prieta epicenter. Although this was not a large event, it did cause some concern because on at least two occasions in the 1800's a large earthquake on one side of San Francisco Bay had been followed within 3 years by a second large earthquake on the opposite side of the bay (for example, Louderback, 1947, Ellsworth, 1990, Sykes and Jaumé, 1990).[1] Since earthquakes on the San Andreas and Hayward faults may have been involved in both of these pairings, there was a possibility that this magnitude 3.7 earthquake might be a precursor to a larger shock, and the question arose as to how the Loma Prieta rupture might have affected stress levels on other Bay Area faults. Could stress changes produced by the Loma Prieta earthquake trigger another large earthquake east of San Francisco Bay or on the San Francisco peninsula?

A working group convened by the U.S. Geological Survey considered in detail the effect of an increase in right-lateral shear stress on segments of the San Andreas fault north of the Loma Prieta earthquake rupture (Working Group, 1990). They concluded that the effect was to shorten the time to the next earthquake on these segments. Because this result was based largely on theoretical models and assumptions about fault behavior, it raised the following additional questions: Were these models and assumptions realistic and consistent with seismicity and other observations? What was the effect of the Loma Prieta earthquake on the Hayward fault? Did a scenario of cross-bay triggering of earthquakes seem plausible?

The location of the Loma Prieta earthquake within a complex section of the San Andreas fault system in central California and in a region monitored by a dense seismograph network was fortuitous. The network provided an enormous quantity of high-quality observations of the aftershock sequence from an area that includes several major active faults in the San Francisco Bay and Monterey Bay regions. These faults are currently loaded by stresses associated with the relative motion of the North American and Pacific plates, and many are constantly producing microearthquakes. When the Loma Prieta earthquake occurred, the level of seismicity on many of these faults suddenly changed, most by increasing. The changes in seismicity provided a natural, in situ indication of the stress changes acting at seismogenic depths on these faults.

Recently, other studies have suggested that changes in the regional stress produced by an earthquake may affect the hypocentral locations or focal mechanisms of its aftershocks. These include Stein and Lisowski (1983), Mavko and others (1985), Poley and others (1987), Oppenheimer and others (1988), Simpson and others (1988), Michael and others (1990), Rydelek and Sacks (1990), Seeber and Armbruster (1990), Michael (1991), and Reasenberg and Simpson (1992). Still others have suggested, through similar analyses, the possibility that stress changes produced by one or a series of earthquakes may be capable of triggering a comparable or larger earthquake on a neighboring fault (Hudnut and others, 1989, Sykes and Jaumé, 1990, Sykes and Jaumé, 1992, Harris and Simpson, 1992, Stein and others, 1992).

In this paper we examine the relationship between the regional changes in static stress produced by the Loma Prieta earthquake and the changes in seismic activity on the nearby faults in central California. To estimate the stress changes, we calculated the stresses produced within an elastic halfspace by slip on a set of model dislocation surfaces. (See Simpson and Reasenberg (1994) for a detailed description of the stress modeling procedures and results for this region using various possible fault structures and source models.) We examine the spatial pattern of the seismicity change and its relation to patterns of stress change predicted by our fault and dislocation models. Because several different faults are involved, we find that the seismicity observations are capable of partially constraining the stress and faulting models. Then, we examine the implications of the favored stress models for the potential for triggering another large earthquake in the Bay Area. Finally, we consider the aftershock-like temporal characteristics of the seismicity after Loma Prieta and find considerable variation among the many faults in the region.

REGIONAL STRESS CHANGES CAUSED BY THE LOMA PRIETA EARTHQUAKE

A detailed discussion of models used to calculate stress changes on other faults after the Loma Prieta earthquake is given in Simpson and Reasenberg (1994). For completeness, we will briefly present the method of calculation, the slip model used, and a definition of the Coulomb failure function (*CFF*).

Our calculations were based on dislocation theory in an elastic half-space (Erickson 1986, Okada, 1992). Central California faults were represented by alignments of vertical (and sometimes dipping) rectangular dislocation surfaces under the traces of major known faults (fig. 1). The

[1]The 1836 (M≈6.8) earthquake on the northern Hayward fault was followed in 1838 by an (M≈7.0) earthquake on the San Francisco Peninsula section of the San Andreas fault, and the 1865 (M≈6.5) earthquake, possibly on the Loma Prieta segment of the San Andreas fault, was followed in 1868 by an (M≈7.0) earthquake on the southern Hayward fault.

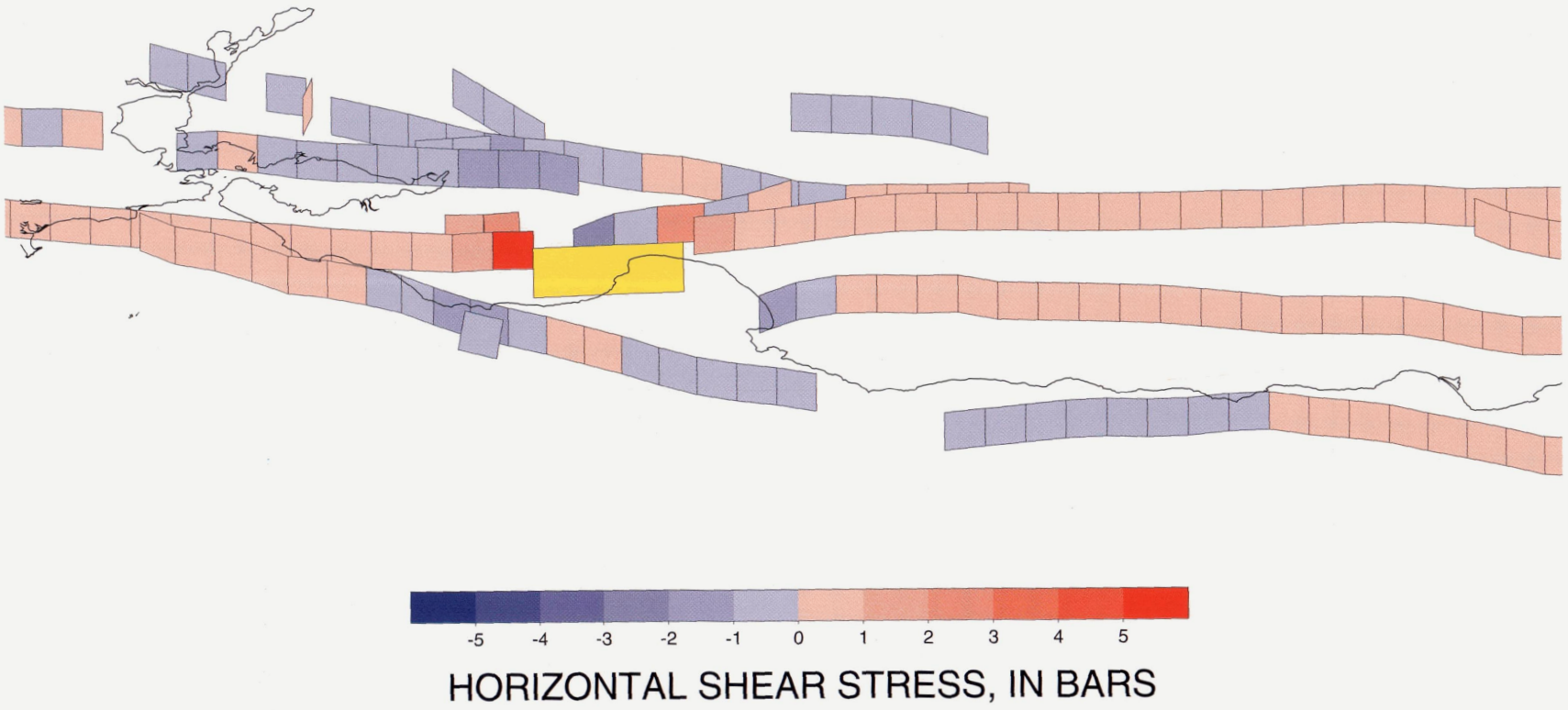

Figure 1.—Change in horizontal shear stress on each fault segment, calculated using Lisowski and others' (1990) model of the Loma Prieta rupture. Red colors indicate increased right-lateral shear; blue colors indicate decreased right-lateral shear.

vertical rectangles were 13 km tall and approximately 10 km long, and the stress changes were calculated at their centers, which lie at about the mean depth of seismicity in the Bay Area. Stress tensors were resolved into three components relative to the rectangular fault patches: a horizontal shear component, an up-dip shear component, and a normal component perpendicular to the surface.

To calculate the stress changes described in this paper, we used a slip model for the Loma Prieta rupture inferred by Lisowski and others (1990) from geodetic observations. Their slip model is a single, uniformly slipping, rectangular dislocation (shown in yellow in fig. 1) striking at N44°W, dipping 70°SW, and extending 37 km horizontally. It has its top at a depth of 5 km and its bottom at a depth of 17.5 km. Geodetically inferred right-lateral slip of 1.66 m and reverse slip of 1.19 m yield a moment of 3.0×10^{19} Nm. More complex models of the rupture slip distribution were also explored but do not substantially change the results of the analysis presented here.

In order to measure the change in the proximity to failure caused by changes in the shear and normal stress components, we defined a *CFF* based on the Coulomb-Ammonton failure criterion (for example, Jaeger and Cook, 1979):

$$CFF = |\bar{\tau}_P| + \mu(\sigma_P + p) - S, \tag{1}$$

where $|\bar{\tau}_P|$ is the magnitude of the shear stress acting on the surface, σ_P is the normal stress acting on the surface (positive for extension), p is the pore-fluid pressure in the medium, μ is the coefficient of friction, and S is the cohesion.

If we assume that the cohesion S and the coefficient of friction μ do not change before and after the Loma Prieta rupture, then the change in *CFF* becomes

$$\Delta CFF = \Delta|\bar{\tau}_P| + \mu(\Delta\sigma_P + \Delta p). \tag{2}$$

If the ambient shear stress acting on a surface is considerably larger than the increment added by the Loma Prieta earthquake, then the quantity $\Delta|\bar{\tau}_P|$ can be approximated by the component of Loma Prieta induced shear, denoted in the following as just $\Delta\tau$, in the direction of the ambient shear field. Armbruster and Seeber (1991) have used a similar quantity in their calculation of encouraging and discouraging stresses. Their assumption is that faults will generally slip in the same directions in which they have slipped previously, so that the appropriate component of shear stress to consider is the one in the direction of the rakes of past earthquakes. Because most of the vertical faults in the Bay Area are thought to be strike-slip faults, we have used the change in horizontal shear stress as the quantity of interest. Certain dipping fault patches discussed below have had ΔCFF calculated using assumed rake directions.

The quantity $(\Delta\sigma_P+\Delta p)$, which is the change in normal stress modulated by the change in pore-fluid pressure, is also referred to as the change in the effective normal stress.

We cannot calculate Δp without some additional assumptions. If the medium is homogeneous, then immediately after the earthquake (in the "undrained state" before the pore fluids have had time to re-equilibrate) the change in pore-fluid pressure can be represented as (Rice and Cleary, 1976)

$$\Delta p = -B\Delta\sigma_{kk}/3, \tag{3}$$

where B is Skempton's coefficient with value between 0 and 1, so that

$$\Delta CFF = \Delta\tau + \mu(\Delta\sigma_P - B\Delta\sigma_{kk}/3). \tag{4}$$

If fault zones are assumed to be formed of more compliant material, then Rice (1992) has shown that $\sigma_{xx}=\sigma_{yy}=\sigma_{zz}$ in the fault zone, so that

$$\Delta\sigma_{kk}/3 = \Delta\sigma_P \tag{5}$$

and

$$\Delta CFF = \Delta\tau + \mu(1-B)\Delta\sigma_P \tag{6}$$

For our analysis, we simplify the above possibilities by defining an apparent coefficient of friction μ' and writing ΔCFF as

$$\Delta CFF = \Delta\tau + \mu'\Delta\sigma_P. \tag{7}$$

For the homogeneous case,

$$\mu' = \mu(1 + \Delta p/\Delta\sigma_P), \tag{8}$$

and for the compliant fault zone case of Rice,

$$\mu' = \mu(1-B). \tag{9}$$

Values of B ranging from 0.23 to 0.99 have been reported for various rock types (Rice and Cleary, 1976, Roeloffs, 1988). A value of $B\approx0.73$ and a value of $\mu=0.75$ close to values observed in the laboratory yield an apparent coefficient of friction $\mu'=0.2$, consistent with correlations described below.

We explored correlations between ΔCFF and seismicity rate changes as a function of μ' by using equation 7.[2] Figures 1 and 2 show changes in shear stress and normal stress on the model fault segments. The normal stress changes will be most effective for high values of apparent coefficient of friction. Figure 3 shows the change in *CFF* for an assumed value of $\mu'=0.2$. Additional plots for other values of μ' are shown in the paper by Simpson and Reasenberg (1994).

REGIONAL SEISMICITY CHANGES AFTER THE LOMA PRIETA EARTHQUAKE

EARTHQUAKE DATA

To accurately measure the fluctuations in seismicity rate in the San Francisco Bay region we must first account for possible artificial rate changes in the catalog. Such artifacts may be produced by changes in the detection capability of the seismograph network or by changes in the way earthquake magnitudes are estimated. While significant growth in the network during the 1970's increased its sensitivity to the smallest earthquakes, the detection level in the study area since 1980 for earthquakes with magnitude 1.5 and larger has remained relatively constant.

Owing to the exponential distribution of earthquake magnitudes (Richter, 1958), the seismicity rate estimated from a magnitude-truncated sample is very sensitive to a systematic error in magnitude. For seismicity with a *b* value of 1, a systematic reduction of 0.1 magnitude units produces approximately a 21-percent apparent reduction in rate. A change in the network occurred in May 1977 when the amplification of certain elements in the Calnet network had been reduced. This change is believed to have introduced an artificial shift in the calculated magnitudes of earthquakes, which were determined from measurements of the coda waves that did not account for the amplification change. Systematic magnitude decreases of between 0.1 and 0.3 units, relative to the magnitudes listed in the Berkeley catalog, were detected by Habermann and Craig (1988) at around this time on the southernmost section of the Calaveras fault, the Sargent fault, and the San Juan Bautista section of the San Andreas fault. Our measurements show that the average rate of earthquakes located on these fault sections and listed in the catalog with magnitude $M \geq 1.5$ decreased 44 percent. This decrease in rate is equivalent to an artificial magnitude shift of 0.25 units when the *b*-value is 1, and is consistent with Habermann and Craig's estimate. No change in network operation affecting magnitude determination is known to have occurred since 1977.

To avoid these potential problems of stability with magnitude estimation and network sensitivity, we shall focus on the $M \geq 1.5$ earthquakes during the 10-year period 1979 to 1989 for our comparisons with the post-earthquake activity. These data represent the best years of the USGS network and provide a stable yardstick for assessing the Loma Prieta-induced changes in the regional seismicity.

On the whole, the pattern of earthquake activity after the earthquake resembles the pattern for the 10 years of seismicity before the earthquake (fig. 4). The major faults are clearly visible in both patterns as narrow alignments of epicenters. Other features that are clearly apparent in the 10-year pattern are also apparent, though perhaps not so obviously, in the shorter-duration postseismic period. Some areas appear to have reduced activity after the Loma Prieta earthquake, but it is difficult to assess this from figure 4 because the time intervals represented in the figure are unequal. In the next section we try to quantify these comparisons.

QUANTIFYING SEISMICITY RATE CHANGES

Because earthquakes occur at discrete locations and times, the concept of a continuously varying "level" of seismicity that parallels our concept of the stress field presents some problems of definition, especially in regions where seismicity is sparse. To compare the seismicity to the regional coseismic stress change we have calculated, we sought a quantitative measure of the seismic activity that would be sensitive to coseismic changes while remaining free from assumptions about the spatial nature and extent of the changes. We compared the average rate of earthquakes in small, overlapping subregions during two specified time intervals—one before and the other after the earthquake. Using the time of the Loma Prieta earthquake to define the intervals assures that the result will be sensitive to the average or DC changes occurring at that time. By finely subdividing the region with a uniform grid, we avoid imposing artificial spatial constraints, as would be introduced by the selection of a few arbitrary "boxes" or subregions, and we allow the spatial pattern of the seismicity change to reveal itself naturally.

We measured the regional coseismic change in seismicity rate using the statistic β, which is sensitive to a

[2]We also attempted to explore the degree of correlation between ΔCFF as defined by equation 4 and seismicity rate changes. In this attempt the degree of correlation was a function of both μ and *B*. The results were inconclusive, suggesting that either the data did not have enough resolving power to yield statistically significant values for both μ and *B* (which could happen because of the approximate parallelism of most Bay Area faults), or the hypothesis being tested in the form of equation 4, with constant values of μ and *B* everywhere, was not correct. Indeed, if equation 9 holds, then μ and *B* cannot be determined separately.

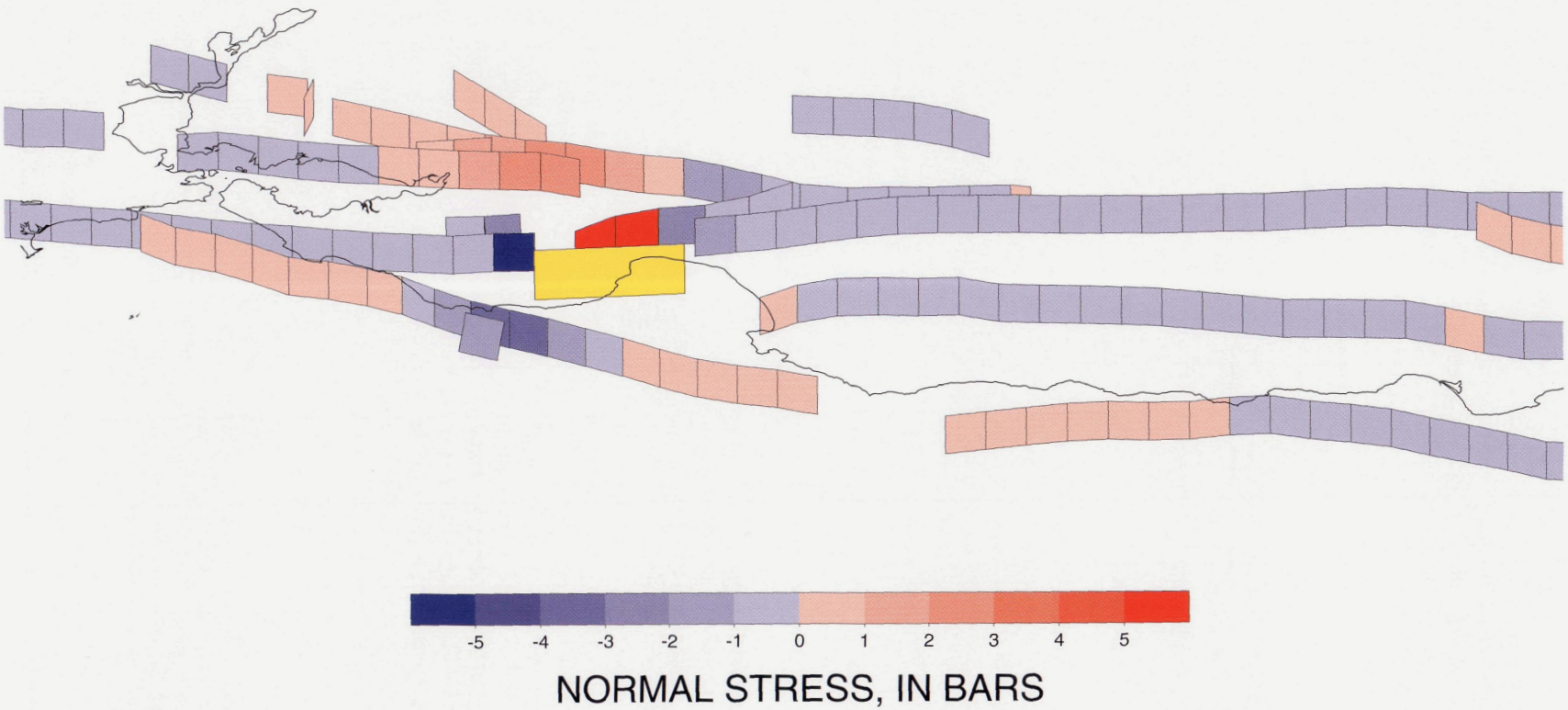

Figure 2.—Change in normal stress on each fault segment, calculated using Lisowski and others' (1990) model of the Loma Prieta rupture. Red colors indicate increased normal extensional stress; blue colors indicate increased normal compressional stress.

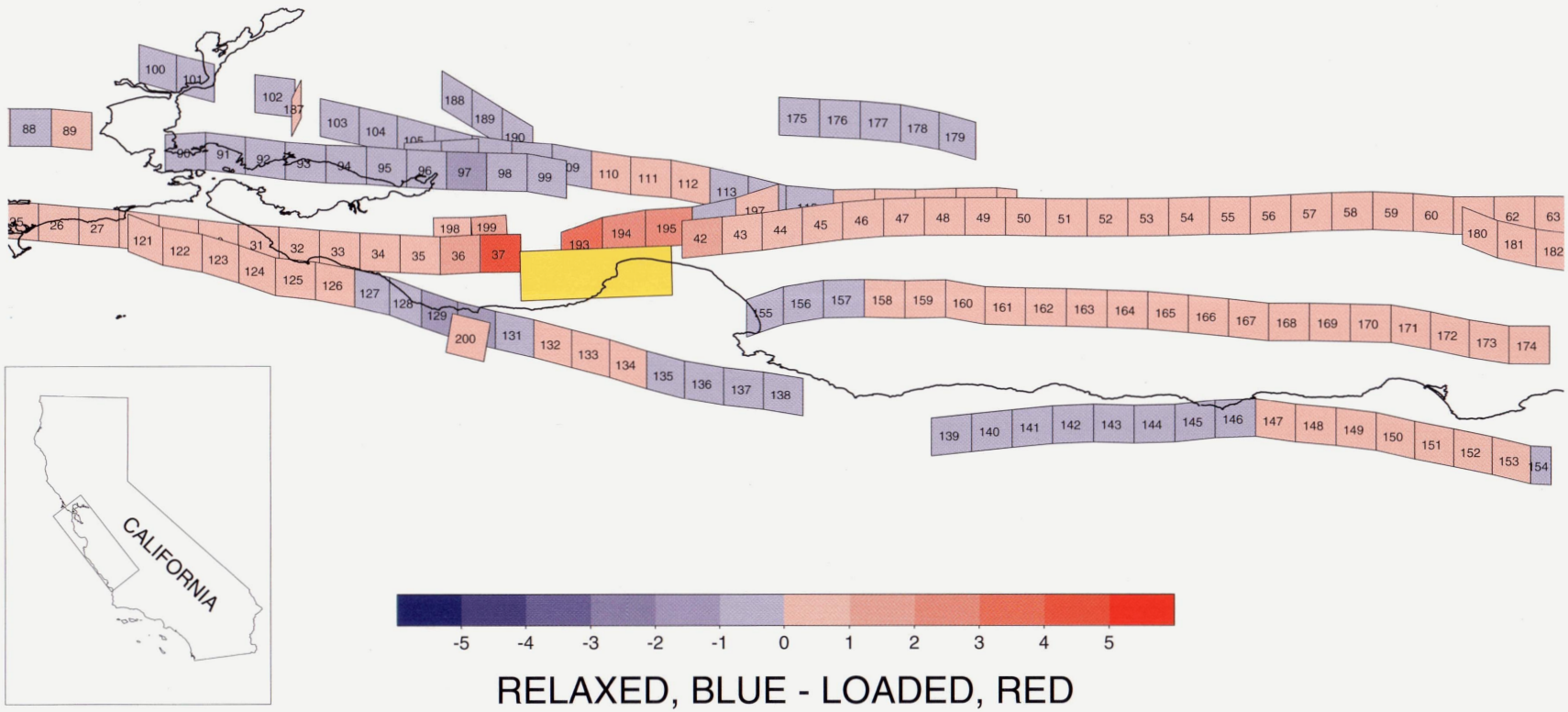

Figure 3.—Change in Coulomb failure function (*CFF*) produced by the Loma Prieta earthquake on rectangular segments representing faults in central California, calculated using Lisowski and others' (1990) model for the Loma Prieta rupture (yellow) derived from geodetic measurments. ΔCFF (in bars) on each fault segment for $\mu'=0.2$ is indicated by color. Segments with increased *CFF* (red) are more likely to produce earthquakes; segments with decreased *CFF* (blue), less likely. This oblique view is from the southwest and down at an angle of 45°. Inset map shows study area. Segment numbers are shown for reference in fig. 9.

contrast of average seismicity rate between two time intervals in a specified area (Matthews and Reasenberg, 1988). We compared the rate r_a in the postseismic interval of duration t_a with the rate r_b in the preseismic interval of duration t_b, where $r_a=n_a/t_a$, $r_b=n_b/t_b$, and n_a, n_b are the numbers of earthquakes occurring in the respective intervals. The rate change is expressed as

$$\beta(n_a, n_b, t_a, t_b) = \frac{n_a - E(n_a)}{\sqrt{var(n_a)}},$$

where *var* denotes variance and $E(n_a)=r_b t_a$ is the value of n_a expected under the null hypothesis of stationary random occurrence. The variance was represented by that of a binomial process: $var(n_a)=n_b t_a$.

We calculated β for fixed t_a and t_b in overlapping 10-km-square cells covering an area 140 by 390 km for the preseismic (background) period between 17 October 1979 and 17 October 1989 and postseismic period between 18 October 1989 and 31 May 1991 (fig. 5). Gaussian spatial smoothing with halfwidth 5 km was applied to the data in each cell to minimize artifacts introduced by the square gridding. Positive values of β indicate that the postseismic rate was higher than the background rate; negative values, lower than the background rate. Significance levels for |β| estimated from its asymptotic (Gaussian) distribution are 1.96 (p=0.05) and 2.57 (p=0.01).

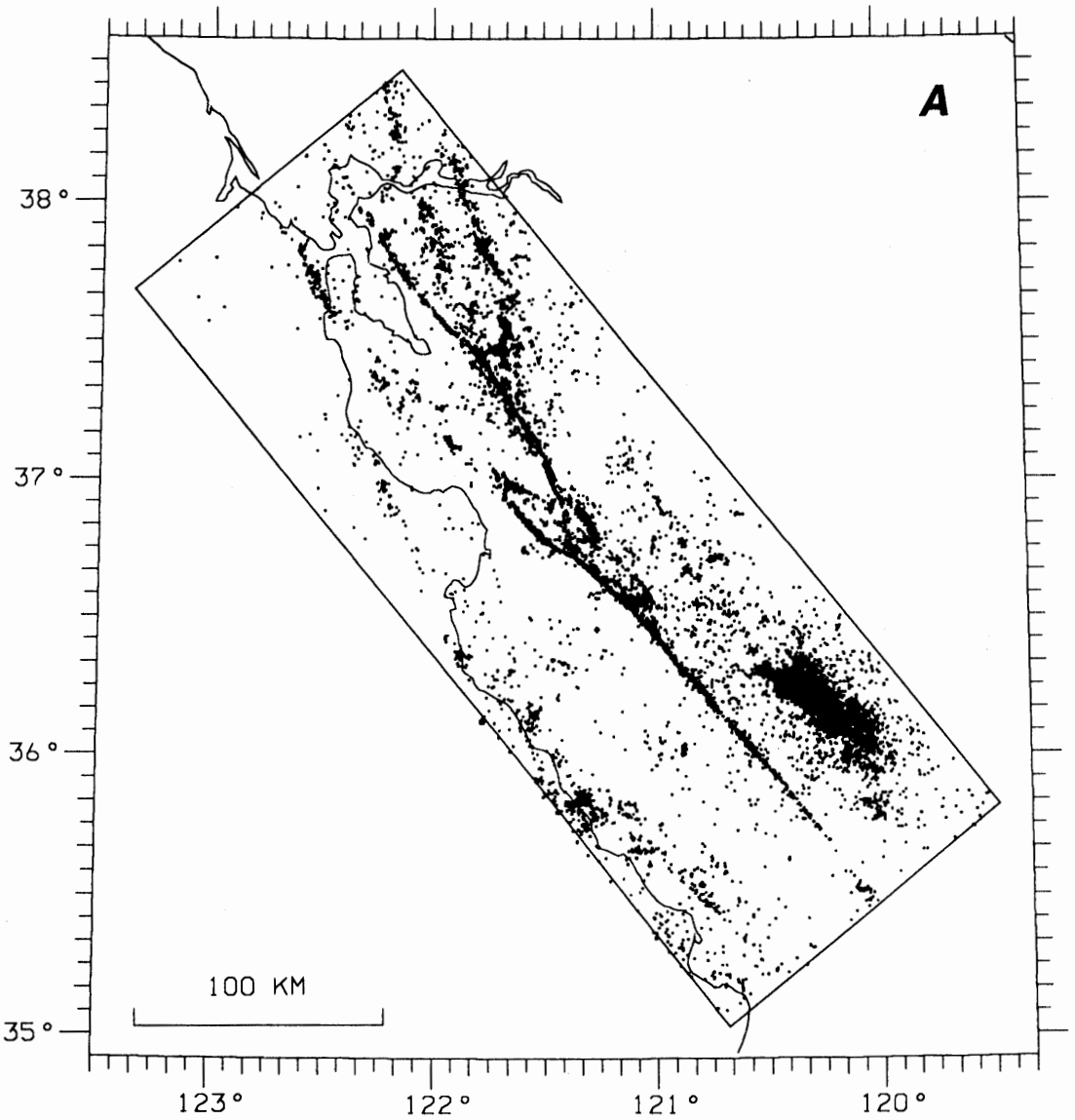

Figure 4.—Earthquakes (M≥1.5) located in the study area 10 years before and 20 months after the Loma Prieta earthquake. (*A*) Earthquakes occurring between 18 October 1979 and 17 October 1989. Some 21,000 events are represented. (*B*) Earthquakes occurring between 18 October 1989 and 31 May 1991. Approximately 5,000 events are represented.

An asymmetry in the definition of β introduces an ambiguity in its interpretation: a relatively low postseismic rate cannot be distinguished from an abnormally high preseismic rate, as would result, for example, from an earthquake swarm or aftershock sequence in the preseismic (background) period. This limitation stems from our use of the empirical background seismicity level as a reference level and presents an inherent difficulty in discerning rate changes in a finite sample of a point process.

In our measurements of San Francisco Bay region seismicity, several artifacts corresponding to the aftershocks of moderate earthquakes in the pre-Loma Prieta background period are apparent (fig. 5). These artifacts appear as dark blue patches and correspond to the 1979 Coyote Lake (M=5.9), 1980 Livermore (M=5.9), 1983 Coalinga (M=6.7), 1984 Morgan Hill (M=6.2), 1985 Kettleman Hills (M=5.5), 1986 Mt. Lewis (M=5.7), 1986 Quien Sabe (M=5.7) and 1988 Alum Rock (M=5.1) (Reasenberg and Ellsworth, 1982, Oppenheimer and others, 1990, Oppenheimer and others, 1988, Eaton, 1990).

We tried varying the choice of background period to avoid these artifacts. When the background is taken as 1969-1979, many of the aftershock zones that were blue in figure 5 became red (fig. 6), indicating that these aftershock sequences may not have fully decayed at the time of the Loma Prieta earthquake. New artifacts, including those associated with earthquake sequences near Danville in 1972, Bear Valley in 1972, and on the Busch fault in 1974, were introduced (Oppenheimer and others, 1990, Ellsworth, 1975, Lee and others, 1971).

We tried to reduce these artifacts by removing aftershocks from the catalog with a computer algorithm

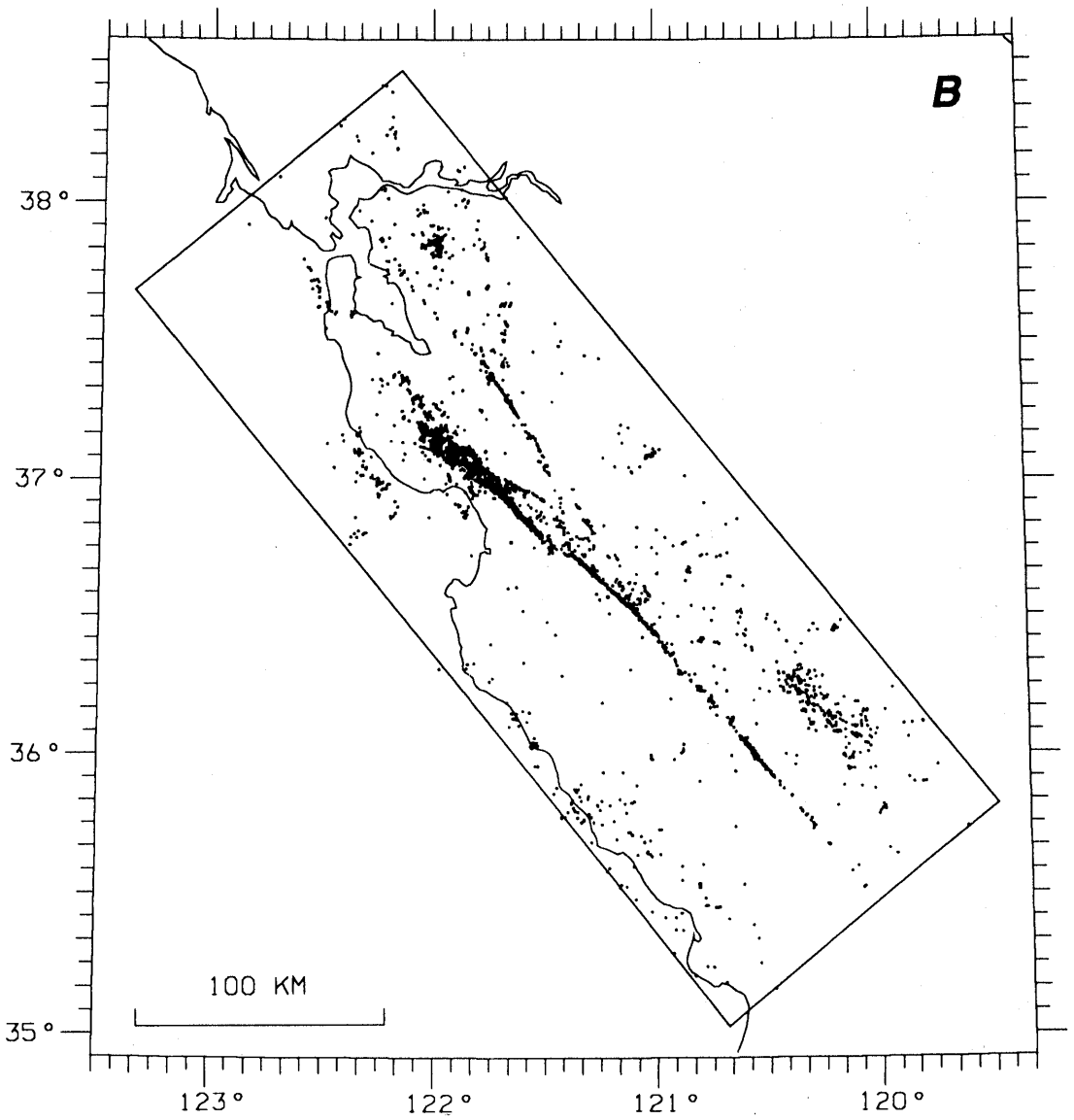

Figure 4.—Continued

(Reasenberg, 1985). Removal of aftershocks apparently eliminated some of the artifacts (for example, the 1983 Coalinga aftershock sequence), but may have only partially eliminated others (fig. 7). The low apparent postseismic rate ($-3 \leq \beta < 0$) remaining along the Calaveras and Mt. Lewis faults in figure 7 may reflect incomplete removal of aftershocks, and this possibility hampers interpretation of these features as postseismic effects.

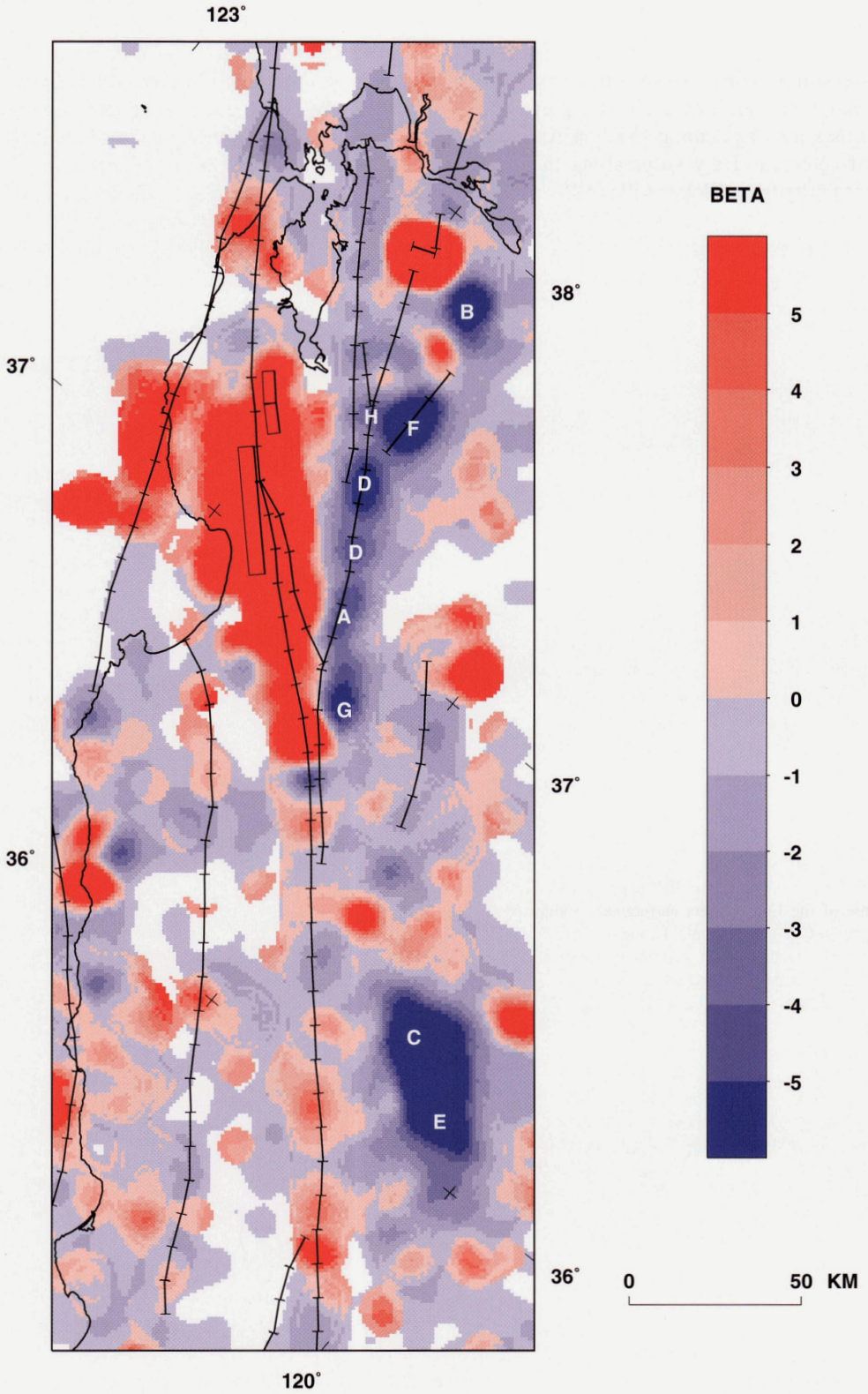

PATTERN OF SEISMICITY RATE CHANGES

Overall, the level of regional seismic activity after the Loma Prieta earthquake increased. The pattern of the increase was highly heterogeneous, with intense postseismic activity occurring on some parts of some faults, and little change or a decrease at comparable distance on others. Areas of high seismicity rate after the earthquake include the immediate aftershock zone (from Los Gatos to Watsonville); the San Francisco peninsula in an area of thrust faults near Los Gatos and along the San Andreas and San Gregorio faults near Daly City; along the San Andreas and Sargent faults from Watsonville to Bear Valley; a partially off-shore segment of the San Gregorio fault near Pt. Ano Nuevo; and along the Alamo fault, near Livermore. With the exception of the activity near Pt. Ano Nuevo, these areas generally coincide with fault segments having increased *CFF*. At Pt. Ano Nuevo, segments 129, 130, and 131 experienced sizable seismicity rate increases and calculated decreases in $CFF(\mu')$ for all values of apparent friction.

Increases in seismicity relative to background activity levels were greatest close to the Loma Prieta rupture, along the San Andreas and Sargent faults (fig. 8). The apparent "S" shape of the area of most intense increase reflects relatively deep activity (below 10 km depth) along the center and northwest parts of the rupture and shallower activity on the southeast part of the rupture and on the Sargent fault (see Dietz and Ellsworth, this volume, for detailed views of the spatial distribution of the aftershocks).

At somewhat greater distances, the apparent disagreement between the seismicity and calculated stress changes near Pt. Ano Nuevo suggested to us that our model for the San Gregorio fault may be inaccurate and prompted us to explore alternate fault models. Because this seismic activity is largely offshore, the ability of the network observations to constrain the fault plane solutions for these earthquakes is somewhat limited. Nevertheless, the set of focal mechanisms obtained for 133 earthquakes occurring between 1984 and 1991 shows a trend of oblique right-lateral thrust solutions (median rake of 120° aligned subparallel to the San Gregorio fault (with approximate strike N20°W) and dipping northeast between 50° and 80°. As illustrated by the dipping segment (200) adjacent to segment 130, such thrust mechanisms would be favored in this vicinity (fig. 3). R. Jachens and A. Griscom (written commun., 1992) report that aeromagnetic data suggest a 50–60 degree northeastward dip for the onland part of the San Gregorio fault and its offshore extension to the south.

Areas that experienced an apparent decrease in seismicity rate after the Loma Prieta earthquake include the southern Calaveras, Hayward, southern Rodgers Creek, and Mt. Lewis faults. These fault segments also have relaxed stress ($\Delta CFF<0$). As discussed in the previous section, however, the effects of other strong aftershock sequences before 1989 preclude unambiguous interpretation of the negative values of β obtained along the southern Calaveras and Mt. Lewis faults in terms of postseismic effects. The Hayward fault, however, was essentially free of significant swarm and aftershock activity during the 1980's (compare fig. 5 and fig. 6). Consequently, the apparent low postseismic rate observed there (strongest on the southern Hayward fault), is not believed to be an artifact, and may be related to the Loma Prieta earthquake. This low postseismic rate is also consistent with an observed slowdown in creep rates on the Hayward fault reported by Galehouse (this chapter) and by Lienkaemper and others (1989, 1991).

◀ Figure 5.—Changes in seismicity rate statistic β in central California occurring at the time of the Loma Prieta earthquake. Values of β (color) compare average rates in the intervals 17 October 1979 to 17 October 1989 and 18 October 1989 to 31 May 1991. Areas that experienced a co-seismic increase or decrease in seismicity rate are shown as red or blue, respectively; areas with insufficient earthquakes for determination of β are white. Absolute value of β indicates the statistical significance of the rate change, taking into account the variance of the background seismicity. Major faults and coastline are indicated by solid lines. Main shock rupture and fault segments 198 and 199 appear as rectangles due to projection of dipping planes onto surface (see fig. 3). The large bright red area includes the Loma Prieta aftershock zone. Values of β in the area close to the rupture greatly exceed 5, but are truncated by color scale (see fig. 8). Bright blue patches along and northeast of the Calaveras fault are artifacts corresponding to strong aftershock sequences that occurred during the background interval, and do not indicate Loma Prieta-related postseismic effects. A, 1979 (M=5.9) Coyote Lake earthquake; B, 1980 (M=5.9) Livermore earthquake; C, 1983 (M=6.7) Coalinga earthquake; D, 1984 (M=6.2) Morgan Hill earthquake; E, 1985 (M=5.5) Kettleman Hills earthquake; F, 1986 (M=5.7) Mt. Lewis earthquake; G, 1986 (M=5.7) Quien Sabe earthquake; H, 1988 (M=5.1) Alum Rock earthquake.

COMPARISON OF REGIONAL STRESS AND SEISMICITY PATTERNS

To investigate the overall dependence between the modeled stress changes and the observed seismicity, we compared, for each fault segment S_j, the mean seismicity rate change index $\overline{\beta}_j$ corresponding to the subset of cells within 5 km of segment S_j to the coseismic static stress change $\Delta CFF_j(\mu')$ calculated on that segment, for various assumed values of the apparent coefficient of friction μ'. We used values of β obtained with aftershocks removed for the background period 1979-1989. We show one of the better fitting comparisons (for μ'=0.2) in figure 9. For this value of the apparent coefficient of friction, concordant changes in stress and seismicity (both increase or both decrease) occurred on 87 fault segments, discordant changes occurred on 54 segments, and a generally

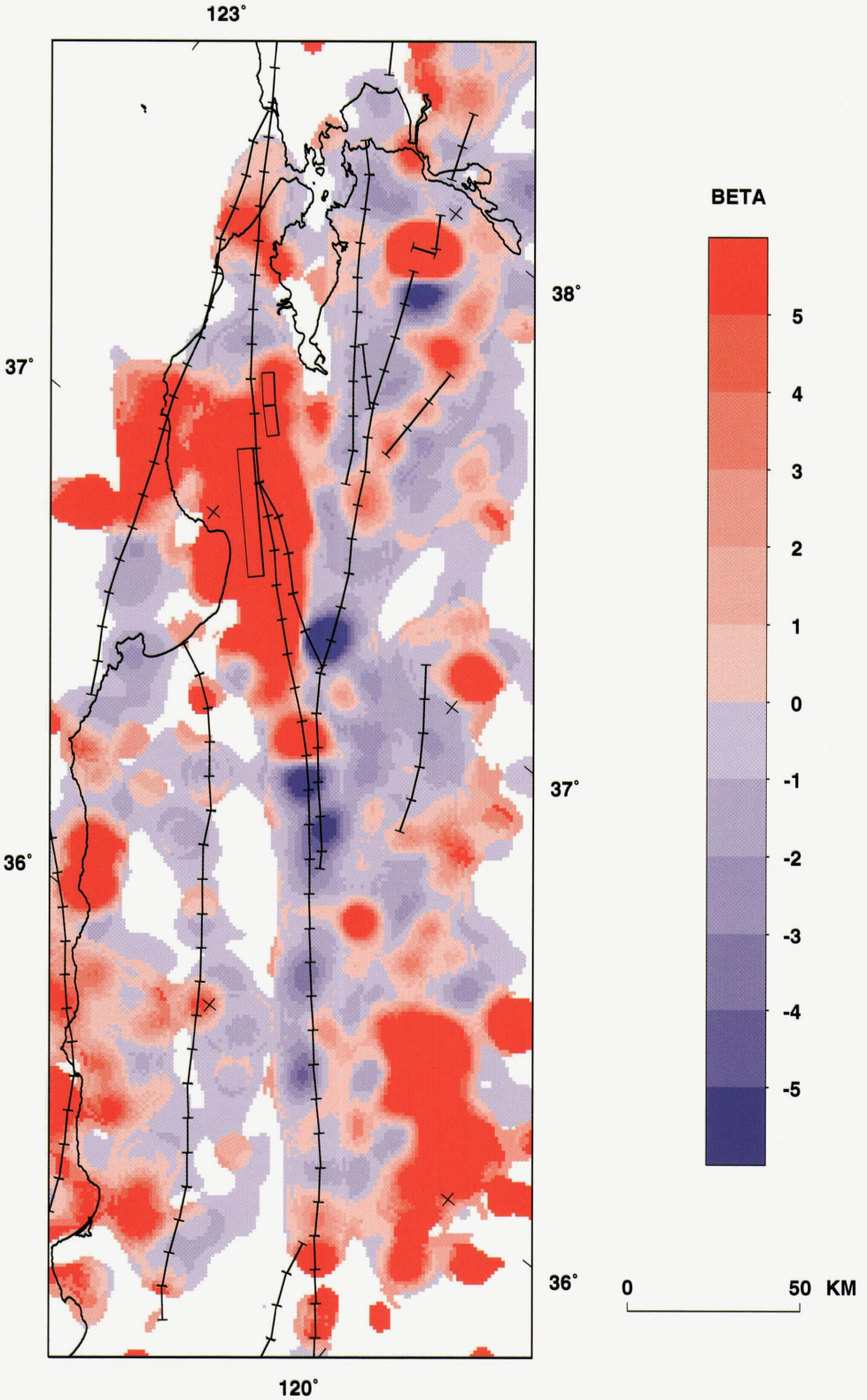

Figure 6.—Changes in seismicity rate, represented as in figure 5, except that the preseismic interval is chosen here to be between 18 October 1969 and 17 October 1979. Switching to this earlier background interval avoids many energetic aftershock sequences in the 1980's. Apparently, however, many of these same areas remain at elevated seismicity levels (red patches), compared to the levels of the 1970's, indicating that these aftershock sequences are not yet over.

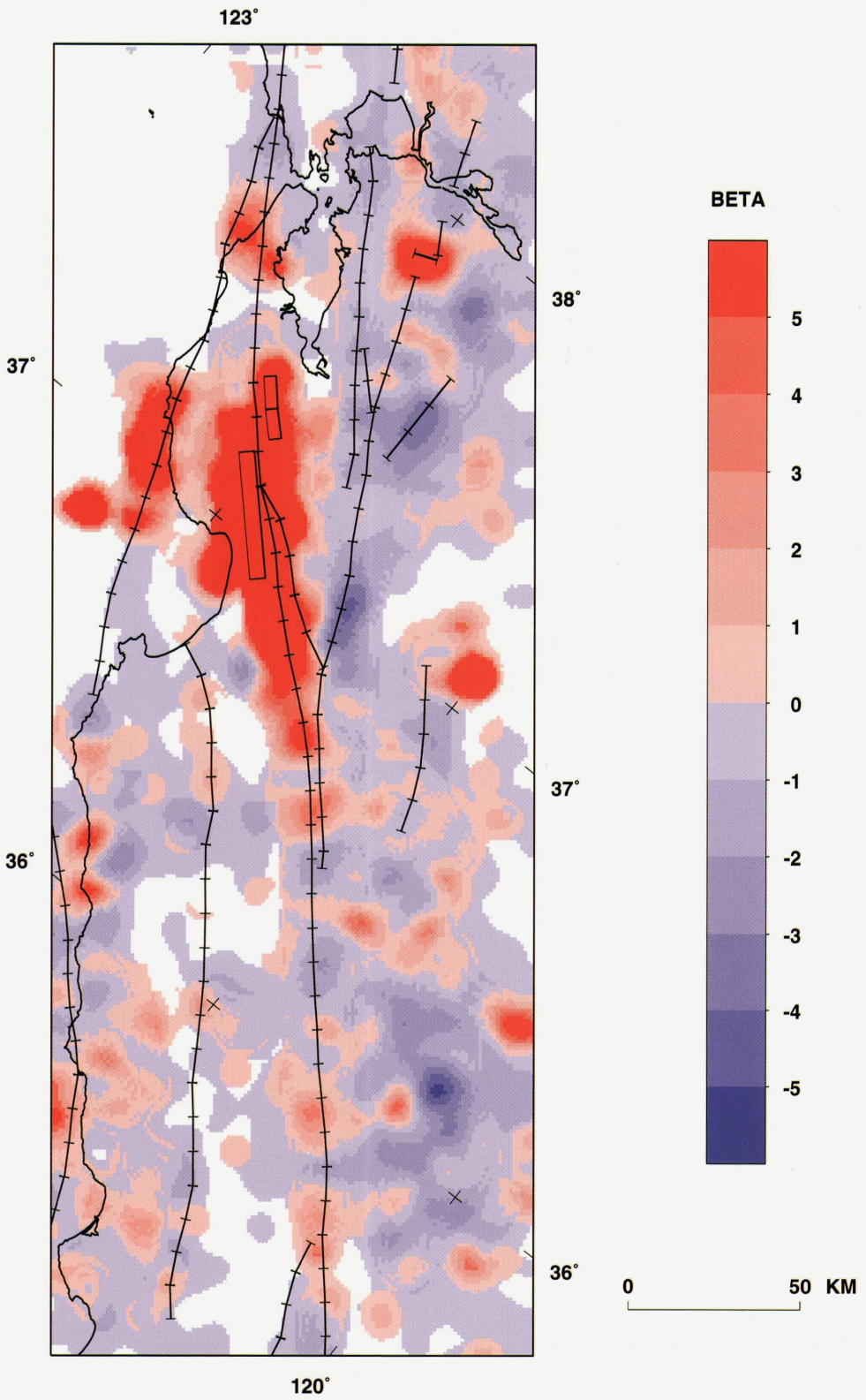

Figure 7.—Changes in seismicity rate, represented as in figure 5 (with background period 1979 to 1989) except that identified earthquake clusters have been removed from the catalog. While removing the clusters reduces the effects of aftershock sequences in the background period, some residual aftershock activity apparently remains, preventing unambiguous interpretation of the postseismic rates in these areas. The depressed rate along the southern part of the Hayward fault, however, is apparently not affected by such aftershock-related artifacts; it is blue in all three representations of the postseismic rate change (figs. 5 to 7).

positive correspondance between $\overline{\beta}$ and ΔCFF is visually apparent.

To quantify the agreement between stress change and seismicity rate change we used the chi-squared statistic in conjunction with a fourfold table. The fourfold table (see, for example, Sachs, 1982) allows a comparison of four relative frequencies, f_1, f_2, f_3, f_4, each representing a subset of the fault segments in our model. In the table, f_1 is the number of fault segments for which $\Delta CFF>0$ and $\beta>0$, f_4 is the number of fault segments for which $\Delta CFF<0$ and

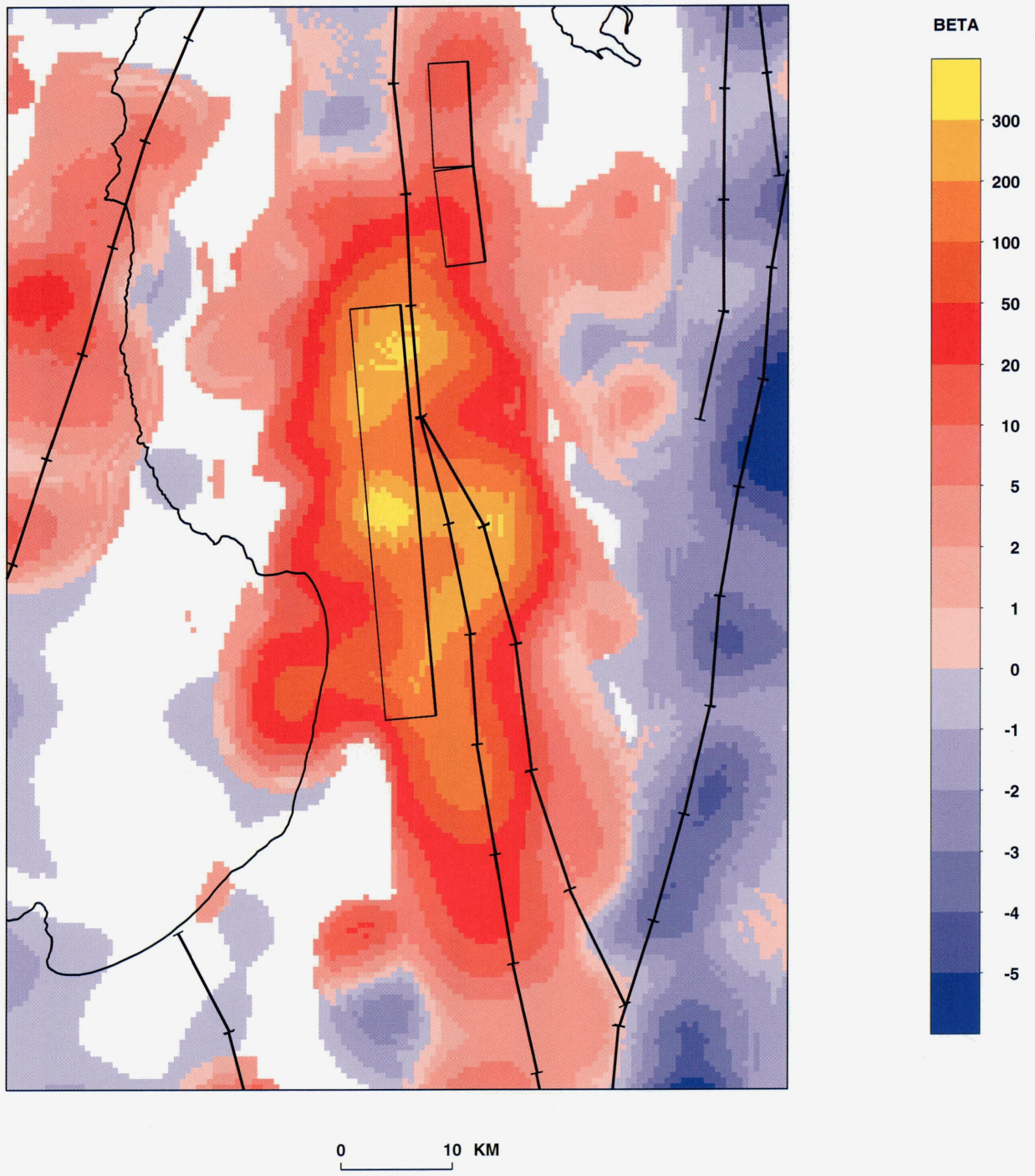

Figure 8.—Changes in seismicity rate in the Loma Prieta aftershock zone relative to the background rate, calculated as in figure 5 but with the full positive range of values of beta shown. Intense increases in seismicity (yellow) near the center and northwest end of the rupture are relatively deep (10 to 18 km depth). Intense aftershock activity is shallower on the Sargent fault and near the southeast end of the Loma Prieta rupture, near the site of the 18 April 1990, M=5.2 Chitenden aftershock.

$\beta<0$, and f_2 and f_3 correspond to the numbers of segments with opposing (different sign) changes of stress and seismicity. High values of χ^2 correspond to high values of f_1 and f_4, low values of f_2 and f_3 and positive correlation between the stress and seismicity rate change. Significance levels for χ^2 are 3.84 (p= 0.05), 6.64 (p=0.01), and 10.83 (p=0.001). An advantage of this formulation of chi-squared is that it makes no assumptions about the functional relationship betweeen the stress changes and seismicity changes, except that they be of the same sign to be in agreement.

Application of the χ^2 test to all 141 fault segments represented in figure 9 rejects the null hypothesis that β and $\Delta CFF(\mu')$ are independent ($p<0.001$ for $0.2\leq\mu'\leq0.3$; $p<0.01$ for $0.1\leq\mu'\leq0.4$) (fig. 10*A*). The correlation coefficient ρ attains its maximum value for $\mu'=0.2$ and exceeds 0.5 for $0.1\leq\mu'\leq0.3$ (fig. 10*B*).

Many of the points plotted in figure 9 indicate absolute changes in stress or seismicity on individual segments comparable to the uncertainties associated with modeling errors (stress) and stochastic variance (seismicity). When the χ^2 and correlation tests were applied to a subset of the fault segments with significant changes in stress and seismicity (numbered points in fig. 9), similar results were obtained (fig. 10). χ^2: $p< 0.01$ for $0.1\leq\mu'\leq0.4$; correlation: ρ exceeds 0.5 for $0.0\leq\mu'\leq 0.3$.

Static stress changes as small as a few tenths of a bar apparently produced detectable changes in seismicity (fig. 11). This level of stress change is about one order of magnitude larger than that of tidally induced stress changes (Heaton, 1982, McNutt and Heaton, 1981, Stacey, 1977) and is comparable to stress changes produced at seismogenic depths by the filling of water reservoirs (Roeloffs, 1988).

The response of seismicity to static stress changes produced by the Loma Prieta earthquake decreases with distance from the rupture and is statistically undetectable (at the p=0.05 level) at distances beyond 80 to 100 km; at this distance the maximum absolute value of ΔCFF is approximately 0.1 bar. To determine this, we calculated χ^2, taking $\mu'=0.2$, for subsets of segments in various ranges of distance from the center of the earthquake dislocation. χ^2 is maximum ($\chi^2>21$) for the 80 segments between 0 and 100 km from the source; χ^2 just fails to exceed the p=0.05 critical point for the farthest 70 segments located 80 or more km from the earthquake. For comparison of this distance range to that of other earthquakes, we calculate that static stress changes of 0.1 bar are produced by M=3 earthquakes at hypocentral distances of approximately 0.4 km, and by M=5 earthquakes at distances of approximately 7 km on favorably oriented planes. Thus, small earthquakes close to the fault segment may have an equally

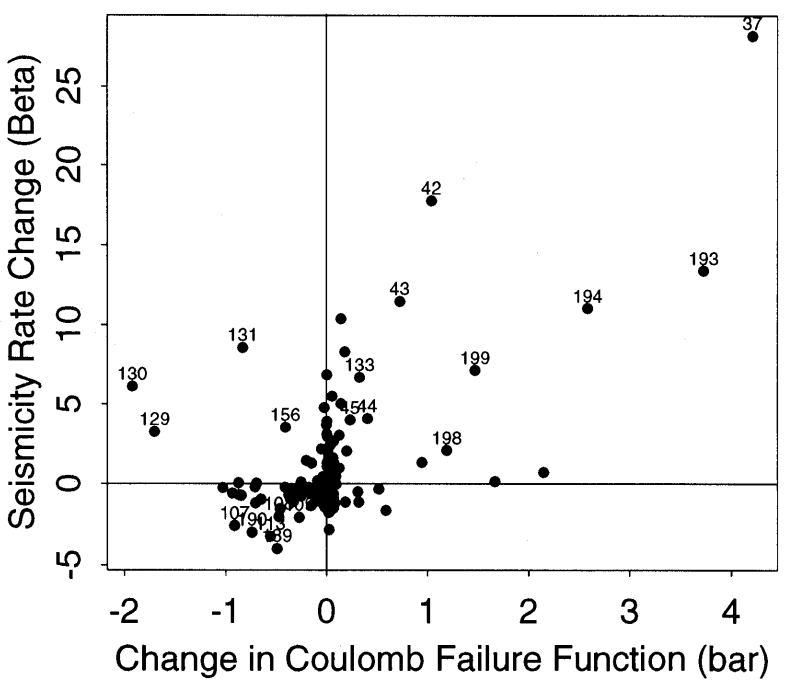

Figure 9.—Seismicity change β and stress change ΔCFF(μ') calculated on 141 model fault segments, assuming $\mu'=0.2$. Numbers (refer to fig. 3) indicate segments experiencing the largest changes ($|\bar{\beta}_j|\geq2$ and $|\Delta CFF_j|\geq0.2$ bar).

intense, but spatially limited, effect on seismicity rate as do large, distant earthquakes.

In a speculative vein, the apparent sensitivity of the central California seismicity to small stress changes suggests that, in general, fluctuations in regional seismicity might also reveal regional, aseismic slip events such as earthquake afterslip, slow earthquakes, slip on the ductile portion of vertical faults, and slip on horizontal detachment surfaces. The feasibility of monitoring the seismicity to infer aseismic strain events obviously would depend on both the sensitivity of the seismic network and the overall level of regional seismicity, and it would certainly be an enormous challenge to future modelers to constrain the location and source parameters of such events solely from seismicity data. There are some suggestions of largely aseismic strain events in the year before Loma Prieta. Galehouse (this volume), in his creep data from the Hayward fault, finds evidence of slowdowns at various sites ranging from 0.3 to 3.6 years before the Loma Prieta earthquake. Gladwin and others (this volume) report the beginning of a shear strain change at a tensor strainmeter near San Juan Bautista in mid-1988.

TEMPORAL CHANGES IN SEISMICITY CAUSED BY THE LOMA PRIETA EARTHQUAKE

Up to this point we have considered the change in regional seismicity as a coseismic step change in rate in order to facilitate comparison to our calculated step changes in stress. Having seen that the sense of change in seismicity and stress agree in many areas, we now focus on the time dependence of the seismicity rate in some of these areas. The time-dependent part of the response of seismicity to the regional stress change may help constrain present and future models of fault behavior and regional deformation.

In this section we examine the rate of $M>1.5$ earthquakes in several geographical zones as a function of time. We defined the zones to be large enough to contain sufficient earthquakes for a statistically significant analysis, yet small enough to resolve areas that appear to have responded coherently to the Loma Prieta earthquake. The

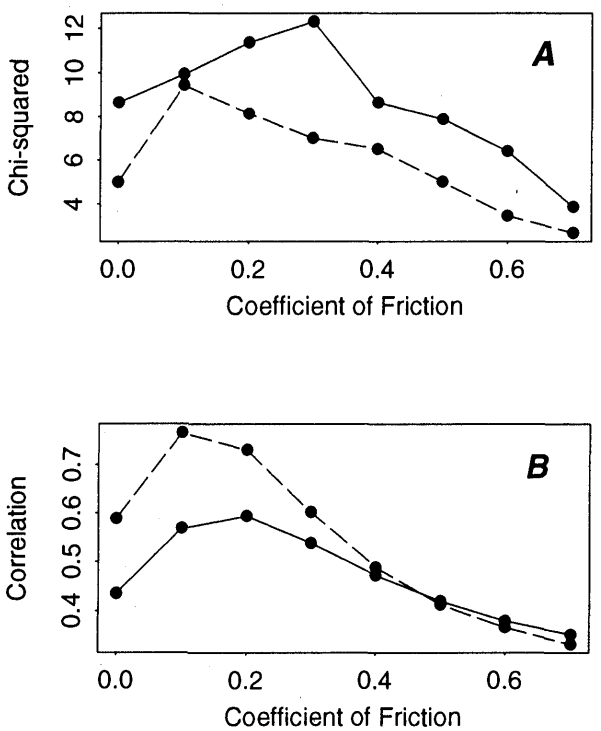

Figure 10.—Measures of agreement between stress changes and seismicity changes on fault segments, shown as a function of the apparent coefficient of friction μ' assumed for the stress calculations. Solid lines, all 141 fault segments; broken lines, fault segments experiencing significantly large changes (numbered points in fig. 9). (*A*) Chi-squared vs. friction. Chi-squared confidence levels are 6.64 (p=0.01) and 10.83 (p=0.001). (*B*) Correlation vs. friction.

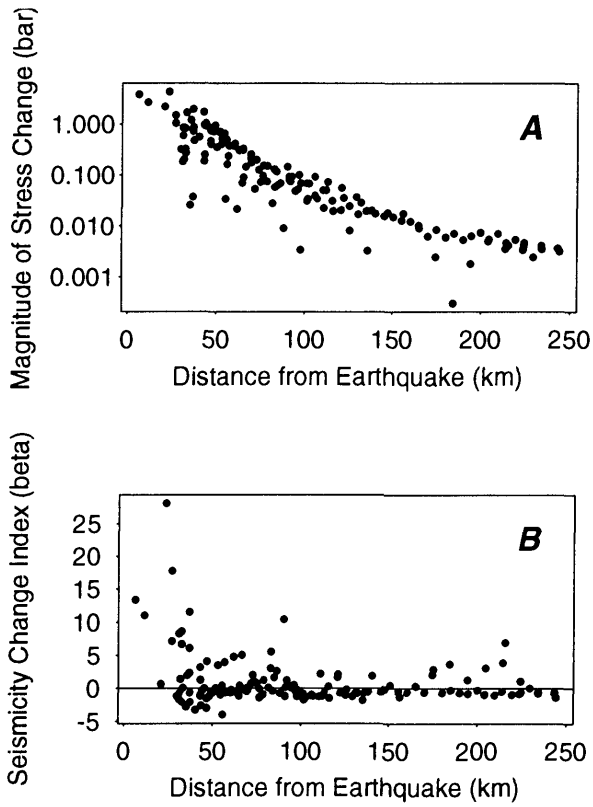

Figure 11.—Absolute levels of stress change and seismicity rate change on individual segments, shown as a function of segment distance from the earthquake epicenter. (*A*) Calculated stress changes (for assumed value of apparent coefficient of friction μ'=0.2). (*B*) Observed seismicity rate change statistic, β. Significant correlation between the stress changes and seismicity rate changes was observed at distances up to 100 km.

zones are defined in terms of subsets of the model fault segments shown in figure 3 and include all $M>1.5$ earthquakes within 5 km of any segment in the subset (table 1). There is a small amount of geographical overlap among the zones. For each zone, we calculated the rate of earthquakes in 30-day, non-overlapping intervals between January 1979 and March 1992 (fig. 12). The choice of 30-day intervals for our rate estimates was subjectively made to provide a balance between resolution and accuracy.

Seismicity during the preseismic period in all zones appears to occur at more or less constant rates punctuated by bursts of activity. For example, the largest four bursts of seismicity along the creeping section of the San Andreas fault (Zones 2N and 2S) before the Loma Prieta earthquake are associated with moderate (M=4.4 to M=4.7) earthquakes near Fremont Peak in April 1980 and near Bear Valley in August and September 1982, May 1986 and July 1988 (fig. 12, table 2). The lower average preseismic rates in the other zones are similarly punctuated by smaller clusters involving smaller earthquakes.

The change in seismicity rate after the Loma Prieta earthquake varied significantly from zone to zone (table 1). For a rough measure of these differences we compared, for each zone, the change in seismicity rate between the 10-year preseismic and 20-month postseismic periods. Of course, the seismicity rates varied greatly during this postseismic period, so our results depend strongly on the choice of intervals, but they serve for comparison. Along the southern portion of the creeping section of the San Andreas fault (zone 2S) the relatively high background rate of 0.58 events/day increased 50 percent after the Loma Prieta earthquake, while farther north and closer to the rupture (zone 2N) the rate increased sevenfold. Within the aftershock zone proper (zone 1) seismicity rate increased nearly twentyfold, and on the southern San Francisco peninsula (zone 3), seismicity rate increased threefold.

We modeled the seismicity in each zone during the background period as a homogeneous (constant rate) Poisson process. While these models generally are not very well fit (in a least-squares sense) by the seismicity rate data due to the presence of bursts of aftershocks, they provide convenient and well-defined reference levels for comparison to the postseismic period. Seismicity rate immediately after the Loma Prieta earthquake in zones 1 to 4 abruptly increased and then decayed in an aftershock-like manner. Accordingly, we modeled the seismicity rate for the postseismic period in zones 1 through 4 as a nonhomogeneous Poisson process with rate $N(t)$ obeying the modified Omori's law (Utsu, 1971):

$$N(t)=\frac{K}{(t+c)^p},$$

where t is time after the main shock, and K, c, and p are positive constants. We estimated these model parameters separately for the seismicity in each zone with a maximum likelihood method (Ogata, 1983) (fig. 13). These models generally provided excellent fits to the first 100 days of data but were incapable of modeling the complexity in seismicity rate in zones 1 and 2N resulting from the strong secondary aftershock sequence that followed the M=5.6 aftershock near Chittenden on 18 April 1990. For these zones, we fit Omori models for the intervals 18 October 1989 to 17 April 1990 (table 1); in zones 3 and 4, data between 18 October 1989 and 31 March 1992 were used.

Our power-law models for the aftershock zone, the southern San Francisco peninsula, and the northern part of the creeping San Andreas fault all have p-values close to the mean value of p previously found for California aftershock sequences of 1.07±0.2 (±1σ) (Reasenberg and Jones, 1989) (fig. 13, table 1). Our model for the decay of seismicity rate on the San Gregorio fault based on earthquakes mostly occurring near segments 131 to 134 is not well constrained, owing to the overall low level of the seismicity response there, and the absence of recorded aftershocks during the first day of the sequence. While the estimate for p there (0.62±0.15) is lower than the California average, these data are too sparse to justify interpreting this model.

From the Omori models and observations of the long term background rates we estimated times at which the seismicity rate in each zone will return to the pre-Loma Prieta level. We defined the end of elevated-rate period as the time when the Omori model rate equals the 1979-1989 background rate. We found that in the aftershock zone (Zone 1) elevated activity will have ended between 1991.3 and 1992.9. The activity on the northern creeping section of the San Andreas fault will have subsided to normal between 1990.4 to 1992.0, and activity on the San Francisco peninsula will have returned to normal between 1990.5 and 1991.3 (table 1). Because the levels of both aftershock activity and background activity vary spatially, our models (and, consequently, these estimates) depend on the particular zones we have used. The zones group together shallow and deep earthquake activity and include multiple fault strands. As a consequence, our results represent subregional averages. In contrast, Dietz and Ellsworth (this chapter) have applied a similar analysis to the seismicity located within approximately 30 km from the main shock epicenter, using $M\geq 1$ earthquakes in smaller and more complexely defined zones, and find significant variations in temporal decay of the aftershock activity associated with specific fault structures.

The post-Loma Prieta seismicity rate along the Hayward fault (zone 5) is the lowest among the regions we have considered, and the coseismic change there was a rate

Table 1.—*Summary of seismicity in selected zones*

Zone	Region	Fault Segments (1)	Preseismic Rate (2) (Events/Day)	Postseismic Rate (3) (Events/Day)	K (Events/Day)	p	c (day)	Return to Preseismic Rate (Years)
1	Aftershock Zone	37–42, 193–195	0.07	1.3	75 ± 7	0.90 ± 0.02	0.21 ± 0.07	6.9 ± 1.5 (4)
					121 ± 20	1.12 ± 0.05	0.57 ± 0.16	2.3 ± 0.3 (5)
2N	Creeping SA fault (Northern Section)	42–44	0.15	1.15	22.1 ± 2.5	0.60 ± 0.02	0.09 ± 0.09	11.2 ± 3.8 (4)
					55.6 ± 16	0.95 ± 0.08	1.1 ± 0.56	1.4 ± 0.8 (5)
2S	Creeping SA fault (Southern Section)	45–50	0.58	0.88	—	—	—	—
3	Southern S.F. Peninsula	32–37, 198–199	0.08	0.27	10.3 ± 1.7	0.81 ± 0.04	0.02 ± 0.04	1.1 ± 0.4
4	San Gregorio fault	128–134	0.02	0.08	2.1 ± 1.8	0.62 ± 0.15	1.83 ± 7.73	7.4 ± 17.4
5	Hayward fault	90–99	0.11	0.06	—	—	—	—
			0.12 (6)	0.07 (7)	—	—	—	—

1. Earthquakes within 5 km of any of the fault segments were used.
2. Mean rate in the 10-year interval 17 October 1979 to 17 October 1989.
3. Mean rate in the 20-month interval 18 October 1989 to 31 March 1992.
4. Model fit to the interval 18 October 1989 to 31 March 1992.
5. Model fit to the interval 18 October 1989 to 17 April 1990.
6. Mean rate in the interval 17 October 1979 to 1 January 1988.
7. Mean rate in the interval 1 January 1988 to 31 March 1992.

decrease, which is inherently more difficult to detect than a rate increase. As a result of these differences, the Hayward fault seismicity rate record is particularly difficult to interpret, and the changes we infer for the Hayward fault are less certain than those for the other zones. After the Loma Prieta earthquake, the seismicity rate on the Hayward fault is about half the rate during the 10-year background period (fig. 12, table 1). In a previous section we interpreted this reduction in rate as support for our stress models. However, the Hayward activity appears to have undergone its most prominent rate decrease around the beginning of 1988, after which time the rate averages 0.07 events/day and does not exceed 0.17 events/day. This decrease, also on the order of 50 percent, coincides roughly with the times of observed decreases in right lateral creep rates between May 1988 and June 1989 at four of five alignment arrays situated along the Hayward fault (Galehouse, 1990, 1992; also, this chapter). While there is considerable uncertainty in the onset times of both our seismicity rate decrease and Galehouse's creep rate reductions, their approximate coincidence suggests a connection and raises the possibility that a separate episode of relaxation on part of the Hayward fault may have begun in this period before the Loma Prieta earthquake. When compared to the relatively low-rate period starting in 1988, the post-Loma Prieta seismicity still shows a decrease, although the size of the decrease is naturally smaller than it is in comparison to the 10-year background period. A possible interpretation of the Hayward fault seismicity is that two relaxation events may have occurred–one related to the 1988-1989 creep retardation and the other related to the Loma Prieta earthquake.

During the period since the Loma Prieta earthquake, the seismicity rate on the Hayward fault has increased slightly (fig. 12). We attempted to model this increase as a linear rate change, suggestive of a constant-rate process of reloading by tectonic forces. We had hoped to be able to estimate the loading rate from the ratio of the average coseismic stress drop calculated for the Hayward fault to the estimated time at which the seismicity rate returns to its preseismic level. This was not possible, however, because of the large uncertainties in the regressed time of

return to the preseismic rate (t_{return}=1994.7±112 years) that result from the low seismicity rates on the Hayward fault.

DISCUSSION AND CONCLUSIONS

The pattern of coseismic changes in seismicity rate in the San Francisco Bay region are positively correlated with the static stress changes calculated for central California faults at distances up to 100 km from the Loma Prieta rupture. The largest increases in seismicity were near the ends of the earthquake rupture on the San Francisco peninsula to the northwest and along the creeping section of the San Andreas fault to the southeast. The seismicity increase on the San Francscio peninsula is consistent with elastic dislocation models for the earthquake, which predict increases in the Coulomb failure function there and support a conclusion of the Working Group (1990) that the probability of a large earthquake on the San Francisco peninsula was increased by the Loma Prieta earthquake.

The correlation between the observed seismicity rate changes and modeled stress changes is best for models involving low apparent friction ($0.1 \leq \mu' \leq 0.3$) on central California faults. In contrast, laboratory experiments on frictional slip in rock typically find high coefficients of friction ($0.5 \leq \mu' \leq 0.8$) (Byerlee, 1978, Dieterich, 1981). Our result is consistent with the idea that low apparent friction is required to explain seismological and other evidence for fault-normal compression in central California (Zoback

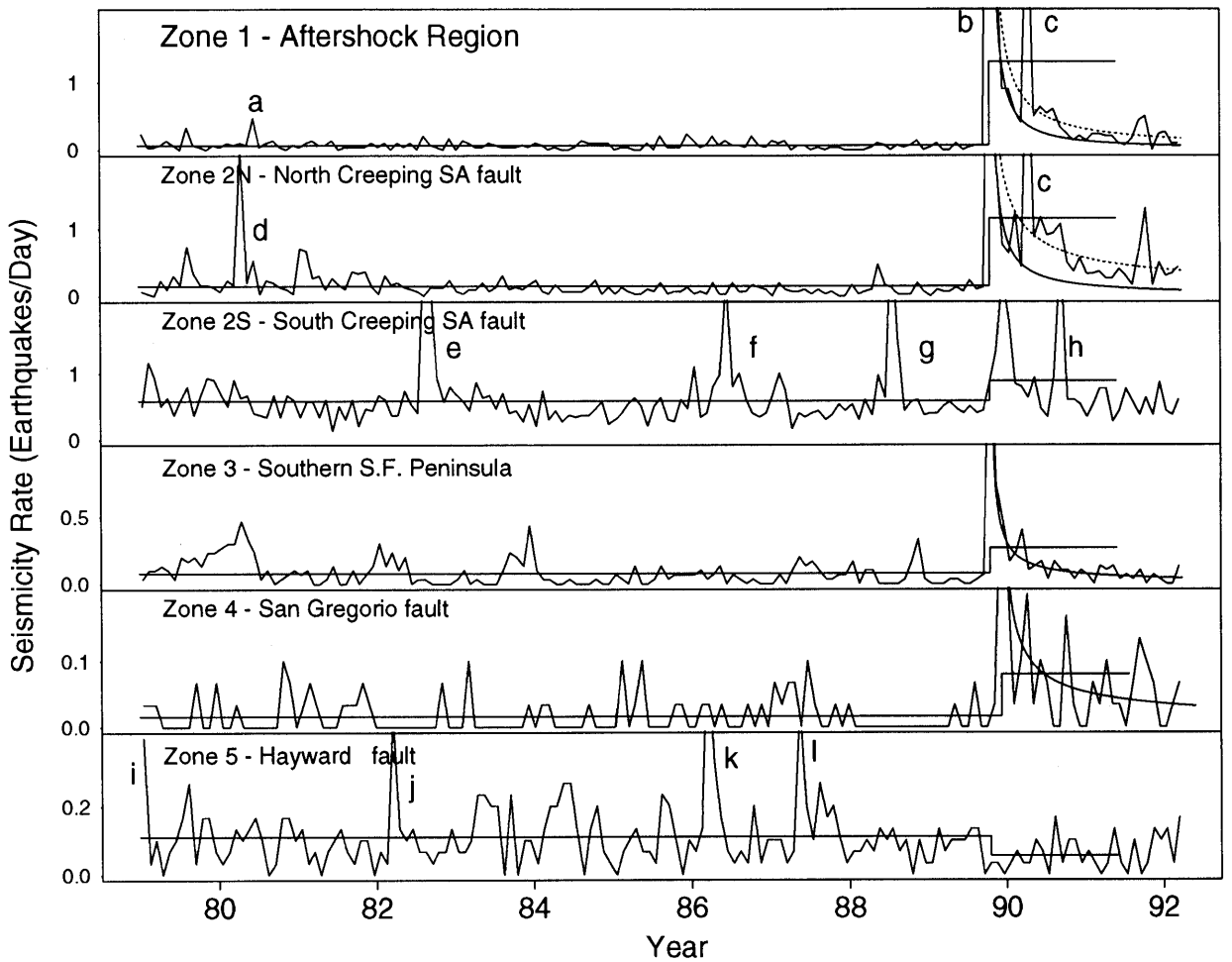

Figure 12.—Rate of $M \geq 1.5$ earthquakes in selected zones (see table 1) between 1 January 1979 and 31 March 1992. Letter symbols "a" through "l" mark significant aftershock sequences in the region (see table 2). Rates were calculated in nonoverlapping, 30-day intervals. Average rates in the 10-year preseismic and 20-month postseismic periods are indicated by horizontal lines. In the postseismic interval in zones 1, 2N, 3 and 4, modified Omori's law (power law) fits to the data are shown by smooth curves. In zones 1 and 2N models representing all data (dashed curve) and data up to the time of the M=5.6 aftershock on 18 April 1990 (solid curve) are shown (See fig. 13). In zones 3 and 4 models representing all data are shown by solid curve. Along the Hayward fault (zone 5), an apparent decrease in rate occurs near the beginning of 1988. In addition, a decrease in seismicity rate at the time of the Loma Prieta earthquake may be present. This decrease and the subsequent gradual increase in rate are modeled by a linear regression (solid increasing straight line).

Table 2.—*Significant regional aftershock sequences (1979-1992) in regions shown in figure 12*

Index (1)	Date	Time	Latitude		Longitude		Depth (km)	Magnitude	Location
a	800618	0452	36	54.3	121	37.8	6.0	3.9	Pajaro Gap
b	891018	0004	37	2.4	121	52.8	17.8	7.1	Loma Prieta
c	900418	1354	36	55.9	121	39.5	5.9	5.2	Watsonville
d	800413	0616	36	46.9	121	30.7	8.8	4.4	Freemont Peak
e	820811	0747	36	39.1	121	16.3	11.0	4.5	Bear Valley
f	860531	0848	36	38.3	121	14.8	5.9	4.7	Bear Valley
g	880726	0327	36	34.7	121	8.8	4.1	4.5	Bear Valley
h	900908	0813	36	40.9	121	18.4	7.5	4.0	Bear Valley
i	790123	0202	37	20.3	121	47.1	3.0	2.4	Calaveras Reservoir
j	820326	1324	37	48.8	122	11.4	5.0	3.3	Piedmont
k	860329	1624	37	52.9	122	12.1	13.4	4.0	Piedmont
l	870511	0646	37	48.6	122	11.2	4.8	3.5	Piedmont

1. Refer to Figure 12.

and others, 1987, and references therein; Oppenheimer and others, 1988) and the lack of an observable heat flow anomaly associated with the San Andreas fault (Lachenbruch and McGarr, 1990). Our low apparent-friction value can be explained by a high coefficient of friction (consistent with laboratory studies) combined with pore-pressure changes in the fault zone (Byerlee, 1990, Rice, 1992) induced by the Loma Prieta stress changes.

Our stress models suggest that for low values of apparent coefficient of friction, most parts of the Hayward fault, especially the southern end, underwent a slight relaxation of the expected right-lateral shear load. While the observed decrease in seismicity rate on the Hayward fault is consistent with such a relaxation, we are unable to determine the precise onset time of the low-rate period; it may have begun before the Loma Prieta earthquake, possibly as early as the beginning of 1988. Measured surface-creep rates at four of five sites along the Hayward fault (Galehouse, 1992) apparently began to decrease during 1988 and 1989, leaving open the possibility that the creep and seismicity on the Hayward fault may have responded to a fault-relaxing event a year or two before the Loma Prieta earthquake, in addition to the coseismic elastic relaxation associated with the Loma Prieta earthquake itself. Because these possible relaxation events might be relatively small compared to stress changes produced by moderate-size earthquakes close to the fault and may already have been eroded by tectonic loading, they are not considered to have significantly affected the long-term estimates for the probability of a large earthquake on the Hayward fault.

For low assumed values of the coefficient of friction, our models do not offer any ready mechanism for the triggering of a large earthquake on the Hayward fault by the Loma Prieta earthquake. The increase in extension calculated for models along the southern part of the Hayward fault would be expected to bring that part of the fault closer to failure if friction were important, and there is one scenario, discussed in more detail by Simpson and Reasenberg (1994), that might be consistent with the inferred low apparent coefficients of friction and yet could offer a mechanism for triggering. This scenario would appeal to the pore-fluid pressure changes induced by the Loma Prieta earthquake as the cause for the low apparent coefficient of friction observed immediately after the earthquake. If these pore fluids are able to re-equilibrate with time (and are not trapped by impermeable barriers in the fault zone as suggested by Byerlee, 1992, Blanpied and others, 1992), then the value for the apparent of coefficient of friction would change with time, eventually reaching high laboratory values when the pore fluids had completely re-equilibrated. At that time the full effect of the unclamping of the southern end of the Hayward fault might be felt, which might advance the time of the next large earthquake on that fault by 5 to 10 years.

We have not considered how increased stresses might produce higher seismicity on a fault, nor have we attempted to quantify the relationship between stress changes and seismicity changes. We used only the fact that the Coulomb stress and seismicity apparently increased and decreased in unison, with their agreement most prevalent for low-apparent-friction faults within about 100 km of the Loma Prieta epicenter. The fact that the seismicity changes correlate with the stresses estimated from homogeneous elastic stress models suggests that the stresses predicted by these models are probably correct in their broad pattern, though not necessarily in detail. The actual stress changes could differ greatly in magnitude (and could

possibly differ in sign in some places) if more complex and geologically realistic mechanisms of mechanical coupling, possibly involving weak fault zones, rigid blocks, fluids, and time-dependent effects, are at work.

Our work raises new questions and suggests some directions for future work. Concerning the sensitivity of San Francisco Bay Area seismicity to small stress changes: Have other large or moderate size earthquakes in the Bay Area and California caused seismicity rate changes on surrounding faults that can be similarly modeled? Using methods similar to the one reported here, one can calculate the static stress changes produced on Bay Area faults by all regional earthquakes for which reliable rupture models can be inferred. In principle, such static models can be combined into a single, time-dependent model that may be capable of explaining a significant portion of the regional background seismicity. After the stress-model-induced seismicity is accounted for, patterns and changes in

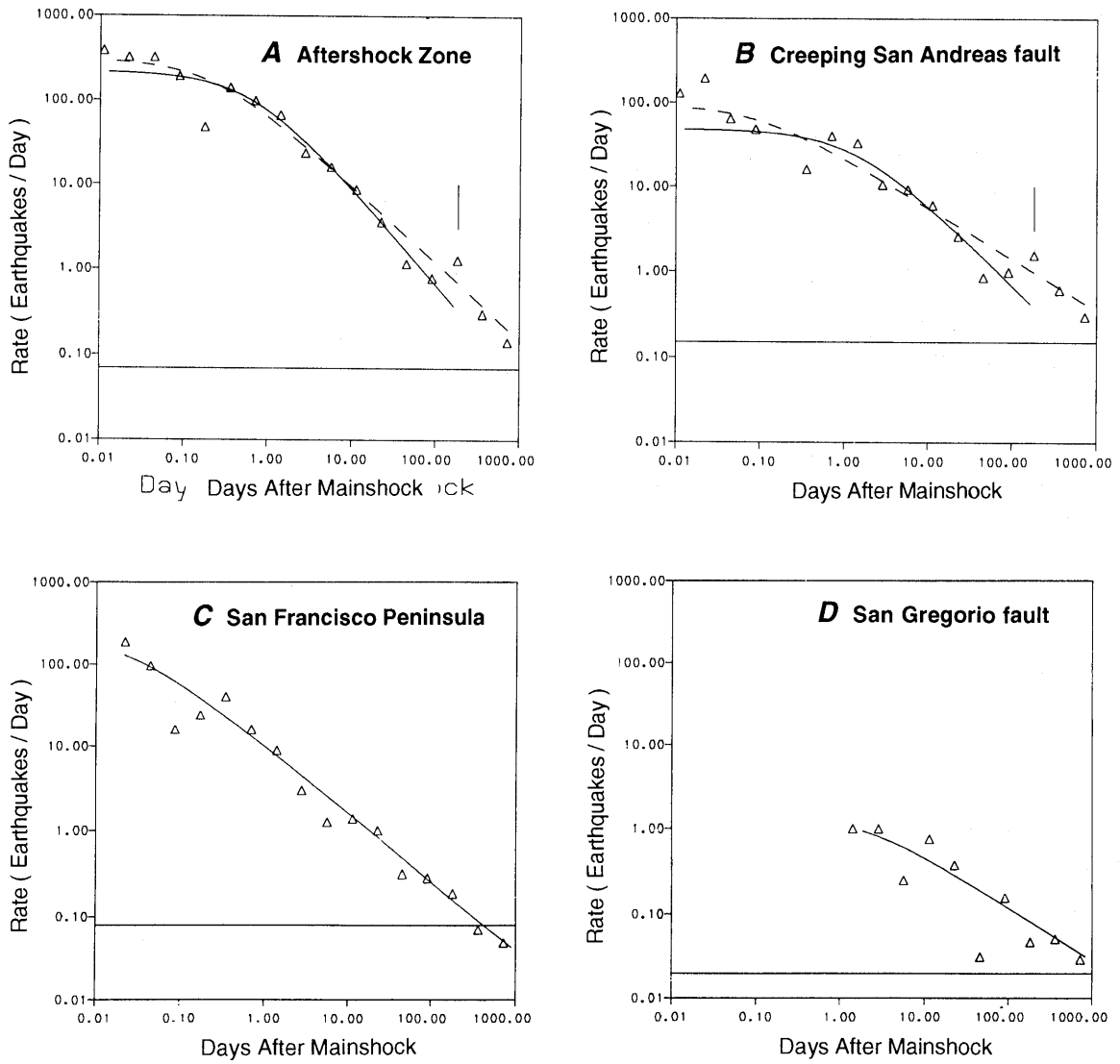

Figure 13.—Rate of $M \geq 1.5$ earthquakes after the Loma Prieta earthquake in zones 1, 2N, 3, and 4 (see table 1) is indicated by triangles. The postseismic decay in seismicity rate in each area is described by Omori's law (curved lines). Horizontal lines represent average seismicity rates in the 10 years preceding the Loma Prieta earthquake. Vertical lines mark time of the 18 April 1990 (M=5.6) aftershock near Chittenden. (*A*) Aftershock zone (Zone 1). Model fit to data between 18 October 1989 and 17 April 1990 is shown by solid curve; model fit to all of the data is shown by dashed curve. (*B*) Northern creeping segments of the San Andreas fault immediately southeast of the Loma Prieta rupture (Zone 2N). Model fit to data between 18 October 1989 and 17 April 1990 is shown by solid curve; model fit to all of the data is shown by dashed curve. (*C*) Southern San Francisco Peninsula (Zone 3). Model reflects data between 18 October 1989 and 31 March 1992. (*D*) San Gregorio fault (Zone 4). Model reflects data between 18 October 1989 and 31 March 1992.

the residual seismicity may provide information on other possible sources of stress, including aseismic slip on or below Bay Area faults.

Concerning the apparent low friction of the faults: Do all faults in the Bay Area have a low effective coefficient of friction, or is this true of only some of the faults? Our result, which relies on earthquakes along all Bay Area faults, does not distinguish among individual faults. Is the low apparent friction on Bay Area faults suggested by our study controlled by the presence of pore fluids in the seismogenic crust? If so, on which faults, and over what characteristic time, will the effective friction change as fluids re-equilibrate in response to the postseismic stresses? Continued close monitoring of the southern Hayward fault seismicity and creep rates may help answer this question. In particular, an increase in the microseismicity and creep rates on the southern Hayward fault might indicate that pore pressure has returned (increased) to the pre-Loma Prieta level and may signal the possible occurrence of a delayed, triggered large earthquake on the Hayward fault.

REFERENCES CITED

Armbruster, J.G., and Seeber, L., 1991, A mechanically modeled seismicity precursor of the Loma Prieta, California earthquake: Eos, Transactions, American Geophysical Union, v. 72, p. 310.

Behr, J., Bilham, R., Bodin, P., Burford, R.O., and Burgmann, R., 1990, Aseismic slip on the San Andreas fault south of Loma Prieta: Geophysical Research Letters, v. 17, p. 1445-1448.

Blanpied, M.L., Locker, D.A., and Byerlee, J.D., 1992, An earthquake mechanism based on rapid sealing of faults: Nature, v. 358, p. 574-576.

Byerlee, J.D., 1978, Friction of rock: Pure and Applied Geophysics, v. 116, p. 615-626.

Byerlee, J., 1990, Friction, overpressure and fault normal compression: Geophysical Research Letters, v. 7, p. 2109-2112.

Byerlee, J.D., 1992, The change in orientation of subsidiary shears near faults containing high pore fluid pressure: Tectonophysics, v. 211, p. 295-303.

Dieterich, J.H., 1981, Constitutive properties of faults with simulated gouge, *in* Carter, N., Friedman, M., Logan, J., D. Stearns, eds., Mechanical behavior of crustal rocks: American Geophysical Union, Washington, D.C., p. 103-120.

Eaton, J.P., 1990, The earthquake and its aftershocks from May 2 through September 30, 1983, *in* Rymer and Ellsworth, eds., The Coalinga, California, earthquake of May 2, 1983: U.S. Geological Survey Professional Paper 1487, p. 113-170.

Ellsworth, W.L., 1975, Bear Valley, California, earthquake sequence of February-March, 1972: Bulletin of the Seismological Society of America, v. 65, p. 483-506.

Ellsworth, W.L., 1990, Earthquake history, 1769-1989, *in* Wallace, R.E., ed., The San Andreas fault system: U.S. Geological Survey Professional Paper 1515, p. 152-187.

Erickson, L., 1986, User's manual for DIS3D: A three-dimensional dislocation program with applications to faulting in the Earth: Stanford University, M.S. thesis, Stanford, Calif., 167 p.

Galehouse, J.S., 1990, Effect of the Loma Prieta earthquake on surface slip along the Calaveras fault in the Hollister area: Geophysical Research Letters, v. 17, p. 1219-1222.

Galehouse, J.S., 1992, Creep rates and creep characteristics on certain North and East Bay faults: 1979-1992: Programs and Abstracts: Second Conference on Earthquake Hazards in the Eastern San Francisco Bay Area, March 25-29, 1992, California State University, Hayward, p. 24.

Habermann, R.E., and Craig, M.S., 1988, Comparison of Berkeley and Calnet magnitude estimates as a means of evaluating temporal consistency of magnitudes in California: Bulletin of the Seismological Society of America, v. 78, p. 1255-1267.

Harris, R.A., and Simpson, R.W., 1992, Changes in static stress on southern California faults after the 1992 Landers earthquake: Nature, v. 360, p. 251-254.

Heaton, T.H., 1982, Tidal triggering of earthquakes: Bulletin of the Seismological Society of America, v. 72, p. 2181-2200.

Hudnut, K.W., Seeber, L., and Pacheco, J., 1989, Cross-fault triggering in the November 1987 Superstition Hills earthquake sequence, southern California: Geophysical Research Letters, v. 16, p. 199-202.

Jaeger, J.C., and Cook, N.G.W., 1979, Fundamentals of rock mechanics [3d ed.]: London, Chapman and Hall, 593 p.

Jaumé, S.C, and Sykes, L.R., 1992, Changes in moderate seismicity in the San Francisco Bay region and stress changes due to large and great earthquakes: Eos, Transactions, American Geophysical Union, v. 73, p. 197.

Lachenbruch, A.H., and McGarr, A., 1990, Stress and heat flow, *in* Wallace, R.E., ed., The San Andreas Fault system: U.S. Geological Survey Professional Paper 1515, p. 261-277.

Lee, W.H.K., Eaton, J.P., Brabb, E.E., 1971, The earthquake sequence near Danville, California: Bulletin of the Seismological Society of America, v. 61, p. 1771-1794.

Lienkaemper, J.J., Borchardt, G., Lisowski, M., 1991, Historic creep rate and potential for seismic slip along the Hayward fault, California: Journal of Geophysical Research, v. 96, p. 18,261-18,283.

Lienkaemper, J.J., Borchardt, G., Wilmesher, J.F., Meier, D., 1989, Holocene slip rate along the Hayward fault, northern California (abstract): Eos, Transactions of the American Geophysical Union, v. 70, p. 1349.

Lisowski, M., Prescott, W.H., Savage, J.C., and Johnston, M.J., 1990, Geodetic estimate of coseismic slip during the 1989 Loma Prieta, California, Earthquake: Geophysical Research Letters, v. 17, p. 1437-1440.

Louderback, G.D., 1947, Central California earthquakes of the 1830's: Bulletin of the Seismological Society of America, v. 37, p. 33-74.

Matthews and Reasenberg, 1988, Statistical methods for investigating quiescence and other temporal seismicity patterns: Pageoph, v. 126, p. 357-372.

Mavko, G.M., Schulz, S., and Brown, B.D., 1985, Effects of the 1983 Coalinga, California, earthquake on creep along the San Andreas fault: Bulletin of the Seismological Society of America, v. 75, p. 475-489.

McNutt, Marcia, and Heaton, T.H., 1981, An evaluation of the seismic-window theory for earthquake prediction: California Geology, v. 34, p. 12-16.

Michael, A.J., 1991, Spatial variations in stress within the 1987 Whittier Narrows, California, aftershock sequence: Journal of Geophysical Research, v. 96, p. 6303-6319.

Michael, A.J., Ellsworth, W.L., and Oppenheimer, D.O., 1990, Coseismic stress changes induced by the 1989 Loma Prieta, California earthquake: Geophysical Research Letters, v. 17, p. 1441-1444.

Ogata, Y., 1983, Estimation of the parameters in the modified Omori formula for aftershock frequencies by the maximum likelihood procedure: Journal Phys.Earth, v. 31, p. 115-124.

Okada, 1992, Internal deformation due to shear and tensile faults in a

half-space: Bulletin of the Seismological Society of America, v. 82, p. 1018-1040.

Oppenheimer, D.H., Reasenberg, P.A., and Simpson, R.W., 1988, Fault-plane solutions for the 1984 Morgan Hill earthquake sequence: Evidence for state of stress on the Calaveras fault: Journal of Geophysical Research, v. 93, p. 9007-9026.

Oppenheimer, D.H., Bakun, W.H., and Lindh, A.G., 1990, Slip partitioning of the Calaveras fault, California, and prospects for future earthquakes: Journal of Geophysical Research, v. 95, p. 8483-8498.

Poley, C.M., Lindh, A.G., Bakun, W.H., and Schulz, S.S., 1987, Temporal changes in microseismicity and creep near Parkfield, California: Nature, v. 327, p. 134-137.

Reasenberg, P.A., 1985, Second-order moment of central California seismicity, 1969-1982: Journal of Geophysical Research, v. 90, p. 5479-5495.

Reasenberg, P.A.. and Ellsworth, W.L., 1982, Aftershocks of the Coyote Lake, California, earthquake of August 6, 1979: a detailed study: Journal of Geophysical Research, v. 87, p. 10,637-10,655.

Reasenberg, P.A., and Jones, L.M., 1989, Earthquake hazard after a main shock in California: Science, v. 243, p. 1173-1176.

Reasenberg, P.A., and Simpson, R.W., 1992, Response of regional seismicity to the static stress change produced by the Loma Prieta earthquake: Science, v. 255, p. 1687-1690.

Rice, J.R., 1992, Fault stress states, pore pressure distributions, and the weakness of the San Andreas fault, *in* Evans, B., and Wong, T.-F., eds., Fault mechanics and transport properties of rock: a festschrift in honor of W.F. Brace: London, Academic Press p. 475-503.

Rice, J.R., and Cleary, M., 1976, Some basic stress diffusion solutions for fluid-saturated elastic porous media with compressible constituents: Review of Geophysics and Space Physics, v. 14, p. 227-241.

Richter, C.F., 1958, Elementary Seismology: San Francisco, W.H. Freeman, 768 p.

Roeloffs, E.A., 1988, Fault stability changes induced beneath a reservoir with cyclic variations in water level: Journal of Geophysical Research, v. 93, p. 2107-2124.

Rydelek, P.A., and Sacks, I.S., 1990, Asthenospheric viscosity and stress diffusion: a mechanism to explain correlated earthquakes and surface deformations in NE Japan: Geophysical Journal International, v. 100, p. 39-58.

Sachs, L., 1982, Applied Statistics: New York, Springer-Verlag, 706 p.

Seeber, L., and Armbruster, J.G., 1990, Fault kinematics in the 1989 Loma Prieta rupture area during 20 years before that event: Geophysical Research Letters, v. 17, p. 1425-1428.

Simpson, R.W., and Reasenberg, P.A., 1994, The Loma Prieta, California, earthquake of October 17, 1989, Tectonic processes and models: U.S. Geological Survey Professional Paper 1550-F, p. 55-89.

Simpson, R.W., Schulz, S.S., Dietz, L.D., and Brown, R.O., 1988, The response of creeping parts of the San Andreas fault to earthquakes on nearby faults: two examples: Pageoph, v. 126, p. 665-685.

Stacey, F.D., 1977, Physics of the Earth [2d ed.]: New York, Wiley, p. 131.

Stein, R.S., King, G.C.P., and Lin, J., 1992, Change in failure stress on the southern San Andreas fault system caused by the 1992 magnitude=7.4 Landers earthquake, Nature: v. 258, p. 1328-1332.

Stein, R.S., and Lisowski, M., 1983, The 1979 Homestead Valley earthquake sequence, California: Control of aftershocks and postseicmic deformation: Journal of Geophysical Research, v. 88, p. 6477-6490.

Sykes L.R., and Jaumé, S.C., 1990, Seismic activity on neighbouring faults as a long-term precursor to large earthquakes in the San Francisco Bay area: Nature, v. 348, p. 595-599.

———1992, Changes in state of stress on thesouthern San Andreas fault resulting from the California earthquake sequence of April to June 1992: Science, v. 258, p. 1325-1328.

U.S. Geological Survey Staff, 1990, The Loma Prieta, California, earthquake: an anticipated event: Science, v. 247, p. 286-293.

Utsu, T., 1969, Aftershocks and earthquake statistics (I): Journal of the Faculty of Science, Hokkaido University, Japan, Series VII, v.3, p. 144-157.

———1971, Aftershocks and earthquake statistics (III): Journal of the Faculty of Science, Hokkaido University, Japan, Series VII, v.3, p. 380-441.

Working Group on California Earthquake Probabilities, 1990, Probabilities of large earthquakes in the San Francisco Bay Region, California: U.S. Geological Survey Circular 1053, 51 p.

Zoback, M.D., Zoback, M.L., Mount, V.S., Suppe, J., Eaton, J.P., Healy, J.H., Oppenheimer, D., Reasenberg, P., Jones, L., Raleigh, C.B., Wong, I.G., Scotti, O., and Wentworth, C., 1987, New evidence on the state of stress of the San Andreas fault system: Science, v. 238, p. 1105-1111.

THE LOMA PRIETA, CALIFORNIA, EARTHQUAKE OF OCTOBER 17, 1989:
EARTHQUAKE OCCURRENCE

AFTERSHOCKS AND POSTSEISMIC EFFECTS

SPATIAL VARIATIONS IN STRESS FROM THE FIRST SIX WEEKS OF AFTERSHOCKS OF THE LOMA PRIETA EARTHQUAKE

By John W. Gephart,
Cornell University

CONTENTS

ABSTRACT

The spatial variation in the state of stress along the main shock rupture plane during the first six weeks after the Loma Prieta earthquake is evaluated by estimating the stress tensor from groups of aftershock focal mechanisms in each of six subregions. Among the best-fitting stresses, two systematic patterns of stress variation are observed: (1) northwest of the main shock hypocenter the inferred stresses are only moderately well constrained but everywhere indicate low shear stress on the main shock fault plane, with σ_1 essentially perpendicular to the plane in most places. The directions of σ_2 and σ_3 appear to vary systematically with position on the fault plane. The mechanisms are generally not consistent with north-south compression and east-west tension, as might be predicted from strike-slip motion on the San Andreas fault if the fault is assumed to be a locus of high shear stress; (2) southeast of the hypocenter the inferred stresses are well constrained and suggest that significant shear stress may have remained on the main shock fault plane after it failed, although the absolute magnitude of the shear traction cannot be determined (and may be very low if the fault is weak, as commonly assumed of the adjacent creeping section of the San Andreas fault). The best-fitting principal stress directions are coincident with the main shock kinematic axes in the region close to the hypocenter but deviate significantly from these with distance to the southeast. The direction of shear stress on the main shock fault plane varies from: (1) alignment with the overall main shock slip vector near the hypocenter to (2) shallow northwest-plunging at the southeast end of the aftershock zone; this variation in shear stress direction (counter-clockwise to the southeast when viewed in the direction of the downward fault pole) is of the same sense as the variation in main shock slip distribution determined by others, but of much smaller magnitude. The mechanisms southeast of the main shock hypocenter generally are not consistent with fault-normal compression, as proposed by some other workers and as might occur if the main shock slip relieved most of the ambient stress in the region. The pattern of stresses observed in this study apparently reflects the distribution of load on the main fault plane shortly after failure. It is possible that the two regions (northwest and southeast of the hypocenter) sample different spatial domains around the main shock fault plane: the diverse events to the northwest reflect the crust adjacent the fault zone, while the well-aligned events to the southeast reflect the fault zone itself. If this is so, then the observations above may support the model of Rice (1992), which predicts spatial heterogeneity in stress around a well-developed fault zone owing to differences in pore pressure and material properties between the fault zone and the adjoining crust.

INTRODUCTION

Aftershocks occurring in the first six weeks following the Loma Prieta earthquake exhibit diverse mechanisms which vary widely with location around the main shock fault plane (Oppenheimer, 1990; Dietz and Ellsworth, 1990). Whereas each event indicates a partial measure of the state of stress at the time and place of its occurrence, the well-constrained focal mechanisms of these data can be used to map out variations in stress in the period immediately following the M=7.1 earthquake. Preliminary investigations of this kind, based on qualitative or approximate quantitative means, infer strongly heterogeneous

postseismic stresses, issuing from the observation of extreme local diversity of mechanisms, which appear to be mutually inconsistent (Oppenheimer, 1990; Michael and others, 1990). Moreover, these studies suggest that the aftershocks may reflect a condition in which the ambient tectonic stress was relieved almost entirely during main shock slip (Michael and others, 1990; Zoback and Beroza, 1993; and Beroza and Zoback, 1993). This study searches for possible spatial heterogeneity of the stress field indicated by 164 well-constrained focal mechanisms of early aftershocks ($M \approx 0.9$-4.0) from around the rupture zone (fig. 1), applying a technique that may resolve subtle stress variations. It appears that while a portion of the main shock fault plane is largely free of shear stress at this time, another part of the fault plane remains loaded, although the absolute magnitude of the deviatoric stress cannot be determined. This work may improve our understanding of the way in which stress is redistributed during large earthquakes.

METHOD

In this study the stress field is inferred from the directions of slip on fault planes, as indicated by the focal mechanisms of earthquakes, following the procedure of Gephart and Forsyth (1984) and Gephart (1990a, 1990b) and based largely on the earlier principles of Wallace (1951), Bott (1959), and McKenzie (1969). The information embodied by focal mechanisms—the orientations of fault planes and associated slip directions—constrains four of the six numbers of the stress tensor. As discussed by Gephart (1990a), these four dimensionless quantities can be expressed as three Euler angles—fixing the principal stress orientations, and one stress magnitude term, R—describing the magnitude of σ_2 relative to σ_1 and σ_3; $R \equiv (\sigma_2-\sigma_1)/(\sigma_3-\sigma_1)$, such that $0 \leq R \leq 1$. The two numbers of the stress tensor that cannot be determined by this approach reflect the magnitudes of a regional normal and shear stress, $\sigma_m \equiv (\sigma_1+\sigma_3)/2$ and $\tau_m \equiv (\sigma_1-\sigma_3)/2$; as these numbers have the dimensions of stress, they cannot be estimated from (dimensionless) orientation data alone. By combining the information expressed in multiple focal mechanism observations, which are assumed to reflect a common stress field, best-fitting values of the four resolvable stress parameters can be determined. In these experiments all the data are grouped in spatially distinct subregions, and independent inversions are performed on each set. The variations in the best-fitting stress fields determined for all the subregions should approximate the continuous variation in stress across the region.

The constraint on the four resolvable stress parameters is derived from the requirements that (1) there be no component of shear stress on any fault plane perpendicular to the direction of slip and (2) the component of shear stress parallel to the direction of slip have the same polarity as the slip. Thus, if s is the (unit) slip vector, b is the (unit) B-axis vector ($b=n \times s$, where n is the unit fault normal),

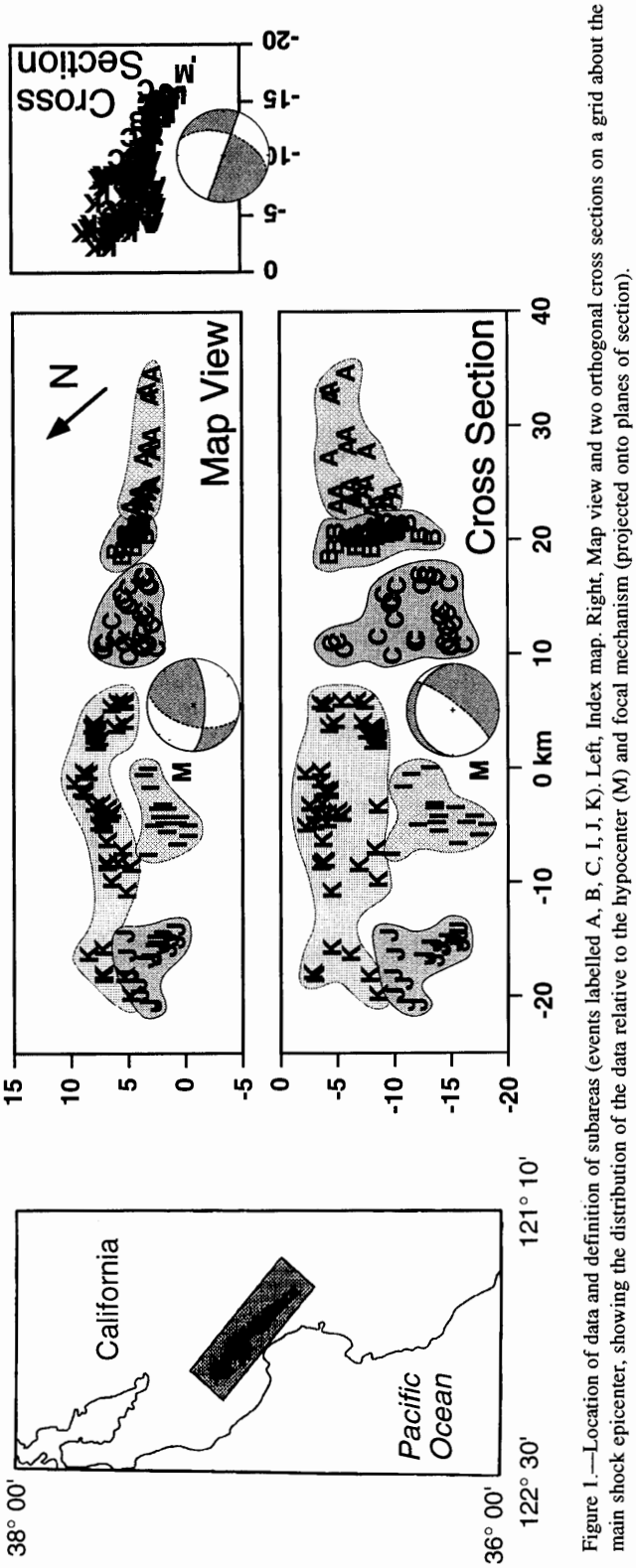

Figure 1.—Location of data and definition of subareas (events labelled A, B, C, I, J, K). Left, Index map. Right, Map view and two orthogonal cross sections on a grid about the main shock epicenter, showing the distribution of the data relative to the hypocenter (M) and focal mechanism (projected onto planes of section).

and τ is the shear stress vector in the fault plane, then it is required that $\tau \bullet b=0$ and $\tau \bullet s>0$. The inverse procedure effects a transformation of the stress tensor from these fault coordinates (unique to each datum) to regional coordinates (common to all data). Following Gephart (1990a), this is performed based on the conventional stress transformation equation, $\sigma_{ij}'=\beta_{ik}\beta_{jl}\sigma_{kl}$ (applying the Einstein summation convention of summing over repeated subscripts), where σ_{ij}' and σ_{ij} are the stress tensor in the two different reference frames, and β_{ij} is the transformation matrix of angle cosines between the two coordinates sets. It is important to note the extreme non-linearity of tensor mechanics that is bound up in the stress transformation equation; this implies that the shear stress direction on a fault plane may vary widely with small variations in the plane or stress tensor, and that there are always many stress tensors that are consistent with any given fault datum based on the two conditions above. As a practical matter, this precludes the possibility of substituting averaged kinematic (P, B, and T) axes for principal stress directions. That is, the maximum and minimum stress (σ_1 and σ_3) directions may not be at large oblique angles (~45°) to the fault plane, and the intermediate stress (σ_2) direction may not be at a small angle to the plane, as is conventionally assumed for simplicity. Thus, as only the direction of shear stress on the fault plane is indicated by the focal mechanisms, and no measure of the magnitude of shear stress, the approach implicitly allows that any of the fault planes may be either strong or weak.

Regarding the extreme non-linearity of the problem, a simple and reliable approach for inverting the fault data is by a grid search over the four resolvable stress parameters (Gephart and Forsyth, 1984). A range of combinations of four stress parameters are tested one-by-one against all of the data. For each set of four parameters (a stress model), the misfit of each datum is determined. Here the misfit is defined as the smallest difference in orientation between the observed mechanism and any one that fits the stress model—in which the slip direction matches the predicted shear stress direction on at least one of the two nodal planes. The difference in orientation between any such observed and predicted mechanisms is equivalent to a rotation in space about some arbitrary axis. The fitness of a particular model relative to all the data is given by the average misfit rotation for the whole data set. The optimum stress model is the one which has the smallest average misfit, and confidence limits can be defined based on the values of the mean misfits using statistics for one-norm procedures (Gephart and Forsyth, 1984). In the course of the inversion, it is necessary to select the fault plane from among the two nodal planes of each focal mechanism. In the absence of an objective means for identifying the true fault plane based on observation, this is done by testing each nodal plane independently against each stress model and selecting the one with the smaller rotation misfit as the preferred fault plane relative to that stress model (the result for the alternate plane is neglected).

To regard the physical properties of particular fault planes (for example, "strong" versus "weak"), it is useful to consider the stress vector that acts on the fault plane. The relation between a stress tensor and a fault geometry can be succinctly illustrated using the Mohr Sphere diagram presented by Gephart (1990a) (fig. 2). This is a generalization of the conventional Mohr Circle diagram for stress (for example, Jaeger and Cook, 1979), which is a plot of normal-versus-shear stress. The Mohr Sphere diagram differs from the Mohr Circle diagram in that it regards two orthogonal components of shear stress, parallel and perpendicular to the observed slip direction, rather than a single component. In both the Mohr Circle and Sphere figures, admissible fault data are represented as points which indicate the magnitudes of normal and shear stresses acting on a fault plane. Whereas the locus of all possible fault orientations in the Mohr Circle diagram is the area between the one large and two small circles which intersect at three crossing points on the normal stress axis (marking the principal stress magnitudes), the locus of all possible fault geometries in the Mohr Sphere diagram is the volume between the corresponding one large and two small spheres. (That no admissible fault geometries are represented by points in the regions within the two smaller circles/spheres or outside the largest one is an intrinsic property of the stress tensor.) Projections of the Mohr Sphere onto planes parallel to the normal stress axis resemble the Mohr Circle diagram. Two orthogonal projections of the Mohr Sphere, each plotting normal stress versus one component of shear stress, are sufficient to illustrate the distribution of fault geometries in this three-dimensional figure. Each fault geometry appears as a single point in each of the two projections. For a particular fault geometry to be consistent with the stress tensor in question, based on matching shear stress and slip directions, the corresponding point must plot above the abscissa in the upper figure ($\tau \bullet s>0$) and on the abscissa in the lower one ($\tau \bullet b = 0$), indicating that the shear stress and slip vectors are aligned and of the same polarity.

TEST

To test for spatial variations in stress, the focal mechanisms of 164 well-constrained Loma Prieta aftershocks were divided among several subsets based on location (fig. 1). To the extent possible, divisions between the subregions were chosen to correspond with distinct spatial gaps among the aftershocks. Some experimentation was applied to establish appropriate domain sizes and boundaries, such that meaningful stress variations could be

determined; however, the separation was defined solely by event location—no consideration was given to the orientations of the mechanisms (and none were rejected as inconsistent, in spite of remarkable local heterogeneity). Three subregions—A, B, and C—were defined along the strike of the main shock rupture zone in the region below and to the southeast of the main shock auxiliary plane (see fig. 1). Subregion A essentially coincides with the northwestern end the central creeping section of the San Andreas fault (U. S. Geological Survey Staff, 1990). The aftershock zone appears to steepen, and its maximum depth shallows, with increased distance to the southeast from a point near the main shock hypocenter; thus the main shock fault plane may vary in orientation and vertical dimension from subregions C to A. Three subregions—I, J, and K—were defined above and to the northwest of the main shock auxiliary plane. Subregion I comprises a group of events immediately northwest of the main shock hypocenter at

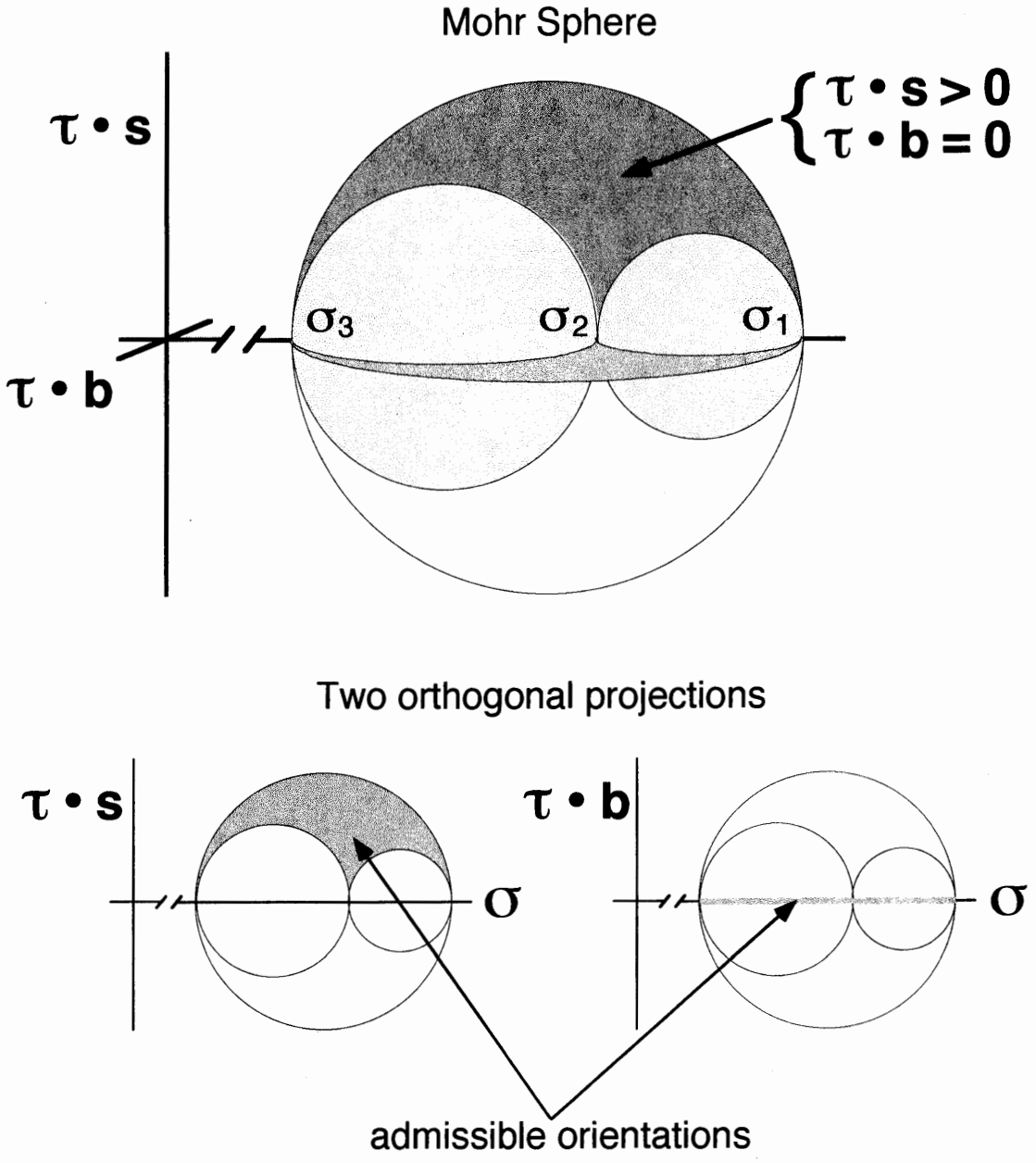

Figure 2.—Mohr Sphere construction: a plot of normal versus two components of shear stress (here parallel to the slip vector, s, and B axis, b, on any fault plane). Fault geometries falling on the [$\tau \bullet s > 0$, $\tau \bullet b = 0$] half-plane relative to any given stress model are admissible, in that shear stress and slip vectors agree in both direction and polarity.

depths >10 km, subregion J comprises a cluster of relatively deep events farther to the northwest, and subregion K comprises all shallow events.

The orientations of aftershock focal mechanisms are illustrated by the P and T axes at the left side of figure 3. The P and T axes of the main shock mechanism are shown for reference on each plot; however, the main shock datum was not included in the inversions of the aftershock data sets. These figures indicate generally modest variation in the character of mechanisms in adjacent subareas, except across the main shock hypocenter where the variation is marked. As noted by Oppenheimer (1990), many of the events southeast of the main shock hypocenter (subareas A, B, and C) are aligned along a steeply-dipping plane and have mechanisms indicating right-lateral strike-slip on a northwest-trending fault, consistent with slip on the San Andreas fault. In contrast, aftershocks to the northwest of the main shock hypocenter (subareas I, J, and K) are distributed widely around the main shock fault plane with mechanisms that vary widely and generally do not resemble that of the main shock, suggesting that these events occurred on a variety of secondary structures (Oppenheimer, 1990).

Independent tests were performed on each of these data subsets in order to observe variations in the stress field across the region. For each data set, an exhaustive search over the ranges of four stress parameters was made to find the model that is most nearly consistent with the data, based on matching observed and predicted slip directions on one of the two nodal planes of each focal mechanism.

RESULTS

The results of the experiments for each of the six subregions are illustrated in the right side of figure 3, which shows the best-fitting stress models, as indicated by the orientations of σ_1 and σ_3 axes on a stereonet, a histogram of R values, and the associated uncertainties of each. The main shock focal mechanism is superimposed on each stereonet for reference. The principal stress directions and value of R of the best-fitting models of each subregion are listed in table 1. Figures 4 and 5 illustrate the variations of the best-fitting stresses among the subregions and emphasize the relation between the inferred stresses and the main shock mechanism. The misfit rotations and the observed and predicted (nearest perfectly fitting) focal mechanisms of each event relative to the best-fitting stress model in each region are given in table 2; this listing indicates the chosen (preferred) fault plane from among the two nodal planes of each mechanism. Based on these results, there appears to be a marked difference in the nature of the stresses on either side of the main shock hypocenter. Thus, in the following discussion the results of the three southeastern and three northwestern subsets are presented separately.

SOUTHEAST OF THE MAIN SHOCK HYPOCENTER

To the southeast of the main shock, the best-fitting stresses fit the data very well, with average rotation misfits of <5°; this suggests that the stresses may be reasonably uniform within each group, as assumed in performing the analysis. Although the aftershock mechanisms of each of the three subsets appear to be qualitatively similar to one another, based on P- and T-axis orientations, the ranges of acceptable stresses vary systematically from one subregion to the next with distance along the main shock fault trace (fig. 3). In subarea C, near the main shock hypocenter, σ_1 is nearly horizontal north-south and σ_3 plunges moderately to the east. In subarea A, at some distance from the main shock hypocenter, σ_1 plunges moderately to the north and σ_3 is nearly horizontal east-west. In subarea B, located between subareas C and A, the principal stresses are intermediate in orientation to those on either side. Although the formal uncertainties in stress orientations are relatively small, the results do not absolutely require that the stresses are smoothly varying from subareas C to A, as there is some overlap at the 95-percent confidence level; however, as the variation in the best-fitting stresses are systematic, the following discussion assumes that this observed trend is meaningful. In all three cases, the acceptable σ_1 directions (within the 95-percent confidence limit) are nearly confined to the main shock dilatational quadrants, and the σ_3 directions to the compressional quadrants. The preferred value of R varies among the subregions from 0.3 to 0.7, but shows no clear systematic spatial trend, as with the stress directions.

The orientations of the best-fitting stresses across the aftershock region appear to be systematically related to the focal mechanism of the main shock, as illustrated in figure 4. In subarea C (adjacent to the main shock hypocenter) the inferred σ_1, σ_2, and σ_3 directions are very nearly aligned with the P, B, and T axes, respectively, of the main shock focal mechanism. Progressively to the southeast of the main shock hypocenter, in subareas B and A, the σ_2 axis remains parallel to the main shock fault plane, but of increasing rake from a northwest strike line. Concomitant variations in the the other two principal stresses are also systematic in space: σ_1 steepens progressively northward, and σ_3 shallows progressively eastward, from subareas C to B to A. Based on these inferred stress models, the predicted slip (shear stress) direction on the main shock fault plane varies from alignment with the observed main shock slip direction in subarea C, to shallow southeast-plunging (with a small reverse dip-slip

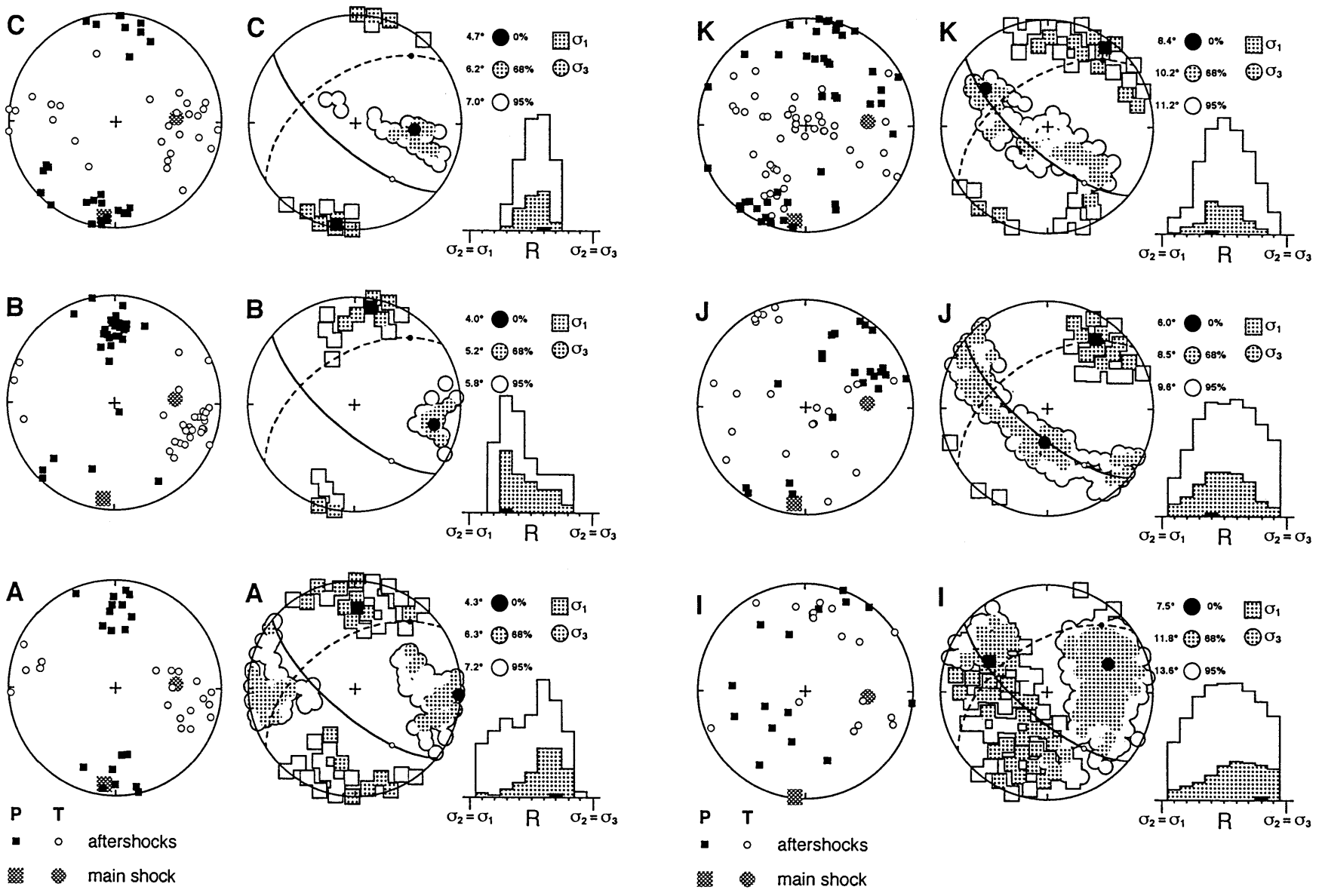

Figure 3.—Data and results for each of six subregions (A, B, C, I, J, K). In each case, on the left are shown the P and T axes of the aftershock focal mechanisms, along with those of the main shock (for reference only—main shock datum was not used in the inversions); on the right are shown the acceptable models, indicated by a strereonet of σ_1 and σ_3 directions and a histogram of R values. Degrees of shading indicate the best model ("0%"), and ranges of the 68-percent and 95-percent confidence limits; the corresponding magnitude of average rotation misfits is shown at the upper right. The main shock focal mechanism is shown on each plot for reference.

Table 1.—*Best-fitting stress models of each subarea*

[Principal stress directions indicated by plunge and azimuth]

Subarea	Principal Stress Directions						R
	σ_1		σ_2		σ_3		
A	27	2	63	187	2	93	0.7
B	9	10	64	261	24	104	0.3
C	4	190	47	284	43	96	0.6
I	40	298	29	180	36	66	0.8
J	22	36	13	301	64	183	0.4
K	9	37	56	140	33	301	0.4

component) in subarea B, to shallow northwest-plunging (with a small normal dip-slip component) in subarea A. It can be shown that if the main shock fault plane in subareas B and A is steeper than shown in figure 4 (but with a slip vector of the same rake), as suggested by the alignment of aftershocks in that region, then the mismatch between the observed and predicted main shock slip is increased in that region; thus we cannot easily associate the along-strike differences among the inferred stresses with variations in main shock fault orientation.

Relative to the best-fitting stress tensor in each subregion, the traction vector on each inferred fault plane is illustrated in the Mohr Sphere diagrams of figure 5 (again, aftershock fault planes were selected from among the two nodal planes of each event in the course of the inversion, so as to minimize the difference between observation and model). That the observed and predicted slip directions are nearly in agreement on most of the aftershock faults is indicated by a clustering of poles on the [$\tau \bullet s > 0$, $\tau \bullet b = 0$] half-plane. For most of the aftershocks in all three subregions, the magnitude of shear stress approaches the maximum for the region (near the top of the largest circle in the plot of $\tau \bullet s$ versus σ); this suggests that the aftershock fault planes may be relatively strong, as they apparently fail only under relatively high shear stress. Of course as described above, the absolute shear stress magnitude is unknown, as the magnitude of τ_m (the radius of the Mohr Sphere) is unconstrained in the present analysis.

Also shown in figure 5 is the traction on the main shock fault plane for the best-fitting stress models of each of the subregions. In all three southeastern subregions the total relative magnitude of shear stress on the main shock is high (nearly the regional maximum), but the magnitude of the components parallel and perpendicular to the observed slip direction vary considerably with location. The main shock fault geometry is consistent with the inferred stresses in subregion C, immediately to the southeast of the main shock hypocenter, but it is progressively less consistent with distance to the southeast in regions B and A, as indicated by the increasing divergence of the main shock datum from the abscissa, [$\tau \bullet b = 0$], in the lower figures. This is consistent with a spatially varying inferred shear stress direction on the main shock fault plane, as shown in figure 4. It is interesting that, while in all three southeastern subregions the main shock P and T axes fall within the scatter of those of the aftershocks (fig. 3), apparently the main shock and aftershock stress tensors are consistent only in subregion C; that is, in terms of the inferred stress tensors, the main shock mechanism is clearly distinct from the aftershocks in subregions B and (especially) A, as indicated in the Mohr Sphere diagrams.

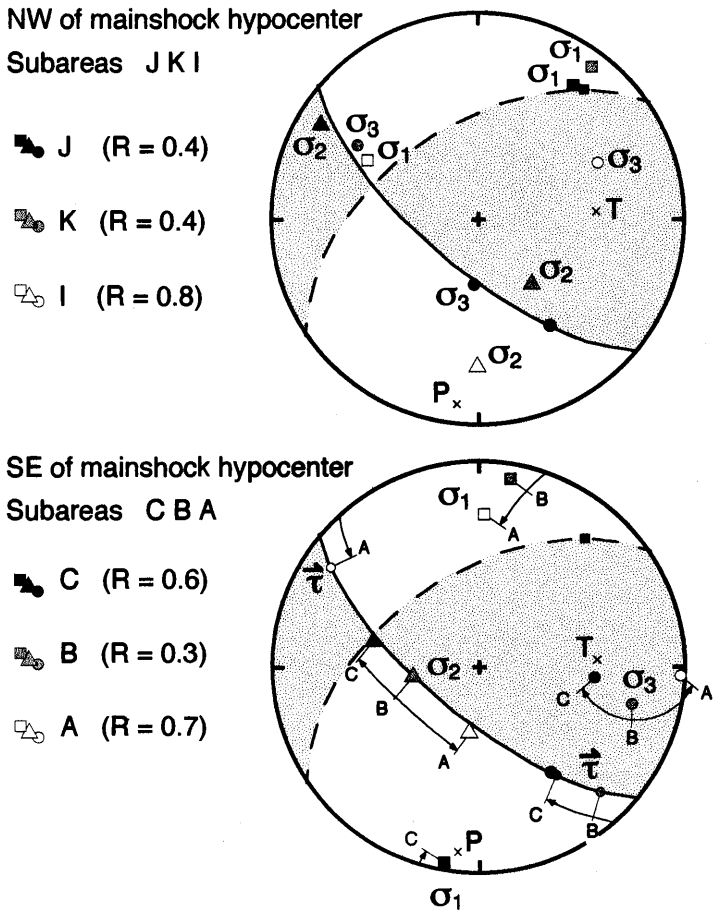

Figure 4.—Summary of best-fitting stress models for each subregion and comparison with main shock focal mechanism. Top, Three northwestern subregions: principal stress axes (σ_1, σ_2, σ_3) tend to align parallel and perpendicular with the main shock fault plane. In all cases the resolved shear stress on the main shock fault plane is very small relative to the regional maximum. Bottom, Three southeastern subregions: principal stress directions in subregion C are aligned with main shock kinematic axes, but drift away in subregions B and A; in all cases the σ_2 axis is nearly parallel to the main shock fault plane. The predicted shear stress direction on the main shock fault plane varies smoothly between subareas C, B, and A, as shown.

NORTHWEST OF THE MAIN SHOCK HYPOCENTER

To the northwest of the main shock hypocenter the average rotation misfits among the best-fitting stress models in each subarea are on the order of 6-9° (fig. 3)—greater than to the southeast but less than the uncertainty in the focal mechanism determinations; thus, the analysis does not preclude the possibility that stresses are essentially uniform within each subregion. Moreover, the stresses appear to be less uniform between subareas I, J, and K than among the subareas to the southeast.

As shown in figure 4, the stresses northwest of the main shock hypocenter appear to bear a very different relationship to the main shock fault plane than to the southeast; here the principal stress directions are nearly parallel and perpendicular to the fault. In subarea I, near the main shock hypocenter, the stresses are especially poorly resolved, although the best-fitting σ_1 and σ_3 directions are nearly aligned with the B and T axes of the main shock, respectively. In an experiment similar to the present one (using a different algorithm to invert for stress), Michael and others (1990) were unable to identify acceptable homogeneous stresses in the region of subarea I, and con-

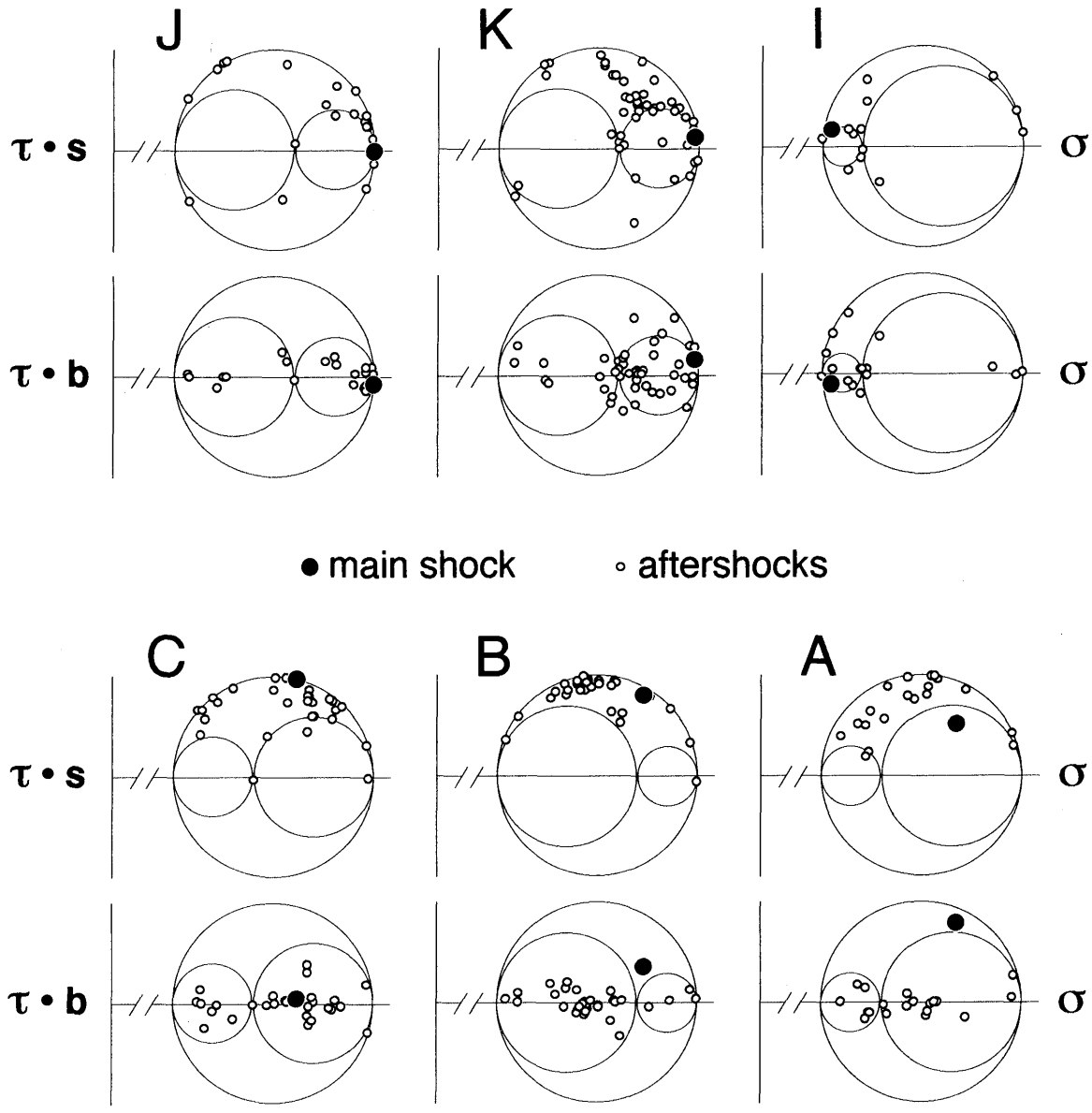

Figure 5.—Two orthogonal projections of the Mohr Sphere construction for the six subregions, corresponding to the best-fitting stresses in each case. Fault geometries that are consistent with the stress model fall on the abscissa in the lower projection and above the abscissa in the top one. Both aftershock (small open circles) and main shock (large filled circles) mechanisms are shown.

cluded that the stresses there were extremely heterogeneous.

In subareas J and K the inferred stress orientations appear to be similar at high confidence levels (for example, 95-percent), with acceptable σ_1 axes clustering about the pole of the fault plane and σ_3 axes distributed in orientations parallel to the fault plane; among the best-fitting stresses, the σ_1 directions of the two subareas are nearly identical but the σ_3 directions are nearly orthogonal to one another. This is illustrated more fully in figure 6, which shows the results of tests based on only a very limited set of stress models—those with σ_1 perpendicular to the main shock fault plane. Among these models, figure 6*A* shows the range of acceptable σ_3 directions parallel to the main shock fault plane, in the same format as in figure 3; the best σ_3 directions are oriented differently along the fault plane for subareas J versus K. This description involves some inherent ambiguity, as each σ_3 direction is associated with several models, spanning a range of values of R (and each value of *R* is associated with a range of σ_3 directions). Figure 6*B* is an unambiguous illustration of the full range of models with σ_1 perpendicular to the main shock fault plane, with each point indicating a single model (a unique combination of stress directions and *R*). At the 95-percent confidence limit, there is nearly a complementary distribution of acceptable models for the two subregions—generally, models acceptable for J are not acceptable for K, and vice versa. Thus, while certain elements of the ranges of acceptable stresses are common to the two regions (σ_1 direction), other elements appear to be mutually exclusive (the combination of σ_3 direction and *R*).

In the Mohr Sphere plots in figure 5, there is considerable scatter of the aftershock data about the [$\tau \bullet s > 0$, $\tau \bullet b = 0$] half-plane among subareas I, J, and K, indicating that the fit to the optimum stress models are only moderately good. In the [$\tau \bullet s$ versus σ] projections, most aftershocks plot at relatively low shear stress magnitudes (at considerable distances from the top of the largest circle), suggesting that the aftershock fault planes may be weak. In all three of these subregions, the main shock fault geometry plots very near to a point of intersection of two of the spheres, indicating that the fault plane is nearly a principal plane—and thus experiences a very low relative shear stress magnitude at the time of the aftershocks. In such cases, the direction of shear stress on the fault plane is of little significance (and so is not shown at the top of figure 4).

DISCUSSION

The above results indicate a systematic spatial variation in stress along the main shock rupture zone, with markedly different expressions on the northwest and southeast sides of the main shock hypocenter. To the northwest of the hypocenter, principal stress axes exhibit large differences in orientations between subregions (an exchange of axes among the principal stresses) but in a manner that everywhere yields relatively low shear stress on the main shock fault plane. To the southeast of the hypocenter, principal stress axes exhibit only minor differences between subregions (small deflections of axes) but in all areas so as to yield relatively high shear stress on the main shock fault plane, and with a shear stress vector of smoothly varying rake with position along the fault. This distinct spatial and geometric association of the main shock and stress inferred from aftershocks implies a physical connection between the main shock failure and the postseismic state of stress.

Presumably, during the main shock the ambient (preseismic) stress was reduced in magnitude and redistributed, although perhaps not completely or evenly; the stress determined from the early aftershocks must reflect the stress state that exists following the main shock stress drop. The marked difference in stress observed on either side of the hypocenter reflects the way that stress was reorganized on the rupture plane. To the northwest, the main shock fault plane appears to be mostly relieved of stress, suggesting that the stress drop was nearly complete (as suggested by Zoback and Beroza, 1993, and Beroza and Zoback, 1993), while to the southeast the fault plane appears to remain loaded, possibly owing to incomplete stress drop on that portion of the fault (in apparent conflict with the interpretation of these workers).

It is interesting that the pattern of the shear stress direction on the main shock fault plane inferred between subareas C and A (fig. 4) bears some resemblance to the interpreted variations in the main shock slip distribution from geodetic-leveling and strong-motion data. The latter, with minor differences among various workers (for example, Beroza, 1991; Hartzell and others, 1991; Marshall and others, 1991; Steidl and others, 1991), indicate predominant thrust slip to the northwest of the main shock hypocenter, and predominant right-lateral strike slip to the southeast (although Wald and others, 1991, find a more uniform slip rake). The inferred postseismic stresses from this study indicate a similar counter-clockwise rotation of predicted slip (shear stress) on the main shock fault plane with distance to the southeast, though of much smaller magnitude than observed in coseismic slip, and limited to a region only southeast of the hypocenter. Assuming that the slip distribution reflects shear stress directions (as implicit in the stress inversion procedure), it is possible that a large spatial variation in preseismic stress, which is reflected in the two disparate domains of main shock slip, evolved into a more subdued and localized variation in postseismic stress observed among the aftershocks.

Table 2.—*Data and results for best-fitting stress models of each subarea*

[All angles in degrees]

	Event #	Misfit Rotation Vector: Misfit Rotations[1] Pref. (Alt.)	Rot. Axis Azim.[2]	Rot. Axis Plunge[2]	Observed Focal Mechanism: Obs. Fault Strike	Obs. Fault Dip[3]	Obs. Aux. Strike	Obs. Aux. Dip[3]	Slip[4]	Rotated Focal Mechanism: Rot. Fault Strike	Rot. Fault Dip[3]	Rot. Aux. Strike	Rot. Aux. Dip[3]	Slip[4]
Subarea A:	1	1.9 (23.4)	116.8	41.5	105.0	55.0	213.3	65.8	T	103.5	53.6	212.7	66.0	T
	2	8.7 (20.1)	137.5	53.1	105.0	60.0	225.8	48.4	T	96.1	55.8	223.5	48.2	T
	3	4.3 (33.9)	106.6	40.3	320.9	40.3	225.0	85.0	R	316.2	43.0	222.4	86.5	R
	4	12.0 (16.0)	170.9	52.5	218.7	63.1	115.0	65.0	T	225.6	67.6	126.8	69.7	T
	5	0.5 (10.9)	89.9	33.6	140.0	55.0	44.2	81.8	R	140.0	54.7	43.9	81.5	R
	6	6.7 (26.8)	136.8	55.3	148.6	30.4	50.0	85.0	R	152.6	34.1	55.8	85.4	R
	7	0.8 (7.6)	119.4	9.5	50.7	80.9	145.0	65.0	L	51.0	81.2	145.0	65.7	L
	8	6.2 (35.0)	134.4	50.9	322.9	60.1	230.0	85.0	R	328.2	56.3	234.5	84.5	R
	9	1.4 (29.6)	229.6	67.5	239.5	54.4	130.0	65.0	T	238.3	53.9	128.5	65.1	T
	10	0.4 (43.8)	165.4	48.2	340.0	70.0	246.5	80.6	R	340.3	69.7	246.8	80.7	R
	11	4.3 (22.4)	131.7	40.2	240.0	81.4	145.0	60.0	L	237.7	82.3	142.7	56.8	L
	12	0.0 (20.4)	152.0	77.2	245.4	67.5	135.0	50.0	T	245.4	67.5	135.0	50.0	T
	13	6.2 (36.8)	204.0	53.3	225.0	65.0	130.7	80.9	L	220.7	61.5	125.2	80.1	L
	14	6.8 (19.5)	86.0	52.6	159.5	54.4	50.0	65.0	R	162.1	55.4	56.3	68.4	R
	15	4.4 (10.9)	124.6	8.1	45.0	85.0	136.8	70.1	L	44.0	84.3	136.6	65.9	L
	16	2.4 (24.1)	149.0	58.6	161.7	31.5	55.0	80.0	R	163.3	32.7	57.3	79.9	R
	17	0.0 (5.4)	102.7	28.9	135.0	75.0	39.6	70.7	R	135.0	75.0	39.6	70.7	R
	18	6.7 (12.1)	121.1	35.1	63.5	82.4	160.0	50.0	L	67.9	85.5	161.1	54.2	L
	19	7.6 (38.0)	109.2	43.2	325.9	40.3	230.0	85.0	R	317.4	45.0	225.1	87.6	R
Subarea B:	1	6.2 (25.6)	332.5	57.0	161.7	31.5	55.0	80.0	R	156.0	34.8	50.4	79.4	R
	2	3.5 (19.4)	211.5	30.1	175.0	75.0	273.5	61.1	R	177.2	77.5	273.8	62.5	R
	3	0.0 (10.4)	340.1	52.1	50.0	90.0	140.0	60.0	L	50.0	90.0	140.0	60.0	L
	4	1.5 (11.2)	52.1	54.1	116.3	63.1	220.0	65.0	T	115.5	62.7	218.9	65.8	T
	5	2.9 (10.8)	11.2	45.0	145.0	50.0	235.0	90.0	R	145.8	48.6	237.0	88.6	R
	6	0.4 (15.1)	4.1	50.5	145.0	45.0	55.0	90.0	R	145.1	44.8	235.3	89.8	R
	7	0.7 (13.0)	331.2	30.4	55.0	81.4	150.0	60.0	L	54.7	81.3	149.6	60.6	L
	8	0.3 (14.0)	330.9	30.0	55.0	80.0	150.7	60.5	R	54.9	80.0	150.6	60.8	R
	9	16.8 (32.1)	204.8	39.0	32.7	51.6	135.0	75.0	N	46.7	39.0	148.1	80.9	L
	10	6.2 (12.5)	334.1	46.9	42.9	82.9	140.0	45.0	L	38.9	81.3	136.6	49.0	L
	11	5.7 (13.1)	324.9	46.9	50.0	75.0	152.3	51.6	L	46.9	74.6	147.8	55.5	L
	12	1.9 (16.2)	332.5	33.3	50.0	81.4	145.0	60.0	L	50.8	81.7	145.9	58.4	L
	13	6.1 (25.0)	326.3	51.3	38.2	73.7	140.0	55.0	L	41.9	74.8	144.6	51.2	L
	14	0.9 (18.3)	326.9	52.6	41.8	74.8	145.0	50.0	L	41.3	74.7	144.3	50.6	L
	15	1.8 (12.3)	7.0	42.4	154.2	50.2	60.0	85.0	R	154.8	49.1	61.1	85.8	R
	16	3.3 (21.3)	352.1	50.3	161.7	41.0	60.0	80.0	R	159.6	43.1	57.8	79.2	R

Table 2.—*Continued*

	17	0.4	(2.5)	347.1	5.5	234.3	80.9	140.0	65.0	L	234.2	81.1	140.0	65.4	L
	18	2.1	(16.1)	350.5	58.1	140.0	40.0	50.0	90.0	R	141.1	39.0	231.8	89.4	R
	19	0.4	(18.8)	205.4	18.5	175.0	75.0	270.4	70.7	R	174.8	74.6	270.4	70.5	R
	20	6.2	(12.5)	334.1	46.9	42.9	82.9	140.0	45.0	L	38.9	81.3	136.6	49.0	L
	21	1.3	(24.2)	270.5	51.3	274.1	33.2	160.0	75.0	T	275.1	34.1	161.2	74.7	T
	22	4.0	(5.7)	280.0	0.0	100.0	85.0	192.9	60.1	R	100.0	81.0	195.2	60.4	R
	23	7.3	(11.8)	313.7	56.9	166.2	38.3	40.0	65.0	N	175.5	35.1	44.2	65.1	N
	24	3.9	(17.1)	338.1	31.3	45.0	85.0	137.9	60.1	L	46.8	86.3	139.2	57.0	L
	25	3.1	(18.5)	309.8	32.8	65.0	75.0	160.4	70.7	L	66.0	73.9	162.6	68.5	L
	26	5.3	(9.9)	5.9	45.8	149.2	50.2	55.0	85.0	R	151.1	47.2	58.6	87.3	R
	27	2.3	(17.2)	319.4	58.4	151.7	31.5	45.0	80.0	R	154.2	30.3	46.8	80.1	R
	28	4.8	(19.4)	334.3	35.8	45.0	81.4	140.0	60.0	L	47.2	82.6	142.2	56.2	L
	29	9.9	(23.8)	3.5	47.6	155.0	40.0	65.0	90.0	R	151.3	45.7	57.9	86.5	R
	30	10.6	(33.6)	255.3	75.8	341.2	62.0	240.0	70.0	R	332.2	61.6	229.3	67.6	R
	31	1.1	(3.5)	270.2	60.1	198.0	50.7	5.0	40.0	N	196.6	50.6	4.7	40.0	N
	32	7.2	(27.4)	272.5	35.4	110.9	80.0	20.0	85.0	R	106.5	85.7	16.2	86.6	R
Subarea C:	1	0.4	(6.9)	255.9	40.3	65.0	65.0	321.3	63.1	T	64.8	65.3	321.2	62.9	T
	2	9.3	(35.2)	294.4	69.0	290.4	85.0	50.0	10.0	R	281.6	81.7	56.7	11.6	R
	3	1.3	(29.2)	281.3	14.9	310.0	80.0	218.2	80.2	R	310.2	81.1	218.8	80.7	R
	4	1.6	(3.4)	132.2	30.7	243.7	63.1	140.0	65.0	T	243.5	63.6	139.2	63.6	T
	5	3.2	(21.9)	37.4	72.3	105.0	65.0	231.2	38.3	T	107.6	65.4	234.6	37.3	T
	6	1.5	(21.7)	92.7	1.7	305.0	90.0	215.0	70.0	R	305.1	88.8	214.6	69.2	R
	7	0.8	(28.3)	274.3	33.1	50.0	80.0	141.8	80.2	L	49.6	80.5	141.2	80.6	L
	8	1.2	(1.3)	164.3	18.7	213.3	50.7	115.0	80.0	L	213.6	50.0	114.5	79.3	L
	9	5.1	(9.9)	21.2	33.6	150.0	50.0	253.2	74.8	R	149.9	47.4	257.0	72.3	R
	10	0.5	(24.2)	317.4	20.1	213.7	71.9	115.0	65.0	L	213.4	72.1	114.9	65.4	L
	11	2.1	(16.4)	24.2	9.1	15.0	45.0	112.1	82.9	R	14.3	43.0	112.0	82.9	R
	12	6.8	(35.3)	252.9	50.1	180.0	80.0	278.3	50.7	R	174.0	78.9	274.6	46.7	R
	13	7.3	(27.2)	280.8	8.1	270.9	80.0	180.0	85.0	L	272.1	87.1	181.7	83.8	L
	14	10.9	(15.0)	76.0	14.7	135.0	85.0	229.2	50.2	R	133.5	79.4	229.7	59.6	R
	15	1.5	(25.2)	283.1	15.2	60.0	90.0	150.0	80.0	L	60.4	88.9	150.6	79.0	L
	16	2.3	(3.5)	313.1	39.9	315.5	54.4	65.0	65.0	T	316.9	56.1	65.7	64.3	T
	17	9.6	(29.1)	257.2	57.3	170.0	75.0	284.1	33.2	R	179.4	75.7	288.7	37.7	R
	18	5.6	(21.4)	281.2	18.1	320.0	85.0	229.1	80.0	R	318.7	80.9	226.5	76.9	R
	19	4.1	(27.6)	264.2	16.8	330.0	90.0	240.0	60.0	R	151.2	88.4	242.0	63.6	R
	20	17.6	(35.9)	263.3	35.9	65.0	60.0	155.0	90.0	L	57.0	73.2	325.3	84.4	L
	21	1.9	(2.7)	305.1	40.4	308.9	64.3	55.0	60.0	R	307.7	62.9	54.6	60.5	R
	22	9.0	(17.5)	191.4	53.7	236.7	41.0	135.0	80.0	L	234.0	37.2	126.8	77.4	L
	23	7.3	(17.8)	290.7	25.8	320.0	80.0	50.0	90.0	R	317.5	74.2	226.7	87.0	R
	24	16.8	(22.3)	263.1	0.8	320.0	85.0	225.8	50.2	R	140.1	85.8	232.2	64.1	R
	25	1.0	(11.4)	229.4	28.4	45.0	45.0	284.3	63.0	T	45.4	44.1	284.4	63.5	T
	26	0.4	(5.9)	46.8	43.0	130.0	60.0	242.8	56.2	T	129.9	60.0	242.4	56.4	T
	27	1.8	(21.3)	88.1	3.0	130.0	90.0	220.0	65.0	R	129.9	88.7	220.5	66.2	R
	28	0.3	(15.8)	233.9	15.1	165.0	65.0	268.7	63.1	R	164.8	64.9	268.7	62.8	R
Subarea I:	1	2.0	(9.9)	198.0	9.2	195.0	40.0	285.0	90.0	L	195.4	41.9	105.3	89.9	L

Table 2.—*Continued*

	2	3.2	(24.6)	144.4	30.3	300.5	68.4	65.0	35.0	N	299.3	70.9	59.4	34.6	N
	3	22.1	(33.7)	39.7	54.1	295.0	55.0	115.0	35.0	T	269.8	60.9	116.2	31.8	T
	4	18.7	(26.1)	314.3	26.9	145.0	70.0	47.9	71.3	L	156.0	54.0	50.5	69.8	L
	5	2.4	(12.9)	29.3	2.9	60.0	50.0	323.5	82.4	R	59.2	52.0	323.9	83.3	R
	6	7.2	(31.8)	124.8	39.5	291.5	80.2	50.0	20.0	N	295.8	74.8	67.4	22.2	N
	7	0.4	(22.4)	202.8	5.8	34.2	50.2	300.0	85.0	R	34.1	50.6	300.0	85.0	R
	8	11.9	(12.9)	313.7	51.3	257.0	56.2	40.0	40.0	N	269.8	60.9	40.5	40.4	N
	9	0.7	(16.7)	40.7	12.5	15.5	54.4	125.0	65.0	N	15.1	53.8	125.2	64.9	N
	10	21.6	(28.8)	165.5	31.5	155.0	80.0	246.8	80.2	R	141.7	62.4	239.2	76.1	R
	11	1.2	(39.7)	168.2	19.9	150.0	55.0	54.2	81.8	R	150.6	56.0	54.8	81.4	R
	12	0.4	(17.8)	187.8	13.0	105.0	70.0	7.9	71.3	L	105.2	70.0	8.0	70.9	L
	13	7.2	(12.4)	43.4	20.7	257.1	42.3	150.0	75.0	L	251.2	48.1	149.1	76.9	L
	14	3.6	(9.6)	279.3	16.4	271.1	64.3	165.0	60.0	T	269.8	60.9	162.2	61.5	T
	15	14.1	(26.2)	168.8	16.9	148.3	41.0	250.0	80.0	R	156.0	54.0	252.0	81.8	R
	16	2.6	(30.1)	121.2	47.5	295.0	85.0	178.7	11.2	N	296.9	83.3	173.7	12.2	N
Subarea J:	1	6.1	(35.9)	285.9	27.1	95.0	45.0	324.9	57.2	T	93.2	50.3	324.5	53.0	T
	2	8.9	(30.5)	326.7	0.2	267.5	80.2	160.0	30.0	L	268.5	84.8	165.1	21.4	L
	3	0.9	(8.0)	29.1	27.9	27.4	80.3	120.0	75.0	R	27.0	79.6	119.8	75.0	R
	4	3.2	(29.1)	120.9	0.3	115.0	65.0	213.7	71.9	L	115.2	68.2	212.7	71.8	L
	5	2.2	(6.7)	319.1	21.3	155.0	81.4	60.0	60.0	R	156.0	79.3	59.6	59.6	R
	6	1.3	(43.1)	124.7	9.0	110.0	70.0	216.0	52.8	N	110.3	71.3	215.2	52.8	N
	7	8.2	(38.9)	285.9	1.5	75.0	75.0	189.1	33.2	L	75.6	82.0	177.2	35.0	L
	8	2.9	(16.0)	295.5	2.9	110.0	70.0	203.5	80.6	L	110.0	67.1	204.1	80.5	L
	9	1.8	(14.7)	291.8	3.0	105.0	65.0	199.3	80.9	L	105.0	66.8	198.9	81.0	L
	10	3.1	(13.6)	292.1	2.8	105.0	70.0	198.5	80.6	L	105.0	66.9	199.1	80.4	L
	11	31.4	(33.7)	51.4	57.7	0.7	63.9	135.0	35.0	N	30.9	77.5	138.4	36.4	L
	12	3.2	(38.2)	297.4	32.8	137.5	80.2	30.0	30.0	R	139.4	77.6	27.1	29.9	R
	13	2.3	(7.0)	46.3	8.6	287.6	39.7	140.0	55.0	T	290.4	38.6	138.7	54.9	T
	14	0.1	(3.2)	41.2	0.7	294.6	52.8	140.0	40.0	T	294.7	52.8	139.9	40.0	T
	15	9.3	(38.4)	322.7	25.3	169.1	85.8	70.0	25.0	R	345.1	86.6	81.5	28.3	R
	16	3.3	(24.4)	114.3	0.2	105.0	65.0	203.7	71.9	L	105.2	68.2	202.7	72.0	L
	17	2.9	(5.2)	131.1	89.6	130.0	50.0	294.7	41.0	T	127.1	50.0	291.7	41.0	T
	18	17.8	(31.5)	344.0	24.7	303.9	35.5	160.0	60.0	N	273.9	26.1	153.3	76.0	R
	19	4.7	(14.2)	72.4	23.4	199.5	22.3	315.0	80.0	L	205.2	25.1	312.5	82.1	L
	20	0.2	(7.7)	225.9	0.1	299.6	52.8	145.0	40.0	T	299.7	52.8	144.8	40.0	T
	21	12.0	(20.3)	304.2	4.4	125.0	80.0	231.7	31.5	R	126.0	68.0	248.7	36.8	R
	22	6.0	(19.0)	257.9	61.5	120.0	70.0	240.6	35.5	R	126.0	68.0	246.8	38.3	R
Subarea K:	1	2.3	(24.1)	78.6	45.2	281.0	45.9	115.0	45.0	T	278.8	47.3	114.4	43.7	T
	2	14.0	(15.7)	33.7	25.5	230.0	50.0	320.0	90.0	L	240.8	38.3	145.6	85.9	L
	3	31.8	(34.7)	322.0	34.3	183.3	46.0	300.0	65.0	N	230.4	34.4	139.5	89.4	L
	4	2.0	(25.2)	175.3	39.0	350.0	40.0	80.0	90.0	R	351.1	38.5	81.2	89.9	R
	5	3.9	(21.1)	170.9	56.1	135.0	55.0	297.9	36.2	T	139.0	56.8	298.7	34.9	T
	6	0.8	(16.3)	167.8	53.9	140.0	60.0	283.9	35.5	T	139.2	59.6	283.9	35.7	T
	7	0.8	(10.3)	71.0	42.7	273.1	48.4	135.0	50.0	T	272.3	49.0	134.9	49.7	T

Table 2.—*Continued*

8	12.9	(32.5)	132.3	30.4	120.0	70.0	300.0	20.0	N	127.0	81.0	295.9	9.2	N
9	24.9	(32.0)	43.6	18.6	15.0	35.0	276.8	84.3	L	31.1	57.2	289.1	72.1	L
10	0.8	(33.0)	190.4	80.4	305.9	85.8	45.0	25.0	R	306.7	85.7	45.9	24.9	R
11	13.5	(42.4)	139.1	76.8	290.6	84.9	40.0	15.0	R	303.6	82.1	64.5	15.2	R
12	9.1	(22.0)	136.9	47.3	120.0	75.0	265.7	18.0	N	127.0	81.0	254.7	14.5	N
13	3.6	(40.9)	142.4	75.4	300.0	85.0	56.3	11.2	R	303.5	84.1	64.4	11.3	R
14	20.1	(25.9)	145.0	62.9	325.0	90.0	235.0	60.0	L	127.0	81.0	222.5	59.0	L
15	34.4	(49.6)	140.7	56.2	335.9	80.0	245.0	85.0	L	127.0	81.0	217.8	85.2	L
16	3.0	(11.5)	26.2	6.9	225.0	30.0	315.0	90.0	R	223.1	32.8	314.6	89.1	R
17	1.0	(21.1)	16.4	1.7	213.3	31.5	320.0	80.0	R	213.8	30.5	320.2	80.5	R
18	12.0	(32.6)	128.2	50.3	254.1	80.0	345.0	85.0	L	262.1	75.1	355.0	79.3	L
19	10.4	(33.3)	106.7	71.4	105.0	30.0	339.0	71.3	T	114.6	33.3	349.9	69.5	T
20	15.4	(26.8)	176.5	68.1	115.0	50.0	324.5	44.0	T	132.8	53.5	335.9	38.8	T
21	8.9	(42.0)	264.7	21.1	218.2	28.0	85.0	70.0	T	230.4	34.4	88.3	61.7	T
22	0.3	(6.9)	168.7	42.9	150.0	55.0	265.7	58.2	T	150.3	55.2	265.8	58.2	T
23	5.3	(24.7)	72.1	32.8	272.9	36.2	110.0	55.0	T	268.3	40.4	109.2	51.5	T
24	2.3	(33.0)	93.3	57.7	293.0	50.7	100.0	40.0	T	290.7	51.9	98.2	38.8	T
25	2.8	(40.5)	93.3	49.0	284.0	45.9	90.0	45.0	T	286.5	44.1	92.2	46.8	T
26	1.1	(36.4)	93.4	51.8	289.0	45.9	95.0	45.0	T	288.0	46.5	94.2	44.3	T
27	19.3	(42.6)	72.4	14.8	249.6	52.8	95.0	40.0	T	254.4	34.2	93.8	57.3	T
28	10.9	(35.5)	157.0	43.7	167.3	51.6	65.0	75.0	R	173.5	59.3	74.6	75.4	R
29	9.1	(33.6)	109.8	60.0	304.5	44.0	95.0	50.0	T	295.9	48.4	85.8	45.7	T
30	0.8	(10.3)	71.0	42.7	273.1	48.4	135.0	50.0	T	272.3	49.0	134.9	49.7	T
31	1.1	(20.6)	208.4	43.5	330.5	54.4	80.0	65.0	R	330.7	53.9	81.1	64.5	R
32	0.5	(13.8)	235.4	45.0	325.0	70.0	71.0	52.8	R	324.8	70.0	70.6	53.2	R
33	20.4	(40.5)	61.4	38.0	10.0	45.0	257.8	69.3	T	31.1	57.2	273.9	54.7	T
34	7.3	(35.5)	179.0	43.0	160.3	41.0	325.0	50.0	T	152.8	36.1	322.4	54.4	T
35	3.5	(11.4)	188.9	2.6	65.0	65.0	326.3	71.9	L	63.5	67.0	326.8	74.6	L
36	4.3	(43.0)	272.9	24.8	224.3	31.6	85.0	65.0	T	230.4	34.4	86.6	61.1	T
37	6.5	(7.2)	12.0	2.4	65.0	60.0	324.7	72.8	L	62.6	64.0	326.2	77.2	L
38	9.2	(24.7)	82.2	45.6	290.0	40.0	110.0	50.0	T	280.7	45.9	106.0	44.2	T
39	5.8	(26.0)	73.3	38.7	267.8	48.4	115.0	45.0	T	272.6	44.1	115.8	48.3	T
40	0.7	(40.0)	90.4	44.8	285.4	41.0	90.0	50.0	T	284.8	41.5	89.6	49.5	T
41	6.3	(23.4)	129.9	17.6	125.0	75.0	270.7	18.0	N	127.0	81.0	257.4	13.7	N
42	9.4	(37.7)	114.6	68.4	290.2	60.2	75.0	35.0	T	298.9	56.8	86.3	37.9	T
43	7.0	(20.2)	168.0	35.2	75.0	90.0	345.0	60.0	L	251.0	89.5	341.2	65.7	L
44	1.9	(34.8)	138.9	58.4	125.0	25.0	347.8	71.1	T	127.1	26.0	349.6	70.2	T
45	8.5	(27.8)	159.4	80.3	135.0	50.0	356.9	48.4	T	126.1	48.7	348.3	49.8	T
46	22.6	(32.8)	148.7	38.3	150.0	45.0	52.9	82.9	R	162.4	62.6	69.1	83.7	R
47	4.1	(14.9)	81.7	49.8	268.7	63.1	165.0	65.0	L	272.1	60.4	166.9	65.3	L

[1]Minimum rotation between the observed mechanism and any one consistent with the model for: preferred (alternate) nodal plane

[2]Rotation axis azimuth and plunge—applies to preferred nodal plane (the one with smaller misfit)

[3]Dip angle; dip direction is 90° clockwise from strike direction

[4]Predominant slip component of preferred nodal plane: N = normal, T = thrust, R = right-lateral, L = left-lateral

Thus, the final stress state may reflect an overall reduced and redistributed pattern of loading on the main rupture plane; the fact that the principal stress axes are not parallel and perpendicular to the plane in subareas A–C suggests that the shear stress is not completely relieved in that region. This differs from the general conclusions of Zoback and Beroza (1993) and Beroza and Zoback (1993), although they included in their analysis all aftershocks from a 21-month period following the main shock, and they did not explore for spatial variations by subdividing the area, as done here. That the southeast end of the aftershock zone approaches the creeping section of the San Andreas might suggest that shear stress magnitudes are low in that region—that is, where the fault is creeping we might surmise that it is weak, as it does not support sufficient ambient stress to allow it to fail in large events. Thus the aftershocks in this region might be induced by even a small static stress change caused by the main shock (for example, as inferred to have occurred on the Calaveras fault in response to the Morgan Hill earthquake, by Oppenheimer and others, 1988); however Beroza and Zoback (1993) found that the Loma Prieta aftershock geometries are inconsistent with this hypothesis.

In subareas J and K, northwest of the main shock hypocenter, the inferred stresses have a common σ_1 direction, essentially normal to the main shock fault plane, indicating that virtually no shear stress remains on that plane in either area (consistent with Zoback and Beroza, 1993, and Beroza and Zoback, 1993). However, the other two principal stress directions, which are parallel to the main shock

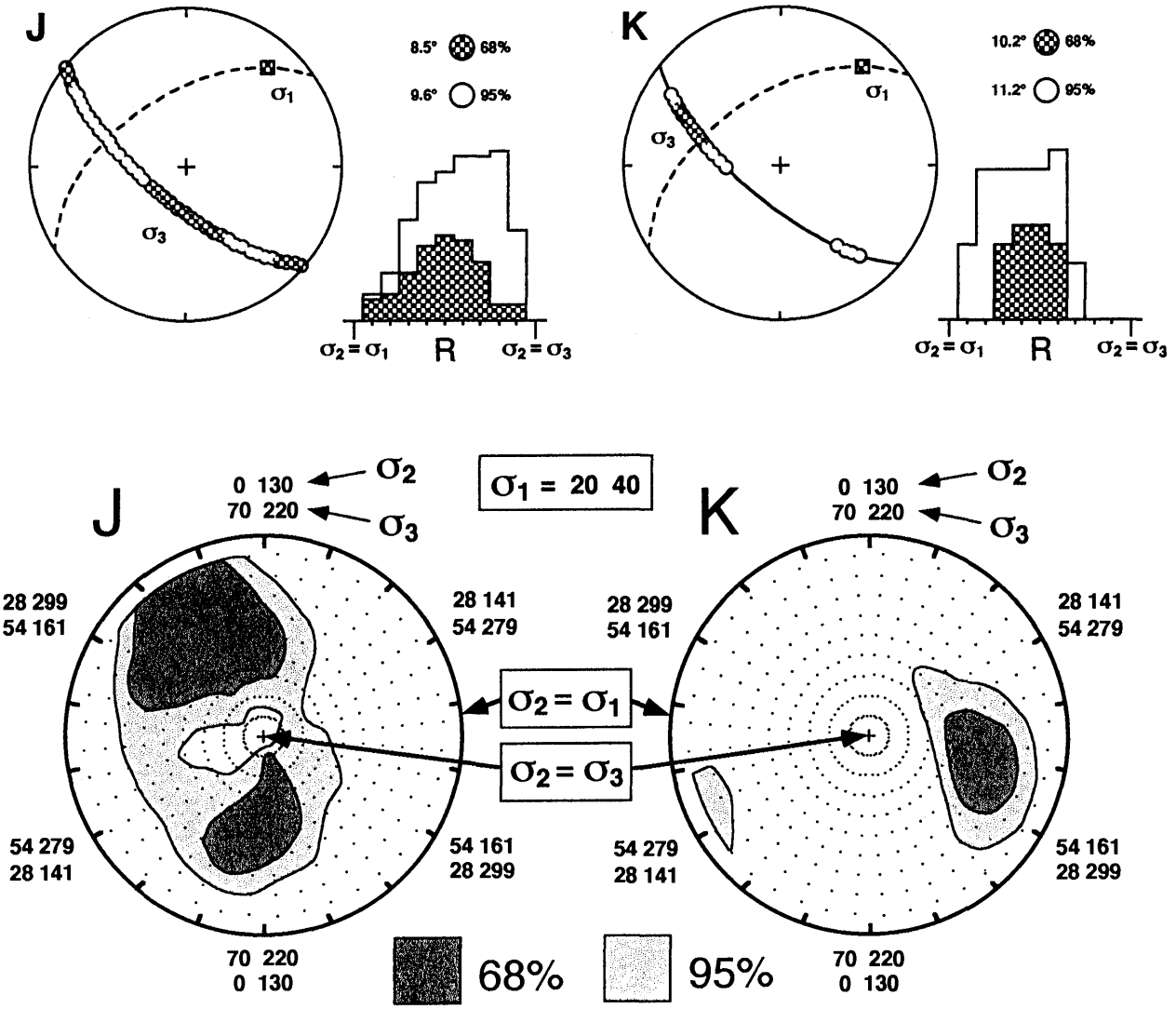

Figure 6.—Details of results for subareas J and K. Top, Results of grid search of stress models with σ_1 direction normal to the main shock fault plane. The optimum σ_3 directions in the two cases are oriented in complementary directions within the fault plane. Bottom, A more detailed illustration of all stress models with σ_1 perpendicular to the fault plane—σ_2 and σ_3 directions vary by azimuth, R varies radially, such that each point represents a unique stress model. (Stress directions are indicated by plunge and azimuth.) There is a strong negative correlation between the ranges of acceptable models for the two subregions.

fault plane and therefore do not contribute to shear stress on it, exhibit different orientations in the two subareas (fig. 6). These observations suggest that at least a small amount of deviatoric stress remains in the region, but that it is of an orientation that cannot be relieved by slip on the main shock fault plane. This might account for the observation that aftershocks in the region exhibit diverse focal mechanisms that are generally dissimilar to that of the main shock (Oppenheimer, 1990).

It is possible that the systematic and complementary distributions of acceptable stresses in subareas J and K shown in figure 6 may reflect variations owing to differences in relative locations along the fault plane, although the mechanical basis for this is not entirely clear. Subarea J is located essentially up the slip vector from the hypocenter (fig. 1), in a region through which the main rupture propagated as a Mode II crack (in-plane shear; Atkinson, 1987); in contrast, subarea K is everywhere significantly up-dip of the hypocenter, where the main rupture had a greater Mode III nature (anti-plane shear). It is unclear why a difference in failure mode should give rise to the observed expression among the aftershock stresses, but the observed symmetry and systematic pattern of inferred stresses in figure 6 is intriguing. In any case, the differences observed between subareas J and K apparently reflect minor heterogeneities in the postseismic stress, of a kind that do not significantly contribute to the shear stress on the main shock fault plane.

An explanation for the difference in stress behavior observed on either side of the main shock hypocenter may emerge from the model of Rice (1992). According to Rice, maturely deformed fault zones such as the San Andreas may exhibit two distinct stress domains, which arise due to spatial variation in pore pressure or physical properties of the region, or both. In his model, the narrow region within the fault zone indicates stress consistent with laboratory-derived frictional properties of rocks (with σ_1 at about 25-30° to the fault plane), while the surrounding region indicates near fault normal compression; this may resolve the long-standing apparent conflict between the inferred weakness of some fault zones, based on the lack of a significant heat flow anomaly, and experimental and theoretical estimates of fault strength. In the present case, it is possible that the heterogeneous aftershocks northwest of the main shock hypocenter record stress off the fault plane, while the more uniform aftershocks southeast of the hypocenter indicate stress inside a well-developed fault zone. If this is so, then the stresses inferred from the early aftershocks, while reflecting real and meaningful spatial variations in stress, may not fully sample all the variation throughout the region.

The determinations of stress in this study may be of some value in assessing the seismic hazard of known faults in the region. If the four stress parameters of interest here are known in a region, together with the orientations of a particular planar zone of weakness, then a forward procedure can be applied to evaluate the relative potential for failure of the prospective faults, as shown in figure 7. As discussed above, Mohr Sphere diagrams can be constructed for each region in which the four stress parameters are known: three principal stress directions and the value of R. These diagrams illustrate the magnitudes of relative normal and shear stress on planes of fixed orientation, normalized by the unknown quantities τ_m and σ_m. Figure 7 shows the projections of the Mohr Spheres on the [$\tau \bullet b$=0] plane, such that shear stress and slip vectors are aligned. The Mohr Spheres for five of the subareas are superimposed; for each of these, the sizes of the two inner spheres are different from those of the other subareas, so none are shown.

On figure 7, the pole of a single plane of orientation, N35°W, vertical, roughly characteristic of the regional San Andreas fault system, is shown relative to the stresses in each region—the pole plots in different places on the Mohr Sphere for each region because the stresses for which the sphere is constructed are different in each case. By requiring that the slip vector match the shear stress direction on the fault plane, the focal mechanisms predicted for each subarea can be determined, as shown. Conventional Mohr or Coulomb fault mechanics (for example, Jaeger and Cook, 1979) suggests that failure should occur on planes of relatively high shear stress and relatively low normal stress. Thus, neglecting the uncertainty of the absolute stress magnitudes, failure is most likely on a fault of this orientation in the vicinity of subarea A, for which the pole falls at the upper left of the Mohr Sphere, and less likely near subareas J and K, with poles at the middle right side of the figure. A number of considerations may limit the utility of this notion, as only local stress and fault geometries are considered; this discussion neglects other relevant physical parameters which are very poorly known, such as possible variation in fault properties and local stress heterogeneities. Perhaps most importantly, the values of τ_m and σ_m, which cannot be estimated in the present analysis of fault geometries (because they are not dimensionless), are of particular significance for the relative magnitudes of shear and normal stress on all planes and thus for the likelihood of failure.

A different experiment regarding the relation between stress and earthquakes, applied by Reasenberg and Simpson (1992), models the Loma Prieta main shock as a dislocation in an elastic half-space and evaluates seismic risk by predicting a spatially-varying pattern of static stress changes on known vertical fault planes of the San Andreas fault system in central California. This analysis, although based on simplified fault orientation data, explicitly considers changes in absolute normal and shear stress magnitudes—quantities that are certainly relevant to the occurrence of fault rupture. The predicted stress changes and consequent seismic risk depend strongly on fault trend

and location; these generally agree well with observed changes in rates of seismicity from before to after the main shock.

The forward procedure employed by Reasenberg and Simpson (1992) and the inverse procedure of this study may be complementary in some respects. Not only do the two analyses apply information in opposite directions (forward versus inverse) and presume different associations between earthquakes with the stress field (active versus passive), but they treat substantially different aspects of the stress tensor. Of the two experiments, the dislocation modeling addresses the aspect of the stress tensor that affects the occurrence of failure on fault planes of known (or assumed) orientation and physical properties, while the inverse approach regards the part of the stress tensor that governs the geometry of fault motion.

CONCLUSIONS

Analysis of the focal mechanisms of groups of aftershocks from the first six weeks after the Loma Prieta earthquake indicates a systematic pattern of postseismic stresses along the main rupture plane. To a first order, the main shock fault plane appears to be nearly completely relieved of shear stress in the region northwest of the main shock hypocenter but may remain loaded by shear stress to the southeast; the direction of shear stress on the fault plane is consistent with the overall main shock slip in the region immediately to the southeast of the hypocenter but deviates from it considerably further to the southeast near the end of the aftershock zone. Within each of these two apparently independent stress domains (northwest and southeast of the main shock hypocenter), some variation in stress is observed at length scales of about 10 km or less. From these observed patterns of stress variation, it appears that steep northwest- or north-northwest-trending faults in the region may be at greater risk of failure near the southeast end of the aftershock zone than to the northwest of the main shock hypocenter. It is important to note that these interpretations are based only on the estimates of the four dimensionless stress parameters derived from the present inverse procedure, including the three principal stress directions and just one measure of stress magnitude; the absolute magnitudes of both normal and deviatoric shear stresses are unconstrained in this analysis. Thus it is possible that, while in some places the main shock fault plane occurs in an orientation that is favorable for renewed slip (in other words, relatively high shear stress and low normal stress compared to other orientations), the absolute shear stress magnitude may be low and the normal stress magnitude may be high, such that the plane might not be likely to fail. The difference in stress inferred on either side of the main shock hypocenter (along strike variation) may indicate a difference in the nature of the two aftershock regions relative to the width of the main shock fault zone (across strike variation), as in the model of Rice (1992). In this case, the aftershocks to the northwest of the hypocenter may reflect the volume surrounding the fault zone, while the ones to the southeast may reflect the condition of the fault zone itself.

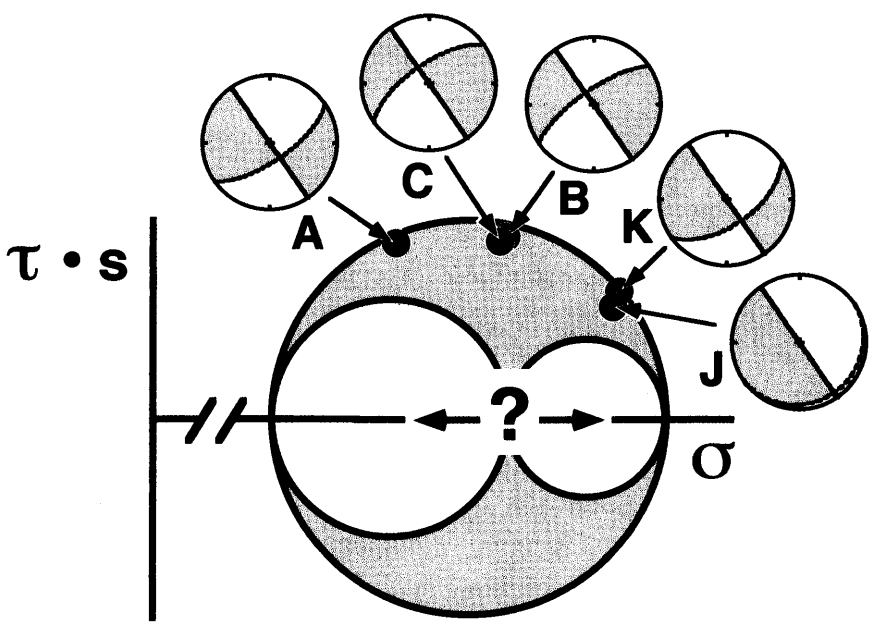

Figure 7.—Projection of Mohr Sphere diagram for five of the subregions (as in fig. 5). The diagram was constructed using the best-fitting stress model found in each region (each with a unique value of R, which would prescribe the size of the two inner circles, but is not shown). Plotted on the projection is the pole of a fault of orientation N35°W, vertical, together with the corresponding focal mechanism that would yield [$\tau \bullet s > 0$, $\tau \bullet b = 0$]. A weak plane of this orientation may be at risk of failure under the stress at subarea A, as it experiences relatively high shear stress and low normal stress, and thus may exceed conventional failure envelopes.

ACKNOWLEDGMENTS

I am grateful to David Oppenheimer and others at the U. S. Geological Survey for compiling and making available the focal mechanism data used in this study and for helpful discussions. David, Andy Michael, and Paul Reasenberg provided thoughtful reviews. This work was supported by USGS Grant 14-08-0001-G1841. INSTOC Contribution 193.

REFERENCES CITED

Atkinson, B.K., 1987, Introduction to fracture mechanics and its geophysical applications, *in* Atkinson (ed.), B.K., Fracture mechanics of rock: London, Academic Press, p. 1-26.

Beroza, G.C., 1991, Near-source modeling of the Loma Prieta earthquake: Evidence for heterogeneous slip and implications for earthquake harzard: Bulletin of the Seismological Society of America, v. 81, no. 5, p. 1603-1621.

Beroza, G.C., and Zoback, M.D., 1993, Mechanism diversity in the Loma Prieta aftershocks and the mechanics of main shock-aftershock interaction: Science, v. 259, p. 210-213.

Bott, M.H.P., 1959, The mechanics of oblique slip faulting: Geological Magazine, v. 96, p. 109-117.

Dietz, L.D., and Ellsworth, W.L., 1990, The October 17, 1989, Loma Prieta, California, earthquake and its aftershocks: Geometry of the sequence from high-resolution locations: Geophysical Research Letters, v. 17, no. 9, p. 1417-1420.

Gephart, J.W., 1990a, Stress and the direction of slip on fault planes, Tectonics, v. 9, p. 845-858.

———1990b, FMSI: A FORTRAN program for inverting fault/slickenside and earthquake focal mechanism data to obtain the regional stress tensor, Computers & Geosciences, v. 16, p. 953-989.

Gephart, J.W., and Forsyth, D.W., 1984, An improved method for determining the regional stress tensor using earthquake focal mechanism data: Application to the San Fernando earthquake sequence, Journal of Geophysical Research, v. 89, p. 9305-9320.

Hartzell, S.H., Stewart, G.S., and Mendoza, C., 1991, Comparixon of L_1 and L_2 norms in a teleseismic waveform inversion for the slip history of the Loma Prieta, California, earthquake: Bulletin of the Seismological Society of America, v. 81, no. 5, p. 1518-1539.

Jaeger, J.C., and Cook, N.G.W., 1979, Fundamentals of rock mechanics: Chapman and Hall, New York, 593 p.

Marshall, G.A., Stein, R.S., and Thatcher, W., 1991, Faulting geometry and slip from co-seismic elevation changes: The 18 October 1989, Loma Prieta, California, earthquake: Bulletin of the Seismological Society of America, v. 81, no. 5, p. 1660-1693.

McKenzie, D.P, 1969, The relationship between fault plane solutions for earthquakes and the directions of the principal stresses: Bulletin of the Seismological Society of America, v. 59, p. 591-601.

Michael, A.J., Ellsworth, W.L., and Oppenheimer, D.H., 1990, Coseismic stress changes induced by the 1989 Loma Prieta, California earthquake: Geophysical Research Letters, v. 17, no. 9, p. 1441-1444.

Oppenheimer, D.H., 1990, Aftershock slip behavior or the 1989, Loma Prieta, California, earthquake: Geophysical Research Letters, v. 17, no. 8, p. 1199-1202.

Oppenheimer, D.H., Reasenberg, P.A., and Simpson, R.W., 1988, Fault plane solutions for the 1984 Morgan Hill, California, earthquake sequence: Evidence for the state of stress on the Calaveras fault: Journal of Geophysical Research, v. 93, p. 9007-9026.

Reasenberg, P.A., and Simpson, R.W., 1992, Response of regional seismicity to the static stress change produced by the Loma Prieta earthquake: Science, v. 255, p. 1687-1690.

Rice, J.R., 1992, Fault stress states, pore pressure distributions, and the weakness of the San Andreas fault, *in* Evans, B., and Wong, T.-F., eds., Fault mechanics and transport properties of rock: London, Academic Press, p. 475-503.

Steidl, J.H., Archuleta, R.J., and Hartzell, S.H., 1991, Rupture history of the 1989 Loma Prieta, California, earthquake: Bulletin of the Seismological Society of America, v. 81, no. 5, p. 1573-1602.

U.S. Geological Survey Staff, 1990, The Loma Prieta event: An anticipated event: Science, v. 247, p. 286-293.

Wald, D.J., Helmberger, D.V., and Heaton, T.H., 1991, Rupture model of the 1989 Loma Prieta earthquake from inversion of strong-motion and broadband teleseismic data: Bulletin of the Seismological Society of America, v. 81, no. 5, p. 1540-1572.

Wallace, R.E., 1951, Geometry of shearing stress and relation to faulting: Journal of Geology, v. 59, p. 118-130.

Zoback, M.D., and Beroza, G.C., 1993, Evidence for near-frictionless faulting in the 1989 (M 6.9) Loma Prieta, California, earthquake and its aftershocks: Geology, v. 21, p. 181-185.

THE LOMA PRIETA, CALIFORNIA, EARTHQUAKE OF OCTOBER 17, 1989:
EARTHQUAKE OCCURRENCE

AFTERSHOCKS AND POSTSEISMIC EFFECTS

LOMA PRIETA AFTERSHOCK RELOCATION WITH *S-P* TRAVEL TIMES FROM A PORTABLE ARRAY

By Susan Y. Schwartz and Glenn D. Nelson,
University of California, Santa Cruz

CONTENTS

ABSTRACT

Aftershocks of the Loma Prieta earthquake are located using *S-P* arrival time measurements from stations of the PASSCAL aftershock deployment. We demonstrate the effectiveness of using *S-P* arrival time data in locating earthquakes recorded by a sparse, three-component network. Events are located using the program QUAKE3D (Nelson and Vidale, 1990) and a three-dimensional *P*-wave velocity model developed independently for this region. Both a constant and a variable vp/vs ratio model are used to generate *S*-wave velocities. The dense coverage of the area around the Loma Prieta rupture zone by instruments of the California Network (CALNET) has allowed the U.S. Geological Survey (USGS) to find *P*-wave earthquake locations, which we compare with our solutions. We also perform synthetic calculations to estimate realistic location errors resulting from uncertainties in both the three-dimensional velocity structure and the timing of arrivals. These calculations provide a comparison of location accuracies obtained using *S-P* arrival times, *S* and *P* arrival times and *P* times alone. We estimate average absolute errors in epicentral location and in depth for the Loma Prieta aftershocks to be between 1 and 2 km using *S-P* phase data and the sparse PASSCAL instrument coverage. The synthetic tests show that these errors are much smaller than those predicted using *P*-wave data alone and are nearly the same as those predicted using *S* and *P* phase data separately. This suggests that future aftershock recording deployments with sparse networks of three-component data can retrieve accurate event locations even if absolute timing is problematic using *S-P* times.

INTRODUCTION

Seismic studies using local networks have revealed important information about earthquake dynamics, fault zone structure, and the effects of near-surface geology on the amplification of strong ground motion. Determination of accurate hypocentral locations is an essential step in analysis of local earthquake data; however, accurate locations are difficult to obtain in the common situation of sparse instrument coverage. Location difficulties arise from several sources: the mathematical instability of solutions due to the interdependence of origin time and depth, inadequacies in the velocity model used in the location process, and uncertainties in arrival times caused by both reading and clock errors. In this paper, we demonstrate the effectiveness of utilizing *S-P* differential arrival-time data in locating earthquakes recorded by a sparse three-component network. The use of *S-P* times for earthquake location removes the trade-off between depth and origin time as well as arrival-time uncertainties arising from clock errors. Furthermore, locations derived from *S-P* arrival times are less sensitive to errors in the velocity model, provided that the Poisson ratio remains relatively constant in the region under consideration.

We use the finite-difference location program QUAKE3D (Nelson and Vidale, 1990) to locate aftershocks of the Loma Prieta earthquake using data recorded by stations of the PASSCAL aftershock deployment (Lerner-Lam and others, 1990; Schwartz and others, 1990). The program QUAKE3D locates earthquakes in regions with complex three-dimensional velocity heterogeneity. The *P*-wave velocity structure in the source region of the Loma Prieta earthquake has been well studied, and both two-dimensional (Dietz and Ellsworth, 1990) and three-dimensional (Eberhart-Phillips and others, 1990a; Lees, 1990) velocity models have been computed. The Loma Prieta earthquake occurred in a region of dense CALNET

instrument coverage, providing accurate locations for most of the aftershocks that we compare with our solutions. Therefore, the aftershock sequence of the Loma Prieta earthquake provides an excellent opportunity to evaluate the effectiveness of using *S-P* arrival times to locate earthquakes in a realistic three-dimensional velocity structure. In this study, we are constrained to use differential arrival times due to uncertainties in the absolute timing of the seismic phases recorded by the PASSCAL instruments. Because such timing uncertainties are often encountered in seismic field deployments, earthquake location techniques that require only the relative timing of phases are useful. The application of an *S-P* location scheme can also substantially reduce the time required to locate earthquakes for studies involving large volumes of data, since time-consuming clock calibrations and corrections are not necessary.

METHOD AND DATA

The location algorithm QUAKE3D has been described elsewhere (Nelson and Vidale, 1990) and will only be summarized briefly here. QUAKE3D is a two-step location procedure where the first step is the discretization of the source volume and the computation of travel times from all recording stations to all points in the grid using the finite-difference method of Vidale (1990). *S*-wave travel times are produced from *P*-wave travel times by assuming a constant Poisson ratio throughout the source volume or by using a three-dimensional model of vp/vs ratios determined for this region by Thurber and Atre (1993). Next, the earthquake hypocenters are determined by finding the position within the source volume that yields the smallest travel time residuals for a set of arrival times for each earthquake. Since QUAKE3D is a grid searching algorithm rather than a least-squares iterative inversion, as are most earthquake location programs, the L1 or L2 norms can be employed with equal ease to determine earthquake locations. Our solutions are computed using the L1 norm, since it is less sensitive to data outliers.

In this study, we use *S-P* times to locate aftershocks of the 1989 Loma Prieta earthquake rather than only *P* times, as in Nelson and Vidale (1990). The *S-P* arrival times are picked by hand from recordings at stations of the Loma Prieta IRIS-PASSCAL aftershock deployment. The recording instruments consisted of Reftek 16-bit digitizers with L-22 (2 Hz) three-component geophones. They were deployed in the northern section of the Loma Prieta aftershock zone from October 20 through November 21, 1989. We locate 50 aftershocks with magnitudes between 1.5 and 3.0 that occurred in the region of dense instrument coverage between October 22 and November 4. In this period, between 10 and 18 widely distributed stations were in operation. Between 4 and 10 stations yielded high-quality *P*- and *S*-wave arrivals for each event. This number is significantly lower than the total number of stations deployed (21) for several reasons: (1) only 10 stations were established during the first week, with instrument coverage expanding southward to a total of 20 stations by the end of the second week; (2) not all stations recorded all events; (3) some stations had instrument problems; and (4) some arrivals were not impulsive enough to accurately read *P*- and *S*-wave times. Figure 1 shows a map of the PASSCAL station locations and the USGS locations (Dietz and Ellsworth, 1990) of the events we analyze.

We locate these events using a three-dimensional velocity model derived through inversion of CALNET *P*-wave arrival-time data from Loma Prieta aftershocks (Eberhart-Phillips and others, 1990b). The three-dimensional velocity model was interpolated from the published model to produce a uniform Cartesian grid (horizontal directions perpendicular and parallel to the strike of the San Andreas Fault and the vertical direction) consisting of $58 \times 100 \times 56$ points with a 0.5-km spacing ($29 \times 50 \times 28$ km) covering the source area. The approximate borders of this travel-time grid are indicated in figure 1. *P*- and *S*-wave travel times were then computed from each station to every one of the 324,800 grid points to be evaluated as potential earthquake sites during the location procedure. *S*-wave travel times were computed either using a constant vp/vs ratio of 1.73 or the three-dimensional vp/vs ratio model of Thurber and Atre (1993).

The PASSCAL instruments recorded both high- and low-gain channels of three-component data that triggered when the ratio of the short term average amplitude (1 s) to the long-term average amplitude (30 s) exceeded a value of 4.5. Once triggered, 60 s of data were recorded, including a pre-trigger length of 10 s. The data sample rate was 200 samples per second during the first week of operation, after which it was reduced to 100 samples per second. We read *P*- and *S*-wave arrival times from the vertical and horizontal components respectively of the high-gain channel. When data recorded on this channel were clipped, we read arrival times from the low-gain channel. In general, data quality was very high; however, for several events, *S*-wave arrival times could not be determined reliably and these events were not located. We estimate our reading errors to be less than 0.05 s and 0.1s for the *P* and *S* waves respectively. Figure 2 shows examples of *P* and *S* waveforms from different earthquakes recorded by several of the PASSCAL stations. In many cases, both *P* and *S* waves are quite complicated; however, initial arrival times can be read very accurately from the vertical and horizontal components, respectively. It is apparent from figure 2 that attempts to read *S*-wave arrival times from the vertical component seismograms would introduce large errors, sometimes exceeding 0.2 s.

SYNTHETIC EXAMPLES

The advantages of using *S* phases to help constrain earthquake location have been recognized for some time (for example, James and others, 1969; Buland, 1976; and Gomberg and others, 1990). Much of the benefit of including *S* phases in the determination of earthquake hypocenters arises from the substantial increase in the range of partial derivatives of travel time with respect to the three spatial parameters of the hypocenter compared with *P* waves. The expanded range of the partial derivative with respect to depth can result in a reduction of the trade-off between depth and origin time, which plagues location schemes that use only *P* waves (Gomberg and others 1990). In situations where exact origin times of earthquakes are unnecessary, the use of *S-P* times for locating earthquakes removes the trade-off between depth and origin time, allowing depth determinations to be better constrained. Also, we show that *S-P* arrival times are less sensitive to uncertainties in velocity models than are *P* and *S* times separately. However, because uncertainties in both velocity structure and timing of arrivals are greater for *S* waves than for *P* waves, the actual benefit of incorporating *S* waves into earthquake location schemes may be substantially diminished compared with noise-free theoretical expectations.

To evaluate the effectiveness of using *S-P* times for earthquake location and to approximate the errors expected from our earthquake locations, we first performed comprehensive synthetic experiments. The first experiment is designed to estimate location errors resulting from uncertainties in the assumed velocity model. Using the same receiver geometry as our data and the three-dimensional velocity model of Eberhart-Phillips and others (1990b), we computed exact *P* - and *S*-wave arrival times from the locations we determined for the 50 events shown in figure 1. We then located these events in a model generated by adding Gaussian-distributed random-velocity perturbations with an RMS value of 5 percent with scale lengths of about 5 km to the model of Eberhart-Phillips and others (1990b) and using the following combinations of phases: *S* and *P*, *S-P*, and *P* alone. When using both *P*- and *S*-wave data to locate earthquakes, we divided the *P*- and *S*-wave residuals by weights of 1 and vp/vs, respectively, prior to choosing the location that minimizes the L1 norm of the residuals. The weighting was applied to equalize

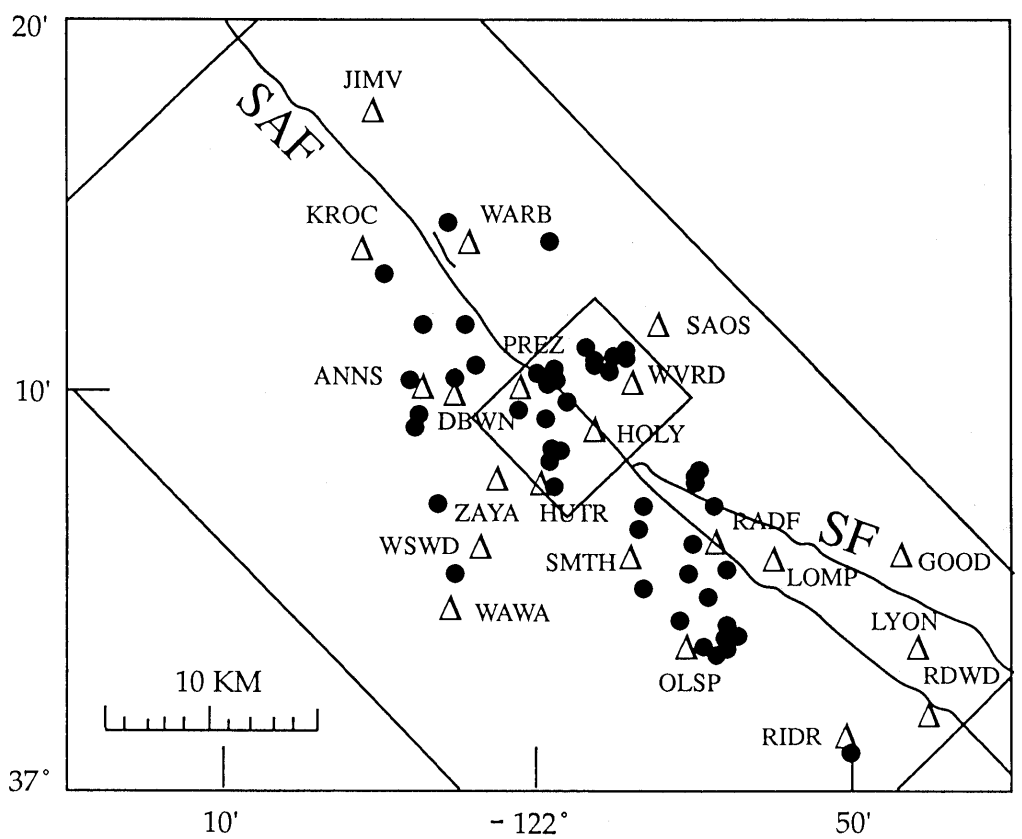

Figure 1.—Map showing sites of PASSCAL stations (triangles) and USGS (Dietz and Ellsworth, 1990) locations of the earthquakes analyzed (solid circles). The boundaries of the finite-difference travel-time grid are indicated by the outer box. SAF is the San Andreas fault and SF is the Sargent fault. Earthquakes within the inner box are the subset of events included in the synthetic calculations.

the constraint imposed on the solution by the *S* and *P* phases. Figure 3 shows cross sections through the original and perturbed three-dimensional velocity models. The inclusion of 5-percent random-velocity perturbations to the original velocity model is expected to adequately reflect realistic uncertainties in crustal velocities. If the true crustal structure contains sharp lateral-velocity contrasts, perturbations to a smoothly varying three-dimensional model may not adequately reflect velocity uncertainties. Further investigation of this possibility is beyond the scope of this paper.

For several of the simulations, *P*- and *S*-wave station delays were computed for each station by averaging the station residuals from all events, as is often done in real earthquake location. These station delays were then subtracted from the arrival-time data and the events were located again. The station delays were applied to account for imperfections in the assumed velocity model. Although the application of station delays had a small effect on the event locations and slightly reduced the L1 residuals, it did not significantly change the estimates of the location errors. Therefore, the results of the synthetic experiments do not include station delays. Since the 50 earthquakes are distributed over a large area, we also compute location errors from a subset of 19 closely spaced events located near the center of our travel-time grid (figure 1). In addition to calculating absolute errors in location resulting from erroneous assumptions about the velocity model we also estimate relative errors. Relative errors are determined by calculating the epicentral distances and depth

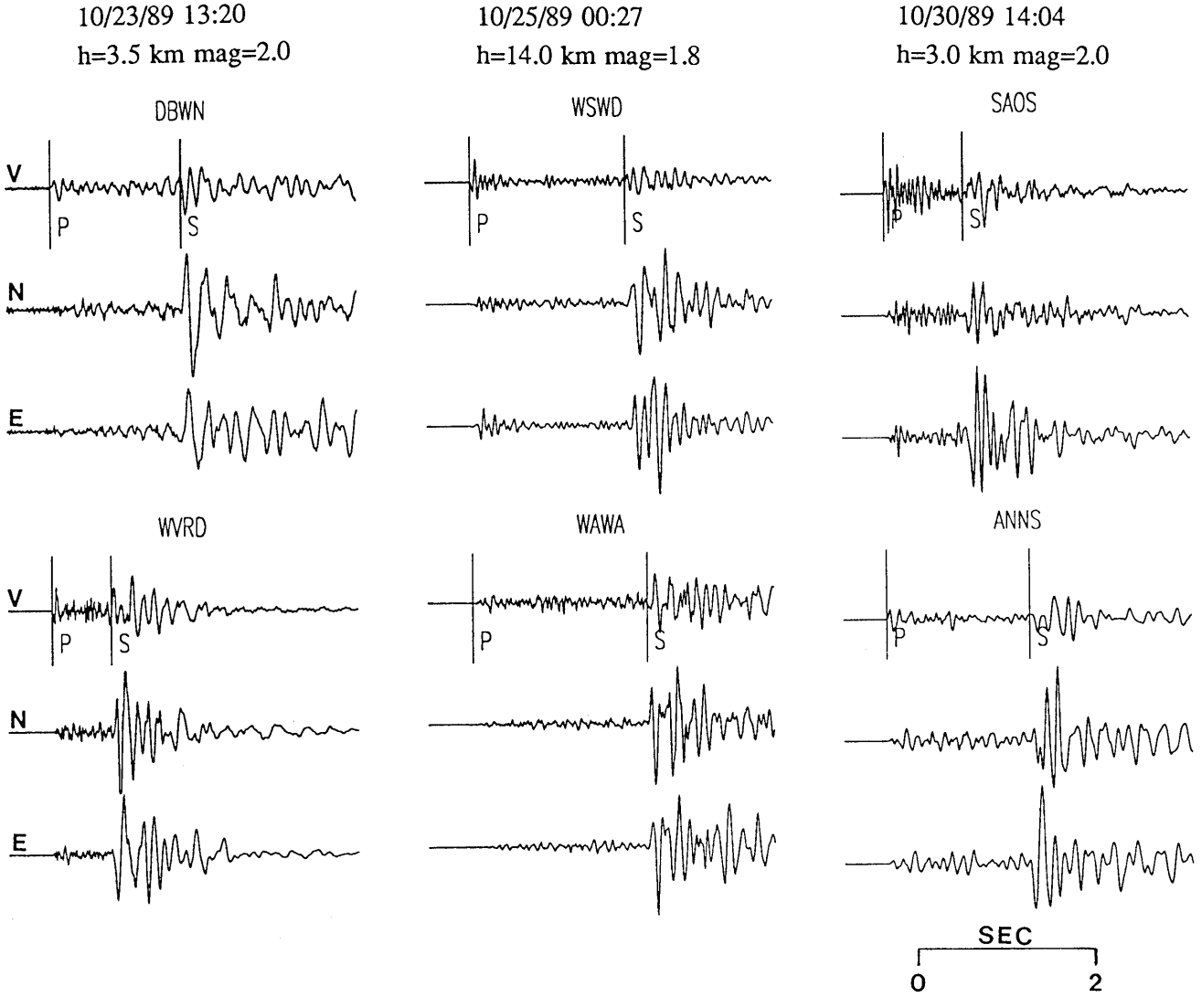

Figure 2—Vertical (V) and horizontal (N and E) component seismograms for three typical earthquakes recorded by six PASSCAL stations. *P*- and *S*-wave arrival times are marked on the vertical components. *S*-wave arrival times can be accurately determined from the horizontal components. h=earthquake depth and mag=magnitude, both determined by the USGS (Dietz and Ellsworth, 1990).

differences between all events in the original synthetic configuration of earthquake locations, subtracting them from the distances and depth differences between events after new locations are computed and averaging these values. If the relative earthquake pattern does not change after the location procedure, then the average of these differences will be zero. The average lengths of the absolute and relative horizontal and depth mislocation vectors for all 50 events and for the subset of nineteen events are summarized in table 1 for the different combinations of phases.

A small component of the error listed in table 1 is due to errors in the finite-difference calculation of travel times and in the interpolation of travel times prior to earthquake location. From a synthetic example with a similar size grid, Nelson and Vidale (1990) estimated average location errors of 0.2 km in the horizontal plane and 0.3 km in depth arising from the computation of finite-difference travel times.

The use of either *S* and *P* or *S-P* phase data yield average lengths of the horizontal and depth mislocation vectors of about 1.2 km and 0.5 km, respectively. The average mislocation increases only slightly when computed for events having observations from only four or five stations and decreases only slightly when computed for events with observations from six or more stations. Only three events have both a horizontal mislocation greater than 2 km and a depth mislocation greater than 1 km. These events are recorded by four stations having a highly unfavorable distribution (either lying along a single line or clustered into two groups). Thus it appears that given reasonable station coverage, nearly comparable location accuracy can be obtained for events recorded by four or five stations as for events recorded by six or more stations using either *S* and *P* or *S-P* phase data. Locations calculated using *P* phases alone produce much larger errors, especially in depth. This is not surprising considering the locations using only *P* arrivals have half the number of observations as locations using *S* and *P* data. The average horizontal and depth mislocation for events located with *P* waves from four or five stations is over twice the average of events located using *P* arrivals from six or more stations. As noted by previous workers, the inclusion of *S*-wave phase data drastically reduces the number of stations necessary to obtain accurate earthquake locations.

The location errors are slightly reduced when only a subset of events with fairly uniform station coverage are considered (table 1). The average lengths of the relative error vectors are larger than the lengths of the absolute error vectors when all earthquakes are considered. The lack of improvement in the relative errors over the absolute errors is due to the rather large region containing the earthquake hypocenters as well as the lack of a consistent set of stations recording each event. The average lengths of the relative horizontal error vectors are smaller than the absolute error vectors for the more closely spaced

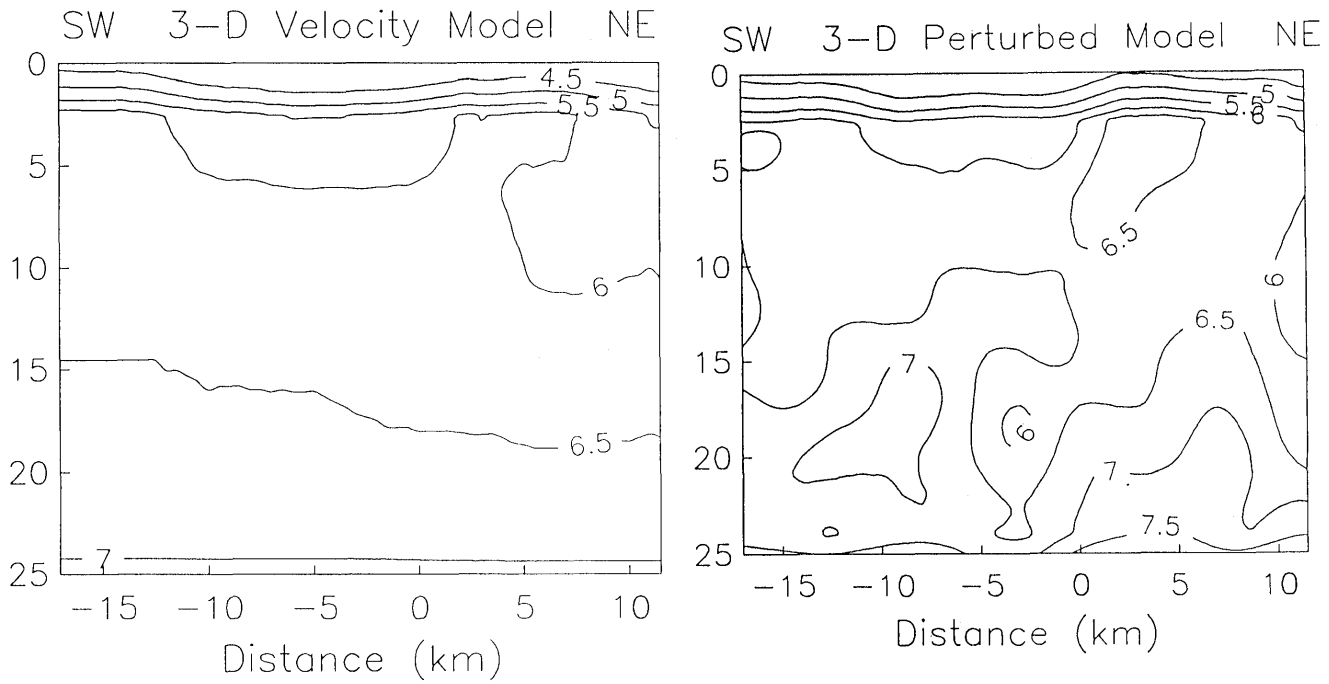

Figure 3—Cross sections through the 3-D model of Eberhart-Phillips and others (1990b) and the velocity model generated by introducing Gaussian-distributed random-velocity perturbations, with an average value of 5 percent over scale lengths of about 5 km, to this model. The cross sections were taken near the intersection of the San Andreas fault with the Sargent fault. Contours are *P*-wave velocities in km/s and distances are measured from the San Andreas fault (0 km).

Table 1.—*Synthetic location errors*

Phases	Error Source	All Events								Subset of Events							
		Absolute Errors				Relative Errors				Absolute Errors				Relative Errors			
		xy	sd	z	sd	xy	sd	z	sd	xy	sd	z	sd	xy	sd	z	sd
S and P	V	1.2	0.9	0.5	0.6	1.5	1.3	0.7	0.8	0.9	0.4	0.3	0.2	0.6	0.4	0.4	0.3
S-P	V	1.2	0.8	0.4	0.5	1.4	1.2	0.6	0.6	1.0	0.4	0.2	0.2	0.7	0.5	0.4	0.3
P	V	1.8	1.5	1.8	2.0	2.2	2.2	2.4	2.3	1.4	0.9	1.3	1.2	1.1	0.9	1.8	1.4
S and P	V & T	1.2	1.0	0.5	0.6	1.5	1.4	0.8	0.8	0.9	0.4	0.4	0.2	0.7	0.5	0.6	0.4
S-P	V & T	1.8	2.4	0.8	1.2	1.9	2.2	1.1	1.3	1.0	0.7	0.5	0.3	0.9	0.7	0.7	0.5
P	V & T	2.2	2.5	2.3	2.5	2.9	3.4	3.0	2.9	1.7	1.7	2.0	2.1	1.6	1.7	2.6	2.5

Error sources result from locating earthquakes in a different velocity model from the one used to calculate the phase data (V) and from the addition of noise to the arrival time data proportional to our estimated reading errors (T). xy=average length of the horizontal error vector, z=average length of the depth error vector and sd=standard deviation of the error. All errors are in km.

subset of events; however, the absolute depth errors are still smaller than the relative depth errors.

Although we expected the inclusion of *S* phases in the location determination to greatly improve their accuracy, the equal success of *S* and *P* and *S-P* arrival times is somewhat surprising considering that the range in the partial derivative of the *S-P* travel time with respect to the hypocentral parameters is substantially decreased compared with *S* or *P* arrival times (Gomberg and others, 1990). The success of *S-P* arrival times is partly due to the diminished sensitivity of this differential measure to the absolute velocity model assumed. Although we located the synthetic earthquakes in a velocity model perturbed from the one used to compute the arrival-time data, both *P*- and *S*-wave velocities were perturbed in the same manner using a constant vp/vs ratio of 1.73. If we locate the synthetic earthquakes using an *S*-wave velocity structure having a vp/vs ratio that differs from that used to compute the arrival time data, the error estimates increase in proportion to the difference between the correct and assumed ratios. In general, the vp/vs ratio is better known than the absolute velocity structure, so the use of *S-P* differential times can provide nearly as accurate locations as those obtained using *S* and *P* arrival times. The magnitude of the location errors resulting from a 3-percent difference between the assumed and actual vp/vs ratios, using *S-P* arrival times, is on the order of 1 km both horizontally and in depth. This error does not increase when 5-percent random velocity perturbations are added to the original model.

To estimate realistic errors to be expected in our aftershock locations, we repeated the first experiment after adding random time delays with an average amplitude determined from our estimated reading errors (0.05 s for *P* and 0.1s for *S*) to the arrival-time data. The results, averaging location errors determined for three separate simulations of random reading errors, are listed in table 1. The inclusion of reading errors had little effect on locations determined using *S* and *P* data but did increase the errors, as expected, when using *S-P* or *P* data. These synthetic calculations indicate that if absolute timing of *S* phases is unavailable, *S-P* arrival times can locate earthquakes with only slightly less accuracy than the use of *S* and *P* phases separately. Previous experiments on synthetic datasets including *S* phases indicated that epicentral parameters were far less sensitive to data inadequacies than depth (Gomberg and others, 1990). Here, we find that the inclusion of *S* phases in earthquake location results in consistently smaller depth mislocation than epicentral mislocations.

LOMA PRIETA AFTERSHOCK LOCATIONS

The synthetic calculations indicated that we can expect average absolute errors in QUAKE3D locations of the Loma Prieta aftershocks to be about 1.8 km in the horizontal plane and 0.8 km in depth using *S-P* phase data and the sparse PASSCAL instrument coverage, provided that the average vp/vs ratio is reasonably well known. We use the three-dimensional velocity model of Eberhart-Phillips and others (1990b) to relocate 50 aftershocks of the Loma Prieta earthquake. We compare QUAKE3D solutions obtained using this velocity model and a constant vp/vs ratio to locations obtained by Eberhart-Phillips and others (1990b) using only *P*-wave arrivals. Associated with all seismicity maps, we show three cross-sections; one parallel to the strike of the San Andreas Fault and two perpendicular to it.

Figures 4 and 5 show locations of 50 aftershocks determined with QUAKE3D using *S-P* arrival time data from

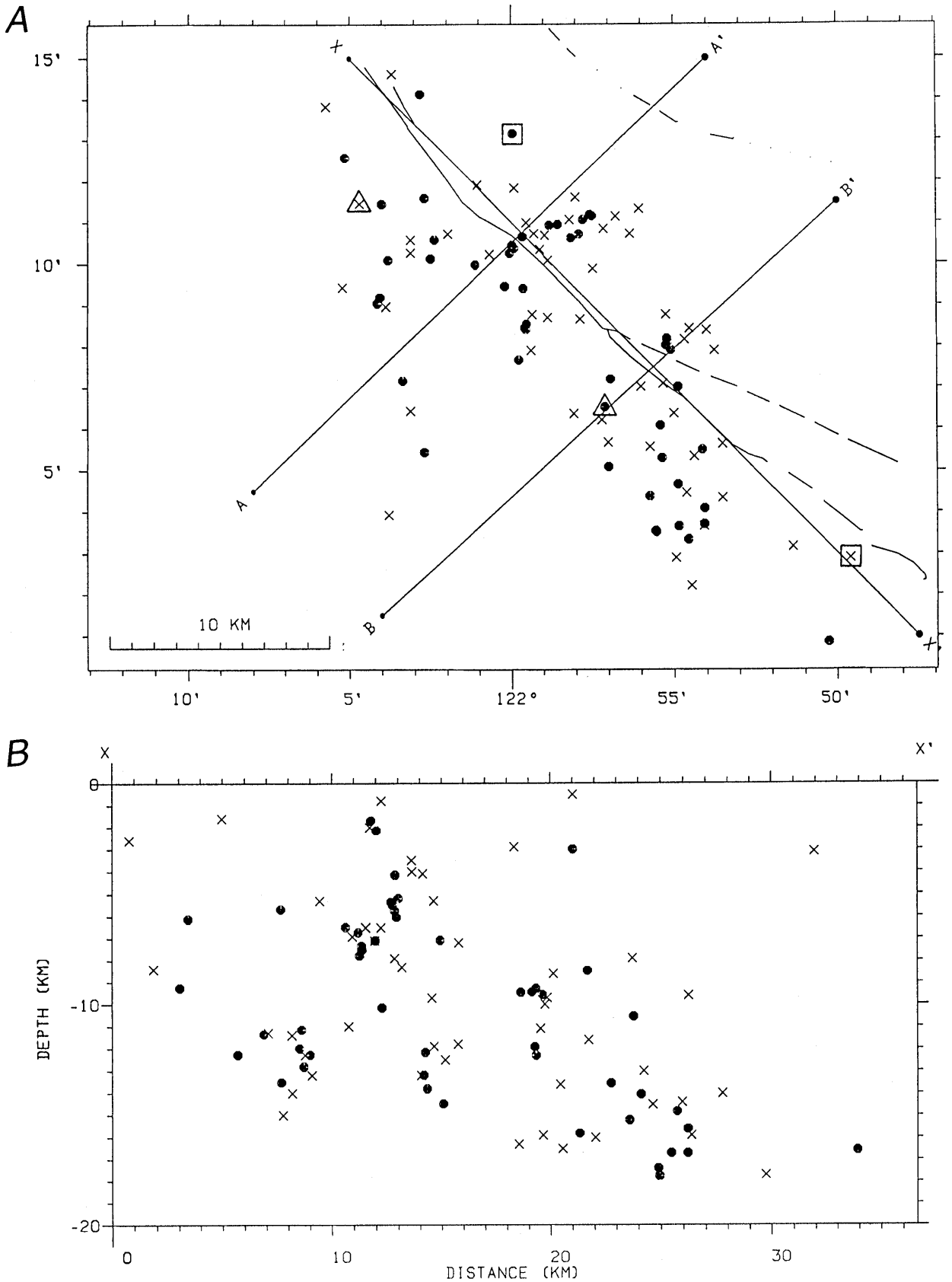

Figure 4.—(*A*) Map view comparing locations determined for the 3-D velocity model using *S-P* finite-difference travel times from the PASSCAL stations (x) and locations from Eberhart-Phillips and others (1990b) (solid dots). The events marked by the boxes and triangles are the two events with very large location discrepancies. Lines *X-X'*, *A-A'* and *B-B'* indicate the location of cross sections. (*B*) Cross section *X-X'* along the length of the San Andreas fault.

the PASSCAL aftershock deployment (×'s) and determined by Eberhart-Phillips and others (1990b) from *P*-waves recorded by stations of the dense California Seismic Network (CALNET). The QUAKE3D locations are indicated in table 2. The average difference in epicentral location and in the absolute value of depth between the two loca-

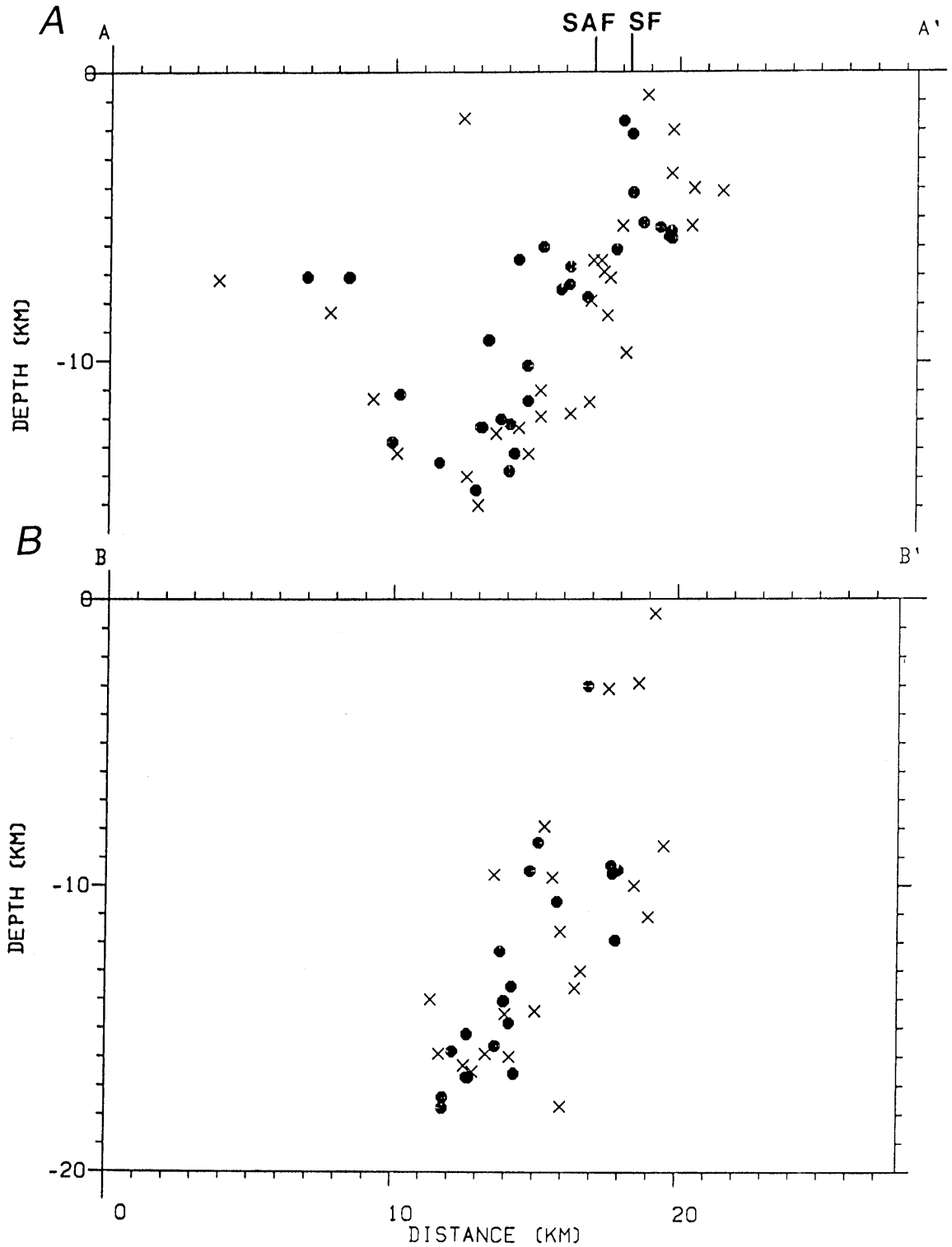

Figure 5.—Cross section *A-A'* (*A*) and *B-B'* (*B*) perpendicular to the San Andreas fault (SAF) showing the seismicity in figure 4. Sections *A-A'* and *B-B'* include all events north and south of the intersection of the SAF with the Sargent fault (SF), respectively.

Table 2.—*Loma Prieta aftershock relocations*

Event		Latitude		Longitude		Depth	Mag	N*
yr mo dy	hr mn	deg	min	deg	min	km		
891023	1320	37	11.61	121	58.01	2.0	2.0	6
891023	1402	37	6.45	122	3.12	8.3	2.3	4
891023	1812	37	14.62	122	3.69	8.4	2.0	4
891023	2127	37	8.40	121	54.00	8.6	3.0	5
891024	0336	37	10.27	122	3.12	14.0	1.8	4
891024	0403	37	8.67	121	57.86	11.8	2.1	5
891024	0702	37	8.78	121	55.24	2.9	2.8	7
891024	0855	37	11.34	121	56.05	4.1	2.5	7
891024	1003	37	10.69	121	58.96	7.1	1.8	6
891024	1003	37	10.85	121	57.15	3.5	1.8	6
891024	1444	37	5.69	121	57.01	16.5	2.3	4
891024	1832	37	8.71	121	58.87	11.9	1.9	5
891024	2225	37	11.15	121	56.77	4.0	2.5	5
891024	2341	37	10.73	121	56.34	5.3	2.3	8
891025	0026	37	8.97	122	3.88	13.2	1.8	4
891025	0305	37	10.73	122	1.97	12.3	1.8	6
†891025	0314	37	11.46	122	4.69	1.6	2.3	4
†891025	1223	37	2.90	121	49.60	3.1	2.1	5
891025	1515	37	10.73	121	59.30	6.5	2.0	4
891025	1926	37	8.78	121	59.35	13.2	2.0	4
891026	0518	37	10.08	121	58.87	7.9	2.1	6
891026	1100	37	6.23	121	57.20	15.9	1.9	4
891026	1208	37	9.89	121	57.48	9.7	1.9	4
891026	1326	37	2.22	121	54.47	14.0	2.4	4
891026	1508	37	5.35	121	54.38	7.9	2.0	6
891026	1544	37	11.84	121	59.92	5.3	2.1	4
891028	0001	37	2.90	121	54.95	15.9	2.1	5
891028	1120	37	9.43	122	5.22	11.3	2.0	7
891028	1947	37	8.17	121	54.67	10.0	2.1	7
891029	1310	37	5.58	121	55.72	16.0	2.9	4
891029	1918	37	3.17	121	51.37	17.7	2.3	6
891029	2043	37	5.65	121	53.52	13.0	2.2	10
891029	2155	37	3.67	121	54.09	9.6	2.9	8
891030	0452	37	4.47	121	54.62	14.5	2.5	7
891030	0710	37	11.00	121	59.54	6.9	1.5	5
891030	1258	37	6.38	121	55.00	11.6	2.1	7
891030	1403	37	11.07	121	58.20	0.8	2.0	10
891030	1541	37	7.91	121	53.76	0.5	2.4	6
891030	1740	37	11.91	122	1.06	11.4	1.7	6
891031	0218	37	7.03	121	56.00	9.7	2.1	7
891031	0302	37	10.58	122	3.12	15.0	2.3	7
891031	0332	37	8.44	121	54.52	11.1	2.3	9
891031	0457	37	13.82	122	5.74	2.6	2.0	5
891031	0649	37	7.91	121	59.39	12.5	2.2	7
891031	1811	37	4.35	121	53.52	14.4	2.5	5
891101	2300	37	7.10	121	55.33	13.6	2.5	5
891102	0423	37	10.35	121	59.11	6.5	2.0	8
891102	1010	37	6.38	121	58.06	16.3	2.1	5
891102	1548	37	3.93	122	3.79	7.2	2.0	6
891103	0257	37	10.23	122	0.68	11.0	1.7	10

*N is number of S-P phases used in location
†Events with large location discrepancies compared with USGS locations.

tion sets is 2.3±1.4 km and 1.3±1.7 km, if two events with large location differences are excluded (these events are indicated by triangles and boxes in figure 4). Eberhart-Phillips and others (1990b) determined locations for both of these events using arrival time data determined with a real time processor (RTP), and it is possible that the RTP missed an emergent first arrival. One of the events (box in figure 4*A*) was located with *P*-wave arrival times from only nine stations; the smallest number of arrivals for any of the 50 events. This event also had the largest rms residual and the largest error estimates of the 50 events. We located these two events with observations from only a small number of stations with a less-than-ideal distribution. Although our synthetic tests indicated that locations using only four or five *S-P* observations were, in general, as accurate as those obtained using many more observations, the largest mislocation vectors determined for our tests were obtained for events with observations from few, poorly distributed stations.

Although there are significant differences in the earthquake locations determined in this study and those determined by Eberhart-Phillips and others (1990b), it is difficult in such a geologically complex region to apply any simple criterion to decide which locations are more accurate. Our synthetic experiments predict that locations determined with *S-P* times should be better constrained than those obtained from *P*-wave data if the event-station geometries are constant and our assumption and assignment of a constant average vp/vs ratio is fairly accurate. However, the locations determined by Eberhart-Phillips and others (1990b) from *P*-wave data used many more *P*-wave observations from more distant stations than the number of nearby *S-P* observations that we used. Also, recent work suggests that our assumption of a constant vp/vs ratio for this region may not be valid. Thurber and Atre (1993) inverted *S-P* arrival times from Loma Prieta aftershocks recorded by stations of the PASSCAL aftershock array to determine a three-dimensional model of vp/vs variations in the Loma Prieta rupture zone. Their results indicate that variations in the vp/vs ratio may be as large as 10 percent in this region. To determine how a variable vp/vs ratio would effect our locations, we calculate earthquake locations using the three-dimensional *P*-wave velocity model of Eberhart-Phillips and others (1990b) and the vp/vs model of Thurber and Atre (1993). A comparison of these locations with those determined using a constant vp/vs ratio of 1.73 are shown in figures 6 and 7. The average difference in position of earthquakes located using the variable vp/vs ratio compared with the constant ratio is 1.5± 0.9 and 1.2± 0.9 km in epicentral location and in depth, respectively. The depth of events located using the variable vp/vs ratio is systematically shallower than those located using a constant ratio. This is because the vp/vs ratio (1.73) of the constant model is smaller than the average ratio in the variable model. Increasing the constant vp/vs ratio would increase the focal depths and eradicate this depth bias. The use of Thurber and Atre's (1993) variable vp/vs ratio to locate Loma Prieta aftershocks does not reduce the travel time residuals compared with a constant vp/vs ratio and results in earthquake locations that are only slightly closer in location to those determined by Eberhart-Phillips and others (1990b).

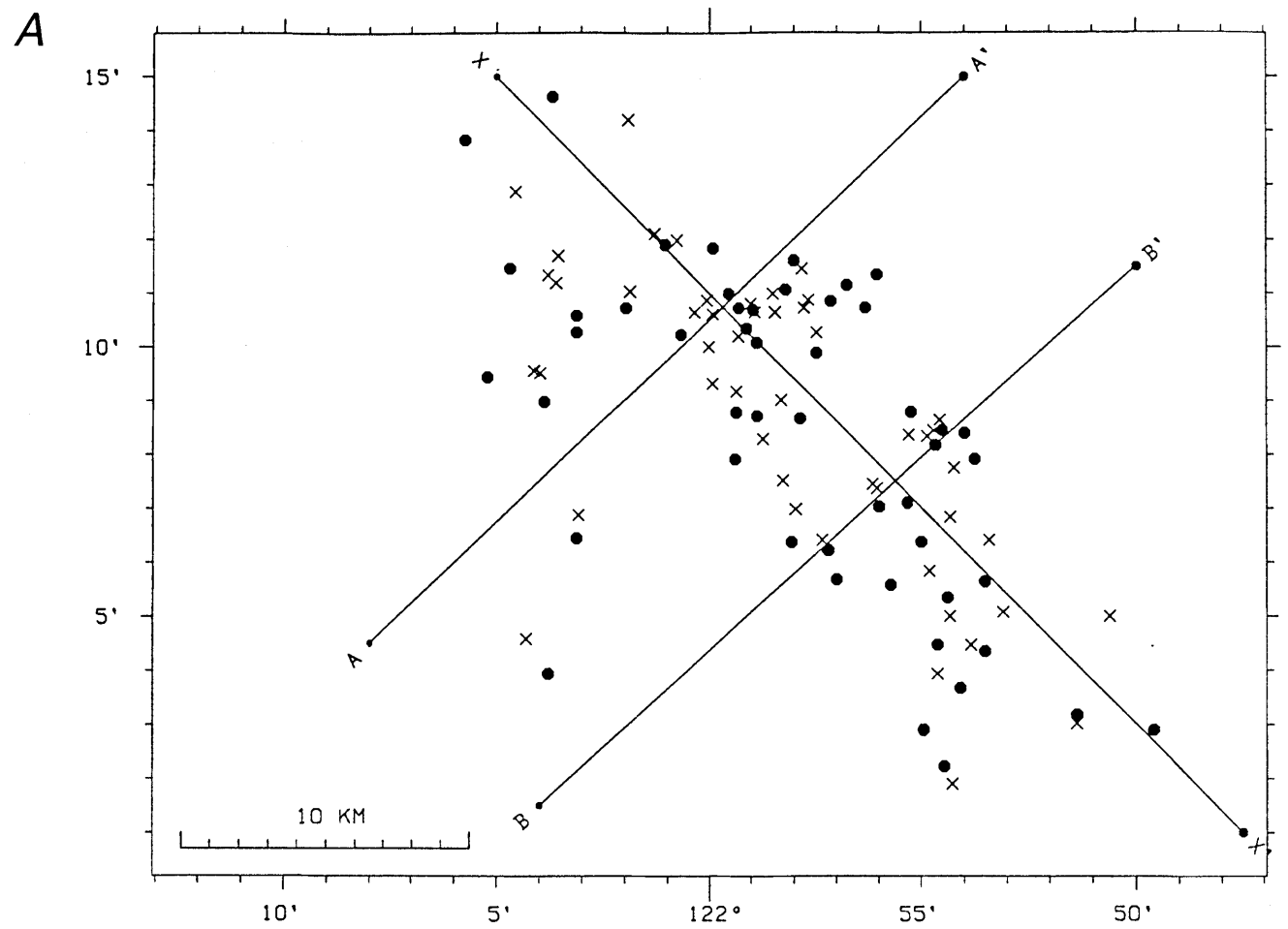
A
15'
10'
5'
A
A'
B
B'
10 KM
10'
5'
122°
55'
50'

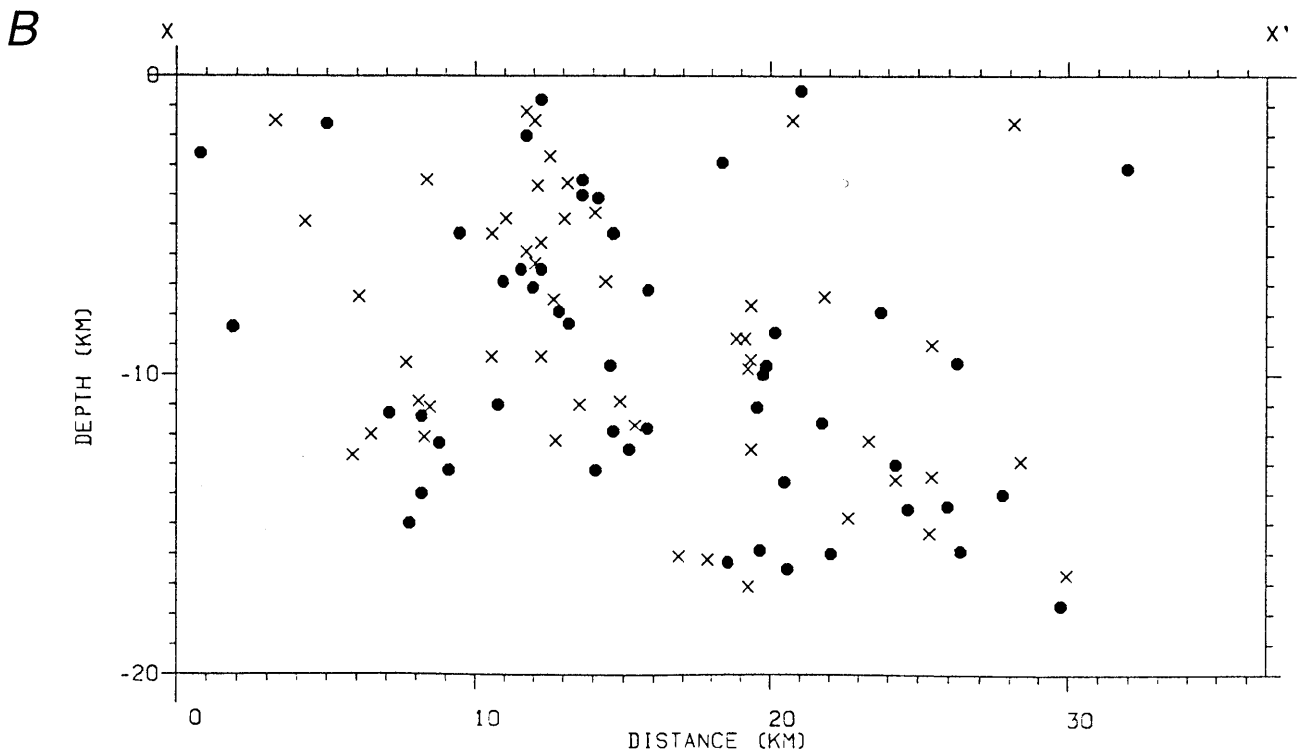
B
X
X'
0
-10
-20
DEPTH (KM)
0
10
20
30
DISTANCE (KM)

◀ Figure 6.—(*A*) Map view comparing locations determined for the 3-D velocity model using *S-P* finite-difference travel times from the PASSCAL stations and a variable vp/vs ratio model (x) with locations computed using a constant vp/vs ratio of 1.73 (solid dots). (*B*) Cross section *X-X'* along the length of the San Andreas fault.

DISCUSSION AND CONCLUSIONS

Although several previous studies have addressed the sensitivity of earthquake locations to uncertainties in assumed velocity models and in the timing of phases, these studies have almost exclusively considered layered velocity structures only. Changes in the lateral velocity

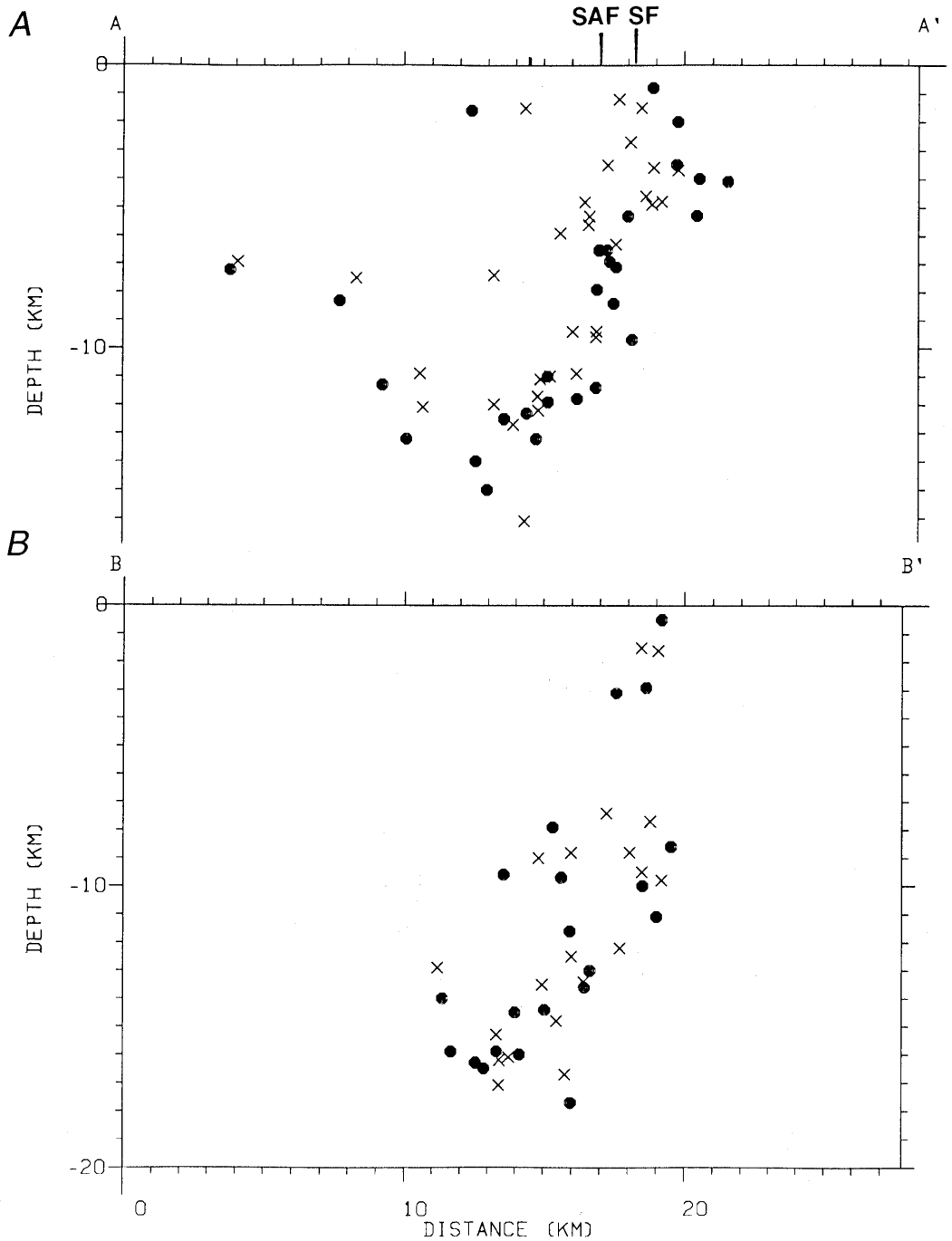

Figure 7.—Cross sections *A-A'* (*A*) and *B-B'* (*B*) perpendicular to the San Andreas fault (SAF) showing the seismicity in figure 6 in the same manner as in figure 5.

gradients will cause raypaths to curve. The effects of ray curvature on travel times are diminished when lateral gradients are not allowed, as in the case of propagation through a layered structure. This can result in an underestimation of location errors when they are assessed in plane-layered media. Here we estimate location error that results from random perturbations in a three-dimensional velocity model, although the model we consider possesses only smooth velocity gradients. Our methods correctly account for ray curvature. We evaluate location errors using the event-station geometries provided by Loma Prieta aftershocks recorded at the PASSCAL instruments. An average of only six *S-P* observations were used in the location determinations. The results are summarized in table 1. Since earthquake locations are often computed from sparse data, an estimation of the location accuracy that can be obtained from so few observations is important. We found that in the absence of reading errors, *S-P* arrival-time data can locate earthquakes with comparable accuracy as *S* and *P* data separately. While the inclusion of realistic timing errors slightly degrades the accuracy of the *S-P* earthquake locations, the differential measure can still locate earthquakes with small uncertainties (< 2 km in epicentral location and <1 km in depth).

The relocation of 50 Loma Prieta aftershocks using *S-P* arrival time data from the PASSCAL aftershock deployment are consistent with several other studies indicating complex faulting at depth within the Loma Prieta rupture zone. Although the locations suggest the existence of many fault segments, a definitive image of the faulting geometry at depth for this structurally complex region requires earthquakes to be located with greater accuracy than we can presently achieve. Such accuracy may be possible if present uncertainties in the velocity structure can be substantially diminished.

Rapid response is essential for the success of aftershock deployments such as those initiated after the 1988 Armenian and 1989 Loma Prieta earthquakes. The installation, testing, and operation of sophisticated clock systems is both expensive and time consuming. Therefore, the assurance of accurate absolute timing can significantly decrease the amount of data recorded during a field operation. In the absence of reliable absolute timing, as was the case for the PASSCAL Loma Prieta aftershock data, where there were many clock problems, we have shown that accurate earthquake locations can be obtained using *S-P* differential travel times from a sparse, three-component network. The Loma Prieta earthquake occurred in a region of very dense pre-existing instrument coverage that was able to provide accurate earthquake locations for the aftershock sequence independent of the PASSCAL deployment. Although the locations we obtained in this study using *S-P* data from the sparse, three-component PASSCAL network may or may not have improved the previous determinations, their accuracy demonstrates the usefulness of *S-P* times to locate earthquakes in more remote regions. In remote locations, such as Armenia, field deployments consisting of sparse instrument coverage may be the only means available to obtain accurate earthquake locations. In these situations the location method discussed here can be very useful.

ACKNOWLEDGMENTS

We are grateful to John Vidale for his excellent advice throughout the course of this project and for his thorough review of this manuscript. We also appreciate and benefited from discussions with Thorne Lay. We thank Cliff Thurber, Lynn Dietz and Donna Eberhart-Phillips for reviewing this manuscript and Zhi Zhang for her help with data processing. This work was supported by USGS Grant no. 14-08-0001-G1836, IRIS Grant SC90115, and a grant from the W.M. Keck Foundation. Contribution 180 of the W.M. Keck Seismological Laboratory and the Institute of Tectonics.

REFERENCES CITED

Buland, R., 1976, The mechanics of locating earthquakes: Bull. Seismol. Soc. Am., v. 66, p. 73-187.

Dietz, L.D. and Ellsworth, W.L., 1990, The October 17, 1989, Loma Prieta, California, earthquake and its aftershocks: Geometry of the sequence from high-resolution locations: Geophys. Res. Lett., v. 17, p. 1417-1420.

Eberhart-Phillips, D.M., Labson, V.F., Stanley, W.D., Michael, A.J., and Rodriguez, B.D., 1990a, Preliminary velocity and resistivity models of the Loma Prieta earthquake region: Geophys. Res. Lett, v. 17, p. 11235-1238.

Eberhart-Phillips, D.M., Michael, A.J., Fuis, G., and Luzitano, R., 1990b, Three-dimensional crustal velocity structure in the region of the Loma Prieta, California, earthquake sequence from inversion of local earthquake and shot arrival times: Seismol. Res. Lett., v. 61, p. 48.

Gomberg, J.S., Shedlock, K.M., and Roecker, S.W., 1990, The effect of *S*-wave arrival times on the accuracy of hypocenter estimation: Bull. Seismol. Soc. Am.,v. 80, p. 1605-1628.

James, D.E., Sacks, I.S., Lazo, E., and Araracio, G., 1969, On locating local earthquakes using small networks: Bull. Seismol. Soc. Am., v. 59, p. 1201-1212.

Lees, J.M., 1990, Tomographic P-wave velocity images of the Loma Prieta earthquake asperity: Geophys. Res. Lett, v. 17, p. 1433-1436.

Lerner-Lam, A., Simpson, D., Menke, W., Kim, W.Y., Hough, S., Pacheco, J., and Estabrook, C., 1990, Initial results of waveform analyses of IRIS/PASSCAL Loma Prieta aftershock data: Trans. Am Geophys. Union, v. 71, p. 289.

Nelson, G.D. and Vidale, J.E., 1990, Earthquake locations by 3-D finite-difference travel times: Bull. Seismol. Soc. Am., v. 80, p. 395-410.

Schwartz, S.Y., Velasco, A., Protti, M., Bonamassa, O., Nelson, G.D., McNally, K.C., Vidale, J.E., Lay , T., and Flatté, S., 1990, A PASSCAL instrument aftershock deployment along the rupture zone of the 18 October 1989 Loma Prieta Earthquake: Trans. Am. Geophys. Union, v. 71, p. 290.

Thurber, C.H., and Atre, S., 1993, Three-dimensional vp/vs variations along the Loma Prieta rupture zone: Bull. Seismol. Soc. Am., v. 83, p. 717-736.

Vidale, J.E., 1990, Finite-difference calculation of travel time in 3D: Geophysics, v. 55, p. 521-526.

AFTERSHOCKS AND POSTSEISMIC EFFECTS

EMPIRICAL GREEN'S FUNCTION STUDY OF LOMA PRIETA AFTERSHOCKS: DETERMINATION OF STRESS DROP

By H. Guo, A. Lerner-Lam, and W. Menke,
Lamont-Doherty Earth Observatory of Columbia University, and
S.E. Hough,
U. S. Geological Survey

CONTENTS

ABSTRACT

This paper presents the estimation of stress drops of aftershocks of the Loma Prieta earthquake recorded by an array of 22 PASSCAL instruments. Using an empirical Green's function analysis, corner frequencies of 98 of the aftershocks are first determined. Brune-model stress drops, $\Delta\sigma$, are calculated from the corner frequencies and moments. A dependence of stress drop on moment is observed.

INTRODUCTION

Estimates of earthquake source spectral parameters can be contaminated by effective attenuation along the source-receiver path, frequency-dependent propagation, and near-receiver site response. The shaping of the spectrum of an arrival by attenuation is known to bias estimates of corner frequency and thus its interpretation in terms of stress drop (Hough and Anderson, 1988). To avoid this bias, a reference measurement technique must be employed when parameterizing the source spectrum, especially in a local aftershock survey. In this paper, we apply an empirical Green's function (eGf) analysis (Frankel and others, 1986; Geller and Mueller, 1980; Hartzell, 1978; Hough and others, 1991; Hutchings and Wu, 1990; Li and Thurber, 1988; Mori and Frankel, 1990; Mueller, 1985; Xie and others, 1991) to aftershock doublets of the Loma Prieta sequence recorded on the IRIS/PASSCAL digital seismographs. The smaller event in each doublet provides the reference signal for correcting the spectral characteristics of the larger source for spectral shaping by attenuation.

In principle, eGf methods provide an efficient technique for quickly parameterizing large amounts of digital data. In practice, however, one has to be careful about the application of the method in the case of inadequate signal-to-noise ratio for the smaller reference signal. We develop a methodology for identifying and mitigating such low-signal problems and show how to assess the possibility of bias in the corner-frequency estimate. In addition, we perform sensitivity tests to demonstrate that the estimate of these spectral parameters is robust with respect to variations in fitting range and noise level.

The combination of extensive coverage of the Loma Prieta aftershock zone with IRIS/PASSCAL instrumentation, coupled with the locating capabilities of CALNET, provides a unique data set for waveform work and eGf analysis of spectral characteristics.

In this paper, a frequency-domain deconvolution using the empirical Green's function method is used to determine the corner frequencies and the stress drops of 98 aftershocks of the Loma Prieta earthquake.

DATA

The Loma Prieta earthquake and its aftershocks are an exceptionally well-recorded earthquake sequence. The aftershocks were recorded not only by the permanent CALNET stations but also by a temporary network. Following the Loma Prieta mainshock, an array of 22 IRIS/PASSCAL (Incorporated Research Institutions for Seismology/Program for Array Seismological Studies of the

Continental Lithosphere) stations was deployed in the epicentral area in the Santa Cruz mountains (see fig. 1). More than 2,000 events were recorded by three-component L-22D 2-Hz velocity sensors paired with IRIS/PASSCAL RefTek model 72A recorders. Two separate geophones, recorded at different gain levels and sampled at 200 samples per second, were deployed at each site. These geophones were calibrated after the Loma Prieta deployment by Menke and others (1991).

A total of 763 of these aftershocks, with local magnitude, M_L, ranging from 1.5 to 4.5 and recorded from October 20 to November 25, 1989, have been time-associated with CALNET data. These associated aftershocks were relocated relative to preliminary CALNET hypocenters by inverting CALNET phase data with a one-dimensional velocity model and a modified HYPOINVERSE program with station corrections dependent on hypocentral location (Seeber and Armbruster, 1990). This method has been shown to give better relative locations (Seeber and Armbruster, 1990; Pujol, 1992).

Candidate pairs for eGf analysis were selected from the relocated hypocenters. The fundamental assumptions of eGf analysis require that (1) the paired events must be closely spaced so that source-receiver paths are nearly coincident, (2) the event pair should have similar focal mechanisms and have similar waveform complexities, and (3) the rupture duration of the smaller or reference event should be short relative to the larger event so that the reference corner frequency is resolvably different from the corner frequency of the large event. This last criterion has implications in terms of signal-to-noise ratio of the quotient spectrum. It is most convenient to interpret this requirement in terms of relative magnitude difference, ΔM_L The ΔM_L values must be large enough to resolve the difference in corner frequencies but not so large as to vitiate the assumption that attenuation and near-receiver effects are linear for two events.

Our criteria for the relocated Loma Prieta aftershocks were (1) the hypocenters must be within 1 km of each other, (2) time- and frequency-domain signals must be

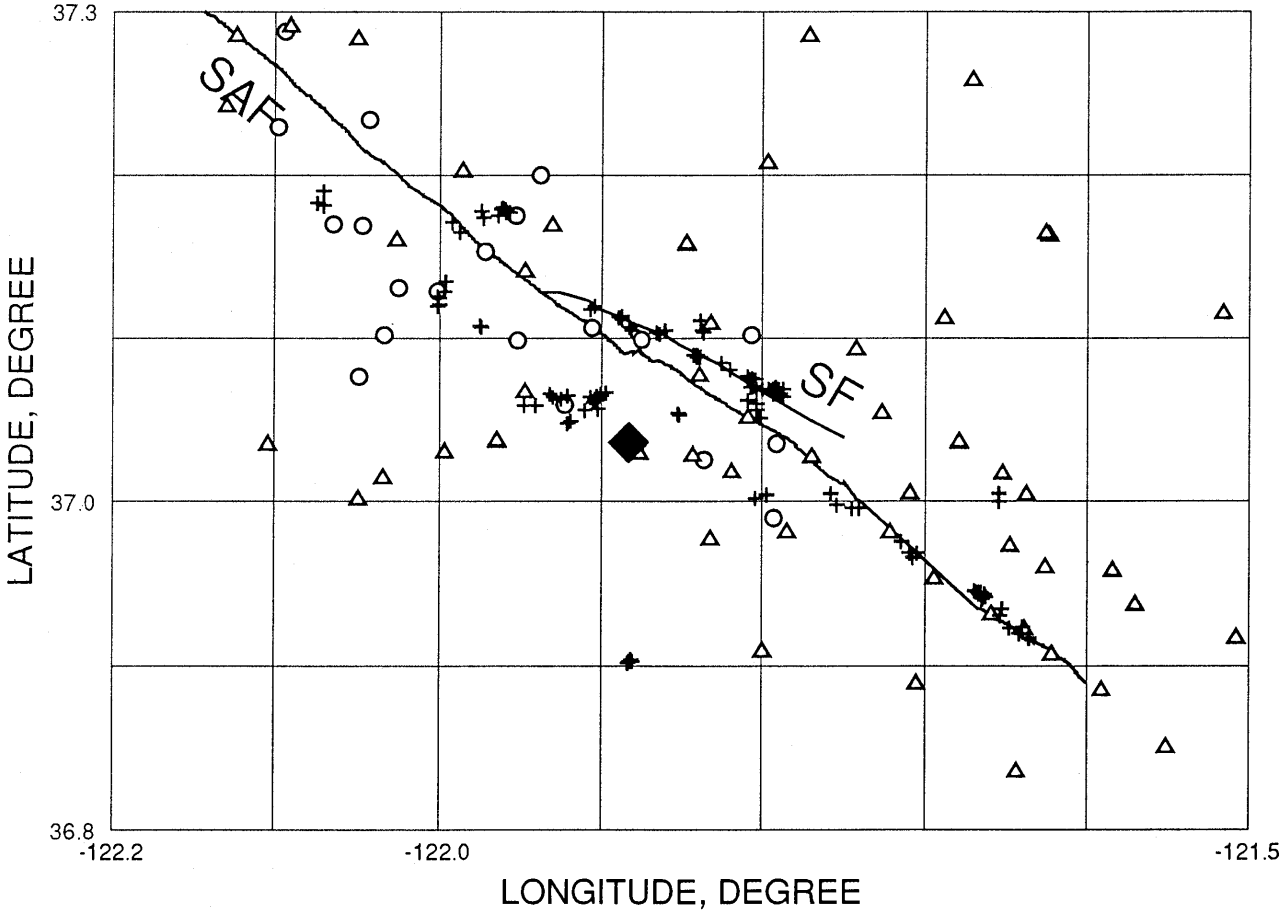

Figure 1.—Portion of the aftershock zone of the Loma Prieta earthquake. Main shock (diamond), 22 PASSCAL stations (circles), 53 closest CALNET stations (triangles), San Andreas Fault (SAF), and Sargent fault (SF) are shown. A total of 124 events recorded by the PASSCAL array with magnitudes larger than 1.5 are used for empirical Green's function analysis and denoted by plus symbols.

visually similar, and (3) $\Delta M_L > 0.7$. Comparable values of this lower bound for ΔM_L have been used in other studies (Li and Thurber, 1988: 0.5; Mueller, 1986: 0.7; Xie and others, 1991: 0.5). The largest ΔM_L for out data set is 2.9, which is small enough to maintain linearity. Of these criteria, the visual check is the most subjective. In the time domain, the comparison emphasizes the first motion direction, the detailed shape of the first several oscillations, and the overall shape of the envelope of the whole seismogram (for example, fig. 2). In the frequency domain, the comparison emphasizes spectral content below 30 Hz because of spurious geophone resonances detected by Menke and others (1991). Only those event pairs that satisfy the above criteria on 80 percent of the seismograms are suitable for further analysis. Seismograms with recording errors or signal-to-noise ratios less than approximately 20 dB were discarded. Low-gain data were used only if the signals were clipped on the high-gain data streams.

Of the 763 relocated aftershocks with $\Delta M_L > 1.5$, 347 pairs were found to meet the hypocentral and ΔM_L restriction, and 226 event pairs were found to meet the subjec-

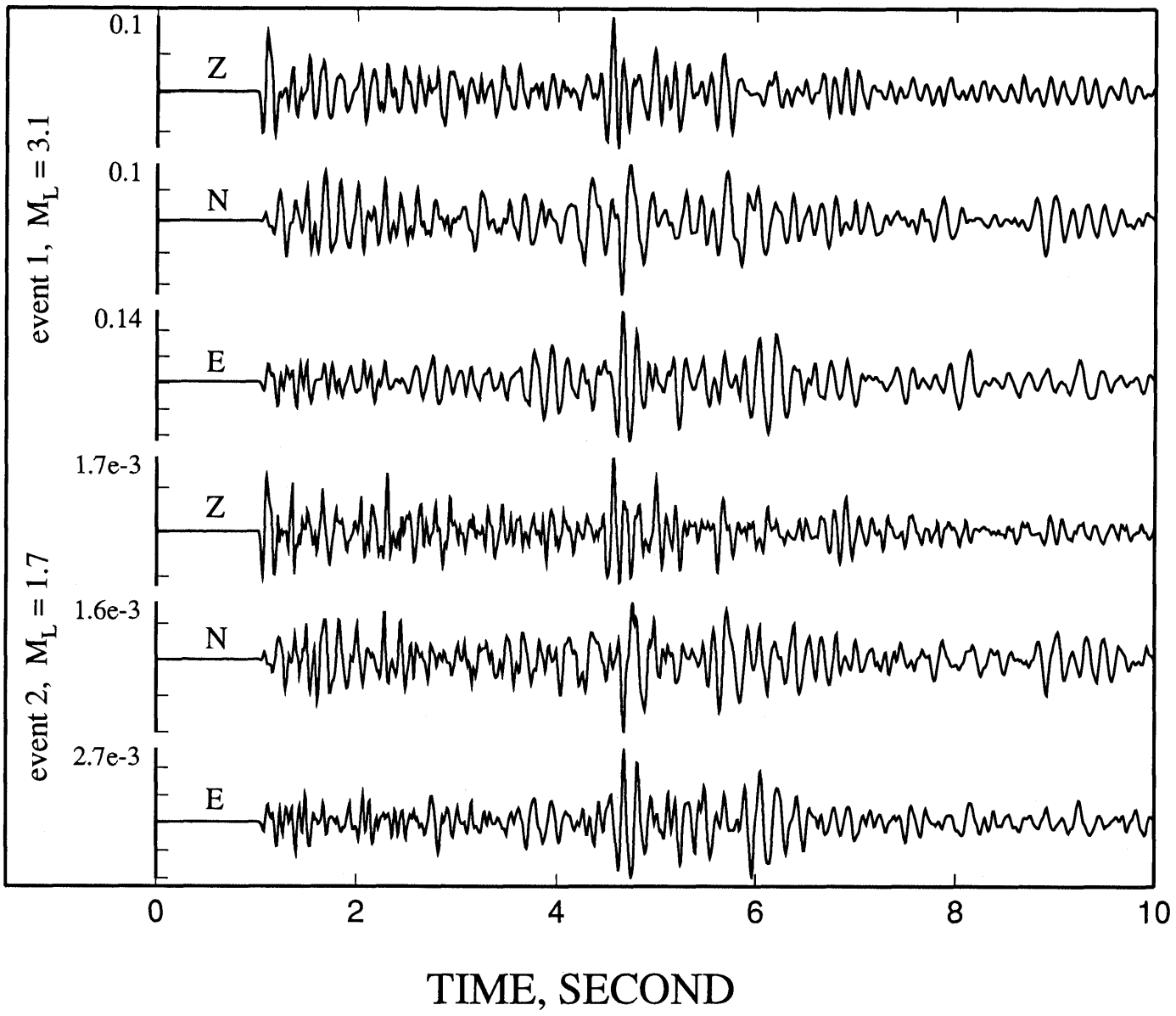

Figure 2.—Three-component seismograms of a typical event pair (events 107 and 106). Amplitude scales differ between seismograms.

tive waveform similarity criteria. The larger events in each pair have magnitudes between 2.2 and 4.4, and the smaller events have magnitudes between 1.5 and 2.9.

ANALYSIS

DETERMINATION OF CORNER FREQUENCY

The *P*-wave spectra were computed for a 2.5-second window starting just before the arrival. The length of the window was derived after experimentation to determine the trade-off between the successful characterization of the long-period signal and the inclusion of too much scattered energy. The spectra were computed using 4π-prolate multitapers, which yield a smooth spectral estimate with good resistance to leakage for relatively short time windows (Park and others, 1987).

The paired spectra were divided to obtain spectral ratios, which should depend only on the relative source characteristics. Spectral ratios from different components and different stations were averaged to reduce the noise. This averaging procedure neglects the effects of directivity, which is not thought to be a large effect.

The parameterization of the spectral ratio in terms of source characteristics is achieved by assuming a Brune spectrum, $A(f)$, for each event (see fig. 3):

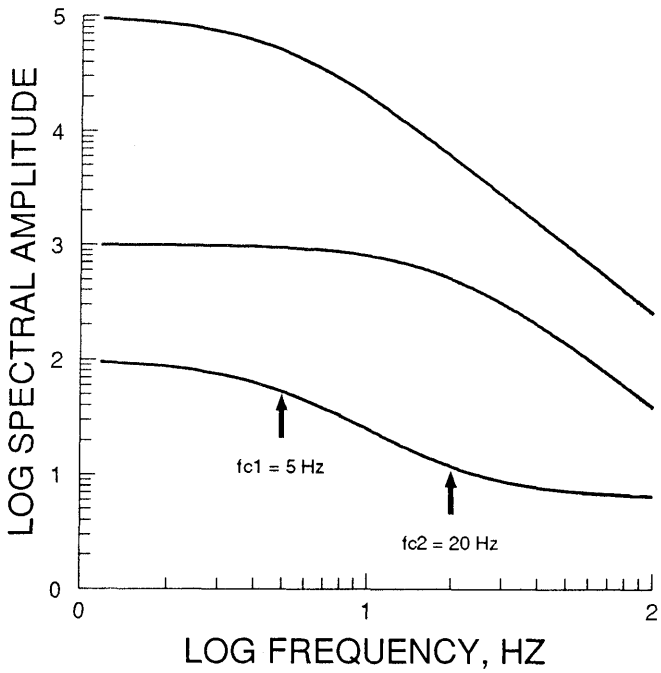

Figure 3. Corner frquencies of a hypothetical event pair, showing spectra as a function of frequency for large event (top), small event (middle), and ratio (bottom). f_{c_1}=5 Hz and f_{c_2}=20 Hz are the corner frequencies of the larger and smaller events, respectively.

$$A(f)=A_o(1+(f/f_c)^2)^{-1}$$

where A_o is the amplitude scaling and f_c is the corner frequency. The spectral domain deconvolution yields the spectral ratio $R(f)$:

$$R(f)=(A_{o_1}/A_{o_2})(1+(f/f_{c_2})^2)(1+(f/f_{c_1})^2)^{-1}$$

where subscripts 1 and 2 (o_1, o_2) denote the larger and smaller members of the event doublet, respectively. Unless f_{c_2} is high enough relative to f_{c_1}, or A_{o2} is below the ambient noise, all four parameters must be included in the representation of the spectral ratio. We do this by finding the amplitude ratio A_{o_1}/A_{o_2} that minimizes the 2-norm of the residual $R'(f)$–$R(f)$, where $R'(f)$ is the observed spectral ratio, while f_{c_1} and f_{c_2} are varied on a grid. The values of f_{c_1} and f_{c_2} that yield the smallest residual are then taken to be estimates of the event corner frequencies. The corner frequencies are first gridded at 1-Hz increments between 1 Hz and a maximum of 100 Hz and 0.1-Hz increments for lower corner frequencies. $R(f)$ is fitted between the instrument corner at 2 Hz and an upper noise-free frequency, which is determined independently for each pair. Poor choice of the fitting range yields obvious instabilities. The morphology of the residual manifold is assessed visually for each event pair studied.

Two examples of this procedure, displayed in figure 4, show that this methodology can be problematic under certain circumstances. Figure 4*A* shows the residuals for the event pair (20, 24). In this case, the corner frequencies (f_{c_1}, f_{c_2})=(3, 16 Hz) are well-resolved. This figure also shows the bias that is possible if we assume the smaller event to be a delta function and the search is gridded only over the corner frequency f_{c_1}. Figure 4*B* shows the residuals for the event pair (58, 60). In this case no closed residual low is observed, and the corner frequency of the smaller event is not resolved at all. However, f_{c_1} has a small variation relative to the poor resolution of f_{c_2}. This is generally true for event pairs where the smaller event magnitude is less than 2 or where the ambient noise is high. In order to get the best estimate of f_{c_1}, we fix f_{c_2} to a value consistent with the average value found in previous studies (Molnar and others, 1973; Boatwright and others, 1991; Fletcher and Boatwright, 1991). Because f_{c_1} in this case is assumed, it is indicated with a blank arrow in figure 5 and excluded from the averaging.

Of the 226 pairs analyzed, 102, which include 124 individual events, are fitted well by the Brune ratio model, shown in figure 5. Averaging of common events and further exclusion of artifacts yielded 98 individual measurements of *P*-wave corner frequencies, with 53 from the larger events (see table 1). These corner frequencies fall in the range 3.8 to 37.5 Hz, with corresponding events having local magnitudes between 1.5 and 4.4.

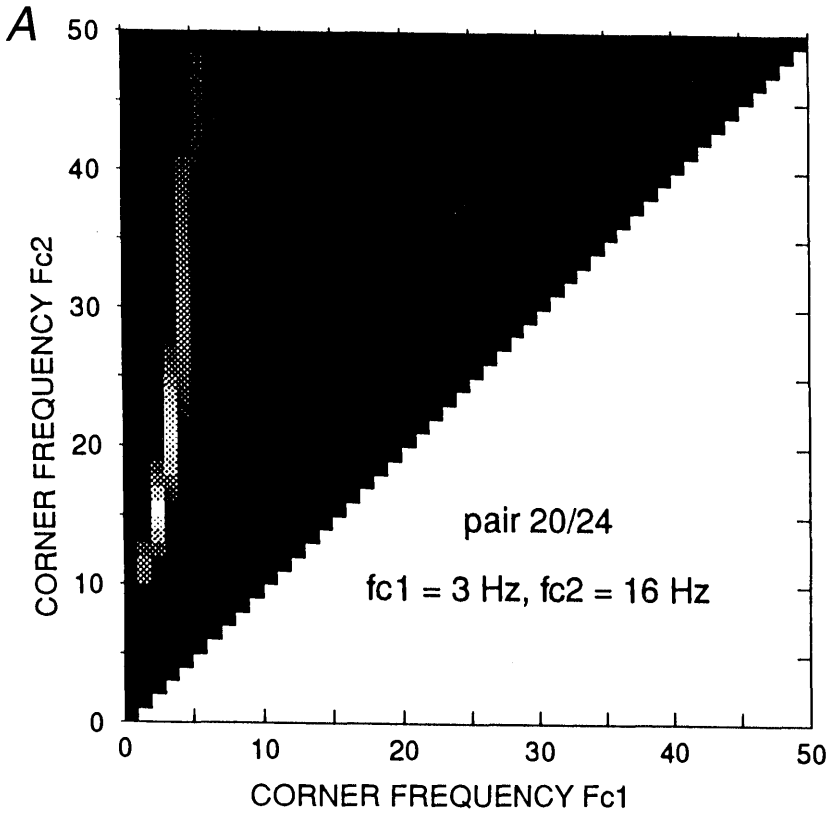

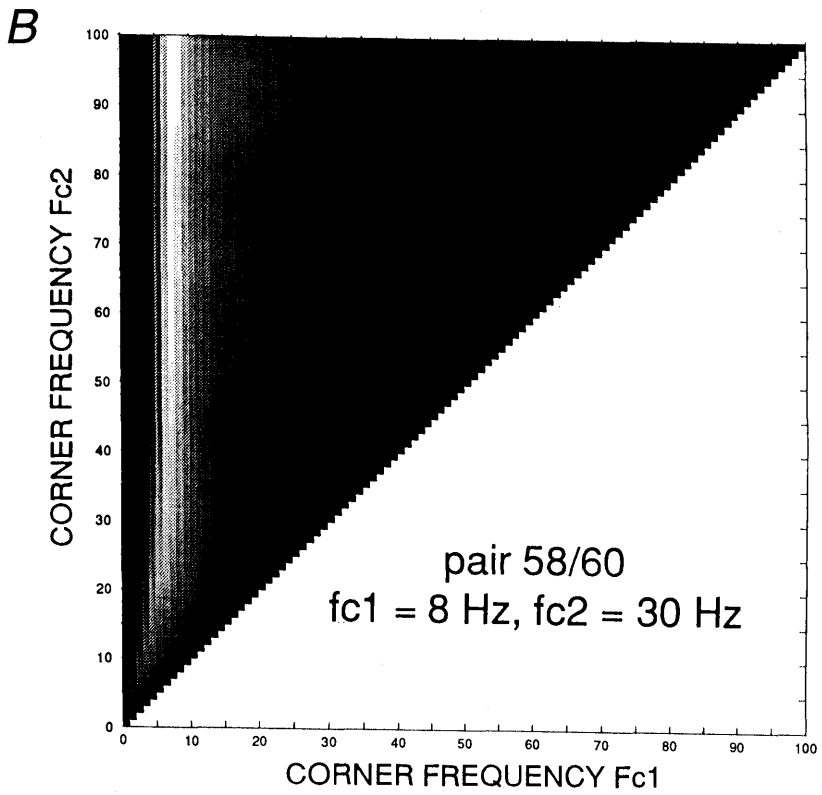

Figure 4.—Typical least-squares residuals as functions of f_{c_1} and f_{c_2}. White represents the minimum residual, and black indicates five times the minimum residual. Variation is linear in logarithmic residual, giving 256 grey scales. (*A*) Fitting for pair 20/24. Low residuals are centered in a very narrow frequency range and give us well-resolved corner frequencies of f_{c_1}=3 Hz and f_{c_2}=16 Hz. (*B*) Fitting for pair 58/60. The residual contour is not closed. The residual increases with increasing f_{c_2}, but f_{c_1} changes less with increasing f_{c_2}. An artifact limit, 30 Hz, is assumed for f_{c_2}, and then f_{c_1}=8 Hz is resolved in this case.

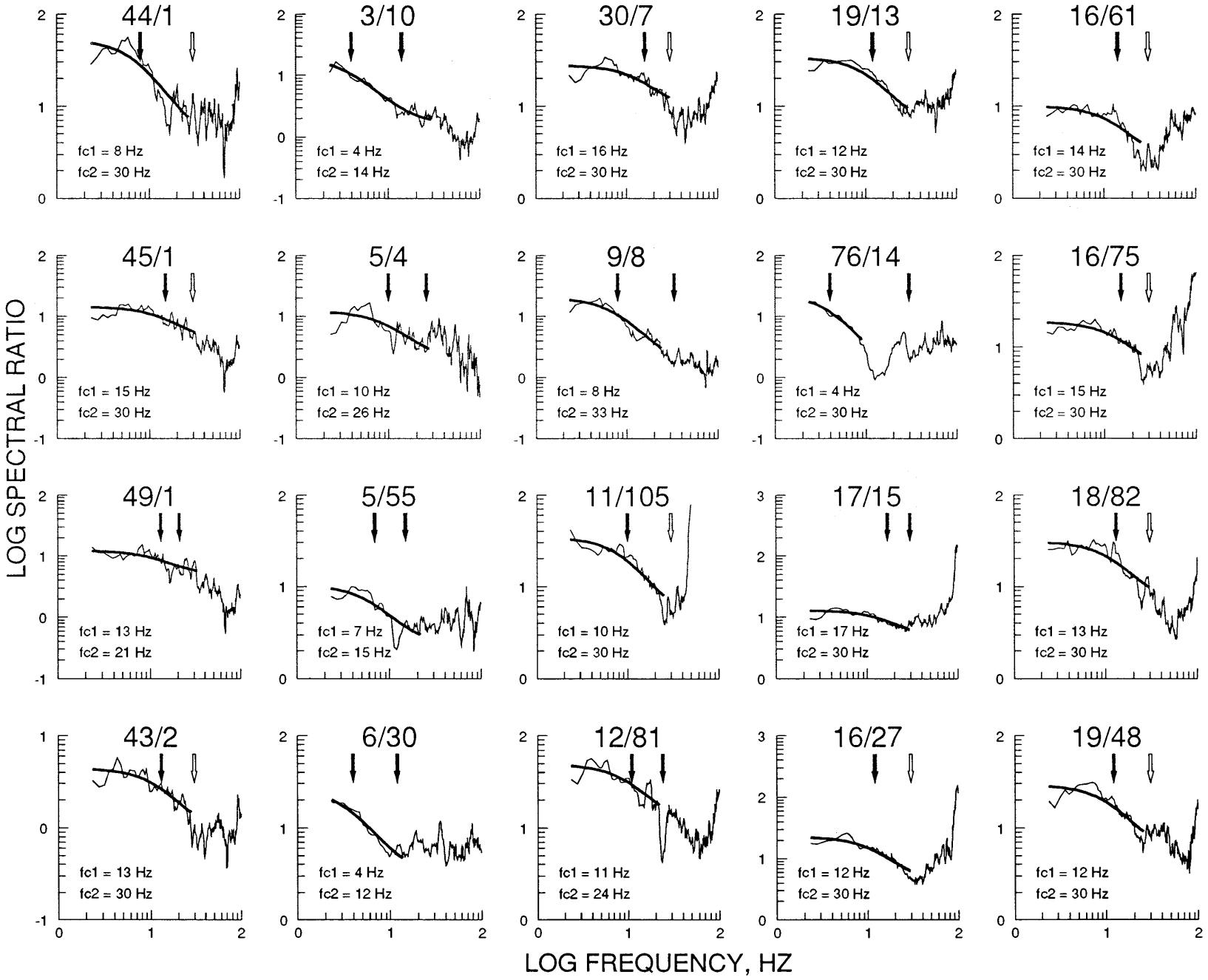

Figure 5.—Spectral ratio as a function of frequency for 102 event pairs (solid line), showing fit to the ratio of omega-square models (bold line). Each pair is indicated by the event number in table 1, with left number for the larger event and right number for the smaller event. Arrows indicate the position of corner frequencies, the left for the larger event and the right for the smaller event. Solid arrow represents a resolved corner frequency, and blank arrow represents an artifact corner frequency for the smaller event. The values of the two corner frequencies are shown in the lower corner for each pair. A total of 124 events are involved in these 102 event pairs.

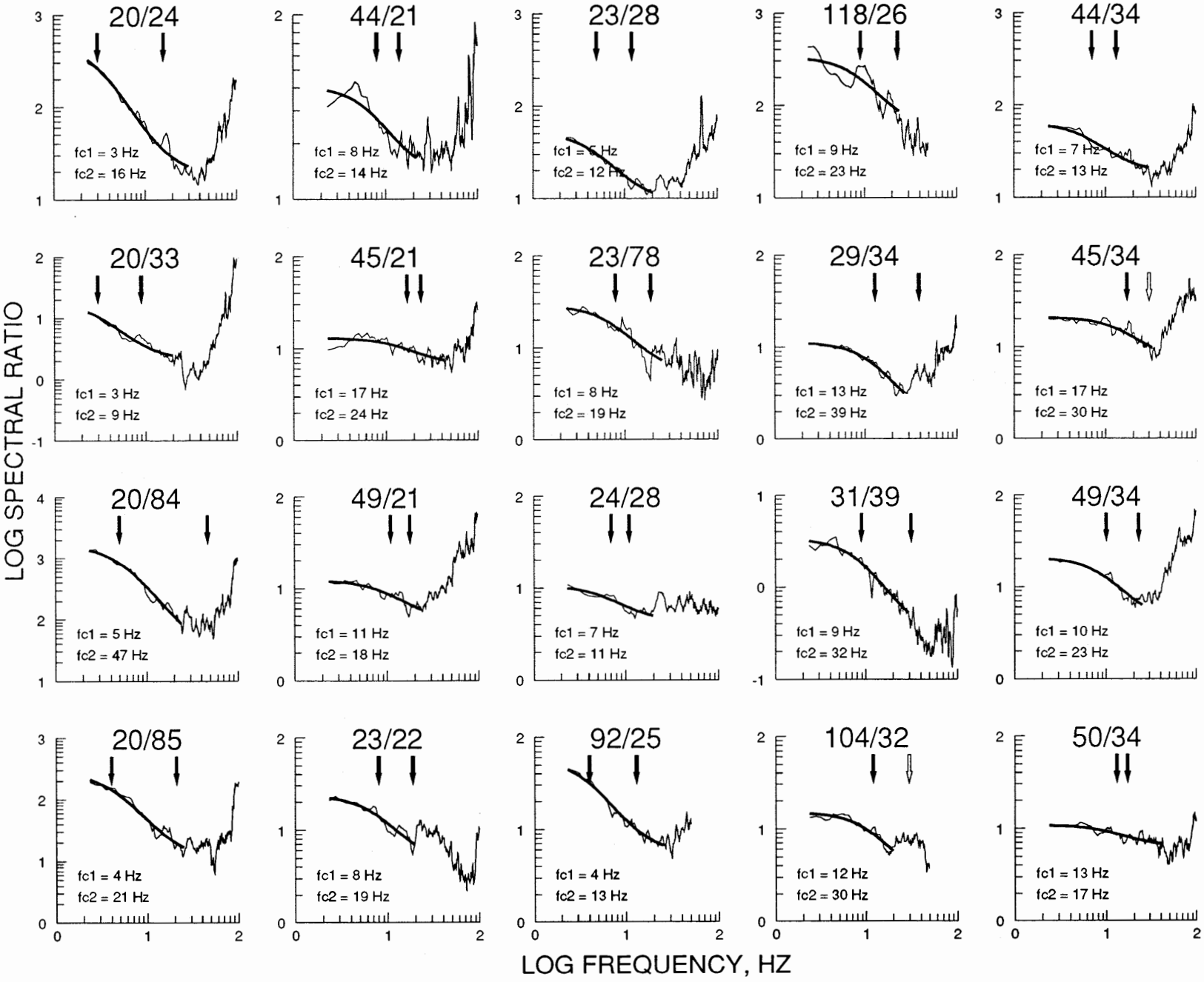

Figure 5.—Continued

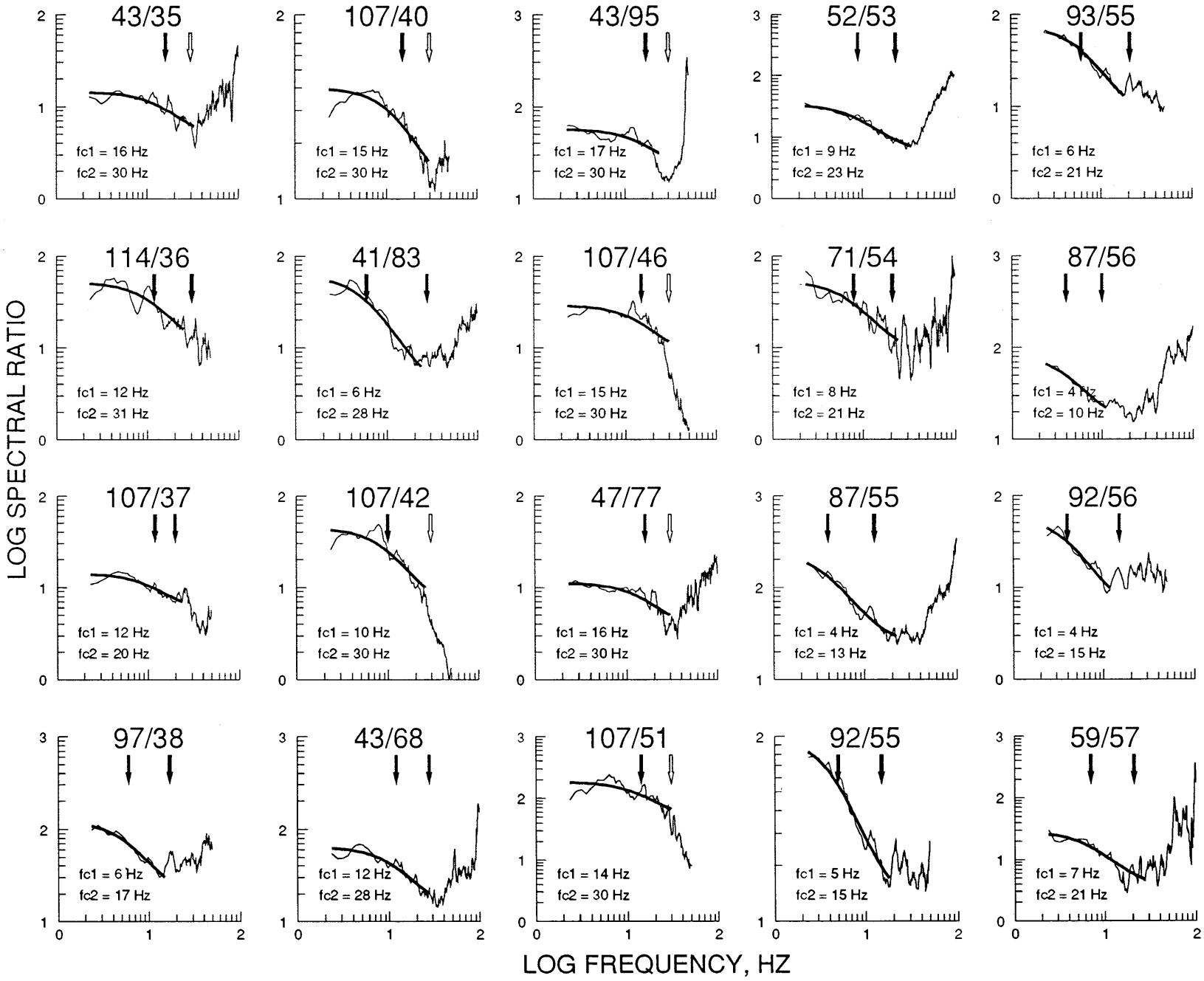

Figure 5.—Continued

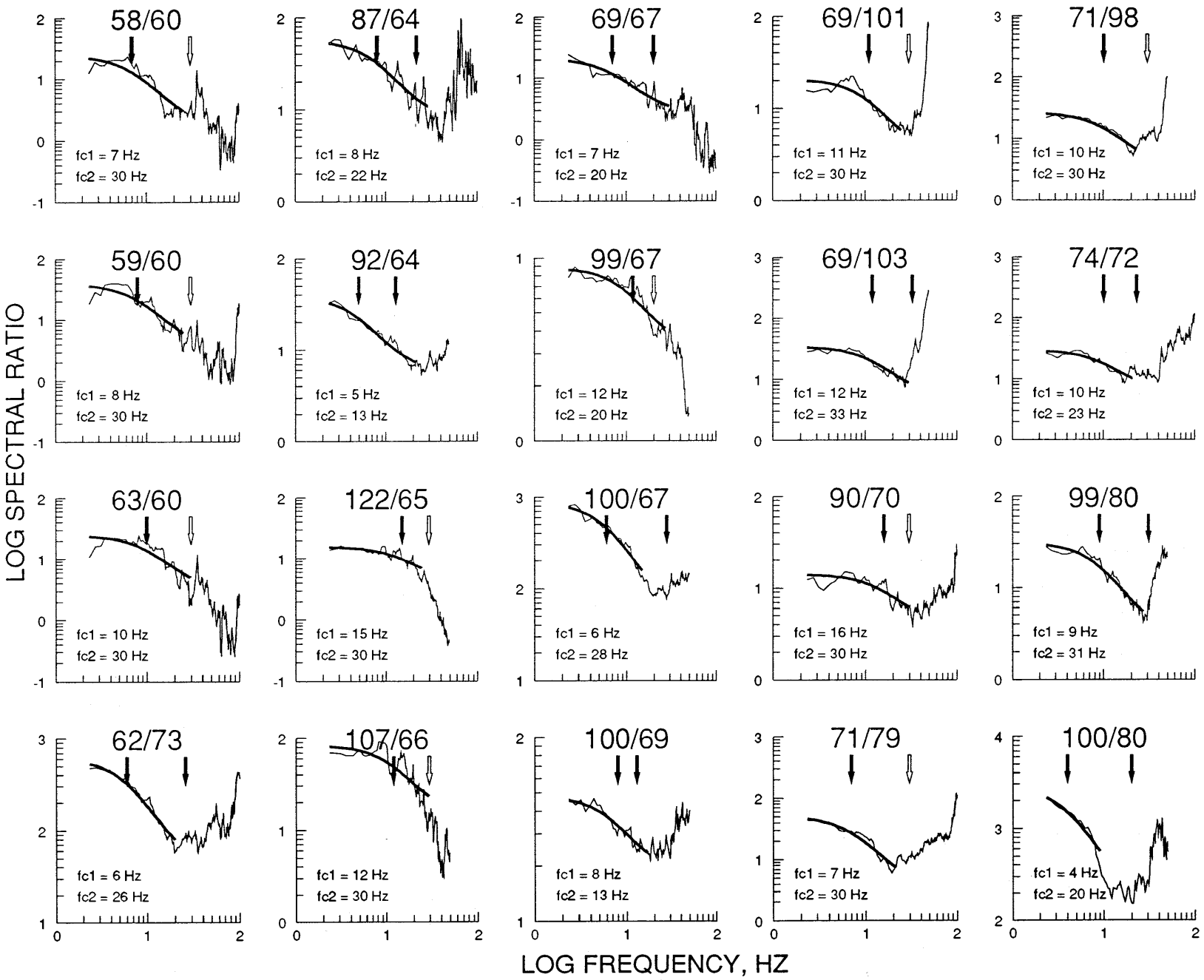

Figure 5.—Continued

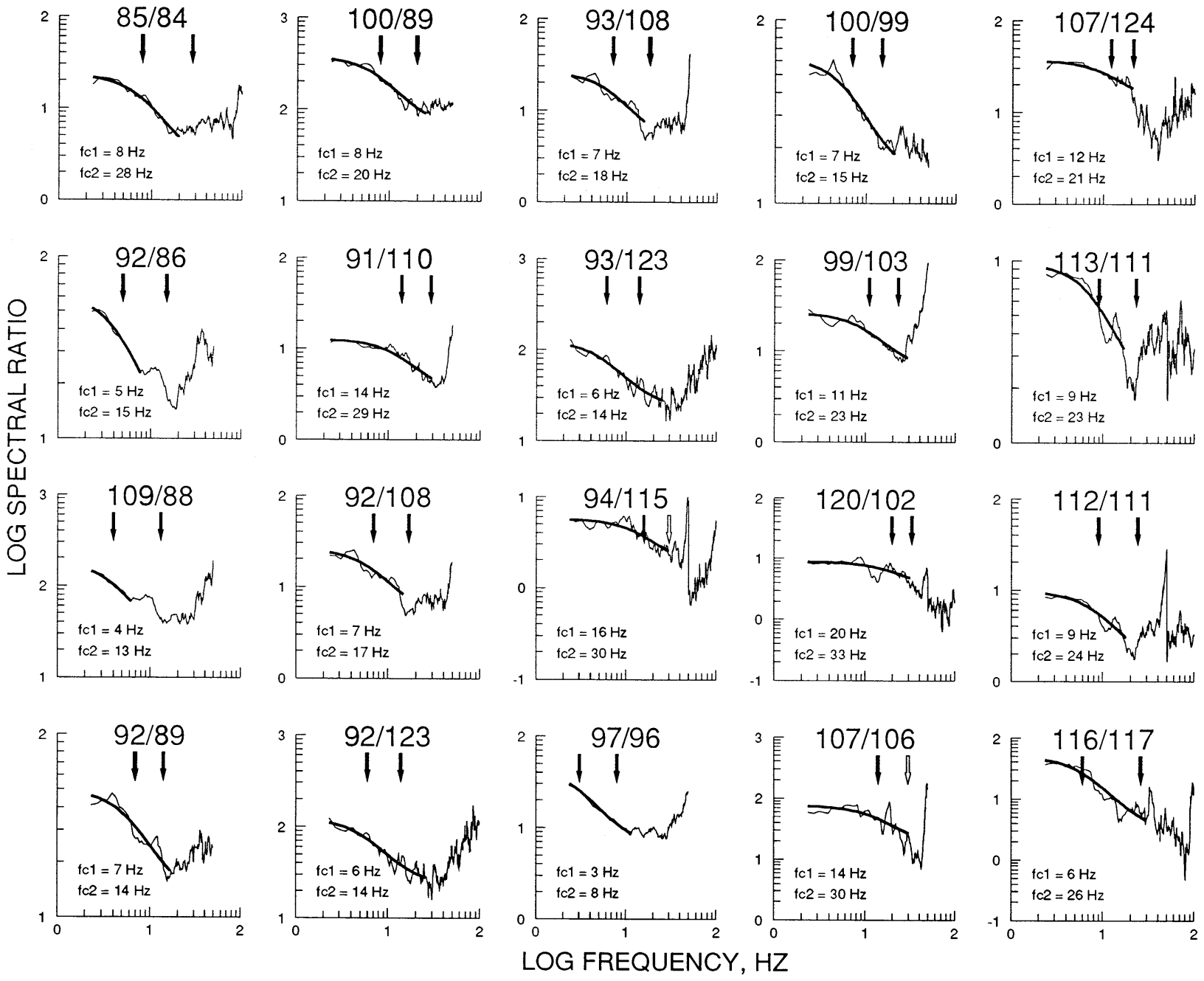

Figure 5.—Continued

CALCULATION OF STRESS DROP

The determination of stress drop for a small earthquake is generally based on a source determination derived from either the corner frequency of the displacement spectrum or the pulse width of the waveform. We model a small earthquake as a circular rupture and estimate the stress drop from the corner frequency, f_{c1}, using the formula (Brune, 1970; Brune, 1971; Kanamori and Anderson, 1975):

$$\Delta\sigma=M_o(f_c/(0.49v_r))^3$$

where the rupture velocity v_r is taken to be 3.5 km/s (Dahlen, 1974; Xie and others, 1991; Hough and others, 1991).

The seismic moment, M_o, is calculated for each event (table 1) from the long-period displacement spectral levels using

$$M_o=(4\pi\alpha^3\rho r\Omega_o)/(FR_{\varphi\psi})$$

where α is the *P*-wave velocity, ρ is the density, r is the hypocentral distance, Ω_o is the long period spectral level, F is the free surface correction, and $R_{\varphi\psi}$ is the average correction for radiation pattern. We use α=6 km/s, ρ=2.7 gm/cm^3, F=2, and $R_{\varphi\psi}$=0.7. We also calculated moment taking into account exact radiation terms as determined from the focal mechanisms, but found these estimates to be less consistent (among moment estimates for the same event at different stations) than those obtained with a constant radiation term. The corner frequency is shown as a function of moment in figure 6.

STRESS-DROP RESULTS

The Brune-model stress drops are found to be highly variable, ranging from approximately 1 to nearly 800 bars (see table 1 and figure 7). The dashed lines on figure 7 indicate the resolution limits corresponding to the frequency range over which we can generally resolve corner frequencies, 1 to 40 Hz. It appears that the apparent upper trend in figure 7 may in fact be an artifact of the high frequency resolution limit. However, the methodology and data should be sufficient to resolve low-stress-drop larger events, if they existed.

A dependence of stress drop on moment can be interpreted in terms of a critical slip distance resulting from fundamental characteristics of established rate and state variable friction laws (for example, Dieterich, 1986). The critical slip distance to achieve dynamic rupture corresponds to a minimum earthquake rupture dimension (for example, Dieterich, 1986; Scholz, 1990), thus leading to a breakdown in the similarity of earthquake rupture processes.

It is also possible to explain the inferred stress drop scaling in terms of tectonic factors. Global compilations (Abercrombie and Leary, 1993) show no resolved systematic scaling of stress drop with moment, implying that globally, there is no preferred earthquake rupture dimension (in other words, breakdown in similarity). However, within a limited tectonic region, it is plausible that a characteristic length scale will exist. If, for example, aftershocks in the Loma Prieta segment are interpreted as activation of cross faults within the fault zone (L. Seeber, 1994, unpub. data), then their rupture dimensions may preferentially correspond to the width of the fault zone.

CONCLUSIONS AND DISCUSSION

It has been demonstrated that eGf analysis is a quick and effective method for estimating the source characteristics of a large number of small- to medium-sized earthquakes with good resolution. The frequency-domain deconvolution removes the effects of travel path, site, and the instrument and isolates the source characteristics of the two events. The Brune spectral ratio model appears sufficient to parameterize the spectral ratio, provided that the differences in magnitude are not too small and the ambient noise at high frequencies is not too large. It is important, moreover, to specifically address the properties of the fitting residual as a function of the gridding variables. The estimate of the large-event corner frequency can be biased by improper selection of the small-event corner frequency, and so it is important to grid additionally over small-event corner frequency. The grid searching yields a well-resolved estimate of the corner frequency of the large event and sometimes of the smaller event as well. The resolution of the corner frequency of the larger event will be much better than that of a single spectrum parameterization of source and path effects if we properly

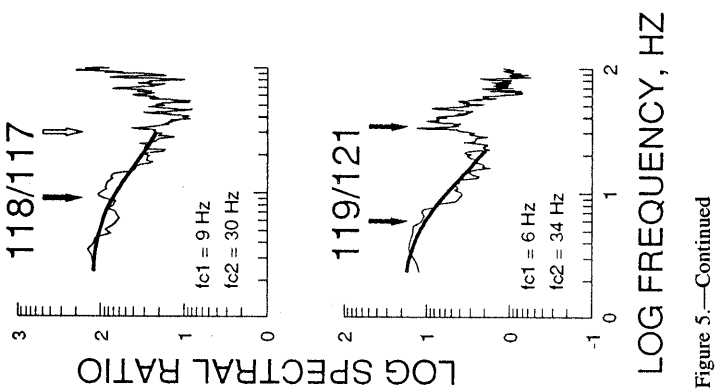

Figure 5.—Continued

Table 1.—*The 124 events used for empirical Green's function analysis*

[The 124 events involved in the 102 event pairs shown in figure 5. Of these, 98 event pairs have resolved corner frequencies, with 53 from the larger events (indicated in column L). The other 26 events are generally smaller events with magnitudes between 1.5 and 2.0. Their corner frequencies are not well-resolved from the ratio fitting and are excluded from the corner frequency averaging and the calculation of stress drops.]

Event	Date (yymmdd)	Time (Gmt)	Long. (W)	Lat. (N)	Depth (Km)	ML	Moment (dyne*cm)	fc (Hz)	Stress (bar)	L
1	891020	0406:04.39	121.957	37.177	6.38	1.7	5.66e+18	21.0	10.39	
2	891020	0513:51.66	121.803	37.060	4.62	2.3	1.58e+19			
3	891020	0617:24.49	121.973	37.174	3.54	2.6	7.94e+19	4.0	1.01	X
4	891020	0646:07.10	121.806	37.076	9.08	1.7	6.21e+18	26.0	21.64	
5	891020	0752:49.06	121.809	37.076	9.42	2.7	4.05e+19	8.5	4.93	X
6	891020	0812:54.07	122.070	37.181	14.13	3.6	1.95e+21	4.0	24.74	X
7	891020	0926:16.93	122.070	37.190	13.47	1.6	1.03e+19			
8	891020	1144:00.45	121.919	37.049	16.92	1.8	3.41e+18	33.0	24.29	
9	891020	1153:29.14	121.921	37.048	17.57	2.7	5.63e+19	8.0	5.71	X
10	891020	1348:28.20	121.974	37.178	2.98	1.7	3.55e+18	14.0	1.93	
11	891021	0011:11.27	121.975	37.108	15.11	2.5	8.69e+19	10.0	17.23	X
12	891021	0102:45.64	121.851	37.053	12.45	2.6	8.75e+19	11.0	23.09	X
13	891021	0257:51.95	121.863	37.103	4.23	1.5	1.66e+19			
14	891021	0320:24.43	121.640	36.924	5.99	2.4	3.98e+19	30.0	213.09	
15	891021	0459:28.71	121.992	37.171	7.86	1.7	1.99e+19	30.0	106.52	
16	891021	0832:19.49	122.000	37.121	14.96	2.7	4.76e+20	13.7	242.65	X
17	891021	1057:04.52	121.987	37.165	8.41	2.6	3.22e+20	17.0	313.62	X
18	891021	1452:24.27	121.881	37.105	3.59	2.5	2.62e+20	13.0	114.11	X
19	891021	1558:45.58	121.860	37.105	4.56	2.6	2.51e+20	12.0	85.99	X
20	891021	2214:56.52	121.905	37.061	15.27	4.4	7.08e+21	3.8	77.02	X
21	891021	2311:19.86	121.957	37.177	6.09	1.7	1.28e+19	18.7	16.59	
22	891021	2329:34.16	121.900	37.065	14.36	1.8	1.34e+19	19.0	18.22	
23	891022	0031:16.48	121.900	37.066	14.41	2.5	2.47e+20	7.0	16.80	X
24	891022	0254:29.59	121.904	37.063	14.36	2.4	6.58e+19	11.5	19.84	X
25	891022	0338:31.35	121.809	37.077	8.79	2.1	4.54e+19	13.0	19.77	
26	891022	0341:09.58	121.842	37.090	4.96	1.6	5.25e+18	23.0	12.66	
27	891022	0433:23.13	122.001	37.126	14.36	1.7	3.00e+19			
28	891022	0641:51.31	121.897	37.067	14.17	1.6	1.04e+19	11.5	3.14	
29	891022	0800:53.26	121.959	37.177	6.02	2.3	1.73e+20	13.0	75.35	X
30	891022	0817:08.47	122.074	37.183	13.65	2.6	2.23e+20	14.0	121.31	X
31	891022	1215:09.50	121.948	37.059	17.21	2.4	1.83e+19	9.0	2.64	X
32	891022	1351:03.20	121.932	37.066	15.19	1.5	3.18e+19			
33	891022	1627:18.20	121.903	37.063	14.60	2.3	1.16e+20	9.0	16.76	
34	891022	1710:32.43	121.961	37.180	6.57	1.5	2.00e+19	23.0	48.24	
35	891022	1720:52.24	121.801	37.051	4.15	1.6	3.75e+19			
36	891022	1938:54.69	121.903	37.062	14.15	1.5	6.42e+18	31.0	37.92	
37	891022	2148:31.54	121.667	36.944	10.97	2.3	1.46e+20	20.0	231.55	
38	891023	0347:04.23	121.838	37.111	4.47	1.9	1.07e+19	17.0	10.42	
39	891023	0541:50.90	121.941	37.059	17.57	1.7	4.61e+19	32.0	299.47	
40	891023	0552:52.55	121.666	36.945	10.97	1.8	6.60e+19			
41	891023	1514:22.93	121.655	37.005	2.71	3.0	2.72e+20	6.0	11.65	
42	891023	1805:59.85	121.665	36.941	10.05	1.6	1.85e+19			
43	891024	0448:11.99	121.803	37.056	4.97	3.2	4.79e+20	14.5		
44	891024	0702:23.52	121.959	37.179	6.14	2.8	5.33e+20			
45	891024	0856:12.93	121.959	37.179	6.04	2.5	1.86e+			
46	891024	1825:32.76	121.668	36.945	11.07	2.1	1.07e+			

Table 1.—*Continued*

Event	Date (yymmdd)	Time (Gmt)	Long. (W)	Lat. (N)	Depth (Km)	ML	Moment (dyne*cm)	fc (Hz)	Stress (bar)	L
47	891024	1930:37.71	121.653	36.935	6.71	2.4	8.95e+19	16.0	72.68	X
48	891024	2213:10.54	121.865	37.104	4.46	1.5	9.29e+18			
49	891024	2226:13.11	121.962	37.179	5.76	2.5	1.61e+20	11.3	46.05	X
50	891024	2342:16.15	121.964	37.175	5.94	2.3	2.82e+19	13.0	12.28	X
51	891025	0051:33.46	121.670	36.946	10.37	1.7	6.10e+18			
52	891025	0127:26.35	121.820	37.081	10.20	4.2	5.50e+21	9.0	794.87	X
53	891025	0538:42.96	121.825	37.085	10.42	2.8	2.46e+20	23.0	593.37	
54	891025	0915:14.31	121.708	36.966	13.99	1.6	1.57e+19	21.0	28.82	
55	891025	0923:31.94	121.806	37.075	9.16	1.7	1.67e+19	16.0	13.56	
56	891025	1314:16.26	121.809	37.075	9.06	1.9	4.96e+19	12.5	19.21	
57	891025	1508:33.00	121.882	36.903	4.31	1.9	3.64e+19	21.0	66.83	
58	891025	1510:54.73	121.881	36.904	4.13	2.6	2.12e+20	7.0	14.42	X
59	891025	1630:51.19	121.882	36.903	4.10	2.8	3.12e+20	7.5	26.09	X
60	891025	1808:58.44	121.880	36.903	4.10	1.6	7.82e+19			
61	891025	1926:36.98	122.001	37.120	14.74	2.0	4.23e+19			
62	891025	2201:49.43	121.797	37.004	17.13	3.7	3.38e+21	6.0	144.74	X
63	891025	2244:41.96	121.883	36.902	4.21	2.6	2.38e+20	10.0	47.18	X
64	891026	0459:19.07	121.808	37.075	9.11	2.0	4.22e+19	17.5	44.84	
65	891026	0727:25.69	121.642	36.920	6.91	1.8	1.10e+19			
66	891026	0840:59.66	121.663	36.942	10.12	1.7	3.55e+18			
67	891026	1303:51.32	121.794	37.068	8.76	1.7	1.94e+19	22.7	44.99	
68	891026	1519:24.88	121.803	37.056	4.57	1.7	7.04e+18	28.0	30.64	
69	891026	1613:25.46	121.793	37.066	9.47	2.9	1.74e+20	10.8	43.45	X
70	891026	1715:11.20	121.904	37.120	4.48	1.6	1.10e+19			
71	891027	1329:51.30	121.710	36.969	14.52	3.0	2.16e+20	8.3	24.48	X
72	891027	1540:03.73	121.754	36.998	15.15	1.6	2.51e+18	23.0	6.06	
73	891027	2206:21.22	121.804	37.002	16.61	1.6	2.79e+19	26.0	97.21	
74	891027	2215:06.83	121.758	37.005	14.84	2.9	2.24e+20	10.0	44.38	X
75	891028	0228:00.68	122.000	37.125	14.48	1.7	3.13e+19			
76	891028	2127:49.47	121.636	36.917	6.22	3.3	8.91e+20	4.0	11.31	X
77	891029	0133:20.15	121.654	36.931	6.75	1.5	3.28e+19			
78	891029	0315:17.60	121.903	37.065	13.82	1.8	2.43e+19	19.0	33.04	
79	891029	0347:37.49	121.705	36.969	13.73	1.8	2.71e+19			
80	891029	0602:04.27	121.793	37.069	8.94	1.5	2.56e+19	25.5	84.15	
81	891029	1107:40.27	121.852	37.054	11.97	1.5	1.62e+19	24.0	44.40	
82	891029	1441:32.57	121.882	37.107	3.58	1.6	1.34e+19			
83	891030	0006:20.04	121.655	37.000	2.16	1.7	1.74e+19	28.0	75.72	
84	891030	0216:06.12	121.910	37.056	15.10	1.6	1.15e+19	37.5	120.23	
85	891030	0452:24.59	121.902	37.057	15.25	2.5	1.35e+20	14.5	81.59	X
86	891030	0946:34.71	121.808	37.075	9.16	1.7	3.55e+18	15.0	2.37	
87	891030	1117:13.54	121.807	37.070	9.66	3.6	3.47e+21	5.3	102.42	X
88	891030	1142:36.59	121.925	37.063	14.47	1.8	3.63e+19	13.0	15.81	
89	891030	1353:59.86	121.804	37.075	9.34	1.5	2.69e+19	17.0	26.20	
90	891030	1541:54.35	121.907	37.118	3.78	2.4	9.08e+19	16.0	73.73	X
91	891031	0650:07.51	121.996	37.135	12.62	2.2	1.30e+20	14.0	70.72	X
92	891031	0834:48.82	121.804	37.071	8.93	3.3	7.23e+20	5.4	22.57	X
93	891031	0834:51.34	121.803	37.069	8.55	3.3	7.23e+20	6.3	35.84	X
94	891031	1729:39.36	121.745	36.996	15.19	2.4	1.21e+20	16.0	98.25	X
95	891101	0323:30.97	121.809	37.062	4.95	1.6	1.00e+19			
96	891101	0616:03.79	121.836	37.104	4.63	2.4	1.17e+20	8.0	11.88	
97	891101	0803:17.43	121.837	37.105	4.62	3.7	1.37e+21	4.5	24.75	X
98	891102	0505:37.90	121.715	36.976	14.26	1.7	3.77e+19			
99	891102	0512:34.29	121.796	37.069	8.93	2.5	3.91e+20	11.8	127.36	X

Table 1.—*Continued*

Event	Date (yymmdd)	Time (Gmt)	Long. (W)	Lat. (N)	Depth (Km)	ML	Moment (dyne*cm)	fc (Hz)	Stress (bar)	L
100	891102	0550:10.87	121.800	37.069	9.08	4.3	1.33e+22	6.6	758.04	X
101	891102	0636:45.27	121.787	37.069	9.35	1.6	1.96e+19			
102	891102	0737:19.50	121.792	37.070	7.40	1.5	1.63e+19	33.0	116.13	
103	891102	0801:57.17	121.791	37.067	8.62	1.5	1.12e+19	28.0	48.74	
104	891102	1011:06.20	121.930	37.064	15.40	2.3	2.29e+20	12.0	78.45	X
105	891102	2019:20.05	121.974	37.107	15.13	1.5	1.46e+19			
106	891103	1014:01.24	121.664	36.944	10.11	1.7	2.17e+19			
107	891103	1047:56.48	121.666	36.944	10.65	3.1	1.65e+21	13.0	718.66	X
108	891104	1613:26.32	121.806	37.070	9.19	1.9	4.03e+19	17.5	42.82	
109	891105	0130:41.94	121.921	37.065	14.31	3.8	2.19e+21	4.0	27.79	X
110	891105	1406:39.68	121.997	37.129	12.90	1.5	1.35e+19	29.0	65.27	
111	891106	0750:16.88	121.887	37.114	4.31	2.0	3.03e+19	23.5	77.96	
112	891106	0827:05.01	121.887	37.112	4.16	2.9	2.47e+20	9.0	35.70	X
113	891106	0827:15.28	121.889	37.113	3.55	2.9	2.47e+20	9.0	35.70	X
114	891106	1548:18.42	121.907	37.064	14.42	2.4	1.94e+20	12.0	66.46	X
115	891111	2116:36.77	121.741	36.996	14.56	1.6	1.83e+19			
116	891114	2041:55.08	121.838	37.089	5.27	2.8	1.13e+20	6.0	4.84	X
117	891114	2053:10.33	121.840	37.090	5.33	1.5	1.38e+19	26.0	48.08	
118	891114	2116:42.70	121.840	37.089	5.53	3.4	5.23e+20	9.0	75.59	X
119	891117	1932:18.88	121.787	37.064	8.12	2.6	7.94e+19	6.0	3.40	X
120	891117	1935:19.16	121.789	37.066	8.13	2.3	5.18e+19	20.0	82.15	X
121	891117	2116:59.77	121.790	37.069	7.43	1.5	1.78e+18	34.0	13.86	
122	891120	1739:57.81	121.648	36.923	7.23	2.8	7.41e+19	15.0	49.58	X
123	891122	1213:52.32	121.805	37.075	9.16	1.6	7.63e+18	14.0	4.15	
124	891122	1757:11.80	121.666	36.944	10.13	2.0	1.38e+19	21.0	25.34	

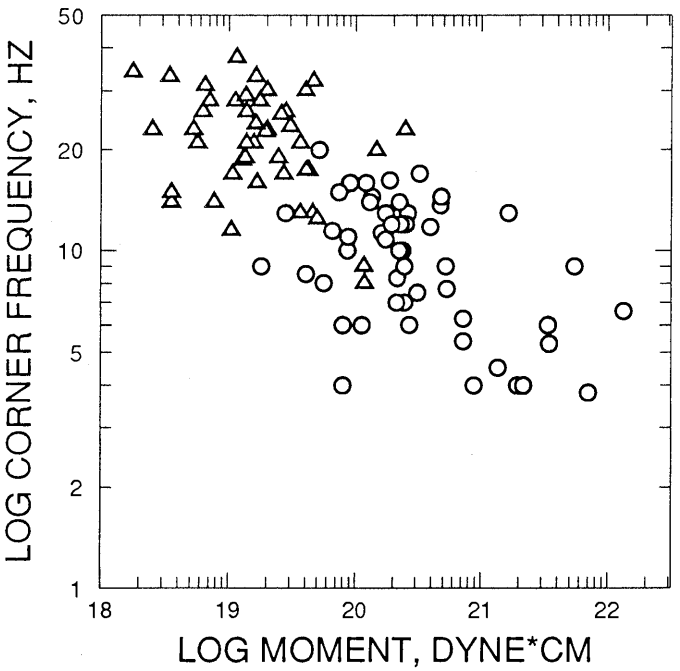

Figure 6.—Corner frequency as a function of seismic moment for 98 Loma Prieta aftershocks. Circles indicate the larger events and triangles indicate the smaller events.

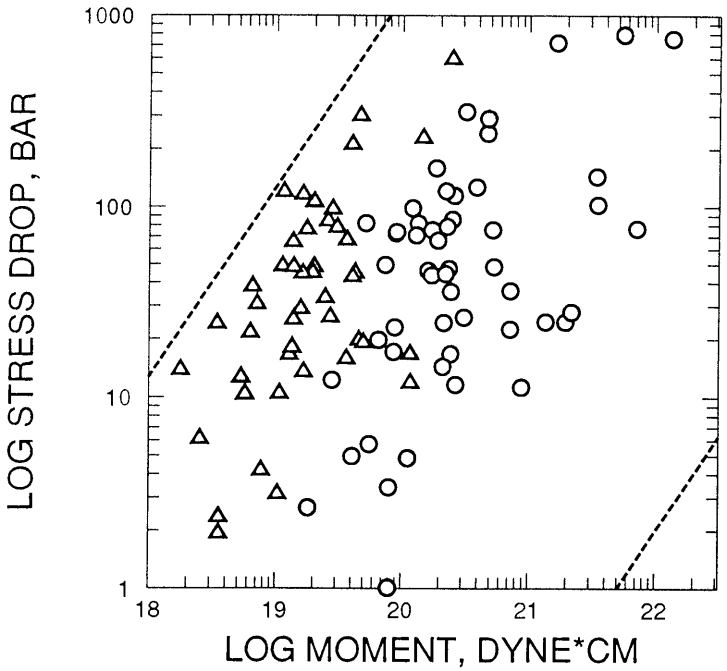

Figure 7.—Brune-model stress drop as a function of seismic moment for 98 Loma Prieta aftershocks. Circles indicate the larger events and triangles indicate the smaller events. The dashed lines are the resolution limits corresponding to fixed corner frequencies of 1 Hz and 40 Hz.

choose the event pair. Although the empirical Green's function method is limited to available event pairs, we have shown that, within a dense aftershock sequence, it can be used for a large-scale investigation of source properties. In this study, we obtain a total of 98 well-resolved corner frequencies for events with magnitudes between 1.5 and 4.4.

ACKNOWLEDGMENTS

We thank the many people who contributed to the successful deployment of the IRIS/PASSCAL network, including David Simpson, Larry Shengold, Robert Busby, and James Fowler. We thank Professor Lynn Sykes for providing helpful comments and suggestions. We thank Leonardo Seeber and John Armbruster for providing relocation data. We also thank David Oppenheimer for supplying CALNET phase data used for relocation. The research was supported by U.S. Geological Survey under Grant 14-08-001-G-1831, and the aftershock data collection was supported by the Incorporate Research Institutions for Seismology and by the National Science Foundation. The PASSCAL aftershock data are available from the IRIS Data Management Center or from the authors at Lamont-Doherty. This is Lamont-Doherty contribution number 5479.

REFERENCES CITED

Abercrombie, L. and P.C. Leary, 1993, Source parameters of small earthquakes recorded at 2.5 km depth, Cajon Pass, California: Implications for earthquake scaling: Geophysical Research Letters 20, p. 1511-1514.

Brune, J.N., 1970, Tectonic stress and the seismic shear waves from earthquakes: Journal of Geophysical Research, v. 75, no. 26, p. 4997-5009.

Brune, J.N., 1971, Correction: Journal of Geophysical Research, v. 76, no. 20, p. 5002.

Boatwright, J., Fletcher, J.B., and Fumal, T.E., 1991, A general inversion scheme for source, site, and propagation characteristics using multiply recorded sets of moderate-sized earthquakes: Seismological Society of America Bulletin, v. 81, no. 5, p. 1754-1782.

Dahlen, A., 1974, On the ratio of P-wave to S-wave corner frequencies for shallow earthquake source: Seismological Society of America Bulletin, v. 64, no. 4, p. 1159-1180.

Dieterich, J., 1986, State variable fault constitutive relations for dynamic slip, *in* Earthquake Source Mechanics: American Geophysical Union Geophysical Monograph 37, p. 311-318.

Frankel, A., Fletcher, J., Vernon, F., Haar, L., Berger, J., Hanks, T., and Brune, J., 1986, Rupture characteristics and tomographic source imaging of ML~3 earthquakes near Anza, Southern California: Journal of Geophysical Research, v. 91, no B12, p. 12633-12650.

Fletcher, J.B., and Boatwright, J., 1991, Source parameters of Loma Prieta aftershocks and wave propagation characteristics along the San Francisco peninsula from a joint inversion of digital seismograms: Seismological Society of America Bulletin, v. 81, no. 5, p. 1783-1812.

Geller, R.J., and Mueller, C.S., 1980, Four similar earthquakes in central California: Geophysical Research Letters, v. 7, no. 10, p. 821-824.

Hartzell, S.H., 1978, Earthquake aftershocks as Green's functions: Geophysical Research Letters, v. 5, no. 1, p. 1-4.

Hough, S.E., and Anderson, J.G., 1988, High frequency spectra observed at Anza, California: Implications for Q structure: Seismological Society of America Bulletin, v. 78, no. 2, p. 692-707.

Hough, S.E., Seeber, L., Lerner-Lam, A., Armbruster, J.G., and Guo, H., 1991, Empirical Green's function analysis of Loma Prieta aftershocks: Seismological Society of America Bulletin, v. 81, no. 5, p. 1737-1753.

Hutchings, L., and Wu, F., 1990, Empirical Green's functions from small earthquakes: a waveform study of locally recorded aftershocks of the 1971 San Fernando earthquake: Journal of Geophysical Research, v. 95, no. B2, p. 1187-1214.

Kanamori, H., and Anderson, D.L., 1975, Theoretical basis of some empirical relations in seismology: Seismological Society of America Bulletin, v. 65, no. 5, p. 1073-1095.

Li, Y., and Thurber, C.H., 1988, Source properties of two microearthquakes in Kilauea volcano, Hawaii: Seismological Society of America Bulletin, v. 78, no. 3, p. 1123-1132.

Menke, W., Shengold, S.L., Guo, H., Hu, G., and Lerner-Lam, A., 1991, Performance of the short-period geophones of the IRIS/PASSCAL array: Seismological Society of America Bulletin, v. 81, no. 1, p. 232-242.

Molnar, P., Tucker, B.E., and Brune, J.N., 1973, Corner frequencies of P and S waves and models of earthquake sources: Seismological Society of America Bulletin, v. 63, no. 6, p. 2091-2104.

Mori, J., and Frankel, A., 1990, Source parameters for small events associated with the 1986 North Palm Springs, California, earthquake determined using empirical Green's functions: Seismological Society of America Bulletin, v. 80, no. 2, p. 278-295.

Mueller, C.S., 1985, Source pulse enhancement by deconvolution of empirical Green's function: Geophysical Research Lettters, v. 12, no. 1, p. 33-36.

Park, J., Lindberg, C.R., and Vernon, F.L., 1987, Multitaper spectral analysis of high-frequency seismograms: Journal of Geophysical Research, v. 92, no. B12, p. 12,675-12,684.

Pujol, J., 1992, Joint hypocentral location in media with lateral velocity variations and interpretation of station correction: Physics of the Earth and Planetary Interiors, v. 75, no. (1-3), p. 7-24.

Scholz, C.H., 1990, The mechanics of earthquakes and faulting: Cambridge, Massachusetts, Cambridge University Press, 441 p.

Seeber, L. and Armbruster, J.G., 1990, Fault kinematics in the 1989 Loma Prieta rupture area during 20 years before that event: Geophysical Research Letters, v. 17, no. 9, p. 1425-1428.

Xie, J., Liu, Z., Herrmann, R.B., and Cranswick, E.D., 1991, Source processes of three aftershocks of the 1983 Goodnow, New York, earthquake: high-resolution images of small, symmetric ruptures: Seismological Society of America Bulletin, v. 81, no. 3, p. 818-843.

AFTERSHOCKS AND POSTSEISMIC EFFECTS

U.S. GEOLOGICAL SURVEY AFTERSHOCK GROUND-MOTION DATA

By Leif Wennerberg,
U.S. Geological Survey

CONTENTS

ABSTRACT

Portable seismographs were deployed to record aftershocks of the Loma Prieta earthquake for studies of earthquake source processes, effects of local geology on ground motions, and crustal and basin wave-propagation effects. This report provides maps and descriptions of specific experimental objectives of the aftershock deployments. Thirty-eight digital seismographs were deployed at 195 sites during the period from the day after the October 17, 1989, main shock until mid-January 1990. Aftershock recordings were obtained at or near 26 sites where the main shock was recorded by permanent strong-motion instruments. Fifteen aftershock recording instruments were at, or near, locations where previous USGS studies have been done; nuclear-explosion recordings and/or borehole geologic and velocity data are available for these sites. There was also a brief deployment of 60 USGS refraction-survey analog instruments in the epicentral area on the night after the main shock.

INTRODUCTION

Aftershock sequences provide a reliable source of earthquake ground motions which can be used to address issues relating to the physics of the seismogenic process and to address practical problems of strong-ground-motion prediction, such as the relevence of weak-motion records to strong-ground motions or the effects of local geologic conditions on ground motion. Following the Loma Prieta earthquake, several groups from the USGS recorded aftershocks in an effort to further our understanding of earthquake hazards in the San Francisco Bay area. The digital data sets include a total of more than 5,000 three-component records from 195 sites in the greater San Francisco Bay area, and have been collected on two CD-ROMs (see Mueller and Glassmoyer, 1990, and Carver and others, 1990, for data access).

In this paper I summarize the USGS data-collection efforts and describe the experimental objectives. Certain recording sites could be used for more than one purpose, some of which may not have been considered, so the objectives listed here cannot be exhaustive. As I discuss the experiments, I refer to any published results I know of that have used these data. I do not discuss the results of these studies. In the "References" section I also list a few analyses not referred to explicitly in the text. There is still a significant amount of work that could be done using these data.

This discussion provides an overview and introduction to the data sets, and supplements Mueller and Glassmoyer's (1990) and Carver and others' (1990) presentations of the digital data. No report has been written specifically devoted to the analog data set. Mueller and Glassmoyer's report (1990), while providing a comprehensive description of a significant portion of the digital data set, provides a much briefer discussion of experimental objectives than presented here. It contains no discussion of previous work or published analyses. My discussion of the data presented in Carver and others (1990) briefly summarizes their report and includes references to relevant work that has appeared since their report was published.

For the purposes of this report, I divide the USGS aftershock investigations into three parts corresponding to three instrumentation groups, one of which collected only a small and quite specialized data set, but which is included for the sake of completeness. The two main data-collection efforts were undertaken by a group using GEOS recorders (Borcherdt and others, 1985; Mueller and Glassmoyer, 1990) and a group using Sprengnether DR-200 recorders (Carver and others, 1986; Carver and others, 1990; Cranswick and others, 1990). The data collected by the GEOS group are mostly from Santa Clara County and the San Francisco peninsula, with some data recorded in Monterey, San Benito, Santa Cruz, and southern Alameda Counties. These data are described in detail in Mueller and Glassmoyer (1990). The DR-200 data are mostly from Santa Cruz and Santa Clara Counties, with some records obtained in Monterey County and are described in Carver and others (1990) and King and others (1990). The GEOS records digital data with 16-bit resolution. The DR-200 has a 12-bit digitizer, but is gain-ranged to give an effective 16-bit recording range. Both types of instruments sampled at 200 samples per second. Three-component velocity transducers with natural periods between 1 and 2 Hz were used. Most GEOS recorders were also deployed with three-component force-balance accelerometers. See Mueller and Glassmoyer (1990) and Carver and others (1990) for details on sensors.

In this paper I discuss the GEOS experiments, presenting station maps and a table of sites and experiments, and note related work done by the USGS. Then I discuss the DR-200 data, presenting maps and discussing experiments and selected sites. Finally, I briefly describe the refraction-survey-instrument data set.

GEOS DATA

Twenty-seven GEOS recorders were deployed at 94 sites during the aftershock studies. 2,615 three-component velocity records were collected, and 2,592 accelerograms were collected from sensors collocated with velocity transducers. Figures 1 through 8, taken from Mueller and Glassmoyer (1990), show the sites occupied by GEOS recorders. Table 1 lists the sites where data were obtained and indicates the reason(s) for each site's occupation. The main shock was recorded by permanent strong-motion instruments at twenty-three GEOS sites. Mueller and Glassmoyer (1990) give more detailed information on site locations and characteristics, instrument parameters, and aftershocks recorded. The following is a somewhat idealized description of the aftershock studies undertaken. Mueller and Glassmoyer (1990) give a clearer indication of how much data relevant to each study were actually obtained.

The topics of interest during the GEOS deployments can be placed in three categories: large-length-scale wave-propagation effects, local site effects, and collocations with strong-motion instruments. The large-scale studies were intended to clarify crustal propagation effects, or the possibility of a distinct seismic response of the sedimentary basin of the south San Francisco Bay. Studies of local site effects were primarily motivated either by damage or by an interest in the shaking properties of common geologic units. These studies typically consisted either of instruments deployed on bay mud and/or alluvium sites with simultaneously recording instrument(s) "nearby" on one or more rock sites, or of dense arrays designed to study wave propagation and (or) the small-scale variability of ground motions. The collocations with strong-motion instruments were intended to collect small-earthquake data that could be used for an empirical-Green's-function analysis of the main shock (for example, Hartzell, 1978), or for information on the relationship between small-earthquake records and large-earthquake ground motions.

LARGE-LENGTH-SCALE SEISMIC-WAVE-PROPAGATION STUDIES

The main large-scale deployment was a line of stations along the San Francisco peninsula from the aftershock zone to San Francisco. The stations are listed in table 1 under the experiment PP. The main interest of this deployment was crustal wave propagation, with a secondary interest in local site response. Results of analysis of the data are presented by Fletcher and Boatwright (1991) and Boatwright and Fletcher (1991a). McGarr and others (1991) also used some of these stations to analyze wave propagation up the peninsula. Two shorter transverse lines, oriented roughly southwest-northeast, were deployed in the south bay: a line from the southern peninsula to the southern east bay flatlands (from SRL on the west to FLB and POR on the east, fig. 4) and a line crossing the northern Santa Clara Valley (from BMT on the west to TUL on the east, fig. 4). The stations involved are listed in table 1 as PE and SV, respectively. These lines were deployed to observe possible basin response.

INFLUENCE OF LOCAL GEOLOGY ON GROUND SHAKING

Most of the aftershock studies focused on the effects of local geology on ground motion. Two particularly significant efforts were studies of the Marina District of San Francisco and of the San Francisco Airport area (Mb and Ms, and SFO in table 1; figs. 7 and 5, respectively). The Marina suffered dramatic damage, which was surprising

given its distance from the main shock, and was the object of quite thorough instrumentation. The USGS was requested by the airport authorities to conduct a study to interpret damage patterns at the facility. Analyses of the Marina data have appeared in Boatwright and others (1991b, 1992). McGarr and others (1991) analyzed the airport data.

A study of San Francisco (SF in table 1) focused on the correlation of site amplification and damage with geology in the city. An analysis of these data appears in Seekins and Boatwright (1994). Instruments were also deployed near Foster City on the bay margin (FC in table 1, fig. 4). These data have been discussed in Çelebi and McGarr (1991a, b). The trans-south-bay line (PE in table 1, fig. 4) was also designed to sample a variety of alluvial units to determine if significant variations in ground shaking occurred. These data were analyzed by Margheriti and others (1994). Six instruments were deployed on or near the

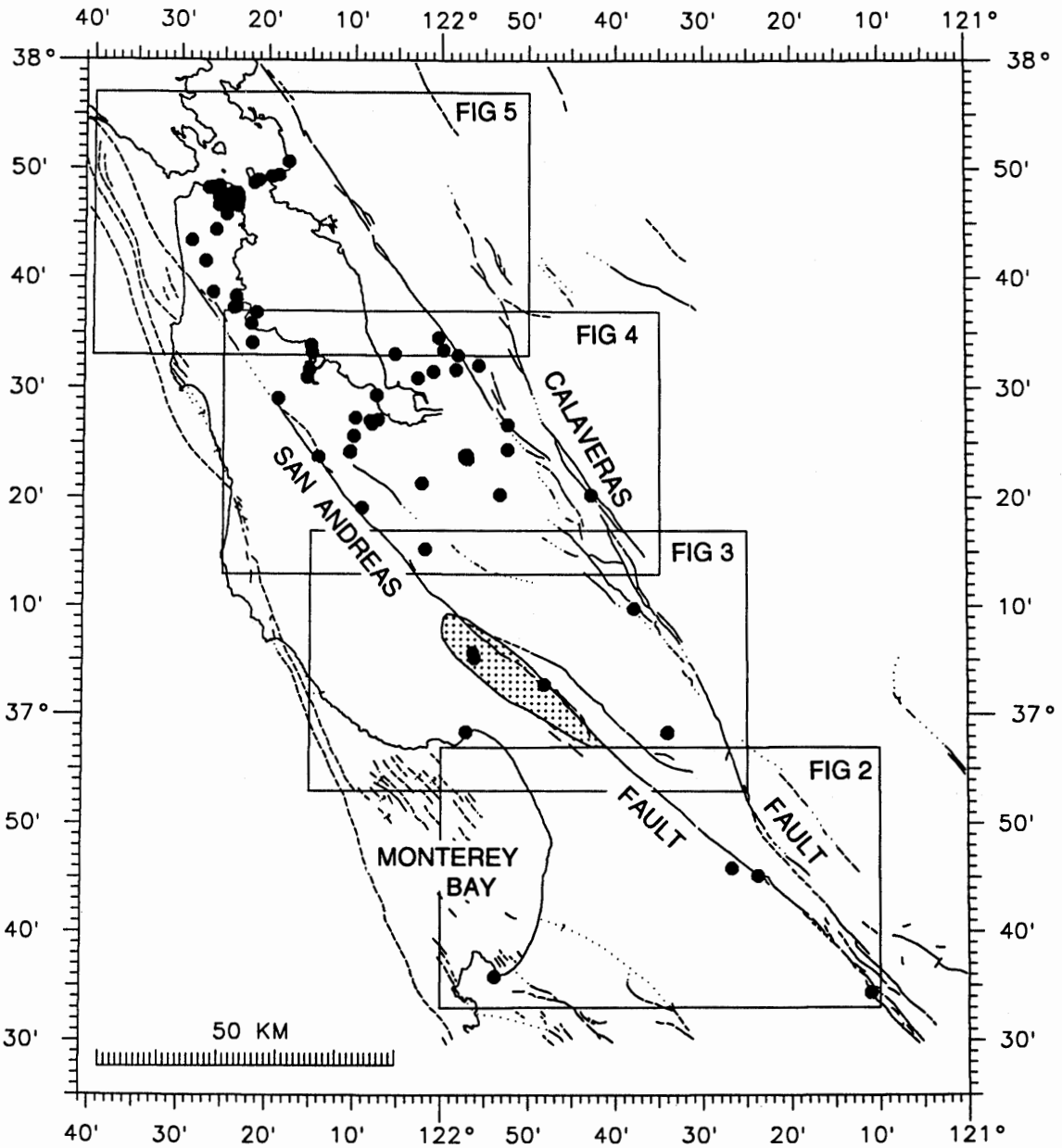

Figure 1.—GEOS station locations (dots) in greater San Francisco Bay area. Main faults are indicated by solid and broken lines. Approximate Loma Prieta aftershock zone is indicated by shaded area. Boxes outline detail maps in figures 2, 3, 4, and 5. Map from Mueller and Glassmoyer (1990).

Oakland Bay Bridge in an effort to gather data relevant to the bridge closure (BB in table 1, fig. 6). Many instruments were located at sites of particular interest due to damage or geologic conditions. These site features are described under the heading U in table 1.

Fifteen instrument locations were the same as, or less than a kilometer away from, sites that have been studied previously by the USGS; one location was the site of a small array (ST1+, figs. 4, 8). These are referred to as Old sites in table 1. The earlier studies began with comparisons of the response of different sites around the bay to nuclear explosions at the Nevada Test Site (Borcherdt, 1970; Gibbs and Borcherdt, 1974; Borcherdt and Gibbs, 1976) and included geologic and velocity logs to 30 meters in depth at selected sites (Gibbs and others, 1975, 1976a, and 1976b). A data analysis indicating that the velocity-log data were useful for interpreting the amplitudes of the explosion data was given by Borcherdt and others (1978). A deeper (180 m) borehole was drilled at station RAV, which has been the subject of quite detailed analysis (Warrick, 1974, and Joyner and others, 1976). Table 2 lists the aftershock-instrument sites that are near to (significantly less than a kilometer), or the same as, sites where nuclear explosions were recorded. It also lists specifically the correspondence between Borcherdt and Gibbs's recordings and the aftershock-instrument sites. The GEOS sites BMT and COY are noteworthy because they were also reference sites for the earlier work.

Also listed in table 2 are sites for which near-surface velocity data are available. Most of these sites were used in the nuclear explosion work. GEOS stations AP7, MAL, and SF1 were not included in the nuclear studies but are the sites of strong-motion accelerometers that recorded the main shock. Recently, a 150-m velocity log was obtained at station SF1 (Gibbs and others, 1992). In addition to a borehole log at SWS (Kayen and others, 1990), simultaneous downhole/uphole small-earthquake data have been recorded there (Liu and others, 1992a, b).

Four sub-kilometer-scale arrays recorded data relevant to spatial variations in ground motions. Three instruments were deployed in the Santa Cruz mountains as part of an attempt to observe topographic effects (SC in table 1 and KK0+ in figs. 3, 8, 14). This deployment was concurrent with DR-200 instruments, as discussed below. Two arrays

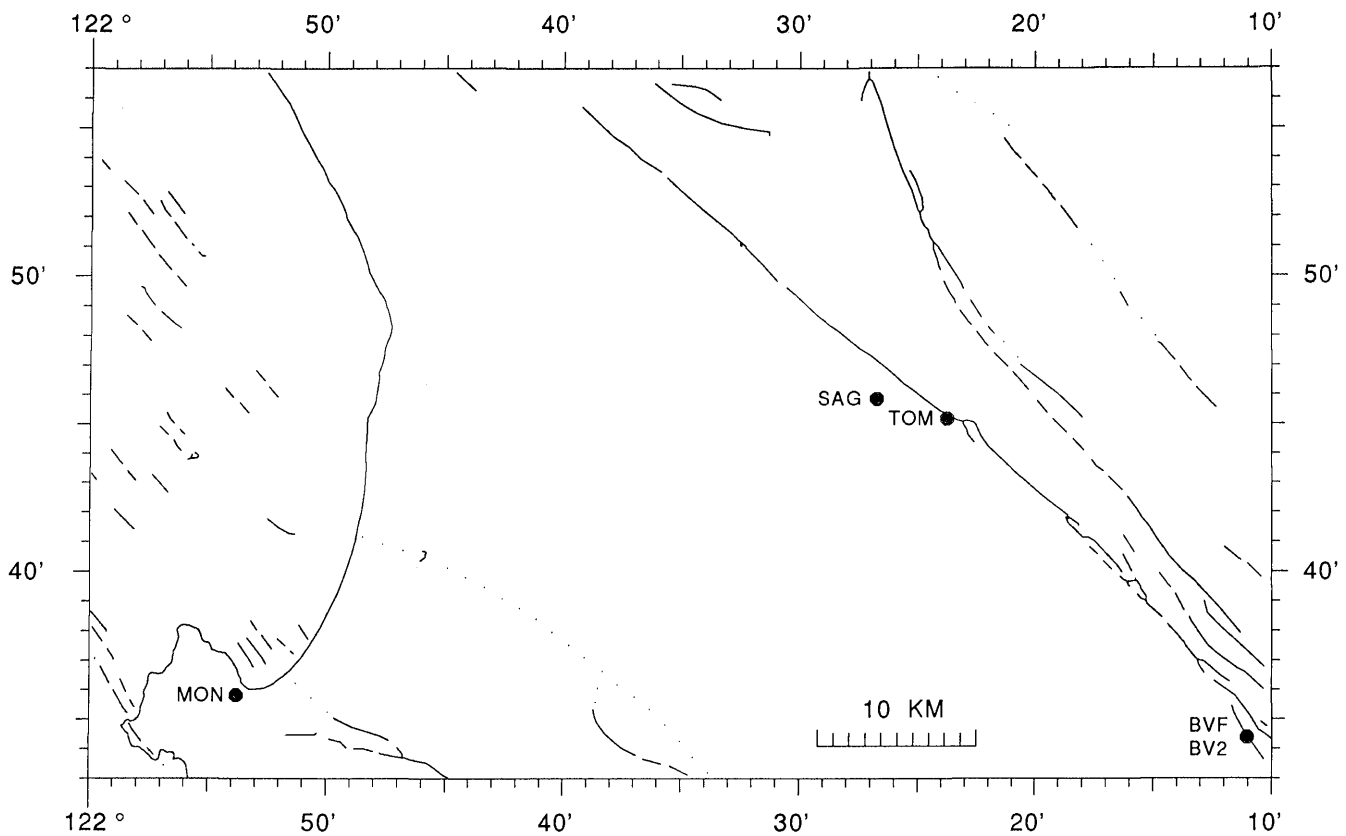

Figure 2.—GEOS stations in Monterey and San Benito Counties (southernmost region in figure 1). Main shock was recorded at MON, SAG, and TOM. Map from Mueller and Glassmoyer (1990).

were intended to study the propagation of surface waves in deeper sediments: a three-component array deployed in Palo Alto (SP in table 1, DUV+ in figs. 4, 8) and a four-component array was deployed in the north central Santa Clara Valley (SA in table 1, AG1+ in figs. 4, 8). A four-component array was deployed near Stanford University, mainly as a test of array instrumentation techniques (ST in table 1, ST1+ in figs. 4, 8. See also table 2).

COLLOCATIONS WITH STRONG-MOTION INSTRUMENTS

Twenty-three GEOS recorders were located where the main shock was also recorded. These sites are designated as CS in table 1. All stations but one were located with strong-motion accelerometers operated by the state of California (Shakal and others, 1989) or by the USGS (Maley and others, 1989). For further information on these strong-motion collocations, see Mueller and Glassmoyer (1990). AMF was deployed across the street from the Hyatt Hotel in Burlingame, where accelerometers operated by the building owners recorded the main shock (Çelebi and McGarr, 1991a, b). The high-rise building in which AMF was located has been razed, apparently because of earthquake damage (Çelebi, oral commun., 1993).

DR-200 DATA

During the aftershock deployment, 11 DR-200 recorders were deployed at 101 sites. A total of 2,926 three-component velocity records were recorded. The main focus of these studies was on local site effects on ground motion. In special studies, data were recorded to investigate topographic effects and sites where liquefaction occurred. Five instruments were collocated with, or very near, sites where the main shock was recorded. Two of these latter sites were also occupied by GEOS recorders. Information analogous to table 1, describing the DR-200 deployments, is available in the detailed reports given by Carver and others (1990) and King and others (1990). Figures 9

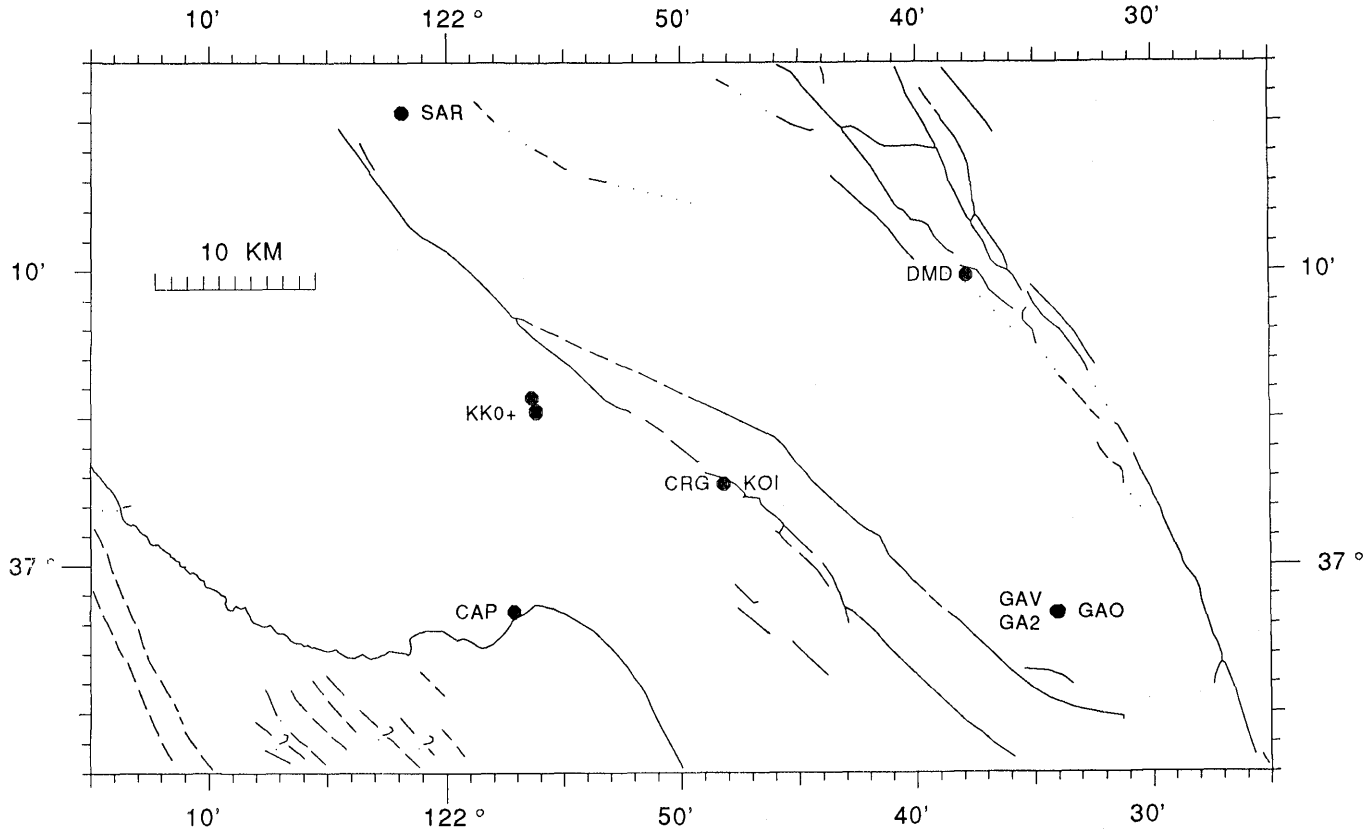

Figure 3.—GEOS stations in Santa Cruz and southern Santa Clara Counties (south-central region in figure 1). KK0+ marks a three-component, sub-kilometer-scale array that was part of a topographic experiment that also included eight DR-200 recorders (see figures 8 and 14). The main shock was recorded at CAP, CRG/KOI (collocated GEOSs), DMD, GA0/GA2/GAV (GEOS's in and around building where main shock was recorded), and SAR. Map from Mueller and Glassmoyer (1990).

through 14, taken from Carver and others (1990), show the locations of the sites they studied.

SANTA CRUZ

Thirty-seven sites were occupied in the Santa Cruz area (fig. 10; Carver and others, 1990). The main objective was to characterize the response of different geologic units in the city. Part of the deployment was a systematic study of site response of the flood plain of the San Lorenzo River (fig. 11). This study was presented by Cranswick and others (1990). Brief comments on some of the sites occupied during this deployment are listed in table 3. In addition to aftershock recordings, King and others (1990) analyzed small-scale refraction studies of 10 sites in the Santa Cruz area. Their results are relevant to velocities at depths of up to approximately 20 to75 meters. See also Williams and others (1994).

MOSS LANDING POWER PLANT

Three DR-200's were deployed at and in the power plant (fig. 9) to gather information regarding this significant site. One instrument was in the free field and two were deployed in the control room in the upper floors of the power plant. These stations are discussed in Carver and others (1990). The Electric Power Research Institute also deployed instruments at the same time as the DR-200's (Schneider, 1990).

LOS GATOS

Twenty-eight sites were occupied to study the effects of local site geology on ground motion in the city of Los Gatos (fig. 12). Stations LG3 and LG6 were located in the area of heaviest damage in the old business district along Santa Cruz avenue. Stations L12 and LEX, which was collocated with the CSMIP strong-motion instrument on

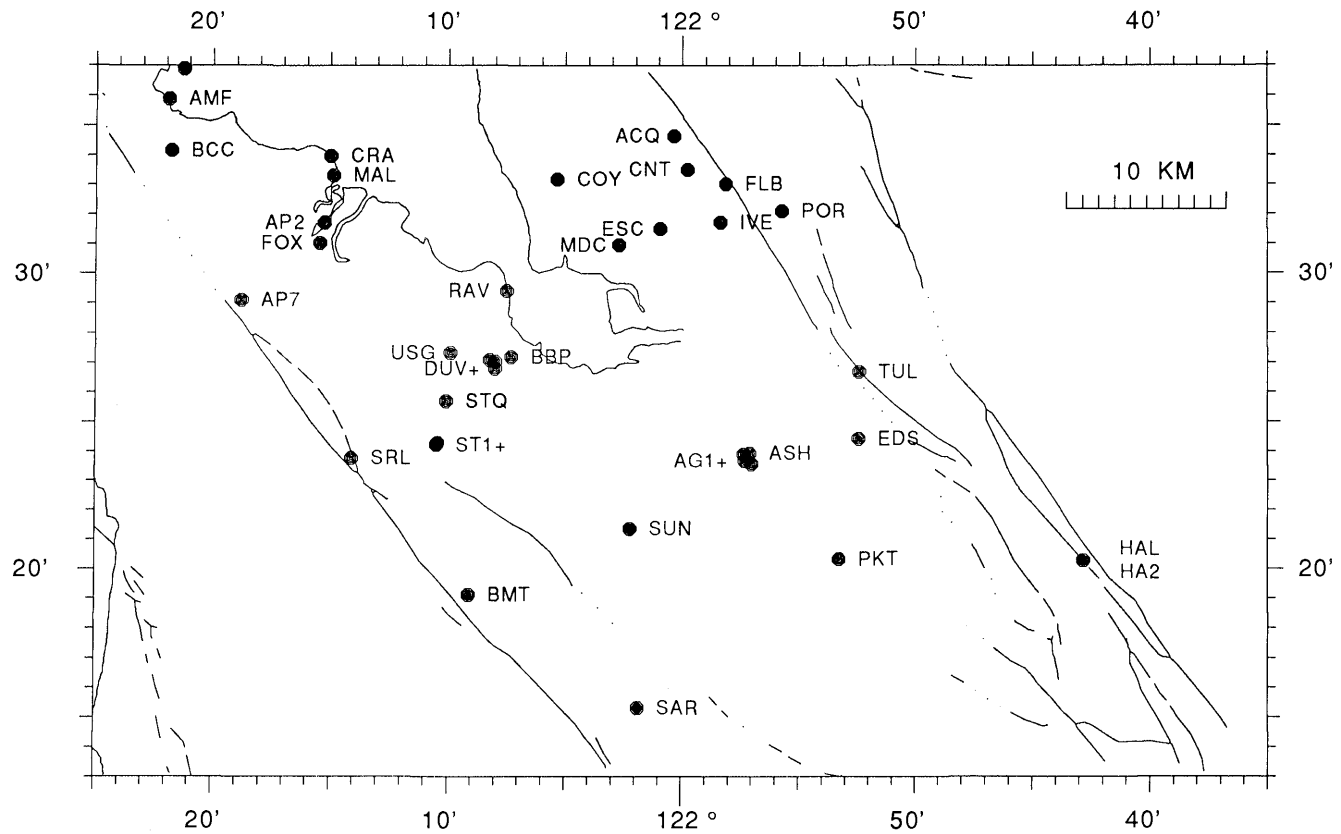

Figure 4.—GEOS stations in San Mateo, southern Alameda, and northern Santa Clara Counties (north-central region in figure 1). Main shock was recorded at AMF, AP2, AP7, ASH, BBP, HAL/HA2, MAL, POR, and SAR. AG1+, DUV+, and ST1+ mark sub-kilometer-scale arrays (see figure 8). Nuclear explosions have been recorded at or near stations AP2, BMT, COY, PKT, RAV, ST1+, and USG. 30-meter velocity logs are available from boreholes near AP7, BMT, MAL, and ST1+. A 180-meter velocity log is available for RAV. See table 2 for references to these data. Map from Mueller and Glassmoyer (1990).

the left abutment of Lexington Dam, served as hard-rock reference sites.

LIQUEFACTION SITES

Seven instruments were installed at sites in Monterey and south Santa Cruz Counties where liquefaction occurred during the main shock. They are sites AIR, ART, BEL, MIL, MOL, MOS, and ORD and are shown in figure 9.

TOPOGRAPHIC EFFECTS STUDIES

Two deployments were made in the Santa Cruz mountains to study variations of ground motion with topography over distances of less than a kilometer. These studies were motivated by dramatic damage to structures along ridge tops. The site locations and topography are indicated in figures 9, 13 and 14.

The study of the ridge topped by Rebecca Drive, east of Boulder Creek (fig. 9), included 15 stations installed along the top and face of the ridge and in the canyons on either side of the ridge (fig. 13). Stations MID and REB were located near minor damage to residences. TOP was placed in an area of significant structural damage, which seemed largely due to its position at the head-scarp of a landslide (King, written commun., 1990). In addition to variations in topography, there were significant variations in site geology among the stations in this study.

The second study was of a ridge topped by Robinwood Lane above Hester Creek off of Old Santa Cruz highway (fig. 9). The ridge appeared to be geologically homogeneous. Eight DR-200's and three GEOS recorders were deployed along the ridge top and descending approximately 45 meters down slope from the site of severely damaged houses near stations LP5 and LP6 (fig. 14). The GEOS sites are denoted by the letters KK in the station name, and the DR-200 sites are denoted by LP.

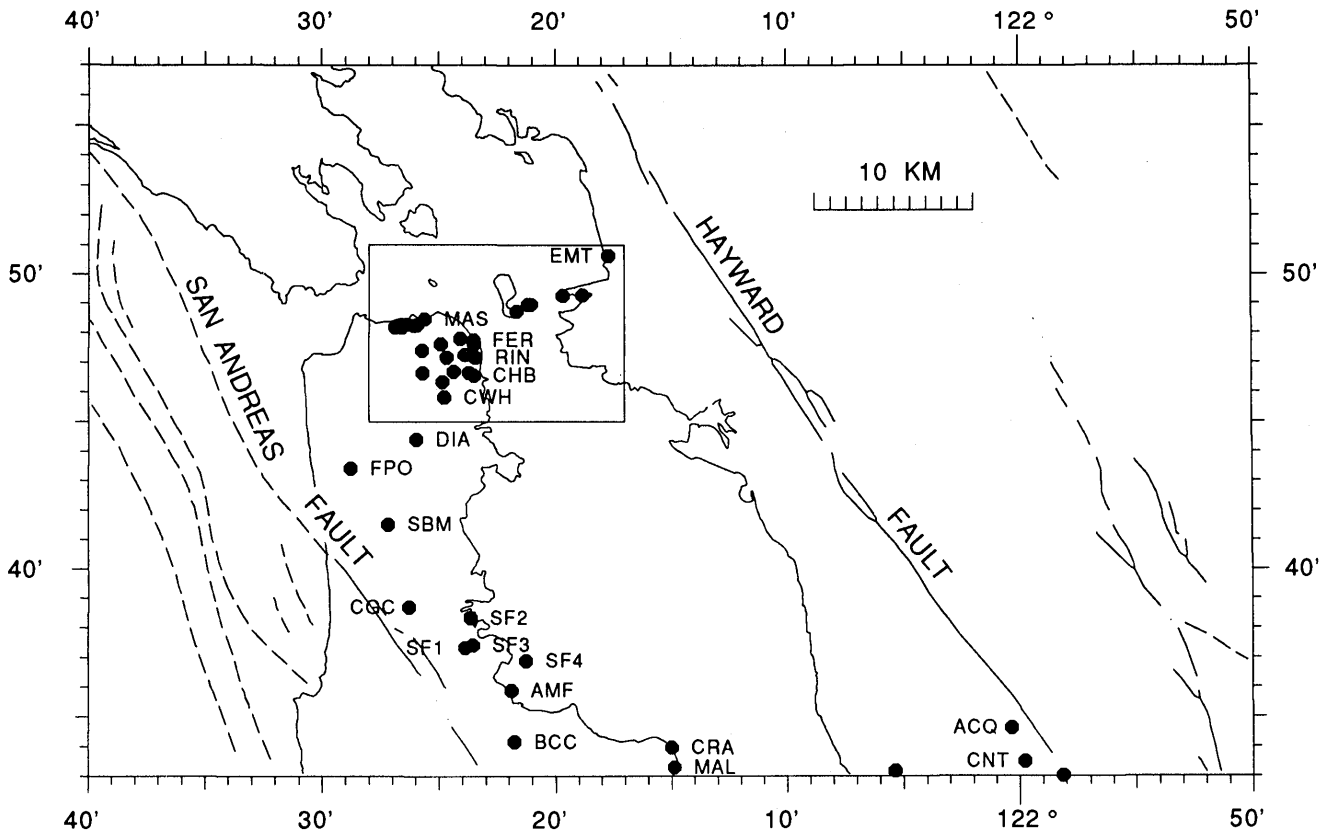

Figure 5.—GEOS stations in San Mateo, San Francisco, and Alameda Counties (northernmost region in figure 1). Area in box is detailed in figure 6. Main shock was recorded at DIA, FPO, MAL, and SF1. A 150-meter velocity log is available for station SF1 (see table 2). No data were obtained from CRA. Map from Mueller and Glassmoyer (1990).

COLLOCATIONS WITH STRONG-MOTION INSTRUMENTS

Instruments were deployed at five sites where, or close to where, the main shock was recorded. Three of the sites are shown in figure 9: HAL, SAL and SAR. Instruments were also collocated with a strong-motion accelerometer on the left abutment of Lexington Dam (LEX in fig. 12) and with the strong-motion accelerometer at UC Santa Cruz (Station LOE in fig. 10). With the exception of SAR (see Maley and others, 1989), the strong-motion instruments were operated by CSMIP (Shakal and others, 1989).

USGS SEISMIC CASSETTE RECORDERS

On the night following the main shock, 60 cassette recorders were deployed in the epicentral area to study crustal structure (fig. 15). These analog recorders were deployed with 2-Hz vertical geophones. See Healy and others (1983) for a description of the instruments. The recorders do not operate in a triggered mode, so they were programmed to turn on for six time intervals lasting 12 to 13 minutes each. The time intervals began at 0600, 0630, 1000, 1030, 2300, and 2300 universal time on October 19, 1989. These data have been digitized and analyzed by Eberhart-Phillips and others (1990). They are also discussed in this professonal paper (Eberhart-Phillips and others, this chapter). No report has been written specifically describing these data.

ACKNOWLEDGMENTS

Paul Spudich suggested that this report would be of use to future workers. Jack Boatwright provided particularly thorough comments on the GEOS data set. Dave Carver and Charles Mueller were helpful by providing copies of

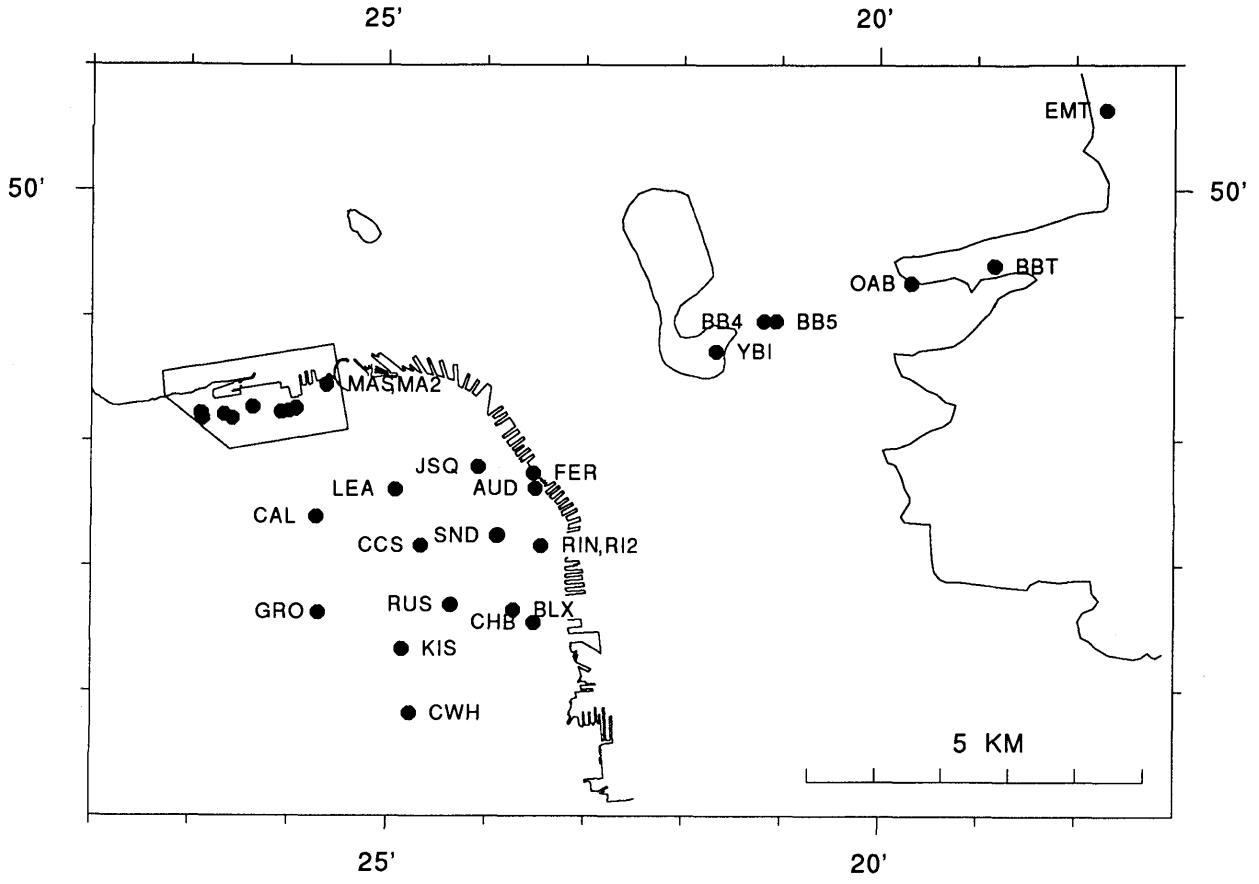

Figure 6.—GEOS stations in San Francisco and Alameda Counties. Marina district is outlined and detailed in figure 7. Main shock was recorded at CAL, EMT, and RIN/RI2. Nuclear explosions have been recorded at or near stations AUD, BLX, EMT, RIN, RI2, and SND (see table 2). No data were obtained at CCS or YBI. Map from Mueller and Glassmoyer (1990).

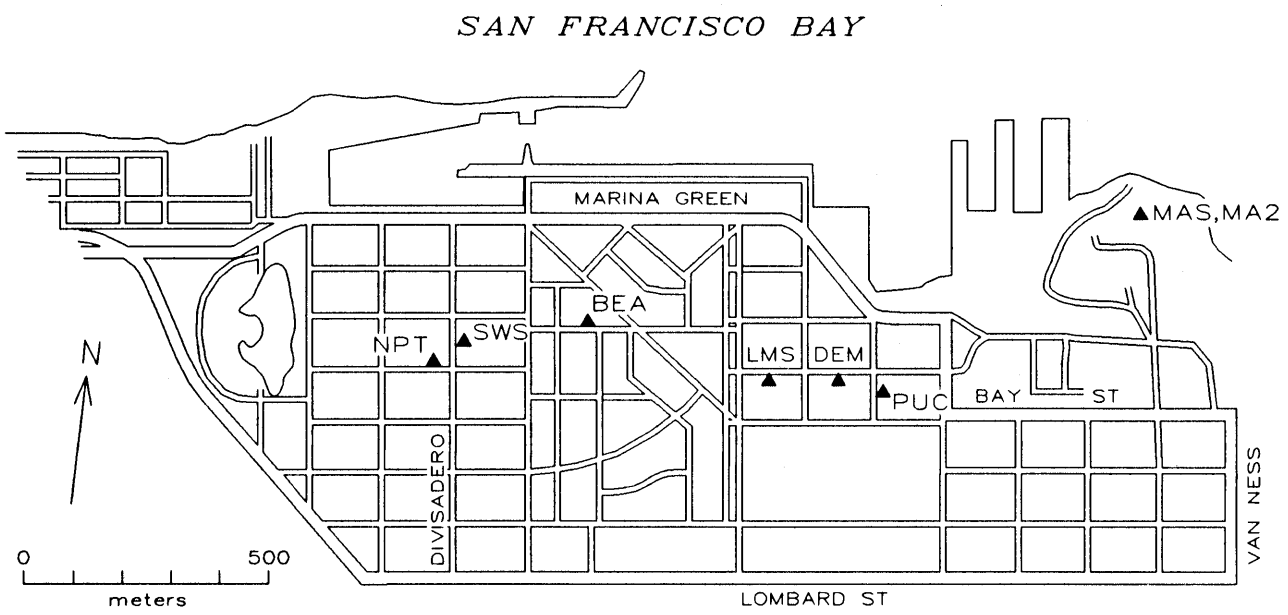

Figure 7.—GEOS stations in the Marina District of San Francisco. Borehole geologic, velocity, and downhole seismic data are available at SWS (see table 2). Map from Mueller and Glassmoyer (1990).

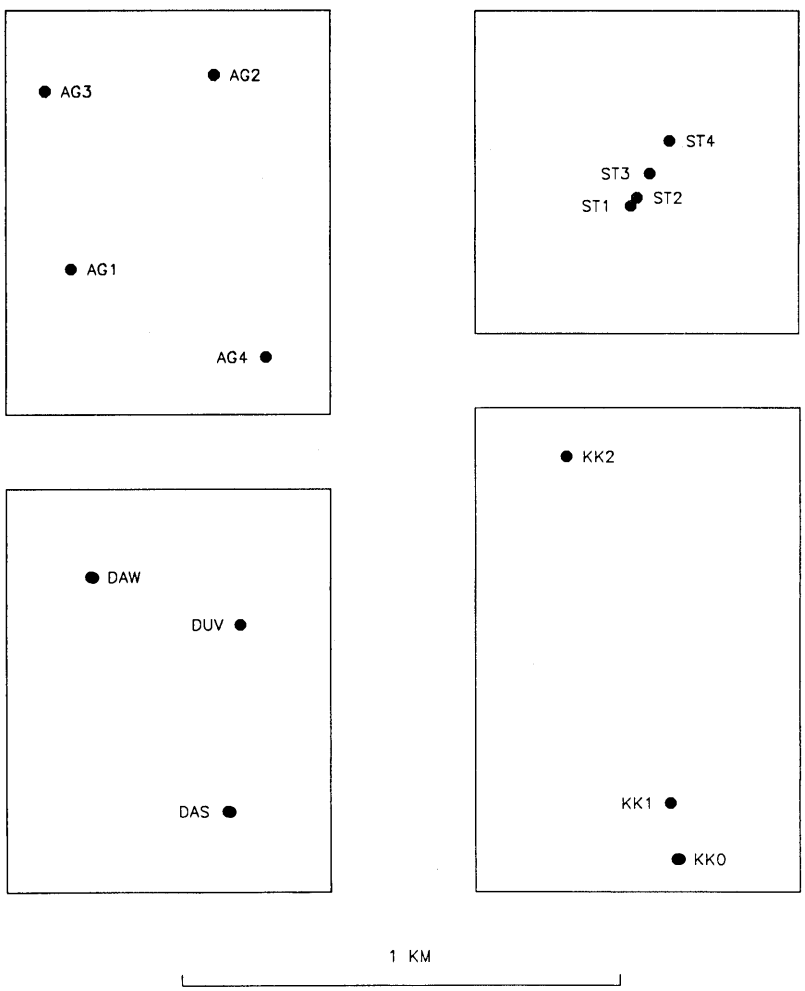

Figure 8.—Details of small GEOS arrays indicating dimensions and relative station postions. North is up. See figures 3 and 4 for array locations. Figure 14 shows topographic detail for, and DR-200 stations recording simultaneously with, the array KK0, KK1, and KK2. Map from Mueller and Glassmoyer (1990).

their figures as well as review comments on an earlier draft. An unpublished report of Ken King's was helpful. Andy Michael provided timing and location information for the cassette recorder data. I would also like to thank Mehmet Çelebi, Chris Dietel, Art Frankel, Jim Gibbs, Gary Glassmoyer, Tom Hanks, Tom Holzer, Art McGarr, and Linda Seekins for their helpful input.

REFERENCES

Boatwright, J., Seekins, L.C., and Mueller, C., 1990, Ground motion amplification in the Marina District, *in* Effects of the Loma Prieta earthquake on the Marina District, San Francisco, California: U. S. Geological Survey Open-File Report 90-253, P. F1-F24.

Boatwright, J., Fletcher, J.B., and Fumal, T., 1991a, A general inversion scheme for source, site and propagation characteristics using multiply recorded sets of moderate-sized earthquakes: Bulletin of the Seismological Society of America, v. 81, no. 5, p. 1754-1782.

Boatwright, J., Seekins, L.C., Fumal, T.E., Liu, H-P., and Mueller, C., 1991b, Ground motion amplification in the Marina District: Bulletin of the Seismological Society of America, v. 81, no. 5, p. 1980-1997.

Boatwright, J., Seekins, L.C., Fumal, T.E., Liu, H-P., and Mueller, C., 1992, Ground motion amplification, *in* The Loma Prieta, California, earthquake of October 17, 1989- Marina District: U.S. Geological Survey Professional Paper 1551-F, p. 35-50.

Borcherdt, R.D., 1970, Effects of local geology on ground motion near San Francisco Bay: Bulletin of the Seismological Society of America, v. 60, no. 1, p. 29-60.

Borcherdt, R.D., and Gibbs, J.F., 1976, Effects of local geological conditions in the San Francisco Bay region on ground motions and the intensities of the 1906 earthquake: Bulletin of the Seismological Society of America, v. 66, no. 1, p. 467-500.

Borcherdt, R.D., Gibbs, J.F., and Fumal, T.E., 1978, Progress on ground motion predictions for the San Francisco Bay region, California, in Proceedings of the Second International Conference on Microzonation for Safer Construction—Research and Application, San Francisco, California: National Science Foundation, UNESCO, American Society Civil Engineers, EERI, SSA, Universities Council for Earthquake Engineering Research, p. 241.

Borcherdt, R.D., Gibbs, J.F., and Lajoie, K.R., 1975, Prediction of maximum earthquake intensity in the San Francisco Bay region, California, for large earthquakes on the San Andreas and Hayward faults: US Geological Survey Miscellaneous Field Studies Map MF-709, scale 1:125,000, 11 p.

Borcherdt, R., Fletcher, J., Jensen, E., Maxwell, G., VanShaak, J., Warrick, R., Cranswick, E., Johnston, M., and McClearn, R., 1985, A general earthquake observation system (GEOS): Bulletin of the Seismological Society of America, v. 75, no. 6, p. 1783-1825.

Carver, D.L., Cunningham, D.R., and King, K.W., 1986, Calibration and acceptance testing of the DR-200 digital seismograph: U.S. Geological Survey Open-File Report 86-340, 28 p.

Carver, D.L., King, K.W. , Cranswick, E., Worley, D.M., Spudich, P., and Mueller, C., 1990, Digital recordings of aftershocks of the October 17, 1989, Loma Prieta, California, earthquake: Santa Cruz, Los Gatos, and surrounding areas: U.S. Geological Survey Open-File Report 90-683, 203 p.

Çelebi, M., and McGarr, A., 1991a, Discussion of site-response at Foster City and San Francisco Airport, in Proceedings of the Fourth International Conference on Seismic Zonation, August 25-29, 1991, Stanford, California: Earthquake Engineering Research Institute, v. III, p. 367-373.

Çelebi, M., and McGarr, A., 1991b, Site-response at Foster City and San Francisco Airport æ Loma Prieta studies, in Soil Dynamics and Earthquake Engineering V, Computational Mechanics Publications: Southampton and London, England, Elsevier Applied Science, p. 35-46.

Clark, J.C., 1981, Geologic map and sections of the Felton-Santa Cruz area, Santa Cruz County, California: U.S. Geological Survey Professional Paper 1168, plate 2.

Cranswick, E., King, K., Carver, D., Worley, D.,Williams, R., Spudich, P., and Banfill, R., 1990, Site response across downtown Santa Cruz, California: Geophysical Research Letters, v. 17, no. 10, p. 1793-1796.

Eberhart-Phillips, D.M., Michael, A. ., Fuis, G., and Luzitano, R., 1990, Three-dimensional crustal velocity structure in the region of the Loma Prieta, California, earthquake sequence from inversion of local earthquake and shot arrival times: Seismological Research Letters, v. 61, no. 1, p. 48.

Fletcher, J.B., and Boatwright, J., 1991, Source parameters of Loma Prieta aftershocks and wave propagation characteristics along the San Francisco peninsula from a joint inversion of digital seismograms: Bulletin of the Seismological Society of America, v. 81, no. 5, p. 1783 -1812.

Gibbs, J.F., and Borcherdt, R.D., 1974, Effects of local geology on ground motion in the San Francisco Bay region, California—a continued study: U.S. Geological Survey Open-File Report 74-222, 146 p.

Gibbs, J.F., Fumal, T.E., and Borcherdt, R.D., 1975, In-situ measurements of seismic velocities at twelve locations in the San Francisco Bay region: U.S. Geological Survey Open-File Report 75-564, 87 p.

———1976 a, In-situ measurements of seismic velocities in the San Francisco Bay region; part II: U.S. Geological Survey Open-File Report 76-731, 145 p.

Gibbs, J.F., Fumal, T.E., Borcherdt, RD., and Roth, E.F., 1976 b, In-situ measurements of seismic velocities in the San Francisco Bay region; part III: U.S. Geological Survey Open-File Report 77-850, 142 p.

Gibbs, J.F., Fumal, T.E., Boore, D.M., and Joyner, W.B., 1992, Seismic velocities and geologic logs from borehole measurements at seven strong-motion stations that recorded the Loma Prieta earthquake: U.S. Geological Survey Open-File Report 92-287, 139 p.

Hartzell, S., 1978, Earthquake aftershocks as Green's functions: Geophysical Research Letters, v. 5, no. 1 p. 1 -4.

Healy, J.H., Mooney, W.D., Blank, H.R., Gettings, M.E., Kohler, W.M., Lamson, and R.J., Leone, L.E., 1983, Saudi Arabian seismic deep-refraction profile: final project report: U.S. Geological Survey Open-File Report 83-390, 360 p., 9 plates.

Helley, E.J. and LaJoie, K.R., 1979, Flatlands deposits of the San Francisco Bay Region, California: their geology and engineering properties and their importance to compreshensive planning: U.S. Geological Survey Professional Paper 943, 88 pp.

Joyner, W.B., Warrick, R.E., and Oliver, A.A. III, 1976, Analysis of seismograms from a downhole array in sediments near San Francisco Bay: Bulletin of the Seismological Society of America, v. 66, no. 3, p. 937-958.

Kayen, R.E., Liu, H-P., Fumal, T.E.,Westerlund, R.E., Warrick, R.E., Gibbs, J.F., and Lee, H.J., 1990, Engineering and seismic properties of the soil column at Winfield Scott School, San Francisco, *in* Effects of the Loma Prieta earthquake on the Marina District, San Francisco, California: US Geological Survey Open-File Report 90-253, p. G1-G18.

King, K., Carver, D., Williams, R., Worley, D., Cranswick, E., and Meremonte, M., 1990, Santa Cruz seismic investigations following

Table 1.—*GEOS data sites described in Mueller and Glassmoyer (1990) and main experimental objectives*

Abbreviations:

BB	Oakland Bay Bridge study
CS	Colocated with a USGS, CSMIP or private strong-motion accelerograph that recorded the mainshock
FC	Foster City study of bay-margin response
IT	Instrumentation test
Mb	Surface instrument near subsequent hole drilled in Marina District of San Francisco
Ms	Site study in the Marina District of San Francisco
NS	Colocated with a strong-motion accelerograph without a mainshock record
Old	In previously published site response study. See table 2.
PE	Line from southern peninsula to the southern East Bay
PP	Peninsula wave-propagation study
SM	Sub-km-scale joint deployment with DR-200 recorders for Santa Cruz mountain topographic study
SA	Sub-km-scale four-station array on alluvium in the central Santa Clara Valley
SV	Line crossing northern Santa Clara Valley
SF	San Francisco site-response study
SFO	Few-km-scale array at San Francisco Airport
SP	Sub-km-scale three-instrument array on the alluvium in the southern peninsula
U	Geologic unit of specific interest. Alluvial unit descriptions from Helley et al (1979)

	BB	CS	FC	IT	Mb	Ms	NS	Old	PE	PP	SA	SM	SV	SF	SFO	SP	U
ACQ									**								gravel quarry
AG1											**		**				
AG2		**			(same location as ASH)						**		**				
AG3											**		**				
AG4											**		**				
AMF		**															bay mud, damaged high-rise
AP2		**	**					**									bay mud
AP7		**	**					**		**							
ASH		**			(same location as AG2)								**				
AUD								**						**			near damaged freeway
BB4	**																
BB5	**																
BBP		**															bay mud
BBT	**																
BCC										**							
BEA						**											hydraulic fill

the October 17, 1989 Loma Prieta earthquake: U.S. Geological Survey Open-File Report 90-307, 59 p.

Liu, H-P., Warrick, R.E., Westerlund, R.E., Sembera, E. D., and Wennerberg, L., 1992a, Observation of local site effects at a downhole-and-surface station, *in* The Loma Prieta, California, earthquake of October 17, 1989—Marina District: U.S. Geological Survey Professional Paper 1551-F, p. 51-74.

Liu, H-P., Warrick, R.E., Westerlund, R.E., Sembera, E.D., and Wennerberg, L., 1992b, Observation of local site effects at a downhole-and-surface station in the Marina District of San Francisco: Bulletin of the Seismological Society of America, v. 82, no. 4, p 1563 -1591.

Maley, R., Acosta, A., Ellis, F., Etheredge, E., Foote, L., Johnson, D., Porcella, R., Salsman, M., and Switzer, J., 1989, U.S. Geological Survey strong-motion records from the northern California (Loma Prieta) earthquake of October 17, 1989: U.S. Geological Survey Open-File Report 89-568, 85 p.

Margheriti, L., Wennerberg, L., and Boatwright, J., 1994, A comparison of coda and S-wave spectral ratios: estimation of site response in the south San Francisco Bay, Bulletin of the Seismological Society of America, v. 84, no. 6, p. 1815-1830.

McGarr, A., Çelebi, M., Sembera, E., Noce, T., and Mueller, C., 1991, Ground motion at the San Francisco International Airport from the Loma Prieta earthquake sequence, 1989: Bulletin of the Seismological Society of America, v. 81, no. 5, p. 1923-1944.

Mueller, C. and Glassmoyer, G.,1990, Digital recordings of aftershocks of the 17 October 1989 Loma Prieta, California, earthquake: U.S. Geological Survey Open-File Report 90-503, 147 p.

Schneider, J., 1990, Aftershock recordings of the Loma Prieta earthquake: project RP 3181-1, EPRI Technical Report.

Seekins, L.C., and Boatwright, J., 1994, Ground motion amplification, geology, and damage from the 1989 Loma Prieta earthquake in the City of San Francisco: Bulletin of the Seismological Society of America, v. 84, no. 1, p. 16-30.

Shakal, A., Huang, M., Reichle, M., Ventura, C., Cao, T., Sherburne, R., Savage, M., Darragh, R., and Peterson, C., 1989, CSMIP strong-motion records from the Santa Cruz mountains (Loma Prieta), California earthquake of 17 October 1989: California Department of Conservation, Division of Mines and Geology, Office of Strong Motion Studies Report OSMS 89-06, 195 p.

Warrick, R.E., 1974, Seismic investigation of a San Francisco Bay mud site: Bulletin of the Seismological Society of America, v. 64, no. 2, p. 375-385.

Williams, R.A., Cranswick, E., King, K.W. , Carver, D.L., and Worley, D.M., 1994, Site-response models from high-resolution seismic reflection and refraction data recorded in Santa Cruz, California, *in* Borcherdt, R.D., ed., Strong ground motion: U.S. Geological Survey Professional Paper 1551-A, p. 217-242.

Table 1.—*Continued*

	BB	CS	FC	IT	Mb	Ms	NS	Old	PE	PP	SA	SM	SV	SF	SFO	SP	U
BLX								**						**			near damage
BMT								**		**							
BVF							**							(BVF inside shed with			
BV2							**							bad resonance. BV2 outside)			
CAL		**				**											
CAP		**															
CGC										**							
CHB														**			bay mud
CNT									**								Holocene coarse-grain alluvium
COY								**	**								hard rock
CRG		**		**	(Guralp accelerometer collocated with KOI)												
CWH														**			near liquefaction
DAS									**							**	Holocene fine-med. alluvium
DAW									**							**	Holocene fine-med. alluvium
DEM						**											on (near?) hydraulic fill
DIA		**												**			
DMD			**														
DUV									**							**	Holocene fine-med. alluvium
EDS													**				
EMT	**	**						**									
ESC									**								Holocene med. grain alluvium
FER														**			building on pilings
FLB									**								near-fault, Pleistocene alluvium
FOX			**														bay margin, near damage?
FPO		**												**			near damage
GAO		**		(GAV and GA2 were													
GAV		**		sequentially deployed													
GA2		**		in and near one structure)													
GRO														**			dune sand near damage
HAL		**		(HA2 same location as HAL,													
HA2		**		but with different sensors)													
IVE									**								Pleistocene alluvium
JSQ														**			bay mud near undamaged unreinforced masonry
KIS														**			dune sand
KK0												**					
KK1												**					

Table 1.—*Continued*

	BB	CS	FC	IT	Mb	Ms	NS	Old	PE	PP	SA	SM	SV	SF	SFO	SP	U
KK2												**					
KOI		**	(Collocated with Guralp, station CRG)							**							
LEA							**							**			
LMS						**											near (but off?) hydraulic fill
MAL		**	**					**									
MAS						**					(MAS and MA2 were sequentially						
MA2						**					near each other on hard rock)						
MDC									**								Holcene fine-med. alluvium
MON			**														
NPT						**											close to greatest damage; fire
OAB	**																
PKT		**						**					**				
POR		**															
PUC						**											off fill, building renovated 1906
RAV				**				**									bay mud
RIN		**						**	(RIN relocated to					**			
RI2		**						**	RI2. Same building)					**			
RUS														**			near damage
SAG		**															
SAR		**								**							
SBM								**		**							
SF1		**						**							**		
SF2															**		hard rock
SF3										**					**		near damage
SF4										**					**		
SND														**			near damage
SRL									**	**							
ST1				**				**									
ST2				**				**									
ST3				**				**									
ST4				**				**									
STQ									**								damage, Pleist. alluvium
SUN													**				
SWS					**	**											
TOM		**															
TUL													**				
USG				**				**									

Table 2.—*GEOS aftershock recording locations at or near previous USGS studies*

[The left column indicates analyses of seismic data from sites collocated with or nearby the listed GEOS aftershock sites. Letter-number combinations denote particular site and nuclear explosion combinations as discussed in Borcherdt (1970), Gibbs and Borcherdt (1974), Borcherdt and others (1975), and Borcherdt and Gibbs (1976). Two more site-specific seismic studies, which analyze borehole data, are explicitly listed. The right column lists velocity and geologic log data sources for the GEOS sites.]

	Nuclear explosion, and borehole seismic studies	Velocity and geologic log data
AP2	I5c (less than 1 km away)	
AP7		"Pulgas Tunnel" in Gibbs and others (1976)
AUD	Q5, P7	
BLX	T5 (less than 1 km away)	
BMT	S3, S4, S5, S16, J17, J18, S19	"Black Mountain" in Gibbs and others (1975)
COY	K1, K12, S13, S14, S15	
EMT	H18 (less than 1 km away)	
MAL		"Audobon School" (~ 1 km away) in Gibbs and others (1977)
PKT	P18	
RAV	I11, Joyner and others (1976)	Warrick (1974)
RIN	J5, J7	
RI2	J5, J7	
SF1		"SF Airport" in Gibbs and others (1992)
SND	R7 (less than 1 km away)	
ST1	L3	"Page Mill" in Gibbs and others (1977)
ST2	L3	"Page Mill" in Gibbs and others (1977)
ST3	L3	"Page Mill" in Gibbs and others (1977)
ST4	L3	"Page Mill" in Gibbs and others (1976b)
SWS	Liu and others (1992a, b)	Kayen and others (1990)
USG	J1	

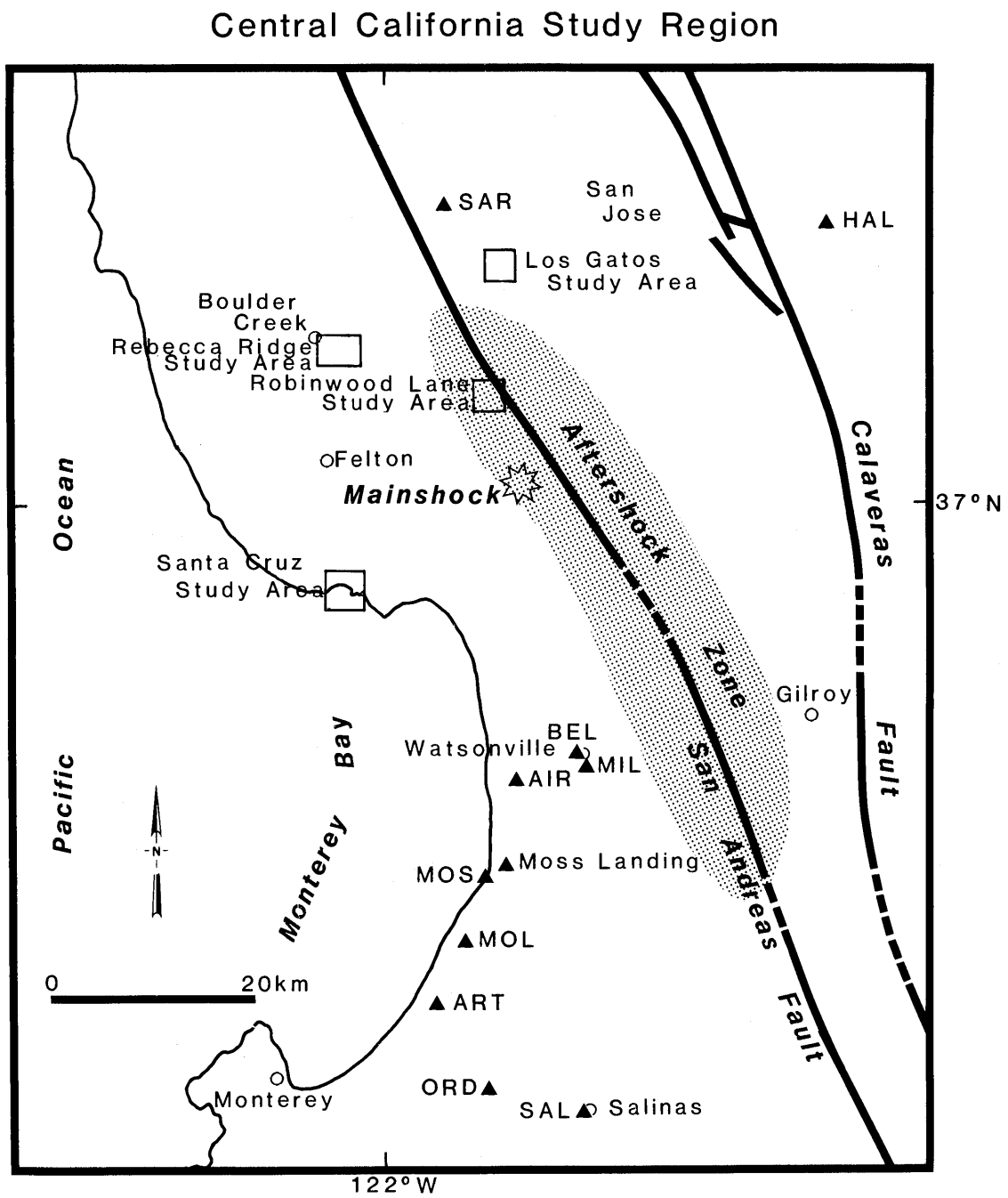

Figure 9.—Locations of DR-200 recorders in Santa Cruz, Monterey and southern Santa Clara Counties. Boxes outline areas detailed in figures 10 to 14. Liquefaction occurred during the main shock at stations AIR, ART, BEL, MIL, MOL, MOS, and ORD. Main shock was recorded at HAL, SAL, and SAR. Map from Carver and others (1990).

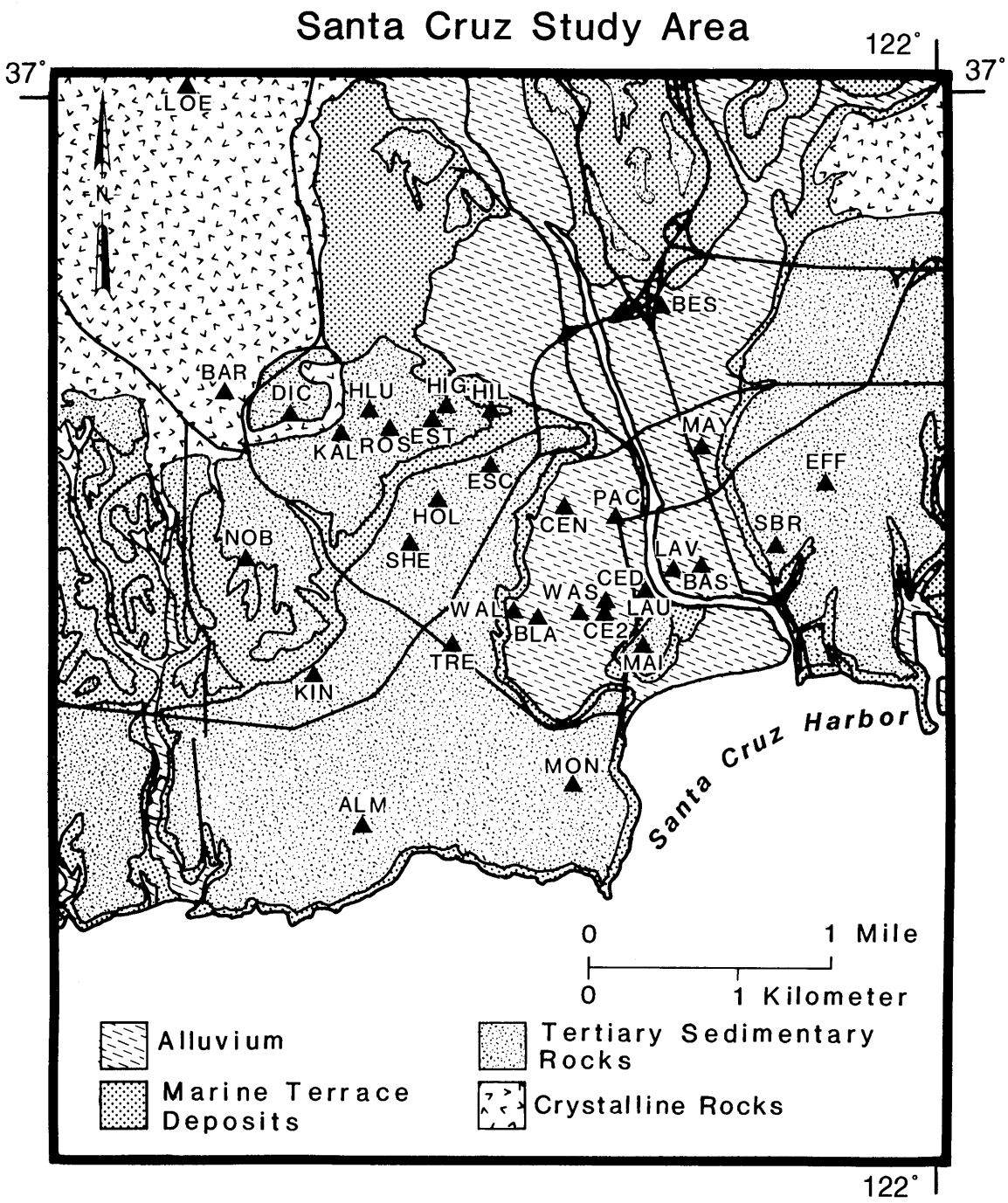

Figure 10.—Locations of DR-200 recorders (triangles) in the city of Santa Cruz. Surficial geology adapted from Clark (1981). Main shock was recorded at LOE. Map from Carver and others (1990).

Santa Cruz Flood Plain Array

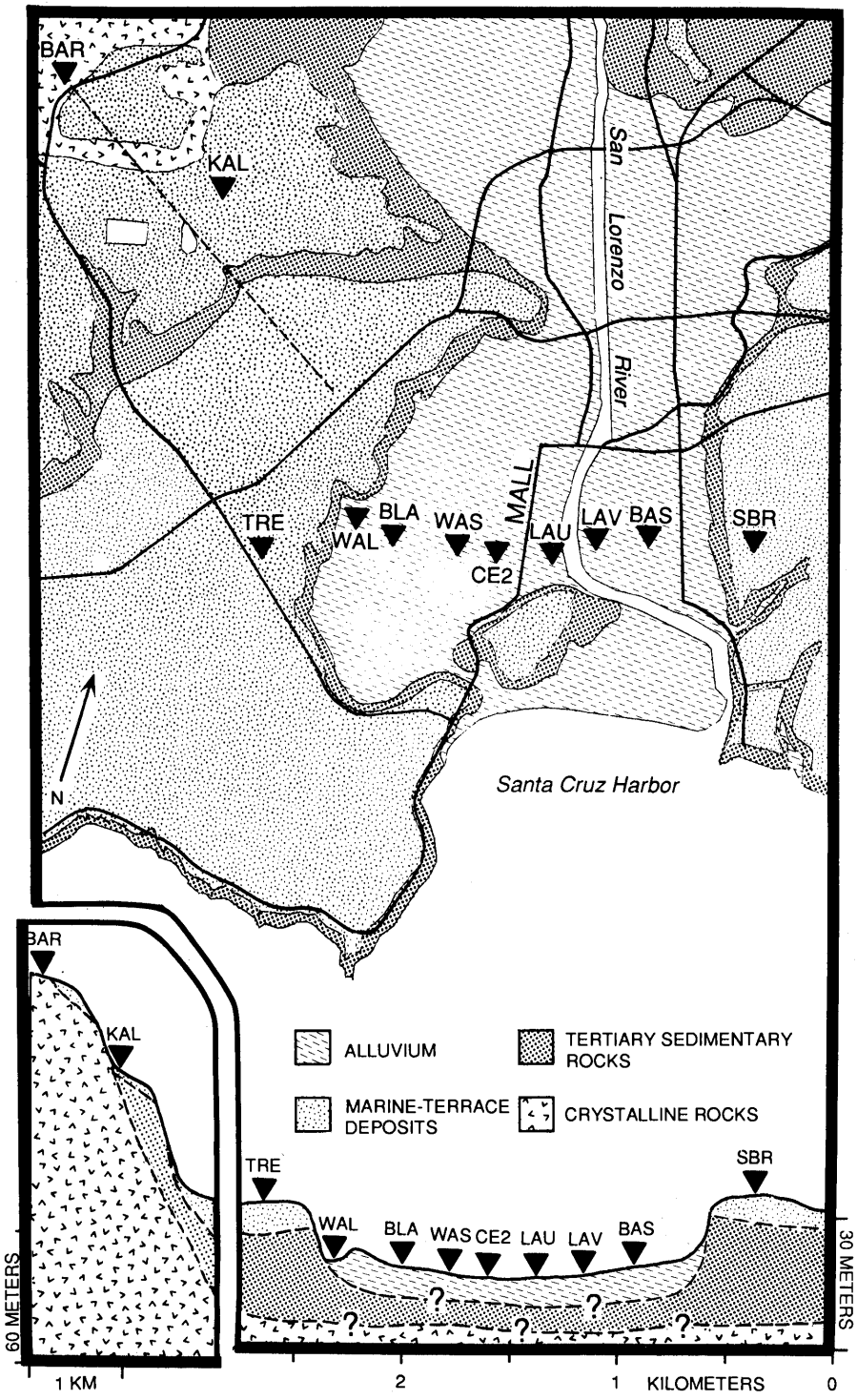

Figure 11.—Locations of DR-200 recorders (triangles) for the study of seismic response of the flood plain of the San Lorenzo River (Cranswick and others, 1990). These sites were occupied simultaneously. Bottom of figure shows idealized geologic cross section, a portion of which is offset and drawn to a different scale than the rest of the figure. Map from Carver and others (1990).

Table 3.—*Noteworthy selected sites in Santa Cruz study*

[See Carver and others (1990) and King and others (1990).]

ALM	Marine terrace, minor chimney damage
BAR	Hard rock
BLA	Heavy damage
CE2	Heavy damage
CED	Heavy damage
KAL	Hard rock
LOE	Mainshock recorded at site
MAI	Marine terrace
MON	Heavy damage
PAC	Heavy damage
WAL	Heavy damage

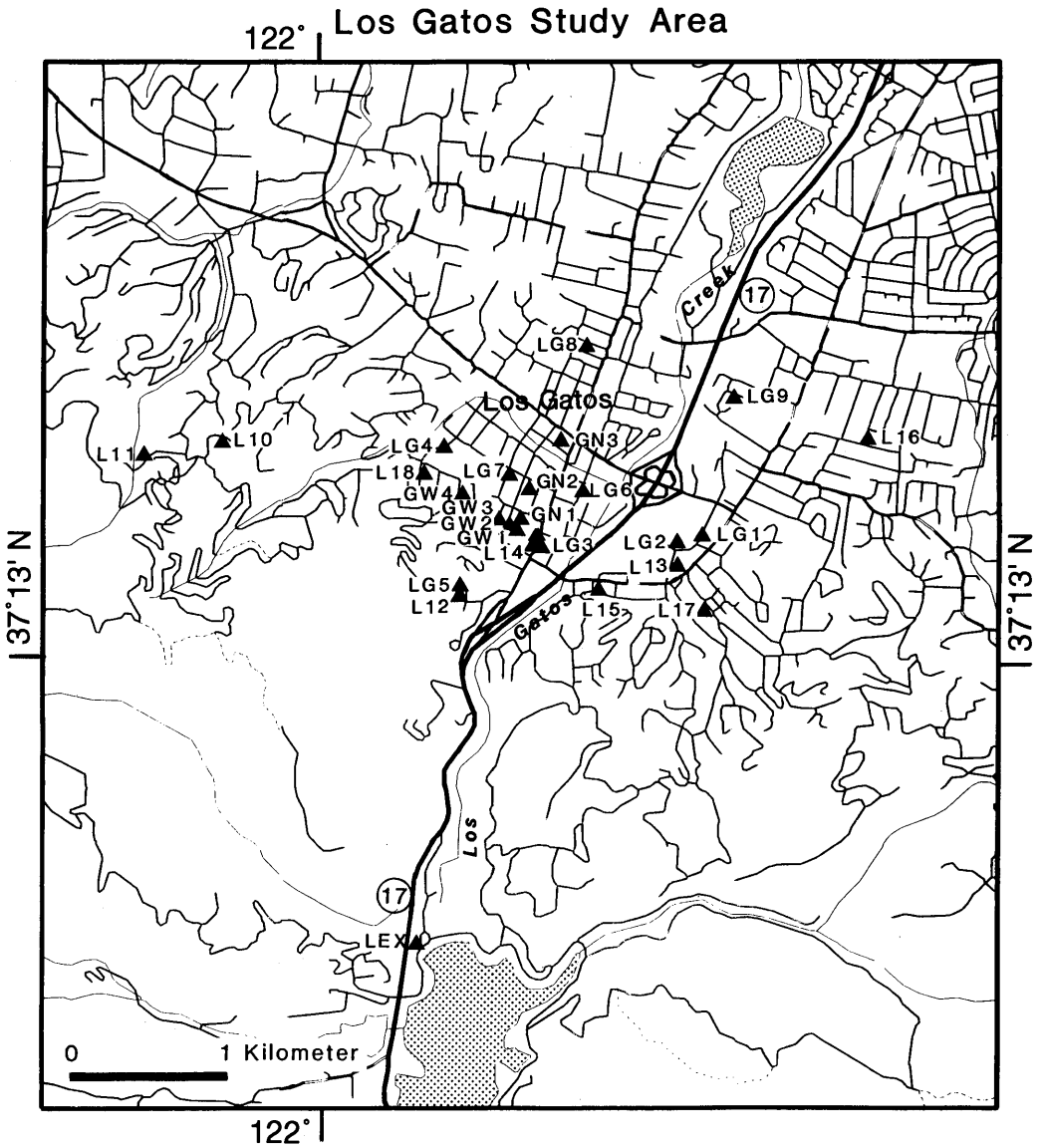

Figure 12.—Locations of DR-200 recorders (triangles) in the city of Los Gatos (roads shown). The shaded areas denote lakes. Highway 17 is indicated. Highway 9 intersects highway 17 at cloverleaf. Main shock was recorded at LEX. Map from Carver and others (1990).

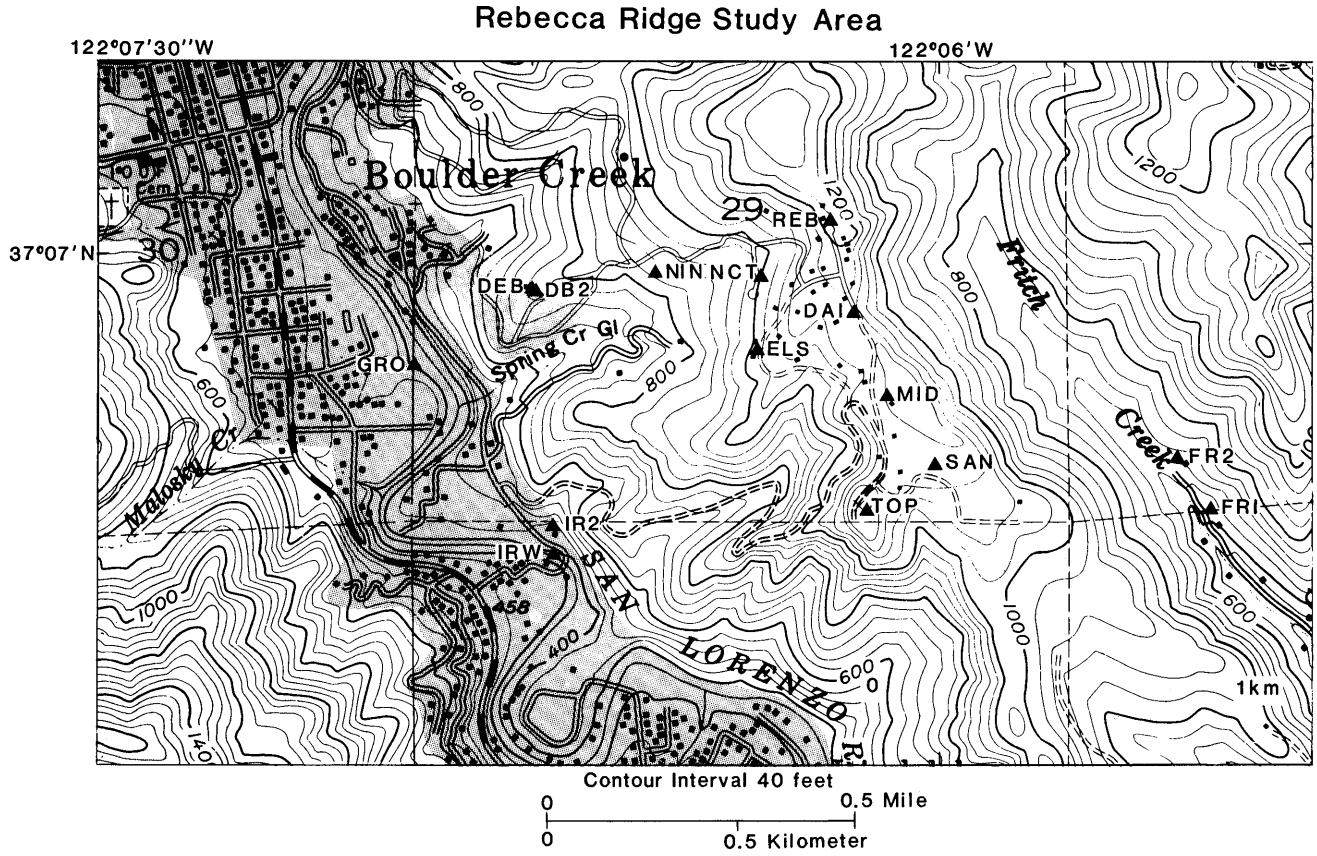

Figure 13.—Locations of DR-200 recorders (triangles) used in the Rebecca Ridge topographic study. See figure 9 for array location. Map from Carver and others (1990).

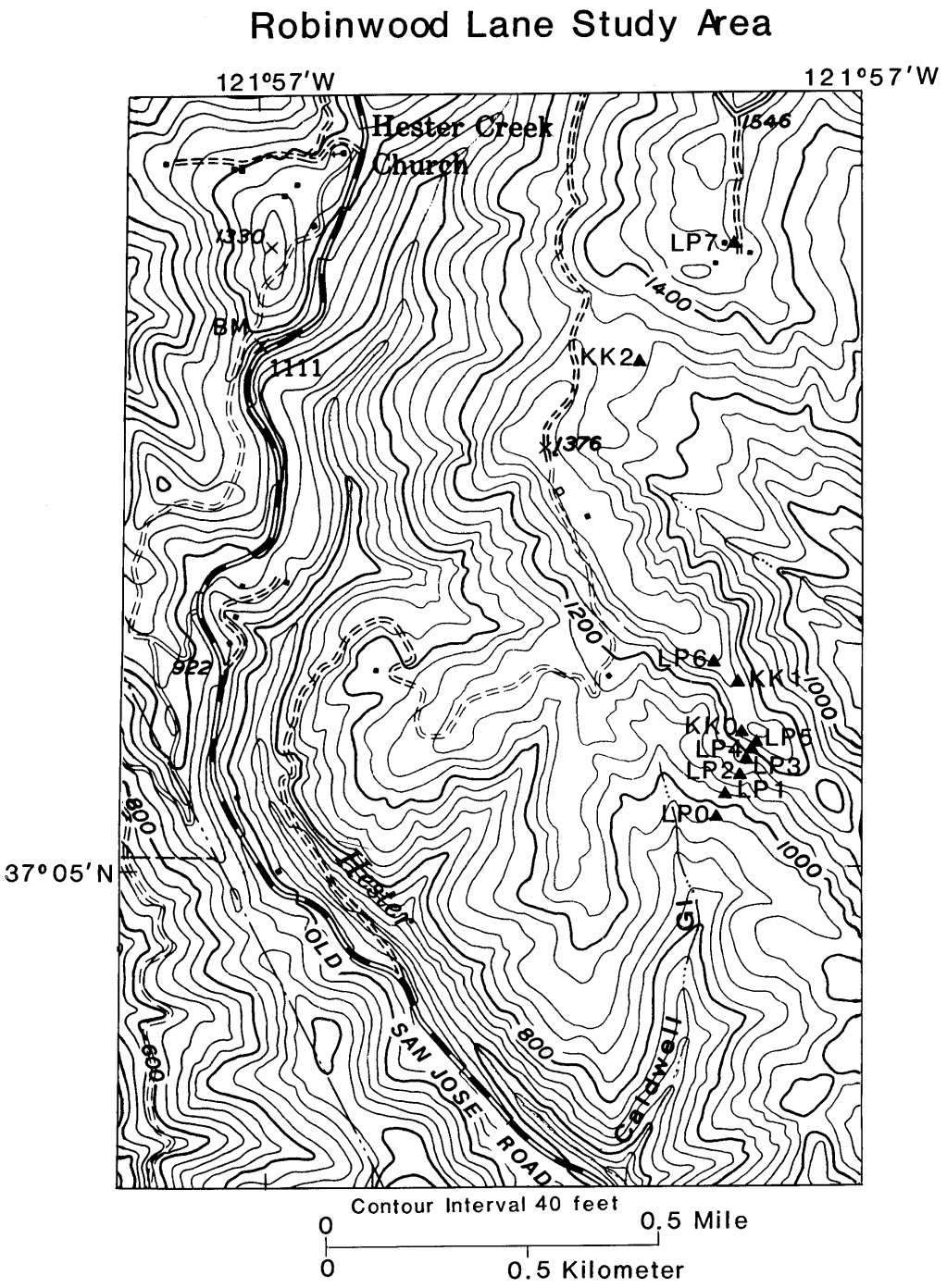

Figure 14.—Locations of DR-200 and GEOS recorders used in the Robinwood Lane topographic study. GEOS instruments are denoted by KK. See figure 9 for array location. Map from Carver and others (1990).

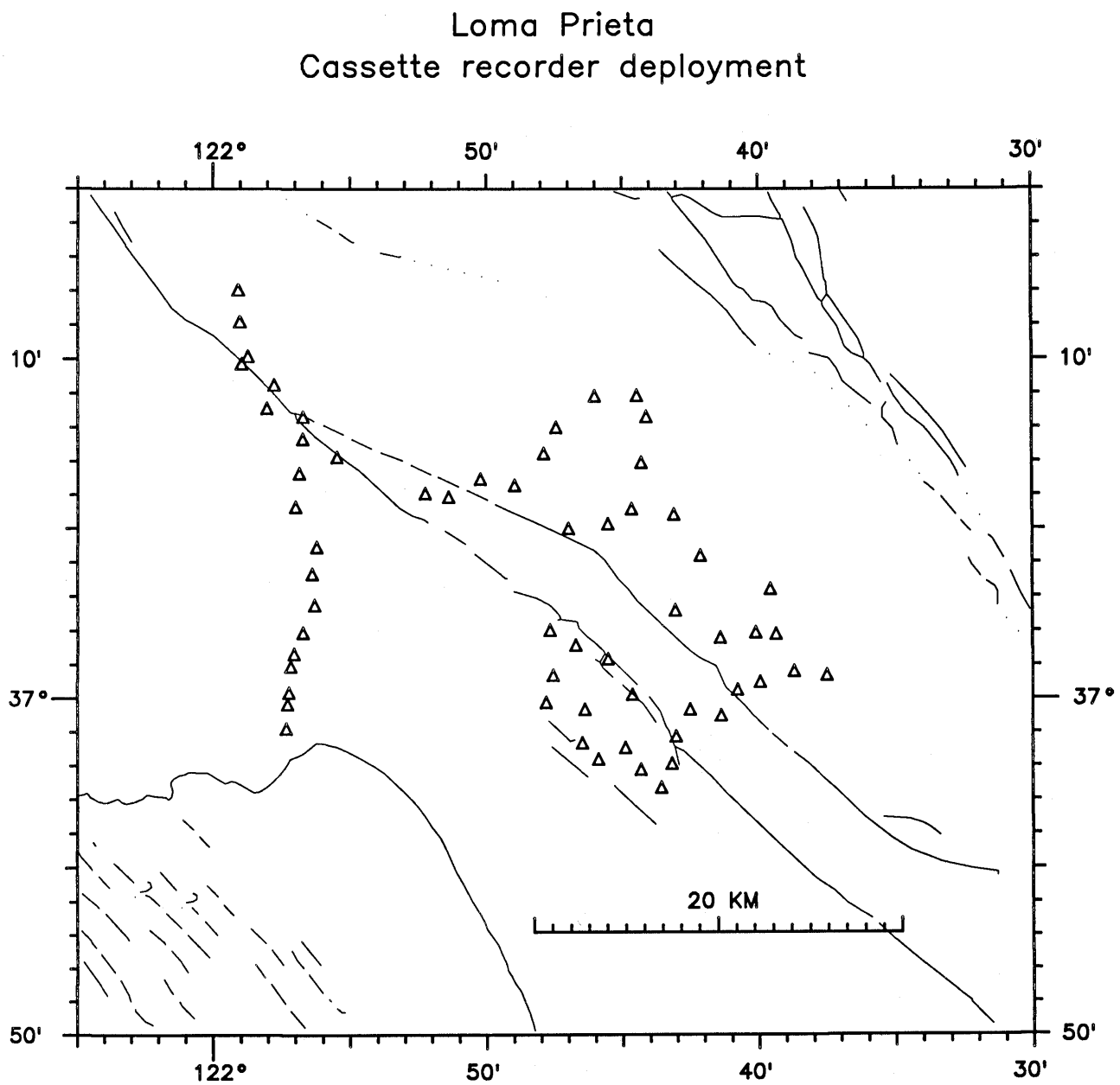

Figure 15.—Locations of USGS seismic cassette recorders deployed the night of October 19, 1989 (triangles). Recordings were made continuously for 12- to 13-minute intervals starting at the following times: 0600, 0630, 1000, 1030, 2300, and 2330 universal time. For comparison, note that the main shock source zone is shown in figure 1 along with the same geologic features as in this figure.

THE LOMA PRIETA, CALIFORNIA, EARTHQUAKE OF OCTOBER 17, 1989:
EARTHQUAKE OCCURRENCE

AFTERSHOCKS AND POSTSEISMIC EFFECTS

RESPONSE OF U.S. GEOLOGICAL SURVEY CREEPMETERS TO THE LOMA PRIETA EARTHQUAKE

By K.S. Breckenridge and R.W. Simpson,
U.S. Geological Survey

CONTENTS

ABSTRACT

At the time of the Loma Prieta earthquake, 18 U.S. Geological Survey creepmeters in central California recorded coseismic steps ranging in size from –0.35 to +6.8 mm. Five of the closest instruments on the San Andreas fault and three on the Calaveras fault also displayed long-term rate changes in the months after the earthquake. The coseismic steps seem to bear little relation in magnitude or sense to static stress changes calculated using dislocation models of the earthquake rupture, but 1-year average creep-rate changes (faster on the San Andreas and slower on the Calaveras) do correlate well with static stress changes. This correlation favors low values of apparent coefficient of friction. Observed advances and deficits in cumulative slip at the closest sites caused by the positive and negative rate changes are in fair agreement with deformation predicted by a three-dimensional dislocation model that requires anomalous slip to extend to depths in excess of 10 km. Rate changes observed at several creepmeters in the years before Loma Prieta may be precursory but are difficult to interpret unambiguously because they fall in a period of extended drought. A 2-year period of retarded creep at the Cienega Winery site before the Loma Prieta earthquake contains an interesting interval with normal right-lateral creep events superposed on unusual left-lateral background drift. Assuming that this behavior was tectonic in origin and not drought- or instrument-related, it can be explained by stresses imposed from two different sources. One source could be slip on the San Andreas fault below the creepmeter, causing the right-lateral creep events. The second could be slip on the subparallel Calaveras fault or other local structures which were caught up in regional tectonic adjustments following the 26 January 1986 Tres Pinos earthquake, causing the left-lateral movement and retarding the cumulative progress of the instrument. In this scenario, the retardation at Cienega Winery could have been a precursor to Loma Prieta in the sense that it too was a manifestation of regional tectonic changes that would eventually trigger the Loma Prieta earthquake.

INTRODUCTION

At the time of the Loma Prieta earthquake, 27 U.S. Geological Survey (USGS) creepmeters were operating within 205 km of the epicenter (fig. 1*A*). Eighteen of these instruments recorded coseismic steps ranging in size from –0.35 to +6.8 mm, and eight instruments located closest to the epicenter recorded significant changes in slip rate in the months after the earthquake (table 1). For several creepmeters, the Loma Prieta signal is the largest anomaly recorded in up to 25 years of operation. Possible precursory rate changes were observed on several instruments (Breckenridge and Burford, 1990).

The USGS creepmeters are of several different designs, and data are collected at various intervals ranging from minutes to months, depending upon the configuration of a particular instrument (table 1). Descriptions of the instruments and sites have been published in Schulz and others (1982, 1983) and more recently in Schulz (1989). Eighteen sites are equipped with satellite telemetry that samples

the creepmeter every 10 minutes (Silverman and others, 1989), while micrometer dial readings at the remaining 9 sites are taken quarterly.

Additional creepmeters on the San Andreas fault installed by researchers from the University of Colorado are discussed by Behr and others (1990) and by Behr and others (this chapter). Alignment arrays on the Calaveras, Hayward, and other Bay Area faults maintained by researchers at the University of California at San Francisco are described by Galehouse (1992, and this chapter).

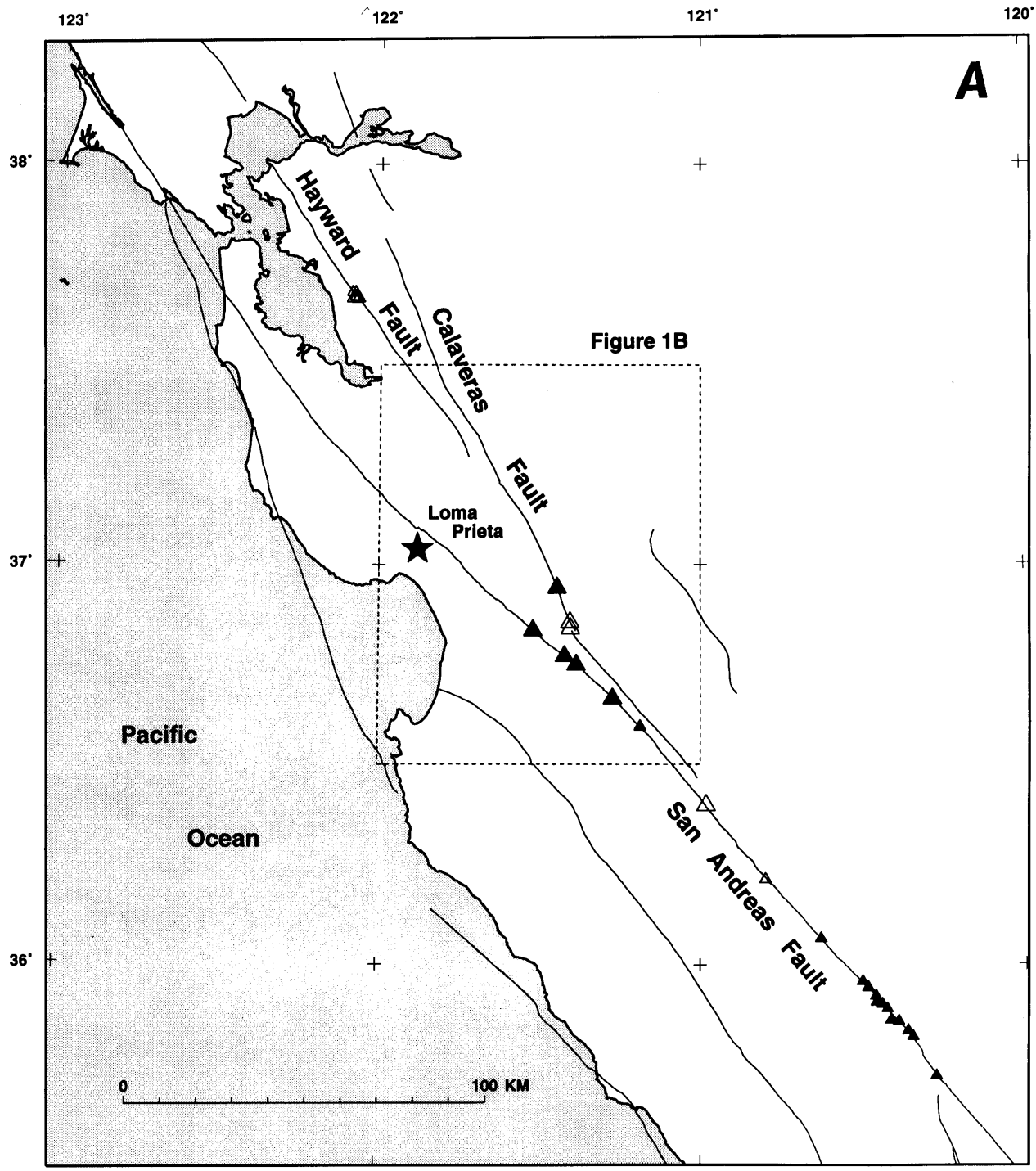

Figure 1.—*A*, Locations of USGS creepmeters in central California operating at the time of the Loma Prieta earthquake. The epicenter of the earthquake is shown by a star. Filled triangles indicate creepmeters which recorded definite coseismic steps; larger triangles indicate creepmeters which experienced long-term rate changes (table 1). *B*, Locations of eight creepmeters lying within 60 km of the Loma Prieta rupture. Epicenters of six earthquakes discussed in the text are also shown as stars.

Numerous instances of triggered slip on fault segments at considerable distances from an earthquake rupture are reported in the literature. For example, such slip occurred after the 1968 Borrego Mountain earthquake (Allen and others, 1972), the 1979 Imperial Valley earthquake (Fuis, 1982; Sieh, 1982; Bilham and Williams, 1985), the 1981 Westmorland earthquake (Sharp and others, 1986a), the 1983 Coalinga earthquake (Mavko and others, 1985; Schulz and others, 1987), the 1984 Morgan Hill earthquake (Schulz, 1984), the 1986 Tres Pinos earthquake (Simpson and others, 1988), the 1986 North Palm Springs earthquake (Fagerson and others, 1986; Sharp and others, 1986b, Wesson and others, 1986; Williams and others, 1986, 1988), the 1987 Superstition Hills earthquake (Sharp, 1989; Hudnut and Clark, 1989; McGill and others, 1989), and the 1989 Loma Prieta earthquake (Behr and others, 1990; Galehouse, 1990; McClellan and Hay, 1990).

If the triggered slip persists, it may be difficult to distinguish from afterslip, although traditionally "afterslip" has been used to describe postseismic slip occurring on the same fault that the earthquake occurred on and localized in the rupture region or in its immediate vicinity (for example, Smith and Wyss, 1968; Scholz and others, 1969; Burford, 1972; Burford and others, 1973; Cohn and others, 1982; Wesson, 1987; Bilham, 1989; Marone and others, 1991).

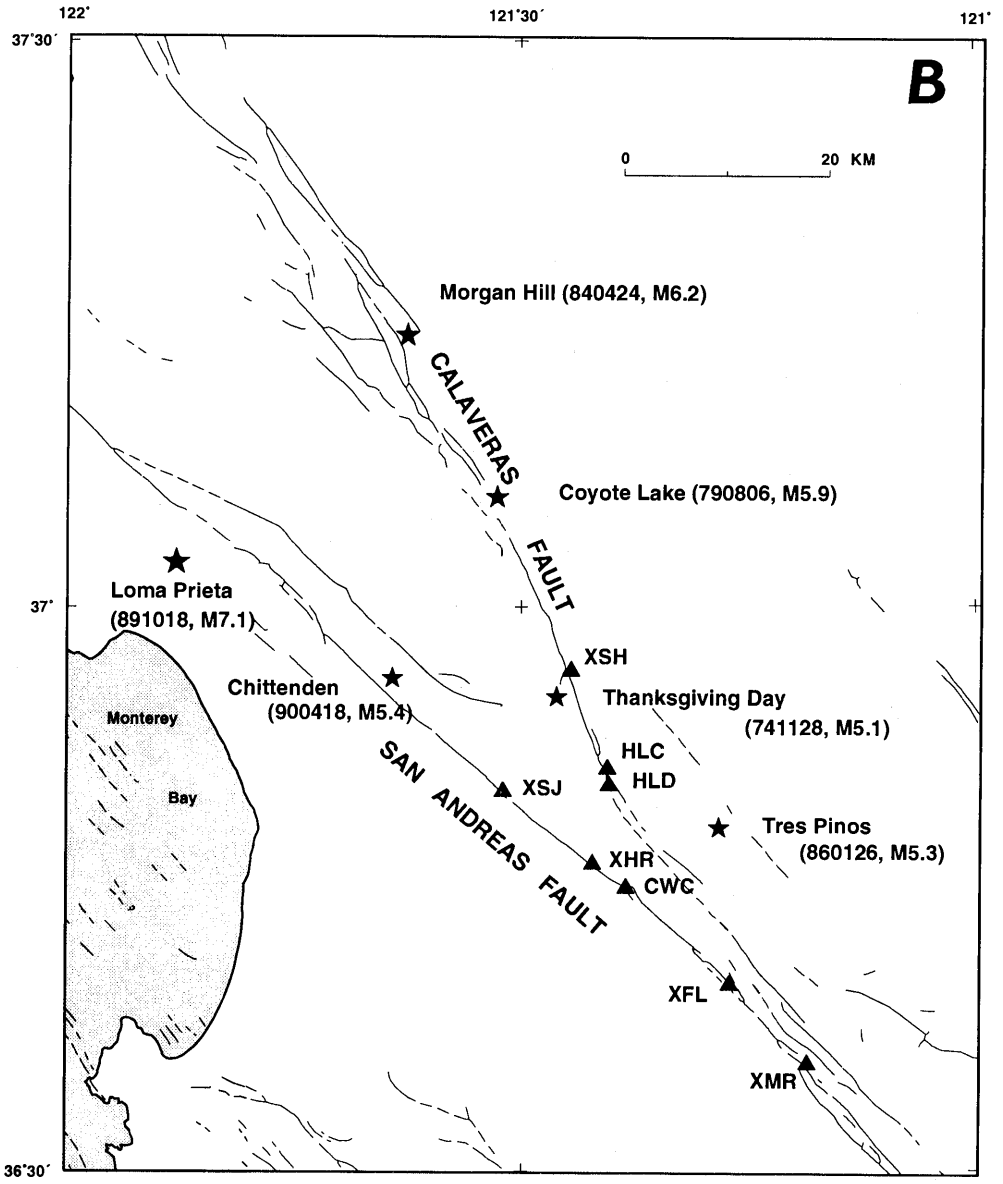

Figure 1.—Continued

Table 1.—*Summary table of all USGS creepmeters in operation at the time of the Loma Prieta earthquake*

[Asterisk (*) in first column indicates a site on the Southwest Fracture near Parkfield. Asterisk (*) in the coseismic change column indicates initial RL movement which was offset by subsequent LL movement within hours to days of the earthquake. Question marks in the coseismic change column indicate lack of data for determining coseismic movement. Negative values indicate left-lateral coseismic steps; positive values, right-lateral.]

Site	Fault	Origin (mo/yr)	Sample Rate	Distance from Loma Prieta (km)	Coseismic Change (mm)	Post-LP Rate Change(?)
XSJ	San Andreas	11/74	10 minute	39	5.2 *	Y
XHR	San Andreas	9/70	10 minute	50	4.3	Y
CWC	San Andreas	10/68	10 minute	54	6.8	Y
XFL	San Andreas	4/73	10 minute	68	-0.35	Y
XMR	San Andreas	6/69	10 minute	79	2.6	?
MRW	San Andreas	10/72	quarterly	80	?	Y
BIT	San Andreas	7/69	quarterly	107	?	N
XMP	San Andreas	6/69	quarterly	133	?	N
XSC	San Andreas	6/69	10 minute	155	0.2	N
XMM	San Andreas	9/79	10 minute	171	0.7	?
XMD	San Andreas	7/86	10 minute	174	1.8	N
XVA	San Andreas	4/87	10 minute	177	3.1	N
XRS*	San Andreas	5/87	10 minute	178	-0.01	N
XPK	San Andreas	9/79	10 minute	180	1.5	N
XTA	San Andreas	9/85	10 minute	182	0.14	N
WKR	San Andreas	9/76	10 minute	186	0.8	N
XHS*	San Andreas	6/87	10 minute	184	0.1	N
CRR	San Andreas	6/66	10 minute	190	0.03	N
XGH	San Andreas	6/69	10 minute	192	0.06	N
X46	San Andreas	8/86	10 minute	204	0.2	N
HWR	Hayward	4/68	quarterly	73	?	N
HWE	Hayward	4/68	quarterly	72	?	N
HWW	Hayward	4/68	quarterly	72	?	Y
HWP	Hayward	5/70	quarterly	71	?	?
XSH	Calaveras	6/71	10 minute	40	5.1 *	Y
HLC	Calaveras	4/70	quarterly	47	?	Y
HLD	Calaveras	4/70	quarterly	48	?	Y

Some of these triggered responses, especially coseismic steps recorded on creepmeters, are most likely produced by the shaking of fault and instrument during passage of the seismic waves (King and others, 1977; Allen and others, 1972; Fuis, 1982; Williams and others, 1988; McGill and others, 1989). Such shaking probably triggers the release of a backlog of slip that had been held in the Earth's near-surface or in the creepmeter itself by friction. Other longer-term responses, including alterations in creep-rate and occasionally in creep direction (Mavko, 1982; Mavko and others, 1985; Simpson and others, 1988), may be caused by static changes in the stress field produced by the distant earthquake's fault offset. The reality of such static stress changes in the earth is not in question, because sensitive strainmeters have detected them at great distances from earthquakes (for example, Johnston and others, 1987; Shimada and others, 1987; Johnston and others, 1990). Microseismicity rate changes on central California faults also appear to correlate with calculated static stress changes after the Loma Prieta earthquake (Reasenberg and Simpson, 1992, and this chapter), suggesting that these faults can and do react to small stress perturbations at seismogenic depths.

In the following sections, we present data for the eight USGS creepmeters that were situated nearest to the Loma Prieta epicenter. One of the largest uncertainties in the interpretation of creepmeter data is introduced by seasonal and rainfall-induced fluctuations. Therefore, rainfall records are also presented, and we explore the possible effects of weather on creepmeter behavior. Because tectonic accelerations or retardations in creep rates may occur before certain earthquakes (for example, Nason, 1973; Burford, 1988), establishing the tectonic as opposed to the rainfall-related significance of creep-rate changes is important, although difficult to accomplish (Goulty and Gilman, 1978, Langbein and others, 1993).

We attempt to relate the observed coseismic steps and longer-term creep-rate changes that occurred at the time

of the Loma Prieta earthquake to static stress changes calculated from simple dislocation models of the rupture in an elastic half-space. To put the Loma Prieta observations into perspective and to improve the statistics, we have compiled creepmeter data for four other moderate-to-large Bay Area earthquakes that occurred before 1989, in addition to the 1990 Chittenden earthquake, which was a large aftershock to the Loma Prieta earthquake. The results described here suggest that although the sense (right-lateral, RL, or left-lateral, LL) of coseismic steps at creepmeter sites seems to bear little relation to the imposed static shear-stress changes, there is a statistically significant relation between the sense (RL or LL) of long-term average creep-rate changes and the sign of coseismic shear-stress changes. For the Loma Prieta earthquake, the magnitudes of these quantities are also well correlated.

We also describe three-dimensional boundary element models used to estimate the total anomalous slip advance or deficit that can be expected at creepmeter sites as a result of the Loma Prieta creep-rate changes. The models suggest that, under some instruments, complex spatial distributions of stress can exist, and the effects of RL stress changes imposed at the surface might be superseded over time by larger LL stresses imposed at depth. These models suggest that for the five creepmeters on the San Andreas fault, cumulative advances ranging from 12 to 60 mm can be expected as a result of the Loma Prieta earthquake, whereas at the three sites on the Calaveras fault, cumulative delays of –6 to –29 mm might be expected. Although post-Loma Prieta adjustments at the creepmeters are not yet complete, these estimates appear to agree with extrapolations of observed advances or deficits in long-term pre-earthquake trends.

DATA FROM EIGHT CREEPMETERS CLOSEST TO THE EARTHQUAKE

In this paper we concentrate our discussion on the responses of the eight closest USGS instruments on the San Andreas and Calaveras faults (fig. 1*B*). Data for all of the operating instruments is available to interested investigators.

Long-term data from the five closest instruments on the San Andreas fault are shown in figure 2*A*. Data from a 3-year time window centered about the Loma Prieta earthquake date are displayed in figure 2*B*. These plots were made using daily data (1 point per day) selected (for the most part) from 10-minute interval data by an automatic algorithm. These daily data have been adjusted to agree with quarterly micrometer readings where data gaps exist or calibrations are in question. Such adjustments are usually unnecessary or small, and none of the significant variations in creep rate presented here are likely to result from instrument calibration problems.

The most obvious features in the long-term data in figure 2*A* are the post-Loma Prieta rate increases at XSJ, XHR, and CWC. Post-seismic changes at XFL and XMR are smaller compared with the other three sites and with other variations recorded at those sites over the years. At the bottoms of figure 2*A* and 2*B*, plots of daily rainfall at Paicines, California, located near the fault between creepmeters CWC and XFL, show that the Loma Prieta earthquake occurred during a drought lasting from 1986 to about 1991 (U.S. Dept. of Commerce).

Figure 3*A* shows cumulative data for the three creepmeters along the Calaveras fault near Hollister. Two traces are plotted for the Shore Road creepmeter; XSH for daily data selected from 10-minute telemetered data and XSHM for approximately quarterly micrometer measurements to facilitate comparison with dial readings from Central Avenue (HLC) and D Street (HLD) in Hollister. The most obvious feature is the slip-rate decrease since the Loma Prieta earthquake at all three sites. There are indications that this decrease began before the earthquake and may be related to the M=5.6 Tres Pinos earthquake on 26 January 1986. These declining slip-rates occur during a period of drought, as shown by the plot of daily rainfall from Paicines, which casts some uncertainty on the tectonic significance of these changes. Galehouse (this chapter) has reported slower creep rates at a number of sites on the Hayward and southern Calaveras faults after the Loma Prieta earthquake.

PRESEISMIC SLIP DEFICITS: PRECURSORY RETARDATION OR DROUGHT?

Small, pre-Loma Prieta rate changes occurred at XHR, CWC, and XMR in the 2–3 years before the earthquake (figs. 2*A*, *B*). It is of some interest to know whether these changes are of tectonic origin, representing precursors to the Loma Prieta earthquake. Burford (1988), for example, discussed the possible significance of retardations in creep rate as precursory signals for magnitude 4–6 earthquakes. Burford also speculated that a larger, more distant shock might be associated with slip deficits across a broader region. The rate reductions seen at several creepmeters before the Loma Prieta earthquake are tantalizing in that respect. However, creepmeters are also known to respond to rainfall, and the prolonged drought that occurred from 1986 to 1991 might also play a role in preseismic creep rates.

Schulz and others (1983) examined the impact of rainfall at XSH, XSJ, and XMR during the 1970's, which includes the drought period from 1976 to 1978. Reviewing 8–11 years of creep data, they found no significant correlation between rainfall and either the total amount of annual creep, the number of annual episodic events, or

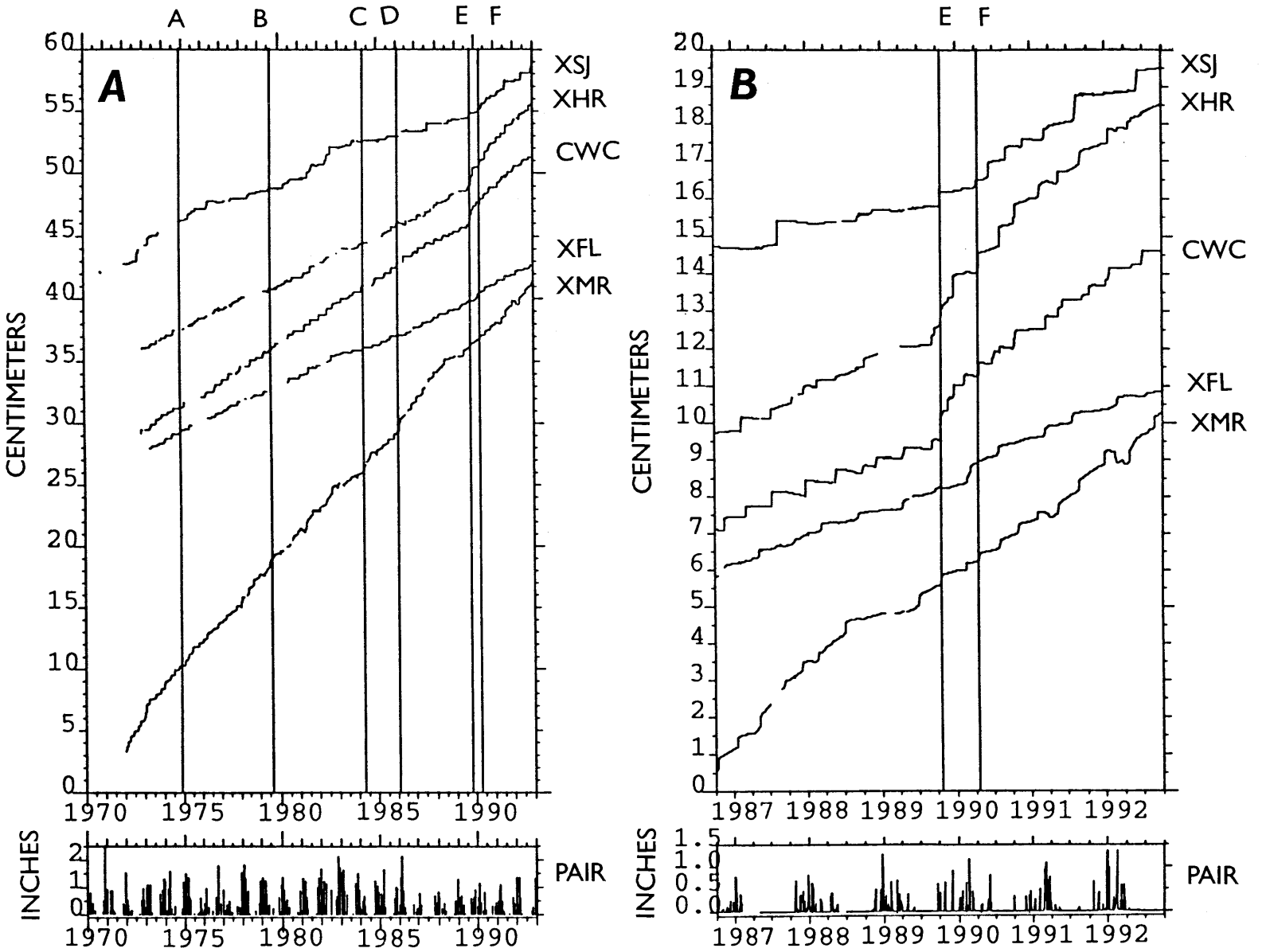

Figure 2.—*A*, Cumulative creep data for five creepmeters on the San Andreas fault from 1970 to 1993. Rainfall occurrences are also shown at the bottom of the plot. Vertical lines A through F mark the times of six moderate to large central California earthquakes discussed in the text and shown in figure 1*B*. *B*, Cumulative creep data for five creepmeters on the San Andreas fault from three years before to three years after the Loma Prieta earthquake. Rainfall occurrences are also shown at the bottom of the plot. Vertical lines E and F mark the times of the Loma Prieta earthquake and the Chittenden aftershock.

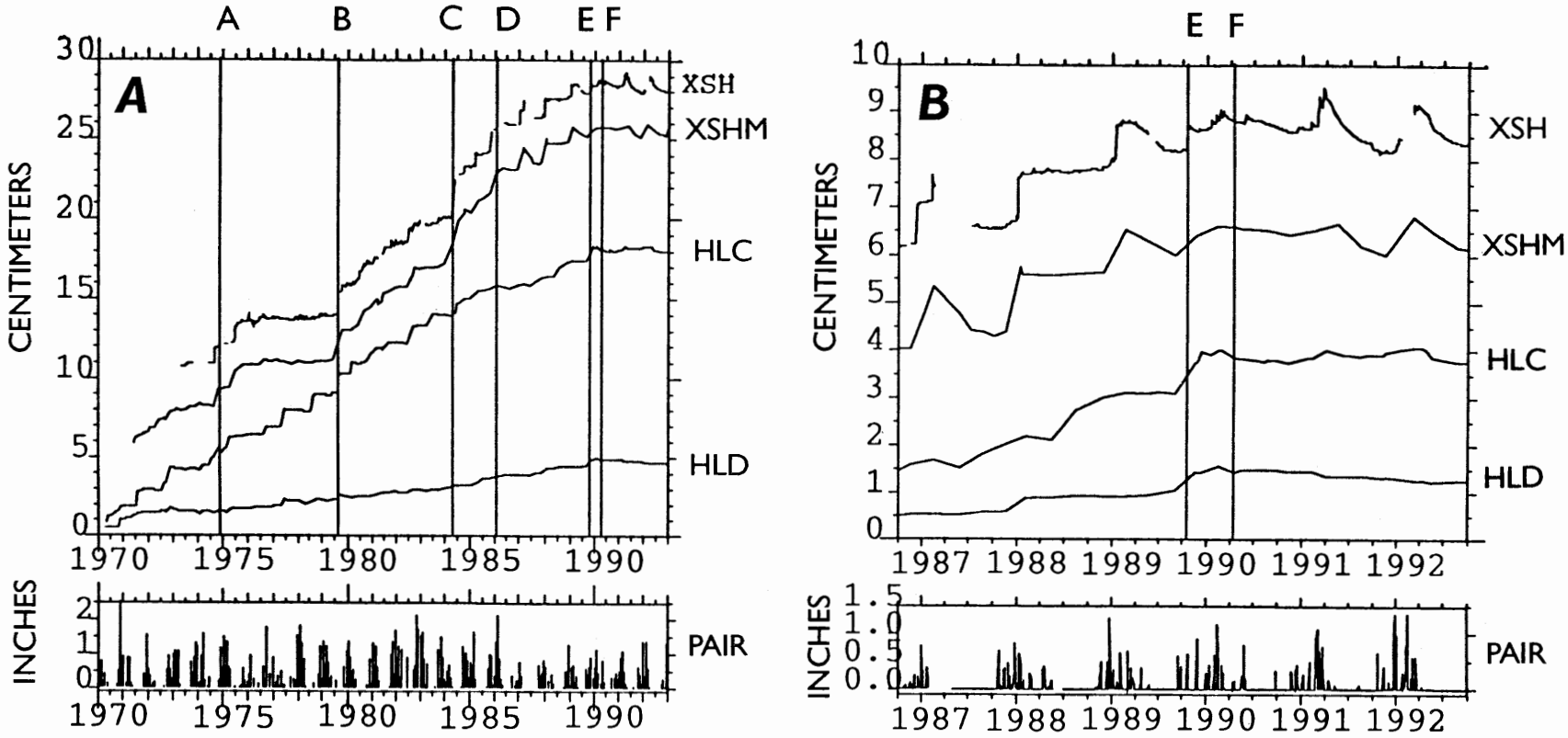

Figure 3.—*A*, Cumulative creep data for three creepmeters on the Calaveras fault from 1970 to 1993. XSHM is micrometer readings at site XSH, presented for easier comparison with the micrometer readings used for HLC and HLD. Rainfall occurrences are also shown at the bottom of the plot. Vertical lines A through F mark the times of six moderate to large central California earthquakes discussed in the text and shown in figure 1B. *B*, Cumulative creep data for three creepmeters on the Calaveras fault from three years before to three years after the Loma Prieta earthquake. Trace XSHM represents quarterly micrometer readings at site XSH, presented for easier comparison with the dial gauge readings from HLC and HLD. Rainfall occurrences are also shown at the bottom of the plot. Vertical lines E and F mark the times of the Loma Prieta earthquake and the Chittenden earthquake.

the total creep accumulated from annual episodic events. The study identified slight RL or LL increases at XSJ and XMR associated with rainfall, and at XSH, oscillatory events of about 1-day duration accompanying rain. No obvious seasonal trends are present at XHR, CWC, or XFL. Figures 4*A* and 4*B* depict residual creep data with residual rainfall from Paicines, located just south of the CWC creepmeter. An annual average rate of 15.4 inches per year has been removed from the rain record to visually enhance seasonal changes. Drought periods, from 1976 to 1978 and from 1986 to 1991, appear as downward trends, and are marked with horizontal bars above the traces.

For San Andreas fault creepmeters in this study, there is no apparent seasonal trend associated with rainfall except at XMR, where strong LL movement occurred dur-

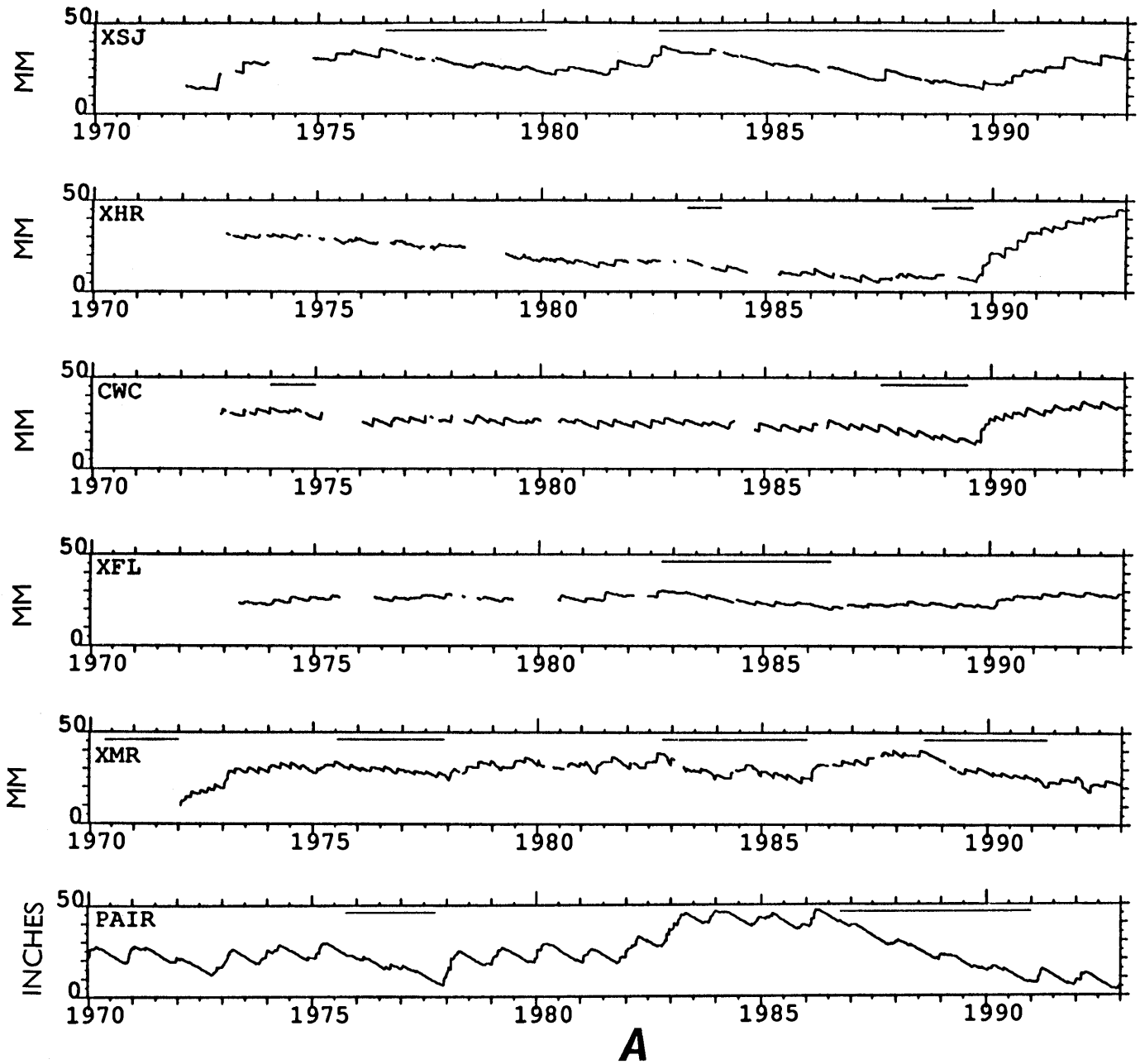

Figure 4.—*A*, Detrended creep data for five creepmeters on the San Andreas fault for the period 1970–1993. Trend was determined by calculating best-fitting least-squares line. Horizontal bars denote periods of creep retardation. Bottom plot shows detrended cumulative rainfall record. *B*, Detrended creep data for three creepmeters on the Calaveras fault for the period 1970–1993. Trend was determined by calculating best-fitting least-squares line. XSHM is micrometer readings at site XSH, presented for easier comparison with the micrometer readings used for HLC and HLD. Horizontal bars denote creep retardation. Bottom plot shows detrended cumulative rainfall record.

ing the 1991 and 1992 rainy seasons. The average creep rate at XMR for those years remains consistent with the long-term average of about 18 mm/yr despite these seasonal fluctuations. On the Calaveras fault, rainfall signals are more pronounced at XSH after 1986, when the instrument was rebuilt. The oscillatory character of the signal remains. Appendix A discusses the reconstruction at XSH in more detail. During the 1976 drought, XSH recorded a slip deficit before the Coyote Lake earthquake in 1979. When normal rainfall resumed in 1978, there was no change in the character of the retardation signal in response to increased precipitation. Schulz and others (1983) note that while lack of rain may delay onset of a creep event, stress build-up from slip at depth will eventually override conditions in the shallow soil to produce a creep event. We find no strong relationship between changes in creep rate and periods of drought or deluge for the creepmeters in this study.

Turning to creep retardation, horizontal bars above creep data in figures 4*A* and 4*B* mark slip deficits identified by Burford (1988), updated through December 1992. Although the definition is subjective, as a general rule we look for rate decreases of at least 30 percent compared to the long-term average rate, using a duration of at least 12 to 18 months to avoid seasonal effects. By this rule, the deficit at XHR in 1988-89 does not qualify as retardation due to its brevity, but we include it nevertheless because of its uniqueness in the long-term data set. On the San Andreas fault, four out of five creepmeters recorded slip retardations of some duration before the Loma Prieta earthquake, though there is little consistency in the onset. However, even in hindsight, it is not clear that these retardations are precursors to the Loma Prieta earthquake or that they could have been used to somehow predict the earthquake. Table 2 lists retardation parameters for these episodes. At two of these sites, XHR and CWC, rate reductions end just

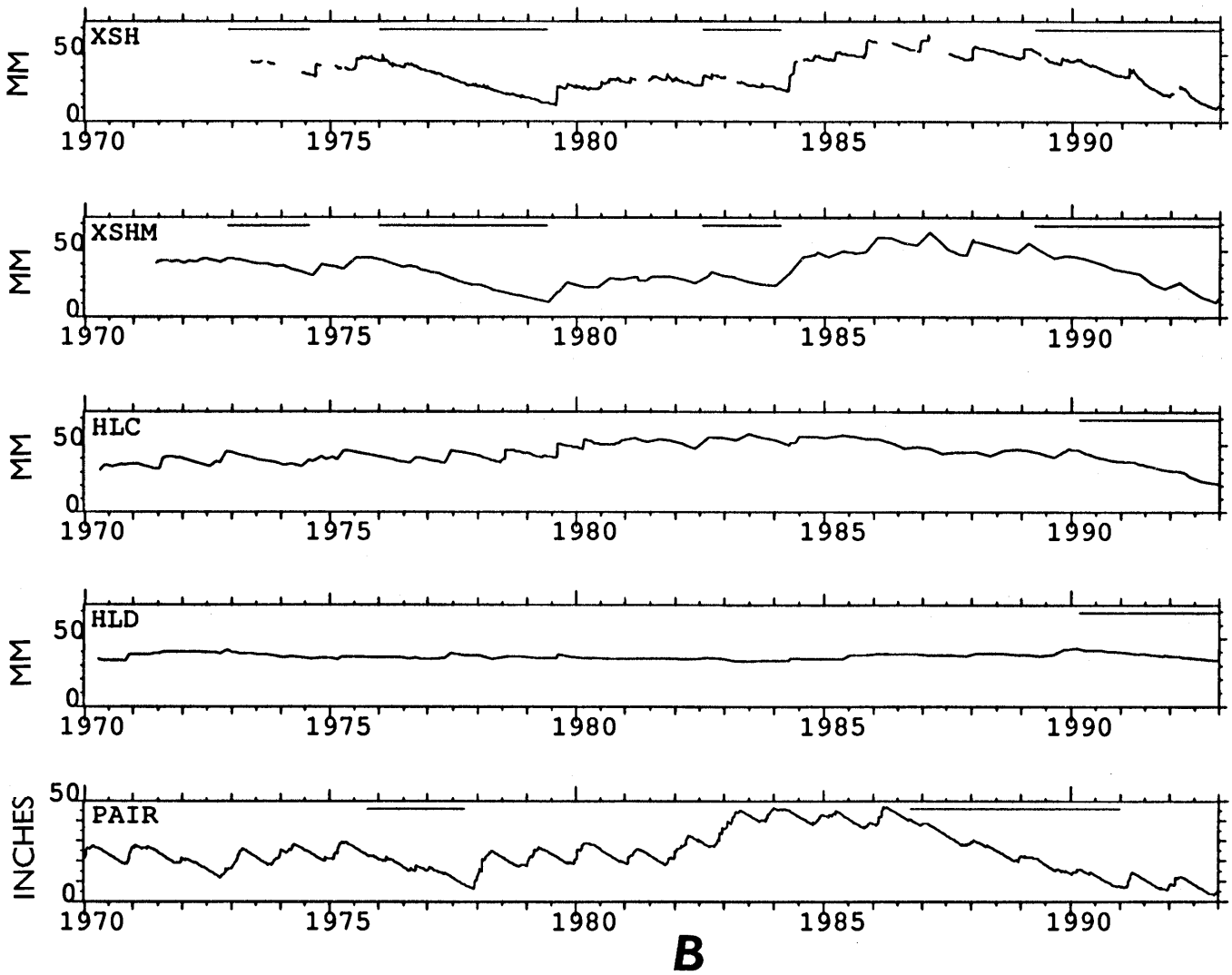

Figure 4.—Continued

Table 2.—*Possible creep retardations before the earthquake*

[The retarded rate and the background rate were determined by fitting least square lines to the intervals of interest. The background interval extends from the origin of the respective meter to 17 October 1989.]

Site	From	To	Duration (months)	Rate (mm/yr)	Background Rate (mm/yr)
XSJ	August 1982	April 1990	92	3.8	6.4
XHR	September 1988	September 1989	12	6.1	7.5
CWC	August 1987	October 1989	26	6.9	10.1
XMR	August 1988	May 1991	36	12.3	18.0
XSH	May 1989	continuing	30	-0.3	11.8

before or with the quake. At XSJ and XMR however, slip rates continued to be lower than the long-term average until 6 months and 19 months after the quake.

Of the Calaveras creepmeters, the rate at XSH began to drop in May 1989, while at HLC and HLD slip deficits are completely postseismic effects. These retardation episodes amount to only a shadowy precursor, given the variability of response across the network. However, since the Loma Prieta is the first M=7 quake in proximity to USGS creepmeters in almost 25 years of monitoring, it is still premature to discount these deficits as local, transitory effects without further rigorous examination.

SIGNAL VERSUS NOISE IN THE CREEP DATA

As is indicated in the above discussion, separating tectonic signals from rainfall-induced signals and noise is an important problem. Langbein and others (1993) have estimated the $1/f^2$ noise of the creepmeters near Parkfield, California, to have a standard deviation of 6 mm/yr. We have attempted to estimate the noise levels for the eight instruments discussed in this report by calculating average creep rates using 6-month and 1-year averaging windows moved across four intervals of interest (table 3).

The standard deviations in table 3 give some indication of noise levels and how large rate changes need to be at particular sites before they can be regarded as significant. Although our analysis is simpler and not directly comparable to that of Langbein and others (1993), the results for XHR, CWC, and XFL show standard deviations consistently below the 6-mm/yr level, suggesting that these instruments may have higher signal-to-noise ratios than typical Parkfield instruments. On the contrary, XSJ, XMR, XSH, and HLC have standard deviations that are typically worse than 6 mm/yr, at least for some intervals.

Another factor that helps convince us that rate changes at the time of Loma Prieta are real is the occurrence of similar changes on a number of instruments. Even though the changes on individual instruments might be called into question because of noise problems, the agreement of a suite of instruments in the sense and magnitude of rate change can be convincing.

COSEISMIC STEPS AND STATIC STRESS CHANGES

Coseismic steps were recorded at the six closest USGS creepmeters on the San Andreas and Calaveras faults with sampling intervals short enough (10 minutes) to detect such steps. These "coseismic" responses occurred within 10-20 minutes of the earthquake origin time, the uncertainty in timing being caused by the coarseness of the sampling interval. Table 1 lists coseismic steps at all creepmeters in the network, and figure 5 shows raw data for the six closest instruments.

Figure 6 compares the coseismic steps at the six creepmeters with the calculated Loma Prieta stress changes, based on a dislocation model of Lisowski and others (1990) used to match geodetic measurements of coseismic surface displacements. Static stress changes at the creepmeter sites were calculated using equations derived by Okada (1992) for dislocations in an elastic half-space. We show only horizontal shear stress changes and normal stress changes because the vertical shear changes are 5–10 times smaller on these vertical faults (Simpson and Reasenberg, 1994). Coseismic steps could not be inferred for HLC or HLD because these instruments are read manually at quarterly intervals. Of six observed coseismic steps, one (at XFL) is LL and all of the others are RL. No strong relation exists between either sign or magnitude of the steps and sign or magnitude of the calculated stress changes, especially in view of the tendency of coseismic steps in RL fault systems to occur in a RL sense.

Five earthquakes other than the Loma Prieta with magnitudes greater than 5 have occurred in the region since 1974 (fig. 1*B*); namely, Thanksgiving Day (M=5.1), Coyote Lake (M=5.9), Morgan Hill (M=6.2), Tres Pinos (M=5.3), and Chittenden (M=5.4). For all six earthquakes, 4 LL and 17 RL coseismic steps were observed (table 4, figure 7). Of the 4 LL steps, two occurred at sites where model calculations predict LL shear-stress changes, and

Table 3.—*Average creep rates for five creepmeters on the San Andreas Fault and three creepmeters on the Calaveras fault*

[Average rate is determined by least square fitting of a line to data in either a 6-month window (A) or in a 1-year window (B); the windows are advanced by 3-month and 6-month increments, respectively, over the period of interest, and the resulting rates are averaged. The first interval is a background period which ends more than 3 years before the earthquake so as to avoid possible precursory Loma Prieta effects. The second interval includes possible precursory Loma Prieta effects. The third interval is for 1 year after the earthquake. The fourth interval is for 2 years after the earthquake. Negative values indicate left-lateral rates; positive values, right-lateral.]

A. 6-Month Average Creep Rates, in mm/yr

[The 6-month sampling interval advances in 3-month steps. First number is average creep rate in mm/yr; second number after ± is one standard deviation; value in parentheses is the number of six-month intervals within the overall interval that was used to calculate average and standard deviation.]

Interval Dates:	01/01/77-01/01/86	01/01/86-10/01/89	11/01/89-11/01/90	11/01/89-11/01/91
XSJ	6.1 ± 7.1 (35)	4.1 ± 5.8 (14)	15.1 ± 7.7 (3)	14.5 ± 6.0 (7)
XHR	7.7 ± 3.7 (25)	8.5 ± 4.0 (12)	22.0 ± 3.3 (3)	19.2 ± 4.4 (7)
CWC	10.3 ± 3.8 (30)	8.1 ± 3.9 (14)	18.4 ± 4.1 (3)	15.8 ± 5.1 (7)
XFL	6.3 ± 3.7 (28)	7.3 ± 3.1 (14)	15.0 ± 3.1 (3)	11.3 ± 4.2 (7)
XMR	17.4 ± 8.0 (34)	18.1 ± 9.3 (14)	12.1 ± 2.0 (3)	13.4 ± 5.3 (7)
XSH	13.1 ±15.9 (33)	9.5 ±15.2 (12)	0.1 ± 5.7 (3)	-1.6 ±10.5 (7)
HLC	12.0 ±12.1 (19)	--- (0)	-1.6 ± 5.3 (3)	0.6 ± 4.5 (6)
HLD	8.0 ± 3.1 (2)	--- (0)	-0.3 ± 1.9 (3)	-1.0 ± 1.5 (6)

B. 1-Year Average Creep Rates, in mm/yr

[The 1-year sampling interval advances in half-year steps. First number is average creep rate in mm/yr; second number after ± is one standard deviation; value in parentheses is the number of six-month intervals within the overall interval that was used to calculate average and standard deviation.]

Interval Dates:	01/01/77-01/01/86	01/01/86-10/01/89	11/01/89-11/01/90	11/01/89-11/01/91
XSJ	6.0 ± 4.9 (17)	4.3 ± 3.4 (6)	15.0 ± -- (1)	14.3 ± 1.0 (3)
XHR	7.9 ± 2.4 (14)	8.5 ± 2.3 (6)	23.0 ± -- (1)	20.2 ± 4.2 (3)
CWC	10.4 ± 1.4 (17)	8.0 ± 1.6 (6)	18.2 ± -- (1)	15.1 ± 2.7 (3)
XFL	6.6 ± 2.1 (14)	7.6 ± 1.3 (6)	14.8 ± -- (1)	11.0 ± 3.3 (3)
XMR	17.0 ± 5.0 (17)	17.7 ± 7.7 (6)	12.8 ± -- (1)	13.6 ± 1.6 (3)
XSH	12.7 ±11.1 (17)	6.6 ± 9.4 (5)	0.1 ± -- (1)	-0.7 ± 4.1 (3)
HLC	10.2 ± 6.3 (15)	4.6 ± 4.1 (6)	-1.3 ± -- (1)	0.7 ± 1.8 (3)
HLD	1.9 ± 2.3 (14)	1.5 ± 1.8 (6)	0.3 ± -- (1)	-0.8 ± 1.0 (3)

two occurred at sites where calculations predict RL shear-stress changes. Conversely, at the six sites with coseismic steps where LL stress changes are predicted, only two showed LL coseismic steps.

These results imply that the sense (RL or LL) of coseismic steps at the six creepmeter sites bears little relation to the imposed static shear-stress changes. If we adopt the null hypothesis that the direction of a coseismic

step is independent of the sign of imposed static stress change, then a two-sided chi-square test (for example, Sachs, 1982) applied to the data displayed in figures 6 and 7 does not allow us to reject the null hypothesis at even the 50-percent confidence level. We conclude that the sense of observed coseismic steps bears no obvious strong relation to the calculated static stress changes. Although all but one of the large coseismic steps did occur for RL static stress changes, there was only one instance of a large imposed LL static change, so the geometry of faults and earthquakes in the region has not lent itself to testing the hypothesis in question.

It does appear from visual inspection of figure 7 that the 26 occurrences of increased RL shear were more likely to have a sizable coseismic step than the 19 occurrences of added LL shear, many of which had a zero step and are not plotted in figure 7. The larger amplitude and the larger number of RL steps presumably reflects the fact that all of the creepmeters are installed across faults that normally creep in a RL sense.

More often than not, the coseismic step probably reflects the triggered release of a backlog of slip either in the near-surface of the earth or in the instrument itself by the shaking that accompanies the passage of seismic waves. The magnitude of the dynamic stress changes associated with the passage of seismic waves is, in general, much larger than the magnitude of the static stress changes (Spudich and others, 1995). On a right-lateral fault, such a backlog would normally be right-lateral, although a few sites might have a left-lateral backlog resulting from seasonal variations in slip direction of the instrument caused by rainfall, local soil conditions, and installation configuration. We cannot rule out the possibility that, because of radiation patterns and ground conditions, those sites with RL shear added also might have been the sites that experienced the greater amount of dynamic shaking during the earthquake. Nevertheless, the results shown in figure 7 suggest that added RL static shear encourages the triggered release of a backlog of slip in a RL system, while added LL static shear can discourage such a triggered release.

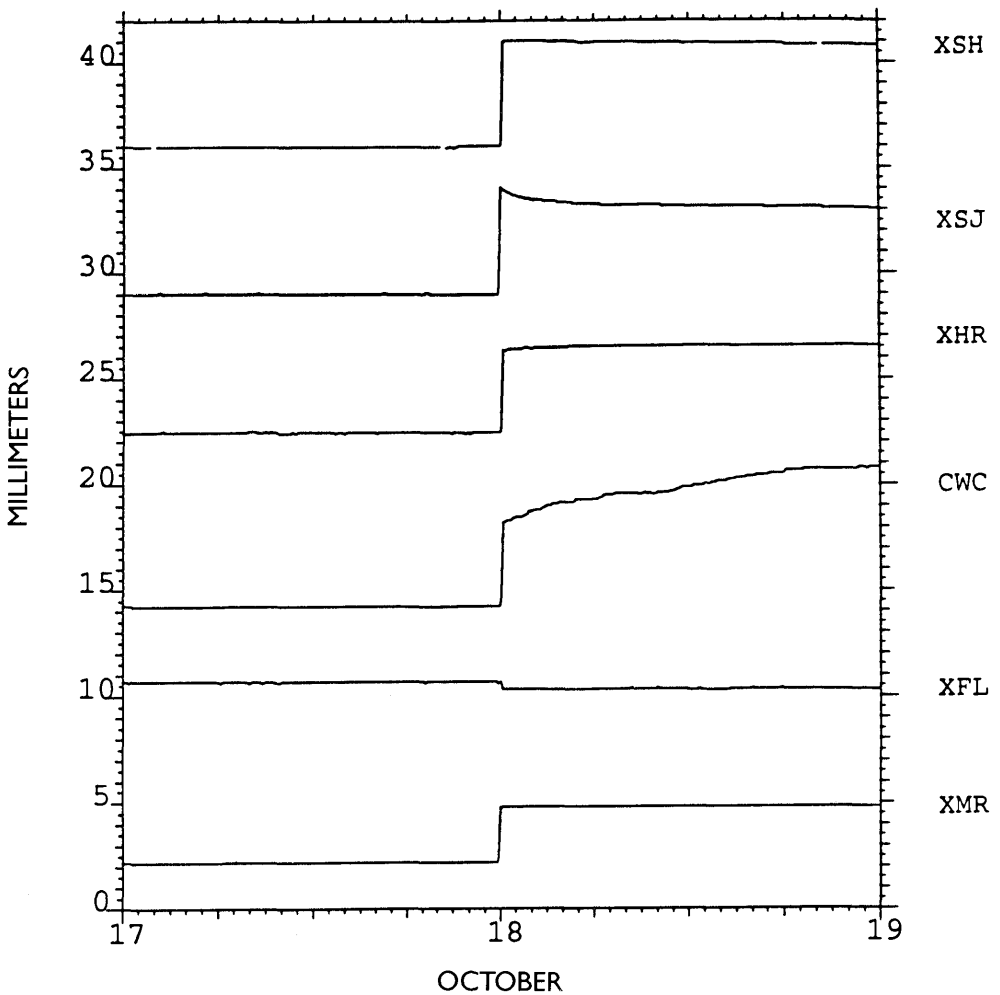

Figure 5.—Coseismic response to the Loma Prieta earthquake for six creepmeters. XSH is on the Calaveras fault, while the others are on the San Andreas fault. Time extends from one day before to one day after the Loma Prieta earthquake.

Williams and others (1988) suggest that the amount of slip triggered on part of the southern San Andreas fault by the 1986 North Palm Springs earthquake agreed well with the size of the slip deficit at the site. McGill and others (1989) suggest that slip deficit is probably only part of the story, because some sites showed triggered events associated with both the 1989 Elmore Ranch and Superstition Hills earthquakes, separated by only 11 hours, whereas one might expect the deficit to have been shaken out by the first shock. We looked for a correlation between the magnitude of the coseismic step and the slip deficit at our eight San Andreas and Calaveras sites, where slip deficit is defined as the difference between the long-term rate at a site and the average rate in the 1-year period preceding the earthquake (fig. 8). (The two points in figure 8 with large negative deficits come from long-term rates before the Chittenden earthquake—an aftershock to the Loma Prieta earthquake. These negative deficits are caused by faster-than-normal rates at the two sites caused by Loma Prieta afterslip.) Although there is a suggestion that the largest steps correlate with the largest deficits as defined here, the strength of the correlation is not great.

We could find no significant agreement between sign of coseismic steps and sign of 1-year average rate changes (fig. 9). The two-sided chi-square test did not allow us to reject the null hypothesis that no relation existed with a confidence level of any greater than 40 percent. The absence of any such a relation is consistent with the idea that, in most cases, coseismic steps largely reflect the release of a backlog of slip rather than a clean response to newly imposed stress changes, although it is not possible to rule out a combination of the two effects.

CREEP RATE CHANGES AND STATIC STRESS CHANGES

Average 1-year slip rates for the five creepmeters on the San Andreas fault increased at the time of the Loma

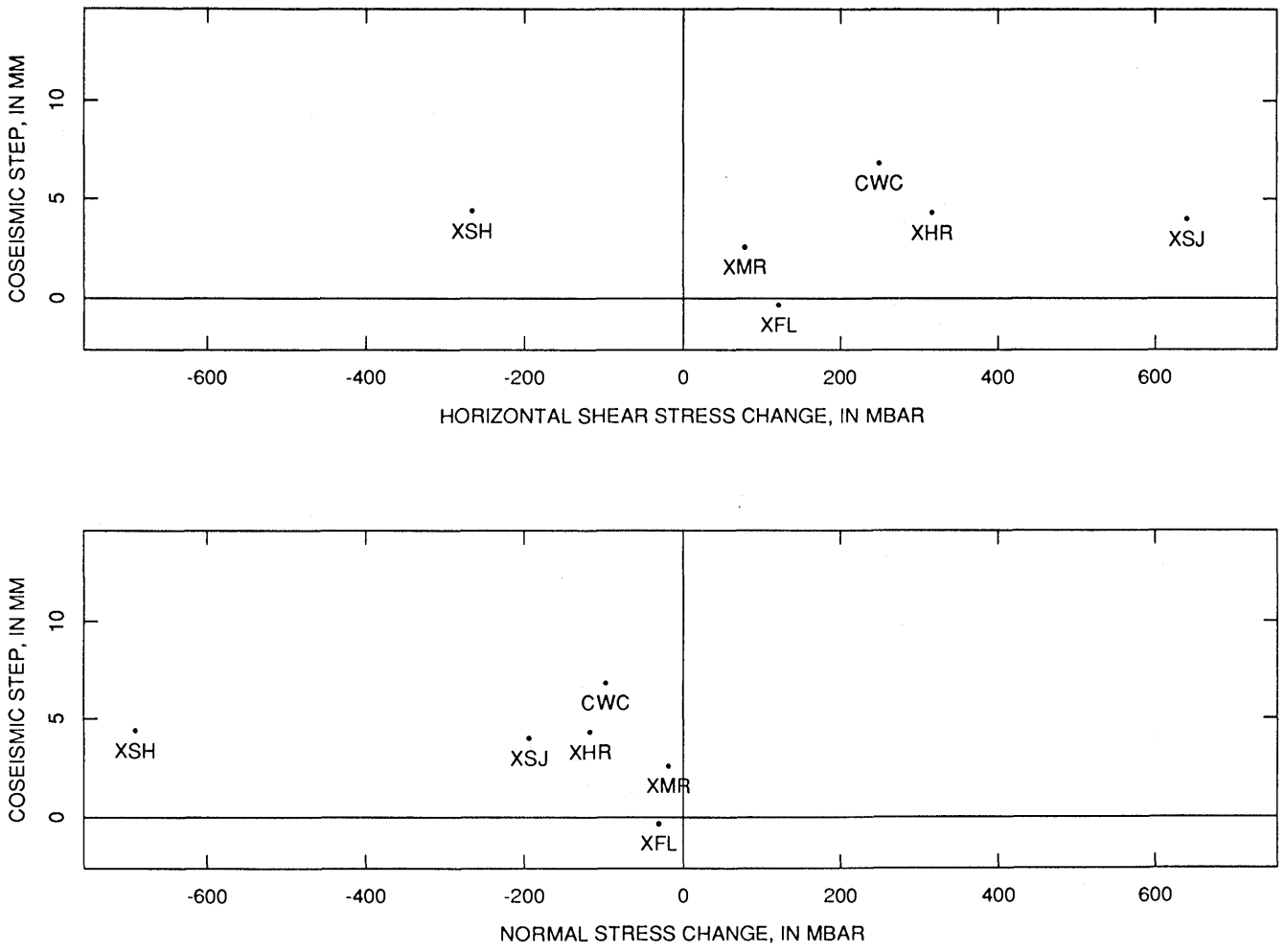

Figure 6.—Coseismic steps for Loma Prieta earthquake at six creepmeters compared with calculated static stress changes. Coseismic steps are + for RL, – for LL. Shear stress is horizontal component, + for RL, – for LL. Normal stress is perpendicular component, + for tension, – for compression.

Table 4.—*Observed coseismic steps and 1-year average rates for eight creepmeters and six earthquakes*

[The earthquakes in column 1 are ch = Chittenden, lp = Loma Prieta, tp = Tres Pinos, mh = Morgan Hill, cl = Coyote Lake, td = Thanksgiving Day. For coseismic steps in column 3, '-' indicates no step, and '?' indicates that the data were not available. 1-year average rates were calculated by fitting a least-squares line to the data in the one year interval and ignoring any coseismic offset. Fractional rate change in column 6 is calculated from columns 4 and 5 as (rate before - rate after)/(rate before). Stress changes in columns 7 and 8 were calculated from dislocation models described in table 3 and in the text. Negative values indicate left-lateral changes or rates; positive values, right-lateral.]

Earthquake	Creep-meter	Coseismic Step (mm)	1-Year Rate Before (mm/yr)	1-Year Rate After (mm/yr)	Fractional Rate Change	Shear Stress (bars)	Normal Stress (bars)
ch	XSH	-0.04	7.0	2.1	-0.70	-0.07	-0.17
ch	HLC	?	12.2	1.5	-0.88	-0.03	-0.01
ch	HLD	?	7.1	-1.1	-1.15	-0.02	0.00
ch	XSJ	-	8.3	13.6	0.64	0.09	-0.02
ch	XHR	5.40	27.6	22.7	-0.18	0.02	0.00
ch	CWC	3.80	27.3	13.5	-0.51	0.01	0.00
ch	XFL	0.15	8.6	9.0	0.05	0.00	0.00
ch	XMR	-	15.6	13.2	-0.15	0.00	0.00
lp	XSH	4.40	2.3	0.8	-0.65	-0.27	-0.69
lp	HLC	?	1.0	-1.3	-2.30	-0.19	-0.17
lp	HLD	?	1.5	0.3	-0.80	-0.15	-0.11
lp	XSJ	4.00	2.0	14.2	6.10	0.64	-0.19
lp	XHR	4.30	6.3	22.8	2.62	0.32	-0.12
lp	CWC	6.80	6.9	18.8	1.72	0.25	-0.10
lp	XFL	-0.35	7.5	14.9	0.99	0.12	-0.03
lp	XMR	2.60	8.7	12.5	0.44	0.08	-0.02
tp	XSH	-	21.8	10.8	-0.50	-0.02	0.00
tp	HLC	-	1.5	-0.7	-1.47	-0.07	-0.03
tp	HLD	?	6.9	1.5	-0.78	-0.06	-0.06
tp	XSJ	-0.05	3.7	3.9	0.05	-0.03	-0.02
tp	XHR	2.68	9.2	4.2	-0.54	0.05	-0.05
tp	CWC	1.54	9.3	8.8	-0.05	0.09	0.00
tp	XFL	-0.05	7.7	7.6	-0.01	0.01	-0.05
tp	XMR	0.35	13.4	22.4	0.67	0.02	-0.01
mh	XSH	13.00	5.0	21.0	3.20	0.18	0.01
mh	HLC	?	1.0	15.9	14.90	0.07	0.01
mh	HLD	?	1.0	1.3	0.30	0.06	0.00
mh	XSJ	-	5.8	1.0	-0.83	-0.10	0.06
mh	XHR	0.50	3.9	6.0	0.54	-0.02	0.00
mh	CWC	0.31	9.4	8.3	-0.12	-0.01	-0.01
mh	XFL	-	3.6	5.1	0.42	0.01	-0.01
mh	XMR	0.27	12.2	14.1	0.16	0.01	0.00
cl	XSH	8.90	2.4	11.6	3.83	0.31	-0.01
cl	HLC	?	1.7	11.2	5.59	0.08	0.00
cl	HLD	?	0.2	0.1	-0.50	0.06	0.00
cl	XSJ	-	3.6	5.2	0.44	-0.10	0.07
cl	XHR	-	3.0	7.8	1.60	-0.01	-0.01
cl	CWC	-	9.9	11.6	0.17	0.00	-0.01
cl	XFL	-	5.8	20.0	2.45	0.01	-0.01
cl	XMR	-	17.1	11.8	-0.31	0.01	0.00
td	XSH	?	18.2	23.8	0.31	-0.19	0.08
td	HLC	?	16.3	13.0	-0.20	-0.15	-0.04
td	HLD	?	1.1	3.4	2.09	-0.10	-0.01
td	XSJ	0.30?	9.0	12.0	0.33	-0.05	-0.13
td	XHR	?	9.0	7.8	-0.13	0.03	-0.01
td	CWC	-	8.8	9.5	0.08	0.01	0.00
td	XFL	-	9.9	8.0	-0.19	0.00	0.00
td	XMR	-	19.0	20.7	0.09	0.00	0.00

Prieta earthquake, whereas rates for the three sites on the Calaveras fault decreased (figs. 2, 3; tables 3, 4). To compare creep-rate changes with calculated static stress changes, three different dislocation models of the Loma Prieta rupture were used, based on geometries and slip distributions proposed by Lisowski and others (1990),

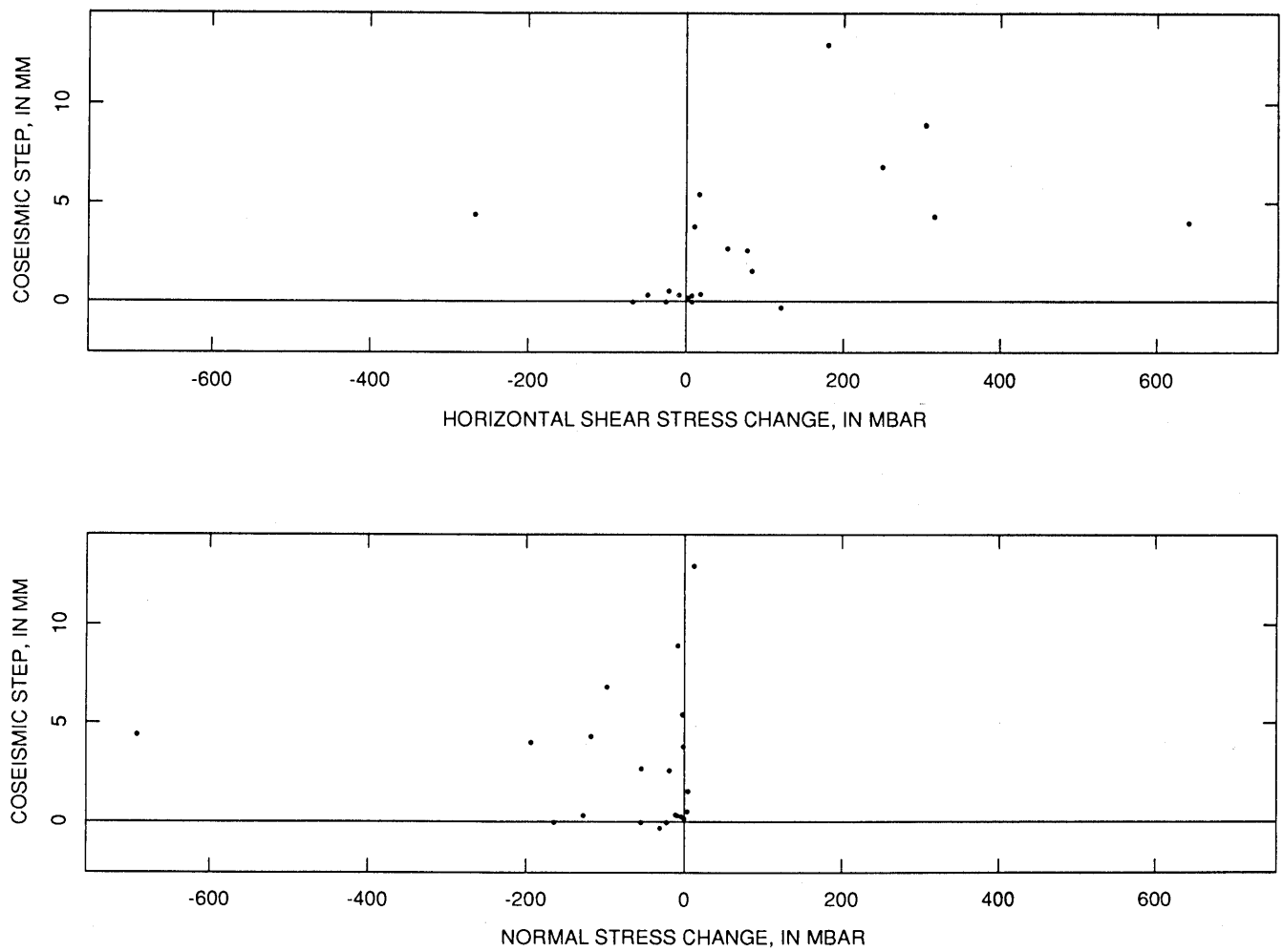

Figure 7.—Coseismic steps for six earthquakes, including Loma Prieta earthquake, compared with calculated static stress changes. Sign conventions as in figure 6.

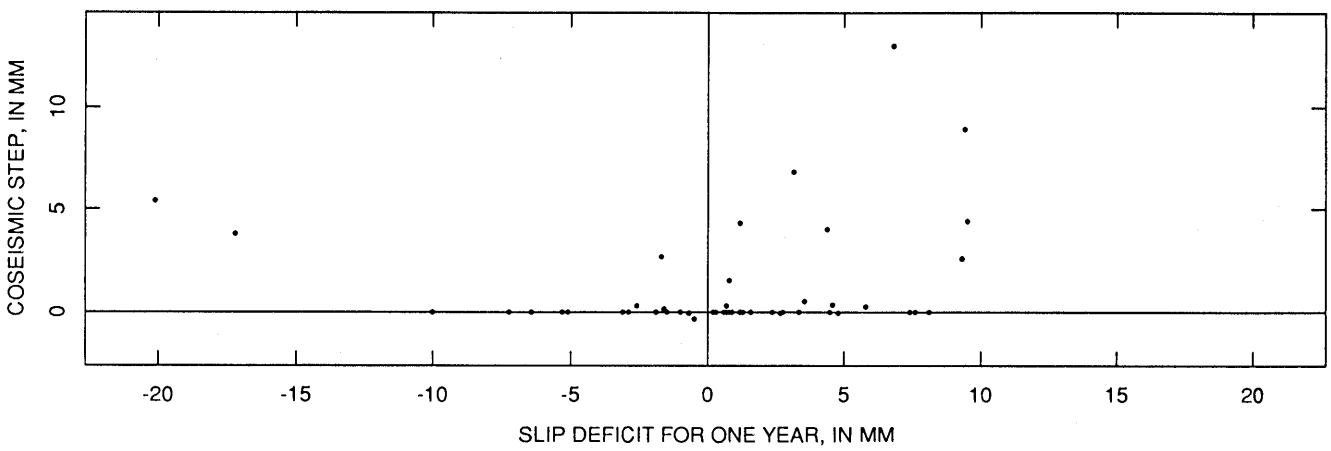

Figure 8.—Coseismic steps for six earthquakes compared with one-year slip deficit (defined as difference between the long term rate and the one-year average rate prior to the earthquake).

Marshall and others (1991), and Beroza (1991). Simpson and Reasenberg (table 1, 1994) tabulate the details of these three Loma Prieta models. For one site, changes in the rupture orientation from model to model changes the sign of calculated shear-stress because this site is near a node in the stress field. In general, the stresses calculated at distances of several rupture lengths from the epicenter are quite comparable model to model.

Figure 10 compares the fractional change in 1-year average creep rates before and after the Loma Prieta earthquake with calculated static stress changes from the three Loma Prieta models. The fractional change in average rate is defined by $\Delta\bar{V}/V_0$ where $\Delta\bar{V}$ is the change in average rate over the given time window and V_0 is the average rate before Loma Prieta over the given time window.

To see if there was any significant relationship between the signs of the rate changes and the signs of the stress changes, we tested the null hypothesis that these quantities were independent by again applying a two-sided chi-square test to the respective fourfold tables.

For shear stresses, the null hypothesis that the quantities are independent can be rejected at the 99-percent, 96-percent, and 83-percent confidence levels (χ^2 values of 8, 4.4, 1.9) for the Lisowski, Beroza, and Marshall models, respectively, when the stresses are calculated at the surface. The confidence limits are even better if the stresses are calculated at greater depths (for example, 10 km) because the horizontal shear-stresses change sign under HLC and HLD in the Marshall model (see fig. 15 and table 6).

For normal stresses, the null hypothesis that the quantities are independent can be rejected at the 0-percent, 52-percent, and 96-percent confidence levels (χ^2 values of 0, 0.5, 4.4) for the Lisowski, Beroza, and Marshall models, respectively. The sense of relation for normal stresses suggested by the Marshall model would yield an increase in creep rate in response to negative values of normal stress which, in the convention used here, would imply more compression. If a relation of this sort exists, it would be counter-intuitive given that Coulomb's law predicts greater friction on the fault as a result of greater compression.

We interpret these results to mean that for the three models tested, there is a good relation between slip-rate change and shear stress change, but that a relation between slip-rate change and normal stress change is unlikely.

In an effort to put this relationship on a firmer footing, we repeated the statistical tests using data for four earlier earthquakes and the Chittenden aftershock, as well as for the Loma Prieta earthquake (table 4). Model ruptures for each earthquake were made using dislocation rectangles positioned and oriented from main shock and aftershock locations and from focal-mechanism information (table 5). Amounts of slip were assigned to these dislocation surfaces to yield the observed seismic moments. By examining the results of six earthquakes together, we hoped that model-dependent effects would be either made apparent or minimized in the statistics. The data for all six earthquakes are shown in figure 11. For shear stress, there is a relation at the 95-percent confidence level (χ^2= 3.88). For normal stress, the null hypothesis of independence cannot be rejected, implying that no strong relation exists.

A slightly sharper result is obtained if the lower calculated values of stress change are discarded. For example, Reasenberg and Simpson (1992, and this chapter) reported that significant correlation exists between shear-stress changes and microseismicity rate changes down to stress levels of about 0.1 bar. If we repeat the statistical tests, eliminating those data points for which the shear-stress changes were less than 0.05 bar (fig. 12), then for shear stresses, there is a relation at the 99-percent confidence level (χ^2= 6.58). These results are summarized in table 6.

Similar statistical tests applied to each of the earthquakes individually show that, not unexpectedly, the largest earthquakes (Loma Prieta and Morgan Hill) give the

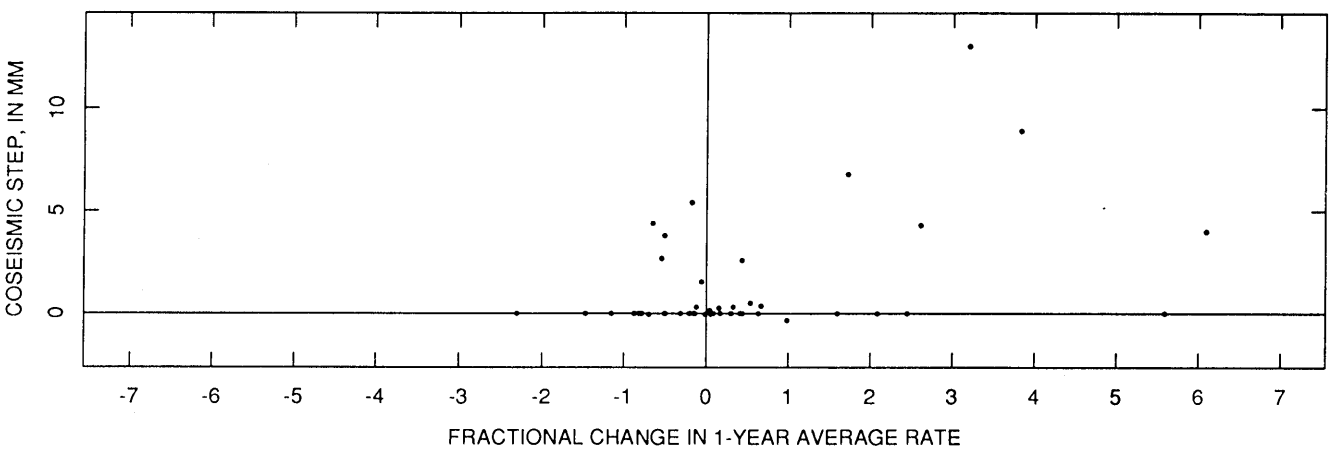

Figure 9.—Coseismic steps for six earthquakes compared with fractional change in 1-year average creep rates. Fractional change is defined as the 1-year average rate before the earthquake minus the 1-year average rate after the earthquake, divided by the 1-year average rate before the earthquake.

most definitive results. The results of such tests are also dependent upon the choice of averaging interval. We used a 1-year interval for the tests described above. For a 3-year window, XMR yields a slower average rate after Loma Prieta compared to the rate before, which worsens the statistical results because the calculated static-stress changes require an increase in rate at XMR. It would be desirable to discover some objective criterion for choosing the averaging interval, but in the absence of such a criterion perhaps the best that can be done is to try a range of reasonable intervals to demonstrate that any results obtained do not depend strongly on the choice of interval length.

The best overall relationship between fractional 1-year average rate changes and applied static stress changes from table 6 can be expressed as $\Delta V/V_0 \approx (8 \text{ bars}^{-1})\Delta\tau$, where $\Delta\tau$ is in bars, although multipliers obtained range from 4 to 9 bars^{-1}. This is not a very general relationship because it is tied to a 1-year averaging window, but the data on the whole do not seem adequate to support a more complex relation. The data from XHR and CWC might be good enough to warrant a fit to some of the empirical relations described below, but we have not done this.

COEFFICIENT OF APPARENT FRICTION

In correlating microseismicity rate changes with Coulomb failure function changes, Reasenberg and Simpson (1992, and this chapter) found that the best correlation was obtained for low assumed values of the apparent coefficient of friction μ'. (In the terminology used by Reasenberg and Simpson (this chapter), the apparent coefficient of friction is the value inferred by neglecting pore fluid pressure changes.) The absence of any significant relationship between creep-rate changes and calculated static stress changes reported in the previous section is consistent with a low value of μ'.

As another way to examine this, we correlated the Coulomb stress for different values of μ' with the fractional rate change. Values of correlation coefficient ρ are weakly

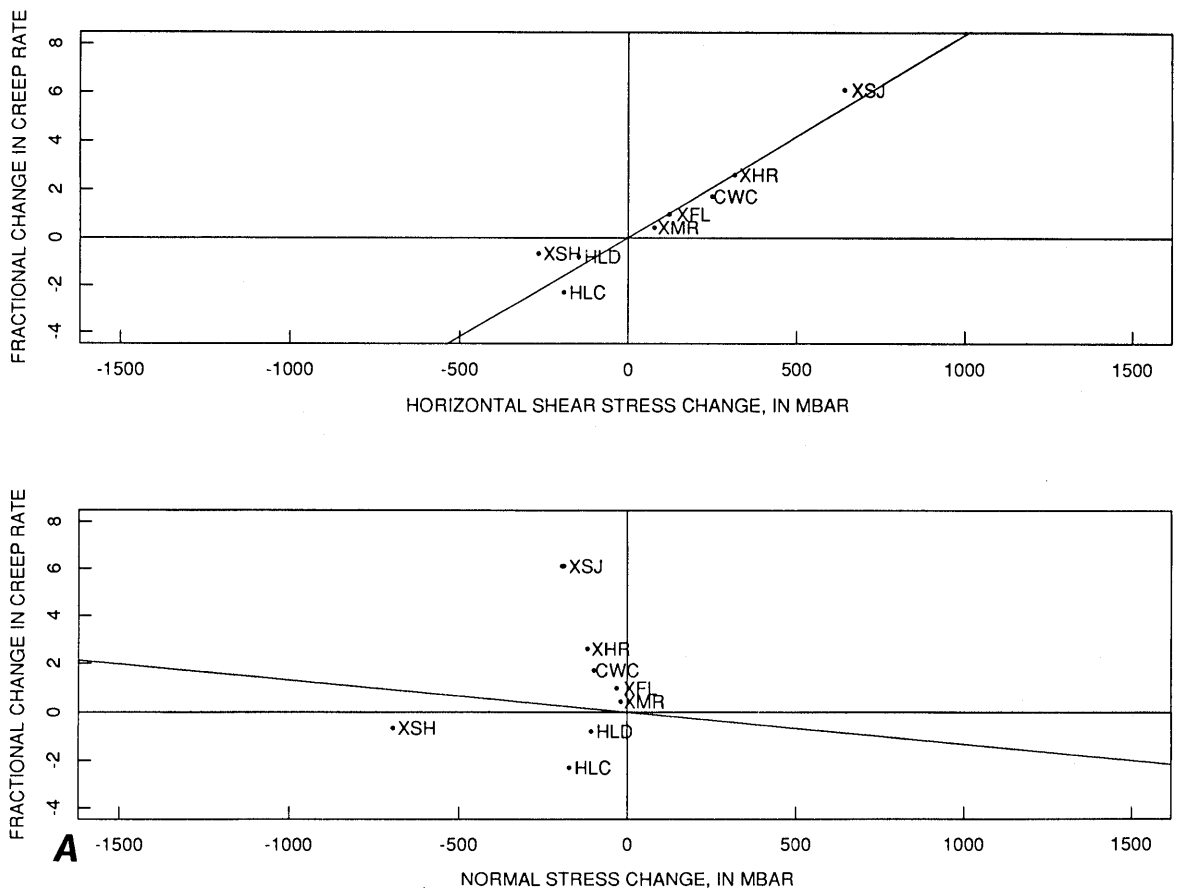

Figure 10.—Comparison of the fractional change in 1-year average creep rate at the time of Loma Prieta earthquake with calculated static stress changes for the three Loma Prieta slip distributions: *A*, Lisowski and others (1990), *B*, Marshall and others (1991), *C*, Beroza (1991). Best fit line passing through the origin is also shown (see table 4 for slopes).

but systematically peaked at low values of the apparent coefficients of friction μ' (fig. 13). The correlation coefficient ρ improves slightly if we delete all values of Coulomb stress less than 0.05 bars. In both cases the correlation is significant at the 95-percent confidence level, although the slight differences for neighboring values of μ' in figure 13 are not likely to be very significant.

CREEP RATE VERSUS STRESS LAW

It would be very desirable to have a rheological law that would allow us to predict how a creeping fault would respond to applied stresses. The calculated stress distributions discussed in the next section suggest that inferring information about such a law from the response of a single creepmeter to a single earthquake will not be easy.

Nason and Weertman (1973) pointed out that although the geometry of fault creep events requires an upper yield point behavior on the part of the fault gouge, a unique constitutive law cannot be inferred from the shape of the creep events alone. Nonetheless, a number of authors have attempted to infer parameters for various plausible types of creep laws by looking at creep events or afterslip decay.

Crough and Burford (1977) used a power law fault-zone rheology to relate the shapes of individual creep events with stress. The power law is

$$dU/dt = C\tau^n,$$

and the resulting displacement for creep events is given by

$$U(t) = U_f\left[1 - 1\Big/\left\{Ct(n-1)U_f^{n-1} + 1\right\}^{1/(n-1)}\right],$$

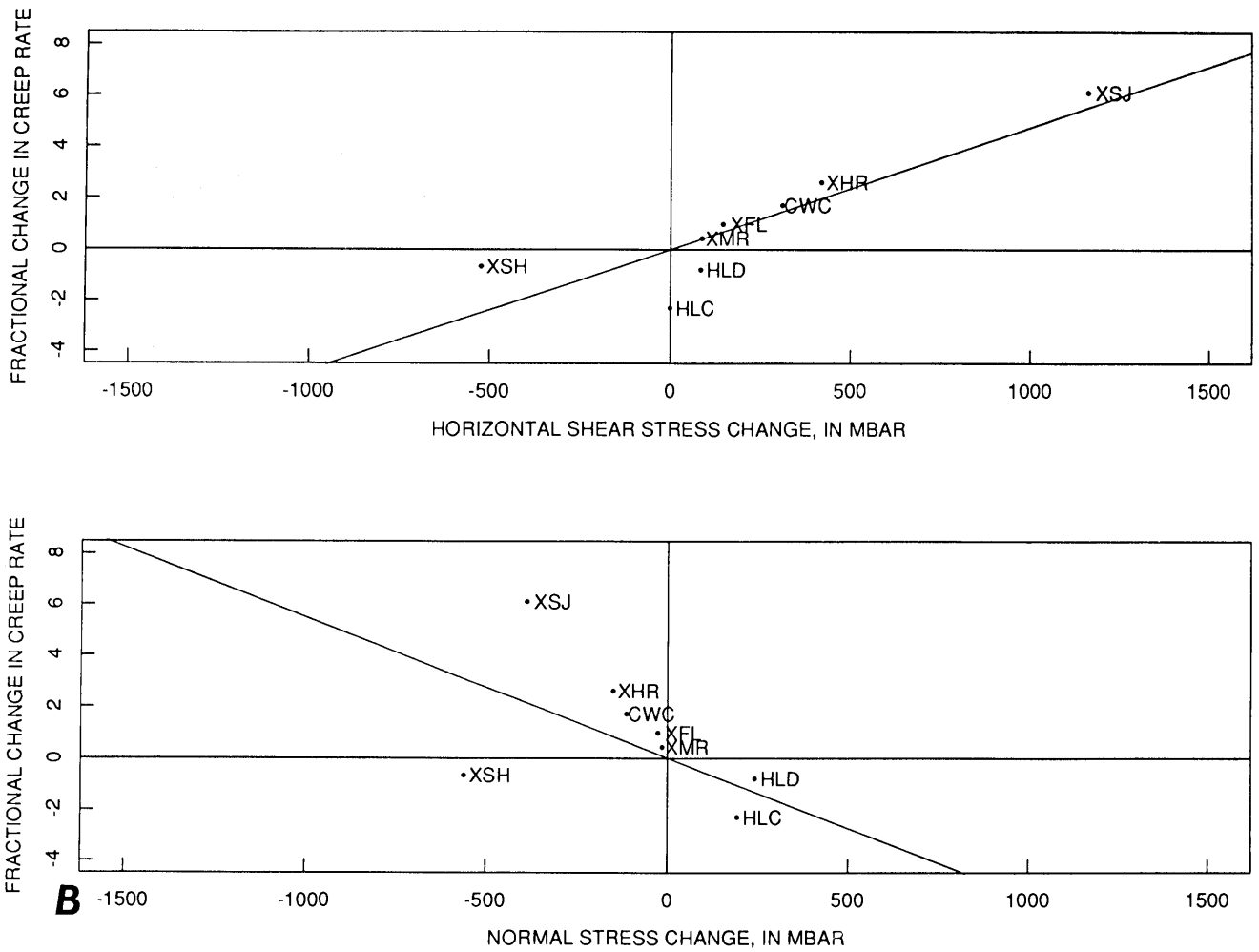

Figure 10.—Continued

where $U(t)$ is the displacement at time t after the onset of the creep event, τ is the driving stress, U_f is the final displacement, C is a constant of proportionality, and n is the power law exponent. Wesson (1987, 1988) used this law for his discussions of fault dynamics and Bilham (1989) used it to fit afterslip data to the 1987 Superstition Hills, California, earthquake. Although the shapes of the Loma Prieta perturbation at XHR and CWC (fig. 14) approximate the shapes of the classic creep event, the shapes of the perturbation at the remaining six sites are far from classic. Wesson (1988) has simulated composite events with somewhat similar shapes to those seen at XSJ and XMR in a model using multiple interacting slip patches, each obeying a power-law rheology.

We note that the power law rheology as written, if applied to the fault at all depths, does not take into account the possibility of a sign change in τ at some depths that might temporarily reverse the creep direction. A better version might be written

$$dU/dt = C\tau|\tau|^{n-1}.$$

For small changes in stress, the power-law yields

$$\frac{\Delta V}{V} = n\left(\frac{\Delta\tau}{\tau}\right),$$

where ΔV is the change in creep rate and $\Delta\tau$ is the change in driving stress, which motivated our use of the fractional creep rate change in the previous section. Comparison with observations (table 6) yields the result that $n/\tau \approx 8$ bars^{-1}.

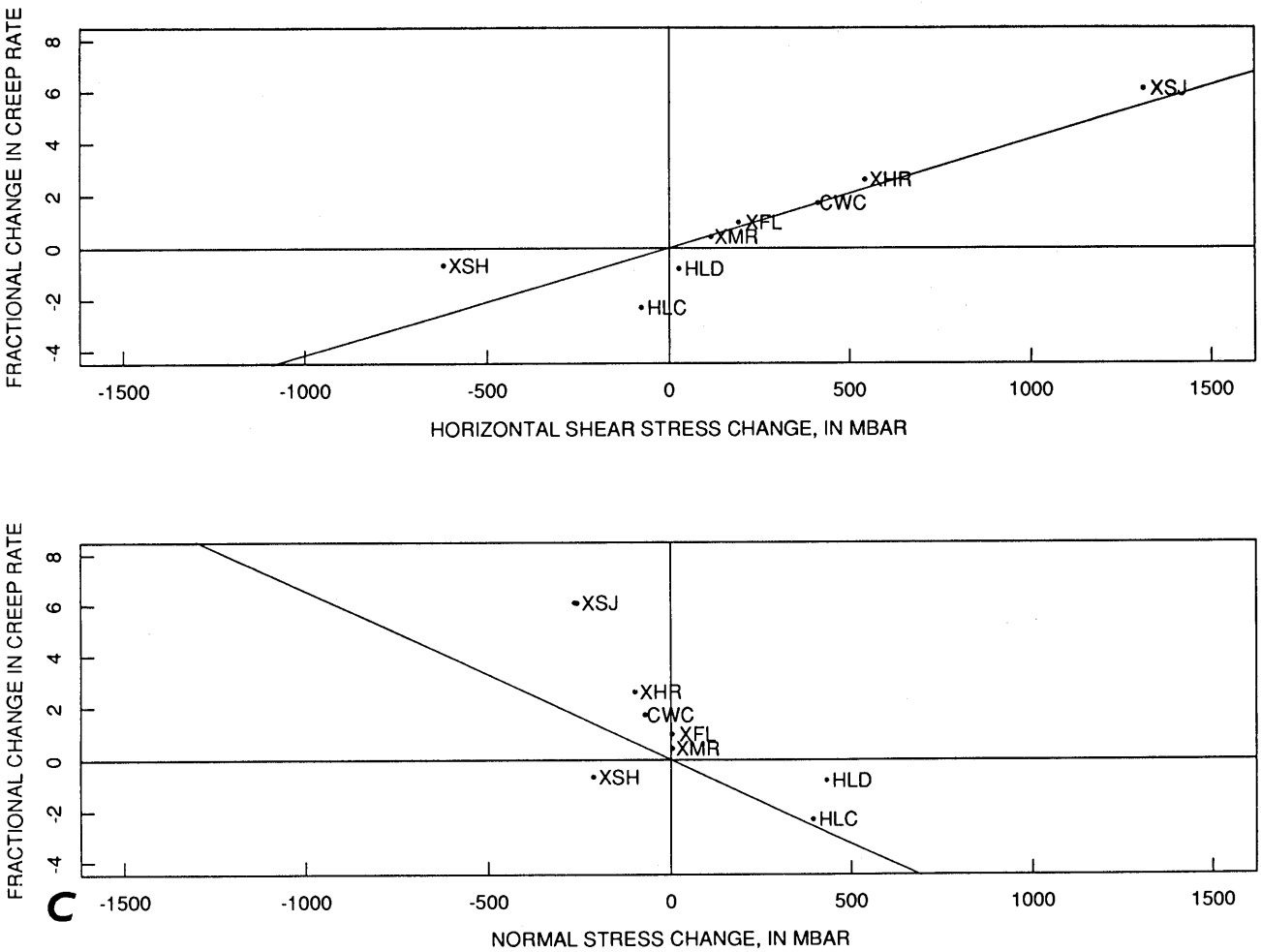

Figure 10.—Continued

Table 5.—*Values used in dislocation models of the six earthquakes*

[Negative horizontal-slip value indicates left-lateral offset; positive values, right-lateral. Negative dip-slip value indicates reverse faulting. Earthquake information from Oppenheimer and others (1990).]

date	name	M	no.	lon (deg)	lat (deg)	depth (km)	len. (km)	ht. (km)	strike (deg)	dip (deg)	horiz slip (m)	dip slip (m)
741128	Thanksgiving Day	5.1	1	121.46	36.92	4.5	1	1	33	90	-1.5	0
790806	Coyote Lake	5.9	1	121.53	37.10	6.0	13	8	335	90	0.2	0
840424	Morgan Hill §	6.2	324	121.61	37.22	-	27	12	328	90	0.24§	0
860126	Tres Pinos	5.3	1	121.28	36.80	7.5	1	1	353	83	3.0	0
891018	Loma Prieta †	7.0	1	121.91	37.06	11.2	37	13.3	136	70	1.66	-1.19
900418	Chittenden	5.4	1	121.64	36.94	4.8	1	1	312	90	4.2	0

M = local magnitude

no. = number of elements in dislocation model

depth = depth to center of model

len. = horizontal length of rectangular dislocation surface

ht. = down-dip dimension of rectangular dislocation surface

strike, dip = orientation of rectangular dislocation surface

horiz. slip = component of slip in horizontal direction

dip slip = component of slip in down-dip direction

§ Model based on Harzell and Heaton (1986) used by Oppenheimer and others (1988). Slip value is average.

† This is the Lisowski model described in Simpson and Reasenberg (1994)

We can infer a value for the "average" ambient stress on the fault plane under the creepmeters by substituting likely values for n. Crough and Burford (1977) report values of n between 1.0 and 2.5 with an average of 1.6 inferred from typical creep events. For such values, τ would lie between 0.1 and 0.3 bars, which seems quite small but which may represent average stress levels at the shallow depths most likely to be reflected in the first year of creep rate change.

Sharp and Saxton (1989) proposed an empirical law to describe the time-evolution of afterslip observed on the Superstition Hills fault after two earthquakes in November 1987

$$U(t) = U_f\left(\frac{Bt}{1+Bt}\right)^c$$

where $U(t)$ is displacement at time t after the earthquake, and U_f, B, and c are constants. (L. Wennerberg, oral commun., 1993, has proposed a refined and better-fitting version of this empirical law.) Boatwright and others (1989) discuss an inversion method to infer the three parameters in the law from field data.

Scholz (1990) and Marone and others (1991) assumed a relation based on constitutive laws developed by Dieterich (1979, 1981), Ruina (1983), and Rice and Gu (1983) to explore the nature of afterslip curves. Their starting constitutive relation is

$$\tau_{SS} = \tau_* + (A-B)\ln(V/V_*),$$

where τ_{ss} is steady state frictional strength, V is sliding speed, A–B is the friction rate parameter, and τ_* is the strength for steady state sliding at speed V_*. The afterslip displacement $U_p(t)$ at time t after the earthquake is given by

$$U_p(t) = \frac{A-B}{k}\ln\left[\left(\frac{kV_{CS}^S}{A-B}\right)t+1\right] + V_o t,$$

where k is the thickness averaged stiffness for the velocity strengthening region, V_{CS}^S is the thickness-averaged coseismic slip velocity within the velocity strengthening region, and V_o is the long-term slip rate.

There is a difficulty in applying the constitutive relation when V becomes zero or negative. A more general

formulation of the constitutive relation suggested by Dieterich (for example, 1992) can allow for these possibilities.

At depths of several kilometers, we would expect that the imposed shear-stress changes under our creepmeter sites (typically tenths of bars or less) are small compared with the usual shear-stress levels driving these faults. If so, then a linearized form of the above laws relating creep-rate changes and stress changes may be appropriate, and the data provided by the creepmeters may not be adequate to distinguish among the various laws or, in fact, to distinguish them from a linear viscous response. The fact that the three sites that were close to regions where the fault surface had LL shear-stress applied actually went LL for varying periods after Loma Prieta suggests that the usual shear-stress levels in the upper meters or kilometers are normally quite small, and that the rheological laws governing this depth range on the fault can probably not be linearized. The behavior of the Middle Mountain creepmeter near Parkfield after the Coalinga earthquake (Mavko and others, 1985; Simpson and others, 1988) provides another example of such behavior.

Clearly, more work needs to be done to propose and test creep-rate laws with the appropriate depth-dependent behaviors, in order to explain the perturbations at these creepmeters. One benefit of such a law is the ability to calculate synthetic creep records at various sites based on the influences of nearby earthquakes. When such a law is calibrated, it can also be used to infer the existence of stressing not obviously associated with seismicity, but perhaps caused by the passage of aseismic tectonic waves. Gwyther and others (1992) describe a post-Loma Prieta shear-strain anomaly near San Juan Bautista recorded on a tensor strainmeter that could perhaps be used in conjunction with creep data to constrain a fault rheology.

If indeed the creep rates are responding to static stress changes caused by earthquakes, including earthquakes on other faults, this raises the question as to whether the effect is shallow or extends to depth. The creepmeters, if they are sitting over low-friction shallow cracks, could just be acting as sensitive strainmeters. The observation that microseismicity rates on Bay Area faults also responded to static stress changes after the Loma Prieta earthquake (Reasenberg and Simpson, 1992), suggests that

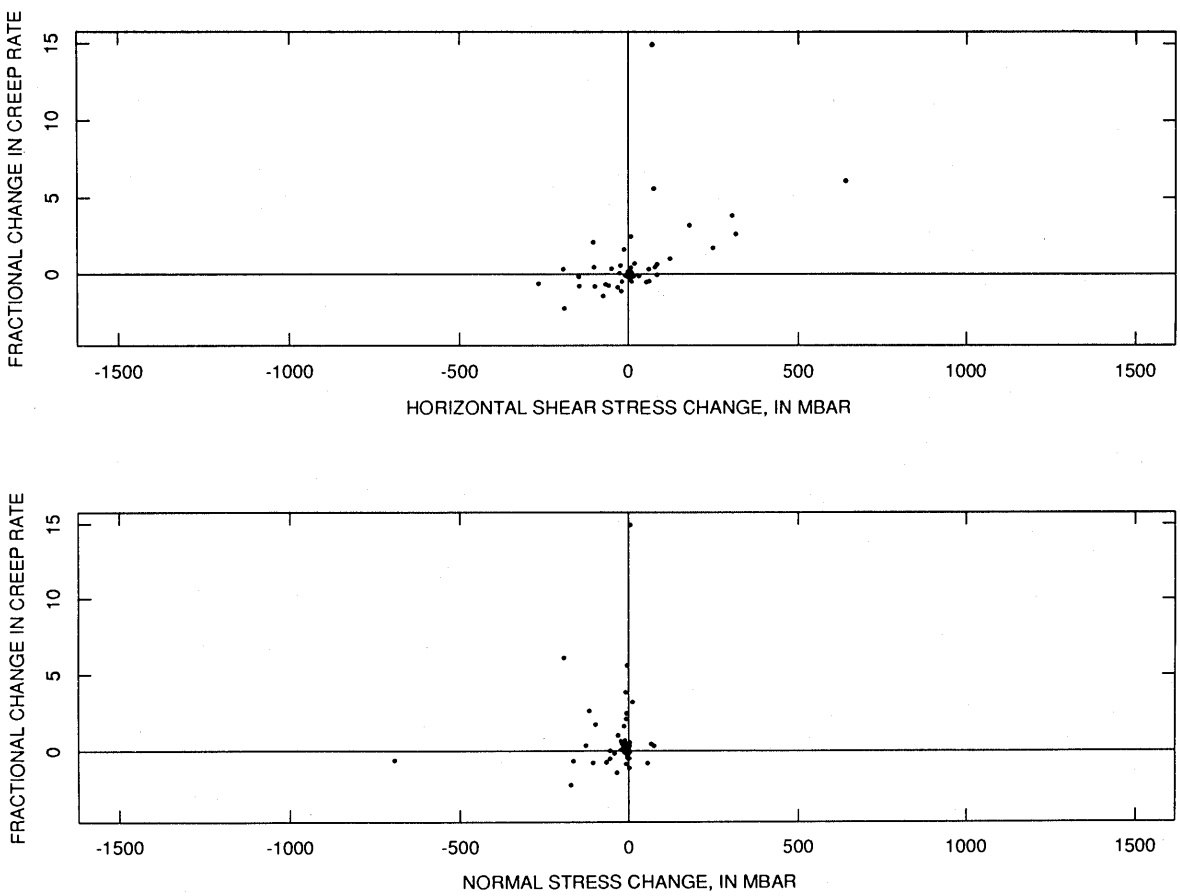

Figure 11.—Comparison of the fractional change in 1-year average creep rate at the times of six earthquakes with calculated static stress changes for simple dislocation models of the earthquakes.

some part of the observed changes in surface creep-rates reflect changes in slip rate at seismogenic depths.

We have not attempted to fit any of these laws to the Loma Prieta perturbations displayed in figure 14, partly because these perturbations are not very cleanly defined, and partly because we believe that the perturbations represent a composite response to sometimes complex stress distributions. We will instead attempt to use some simple dislocation models to put bounds on the total amount of perturbed slip that might occur at the various sites, and to estimate the depths from which the slip might be coming as a function of time.

MODELS EXPLORING DEPTH-ORIGIN OF LOMA PRIETA AFTERSLIP

Although it is difficult to infer fault-zone rheology from the available "afterslip" observations, it is possible to estimate the depth to which the earthquake-induced anomalous slip extends. It might be the case, for example, that the afterslip recorded at the creepmeters was a superficial phenomenon, confined to the upper kilometer or two of the crust.

To bound the possible depth to which anomalous slip might extend, we used Okada's (1992) dislocation subroutines and the Loma Prieta slip distribution of Marshall and others (1991) to make a model of the San Andreas and Calaveras faults (fig. 15). Stress changes were calculated at the centers of 2 km by 2 km square dislocation patches extending down to 20 km. We permitted the dislocation squares between the Earth's surface and some chosen depth to slip freely in response to the earthquake-induced static stress changes, so that the stress at their centers was canceled. All squares below the chosen depth were not allowed to slip. No squares farther than 9 km north of creepmeter XSJ were allowed to slip in response to the stress changes. We assumed that the total slip in response to the stress changes would occur instantaneously, although, in fact, the slip must occur in viscous fashion over the space of several years.

The model contains an interruption in the Calaveras fault between HLC and HLD. This discontinuity, although

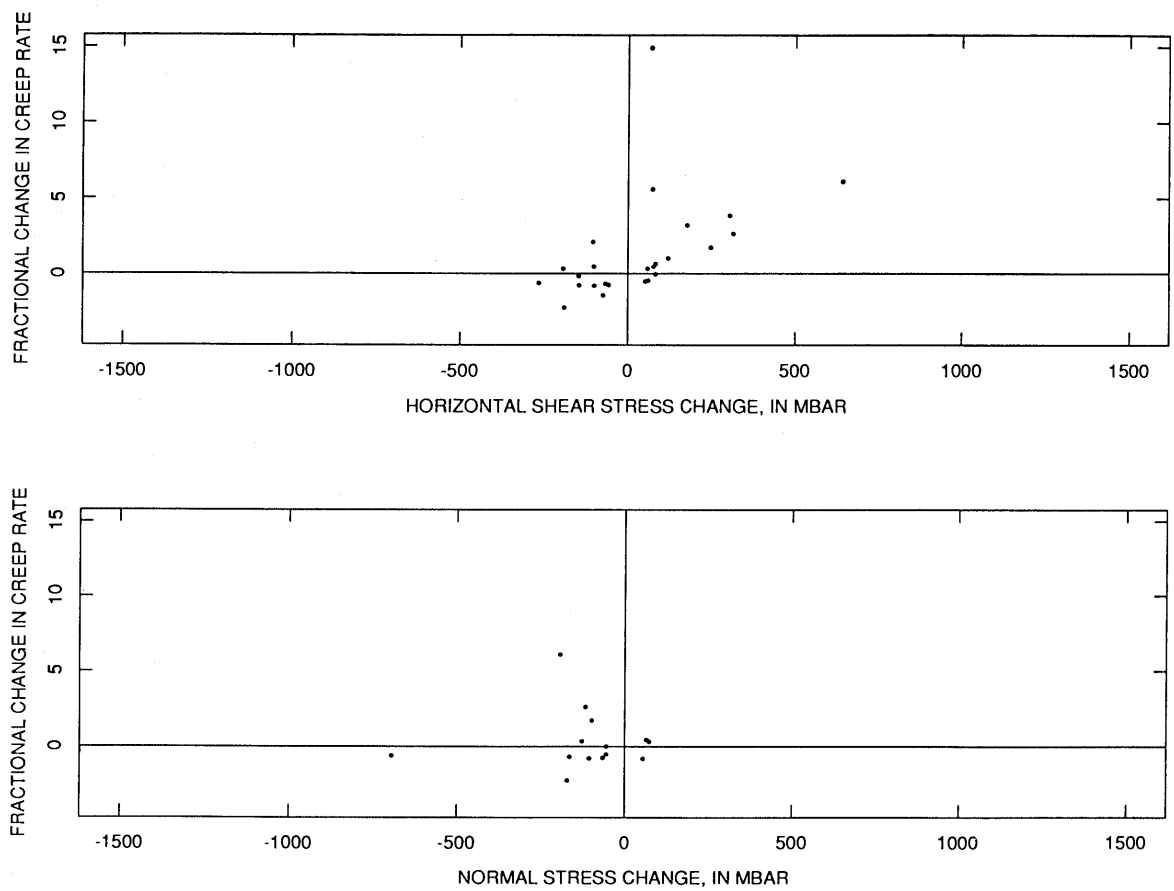

Figure 12.—Comparison of the fractional change in 1-year average creep rate at the times of six earthquakes with calculated static stress changes greater than 0.05 bars in amplitude for simple dislocation models of the earthquakes.

Table 6.—Statistical tests to determine significance of relation between changes in one-year average creep rates and calculated changes in static stress

Earthquake Model(s)	Stress Component	Depth (km)	Two-Sided Chi-sq	Confidence (%)	Rho	N	Conf (%)	Slope0 (bar^{-1})	Slope (bar^{-1})	Intercept
L	horiz. shear	0	8.00	99	0.96	8	99	8.38	8.16±0.97	0.19±0.29
B	"	"	4.44	96	0.90	8	99	4.16	4.14±0.83	0.03±0.48
M	"	"	1.90	83	0.87	8	99	4.75	4.74±1.08	0.01±0.53
L	normal	0	NA	0	0.18	8	<50	-1.32	2.10±4.80	1.39±1.29
B	"	"	0.53	53	-0.71	8	95	-6.55	-7.04±2.88	1.19±0.70
M	"	"	4.44	96	-0.50	8	<80	-5.50	-4.77±3.35	0.53±0.92
L	horiz. shear	10	8.00	99	0.88	8	99	6.50	6.34±1.36	0.88±0.46
B	"	"	8.00	99	0.86	8	99	4.38	4.17±1.02	0.71±0.51
M	"	"	8.00	99	0.85	8	99	5.05	4.79±1.21	0.66±0.52
L	normal	10	NA	0	0.30	8	~50	-0.03	2.48±3.22	1.54±1.16
B	"	"	0.53	53	0.13	8	<50	0.28	0.78±2.50	1.14±1.06
M	"	"	1.90	83	0.08	8	<50	0.74	0.57±2.79	1.12±1.10
ALL	horiz. shear	0	3.88	95	0.48	48	99	9.35	8.81±2.36	0.60±0.34
ALL>0.05	"	"	6.58	98	0.48	25	98	9.39	8.38±3.23	1.06±0.64
ALL	normal	0	0.30	41	0.07	48	<50	-0.82	1.58±3.50	0.83±0.41
ALL>0.05	"	"	0.88	65	0.00	14	0	-0.88	0.02±3.16	0.35±0.68
ALL	horiz. shear	10	6.50	99	0.45	48	99	8.51	8.09±2.36	0.66±0.34
ALL>0.05	"	"	9.38	99	0.46	20	96	8.48	7.72±3.52	1.45±0.79
ALL	normal	10	0.23	36	0.08	48	<50	0.24	1.48±2.57	0.82±0.39
ALL>0.05	"	"	0.20	34	0.13	11	<50	0.28	1.06±2.64	0.52±0.84

Models: L=Lisowski, B=Beroza, M=Marshall, ALL=Lisowski plus 5 other earthquakes, ALL>0.05 = same as ALL except with stress changes less than 0.05 bar omitted.

Depth = depth at which static stress changes were calculated.

Two-sided Chi-sq = Confidence that the fractional creep rate and change in stress component are not independent based on the two-sided Chi sqaured test applied to the respective four-fold table (Sachs, 1982).

Rho = Correlation coefficient for fractional creep rates and static stress change values.

N = number of samples.

Conf = Confidence in best fit line.

Slope0 = Slope of best fit line forced to pass through the origin.

Slope, Intercept = Parameters for best fit line not forced to pass through the origin.

small, will reduce the total slip estimated for nearby sites because of the fault connectivity effect of Bilham and Bodin (1992). (Sites on model faults that are distant from fault ends can slip farther than points close to ends of discontinuous segments.)

The results (table 7, fig. 16) show, for example, that at CWC, a maximum of 5 mm of anomalous surface slip will occur if only the upper 2 km of the fault are able to respond to the stress changes. Figure 14 shows that slip at CWC had exceeded the amount expected at the pre-earthquake creep rate by this amount within several months of the earthquake, even if the coseismic step is not included. Compared to the creep rate in the year before the earthquake, at the beginning of 1993, anomalous excess slip of 30–35 mm had occurred at CWC (fig. 14), requiring anomalous slip to have occurred to depths in excess of 10 km in our model. Note that anomalous slip at some sites is highly dependent on the choice of background interval (compare last two columns in table 7).

Figure 16 suggests that the total anomalous slip at the surface would not get much larger if even deeper levels were allowed to slip. We anticipate that the results obtained from a model where slip could extend to 50 km or 100 km would not be greatly different from the results

observed at 20 km. As of 1 July 1992, observed anomalous slip advances and deficits were estimated to range from –25 to +45 mm for the 8 creepmeters on the San Andreas and Calaveras faults (table 7). These observations fall within the calculated extremes of –28 to +60 mm in the 20-km column of table 7. Because the anomalous slip is continuing, further comparisons will be needed.

The three-dimensional distribution of earthquake-induced shear-stress in our model (fig. 15) suggests that efforts to infer fault-zone rheology from afterslip behavior recorded at the Earth's surface need to take into account the geometry of the stress field both laterally and with depth on the fault surface. For example, using the slip distribution of Marshall and others (1991), the stresses imposed by the earthquake close to HLC and HLD are RL in the upper 6 km and LL from 6 to at least 20 km (fig. 15). The expected signal at these sites would initially be an increase in creep rate as the upper levels of the fault move faster in response to the added RL shear, followed by a slowing creep rate as the LL shear imposed at greater depths and to the north retards creep in these regions—which eventually propagates to the creepmeter sites. One can see suggestions of such behavior in figure 14 at sites HLC and HLD, although the noise level in these records is large enough to cast some doubt on this interpretation.

RETARDATION AND ANOMALOUS BEHAVIOR BEFORE THE EARTHQUAKE?

A number of possible precursors to the Loma Prieta earthquake have been suggested. For example, Fraser-Smith and others (1990) reported anomalous electromagnetic radiation in the days and hours before the earthquake. Gladwin and others (1991) described a strain anomaly near creepmeter XSJ that began mid-way through 1988. Galehouse (this chapter) suggested that some alignment arrays along the Hayward fault might have slowed down in the months before Loma Prieta, and Reasenberg and Simpson (this chapter) reported a possible slowdown in Hayward fault seismicity beginning in 1988.

We have listed five possible creep retardations (table 2, fig. 4) that might have foreshadowed the Loma Prieta earthquake. We examined the retardation at CWC in detail because the behavior of CWC (fig. 17) had been so consistent from about 1975 to 1987 that the retardation appears more convincing than do some of the others. We cannot rule out the possibility that drought conditions caused the slowdown at this site, but in the following discussion we assume a tectonic origin and see where that leads.

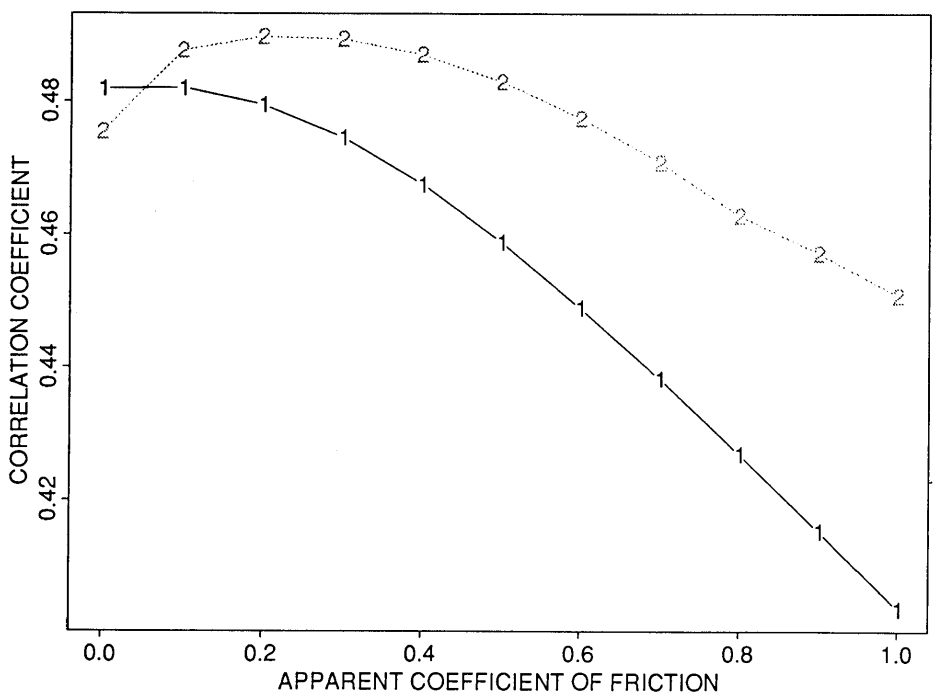

Figure 13.—Correlation coefficient as a function of apparent coefficient of friction for correlation of fractional changes in 1-year creep rates with calculated shear stress change. Curve 1 represents results for all data. Curve 2 is for data with Coulomb failure function values greater than or equal to 0.05 bars.

An important observation is that in spite of possible retardations identified at XHR and XSJ (4 and 15 km northwest of CWC, respectively), the anomaly at CWC does not correspond very well in duration or character with the behaviors of neighboring creepmeters (figs. 2, 3, 4), suggesting that whatever is happening at CWC is mostly local in scope.

The Tres Pinos earthquake of 26 January 1986 ought to have increased the static shear-stress at CWC by about one-third as much as the Loma Prieta event (table 4), and

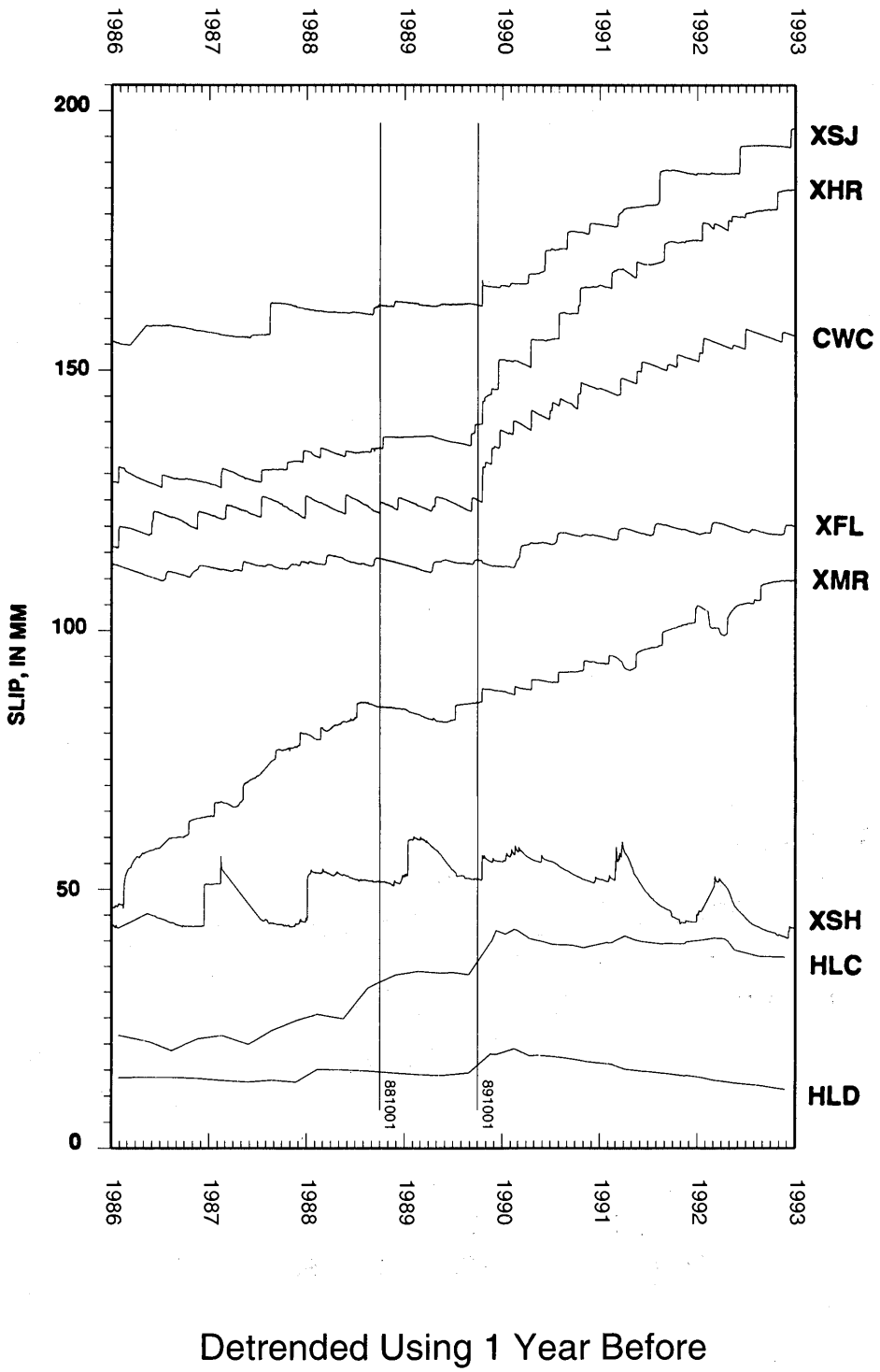

Figure 14.—Plots of the Loma Prieta perturbation for eight creepmeters with 1-year average rates for the year before the Loma Prieta earthquake subtracted to enhance the perturbations.

our model suggests that these stress changes at CWC should have increased the creep-rate just as the Loma Prieta earthquake did, rather than retard it. (A small increase in rate is apparent immediately after the Tres Pinos earthquake, but it was soon followed by the more obvious decrease.)

Another clue is offered in the detailed behavior of CWC during part of the retardation period (fig. 18). Although discrete RL events continued at about the same rate and size as before, a trend change in background movement beginning soon after a M=3 earthquake on 871102 carries the instrument in a LL sense between the RL events. Histograms of creep step sizes for part of this period and for a more normal period are shown in figure 19. Left-lateral movement between RL events at CWC also took place between 1978 and 1981, but such behavior has not been the norm.

Bilham and Behr (1992) proposed a two-layer model for creep observed on the Superstition Hills fault. They described episodic creep events superimposed on a more constant background slip rate, and they proposed that the episodic slip is coming from deeper layers on the fault, while the background slip represents steady sliding in a near-surface layer. One plausible explanation for the CWC retardation would be to have the RL events produced by slip propagating to the surface from some region on the San Andreas fault under or adjacent to CWC. The LL slip between RL events would be produced by stress transferred to the San Andreas fault under CWC by slip on some other fault. The most obvious source is the Tres Pinos earthquake, which was followed by a diffuse set of aftershocks (fig. 20), suggesting regional stress changes in the complex region between the San Andreas and Calaveras faults (Burford and Savage, 1972). Afterslip on the Tres Pinos fault plane itself does not produce LL stresses near CWC with our model geometry. But if the Tres Pinos earthquake triggered RL slip on parts of the subparallel Paicines fault, the resultant stresses at CWC could be LL. Figure 21 shows regions on nearby vertical faults where RL slip (red) would produce LL stress at CWC.

A second scenario would be to have the Tres Pinos earthquake induce slip on some other structure even closer to CWC that could again induce LL stress changes on the San Andreas fault in the near surface under CWC. Small earthquakes define several such structures just to the north and east of CWC (fig. 20). Activation of a small structure close to CWC could explain why the effect is not seen with the same character on other nearby creepmeters. The next creepmeter 4 km to the north (XHR) might in fact see stresses of opposite polarity depending on the geometry and location of the slipping region. Future models will be constructed to test the magnitudes of slip needed on various nearby faults to produce the observed rates of LL stepping.

A third scenario would have regional, mostly aseismic slip on a sub-horizontal detachment structure following

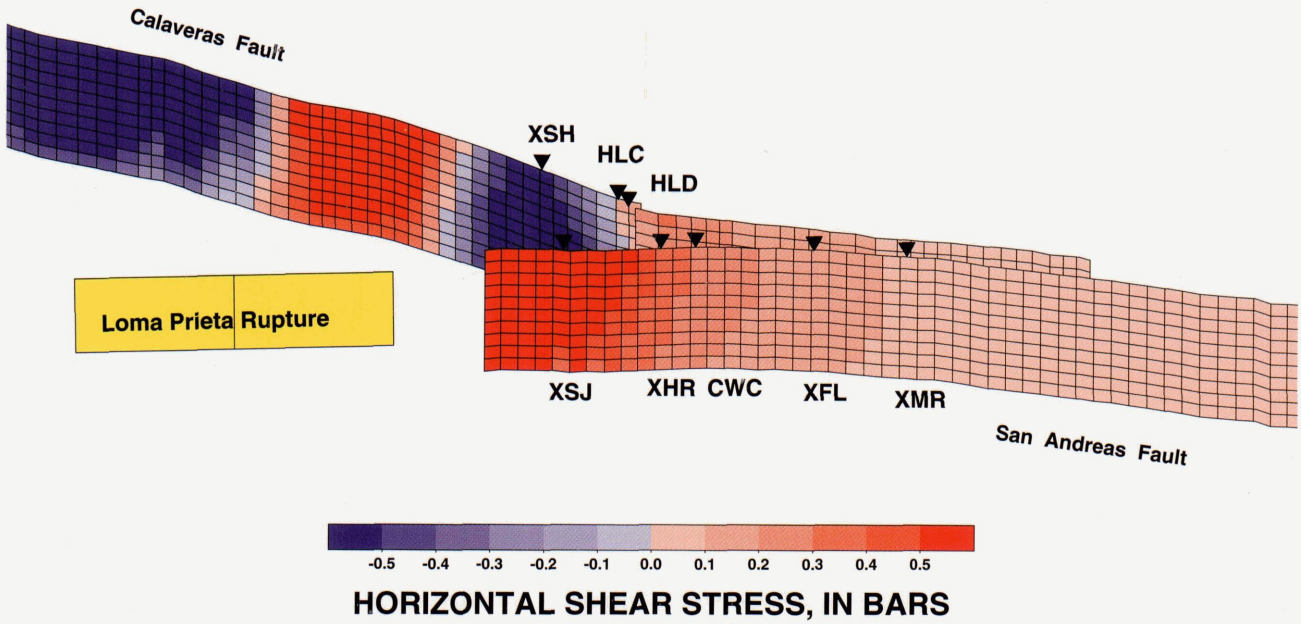

Figure 15.—Geometry of one model used to estimate total size of post-Loma Prieta slip perturbation for various depths to the bottom of the freely slipping layer. This is an oblique view from the southwest, with the San Andreas fault south of the Loma Prieta rupture in the foreground, and the Calaveras fault in the background. Horizontal shear stresses calculated using the Marshall and others (1991) slip distribution are shown plotted in color. Red colors indicate right-lateral stress changes, blue colors indicate left-lateral changes. Each small rectangle is approximately 2-km by 2-km in size. The fault planes in this model extend to a depth of 20 km. Locations of eight creepmeters discussed in the text are shown by triangles.

Table 7.—Total post-Loma Prieta anomalous slip, in millimeters, at eight creepmeters predicted for various depths to the bottom of the freely slipping layer

[Calculations based on a dislocation model using the Loma Prieta slip distribution of Marshall and others (1991). Negative values indicate left-lateral slip; positive values, right-lateral. The values shown in the last two columns are observed anomalous slip as of 1 July 1992 relative to a 1-year average rate before Loma Prieta (figure 14) and relative to a 3-year average rate before Loma Prieta.]

depth->	2km	4km	6km	10km	20km	Observed(1)	Observed(3)
XSJ	18.8	30.8	39.1	49.4	60.3	30	25
XHR	6.2	12.1	17.7	27.5	41.8	45	33
CWC	4.7	9.0	13.5	21.9	35.4	30	33
XFL	1.9	3.5	5.4	9.7	19.4	7	7
XMR	1.2	2.1	3.1	5.6	12.2	20	-10
XSH	-7.0	-11.4	-14.6	-19.7	-28.6	-7	-25
HLC	0.1	-1.2	-2.8	-5.9	-10.5	5	-15
HLD	0.2	-0.7	-1.6	-3.3	-5.7	-5	-5

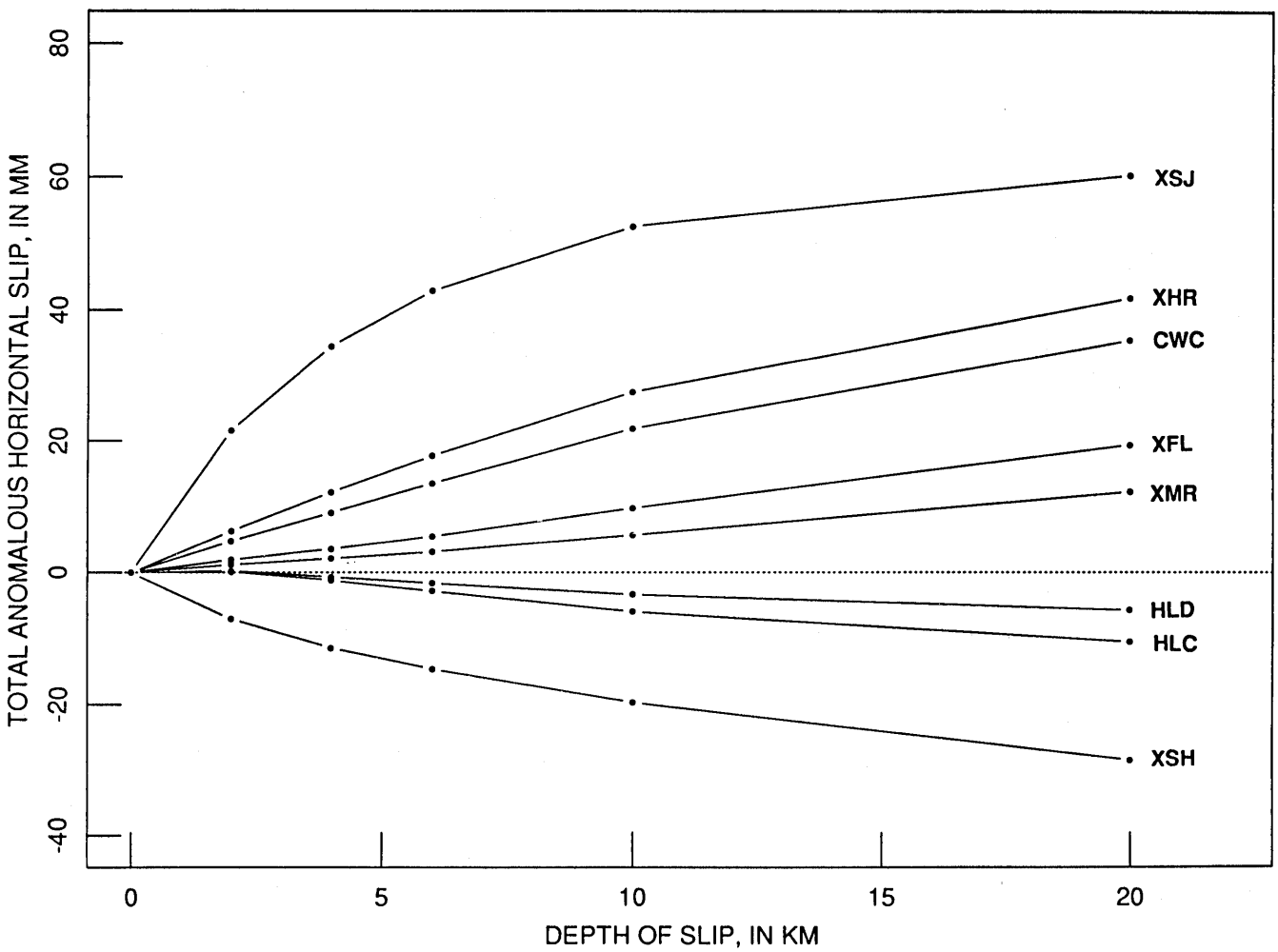

Figure 16.—Plot of total post-Loma Prieta anomalous slip predicted at eight creepmeter sites as a function of the depth to the bottom of the freely slipping layer in model.

the Tres Pinos earthquake. Again, slip in the proper regions of such a structure could probably induce LL stress at CWC.

In all of these scenarios we suggest that the Tres Pinos earthquake caused or accompanied regional stress changes in the triangular wedge between the San Andreas and Calaveras faults which could have been recorded at CWC as LL drift. Thus CWC retardation might have reflected large-scale stress changes that could also have triggered the Loma Prieta earthquake.

Perhaps it is significant that the region south of San Juan Bautista in which most creep retardations have been described (Burford, 1988) contains subparallel fault strands (San Andreas and Paicines/Calaveras). If RL slip were to alternate on these strands, then creepmeters on the moving strand would speed up, while those on the other would

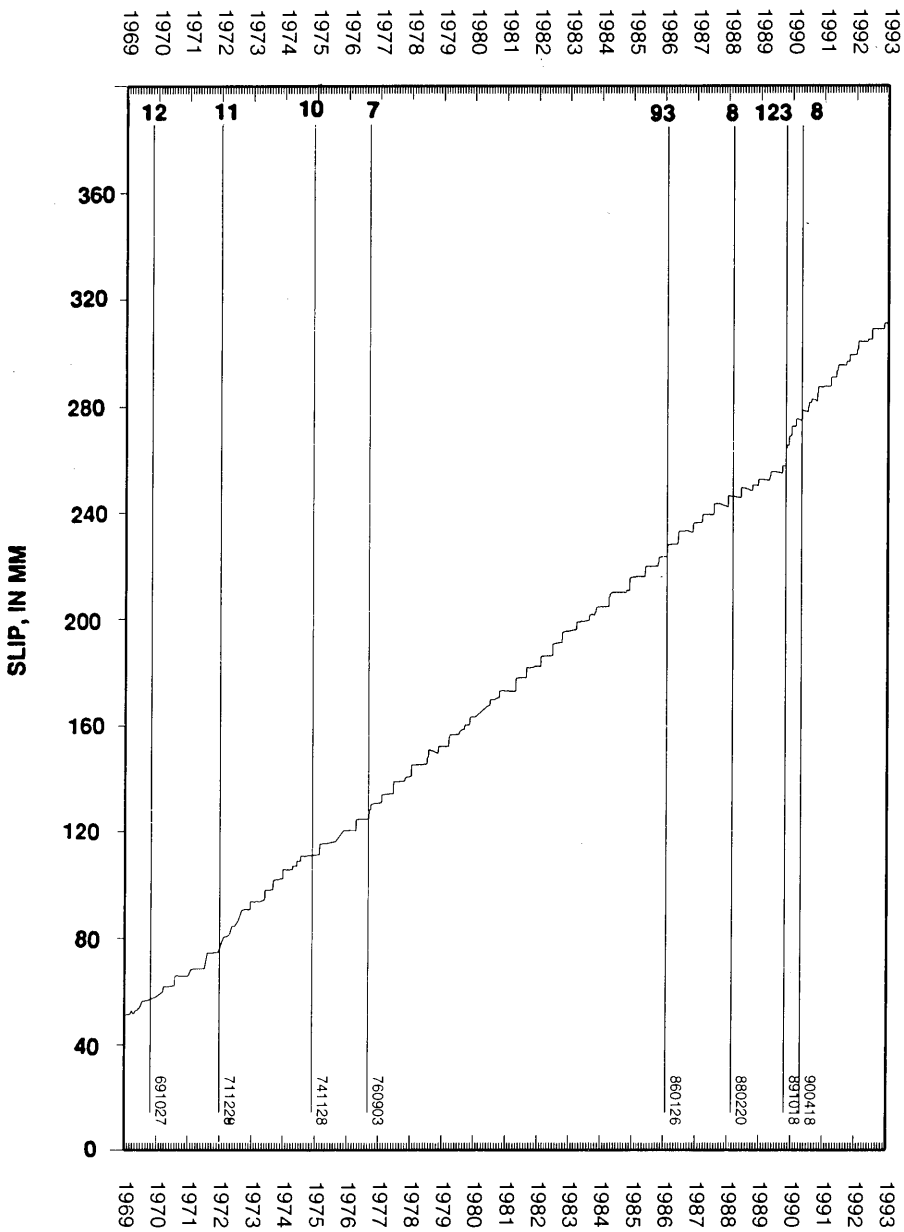

Figure 17.—Plot of creep record for CWC showing times of earthquakes that might have had an effect at this site. Earthquakes were selected from the CALNET catalog by scaling their moment by distance^{-3}, which is the fall-off of maximum stress from a point dislocation, disregarding orientation. Numbers at tops of lines compare potential impact of the earthquake's static stresses (without regard to orientation information, so the value is an upper bound) to the impact expected from an optimally oriented magnitude 4.0 earthquake at a distance of 10 km.

slow down. Perhaps when the slowed strand begins to move again the fault might have become more brittle because it has had a chance to heal, so that if sufficient stress has accumulated to produce an earthquake, then one would be more likely to occur at the end of a retardation period than at other times.

Burford (1988) suggested fault interactions of this sort as a possible explanation for the observed retardations. He also offers other explanations for the phenomenon, including growth of asperities, strain hardening, stress waves, and fluctuation in driving stress. There appears to be some hope of evaluating these possibilities using simple dislocation models to explore plausible sources of imposed stresses.

CONCLUSIONS

Four mechanisms have been proposed to explain triggered slip on faults (Allen and others, 1972; Fuis, 1982; Williams and others, 1988; McGill and others, 1989): (1) static stress changes produced by the earthquake rupture, (2) dynamic stresses from the passage of seismic waves, (3) creep migrating from the earthquake source region, and (4) a regional strain event that produces both aseismic slip on some faults as well as earthquakes on others.

The Loma Prieta earthquake produced coseismic steps on many of the central California creepmeters. We think that these steps were caused by shaking of the sites and

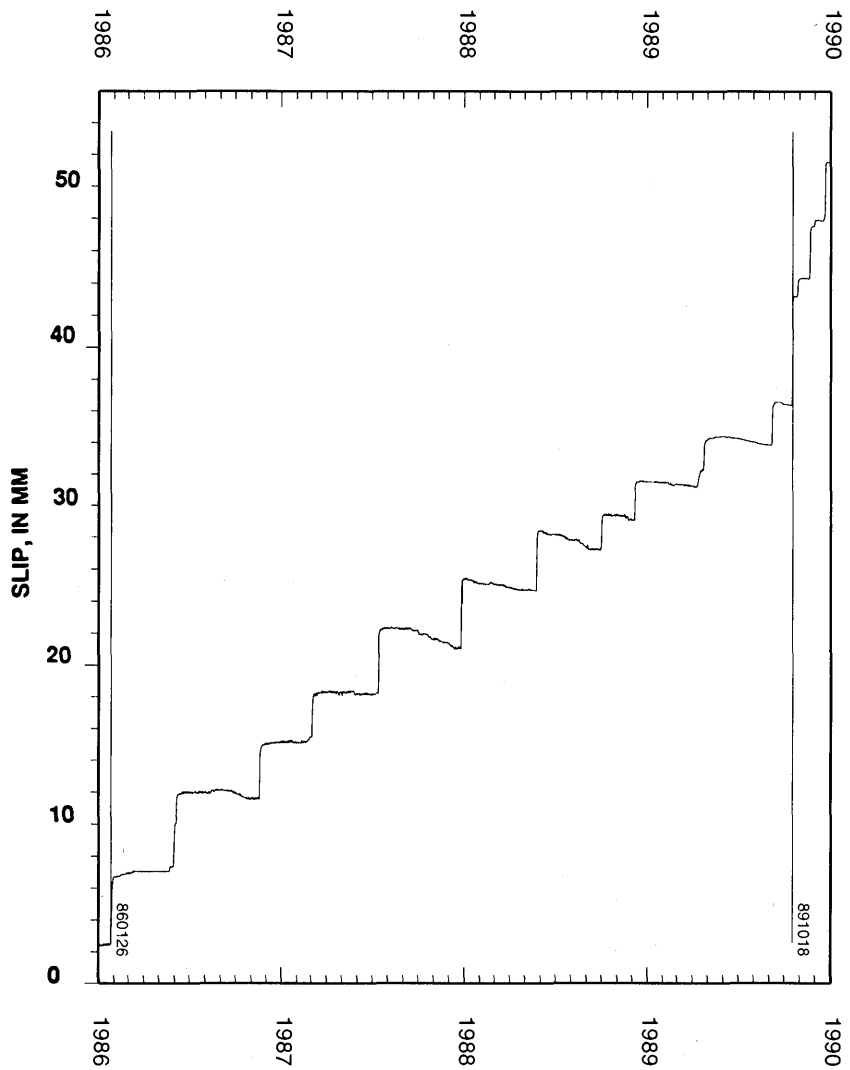

Figure 18.—CWC creep record from 1986–1989 showing pre-Loma Prieta retardation beginning in mid-1987. Times of the Tres Pinos and Loma Prieta earthquakes are indicated by vertical lines.

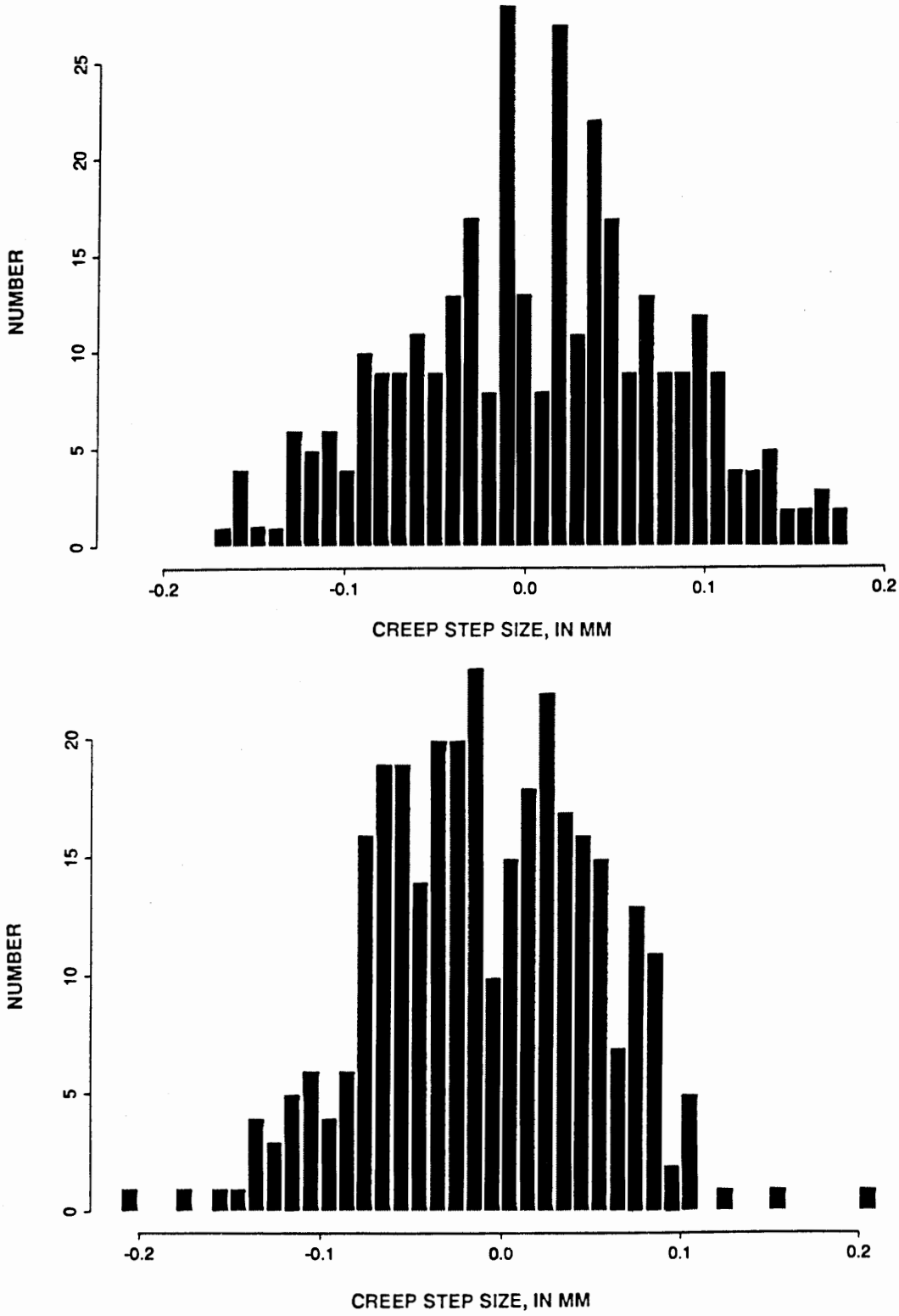

Figure 19.—Histogram of creep step sizes smaller than 0.25 mm from daily data between 1 October 1987 and 1 October 1988 (bottom) compared with a similar histogram for the period from 1 January 1981 to 1 January 1982 (top).

the instruments because they do not seem to correlate very well in either size or direction with calculated static stress changes, favoring explanation (2) above.

The Loma Prieta earthquake produced significant changes in average creep rate at a number of sites on the San Andreas, Calaveras, and Hayward faults (Galehouse, this chapter). These changes are generally consistent in magnitude and sign with the static shear-stress changes, and statistically significant correlation exists for three different models of the Loma Prieta rupture, although the quality of the correlation varies to some degree from model to model. The change in horizontal shear-stress appears to

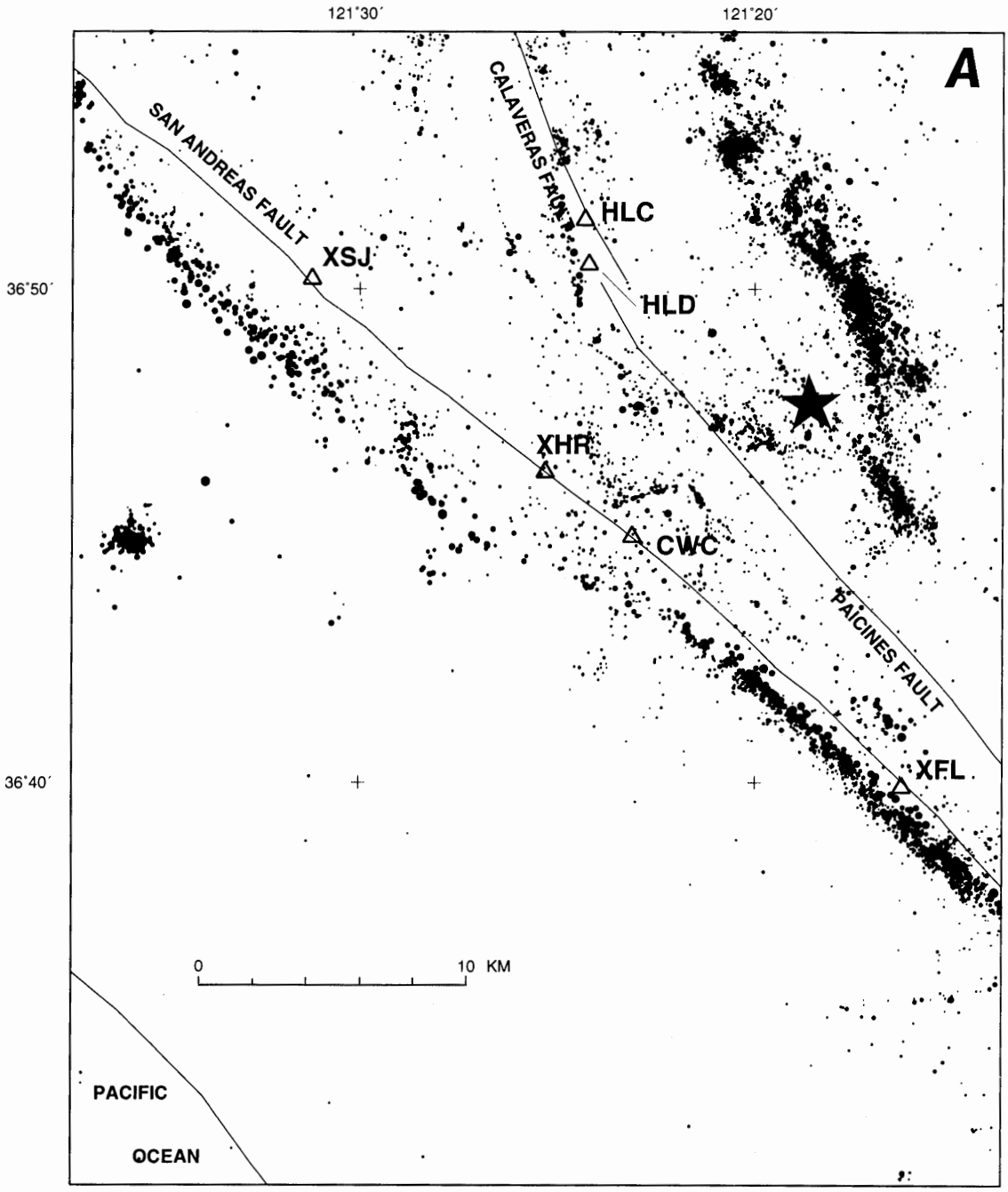

Figure 20.—*A*, Earthquakes in the area of creepmeter CWC during the period from 1983–1988 from the CALNET catalog. *B*, Earthquakes for the same area from 1 January 1987 to 1 September 1988 during the period of retardation observed on creepmeter CWC when left-lateral steps were most obvious. Earthquakes do not lie exactly under the fault traces, probably in part because of deficiencies in the velocity models and in part because the faults may not be vertical. A star marks the epicenter of the 26 January 1986 Tres Pinos earthquake.

be the significant variable. Changes in calculated normal stress do not seem to correlate at significant confidence levels, which suggests that coefficients of apparent friction are low for creep on these faults. A comparison of correlation coefficients for various assumed values of apparent coefficient of friction finds the best correlation for low values in the range 0.0-0.3. These observations seem consistent with explanation (1) above. Explanation (3) might explain rate changes for creepmeters on the San Andreas fault, but hardly seems to explain the rate changes on the Calaveras or Hayward faults.

A three-dimensional boundary element model was used to examine the depths that were being sampled by surface slip. This model can only put approximate limits on the depths that slip is "coming from" but suggests at CWC, for example, that by 1 year after the earthquake at the latest, slip from 10 km depth was being sampled at the surface. Total expected anomalous slip at the creep sites

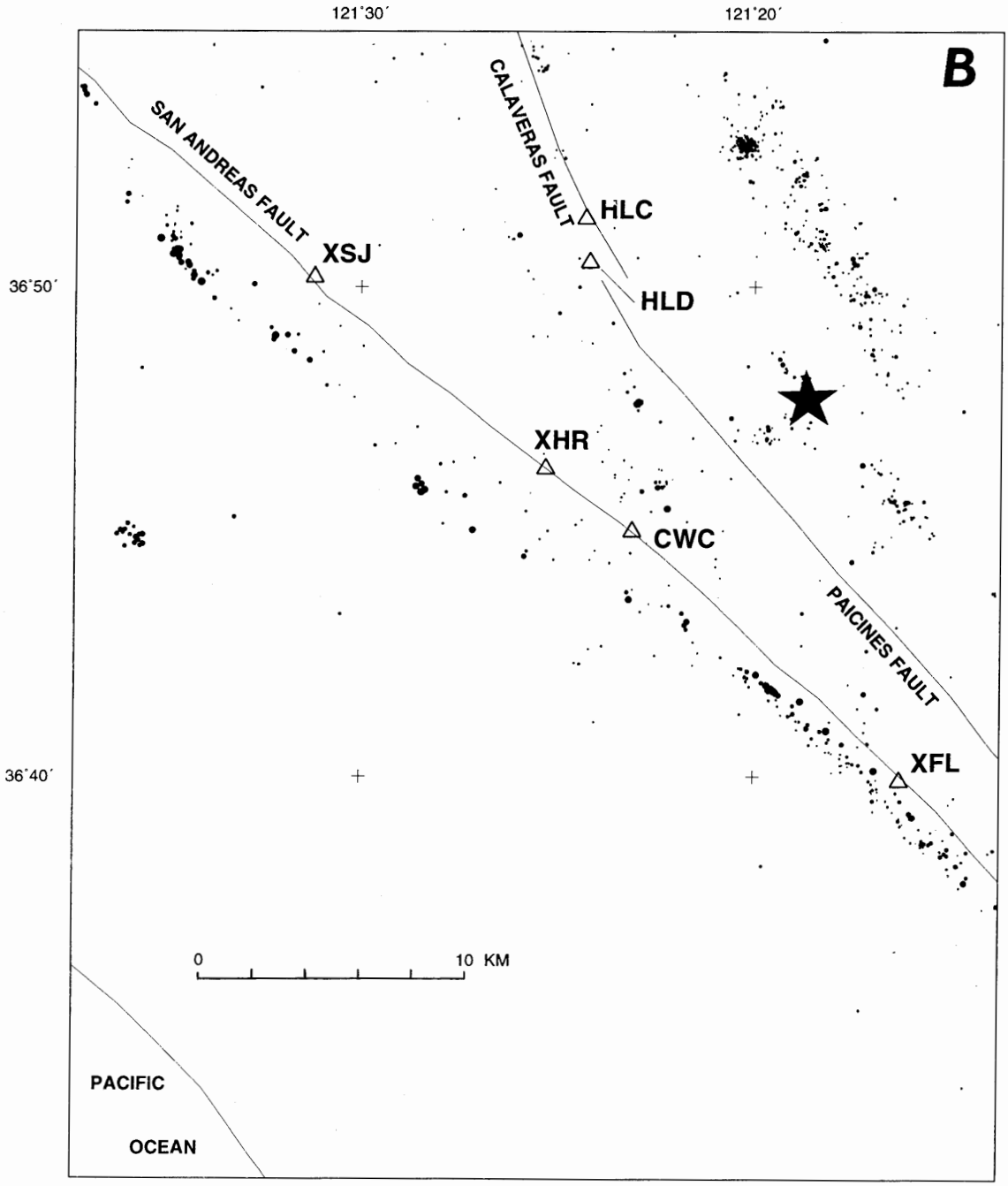

Figure 20.—Continued

can also be estimated from this three-dimensional model. The estimates range in value from –6 mm to +60 mm, which are in fair agreement with observed slip deficits and advances observed at the sites.

Rainfall-induced and seasonal variations in creepmeter behavior are considerable and raise the possibility that some rate variations that might be interpreted as precursors to earthquakes are weather related. Because the drought conditions starting in 1987 were especially severe, creep retardations observed at four sites are suspect to some degree. We attempted to use creep behavior during the earlier drought years of 1976-1977 to calibrate the more recent drought but found no strong link between climate and slip fluctuations.

Burford (1988) has proposed that creep retardations can occur at creep sites before local earthquakes and has tabulated 25 instances of possible retardations on the San Andreas and Calaveras faults between 1957 and 1983. Assuming that a possible retardation at CWC that began in 1986-1987 and ended with the Loma Prieta earthquake might be of tectonic origin, we considered some possible tectonic causes of this retardation. The instrument continued to record large RL events during this interval but small LL slip events in the intervals between the large RL events slowed the total creep-rate. This behavior is similar to that described by Bilham and Behr (1992), who ascribe the large creep steps and the background creep at creepmeter sites on the Superstition Hills fault to different sources. If such an explanation holds here, it would seem likely that the large RL steps that represent fairly normal behavior at CWC come from slip on nearby parts of the San Andreas fault. We propose three scenarios for the origin of the LL drift: slip triggered on the Paicines fault, slip on a nearby structure to CWC revealed in the seismicity, or slip on a regional subhorizontal detachment. In all three scenarios, this movement would be triggered by regional tectonic adjustments following the 26 January 1986 Tres Pinos earthquake in the complex triangle (Burford and Savage, 1972) between the San Andreas and Calaveras faults. If this is correct, then the retardation at CWC could be regarded as a precursor to the Loma Prieta earthquake if these same adjustments ultimately brought that earthquake closer to fruition. This scenario would also seem to give some credence to explanation (4) above as a viable mechanism.

The ability of the creepmeters to respond to Loma Prieta stress changes in predictable ways suggests to us that other regional stress-change information is contained in the creepmeter signals. It becomes increasingly important to understand the effects of weather and seasons on the instruments so that the true signals of tectonic origin can be extracted and interpreted.

ACKNOWLEDGMENTS

This paper was greatly enhanced by discussion with Paul Reasenberg, Evelyn Roeloffs, John Langbein, Roger Bilham, Bob Burford, and Jeff Behr. We are also grateful to Rich Liechti, whose expertise in creepmeter maintenance ensures a foundation for this and other studies, and to Jon Galehouse and his students at San Francisco State

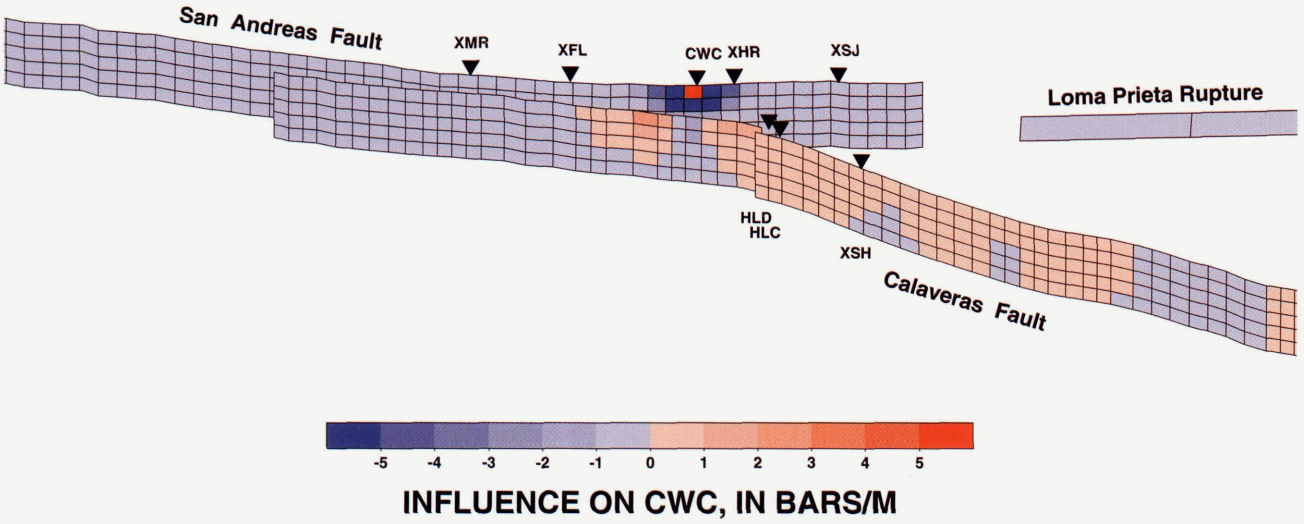

Figure 21.—Oblique view from the northeast with the Calaveras fault in the foreground and the San Andreas fault in the background, showing influence coefficients relative to the rectangular patch under creepmeter CWC. Red indicates fault patches where RL slip would induce LL stress changes at CWC; blue indicates patches where RL slip would induce RL stress changes at CWC. Note that on the parts of the San Andreas fault shown in the figure, LL slip would be required to produce LL stress at CWC, whereas on the Calaveras fault, there are regions (red) where RL slip can produce LL stress at CWC. Each small rectangle is approximately 2-km by 2-km in size. The fault planes in this model extend vertically to a depth of 10 km.

University for reading the creepmeters manually during their surveying expeditions.

APPENDIX A: SITE NOTES

The following section provides further detail on conditions influencing the data from different creepmeters. These aspects are typically site-specific and modulate the way we interpret the long-term record. As such they form the basis of several assumptions in this paper.

XHR: COMBINED DATASETS

The record for XHR used in the study is a composite of data from XHR1 and XHR2. Zero was lost on creepmeter XHR1 when it was destroyed in 1984 (Schulz 1989). To estimate a projected starting point for XHR2 data we calculated the amount of movement in a 245 day window, which is the duration of the gap between instruments, sliding the window every 10 days. The greatest change in a window with continuous data was 9.4 mm for the period ending 811102. We chose instead a correction value of 5.4 mm, which occurred most often in the series of windows. Comparison with creep data from Cienega winery, 3 km southeast of the site supports this as a reasonable adjustment for the level of activity at the time.

CWC: INSTRUMENT CHARACTERISTICS AND RAINFALL

At the winery, creepmeters actually measure offset of adjacent concrete floor slabs separated by the fault trace. Individual rainstorms produce only nominal changes in creep at this site. It is possible that a sustained drought might be expressed as a decrease in the background slip pattern such that episodic events, an indication of slip at depth, would be of normal amplitudes, while inter-event slip could be more sensitive to changing conditions in the shallow soil. De-coupling between the instrument and the fault at this site makes the association between drought and slip deficit tentative at best. In fact, we could argue that the retardation seen at the winery from 1987 to 1989 is caused by the same phenomenon that produced the slip deficit at XHR from late 1988 to September 1989. Perhaps both sites were responding to drought. Alternatively, these instruments may have been sensing a local perturbation in fault activity that was overridden by the Loma Prieta earthquake.

Another instrument at the winery, CWN, is not included in this study. At this creepmeter, located about 30 meters northwest of CWC, an obstruction gradually developed inside the instrument enclosure which inhibited the amount of movement recorded. Approximate onset of this condition is difficult to determine, and the slip released when the problem was corrected in February 1990 was insufficient to resolve the discrepancy between what was recorded on CWN and what was observed on CWC. Prior to 1987 the two instruments tracked each other very well, both in rate of slip and in creep event characteristics—onset, duration, and amplitude.

XSH: SITE MODIFICATIONS AND RAINFALL

In spring 1986 a new creepmeter was installed at Shore Road, slightly south of the original site and spanning an additional five meters of fault zone (Schulz 1989). The anchor pier of the new instrument is now within a few meters of an adjacent slough embankment. The stronger RL movement occurring during winter and spring may be related to increased movement of the anchor pier during wet weather. The fact that this pattern of activity was not seen at the site before 1987 adds credence to this account.

REFERENCES CITED

Allen, C.R., Wyss, M. Brune, J.N., Grantz, A., and Wallace, R.E., 1972, Displacements on the Imperial, Superstition Hills and the San Andreas faults triggered by the Borrego Mountain earthquake, *in* The Borrego Mountain earthquake of April 9, 1968: U.S. Geological Survey Professional Paper 787, p. 87–104.

Behr, J., Bilham, R., Bodin, P., Burford, R.O., and Burgmann, R., 1990, Aseismic slip on the San Andreas fault south of Loma Prieta: Geophysical Research Letters, v. 17, p. 1445–1448.

Beroza, G.C., 1991, Near-source modeling of the Loma Prieta earthquake: Evidence for heterogeneous slip and implications for earthquake hazard: Bulletin of the Seismological Society of America, v. 81, p. 1603–1621.

Bilham, R., 1989, Surface slip subsequent to the 24 November 1987 Superstition Hills, California, earthquake monitored by digital creepmeters: Bulletin of the Seismological Society of America, v. 79, p. 424–450.

Bilham, Roger, and Behr, Jeffrey, 1992, A two-layer model for aseismic slip on the Superstition Hills fault, California: Bulletin of the Seismological Society of America, v. 82, p. 1223–1235.

Bilham, Roger, and Bodin, Paul, 1992, Fault zone connectivity: Slip rates on faults in the San Francisco Bay Area, California: Science, v. 258, p. 281–284.

Bilham, Roger, and Williams, Patrick, 1985, Sawtooth segmentation and deformation processes on the southern San Andreas fault: Geophysical Research Letters, v, 12, no. 9, p. 557–560.

Boatwright, John, Budding, K.E., and Sharp, R.V., 1989, Inverting measurements of surface slip on the Superstition Hills fault: Bulletin of the Seismological Society of America, v. 79, p. 411–423.

Breckenridge, K.S., and Burford, R.O., 1990, Changes in fault slip near San Juan Bautista, California before the October 17, 1989 Loma Prieta earthquake—A possible precursor?: Eos, Transactions, American Geophysical Union, v. 71, p. 1461.

Burford, R.O., 1972, Continued slip on the Coyote Creek fault after the Borrego Mountain earthquake, in The Borrego Mountain Earthquake of April 9, 1968: U.S. Geological Survey Professional Paper 787, p. 105–111.

———1988, Retardations in fault creep rates before local moderate earthquakes along the San Andreas fault system, central California: Pageoph, v. 126, p. 499–529.

Burford, R.O., Allen, S.S., Lamson, R.J., and Goodreau, D.D., 1973, Accelerated fault creep along the central San Andreas fault after moderate earthquakes during 1971–1973, *in* Kovach, R.L., and Nur, Amos, eds., Proceedings of the Conference on Tectonic Problems of the San Andreas Fault System: Geological Sciences, Volume XIII, School of Earth Sciences, Stanford University, p. 275–285.

Burford, R.O., and Savage, J.C., 1972, Tectonic evolution of a crustal wedge caught within a transform fault system: Geological Society of America Abstracts with Programs, v. 4, p. 134.

Cohn, S.N., Allen, C.R., Gilman, R., and Goulty, N.R., 1982, Preearthquake and postearthquake creep on the Imperial fault and the Brawley fault zone, in The Imperial Valley, California, Earthquake of October 15, 1979: U.S. Geological Survey Professional Paper 1254, p. 161–167.

Crough, S.T., and Burford, R.O., 1977, Empirical law for fault-creep events: Tectonophysics, v. 42, p. 53–59.

Dieterich, J.H., 1979, Modeling of rock friction, 1. Experimental results and constitutive equations: Journal of Geophysical Research, v. 84, p. 2161–2168.

———1981, Constitutive properties of faults with simulated gouge, in Carter, N.L., Friedman, M., Logan, J.M., and Stearns, D.W., eds., Mechanical Behavior of Crustal Rocks: American Geophysical Union, Geophysical Monograph 24, p. 103–120.

———1992, Earthquake nucleation on faults with rate- and state-dependent strength: Tectonophysics, v. 211, p. 115–134.

Fagerson, S.H., Louie, J.N., Allen, C.R., Sieh, K.E., 1986, Measurements of triggered slip on the southern San Andreas fault associated with the North Palm Springs earthquake: Eos, Transactions, American Geophysical Union, v. 67, p. 1090.

Fraser-Smith, A.C., Bernardi, A., McGill, P.R., Ladd, M.E., Helliwell, R.A., and Villard, O.G., Jr., 1990, Low-frequency magnetic field measurements near the epicenter of the Ms 7.1 Loma Prieta earthquake: Geophysical Research Letters, v. 17, p. 1465–1468.

Fuis, G.S., 1982, Displacement on the Superstition Hills fault triggered by the earthquake, in the Imperial Valley, California, Earthquake of October 15, 1979: U.S. Geological Survey Professional Paper 1254, p. 145–154.

Galehouse, J.S., 1990, Effect of the Loma Prieta earthquake on surface slip along the Calaveras fault in the Hollister area: Geophysical Research Letters, v. 17, p. 1219–1222.

———1992, Creep rates and creep characteristics on certain North and East Bay faults: 1979–1992: Programs and Abstracts, Second Conference on Earthquake Hazards in the Eastern San Francisco Bay Area, March 25–29, 1992, California State University, Hayward, p. 24.

Gladwin, M.T., Gwyther, R.L., Higbie, J.W., and Hart, R.G., 1991, A medium term precursor to the Loma Prieta Earthquake?: Geophysical Research Letters, v. 18, p. 1377–1380.

Goulty, Neil R., and Gilman, Ralph, 1978, Repeated creep events on the San Andreas Fault near Parkfield, California, recorded by a strainmeter array: Journal of Geophysical Research, v. 83, no. B11, p. 5414–5419.

Gwyther, R.L., Gladwin, M.T., and Hart, R.G., 1992, A shear strain anomaly following the Loma Prieta earthquake: Letters to Nature, v. 356, p. 142–144.

Hartzell, S.H., and Heaton, T.H., 1986, Rupture history of the 1984 Morgan Hill, California, earthquake from the inversion of strong motion records: Bulletin of the Seismological Society of America, v. 76, 649–674.

Hudnut, K.W., and Clark, M.M., 1989, New slip along parts of the Coyote Creek fault rupture, California: Bulletin of the Seismological Society of America, v. 79, p. 451–465.

Johnston, M.J.S., Linde, A.T., and Gladwin, M.T., 1990, Near-field high resolution strain measurements prior to the October 18, 1989, Loma Prieta Ms 7.1 earthquake: Geophysical Research Letters, v. 17, p. 1777–1780.

Johnston, M.J.S., Linde, A.T., Gladwin, M.T., and Borcherdt, R.D., 1987, Fault failure with moderate earthquakes: Tectonophysics, v. 144, p. 189–206.

King, C.Y., Nason, R.D., and Burford, R.O., 1977, Coseismic steps recorded on creep meters along the San Andreas fault: Journal of Geophysical Research, v. 82, p. 1655–1662.

Langbein, John, Quilty, Eddie, and Breckenridge, Katherine, 1993, Sensitivity of crustal deformation instruments to changes in secular rate: Geophysical Research Letters, v. 20, no. 2, p. 85–88.

Lisowski, M., Prescott, W.H., Savage, J.C., and Johnston, M.J., 1990, Geodetic estimate of coseismic slip during the 1989 Loma Prieta, California, Earthquake: Geophysical Research Letters, v. 17, p. 1437–1440.

Marone, C.J., Scholz, C.H., and Bilham, R., 1991, On the mechanics of earthquake afterslip: Journal of Geophysical Research, v. 96, p. 8441–8452.

Marshall, G.A., Stein, R.S., and Thatcher, Wayne, 1991, Faulting geometry and slip from co-seismic elevation changes: the 18 October 1989, Loma Prieta, California, earthquake: Bulletin of the Seismological Society of America, v. 81, p. 1660–1693.

Mavko, G. M., 1982, Fault interaction near Hollister, California: Journal of Geophysical Research, v. 87, p. 7807–7816.

Mavko, G.M., Schulz, S., and Brown, B.D., 1985, Effects of the 1983 Coalinga, California, earthquake on creep along the San Andreas fault: Bulletin of the Seismological Society of America, v. 75, p. 475–489.

McClellan, P.H., and Hay, E.A., 1990, Triggered slip on the Calaveras fault during the magnitude 7.1 Loma Prieta, California, earthquake: Geophysical Research Letters, v. 17, p. 1227–1230.

McGill, S.F., Allen, C.R., Hudnut, K.W., Johnson, D.C., Miller, W.F., and Sieh, K.E., 1989, Slip on the Superstition Hills fault and on nearby faults associated with the 24 November 1987 Elmore Ranch and Superstition Hills earthquakes, southern California: Bulletin of the Seismological Society of America, v. 79, p. 362–375.

Nason, R.D., 1973, Fault creep and earthquakes on the San Andreas fault, *in* Kovach, R.L., and Nur, Amos, eds., Proceedings of the Conference on Tectonic Problems of the San Andreas Fault System: Geological Sciences, Volume XIII, School of Earth Sciences, Stanford University, p. 275–285.

Nason, R.D., and, Weertman, Johannes, 1973, A dislocation theory analysis of fault creep events: Journal of Geophysical Research, v. 78, p. 7745–7751.

Okada, 1992, Internal deformation due to shear and tensile faults in a half-space: Bulletin of the Seismological Society of America, v. 82, p. 1018–1040.

Oppenheimer, D.H., Bakun, W.H., and Lindh, A.G., 1990, Slip partitioning of the Calaveras fault, California, and prospects for future earthquakes: Journal of Geophysical Research, v. 95, p. 8483–8498.

Oppenheimer, D.H., Reasenberg, P.A., and Simpson, R.W., 1988, Fault plane solutions for the 1984 Morgan Hill, California, earthquake sequence: Evidence for the state of stress on the Calaveras fault: Journal of Geophysical Research, v. 93, p. 9007–9026.

Reasenberg, P.A., and Simpson, R.W., 1992, Response of regional seismicity to the static stress change produced by the Loma Prieta earthquake: Science, v. 255, p. 1687–1690.

Rice, J.R., and Gu, Ji-cheng, 1983, Earthquake aftereffects and triggered seismic phenomena: Pageoph, v. 121, p. 185–219.

Ruina, A.L., 1983, Slip instability and state variable friction laws: Journal of Geophysical Research, v. 88, p. 10359–10370.

Sachs, Lothar, 1982, Applied statistics—A handbook of techniques: New York, Springer-Verlag, 706 p.

Scholz, C.H., 1990, The mechanics of earthquakes and faulting: Cambridge, U.K., Cambridge University Press, 439 p.

Scholz, C.H., Wyss, M., and Smith, S.W., 1969, Seismic and aseismic slip on the San Andreas fault: Journal of Geophysical Research, v. 74, p. 2049–2069.

Schulz, S.S., 1984, Triggered creep near Hollister after the April 24, 1984, Morgan Hill, California, earthquake, *in* Bennett, J.H., and Sherburne, R.W., eds., The 1984 Morgan Hill, California Earthquake: California Division of Mines and Geology Special Publication 68, p. 175–182.

Schulz, S.S., 1989, Catalog of creep measurements in California from 1966 to 1988: U.S. Geological Survey Open-File Report 78–203, 193 p.

Schulz, S.S., Burford, R.O., and Mavko, B., 1983, Influence of seismicity and rainfall on episodic creep on the San Andreas fault system in central California: Journal of Geophysical Research, v. 88, p. 7475–7484.

Schulz, S.S., Mavko, G.M., Brown, B.D., 1987, Response of creepmeters on the San Andreas fault near Parkfield to the May 2, 1983, Coalinga earthquake: U.S. Geological Survey Professional Paper 1487, p. 409–417.

Schulz, S.S., Mavko, G.M., Burford, R.O., and Stuart, W.D., 1982, Long-term fault creep observations in central California: Journal of Geophysical Research, v. 87, p. 6977–6982.

Sharp, R.V., 1989, Pre-earthquake displacement and triggered displacement on the Imperial fault associated with the Superstition Hills earthquake of 24 November 1987: Bulletin of the Seismological Society of America, v. 79, p. 466–479.

Sharp, R.V., Rymer, M.J., and Lienkaemper, J.J., 1986a, Surface displacements on the Imperial and Superstition Hills faults triggered by the Westmorland, California, earthquake of 26 April 1981: Bulletin of the Seismological Society of America, v. 76, p. 949–965.

Sharp, R.V., Rymer, M.J., and Morton, D.M., 1986b, Trace-fractures on the Banning fault created in association with the 1986 North Palm Springs earthquake: Bulletin of the Seismological Society of America, v. 76, p. 1838–1843.

Sharp, R.V., and Saxton, J.L., 1989, Three-dimensional records of surface displacement on the Superstition Hills fault zone associated with the earthquakes of 24 November 1987: Bulletin of the Seismological Society of America, v. 79, p. 376–389.

Shimada, Seiichi, Sakata, Shoji, and Noguchi, Shin'ichi, 1987, Coseismic strain steps observed by three-component borehole strainmeters: Tectonophysics, v. 144, p. 207–214.

Sieh, K.E., 1982, Slip along the San Andreas fault associated with the earthquake, *in* The Imperial Valley, California, Earthquake of October 15, 1979: U.S. Geological Survey Professional Paper 1254, p. 155–159.

Silverman, S., Mortensen, C., and Johnston, M., 1989, A satellite-based digital data system for low-frequency geophysical data: Bulletin of the Seismological Society of America, v. 79, p. 189–198.

Simpson, R.W., Schulz, S.S., Dietz, L.D., and Burford, R.O., 1988, The response of creeping parts of the San Andreas fault to earthquakes on nearby faults: Two examples: Pageoph, v. 126, p. 665–685.

Smith, S.W., and Wyss, Max, 1968, Displacement on the San Andreas fault subsequent to the 1966 Parkfield earthquake: Bulletin of the Seismological Society of America, v. 58, p. 1955–1973.

Spudich, Paul, Steck, L.K., Hellweg, Margaret, Fletcher, J.B., and Baker, L.M., 1995, Transient stresses at Parkfield, California, produced by the M7.4 Landers earthquake of June 28, 1992: Observations from the UPSAR dense seismograph array: Journal of Geophysical Research, v. 100, p. 675-690.

U.S. Department of Commerce, National Oceanic and Atmospheric Administration. Climatological Data, California. Ashville, NC: National Climatic Data Center, 1970–1992.

Wesson, R.L., 1987, Modelling aftershock migration and afterslip of the San Juan Bautista, California, earthquake of October 3, 1972: Tectonophysics, v. 144, p. 215–229.

———1988, Dynamics of fault creep: Journal of Geophysical Research, v. 93, p. 8929–8951.

Wesson, R.L., Jibson, R.W., Morton, D., Campbell, R.H., and Nicholson, C., 1986, Interpretation of surface cracks and other fault-line surface deformation associated with the North Palm Springs earthquake of July 8, 1986: Eos, Transactions, American Geophysical Union, v. 67, p. 1090.

Williams, P., Fagerson, S., and Sieh, K., 1986, Triggered slip of the San Andreas fault after the July 8, 1986 North Palm Springs earthquake: Eos, Transactions, American Geophysical Union, v. 67, p. 1090.

Williams, P.L., McGill, S.F., Sieh, K.E., Allen, C.R., and Louie, J.N., 1988, Triggered slip along the San Andreas fault after the 8 July 1986 North Palm Springs earthquake: Bulletin of the Seismological Society of America, v. 78, p. 1112–1122.

THE LOMA PRIETA, CALIFORNIA, EARTHQUAKE OF OCTOBER 17, 1989:
EARTHQUAKE OCCURRENCE

AFTERSHOCKS AND POSTSEISMIC EFFECTS

INCREASED SURFACE CREEP RATES ON THE SAN ANDREAS FAULT SOUTHEAST OF THE LOMA PRIETA MAIN SHOCK

By Jeff Behr, Roger Bilham, and Paul Bodin,
University of Colorado, Boulder;
Kate Breckenridge,
U.S. Geological Survey; and
Arthur G. Sylvester
University of California, Santa Barbara

CONTENTS

ABSTRACT

Surface creep rates increased substantially on the northwestern 50 km of the creeping section of the San Andreas fault following the Loma Prieta earthquake. Although postseismic creep southeast of the rupture zone initially resembled previously observed earthquake afterslip, creep rates between October 1990 and September 1992 have remained nearly constant at rates higher than pre-event values. Two-dimensional elastic boundary element models indicate that if the San Andreas and Calaveras faults were frictionless, vertical dislocations, then more than 20 cm of surface slip would be induced on the northwesternmost 20 km of the creeping section in response to strain changes accompanying the Loma Prieta event. Induced additional postseismic surface slip nowhere exceeds 4 cm, indicating that much of the potential fault displacement in the northwestern creeping section has not occurred. Whereas postseismic displacements up to September 1992 have attained only 10 to 20 percent of modeled values, the spatial distribution of postseismic surface slip rate increases reflects the results of these simple models. In particular, potential slip and creep rates are predicted to be much reduced south of the San Andreas' intersection with the Calaveras fault. Changes in borehole strain and creep rates recorded along a 3.1-km-long section of the northwestern San Andreas creeping section provide strong indications of the depths of pre- and post-event shallow surface creep but satisfy a wide range of models in which the fault may be slipping at depth. The substantial difference in creep rate in that region suggests that observed strain changes may be locally enhanced by elastic inhomogeneity or local fault-slip processes.

INTRODUCTION

The Loma Prieta earthquake was not associated with a throughgoing surface rupture even though numerous discontinuous surface cracks were manifest near the surface fault trace (U.S. Geological Survey Staff, 1990). It is possible that distributed shear could have absorbed surface displacements over a several kilometer wide zone, although geodetic data indicate that the Loma Prieta rupture did not reach the surface (Lisowski and others, 1990). In several recent strike-slip earthquakes in California, the amplitude of surface fault displacement has increased in the weeks to years following the main shock (Smith and Wyss, 1968; Burford, 1972; Cohn and others, 1982; Bilham, 1989; Sharp and others, 1989; Williams and Magistrale, 1989). Anticipating the possible development of post-event surface slip, we installed three digital creepmeters (Bilham, 1989) within 2 to 17 days after the Loma Prieta earthquake. Two of these, Madonna Road and Chittenden Bridge, were installed over the southeastern rupture zone, whereas the other, at Nyland Ranch, was installed near the northwestern end of the San Andreas fault creeping section (Behr and others, 1990) (fig. 1).

Although the two instruments over the rupture zone have not recorded significant post-event tectonic slip, the

Nyland Ranch creepmeter and several USGS creepmeters installed on the San Andreas fault creeping section southeast of the rupture zone (creepmeters XSJ2, XHR2, CWC3, XFL1 and XMR1) have recorded substantial changes in creep rate since the event. The form of this creep signal exhibits a decay in slip rate characteristic of postseismic slip observed following other earthquakes (Smith and Wyss, 1968; Sylvester, 1986; Marone and others, 1991). Although the term "afterslip" has hitherto been used to describe this characteristic surface slip behavior over the rupture zone, it conveniently describes the impulsive initiation of slip and subsequent decay in slip rate observed on adjacent fault segments. In the case of the Loma Prieta earthquake, however, the increased surface slip rates on the northwestern 50 km of the creeping section have not continued to decay toward pre-event levels, but have remained elevated and roughly constant during the ≈500 to 1,100 days following the main shock.

The response of the creeping section of the San Andreas fault to previous earthquakes was examined by Mavko and others (1985), Burford (1988), and Simpson and others (1988). The northwestern creeping section, which terminates a few kilometers northwest of San Juan Bautista, defines an area of high surface creep rate on the San Andreas fault. The Loma Prieta earthquake epicenter was located approximately 50 km northwest of San Juan Bautista, and its aftershocks define a rupture zone that extends to within approximately 10 km of that town (fig. 1). In this paper, we describe the nature of fault creep observed in the northwestern 50 km of the creeping section and estimate the additional fault slip induced by the Loma Prieta earthquake. Using two-dimensional boundary element methods, we examine the possible effect of

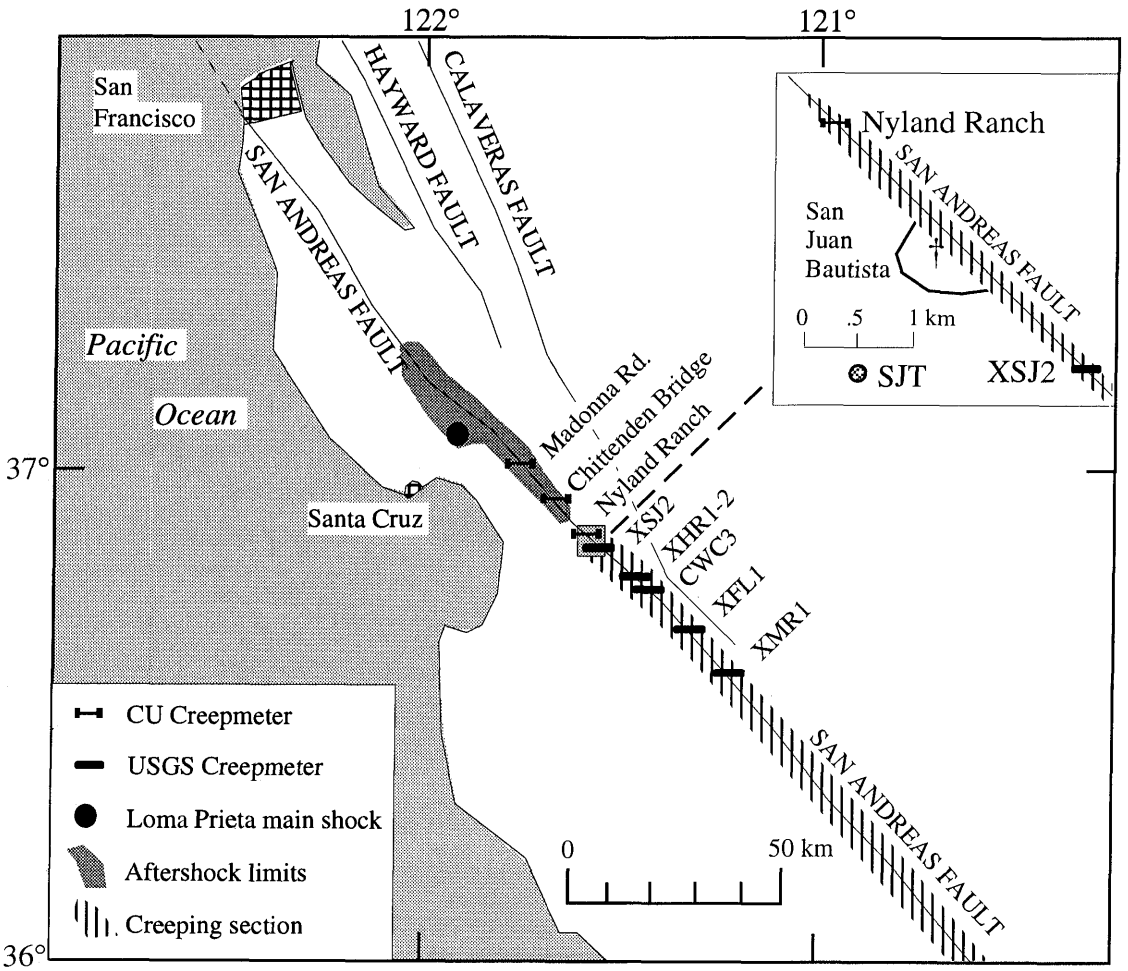

Figure 1.—Location map showing University of Colorado (CU) digital creepmeters and U.S. Geological Survey (USGS) creepmeters used in this study in relation to the Loma Prieta main shock and aftershock zone (shaded), the San Andreas fault creeping section (hachured), and the principal San Francisco Bay area faults. The inset map shows the relationship between creepmeters at Nyland Ranch and XSJ2, and the borehole strainmeter, SJT, near San Juan Bautista; San Juan Bautista Mission is marked by a cross (†).

variable San Andreas and Calaveras fault geometries on the amplitude and spatial distribution of surface creep southeast of the Loma Prieta rupture. We further estimate the potential amplitude of slip induced by the Loma Prieta main shock on the San Andreas fault using simple frictionless models of the San Andreas and Calaveras faults. Finally, we attempt to reconcile changes between pre- and postseismic creep and strain rates near San Juan Bautista with changes in the depths of shallow and deep slip on the creeping fault .

POSTSEISMIC SURFACE SLIP ABOVE THE SOUTHERN LOMA PRIETA RUPTURE ZONE

The longest of the discontinuous surface fractures in the San Andreas fault zone associated with the Loma Prieta earthquake was at Madonna Road (Rymer, 1990). This crack, which displayed right-lateral offset of ≈2 cm, was instrumented 2 days after the event with a 10-m-long digital creepmeter. Even though right-lateral slip increased by 8 mm on this fracture during the 10 months following the earthquake, slip since September 1990 has displayed significant apparent left-lateral displacement (fig. 2*A*). We interpret this apparent left-lateral signal as contraction during periods of heavy rain, followed by extension, or right-lateral motion, during dry spells. We suspect that much of the signal monitored by this instrument is related to hillslope instability.

The Chittenden rail bridge crossing the Pajaro River at Pajaro Gap was instrumented in early November 1989 on the assumption that the structure crosses the 1906 fault break (Behr and others, 1990). Since mid-1990 the instrument has monitored no cumulative displacement other than an annual signal considered to be thermoelastic response of the bridge box-girder. If we consider that signal to be typical annual behavior, then during the first several months of instrument operation this creepmeter recorded a cumulative bridge contraction of approximately 3 cm (fig. 2*B*). Several mapped strands of the San Andreas fault do not pass beneath the bridge and, although it was pulled from its abutment during the 1906 earthquake, it is possible the Chittenden Bridge may not cross the main active fault trace (Prentice and Schwartz, 1991).

ASEISMIC SURFACE SLIP ON THE SAN ANDREAS FAULT SOUTHEAST OF THE LOMA PRIETA RUPTURE

A wooden fence at Nyland Ranch (1.4 km northwest of San Juan Bautista Mission), offset at a rate of 8 mm/year between 1942 and 1978 (Burford and Harsh, 1980), represents the northwesternmost location of aseismic creep observed on the San Andreas fault. A 43-m-long alignment array was established adjacent to this wooden fence in 1967 (Nason and Tocher, 1970). The periodic measurement of this array was supplemented by a biaxial rod extensometer with a dial gauge read-out installed 5 m southeast of the alignment array, and by a continuously operating creepmeter (USGS instrument SJN1) that was discontinued in 1985 due to repeated flooding of the instrument. Infrequent measurement data from the alignment array reveal an approximately linear slip rate of 7.0 mm/year prior to 1989, although over short periods the sense of motion fluctuates in rate and sign (fig. 3*A*). Between 1968 and 1985 the creepmeter SJN1 recorded somewhat more rapid creep at 8.1±0.2 mm/year, with rare creep events of amplitude approaching 1 mm (Schulz and others, 1982; Schulz, 1989). An M_L=4.6 earthquake near the site in 1972 resulted in accelerated creep with a duration of several months and with a decaying rate typical of earthquake afterslip (Burford and others, 1973).

Surface cracks were not present near the alignment array at Nyland Ranch a few hours after the Loma Prieta main shock, although they were evident on the fault through the town of San Juan Bautista to the southeast. Measurement of the alignment array a few days after the main shock revealed a small (≈1 mm) left-lateral signal. On October 22, 1989, we installed a digital creepmeter (Bilham, 1989) next to the east-west arm of the dial-gauge creepmeter to provide a continuous record of creep at this location. During the three years following the Loma Prieta earthquake, the creep rate at Nyland Ranch has averaged more than 20 mm/year (fig. 3). This increased slip rate did not begin until 44 days after the main shock; in the first 10 days of operation the creepmeter recorded less than 0.1 mm of left-lateral signal (possibly a response to instrument installation), subsequently replaced by slow right-lateral displacement of less than 10 microns per day. An abrupt increase in creep rate, which began 44 days after the main shock, exhibits the characteristic decay in rate described as earthquake afterslip. However, the creep rate has not continued to decay in the manner of previously described earthquake afterslip but instead has established an approximately linear 13.4-mm/year rate between 480 and 1,120 days after the main shock (fig. 3*B*). If the mean pre-earthquake creep rate of 7 mm/year is subtracted from the mean post-earthquake rate of nearly 20 mm/year, then an additional 3.9 cm of surface slip is inferred to have been induced by the Loma Prieta main shock in the three years since the event.

Rainfall clearly modulates the short-term creep rate at Nyland Ranch. At times of rainfall, the single-component creepmeter displays significant shortening (1-5 mm). Following these periods, however, the instrument recovers and resumes recording dextral slip. These rainfall-induced transients have been removed from the record (fig. 3*B*) to

allow for more precise least-squares estimation of the overall creep rate. In an attempt to suppress signals related to soil expansion induced by rainfall, the digital creepmeter was supplemented by a differential creepmeter in March 1990 (Bilham and Behr, 1992). Data from the differential creepmeter are significantly less contaminated by rainfall signals. However, the continuous records from this instrument and from the single creepmeter have been interrupted by flooding of the instruments at times of high water table, a problem responsible for discontinuing op-

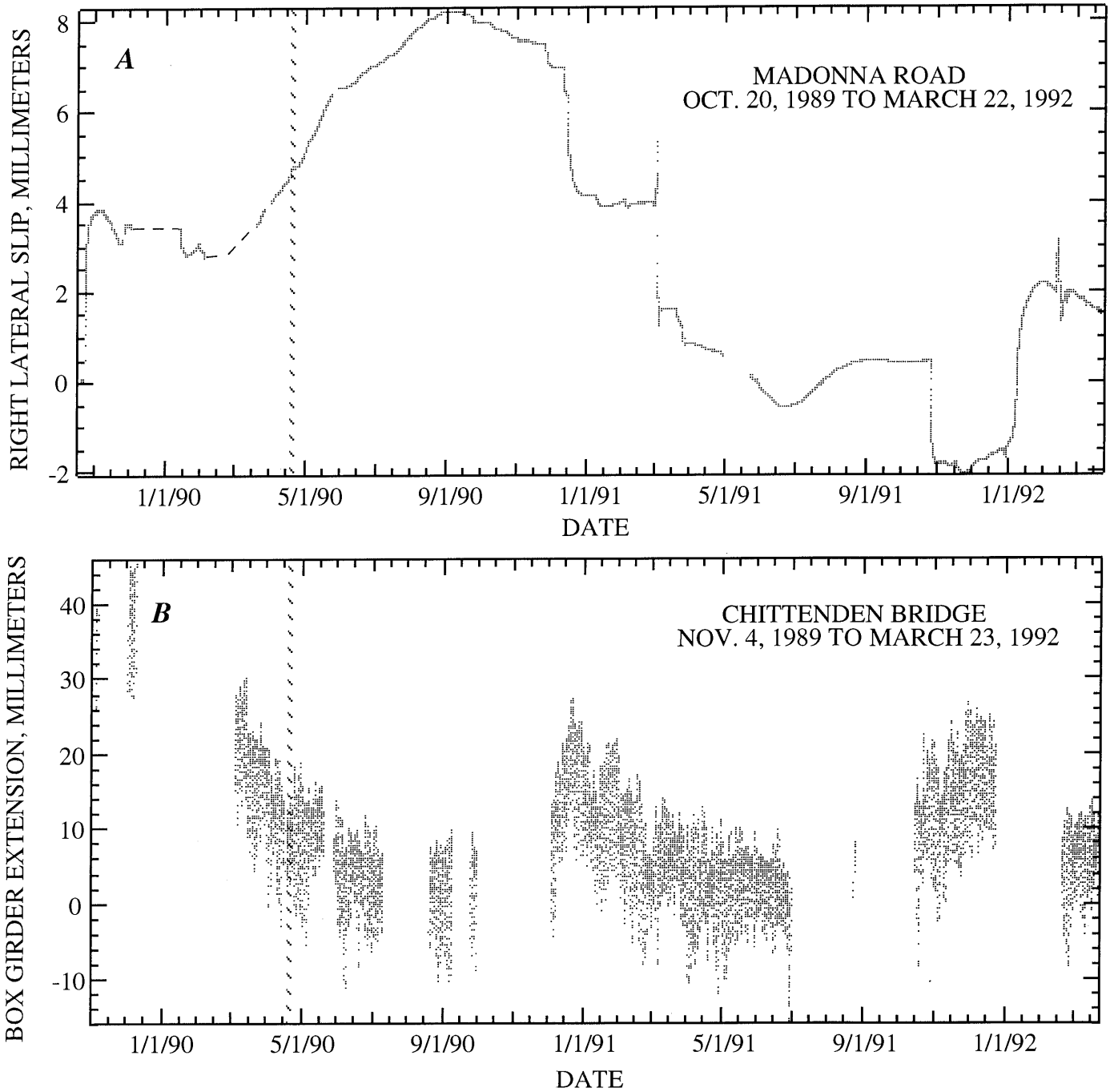

Figure 2.—*A*, Digital creepmeter record from Madonna Road, 20 October 1989 to 22 March 1992. Right-lateral displacement is positive. The cumulative displacement is believed to result from ground failure of the sediments in which the instrument is installed. *B*, Digital extensometer record from Chittenden Bridge, 4 November 1989 to 23 March 1992. Extension of the bridge and corresponding right-lateral displacement is positive. The high-amplitude diurnal and annual signal is due to thermal expansion of the 110-m-long box girder to which the instrument rod is attached. The vertical hachured lines in both *A* and *B* mark the April 1990 Loma Prieta aftershock sequence. Gaps in the data are caused by instrument malfunction and are constrained by jaw separation readings of the instrument's digital caliper sensor.

eration of USGS creepmeter SJN1 in 1985. The data segments in figure 3 represent a composite record constructed from discontinuous data from both creepmeters. Surface displacements during gaps in the recorded data are recovered by measuring changes in the physical separation of the jaws of the digital caliper-displacement sensors.

We examine data from the five northwesternmost USGS creepmeters on the San Andreas fault (fig. 1) from the

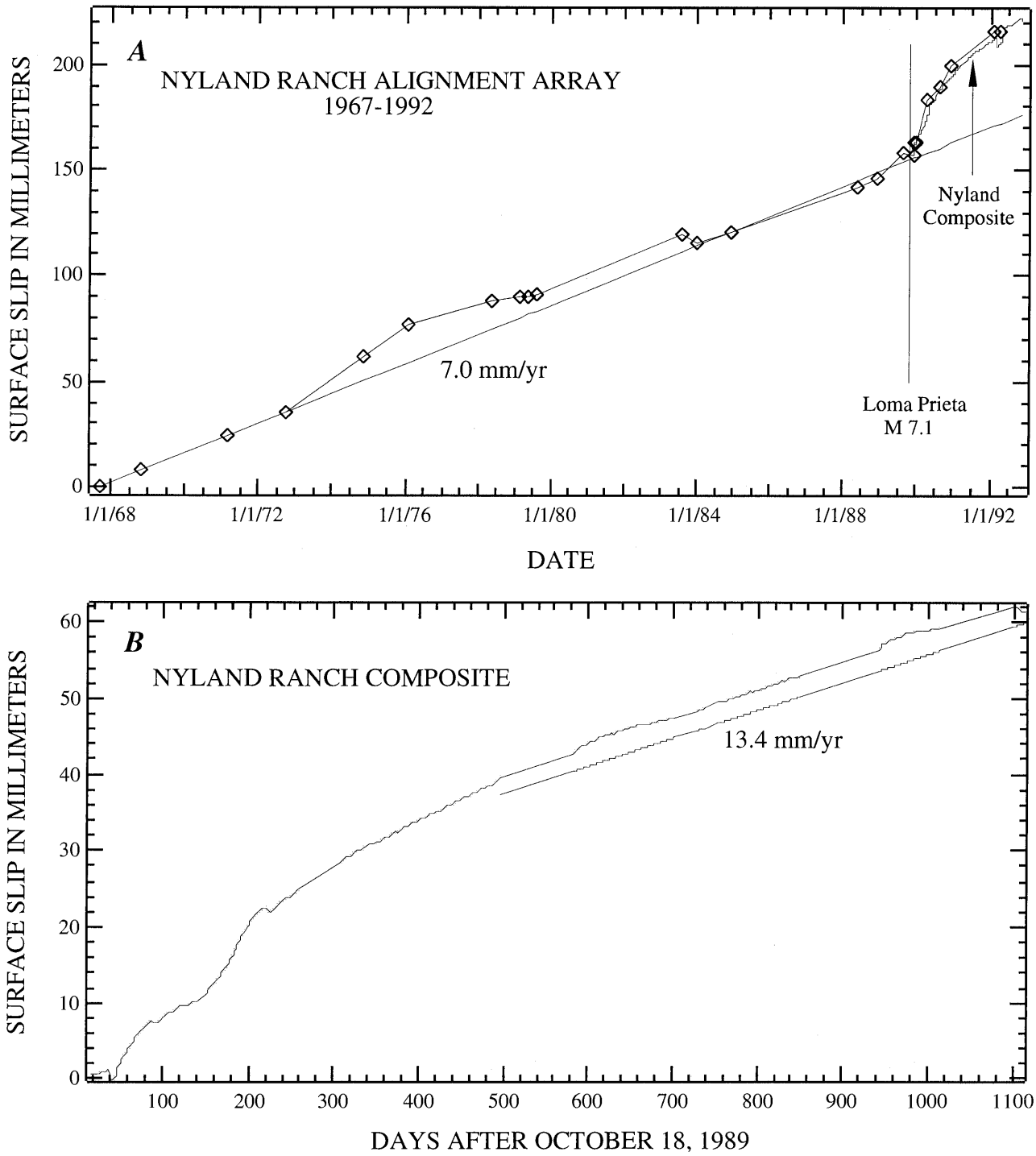

Figure 3.—*A*, Record of alignment array offset (diamonds) at Nyland Ranch from 1967 to 1992. The straight line represents the 7.0-mm/yr average creep rate at Nyland Ranch from 1967 to 1990. A composite record of post-Loma Prieta creep from the single- and double-rod digital creepmeters at Nyland Ranch has been appended to the alignment array record. *B*, Nyland Ranch digital composite record, 4 November 1989 to 5 November 1992. Transient rainfall-induced signals are omitted from the record with all interruptions to the observed data constrained by manual caliper readings. The data after January 1991 are linearly fit by a creep rate of ~13.4 mm/yr.

time of the May 2, 1983, Coalinga earthquake until 2.8 years after the Loma Prieta earthquake (fig. 4). These creepmeters recorded coseismic offsets ranging from -0.35 mm to 6.8 mm of triggered dextral slip (Schulz, 1989; table 1). During the 6 years prior to the Loma Prieta main shock, creep rates at XSJ2, CWC3, XFL1 and XMR1

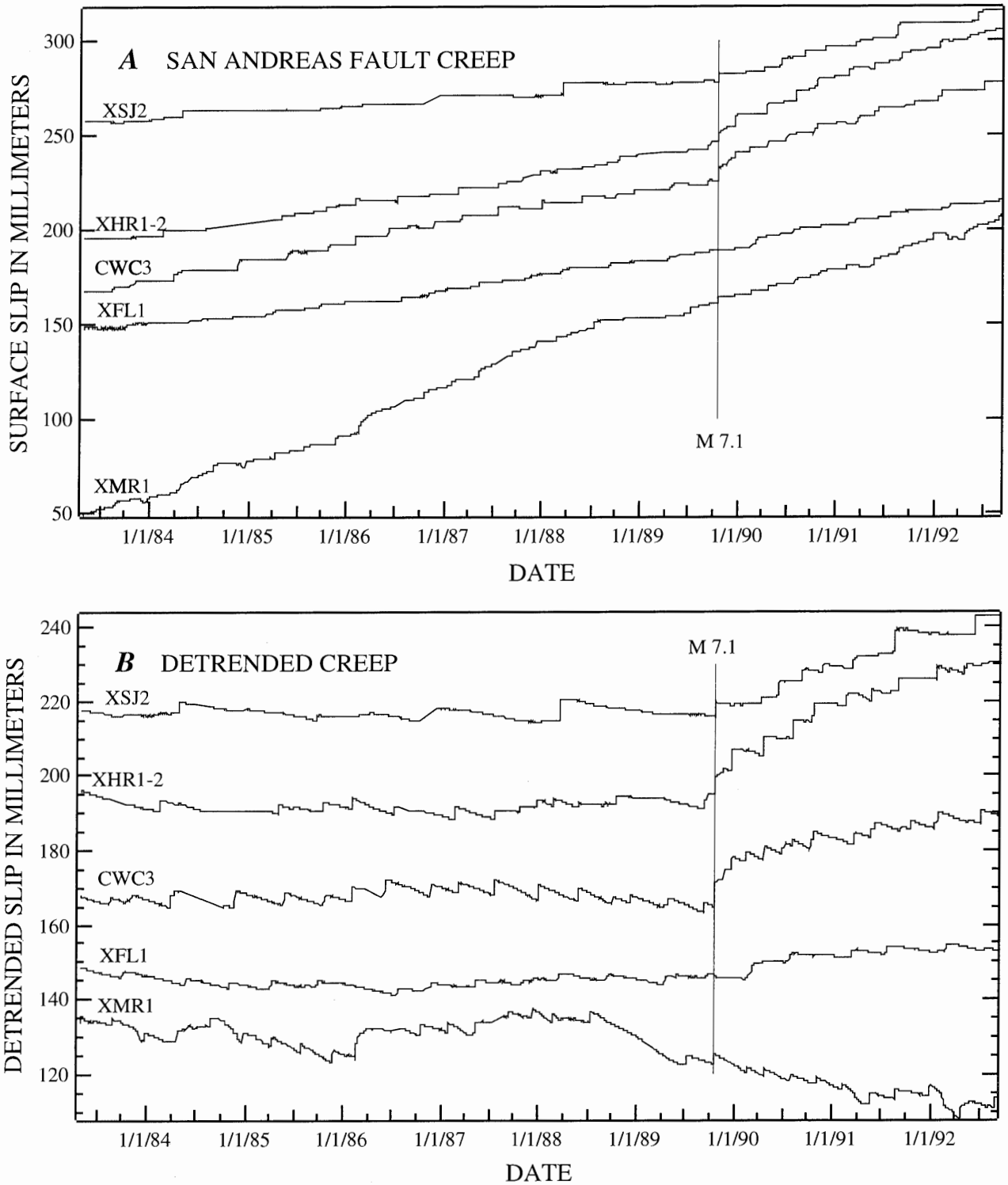

Figure 4.—*A*, USGS creepmeter records from the northwestern 45 km of the creeping section of the San Andreas fault, 2 May 1983 to 1 September 1992. The vertical line marks the Loma Prieta main shock. *B*, Records from *A*, detrended by subtracting the least squares estimated pre-event (1983–1989) creep rate (see table 1). The detrended creep records show significant changes in creep rate at about the time of the Loma Prieta earthquake.

Table 1.—*Creep rates before and after the Loma Prieta earthquake determined from least squares analyses and end-point values*

[The pre-event data begin after the Coalinga earthquake (2 May 1983). Post-event data include a transient period marked by decreasing slip rate (cumulative afterslip column) and a period of approximately constant rate beginning in October 1990 (least squares and end-point fits, 1990-1992). The triggered slip estimates are from Schulz (1989). The last column shows estimates of the change in creep rate between the six years prior to Loma Prieta and the steady rate established after October 1990. Uncertainties reflect the range of differences obtained through the least squares and end-point fit methods.]

Creepmeter	Distance south of San Juan (km)[1]	Least squares 1983-89 (mm/yr)[2]	End-point fit 1983-89 (mm/yr)[2]	Triggered slip 18 Oct. '89 (mm)	Cumulative afterslip 1989-90 (mm)	Least squares 1990-92 (mm/yr)[3]	End-point fit 1990-92 (mm/yr)[3]	Rate change 1990-92 minus 1983-89 (mm/yr)
Nyland	-1.4	7.0	7.0	<2.0	35	13.4	12.9	+6.2±0.2
XSJ2	1.7	3.5	3.2	5.18	22	14.0	11.4	+9.5±1.7
XHR1-2	12.8	8.1	7.9	4.25	40	15.7	17.2	+8.4±0.8
CWC3	16.9	9.5	9.1	6.8	40	13.2	14.0	+4.3±0.6
XFL1	30.3	6.6	6.4	-0.35	20	8.5	7.3	+1.4±0.7
XMR1	41.7	18.9	17.4	2.6	35	16.3	18.3	-0.8±1.8

[1] Distance along San Andreas fault trace south of Mission, San Juan Bautista.

[2] Least-squares and end-point fits to creep data from May 2, 1983 to October 17, 1989. Rates at Nyland Ranch are long-term averages established from alignment array data.

[3] Least-squares and end-point fits to creep data from October 1990 to September 1992.

ranged from 4.0 to 0.75 mm/year lower than previously estimated long-term averages (Schulz and others, 1982). An apparent increase in creep rate of 0.9 mm/year at Harris Ranch (HR) about the time of the Coalinga earthquake may be a consequence of instrumental friction in creepmeter HRS3. The record from HRS3 was used by Schulz and others (1989) to estimate the creep rate from 1970 to 1982, whereas the rate estimate between the Coalinga and Loma Prieta earthquakes was calculated from the records of XHR1, active from 1980 to 1984, and its replacement, XHR2, installed in 1985. Overall, Schulz (1989) noted that the long-term creep rate at Harris Ranch averages from 6 to 9 mm/yr, depending on the time period considered. A further decrease in creep rate prior to the Loma Prieta event, noted by Burford and Schulz (1988) and by Sylvester and others (1990), is evident in the creep records at XSJ2, CWC3 and XMR1 (fig. 4, table 1). As at Nyland Ranch, surface slip at XHR2 and CWC3 appeared in a form similar to earthquake afterslip for approximately 1 year after the earthquake. However, creep rates over the whole of the northwestern creeping section were significantly altered, with rates increased by a factor of 3.3 near the rupture zone (XSJ2), to a 10 percent reduction distant from the rupture (XMR1). Following the initial postseismic increases on the four northwesternmost USGS instruments, slip rates decreased until the fall of 1990. From then through September 1992, surface slip rates remained nearly constant along the northwestern 35 km of the creeping section at rates significantly increased above pre-event velocities (fig. 4, table 1). Because of seasonal variations in creep rate and the occurrence of episodic creep in some of the records, the mean rates in table 1 are sensitive to the methods by which they are estimated. As noted by Schulz and others (1982) the mean rate obtained by least-squares analysis yields a different value from that obtained by taking the end-point values and dividing by the appropriate time interval. This is because of the "staircase" character of creepmeter records consisting of a cumulative signal formed by minor contributions from steady creep and substantial contributions from large episodic events. The resultant uncertainty in the actual change in creep rate initiated by the Loma Prieta earthquake is indicated by a range of values for each creepmeter (column 9, table 1). Because we have used different averaging windows, the mean, pre-Loma Prieta creep rates we present in table 1 differ from those reported by Schulz and others (1982) and Schulz (1989).

We are unable to offer a satisfactory explanation for the 44-day delay between the Loma Prieta main shock and the sudden emergence of rapid dextral creep at Nyland Ranch. If it were a propagating phenomenon, then creepmeters farther to the southeast should experience a sequential delay in their response to the main shock. Although there were similar 67- and 42-day delays in the onset of increased creep rates at XSJ2 and XFL1, respectively, a search for a ubiquitous southeastward (or northwestward) propagating process was unsuccessful. We do, however, exclude rainfall as the triggering process for

initiating creep, because heavy periods of rain occurred twice during the 44 days of creep quiescence with no significant perturbation to the creep record.

ELASTIC MODEL ESTIMATES FOR ASEISMIC SLIP IN CENTRAL CALIFORNIA ASSOCIATED WITH THE LOMA PRIETA EARTHQUAKE

Stress changes on faults in central California resulting from the Loma Prieta rupture (Reasenberg and Simpson, 1992) cannot be used directly to estimate potential aseismic slip along the creeping section because slip locally modifies the calculated stress, which in turn leads to an incorrect estimate for potential slip. To overcome this problem, we use boundary element methods (Mavko, 1982) to estimate the slip at various locations along the northwestern San Andreas fault creeping section. Our approach (Bilham and King, 1989a) minimizes the stress in the medium surrounding the fault generated both by slip on the Loma Prieta rupture plane and by slip adjustment on segments of the Calaveras and San Andreas faults. That is, we ignore the steadily accumulating plate boundary loading rate responsible for the pre-event creep rates in central California. The creeping zone is simplified as a two-dimensional frictionless vertical cut in an elastic halfspace (fig. 5) with the observed geometry of the San Andreas creeping section. We confine the model to these two faults, which further simplifies the analysis compared to that reported by Mavko (1982). We represent the Loma Prieta rupture as a vertical, rectangular dislocation with a length of 38 km on which is imposed a dextral slip of 1.66 m and a convergent displacement of 41 cm to simulate 1.2 m of dip slip on a fault surface dipping 70° to the southwest (Lisowski and others, 1990). This simplified model for the Loma Prieta earthquake implies that rupture extends throughout a uniformly thick elastic crust which will consequently overestimate strain changes associated with a rupture confined to depths of 4 to 20 km.

The geometry of the faults near San Juan Bautista have been interpreted differently in various maps of the region, and there is no consensus on the relationship between surface faults and active dislocations at depth (Mavko, 1982). We use a creeping section represented by a series of contiguous, straight, vertical segments corresponding to line segments listed in Bilham and King (1989b). The displacements calculated for that model and for the current models are those that would result if aseismic and/or seismic slip extended throughout the elastic crust and completely released the calculated fault driving stresses. Our models consequently provide an upper limit to the slip anticipated from the Loma Prieta rupture.

In two boundary element models (fig. 6), slip on the creeping faults is driven only by the Loma Prieta rupture. In one model the Calaveras fault is locked, while in the other model the Calaveras fault slips freely and intersects the San Andreas fault. Whether or not slip occurs on the Calaveras fault, we find that the resulting characteristic slip distribution on the creeping section of the San Andreas fault reaches a maximum of 30 cm, 10 to 20 km southeast of San Juan Bautista. From that point southeastward, the potential slip with the Calaveras fault locked decays nearly linearly over the length of the creeping section. If the Calaveras fault is introduced as a freely slipping dislocation that nowhere approaches closer than 10 km to the San Andreas fault, then maximum slip on the San Andreas is slightly reduced (25 cm), and the location of maximum slip is skewed 10 km to the northwest (model results not shown). If a slipping Calaveras fault contacts the San Andreas fault, then this abruptly reduces potential slip southeast of their intersection and significantly increases slip to the northwest. This result is counter-intuitive and contrasts with the finding reported by Mavko

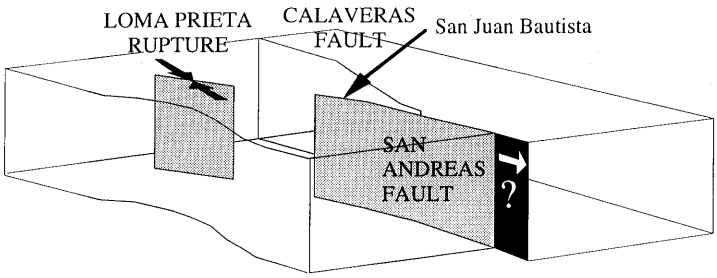

Figure 5.—Block diagram of the two-dimensional boundary element model used to estimate slip on the creeping segments of the Calaveras and San Andreas faults. Dextral slip with convergence is imposed on a vertical segment to emulate the Loma Prieta rupture northwest of the creeping section. In all models, the San Andreas and Calaveras faults are permitted to slip freely in response to strain changes calculated for the rupture.

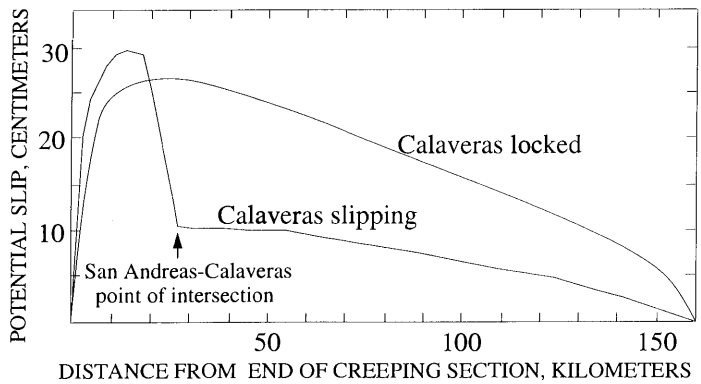

Figure 6.—Slip induced on a freely slipping San Andreas fault by strain changes accompanying the Loma Prieta rupture. Model results are shown for a system with both a locked and a freely slipping Calaveras fault, which intersects the San Andreas. For the slipping Calaveras model, an abrupt decrease in potential slip occurs southeast of the intersection of the San Andreas and Calaveras faults.

(1982) that slip increases on the San Andreas fault southeast of its junction with the Calaveras fault. The reason for this difference is that our model is driven by stresses associated with the Loma Prieta rupture northwest of the Calaveras-San Andreas fault intersection, whereas slip in Mavko's (1982) model is driven by remote antisymmetric shear displacements.

In models where the Calaveras fault is permitted to slip freely, we find that the mean slip on that fault is approximately 13 cm in a left-lateral sense, varying from a few centimeters to more than 20 cm at the latitude of the Loma Prieta rupture. Extending the fault model to include the southern 30 km of the Hayward fault permits an additional mean left-lateral slip of 5 cm on the Calaveras fault, but it increases the slip on the northwestern San Andreas fault by less than a few percent. Creepmeters and alignment arrays on the southern Calaveras recorded a reduction in right-lateral creep rates following the Loma Prieta main shock but no significant left-lateral slip (Galehouse, this chapter). If, prior to the earthquake, the Calaveras fault behaved as a frictionless surface and entirely released the applied dextral strain induced by plate motions, then we might anticipate that left-lateral slip induced by the main shock would be manifest on the fault. The absence of sinistral slip indicates that the dextral shear strain applied to the Calaveras fault prior to the earthquake exceeded the sinistral shear component applied to the fault by the earthquake. Creep retardation, a decrease in slip rate relative to long-term slip rates, presumably represents the expression of these combined strain fields. Our two-dimensional elastic models indicate that left-lateral slip would also be expected on the southern Hayward fault. As much as 1 cm of left-lateral slip has been manifest on that fault since the Loma Prieta earthquake (Lienkamper, oral commun., 1992), indicating that dextral strain applied to the Hayward fault prior to the earthquake was less than the sinistral strain generated by the earthquake.

Our models yield surprisingly large estimates for the amplitude of induced slip anticipated on the San Andreas fault, exceeding 20 cm in the northwestern 20 km of the creeping section. Using three-dimensional models in which coseismic strains fall off with distance much faster ($\sim R^{-3}$) than they do in two-dimensional models ($\sim R^{-2}$), Breckenridge and Simpson (this chapter) estimate maximum values of approximately 6 cm for induced right-lateral slip on the northwestern creeping section, with proportionately smaller slip induced on surrounding faults. Strain changes induced within the surrounding crustal volume by an earthquake evolve with time due either to viscous relaxation of the lower crust, or to time-dependent deep slip on faults within an otherwise elastic lithosphere (for example, Stein and others, 1992). The amplitude of slip on faults driven by such strains should evolve as well. Two-dimensional models of this system yield high estimates because in some sense they represent an extreme case in which all of the strain induced by the earthquake is manifest as slip. The introduction of a third dimension requires numerous other parameters to be estimated that we avoid in a two-dimensional approach; precise values computed in Breckenridge and Simpson's three-dimensional models are sensitive not only to which surrounding faults are assumed to slip, but also to the depth to which slip is assumed to occur. Nevertheless, our analysis permits the interpretation that less than 25 percent of the slip estimated by the two-dimensional models has occurred on the northwestern 20 km of the creeping San Andreas fault, and perhaps as little as 10 percent. At current creep rates, the slip modeled in two dimensions would not be manifest for decades, and if creep rates decrease over time, then potential slip will be delayed further.

Frictional and viscous processes moderate the rate at which the estimated postseismic induced displacement will be manifest on the fault. However, since creep rates depend in part on the strain applied to the fault, we anticipate that observed postseismic slip rates will be proportional to the modeled potential slip amplitudes. In figure 7, observed surface creep rate changes in the northwestern 50 km of the creeping section are superposed on curves fit to two-dimensional model displacements calculated for three geometries of Calaveras fault/San Andreas fault interaction. Although the relative positions of the creepmeter data are exact, there is some uncertainty about the northwestern terminus of creep entered in the models, and in the location and proximity of approach of the Calaveras and San Andreas faults. For these reasons, we should not expect a precise correspondence between predicted slip data and slip-rate observations. Nevertheless, the predicted displacements and observed creep rate increases are reasonably close, suggesting our models may represent appropriate simplifications of the regional slip mechanism. Indeed, the fit of the creep data to the slip estimates in figure 7 suggest a best-fit model in which aseismic slip on the Calaveras fault may have occurred fewer than 3 km from the creeping San Andreas fault. It would appear that more detailed models may provide a better estimate of the connectivity (Bilham and Bodin, 1992) between the San Andreas and Calaveras faults. Although our two-dimensional methodology provides insight into the behavior of faults with approaches that are closer than the thickness of the elastic plate, in practice, three-dimensional subsurface geometry and analysis methods will more accurately characterize the detailed behavior of such systems.

CREEPMETER AND BOREHOLE STRAINMETER DATA

The mean creep rates at XSJ2 and Nyland Ranch for the year preceding the Loma Prieta main shock were 3.2 to 3.5 mm/year and 7 mm/year, respectively. From Octo-

ber 1990 to September 1992, the mean rates were approximately 12.7 mm/year and 13.1 mm/year, respectively. Thus, although recent post-event slip rates at these two creepmeters are similar, they differ before the main shock by a factor of two. Moreover, a change in the characteristics of slip at XSJ2 occurs at the time of Loma Prieta in that during nearly 3 years of observed postseismic displacement there have been as many as eight creep events (episodic creep), whereas only two creep events were recorded in the 3 years preceding the main shock and none during the immediately preceding 18 months.

In view of the limited data available to study the event, models of the fault-slip process must inevitably remain non-unique. We use a simple two-dimensional analysis to test whether the strain and creep rates at the northwestern end of the fault are mutually consistent. A triaxial borehole strainmeter (SJT) operating 1.13 km from the fault, at 200 m depth, and within 3 km along strike from XSJ2 and Nyland Ranch recorded a shear strain rate of 1.2±0.1 μstrain/year during the 10 months prior to the earthquake and 1.9±0.1 μstrain/year from January 1990 through at least July 1991 (Gladwin and others, 1991; Gwyther and others, 1992). If we assume that observed strain rates ($\partial\varepsilon/\partial t$) result from annual antisymmetric displacements applied remotely to the region and that they are monitored by a surface strainmeter y km from the fault (fig. 8), then we may estimate the remotely applied strain load σ/μ and the depths, b and H-a, between which the fault is locked (Tse and others, 1985):

$$\varepsilon = 2\frac{\sigma}{\mu}\sinh\left(\frac{\pi y}{H}\right)\left[\left(2\cosh\left(\frac{\pi y}{H}\right)+\cos\left(\frac{\pi a}{H}\right)-\cos\left(\frac{\pi b}{H}\right)\right)^2-\left(\cos\left(\frac{\pi a}{H}\right)+\left(\frac{\pi b}{H}\right)\right)^2\right]^{-1/2}$$

The surface slip, Δu, on a fault subject to the same applied strain load is

$$\Delta u = 2\frac{\sigma H}{\pi\mu}\cosh^{-1}\left(\frac{2+\cos\frac{\pi a}{H}-\cos\frac{\pi b}{H}}{\cos\frac{\pi a}{H}+\cos\frac{\pi b}{H}}\right)$$

(Tse and others, 1985).[1]

Thus, the surface strain rate and surface creep rates provide certain limits to the applied strain loading rate and the locked depths of the fault. We use a mean post-earthquake creep rate of 12.9 mm/year for XSJ2 (11.4–14 mm/year) and Nyland Ranch (12.9–13.4 mm/year) in the following estimates. For y = 1.13 km (neglecting the 200-m depth of the borehole strainmeter SJT), a surface creep rate of 12.9 mm/year is consistent with a fault locked below 1.57 km, subject to an applied shear strain rate of 3.2 μstrain/year. However, the observed strain and creep rates are compatible with a range of increased depths for subsurface slip (H-a) with correspondingly reduced loading rates as shown in figure 9. For elastic plate thicknesses (H) greater than 10 km, it is evident that the depth of surface slip is only marginally sensitive to slip at depth, varying by less than 10 percent for subsurface creep extending from the base of the elastic plate to within 3 km of the surface. The lowest applied shear-strain signal consistent with a creep rate of 12.9 mm/year and a strain rate of 1.9 μstrain/year observed 1.13 km from the fault is 0.7 μstrain/year (fig. 9*A*). This value occurs for creep in a 15-km-thick elastic plate with a narrow region locked between 1.2 km and 2 km depth. Thus, from figure 9*A*, we deduce that post-earthquake shallow creep can occur to depths of 1.2 to 1.57 km for applied strain rates of 0.7 to 3.2 μstrain/year, respectively, depending upon whether or not the fault creeps below 2 km depth.

Assuming that the creep and strain are driven by remote loading of the fault, the difference in creep rates between Nyland Ranch (7.0±2.0 mm/year) and XSJ2 (3.4±2.0 mm/year) in the years prior to the main shock require different depths for slip at these two locations. The rate of shear strain parallel to the fault (Gamma 1 of Gladwin and others, 1991) recorded by SJT after mid-1986 was near zero until one year before the main shock when strain rates increased to 1.2 μstrain/year. An observed strain rate of 1.2 μstrain/year is consistent with the observed creep rate at Nyland Ranch for a depth of shallow creep of ≈1.4 km and an applied strain loading rate of 1.9 μstrain/year (see fig. 9*B*). Again a suite of possible combinations of creep at depth and applied strain rate can satisfy the observed creep and borehole strain data, one of which requires a low strain loading rate (0.41 μstrain/year) for a model in which a narrow zone remains locked between 1.1 and 2 km (fig. 9*B*). During this time, however, the lower XSJ2 creep rate required a significantly shallower depth of creep compared to that inferred for Nyland Ranch (fig. 9*C*). The range of acceptable applied strain rates is not changed much given this reduced creep rate, but the range of shallow creep depths is reduced to 330 to 500 m, depending on the applied loading rate (fig. 9*C*). Although other interpretations are possible, a plausible explanation is that the depth of shallow creep increased by approximately a factor of three at XSJ2 at the time of the Loma Prieta earthquake (from ≈500 m to ≈1.5 km), but remained substantially unchanged at Nyland Ranch (from ≈1.5 km to ≈1.4 km depth).

These inferred changes for depth of shallow creep are reasonably well indicated by the observed combination of

[1] The cosine terms in this expression were incorrectly excluded in Bilham and Behr (1992)

strain and creep data. In contrast, the rate and extent of creep below a locked region of the fault, and the appropriate strain loading rates are poorly constrained. Thus if the two-dimensional model of figure 9 is applicable, then the creep data require that the strain rate increase at the time of the Loma Prieta main shock noted by Gwyther and others (1992) was accompanied by a threefold increase in the depth of near-surface creep at XSJ2. In prin-

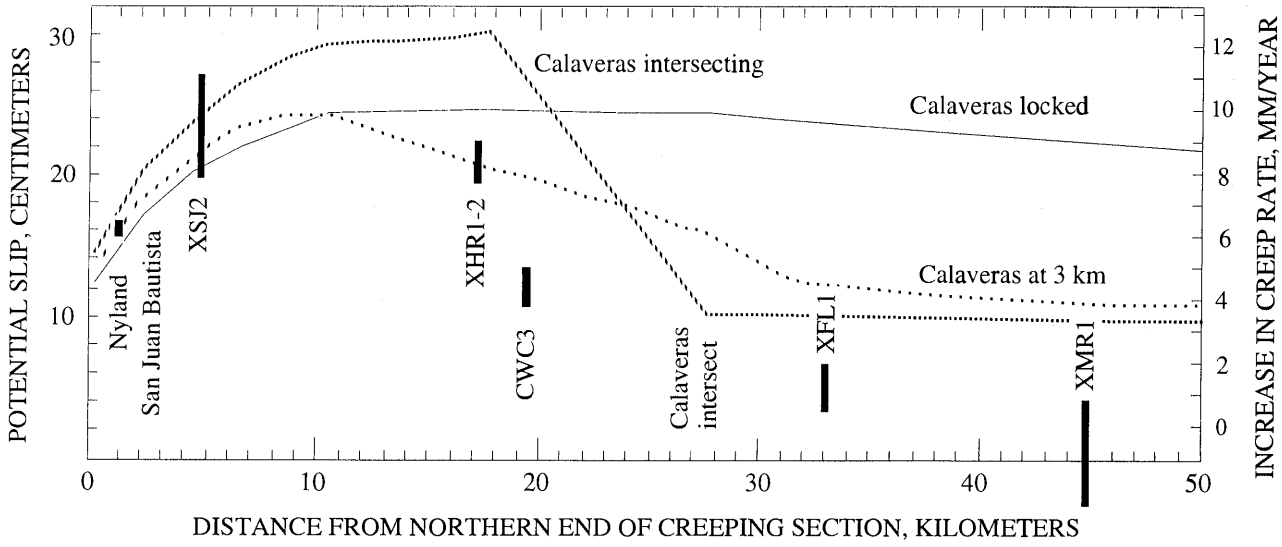

Figure 7.—Estimates of potential slip and observed creep rate changes on the northwestern 50 km of the San Andreas fault. Potential slip is estimated using three boundary element models involving different Calaveras fault geometries: Calaveras locked, Calaveras approaching San Andreas to within 3 km, Calaveras intersecting San Andreas at kilometer 27.5. Estimates of the change in creep rate following the Loma Prieta earthquake (column 9 of table 1) are shown as vertical bars.

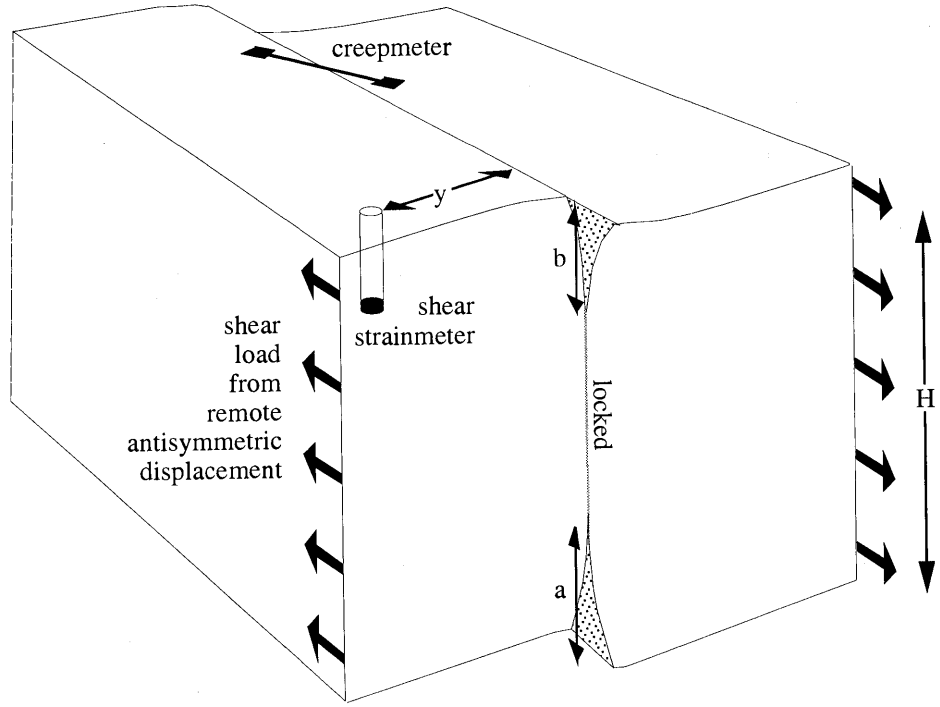

Figure 8.—Block diagram representing an elastic plate of thickness H undergoing antisymmetric shear displacement with a locked patch between depths b and H-a, after Tse and others (1985). This model is used in the analysis of surface creep and strain rates observed near San Juan Bautista.

ciple, by estimating the elastic strain changes induced by the Loma Prieta event at Nyland and XSJ2, it is possible to determine the increment in loading rate and thereby limit the possible range in creep depth on the subsurface fault. We do not pursue this here because the starting geometry is determined by the background loading rate, which is insufficiently established. Certainly additional strain measurements would permit a substantial improvement in our ability to interpret the ranges of fault slip at depth.

An important feature in the XSJ2 data is the absence of episodic creep events in the data in the 18 months prior to the main shock. Episodic creep is defined as an abrupt increase in slip velocity with a duration of a few hours to a few days, commonly manifest as a transient acceleration followed by a gradual decay in slip rate. In previous years, the slip rate at XSJ2 was formed from a combination of episodic creep and background creep, a slow, continuous slip of the surface fault. Bilham and Behr (1992) proposed that steady background creep and episodic creep may be generated at different depths on a creeping fault, and that the ratio of the rates of background to episodic creep is approximately proportional to the ratio of the depths to which these processes occur. The ratio of cumulative background creep to cumulative episodic creep recorded by XSJ2 is 0.29 for the period 1983-1989, and 0.37 after the Loma Prieta main shock, yielding a mean value of 0.33. That is, the long-term contribution to creep from episodic events is three times greater than the contribution from background creep. This implies that the depth of episodic creep is three times greater than the depth of background creep. If one of these depths is known, it is possible to estimate the other. From the preceding estimate of depth of shallow creep at XSJ2, the lack of episodic creep in the 18 months prior to the main shock suggests a maximum depth of ≈500 m for background creep. Following the main shock, episodic creep resumed and we inferred a creeping depth of ≈1.5 km. Thus, the ratio of depths derived from the long-term ratio of episodic and background creep agrees with the ratio of depths determined from reconciling the strain and creep rates before and after the main shock. We conclude that the creep retardation near San Juan Bautista in the late 1980's, as noted by Sylvester and others (1990) (fig. 4), was caused by the cessation of episodic creep in the depth range 0.5 to 1.5 km. We interpret the return of episodic creep at XSJ2 after the Loma Prieta main shock as the resumption of surface creep to a depth of 1.5 km. Several factors affecting the fault zone could be responsible for arresting episodic creep prior to the main shock, including an in-

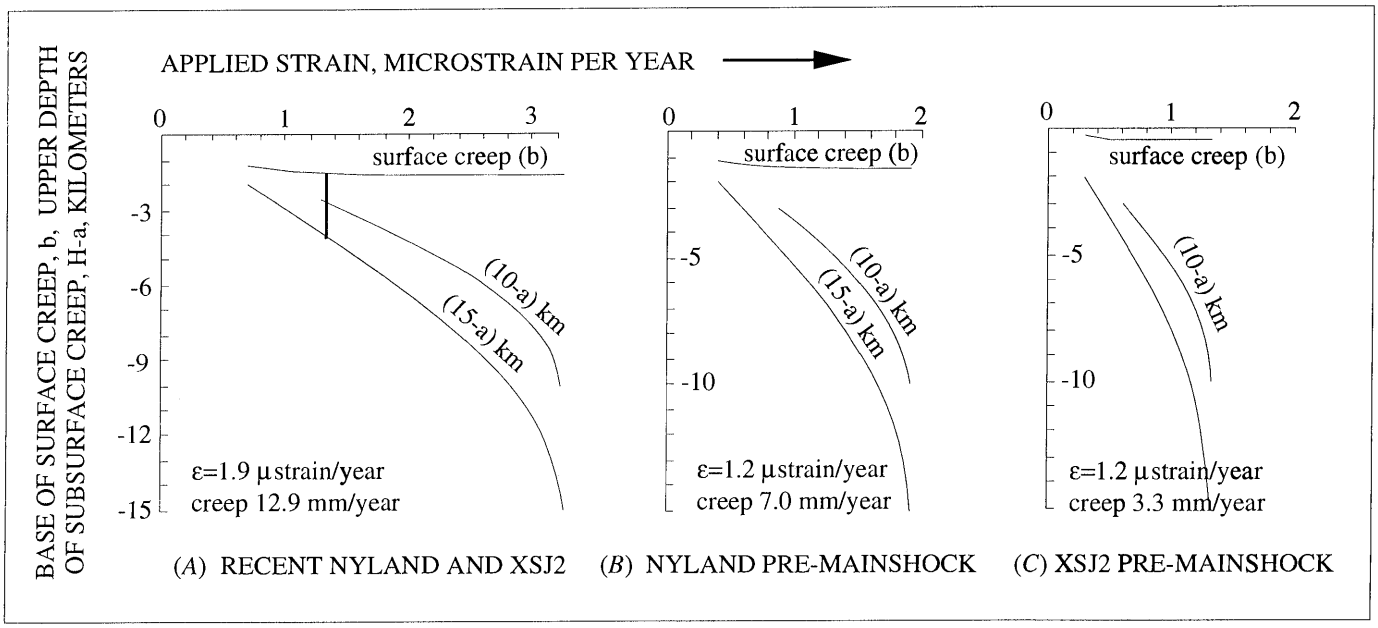

Figure 9.—Analytic solutions for applied strain and depths of surface (*b*) and subsurface (*H-a*) creep that satisfy observed creepmeter and borehole strain rates (indicated). The three curves in each graph correspond to the depth of surface creep (*b*) and the upper depths of a subsurface creeping zone (*H-a*) for crustal thickness (*H*) of 10 and 15 km. The vertical bar in 9*A* corresponds to a fault creeping above and below a region locked between 1.49 km and 4 km in a 15-km-thick elastic plate. In 9*A*, a shear strain loading rate of 1.32 μstrain/year generates creep of 12.9 mm/year with strain of 1.9 μstrain/year observed 1.13 km from the fault. The same load rate generates similar creep and strain rates in a 10-km-thick elastic plate with a narrower locked region. Examples *B* and *C* correspond to the pre-Loma Prieta creep rates observed at Nyland Ranch and XSJ2, respectively, and an observed strain rate of 1.9 μstrain/yr.

crease in fault normal stress, a decrease in pore pressure, or other physical changes in the rheology of the fault zone.

Despite the persuasive consistency of the above results and the potential existence of bimodal slip at XSJ2, several alternative explanations for the observed strain and creep data may be considered. Alignment array data recorded between 1968 and 1977 at Mission Vineyard Road, site of the XSJ2 creepmeter, indicated a diffuse shear zone (Burford and Harsh, 1980) in which the primary slip zone spanned by XSJ2 (13-m fault normal aperture) exhibited a creep rate of 7.6 mm/yr, while the alignment array (79-m aperture) recorded an average of 13.4 mm/yr of shear deformation. It is therefore possible that the observed pre-event slip deficit at XSJ2 results from a lack of coverage of the entire deformation zone. Whether or not this is the case, XSJ2 has been recording all slip within ± 40 m of the primary fault trace since Loma Prieta. This seems especially to be the case during a period of significantly increased surface slip from December 1992 through June 1993, when records from XSJ2 and the Mission Vineyard Road alignment array indicate 16.8 mm and 16.9 mm of right-lateral shear, respectively (Galehouse, oral commun., 1993). The suggestion that XSJ2 was not monitoring the entire deformation zone prior to Loma Prieta, but has been since, requires a change over time in the location, or the nature, of principal shear deformation at that latitude.

Additional alternatives may be assessed by examining transient strain and creep data at the time of episodic creep events to determine the regions where such events are generated. The very low strain rates recorded by the borehole strainmeter prior to 1988 require a different depth of slip to be applicable at that time. Strain rates recorded by SJT are lower than the 0.3 μstrain/year measured geodetically by the USGS in the region northwest of San Juan Bautista (Lisowski and Prescott, 1981; Prescott and others, 1981). If we assume that the applied strain rate from 1986 to 1988 was 0.3 μstrain/year, then an estimated maximum observed borehole strain rate of 0.1 μstrain/year requires the fault at Nyland Ranch to slip above 4.8 km and below 5.1 km, whereas under the same conditions, the slip rate of 3.3 mm/year at XSJ2 implies that the fault is locked below 4.8 km. These large depths for surface creep appear to us implausible in the extreme northwestern end of the creeping section because the surface fault is completely locked less than 3 km to the northwest of Nyland Ranch. We conclude that the borehole strain rates reported by Gwyther and others (1992) may signify changes in the fault zone which are more complex than those modeled here. In the 6 months prior to the Loma Prieta event, slip was apparently confined to shallow depths. The transient responses of the creepmeters in the months following the main shock confirm that the fault is responding differently along strike to strain changes induced by the Loma Prieta earthquake.

CONCLUSIONS

Aseismic slip rates on the northwestern part of the San Andreas fault creeping section in central California increased substantially following the Loma Prieta earthquake and continue, three years after the main shock, to be above their mean pre-earthquake values. Farther southeast in central California, creep rates are substantially unaltered by the earthquake. Our two-dimensional elastic models indicate that maximum displacements of 20 cm on the northwestern creeping section will result from strain changes accompanying the Loma Prieta main shock. Although these models differ from the creeping San Andreas and Calaveras fault systems in that they are simulated as frictionless, vertical planes, they suggest that southeast of the San Andreas fault's intersection with the Calaveras fault, displacements induced on the creeping section should be significantly reduced in comparison to those northwest of the intersection. This finding qualitatively agrees with observed creep-rate increases. At current surface creep rates, the induced fault displacements predicted by two-dimensional models of the Loma Prieta earthquake will take a minimum of two decades to eliminate by creep processes alone, although three-dimensional models indicate that most, if not all, of the induced slip will occur within the next few years. Another possibility is that slip predicted for the northwestern creeping section, which has not yet occurred aseismically, may occur during future seismic activity.

Our two-dimensional analysis of strain and creep data suggests that slip was apparently confined to shallow depths beneath creepmeter XSJ2 during the 6 months prior to the Loma Prieta earthquake. High strain rates reported near the northwestern end of the creeping section by Gwyther and others (1992) can be reconciled with high creep rates by permitting a substantial fraction of the San Andreas fault to slip below a locked zone from 1 to 2 km depth. However, we consider that the substantial aseismic slip at depth that is implied by these models is inconsistent with the setting at the northwestern end of the creeping section in that surface creep is not observed more than a few kilometers northwest of Nyland Ranch. We conclude that the observed high strain rates recorded near San Juan Bautista must be related to a local strain adjustment process, perhaps caused by the concentration of strain near the creeping fault as it adjusts to the new strain conditions resulting from the Loma Prieta main shock.

ACKNOWLEDGMENTS

This work was funded by the U.S. Geological Survey grant 14-08-001-G1876. We wish to thank three anonymous reviewers for their perceptive, insightful, and help-

ful comments. We thank Mr. Frank Avilla and his family for the use of the pasture and barn at Nyland Ranch.

REFERENCES CITED

Behr, J., Bilham, R., Bodin, P., Burford, R.O., and Burgmann, R., 1990, Aseismic slip on the San Andreas fault south of Loma Prieta: Geophysical Research Letters, v. 17, no. 9, p. 1445–1448.

Bilham, R., 1989, Surface slip subsequent to the 24 November 1987 Superstition Hills, California, earthquake monitored by digital creepmeters: Bulletin of the Seismological Society of America, v. 79, no. 2, p. 424–450.

Bilham, R., and King, G., 1989a, The morphology of strike slip faults: examples from the San Andreas fault, California: Journal of Geophysical Research, v. 94, no. B8, p. 10204–10216.

——— 1989b, Slip distribution on oblique segments of the San Andreas Fault, California: observations and theory: U.S. Geological Survey Open-File Report 89–315, 447 p.

Bilham, R., and Behr, J., 1992, A two-layer model for aseismic slip on the Superstition Hills fault, California: Bulletin of the Seismological Society of America, v. 82, no. 3, p. 1223–1235.

Bilham, R., and Bodin, P., 1992, Fault zone connectivity: slip rates on faults in the San Francisco Bay area, California: Science, v. 258, p. 281–284.

Burford, R.O., 1972, Continued slip on the Coyote Creek fault after the Borrego Mountain earthquake: U.S. Geological Survey Professional Paper 787, p. 105–111.

———1988, Retardations in fault creep rates before local moderate earthquakes along the San Andreas fault system, central California: Pure Applied Geophysics, v. 126, nos. 2-4, p. 499–529.

Burford, R.O., Allen, S.S., Lamson, R.J., and Goodreau, D.D., 1973, Accelerated fault creep along the central San Andreas fault after moderate earthquakes during 1971–1973, *in* Kovach, R.L., and Nur, Amos, eds., Proceedings of the conference on tectonic problems of the San Andreas fault system: Stanford University Publications in the Geological Sciences, v. 13, p. 268–274.

Burford, R.O., and Harsh, P.W., 1980, Slip on the San Andreas fault in central California from alignment array surveys: Bulletin of the Seismological Society of America, v. 70, no. 4, p. 1233–1261.

Burford, R.O. and Schulz, S.S., 1988, A current retardation rate of aseismic slip on the San Andreas fault at San Juan Bautista, California: E O S, Transactions of the American Geophysical Union, v. 69, no. 44, p. 1424.

Cohn, S.N., Allen, C.R., Gilman, R., and Goulty, N.R., 1982, Preearthquake and postearthquake creep on the Imperial fault and the Brawley fault zone: U.S. Geological Survey Professional Paper 1254, p. 161–168.

Gladwin, M.T., Gwyther, R.L., Higbie, J.W., and Hart, R.G., 1991, A medium term precursor to the Loma Prieta earthquake?: Geophysical Research Letters, v. 18, no. 8, p. 1377–1380.

Gwyther, R.L., Gladwin, M.T., and Hart, R.G., 1992, A shear strain anomaly following the Loma Prieta earthquake: Letters to Nature, v. 356, no. 6365, p. 142–144.

Lisowski, M. and Prescott, W.H., 1981, Short-range distance measurements along the San Andreas fault system in central California, 1975–1979: Bulletin of the Seismological Society of America, v. 71, no. 5, p. 1607–1624.

Lisowski, M., Prescott, W.H., Savage, J.C., and Johnston, M.J., 1990, Geodetic estimate of coseismic slip during the 1989 Loma Prieta, California, earthquake: Geophysical Research Letters, v. 17, no. 9, p. 1437–1440.

Marone, C.J., Scholz, C.H., and Bilham, R., 1991, On the mechanics of earthquake afterslip: Journal of Geophysical Research, v. 96, no. B5, p. 8441–8452.

Mavko, G.M., 1982, Fault interaction near Hollister, California: Journal of Geophysical Research, v. 87, no. B9, p. 7807–7816.

Mavko, G.M., Schulz, S., and Brown, B.D., 1985, Effects of the 1983 Coalinga, California, earthquake on creep along the San Andreas fault: Bulletin of the Seismological Society of America, v. 75, no. 2, p. 475–489.

Nason, R.D., and Tocher, D., 1970, Measurement of movement on the San Andreas fault, *in* Earthquake Displacement Fields and Rotation of the Earth, L. Mansinha and others, eds., Riedal, Dordrecht, Holland.

Prentice, C.S., and Schwartz, D.P., 1991, Re-evaluation of 1906 surface faulting, geomorphic expression, and seismic hazard along the San Andreas fault in the southern Santa Cruz Mountains: Bulletin of the Seismological Society of America, v. 81, no. 5, p. 1424–1479.

Prescott, W.H., Lisowski, M., and Savage, J.C., 1981, Geodetic measurement of crustal deformation across the San Andreas, Hayward, and Calaveras faults near San Francisco, California: Journal of Geophysical Research, v. 86, no. B11, p. 10853–10869.

Reasenberg, P.A., and Simpson, R.W., 1992, Response of regional seismicity to the static stress change produced by the Loma Prieta earthquake: Science, v. 255, p. 1687–1690.

Rymer, M., 1990, Near-fault measurement of postseismic slip associated with the 1989 Loma Prieta, California, earthquake: Geophysical Research Letters, v. 17, no. 10, p. 1789–1792.

Schulz, S.S., Mavko, G.M., Burford, R.O., and Stuart, W.D., 1982, Long-term fault creep observations in central California: Journal of Geophysical Research, v. 87, no. B8, p. 6977–6982.

Schulz, S.S., 1989, Catalog of creepmeter measurements in California from 1966 through 1988: U. S. Geological Survey Open-File Report 89-650, 193 p.

Sharp, R.V., K.E. Budding, J. Boatwright, M.J. Ader, M.G. Bonilla, M.M. Clark, T.E. Fumal, K.K. Harms, J.J. Lienkaemper, D.M. Morton, B.J. O'Neill, C.L. Ostergren, D.J. Ponti, M.J. Rymer, J.L. Saxton and J.D. Sims, 1989, Surface faulting along the Superstition Hills fault zone and nearby faults associated with the earthquakes of 24 November 1987: Bulletin of the Seismological Society of America, v. 79, no. 2, p. 252–281.

Simpson, R.W., Schulz, S.S., Dietz, L.D., and Burford, R.O., 1988, The response of creeping parts of the San Andreas fault to earthquakes on nearby faults: two examples: Pure Applied Geophysics, v. 126, nos. 2–4, p. 665–685.

Smith, S.W., and Wyss, M., 1968, Displacement on the San Andreas fault subsequent to the 1966 Parkfield earthquake: Bulletin of the Seismological Society of America, v. 58, no. 6, p. 1955–1973.

Stein, R.S., King, G.C.P., and Lin, J., 1992, Change in failure stress on the Southern San Andreas fault system caused by the 1992 magnitude = 7.4 Landers earthquake: Science, v. 258, p. 1328–1332.

Sylvester, A.G., 1986, Near-field tectonic geodesy, *in* Wallace, K.E., Active Tectonics, ed.: Washington, D.C., National Academy Press, p. 164–180.

Sylvester, A.G., Burford, R.O., and Schulz, S.S., 1990, Almost no surface displacement occurred at San Juan Bautista as a result of the Loma Prieta earthquake: E O S, Transactions of the American Geophysical Union, v. 71, no. 8, p. 290.

Tse, S.T., Dmowska, R., and Rice, J.R., 1985, Stressing of locked patches along a creeping fault: Bulletin of the Seismological Society of America, v. 75, no. 3, p. 709–736.

U.S. Geological Survey Staff, 1990, The Loma Prieta, California, earthquake: an anticipated event: Science, v. 247, p. 286–293.

THE LOMA PRIETA, CALIFORNIA, EARTHQUAKE OF OCTOBER 17, 1989:
EARTHQUAKE OCCURRENCE

AFTERSHOCKS AND POSTSEISMIC EFFECTS

EFFECT OF THE LOMA PRIETA EARTHQUAKE ON FAULT CREEP RATES IN THE SAN FRANCISCO BAY REGION

By Jon S. Galehouse,
San Francisco State University

CONTENTS

ABSTRACT

We have been measuring creep on San Francisco Bay region faults since 1979. Virtually no creep preceded the Loma Prieta earthquake (LPEQ) on the San Andreas fault northwest of the aftershock zone and virtually none has occurred since. In contrast, the post-LPEQ creep rate of 13.5 mm/yr near the northwestern end of the creeping segment of the San Andreas fault near San Juan Bautista is about twice the pre-LPEQ average. About 5 mm of coseismic right slip was triggered here by the LPEQ. Most of the Hayward fault creeps at a long-term rate of about 5 mm/yr. The median rate at five sites along the Hayward fault that we had been measuring for the decade before the LPEQ was 4.9 mm/yr. The median rate at these same sites for the 3.4 yr following the LPEQ is 3.6 mm/yr. The rate has been particularly low at a site near the northwestern end of the fault in San Pablo and at sites near the southeastern end in Fremont. In fact, left-lateral slip of a few centimeters associated with the LPEQ may have occurred in southern Fremont along this previously rapid, right-lateral-creeping segment of the fault. Small amounts of left-lateral slip have continued there since the LPEQ (through March 1993). The average creep rate on the southern Calaveras fault in the Hollister area before the LPEQ was 6.4 mm/yr at one site and 12.2 mm/yr at another. More than 10 mm of right-lateral slip was triggered here by the M=6.3 Morgan Hill earthquake (MHEQ) in 1984 and again in 1989 by the M=7.1 LPEQ. Since the LPEQ-triggered slip, one site has slowed to 4.2 mm/yr and the other site has stopped creeping (the one that was creeping at 12.2 mm/yr), which has resulted in a slip deficit of more than 2 cm. The Concord fault creeps at an overall long-term average rate of about 3 mm/yr and the Green Valley fault at about 5 mm/yr. Both move episodically and both have post-LPEQ rates of about 1–2 mm/yr slower than the longer-term averages. No creep has occurred at a site on the northern Calaveras fault in San Ramon either before or after the LPEQ. The same is true for sites on the noncreeping Seal Cove-San Gregorio, Rodgers Creek, West Napa, and Antioch faults. The changes in creep rates on San Francisco Bay area faults after the LPEQ are consistent with the static shear stress changes estimated for the LPEQ.

INTRODUCTION

My student research assistants and I have been measuring creep (aseismic slip) on active faults throughout the greater San Francisco Bay region since 1979. Over the past 13.5 yr (September 1979 to March 1993) we have made about 1,325 creep measurements at about two dozen sites (fig. 1). About 850 measurements were made in the decade preceding the Loma Prieta earthquake (LPEQ) and about 475 were made in the 3.4 yr following the quake. This data set enables us to determine the detailed creep rates and characteristics at each site and to compare measurements made after the LPEQ with those made previously in order to determine the effects, if any, of the LPEQ. An earlier summary of the effects of the LPEQ on creep rates during the first 6 months after the quake is in Galehouse (1990).

We use a theodolite triangulation method (Galehouse and others, 1982), which allows us to determine the amount of strike-slip surface creep by noting changes in angles between sets of measurements taken across a fault at

different times. Most of the sites span a fault width of 50-225 m, but a few must span a greater width because of site considerations. The precision of the measurement method is such that we can detect with confidence any movement more than 1–2 mm between successive measurement days.

The M=7.1 LPEQ is the largest earthquake to have occurred in the San Francisco Bay region since 1906 (Plafker and Galloway, 1989). Before 17 October 1989, we had been remeasuring sites about once every 2–3 months. Because of augmented funding following the LPEQ, we were able to increase the measurement frequency at sites on the San Andreas, Hayward, and southern Calaveras faults to about once every 5–6 weeks through 1990. Since then we are again occupying all sites about once every 2–3 months.

Results are presented in figures 2–5, which give the average creep rate at each site as determined by the slope of the least-squares line. These figures also indicate the fault width spanned (W) and the time of the LPEQ (shown as a vertical line). All creep rates presented in this paper should be considered minimum rates because undetected creep on additional active fault traces could be occurring outside of the fault width spanned. Most sites are located in low-relief areas, so creep due to mass movement is probably not significant. Even though our data include some of the area's wettest and driest years, the long-term

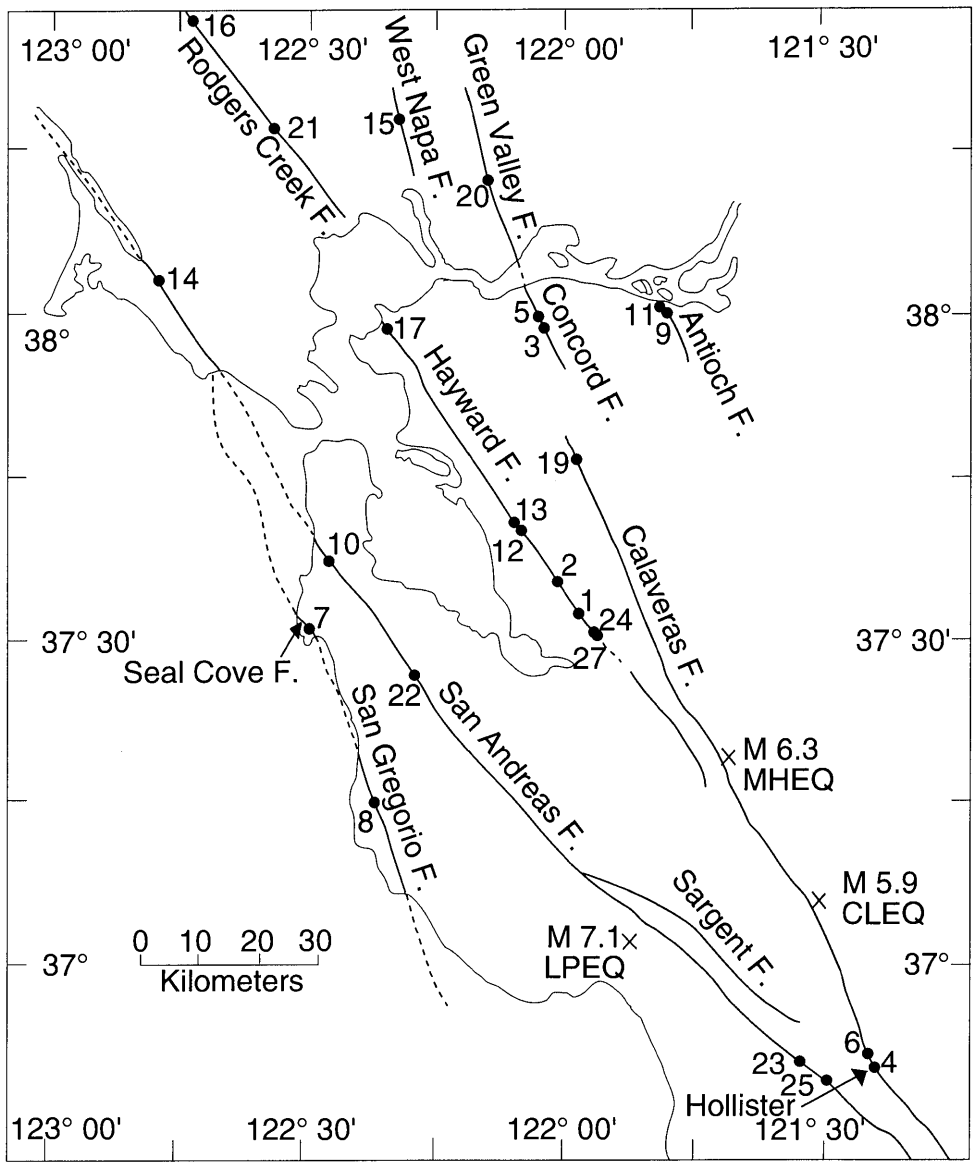

Figure 1.—Map of San Francisco State University creep measurement sites (numbered dots). Epicenters and magnitudes are indicated for the 6 August 1979 Coyote Lake earthquake (CLEQ), the 24 April 1984 Morgan Hill earthquake (MHEQ), and the 17 October 1989 Loma Prieta earthquake (LPEQ).

trends in creep rates do not seem to be significantly affected by these surficial weather conditions. We think that at most sites, the measured creep rate closely approximates the right-lateral, strike-slip component of the tectonic creep rate. All creep and slip mentioned in this paper are strike slip with right-lateral slip defined as positive.

SAN ANDREAS FAULT

We presently measure six sites on the San Andreas fault, five of which are shown in figure 1. Measurements for the past 8.0 yr at Site 14 at the Point Reyes National Seashore Headquarters and for the past 12.9 yr at Site 10 in South San Francisco suggest that the segment of the San Andreas fault is locked between these two sites that are about 135 km and 80 km northwest of the LPEQ epicenter. Virtually no creep was occurring prior to 17 October 1989 and virtually none has occurred thus far in the 3.4 yr since the quake (fig. 2). The same is true for our most northerly site (18) on the San Andreas fault in the Point Arena area (not shown in fig. 1).

Langbein (1990) detected a few millimeters of postseismic slip within a small, multi-kilometer-long geodetic network spanning the San Andreas fault at the northwestern end of the LPEQ aftershock zone in the 7–200 day interval following the quake. In November 1989 in order to detect any post-LPEQ creep closer to the epicentral area, we began measuring a previously established U.S. Geological Survey (USGS) site in Woodside (Site 22) slightly northwest of the aftershock zone. Our results for the past 3.3 yr, when compared to unpublished USGS measurements in 1977 and 1980 (R. Burford, oral commun., 1989), show that little creep occurred at this site before, during, or after the LPEQ (through 13 February 1993). The rate that we measure is <1 mm/yr (fig. 2).

We also established a new site (23) on the San Andreas fault near the southeastern end of the LPEQ aftershock zone just northwest of San Juan Bautista. Virtually no post-LPEQ creep has occurred at this site either (through 20 February 1993).

In July 1990, we established Site 25 on the creeping segment of the San Andreas fault just southeast of San Juan Bautista and the LPEQ aftershock zone. This site spans the location of USGS creepmeter XSJ2, which showed a slip of 5.2 mm triggered by the LPEQ shaking (Schulz, 1989). Our measurements give a creep rate of 13.5±1.0 mm/yr for the past 2.6 yr (through 20 February 1993). This rate is about the same as the creepmeter-determined rate of 12.4 mm/yr following the LPEQ and considerably faster than the pre-LPEQ longer-term creepmeter rate of about 7 mm/yr (Schulz, 1989; Breckenridge and Burford, 1990; Gladwin and others, 1991; Breckenridge and Simpson, 1992). Bilham (1992) reports that the creepmeter-determined rate at Nyland Ranch, between our Site 23 and Site 25, was 20 mm/yr in the 2 years following the LPEQ which is approximately 3 times the mean creepmeter rate at this site from 1968-85 (Schulz, 1989).

In summary, the San Andreas fault at five sites (18, 14, 10, 22, 23) along the locked portion of the fault both northwest and southeast of the LPEQ aftershock zone does not appear to have been affected by the LPEQ. Virtually no surface creep has been detected thus far. In contrast, the northwestern portion of the creeping segment of the fault at Site 25 near San Juan Bautista had about 5 mm of slip triggered by the LPEQ and has continued creeping at a post-LPEQ rate that is about twice the longer-term, pre-LPEQ creepmeter average.

HAYWARD FAULT

We have been measuring creep at five sites along the Hayward fault for about 13 years and have determined that the average long-term rate is slightly less than 5 mm/yr (fig. 3). Although creep characteristics (steady or episodic) differ from site to site, the average rates for all sites are similar. Table 1 gives the relationship between creep on the Hayward fault and the LPEQ and is a summary of much of the following discussion. The Hayward fault at Site 17 at Contra Costa College in San Pablo was creeping at a rate of 4.7 mm/yr for the 9 years before the LPEQ. Since the LPEQ, however, the rate has been only 2.2 mm/yr, which has brought the overall average down to 4.2 mm/yr for the past 12.6 yr.

The Hayward fault at Site 13 at Rose Street in Hayward has also moved episodically at an overall average rate of 4.9 mm/yr since June 1980; the same as the average in the 9.3 yr before the LPEQ. With J. Lienkaemper of the USGS, we remeasured curb offsets and old city of Hayward arrays at Rose Street in late 1992 and determined that the overall creep rate there since 1930 is 5 mm/yr. A least-squares line through our theodolite-measured data points collected after the LPEQ, however, indicates a rate of 6.8 mm/yr. This higher rate may be partly due to a statistical phenomena because of the episodic nature of creep events at this site. The overall rate of 4.9 mm/yr that includes all the theodolite data is the same as the pre-LPEQ rate. The total displacement since the LPEQ, however, is 20.1 mm in 3.37 yr, which gives an average of 6.0 mm/yr, closer to the long-term average rate but still about 1 mm/yr higher. The Hayward fault at Site 12 at D Street in Hayward has two active traces and moves fairly steadily and uniformly, unlike the episodic creep at Rose Street just 1.3 km to the northwest. At D Street the fault was creeping at a rate of 4.9 mm/yr for the 9.3 yr before the LPEQ. Since the LPEQ, however, the rate has dropped to 3.6 mm/yr, which has

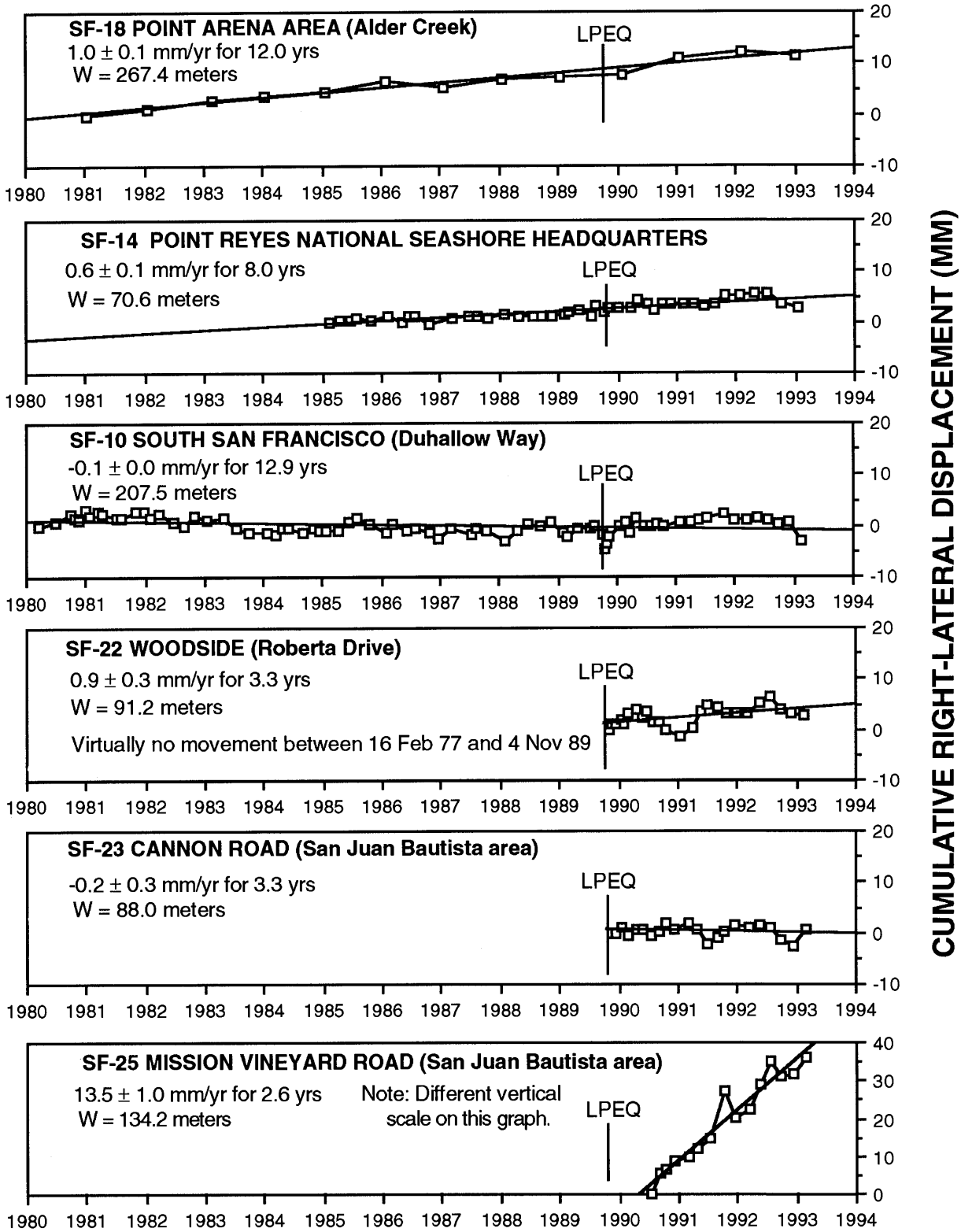

Figure 2.—San Andreas fault displacement measurements at six sites between 1980 and 1993. LPEQ = Loma Prieta earthquake of 17 October 1989. Squares represent individual measurements at each site. The ±1 standard deviation for each measurement almost always falls within its square. A straight line represents the least-squares fit to all the pre- and post-LPEQ measurements at each site and its slope indicates the overall average creep rate. W is the width of the fault zone spanned by the theodolite measurements.

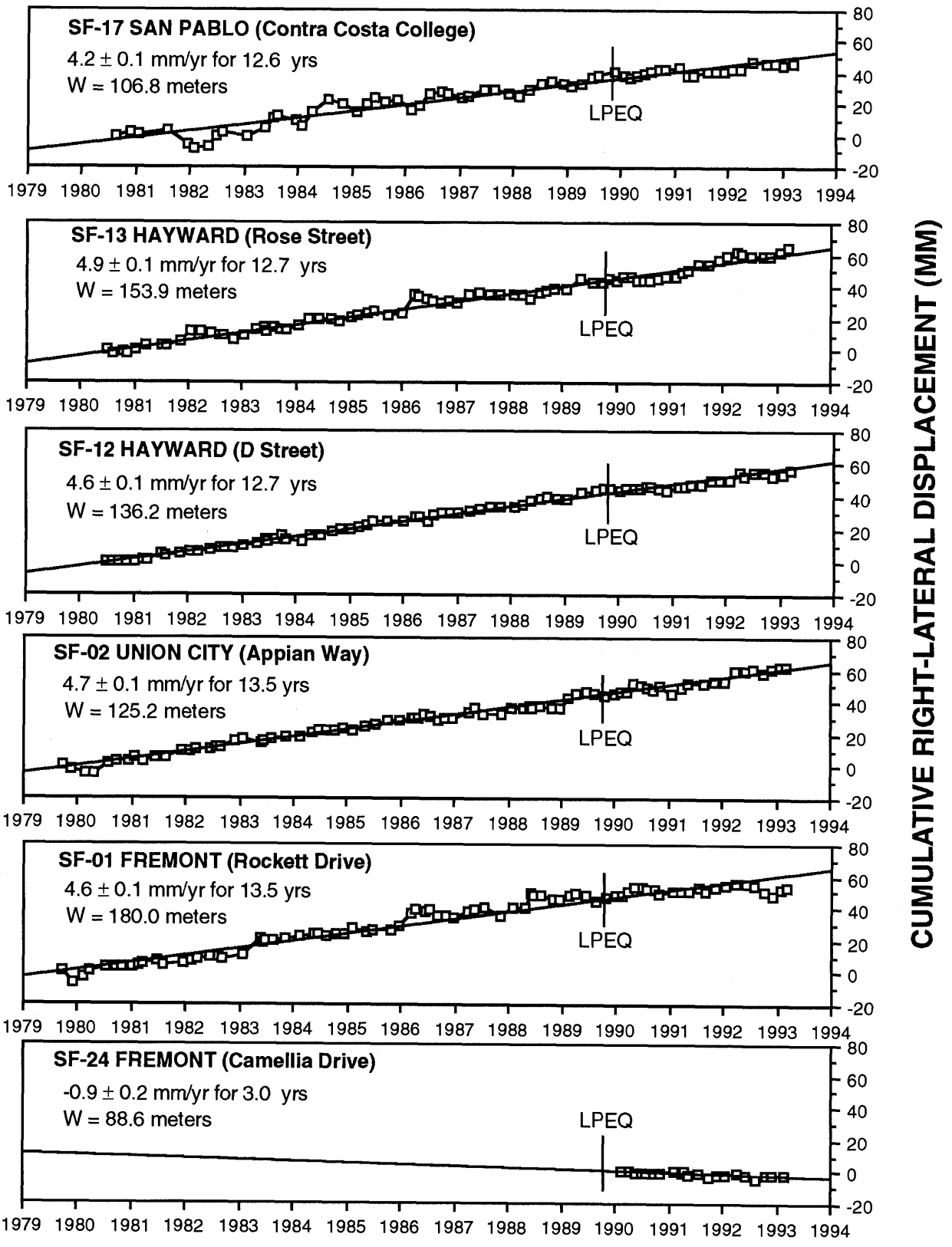

Figure 3.—Hayward fault displacement measurements at six sites between 1979 and 1993. See fig. 2 for further explanation.

Table 1.—*Hayward fault creep rates measured by theodolite between 1979 and 1993*

[See fig. 1 for site locations.]

Site	Pre-Loma Prieta			Post-Loma Prieta			All Measurements	
	Measurement		Average	Measurement		Average	Total	Average
	First (yr)	Last[a] (yr)	Rate (mm/yr)	First[a] (yr)	Last (yr)	Rate (mm/yr)	Years	Rate (mm/yr)
17 San Pablo	1980.609	1989.597	**4.7±0.3**	1989.866	1993.200	**2.2±0.4**	12.6	**4.2±0.1**
13 Hayward Rose St.	1980.481	1989.748	**4.9±0.1**	1989.847	1993.216	**6.8±0.6**	12.7	**4.9±0.1**
12 Hayward D St.	1980.478	1989.748	**4.9±0.1**	1989.847	1993.216	**3.6±0.3**	12.7	**4.6±0.1**
2 Union City	1979.729	1989.595	**4.7±0.1**	1989.808	1993.178	**5.0±0.4**	13.5	**4.7±0.1**
1 Fremont Rockett Dr.	1979.726	1989.595	**5.4±0.1**	1989.808	1993.178	**1.1±0.5**	13.5	**4.6±0.1**
24 Fremont Camellia Dr.	1967	1987	**9.5±0.3** [b]	1990.115	1993.123	**-0.9±0.2**	3.0	**-0.9±0.2**
27 Fremont Parkmeadow Dr.	1968	1982	**8.2±0.2** [c]	1992.262	1993.123	**-4.0±3.8**	0.9	**-4.0±3.8**

[a]The Loma Prieta earthquake occurred at 1989.795.

[b] Pre-Loma Prieta rate from Lienkaemper and others (1991) from curb offsets for the 20 years from 1967-1987.

[c] Pre-Loma Prieta rate from Harsh and Burford (1982) from alignment array data from 1968-1982 at a site 0.3 km southeast of Parkmeadow Drive in Fremont.

brought the overall average down to 4.6 mm/yr for the past 12.7 yr. It is interesting to note but difficult to explain why the Rose Street and D Street sites that are so close together and had the same pre-LPEQ creep rate should be so different in the 3.4 yr following the quake, with Rose Street apparently speeding up and D Street slowing down.

The Hayward fault at Site 2 at Appian Way in Union City also moves fairly steadily, though not as uniformly as at D Street in Hayward. The LPEQ appears to have had little effect on the fault at Site 2. Even though the post-LPEQ rate is 0.3±0.4 mm/yr higher than the average before the LPEQ, the overall average rate has remained at 4.7 mm/yr since September 1979. The Hayward fault at

Site 1 at Rockett Drive in Fremont moves episodically and was creeping at a rate of 5.4 mm/yr for the decade prior to the LPEQ. With J. Lienkaemper of the USGS, we measured the amount of curb offset along Rockett Drive in January 1993 and determined that the overall creep rate since 1964 is 5.3 mm/yr. This projects to a rate of about 5.8 mm/yr for the 25 years prior to the LPEQ, because the extremely low creep rate at this site since the LPEQ has brought the overall average down. The creep rate at Rockett Drive has been only 1.1 mm/yr since the LPEQ, which has reduced the average rate for the past 13.5 yr to 4.6 mm/yr.

Although the creep data are equivocal because of their scatter and the normal episodic nature of movement at most sites, there is a possibility that a slowdown in creep on the Hayward fault began before the LPEQ. A crude estimate of the time when a slowdown may have begun can be made by noting the time of the last previous (before the LPEQ) significant creep event at each site. Even though the results are highly subjective and other investigators could pick different times for the onset of the possible slowdown, the following times were picked by "eyeball" from figure 3. The creep rate may have slowed about 0.3 yr before the LPEQ at Site 17, about 3.6 yr before at Site 13, about 1.4 yr before at Site 12, about 0.7 yr before at Site 2, and about 1.4 yr before at Site 1. Although these eyeball estimates are suggestive that a slowdown in creep on the Hayward fault may have begun a few months to a few years before the LPEQ, more objective methods of evaluating the onset times of rate changes and a statistical measure of the confidence level of the proposed changes need to be developed before any pre-LPEQ slowdown can be considered likely.

At the more recently installed Site 24 at Camellia Drive about 4 km southeast of Rockett Drive (Site 1) in Fremont, creep has only been measured subsequent to the LPEQ (first measurement on 11 February 1990). For the past 3 years, the fault has shown 0.9 mm/yr of left-lateral creep. Measurements for the past year at Parkmeadow Drive in Fremont (Site 27) only 0.4 km southeast of Camellia Drive also indicate a small amount of left-lateral creep (not shown on fig. 3). Sites 24 and 27 are along a 4-km-long segment in Fremont near the southeastern end of the fault that before the LPEQ had been creeping right laterally at about 8-11 mm/yr since at least the 1920's (Harsh and Burford, 1982; Burford and Sharp, 1982; Lienkaemper and others, 1991; Lienkaemper and Borchardt, 1992). Lienkaemper and Borchardt (1992) consider this rate significant because they think it may reflect the long-term surficial slip rate and the deep slip rate that controls the recurrence between large earthquakes on the Hayward fault. Recent measurements of an offset fence along Union Street in Fremont (about 0.9 km southeast of Rockett Drive and 3.2 km northwest of Camellia Drive) by J. Lienkaemper and us suggest that a few centimeters of left-lateral slip may have occurred here in conjunction with the LPEQ.

In summary, our measurements at five sites (17, 13, 12, 2, 1) along the Hayward fault show that the right-lateral creep rate ranged from 4.7 to 5.4 mm/yr for the decade preceding the LPEQ. Equivocal data suggest the possibility that a slowdown in creep may have occurred at these sites a few months to a few years before the LPEQ. No slip events appear to have been triggered at any of these sites by the quake. Since the LPEQ, however, rates have changed significantly at four of these five sites (see table 1). The pre- to post-LPEQ rate decreased in San Pablo from 4.7 to 2.2 mm/yr, at D Street in Hayward from 4.9 to 3.6 mm/yr, and at Rockett Drive in Fremont from 5.4 to 1.1 mm/yr. The rate increased at Rose Street in Hayward from 4.9 to 6.8 mm/yr and stayed nearly constant at 4.7 mm/yr in Union City. In addition, it appears that a few centimeters of left-lateral slip associated with the LPEQ in southern Fremont may have occurred along the previously rapid, right-lateral-creeping southeastern segment of the fault. Slow, left-lateral creep at 0.9 mm/yr has continued since the LPEQ along this segment of the fault at Site 24, and Site 27 has also shown left-lateral creep since we began measurements in April 1992.

Historic creep rates for the Hayward fault determined over the years by various investigators from alignment arrays and offset cultural features have been summarized recently by Lienkaemper and others (1991). The rate of right-lateral creep for the 40–50 years before the LPEQ has been between 3.5 and 6.5 mm/yr for most of the Hayward fault, with a higher rate of about 9 mm/yr along a 4-km-long segment in southern Fremont. All of our pre-LPEQ measurements fall within the 3.5–6.5 mm/yr range. As pointed out above, however, several sites along the fault are now creeping at rates below this range, including slow left-lateral creep in southern Fremont. This indicates that the LPEQ has had a significant effect on creep rates along the Hayward fault.

CALAVERAS FAULT

San Francisco State University began measuring creep at Sites 4 and 6 on the southern Calaveras fault in the Hollister area (fig. 1) in 1979. During the 10 years of measurements before the LPEQ, creep at both sites was quite episodic, with intervals of fast creep typically lasting a couple months or less, alternating with longer periods when little creep occurs (fig. 4).

More specifically, in the decade before the LPEQ, Site 4 along Seventh Street in the city of Hollister had nine episodes of fast creep of about 5 mm or more. This mode of movement had been noted previously by Langbein (1981), based on data from a precision multi-wavelength distance-measuring instrument. He reported that four strain

episodes of creep of about 4–6 mm per episode occurred over time intervals of about 2 months or less during 1975 and 1976 along the Calaveras fault in the Hollister area. He concluded that aseismic slip was the dominant mechanism for strain release, rather than slip associated with earthquakes. At Site 4, times of relatively rapid movement since at least 1979 alternate with intervals of little net movement typically lasting about 8–12 months, with one lasting 2 years between January 1986 and January 1988. The LPEQ apparently triggered 14 mm of right-

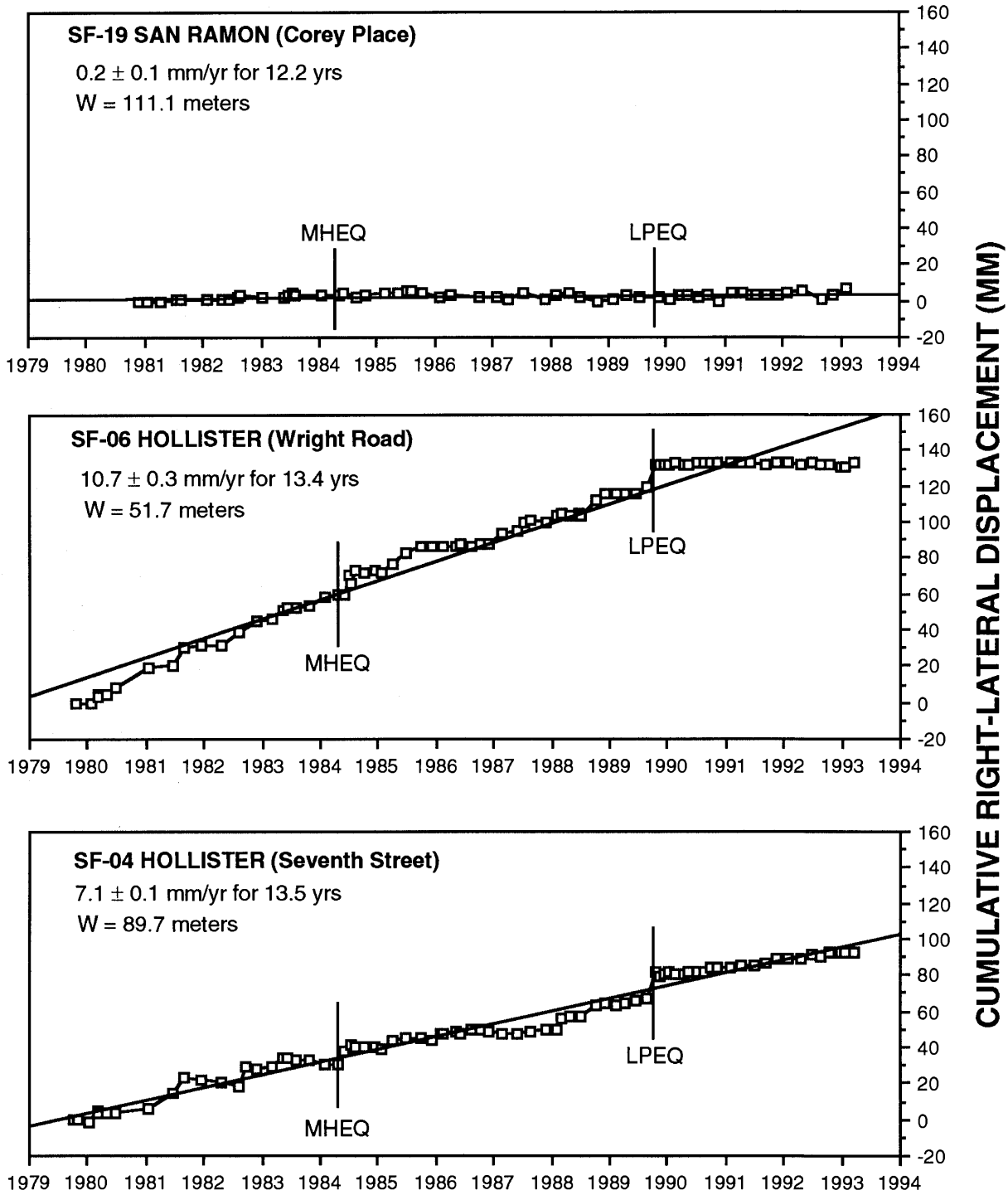

Figure 4.—Calaveras fault displacement at three sites between 1979 and 1993. MHEQ = Morgan Hill earthquake of 24 April 1984. See fig. 2 for further explanation.

lateral slip at Site 4 that marked the abrupt end of an interval of slow creep that had persisted for about a year. Total cumulative displacement from the time of the first measurement in 1979 went from 67 to 81 mm. Following this triggered slip, Site 4 has been creeping at a rate of 4.2 mm/yr for the past 3.4 yr (through 13 March 1993). This is considerably lower than the pre-LPEQ rate of 6.4 mm/yr.

Creep at Site 6 along Wright Road, located 2.3 km northwest of Site 4, included 11 episodes of fast creep of about 5 mm or more in the 10 years before the LPEQ. This faster creep alternates with intervals of little net movement that typically last about 3–12 months at Site 6, with one lasting 18 months between June 1985 and December 1986. The LPEQ marked the end of an interval of slow creep that had persisted for about a year at Site 6, similar to the situation at Site 4. The earthquake apparently triggered 12 mm of right-lateral slip, and cumulative displacement increased from 119 to 131 mm. Following this triggered slip, the fault at Site 6 has virtually stopped creeping for the past 3.4 yr (through 13 March 1993). This has brought the pre-LPEQ average rate of 12.2 mm/yr down to 10.7 mm/yr for the past 13.4 yr. As shown in figure 4, the fault at Site 6 now has a "slip deficit" of more than 2 cm.

Creepmeter data also show that relatively long periods of time with little net movement have occurred along the Calaveras fault in the Hollister area. Evans and others (1981) note that the USGS creepmeter across the Calaveras fault at Shore Road 10 km north of Hollister showed virtually no net creep for a 3-year period from July 1976 to July 1979. They point out that this period of no movement ended with a small slip event coincident with the 6 August 1979 M=5.9 Coyote Lake earthquake (CLEQ) on the Calaveras fault about 12 km northwest of the creepmeter site. Accelerated afterslip in the form of a cluster of creep events followed the small slip event (Raleigh and others, 1979).

Our theodolite data alone cannot prove that the LPEQ on the nearby San Andreas fault coseismically triggered aseismic slip on the Calaveras fault. Our last measurement before the earthquake was on 19 August 1989 and our first measurement after the quake was on 21 October 1989. Strictly speaking, we can only say that 12–14 mm of displacement in the Hollister area occurred between these two dates. Other evidence, however, suggests that the timing of the slip was at least partially coseismic. We detected fresh en echelon cracks on Highway 25 near Hollister on the morning of 21 October 1989. These cracks extended from the asphalt into the dirt shoulder of the road. Fortunately, we were able to photograph them before they were obliterated by rainfall that occurred that afternoon. The cracks had to have formed sometime after the last previous rainfall on 29 September 1989 (McClellan and Hay, 1990) and probably formed shortly after the LPEQ (see the following discussion).

The strongest evidence for coseismic slip on the Calaveras fault due to the LPEQ comes from the USGS creepmeter at Shore Road, 8.5 km northwest of Wright Road (Site 6). The LPEQ occurred at 1704 hours, Pacific Daylight Time (Plafker and Galloway, 1989). The Shore Road creepmeter recorded slip of 5.0 mm within a 10-minute interval from 1700 to 1710 hours (Schulz, 1989). It is unlikely that slip on the Calaveras fault preceded the LPEQ. It is more likely that shaking from the LPEQ triggered slip on the Calaveras fault at the exact time of the earthquake or within a few minutes after it. Additional evidence that slip on the Calaveras fault was triggered by the LPEQ comes from field observations made by McClellan and Hay (1990), who observed fresh en echelon cracks and offset cultural features that indicated at least 5 mm of movement along 17 km of the Calaveras fault from the city of Hollister northwest to Highway 152.

Table 2 shows a comparison of Calaveras fault creep rates in the Hollister area determined by USGS creepmeters and San Francisco State University (SFSU) theodolite measurements. Both data sets span 10 years or more and overlap from the late 1970's to mid 1980's. The SFSU data exclude the LPEQ coseismic slip. Even though the measurement methods and time intervals are different, the creep rates determined by the USGS and SFSU are quite similar. Both indicate that the long-term creep rate at Wright Road (Site 6) is about 6 mm/yr faster than the rate at nearby Seventh Street (Site 4). Either the creep rate on the Calaveras fault decreases significantly from Wright Road southeast to Seventh Street or undetected surface movement is occurring outside our 89.7-m-long survey line at Seventh Street, which encompasses the former USGS creepmeter site. Since the slip triggered by the LPEQ, the creep rate at both sites has decreased and the sites with faster and slower creep have reversed. Site 4 is now creeping at 4.2 mm/yr, whereas Site 6 has stopped creeping.

In contrast to the evidence for creep and triggered slip along the southern segment of the Calaveras fault near Hollister, Site 19 in San Ramon near the northwestern terminus of the Calaveras fault has shown virtually no creep since measurements began in 1980 (fig. 4).

Previous investigators have determined that significant earthquakes occurring on particular faults in California have triggered coseismic slip or afterslip on other nearby faults. Examples of such earthquakes include the Borrego Mountain earthquake of 9 April 1968 (Allen and others, 1972), the Imperial Valley earthquake of 15 October 1979 (Fuis, 1982; Sieh, 1982), the Livermore Valley earthquakes of late January 1980 (Harsh and Burford, 1982), the Coalinga earthquake of 2 May 1983 (Mavko and others, 1985), the Tres Pinos earthquake of 26 January 1986

Table 2.—*Calaveras fault creep rates in the Hollister area measured by creepmeter and theodolite between 1970 and 1993*

[See fig. 1 for site locations.]

Site	Average creep rate (mm/yr)
Wright Road (SF-6)	
USGS (1971 - 1983)[a]	13.1
SFSU (1979 - LPEQ)[b]	12.2
SFSU (LPEQ - 1993)[b]	0.0
Seventh Street (SF-4)	
USGS (1970 - 1987)[a]	6.8
SFSU (1979 - LPEQ)[b]	6.4
SFSU (LPEQ - 1993)[b]	4.2

[a] U. S. Geological Survey (USGS) creepmeter data from Schulz and others (1982) and Schulz (1989).

[b] San Francisco State University (SFSU) theodolite data before and after the Loma Prieta earthquake (LPEQ) from this paper.

(Simpson and others, 1988), the North Palm Springs earthquake of 8 July 1986 (Williams and others, 1988), and the Superstition Hills earthquake of 24 November 1987 (Sharp, 1989).

In central California, USGS creepmeters on the San Andreas, Hayward, and Calaveras faults have recorded small, abrupt movements during or shortly after nearby moderate earthquakes as well as increased or decreased creep rates either before or after some of these quakes (Schulz and others, 1982). King and others (1977) point out that during 1971-73, creepmeters along the creeping portion of the San Andreas fault in central California often recorded minor coseismic steps (<1 mm) at times of local earthquakes of magnitudes 4–5. Although most of the nine moderate earthquakes that occurred locally during this time interval were on the San Andreas fault, some were not. In contrast, many larger creep events (≥1 mm) occurred during this same interval at times of no local seismic events. King and others (1977) concluded that during 1971–73, coseismic slip was negligible compared to slip by episodic and continuous creep processes. They also concluded that creep episodes often follow seismic events at depth, suggesting that some creep may be afterslip delayed by different fault rheology near the surface.

In our observations, some phases of rapid creep on the Calaveras fault in the Hollister area are apparently related to nearby seismic events, but others are not. Our data suggest that some significant nearby earthquakes trigger slip on the Calaveras fault, but others do not. In addition to the relationship between the LPEQ and triggered slip on the Calaveras fault discussed above, there also appears to have been a period of rapid creep on the fault near Hollister that was related to the 1984 M=6.3 Morgan Hill earthquake on the Calaveras fault. However, no immediate surface displacement was observed at either of the Hollister sites when they were remeasured on 25 April 1984, the day after the MHEQ (Galehouse, 1987), even though surface displacement had occurred 2.7 km northwest of Site 6 (Galehouse and Brown, 1987). However, within the following 2.5 months, Site 4 showed 11 mm of creep and Site 6 showed 10 mm of creep. This relatively large amount of post-seismic creep was about the same as the slip (13 mm) recorded in the 18 hours following the earthquake at the USGS creepmeter at Shore Road 8.5 km northwest of Site 6 (Schulz, 1987).

Since detailed monitoring began more than 20 years ago, the southern Calaveras fault has had several intervals with relatively large amounts of creep (≥ 1 cm) occurring within a relatively short time interval (months), but these intervals were apparently unrelated to any nearby significant earthquakes. Fast creep was recorded by two USGS creepmeters in Hollister in May-August 1977 (Evans and others, 1981). This rapid creep occurred during a 3-year interval when the Calaveras fault at Shore Road, 10 km to the northwest, was in a period of no movement. It also occurred with no apparent relationship to any significant earthquake(s) in the area.

Another example of distinctly aseismic rapid creep occurred in the 14-month interval between June 1980 and August 1981 (fig. 4). The Calaveras fault at Site 4 showed creep of 19 mm during this interval, more than twice the predicted slip of about 8 mm obtained for this 14-month interval by extrapolating the pre-LPEQ least-squares average rate (6.4 mm/yr). The fault at Site 6 showed creep of 23 mm, also considerably larger than the expected slip of 14 mm, based on the average rate (12.2 mm/yr) for this interval. This rapid creep began 10 months after the M=5.9 CLEQ on the Calaveras fault (epicenter about 30 km northwest of Hollister) and ended about 32 months before the M=6.3 MHEQ on the Calaveras fault (epicenter about 55 km northwest of Hollister). Thus, this interval of rapid creep in the Hollister area appears to be unrelated to either large regional earthquakes (CLEQ, or MHEQ, or both), or any significant local earthquakes.

CONCORD FAULT

Sites 3 and 5 are in the city of Concord on what is known as the Concord segment of the Concord fault (Sharp, 1973). A detailed discussion of creep characteristics on the Concord fault is in Galehouse (1992). In general, the Concord fault creeps episodically, with intervals

of fast creep of about 7–10 mm over a period of a few months alternating with intervals of slow creep of about 1–2 mm/yr over a period of several years (fig. 5). This pattern of episodic creep was slightly more pronounced during the first eight to nine years of measurements. The average creep rate on the Concord fault for at least the past 13.4 yr is about 3 mm/yr (3.4 at Site 3 and 2.6 at Site 5). Because of the episodic nature of creep on the Concord fault and the lack of any triggered slip, it is difficult to assess any effect(s) of the LPEQ. Both sites completed

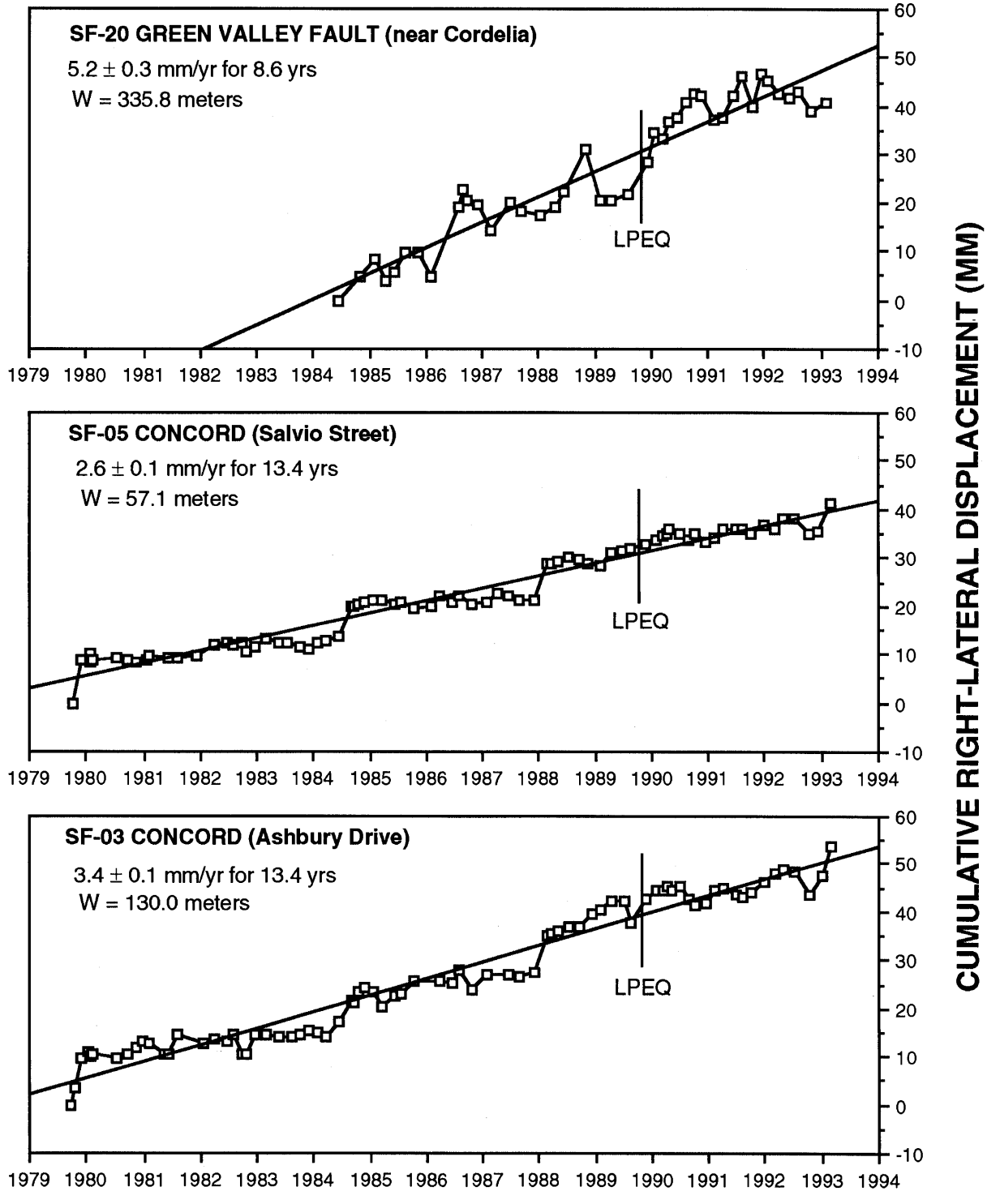

Figure 5.—Concord fault displacement at two sites between 1979 and 1993 and Green Valley fault displacement at one site between 1984 and 1993 . See fig. 2 for further explanation.

their latest phase of fast creep in February 1988 and overall have been creeping at about their longer-term average rate since then (through 7 March 1993). A least-squares line through only the post-LPEQ data points, however, shows a rate at both sites that is about 1–1.5 mm/yr lower than the long-term average. However, given the episodic nature of the fault movement recorded over the years at Sites 3 and 5, we cannot definitely state that the rate has slowed due to the LPEQ.

GREEN VALLEY FAULT

Frizzell and Brown (1976) and Helley and Herd (1977) suggest that the southern extension of the Green Valley fault connects to the northern extension of the Concord fault by a relatively short (<3 km) right step (fig. 1). The overall average rate of creep for the past 8.6 yr on the Green Valley fault is 5.2 ± 0.3 mm/yr. This is virtually the same rate (5.4 mm/yr between 1922 and 1974) that Frizzell and Brown (1976) determined from offset power transmission lines about 3 km south of Site 20. Although the creep rates are different, creep characteristics of the Green Valley fault are crudely similar to those of the Concord fault (fig. 5), although there is more "noise" in the Green Valley data, which is at least partly due to the relatively large fault width being measured (335.8 m). A detailed comparison is in Galehouse (1991 and 1992). In general, the Green Valley fault also creeps episodically, with intervals of fast creep of 10 mm or more over a few months alternating with intervals of slower creep up to about 3 mm/yr over a few years. In the 8.6 yr since we began our measurements, there have been two intervals of fast creep and three of slow creep. The most recent fast creep interval began sometime between 6 August 1989 and 2 December 1989. Although there is a possibility that shaking from the 17 October 1989 LPEQ triggered the onset of this fast creep as it apparently did in Hollister, it is probably only a coincidence that the Green Valley fault began a period of faster creep at a time that can be crudely related to the quake that was centered more than 125 km away. Our measurement intervals on the Green Valley fault were too far apart to pin down the exact time when rapid creep started, and we know of no other evidence suggesting a relationship. The latest phase of slow creep is continuing, and in fact there has been no net slip on the Green Valley fault for the past 2.5 yr (through 30 January 1993), giving a post-LPEQ rate of only 2.9 mm/yr.

OTHER FAULTS

We also have measurement sites on the Seal Cove-San Gregorio, Rodgers Creek, West Napa, and Antioch faults (fig. 1). None of these faults show unequivocal evidence of fault creep and none have shown any effects from the LPEQ thus far.

SUMMARY AND CONCLUSIONS

Reasenberg and Simpson (1992) point out that because the major San Francisco Bay area faults are probably loaded by right-lateral shear, the stress changes due to the LPEQ would either increase the shear load if the change was right-lateral or decrease the shear load if the change was left-lateral. Consequently, a right-lateral static stress change would tend to be associated with a post-LPEQ increase in seismicity rate and an increase in creep rate. A left-lateral change would tend to be associated with a decrease in seismicity rate and either a decrease in creep rate or even a reversal in creep direction if the static stress change was particularly significant. Reasenberg and Simpson (1992) found that their calculations of stress changes agreed closely with changes in the regional seismicity rate after the LPEQ. The data we have been collecting since the LPEQ are exactly what are needed to evaluate further the Reasenberg and Simpson (1992) calculations for static stress changes. For sites which clearly showed proposed stress changes, we compared our data with the Reasenberg and Simpson (1992) model. None of the stress changes were evidently large enough to cause noncreeping segments of faults to begin creeping. Whether the stress change was right-lateral or left-lateral, none of our measurement sites with pre-LPEQ rates less than 1 mm/yr increased in rate after the LPEQ. In other words, fault segments that were virtually locked before the LPEQ remained locked after the quake. This suggests that none of the noncreeping areas that experienced an increase in right-lateral stress were loaded to their breaking (fault slip) stress level. Those that received a left-lateral change probably had their next time of surface rupture delayed. The amount of static stress change and degree of shaking from the earthquake were not enough to induce movement at any of these noncreeping fault sites. In areas that were already creeping, we can compare the creep rates before and after the LPEQ to see if the changes correspond to the Reasenberg and Simpson (1992) model. In 11 of 13 cases, the changes in creep rates are consistent in sign with their model. In one additional case the data are consistent with the model, and in only one case is the change inconsistent.

The San Andreas fault northwest of the LPEQ aftershock zone was not creeping before the quake, did not have any surface slip during the quake, and is still not creeping. There also has been no post-LPEQ creep at a site (23) just southeast of the aftershock zone. In contrast, about 42 km southeast of the epicenter, approximately 5

mm of slip was triggered by LPEQ shaking near the northwestern end of the creeping segment of the fault near San Juan Bautista and the post-LPEQ creep rate at this site (25) is about twice the pre-LPEQ average. It appears that right-lateral shear stress from the Loma Prieta region was transferred to the region southeast of the rupture following the LPEQ.

Most of the Hayward fault creeps at a long-term rate of about 5 mm/yr. Five sites along the fault that we had been measuring for the decade before the LPEQ had rates between 4.7 and 5.4 mm/yr, with a median rate of 4.9 mm/yr. These same sites have a median rate of only 3.6 mm/yr during the 3.4 yr since the quake. The post-LPEQ rate is particularly low in San Pablo and Fremont, at either end of the fault. A few centimeters of left-lateral slip associated with the LPEQ may have occurred in southern Fremont, and small amounts of left-lateral creep are continuing. This left-lateral displacement is along the segment of the Hayward fault that was creeping right-laterally at about 9 mm/yr for at least 50 yr before the LPEQ. Simpson and others (1988) point out two possible explanations for earthquake-related steps in creep (slip) along faults. Either the slip was triggered by earthquake shaking or the slip occurred in response to changes in static stress fields accompanying the earthquake. This left-lateral slip of a few centimeters in southern Fremont almost certainly would not have occurred as triggered slip. It is unlikely that the segment of the Hayward fault that had been creeping right-laterally at about twice the rate on the rest of the fault would have been loaded left-laterally and been primed to move in that direction. The left-lateral slip was almost certainly due to the nature of the static stress changes imposed upon the fault by the LPEQ, although stress changes due to unknown factors unrelated to the LPEQ cannot be completely ruled out. A decrease in right-lateral static stress on the fault following the LPEQ was suggested by Reasenberg and Simpson (1992) based on their computer simulation of the earthquake and the post-LPEQ decrease in microseismicity along the Hayward fault. Their model assumes low values for the apparent coefficient of friction along the fault and agrees well with our measurements of low creep rates following the LPEQ. The segment of the Hayward fault in Fremont that moved and is continuing to move left-laterally, however, probably had a larger left-lateral stress change than indicated in the Reasenberg and Simpson (1992) model. The post-LPEQ slowdown in right-lateral creep over much of the rest of the Hayward fault is fully consistent with the sign of the predicted LPEQ stress change in their model. The model, however, does not help explain the puzzling post-LPEQ increase in creep rate at Rose Street in Hayward or a pre-LPEQ slowdown along the Hayward fault, if that indeed occurred.

The average creep rate on the southern Calaveras fault in the Hollister area before the LPEQ was 6.4 mm/yr at Site 4 and 12.2 mm/yr at Site 6. The LPEQ triggered 12-14 mm of slip here, less than 50 km from the epicenter. A similar amount of slip occurred at these sites after the MHEQ in 1984. It appears that the rapid slip that occurred in the Hollister area on the Calaveras fault in conjunction with the MHEQ in 1984 and the LPEQ in 1989 were of different character. The rapid slip associated with the MHEQ occurred during the 2.5 months following the quake, but no slip had occurred when measurements were taken the first day after the quake. This rapid slip was most probably in response to a change in the static stress field. In contrast, the rapid slip associated with the LPEQ almost certainly was triggered by earthquake shaking. For decades, the typical mode of movement has been episodic in the Hollister area, with longer periods of slower creep alternating with shorter periods of faster creep. When no significant earthquakes occur in the Hollister area over a relatively long period, a rapid phase of movement will occur with no association with any seismic event(s). When a significant earthquake occurs on either the Calaveras or another nearby fault and the Hollister area segment of the Calaveras fault is primed to move anyway, the earthquake will probably trigger a relatively rapid phase of movement. This may occur as coseismic slip triggered by shaking (as with the LPEQ) or as accelerated creep when a change in the static stress field caused by the earthquake is right-lateral (as with the MHEQ). On the other hand, when the fault is not primed, a nearby earthquake will not trigger any slip. Because the lengths of time of the slower and faster phases are so variable, predicting whether or not the southern Calaveras fault is "primed and ready to go" is extremely difficult. At the present time (March 1993), there appears to be a "slip deficit" of more than 2 cm at Site 6 in the Hollister area (fig. 4). A post-LPEQ decrease in the rate of right-lateral creep on the Calaveras fault in the Hollister area is qualitatively consistent with the static stress change following the LPEQ proposed by Reasenberg and Simpson (1992).

The observed decrease in creep rates on the Concord and Green Valley faults is also qualitatively consistent with the stress changes estimated for these sites with the Reasenberg and Simpson (1992) model. The noncreeping northern Calaveras, Seal Cove-San Gregorio, Rodgers Creek, West Napa, and Antioch faults were apparently not affected by the LPEQ.

In summary, changes in creep rates on San Francisco Bay region faults after the LPEQ are consistent with stress changes estimated for the LPEQ by Reasenberg and Simpson (1992). At one measurement site (25) on a creeping fault where Reasenberg and Simpson (1992) show a right-lateral static shear stress increase, the creep rate has doubled since the LPEQ. Among 12 sites on creeping faults where Reasenberg and Simpson (1992) calculate a left-lateral change (a decrease in right-lateral shear load), the post-LPEQ creep rate slowed significantly (>1.2 mm/

yr) at ten of these sites (1, 3, 4, 5, 6, 12, 17, 20, 24, 27), stayed virtually the same at one (2), and increased at only one (13). As Simpson and others (1988) conclude, it is not yet possible to explain unambiguously all the observed creep on certain faults during and after earthquakes on other faults. We do, however, seem to be making some progress in understanding and predicting these relationships.

ACKNOWLEDGMENTS

I thank the many geology students at San Francisco State University who have been instrumental in helping collect this theodolite data since 1979. I am particularly grateful to Carolyn Garrison, Oliver Graves, Theresa Hoyt, and Carl Schaefer, who are presently working with me on this ongoing research effort. I also thank J. Lienkaemper, P. Reasenberg, and R. Simpson of the USGS for helpful suggestions and thoughtful reviews of the manuscript. The present work is supported by the USGS, Department of the Interior, under award number 14-08-0001-G1992.

REFERENCES

Allen, C.R., Wyss, M., Brune, J.N., Grantz, A., and Wallace, R.E., 1972, Displacements on the Imperial, Superstition Hills and the San Andreas faults triggered by the Borrego Mountain earthquake, *in* The Borrego Mountain earthquake of April 9, 1968: U.S. Geological Survey Professional Paper 787, p. 87-104.

Bilham, R., 1992, Creepmeters on California faults: U.S. Geological Survey Open-File Report 92-258, p. 153-156.

Breckenridge, K.S., and Burford, R.O., 1990, Changes in fault slip near San Juan Bautista, California, before the October 17, 1989, Loma Prieta earthquake-a possible precursor? [abs.]: Eos (American Geophysical Union Transactions), v. 71, no. 43, p. 1461.

Burford, R.O., and Sharp, R.V., 1982, Slip on the Hayward and Calaveras faults determined from offset powerlines, *in* Hart, E.W., Hirschfeld, S.E., and Schulz, S.S., eds., Proceedings - Conference on Earthquake Hazards in the Eastern San Francisco Bay Area: California Division of Mines and Geology, Special Publication 62, p. 261-269.

Evans, K.F., Burford, R.O., and King, G.C.P., 1981, Propagating episodic creep and the aseismic slip behavior of the Calaveras fault north of Hollister, California: Journal of Geophysical Research, v. 86, p. 3721-3735.

Frizzell, V.A., Jr., and Brown, R.D., Jr., 1976, Map showing recently active breaks along the Green Valley fault, Napa and Solano Counties, California: U.S. Geological Survey Miscellaneous Field Studies Map MF-743, scale 1:24,000.

Fuis, G.S., 1982, Displacement on the Superstition Hills fault triggered by the earthquake, *in* The Imperial Valley, California, earthquake of October 15, 1979: U.S. Geological Survey Professional Paper 1254, p. 145-154.

Galehouse, J.S., 1987, Theodolite measurements, *in* Hoose, S.N., ed., The Morgan Hill, California, earthquake of April 24, 1984: U.S. Geological Survey Bulletin 1639, p. 121-123.

———1990, Effect of the Loma Prieta earthquake on surface slip along the Calaveras fault in the Hollister area: Geophysical Research Letters, v. 17. no. 8, p. 1219-1222.

———1991, Present-day creep on the Green Valley fault, *in* Figuers, S.H., ed., Field Guide to the Geology of Western Solano County: Northern California Geological Society and Association of Engineering Geologists Guidebook, p. 12-16.

———1992, Creep rates and creep characteristics of eastern San Francisco Bay area faults: 1979-1992, *in* Borchardt, G. and others, eds., Proceedings of the Second Conference on Earthquake Hazards in the Eastern San Francisco Bay Area: California Division of Mines and Geology, Special Publication 113, p. 45-53.

Galehouse, J.S., and Brown, B.D., 1987, Surface displacement near Hollister, California, *in* Hoose, S.N., ed., The Morgan Hill, California, earthquake of April 24, 1984: U.S. Geological Survey Bulletin 1639, p. 69-72.

Galehouse, J.S., Brown, B.D., Pierce, B., and Thordsen, J.J., 1982, Changes in movement rates on certain East Bay faults, *in* Hart, E.W., Hirschfeld, S.E., and Schulz, S.S., eds., Proceedings - Conference on Earthquake Hazards in the Eastern San Francisco Bay Area: California Division of Mines and Geology, Special Publication 62, p. 239-250.

Gladwin, M.T., Breckenridge, K.S., Hart, R.H.G., and Gwyther, R.L., 1991, Recent acceleration of characteristic creep-strain events at San Juan Bautista [abs.]: Eos (American Geophysical Union Transactions), v. 72, no. 44, p. 484.

Harsh, P.W., and Burford, R.O., 1982, Alinement-array measurements of fault slip in the eastern San Francisco Bay area, California, *in* Hart, E.W., Hirschfeld, S.E., and Schulz, S.S., eds., Proceedings - Conference on Earthquake Hazards in the Eastern San Francisco Bay Area: California Division of Mines and Geology, Special Publication 62, p. 251-260.

Helley, E.J., and Herd, D.G., 1977, Map showing faults with Quaternary displacement, northeastern San Francisco Bay region, California: U.S. Geological Survey Miscellaneous Field Studies Map MF-881, scale 1:125,000.

King, C.Y., Nason, R.D., and Burford, R.O., 1977, Coseismic steps recorded on creep meters along the San Andreas fault: Journal of Geophysical Research, v. 82, p. 1655-1662.

Langbein, J.O., 1981, An interpretation of episodic slip on the Calaveras fault near Hollister, California: Journal of Geophysical Research, v. 86, p. 4941-4948.

———1990, Post-seismic slip on the San Andreas fault at the northwestern end of the 1989 Loma Prieta earthquake rupture zone: Geophysical Research Letters, v. 17, no. 8, p. 1223-1226.

Lienkaemper, J.J., and Borchardt, G., 1992, Hayward fault: Large earthquakes versus surface creep, *in* Borchardt, G. and others, eds., Proceedings of the Second Conference on Earthquake Hazards in the Eastern San Francisco Bay Area: California Division of Mines and Geology, Special Publication 113, p. 101-110.

Lienkaemper, J.J., Borchardt, G., and Lisowski, M., 1991, Historic creep rate and potential for seismic slip along the Hayward fault, California: Journal of Geophysical Research, v. 96, no. B11, p. 18, 261-18, 283.

Mavko, G.M., Schulz, S.S., and Brown, B.D., 1985, Effects of the 1983 Coalinga, California earthquake on creep along the San Andreas fault: Seismological Society of America Bulletin, v. 75, p. 475-489.

McClellan, P.H., and Hay, E.A., 1990, Triggered slip on the Calaveras fault during the magnitude 7.1 Loma Prieta, California, earthquake: Geophysical Research Letters, v. 17, no. 8, p. 1227-1230.

Plafker, G., and Galloway, J.P., eds., 1989, Lessons learned from the Loma Prieta, California, earthquake of October 17, 1989: U.S. Geological Survey Circular 1045, 48 p.

Raleigh, C.B., Stuart, W., and Harsh, P., 1979, Creep on the Calaveras

fault near Coyote Lake [abs.]: Eos (American Geophysical Union Transactions), v. 60, p. 890.

Reasenberg, P.A., and Simpson, R.W., 1992, Response of regional seismicity to the static stress change produced by the Loma Prieta earthquake: Science, v. 255, p. 1687-1690.

Schulz, S.S., 1987, Response of U.S. Geological Survey creepmeters near Hollister, California, *in* Hoose, S.N., ed., The Morgan Hill, California, earthquake of April 24, 1984: U.S. Geological Survey Bulletin 1639, p. 111-115.

———1989, Catalog of creepmeter measurements in California from 1966 through 1988: U.S. Geological Survey Open-File Report 89-650, 193 p.

Schulz, S.S., Mavko, G.M., Burford, R.O., and Stuart, W.D., 1982, Long-term fault creep observations in central California: Journal of Geophysical Research, v. 87, p. 6977-6982.

Sharp, R.V., 1973, Map showing recent tectonic movement on the Concord fault, Contra Costa and Solano Counties, California: U.S. Geological Survey Miscellaneous Field Studies Map MF-505, scale 1:24,000.

———1989, Pre-earthquake displacement and triggered displacement on the Imperial fault associated with the Superstition Hills earthquake of 24 November 1987: Seismological Society of America Bulletin, v. 79, p. 466-479.

Sieh, K.E., 1982, Slip along the San Andreas fault associated with the earthquake, *in* The Imperial Valley, California, earthquake of October 15, 1979: U.S. Geological Survey Professional Paper 1254, p. 155-159.

Simpson, R.W., Schulz, S.S., Dietz, L.D., and Burford, R.O., 1988, The response of creeping parts of the San Andreas fault to earthquakes on nearby faults: two examples: Pageoph, v. 126, nos. 2-4, p. 665-685.

Williams, P.L. and others, 1988, Triggered slip along the San Andreas fault after the 8 July 1986 North Palm Springs earthquake: Seismological Society of America Bulletin, v. 78, p. 1112-1122.

THE LOMA PRIETA, CALIFORNIA, EARTHQUAKE OF OCTOBER 17, 1989:
EARTHQUAKE OCCURRENCE

AFTERSHOCKS AND POSTSEISMIC EFFECTS

POSTSEISMIC STRAIN FOLLOWING THE LOMA PRIETA EARTHQUAKE FROM REPEATED GPS MEASUREMENTS

By Roland Bürgmann, University of California, Davis;
Paul Segall, Stanford University; and
Mike Lisowski and Jerry L. Svarc, U.S. Geological Survey

CONTENTS

ABSTRACT

The postseismic velocity field in the epicentral region of the Loma Prieta earthquake differs significantly from displacement rates measured in the two decades preceding the event. The post-earthquake displacement rates along the Black Mountain profile, which crosses the San Andreas fault 44 km northwest of the Loma Prieta epicenter, do not differ significantly from those determined from 20 years of trilateration measurements. However, station velocities along the Loma Prieta profile, which passes through the epicentral region, significantly exceed pre-earthquake rates within 20 km of the Loma Prieta rupture. There is also significant San Andreas normal shortening centered near Loma Prieta. Aseismic right-lateral strike slip at a rate of 0.10 m/yr on the Loma Prieta rupture and reverse slip at a rate of 0.12 m/yr on a reverse fault of the Foothills thrust belt can explain the observed postseismic deformation. Slip within the Foothills thrust belt appears to have been triggered by the stressing during the Loma Prieta main shock.

INTRODUCTION

Geodetic observations have shown accelerated strain rates adjacent to faults in the years to decades following some large earthquakes (for example, Thatcher, 1986). Following the 1906 San Francisco earthquake, which ruptured a 400 km segment of the San Andreas fault (Lawson, 1908), shear strain rates near Point Reyes and Point Arena were 2 to 3 times greater than rates measured in the 1970's (Thatcher, 1974). Postseismic transients have also been observed following some subduction-zone earthquakes in Japan (Kasahara, 1981; Thatcher, 1986).

Transient postseismic deformation has generally been explained either by viscous relaxation of a ductile (asthenospheric) layer underlying an elastic (lithospheric) plate, or by downward propagation of aseismic slip along an extension of the fault zone into the lower crust (Bott and Dean, 1973; Nur and Mavko, 1974; Thatcher, 1974; Anderson, 1975; Budianski and Amazigo, 1976; Rundle and Jackson, 1977; Savage and Prescott, 1978; Cohen, 1979; Lehner and others, 1981; Thatcher, 1983; Li and Rice, 1987). Unfortunately, there is a lack of adequate data to test and differentiate among the various kinematic models.

Earthquakes have been observed to propagate along fault zones, rupturing adjacent fault segments over the time span of several years. Examples involving strike-slip faults have been reported in northeast China preceding the 1975 Haicheng earthquake (Scholz, 1977), and along the North Anatolian (Toksöz and others, 1979), the Calaveras (Oppenheimer and others, 1990), and the San Andreas (Savage, 1971; Wood and Allen, 1973) fault zones. In the 19th century, earthquakes along the San Andreas fault and the Hayward fault in the San Francisco Bay area occurred in clusters spread over several years (Ellsworth, 1990). These observations suggest the existence of transient loading processes that occur with characteristic time scales of several years. However, without more data on time-dependent deformation following large earthquakes, we can only speculate on the mechanics of postseismic

deformation and the relation between strain transients and the clustering of earthquakes.

The Loma Prieta earthquake was the largest earthquake in California in 40 years and the largest earthquake in the San Francisco Bay area since 1906. The horizontal deformation field in the epicentral region prior to the 1989 earthquake was already well established on the basis of 20 years of Geodolite measurements (Lisowski and others, 1991a) and several years of Global Positioning System (GPS) measurements (Davis and others, 1989; Lisowski and others, 1990b). Because of the extensive pre-earthquake monitoring, it is possible to identify features in the present-day deformation field that are attributable to the earthquake. Furthermore, the source characteristics of the Loma Prieta earthquake itself are well established by both seismic and geodetic measurements (Beroza, 1991; Hartzell and others, 1991; Steidl and others, 1991; Wald and others, 1991; Lisowski and others, 1990a; Marshall and others, 1991; Williams and others, 1993; Arnadottir and Segall, 1994). The magnitude of the earthquake, together with the extensive pre- and co-seismic geodetic monitoring, make the Loma Prieta earthquake an important source of data for the study of postseismic processes. The possibility that accelerated postseismic straining could advance the occurrence of other earthquakes in the San Francisco Bay area adds additional importance to the study.

Postseismic slip at shallow depths along the trace of the San Andreas fault was generally less than 1 cm in the first year following the Loma Prieta earthquake (Behr and others, 1990; Langbein, 1990; Rymer, 1990). The cumulative slip of aftershocks on the Loma Prieta rupture and adjacent faults is about 5 mm (King and others, 1990), which is too small to be detected geodetically. Behr and others

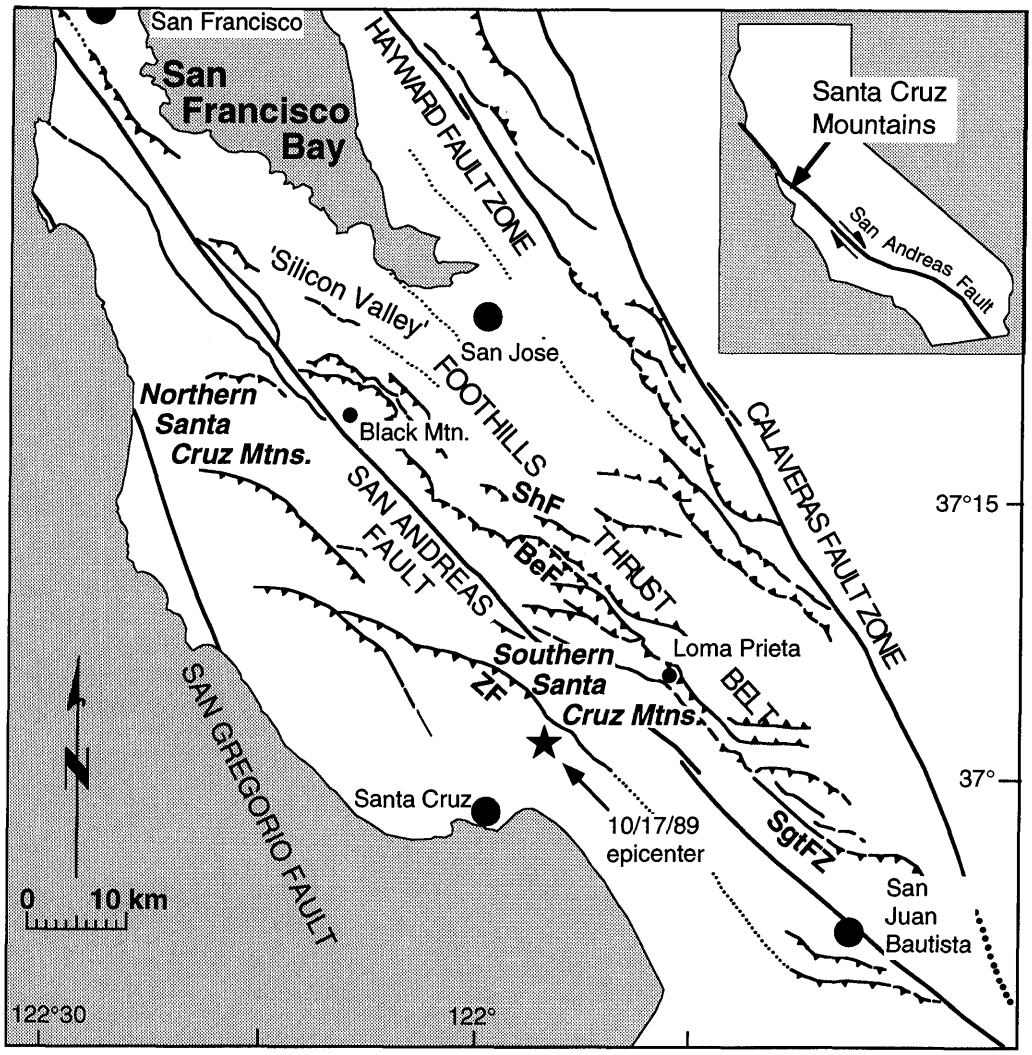

Figure 1.— Location map of San Francisco Bay area showing major fault zones and localities discussed in text. BeF = Berrocal fault, SgtFZ = Sargent fault zone, ShF = Shannon fault, ZF = Zayante fault.

(this chapter) find that slip rates on the creeping section of the San Andreas fault near San Juan Bautista accelerated from a pre-earthquake rate of 7 to 8 mm/yr to a rate of about 13 mm/yr following the earthquake. About 2 to 3 cm of excess slip occurred on the northernmost 15 km of the creeping section in the 3 years following the earthquake, probably down to a depth of 1 to 3 km (Behr and others, this chapter; Gwyther and others, 1992). Surficial creep rates on the southern Hayward fault have decreased to about half the pre-earthquake rates of 3 to 9 mm/yr. Near the southeast end of the Hayward fault, where the pre-earthquake-creep rate was highest, the fault has been slipping left-laterally since the earthquake (Lienkaemper and others, 1992) with a possible reversal in early 1993 (Lienkaemper, oral commun.,1993).

In this study we report on post-earthquake GPS measurements from the Black Mountain profile, which crosses the San Andreas fault 44 km northwest of the Loma Prieta epicenter. We analyze these data together with GPS data from a similar profile (the Loma Prieta profile) which crosses the SAF through the epicentral region (Savage and others, 1994), as well as from the San Francisco Bay area monitor network (fig. 2). The post-earthquake network geometry was chosen to measure postseismic transients away from and along the San Andreas fault trace. Twenty years of trilateration measurements prior to the earthquake constrain the preseismic displacement field (Lisowski and others, 1991a). The five-station San Francisco Bay area monitor network and two VLBI (Very Long Baseline Interferometry) sites had also been repeatedly measured for several years prior to the earthquake (Lisowski and others, 1990b; Clark and others, 1990).

Our objectives are to characterize the deformation of the crust following the Loma Prieta earthquake, to determine the sources of the postseismic deformation, and to assess the implications of these results for earthquake hazards in the San Francisco Bay region.

METHODS: GPS DATA COLLECTION, PROCESSING, AND ERROR ANALYSIS

DATA COLLECTION

A total of 17 occupations during 11 campaigns of the Black Mountain profile (fig. 2) were carried out with dual frequency C/A-code Trimble 4000, P-code TI 4100, and C/A-code Ashtech LM-XII receivers. The results we present here are derived from 9 campaigns between January 1990 and January 1993 (fig. 3). We also interpret data from 9 occupations of the Loma Prieta profile during the first 2 years following the Loma Prieta earthquake (Lisowski and others, 1991b; Savage and others, 1994), and 12 to 14 occupations of the San Francisco Bay area monitor network baselines (fig. 4). Table 1 shows the names and site coordinates of the postseismic GPS stations. Table 2 details the occupation dates and receiver type used in the Black Mountain profile. The Loma Prieta profile and the monitor network were surveyed by the U.S. Geological Survey with TI 4100 receivers until August 1991 and Ashtech receivers since that time.

TI 4100 and Ashtech carrier phase and pseudorange data were collected at 30-s intervals for approximately 6 hours, whereas the Trimble receivers recorded data at 15-s intervals for 6 to 14 hours. Occupations exceeding 8 hours in the May 1992 campaign appear to have contributed significantly to the precision (see below) of this survey. Survey times were chosen to maximize the number of satellites visible during an experiment.

DATA ANALYSIS

Our analysis of the GPS data follows the methods described by Davis and others (1989). Doubly differenced, ionosphere-free carrier phase observations were processed to estimate station coordinates, tropospheric zenith delays, satellite orbit parameters, and integer phase ambiguities. We used the Bernese GPS analysis software (Versions 3.2 and 3.3) for parameter estimation (Beutler and others, 1987; Rothacher and others, 1990).

Errors in the orbit information broadcast by the GPS satellites can be significantly reduced by monitoring the satellites from global tracking networks with well known station coordinates (for example, Larson and others, 1991). We improved GPS satellite orbits using data from fiducial stations of the CIGNET network; usually Mojave, California, Westford, Massachusetts, and Richmond, Florida. The fiducial sites were constrained to their SV6 coordinates (M. Murray, written commun., 1992). During the June 1991 campaign we added data from tracking stations at Penticton and Yellowknife in Canada, and from Kokee in Hawaii to compensate for the lack of data from the three North American stations. In three campaigns (January and September, 1990 and February, 1991) we have not been able to produce reliable improved orbits with the tracking data from the CIGNET stations. In these campaigns, broadcast orbits with inferred precision of about 5 parts in 10^7 (Hager and others, 1991) were used.

For the Trimble and Ashtech data, we determined receiver clock corrections at each measurement point using C/A-code pseudorange data. For the TI 4100 data we estimated corrections with a polynomial in time using P-code pseudorange data (Davis and others, 1989). The data were processed with an automatic program to fix cycle slips, and then all doubly differenced carrier-phase residuals were visually inspected to remove any remaining cycle slips and outliers.

All data were processed with a satellite elevation cut-off angle of 15°, because higher cut-off angles appear to reduce the short-term repeatability of the station coordinates in the June 1991 survey. Carrier phase data from GPS satellites are known only up to an integer number of wavelengths. We resolve these so-called integer ambiguities using phase and pseudorange measurements (Blewitt, 1989). We initially resolved "wide-lane" ambiguities—a linear combination of the L1 and L2 carrier frequencies—with a wavelength of 86 cm. Using the resolved wide-lane ambiguities, we fixed the remaining linearly independent integer-cycle ambiguities using the ionosphere-free linear combination. This combination of the two L-band frequencies (L3) eliminates the first-order effects of the dispersive ionospheric delays. Practically all integer-cycle ambiguities in the doubly differenced phase

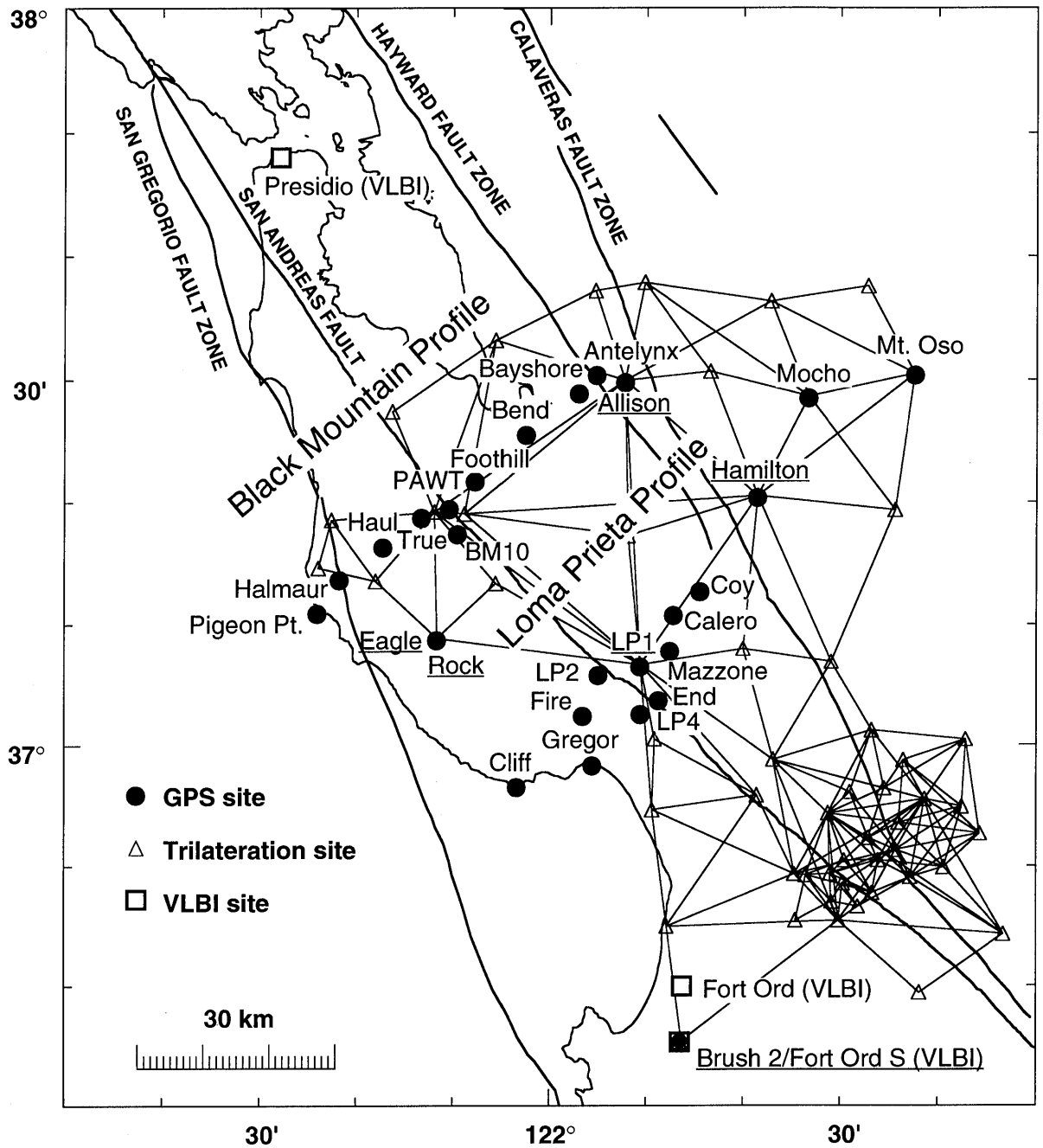

Figure 2.— Trilateration network, GPS, and VLBI station locations in the south San Francisco Bay-Monterey Bay area. Pre-earthquake data are available from the trilateration network, VLBI measurements at Presidio and Ft. Ord, and GPS occupations of the Bay area monitor network (underlined station names). Postseismic measurements are available from the VLBI sites, the Bay area GPS monitor network, the Black Mountain profile, and the Loma Prieta profile.

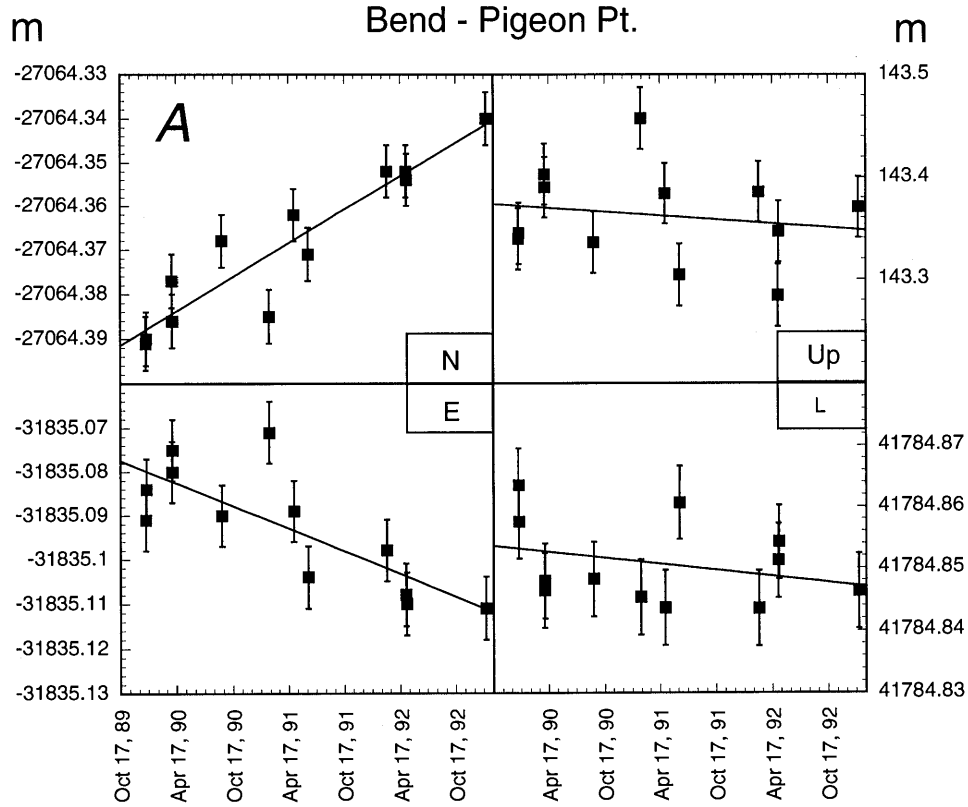

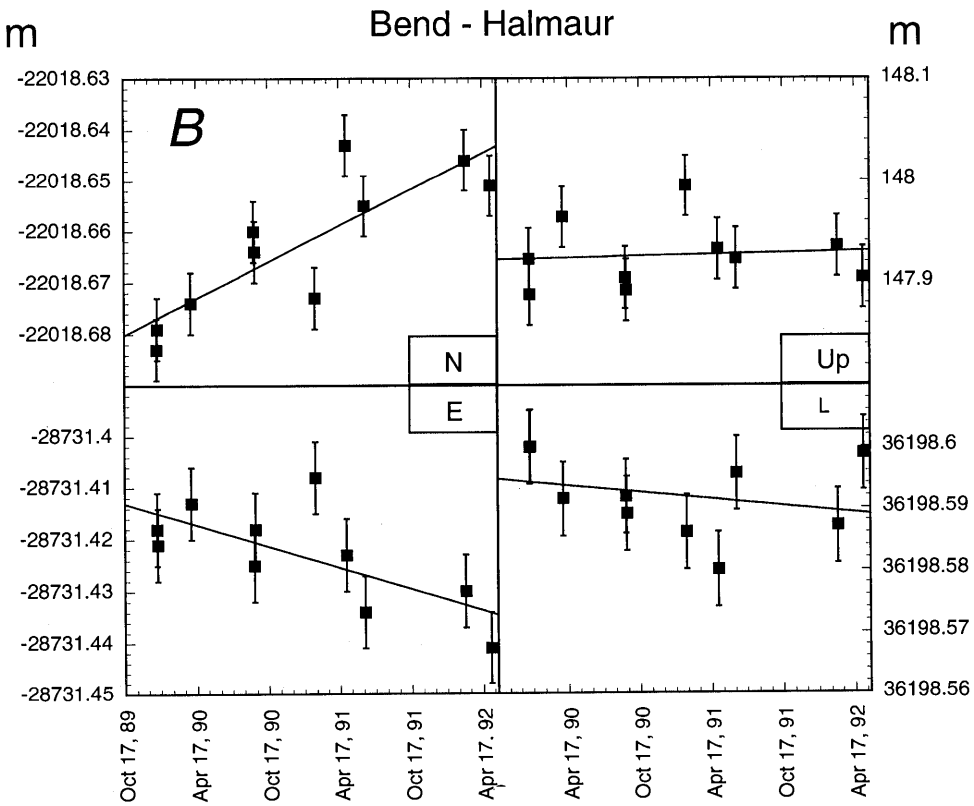

Figure 3.— Relative changes in the north, east, and vertical baseline components and line length changes in the Black Mountain profile with respect to station Bend as a function of time. The line is a least-squares fit to the data. Error bars are ± 1 sigma based on the observed residuals to the linear fit. Standard errors are 6 mm in the north and 7.1 mm in the east component. The line fit in fig. 3I is based on the data collected after a benchmark disturbance at Bayshore in 1990.

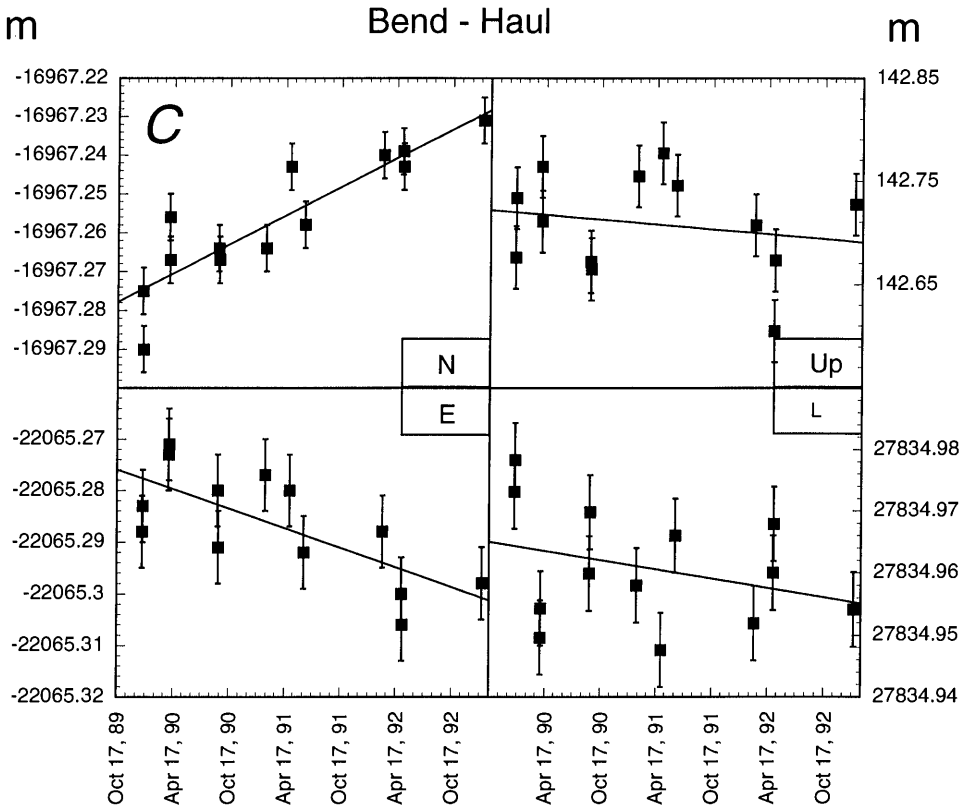

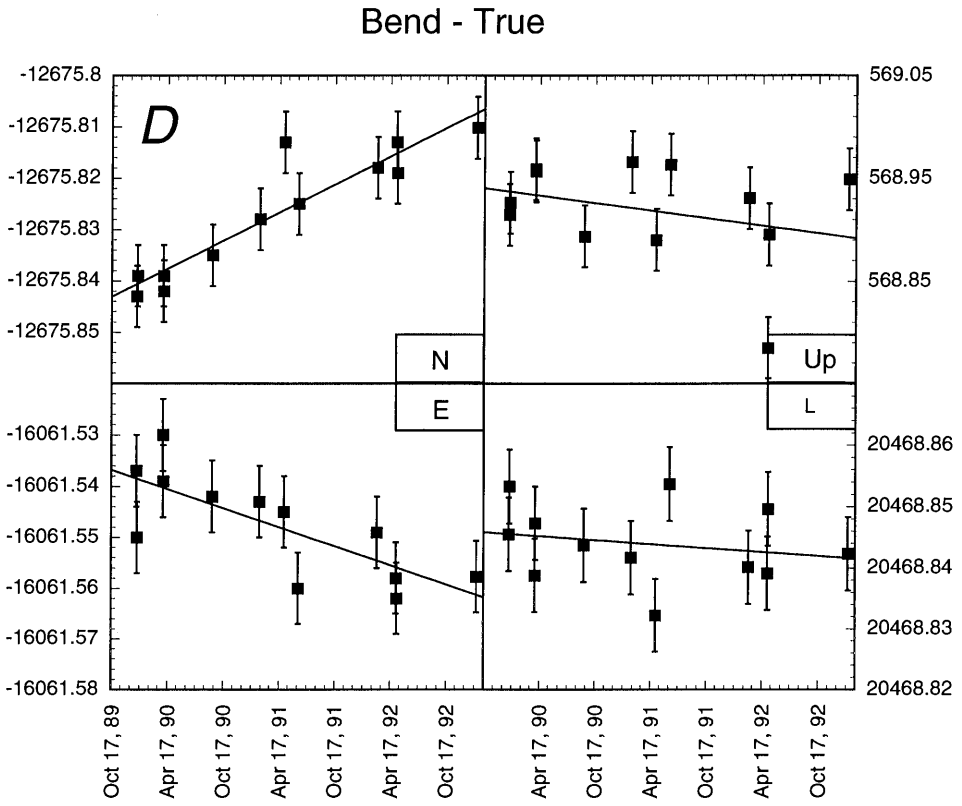

Figure 3.— Continued

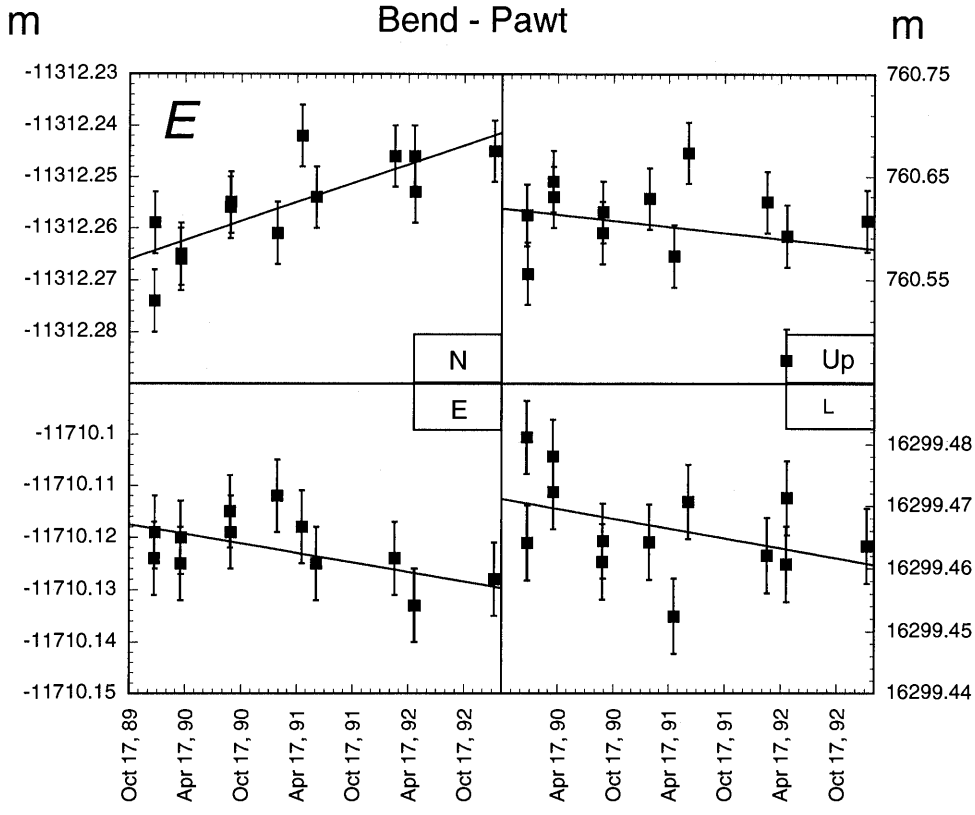

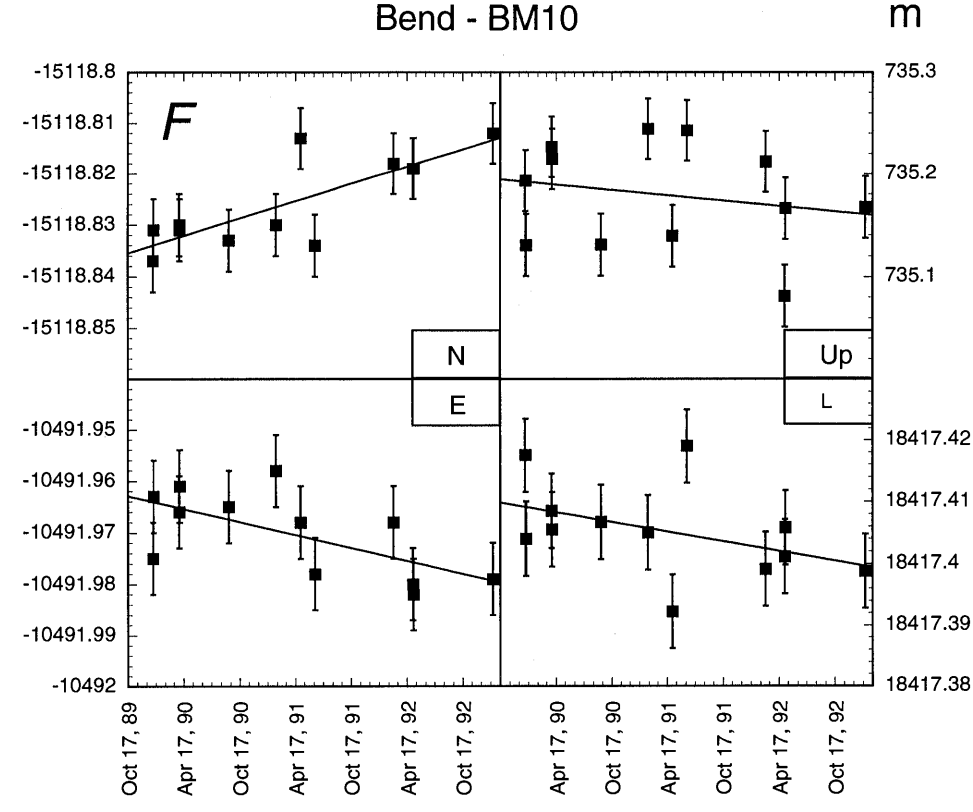

Figure 3.— Continued

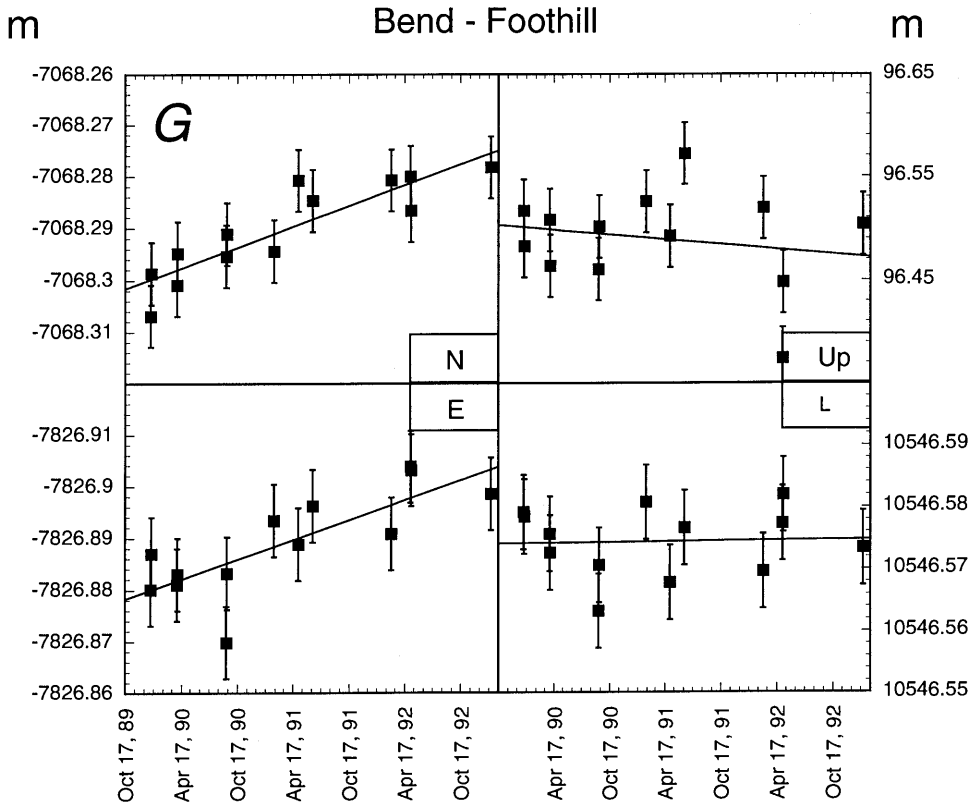

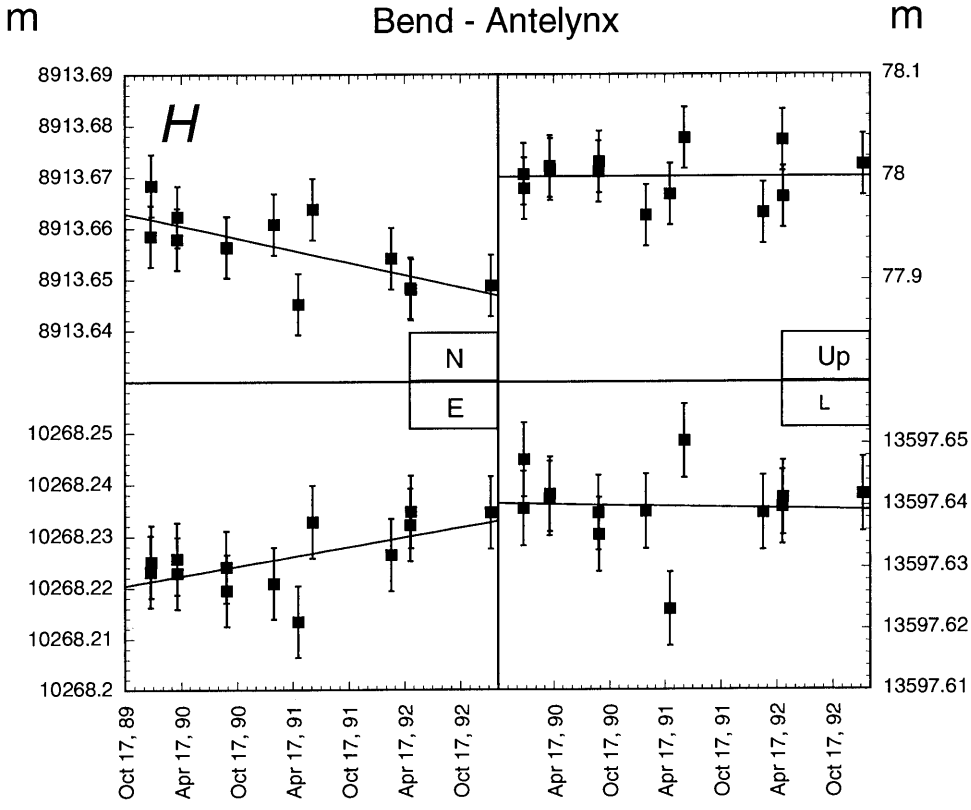

Figure 3.— Continued

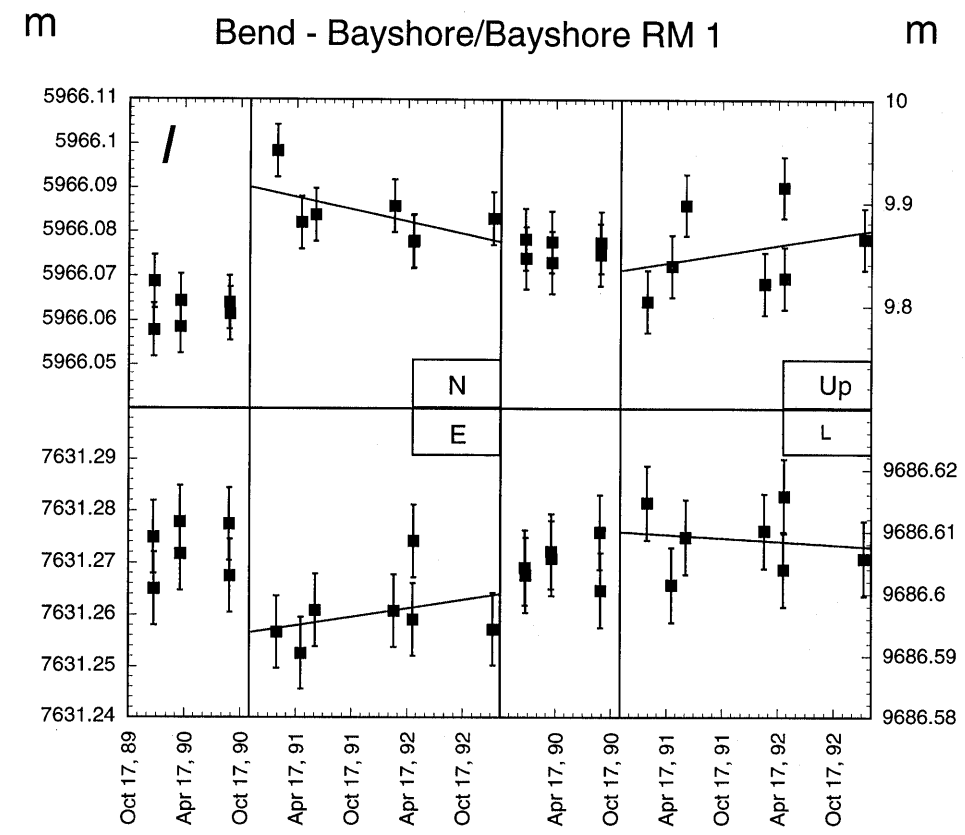

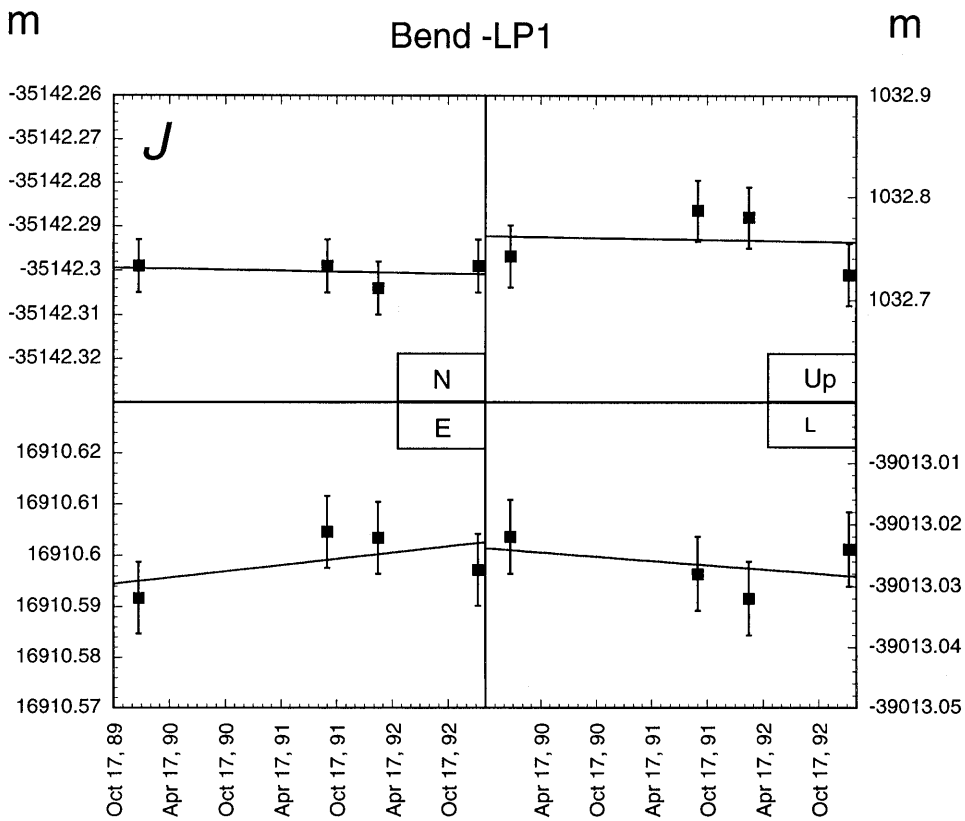

Figure 3.— Continued

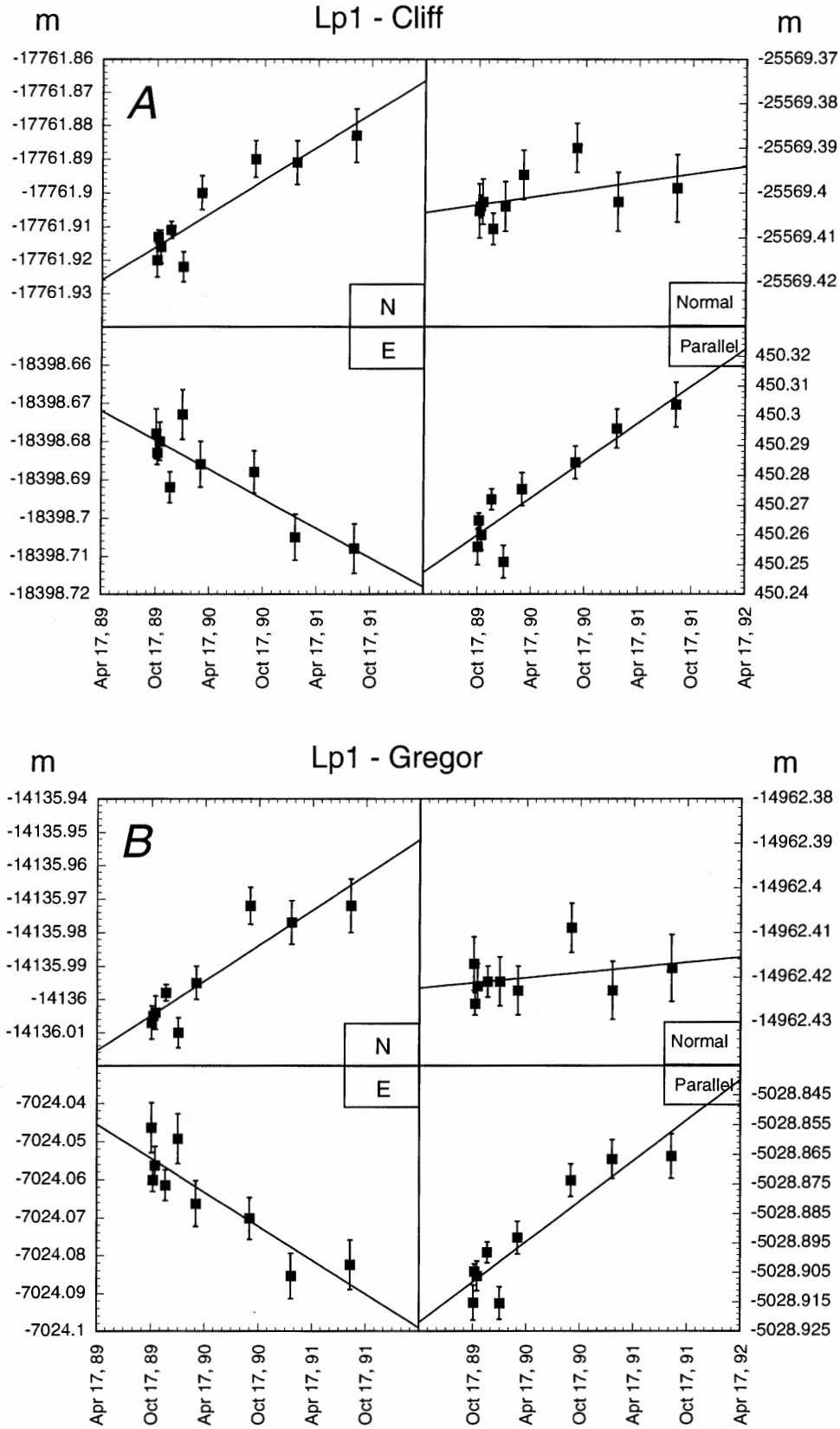

Figure 4.— Relative changes in the north, east, San Andreas fault-normal and fault-perpendicular baseline components in the Loma Prieta profile with respect to station LP1 as a function of time. The line is a least-squares fit to the data. Error bars are ± 1 sigma based on Bernese formal errors scaled by a factor of 5. Significant fault-normal motions occur at sites within about 20 km of the Loma Prieta rupture.

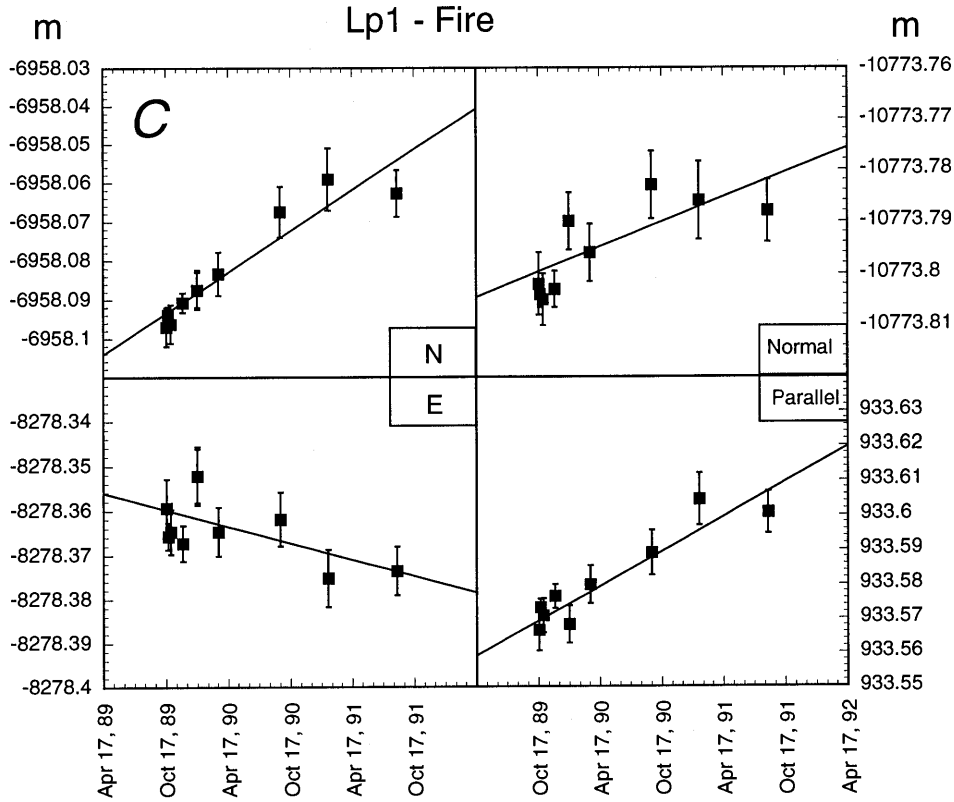

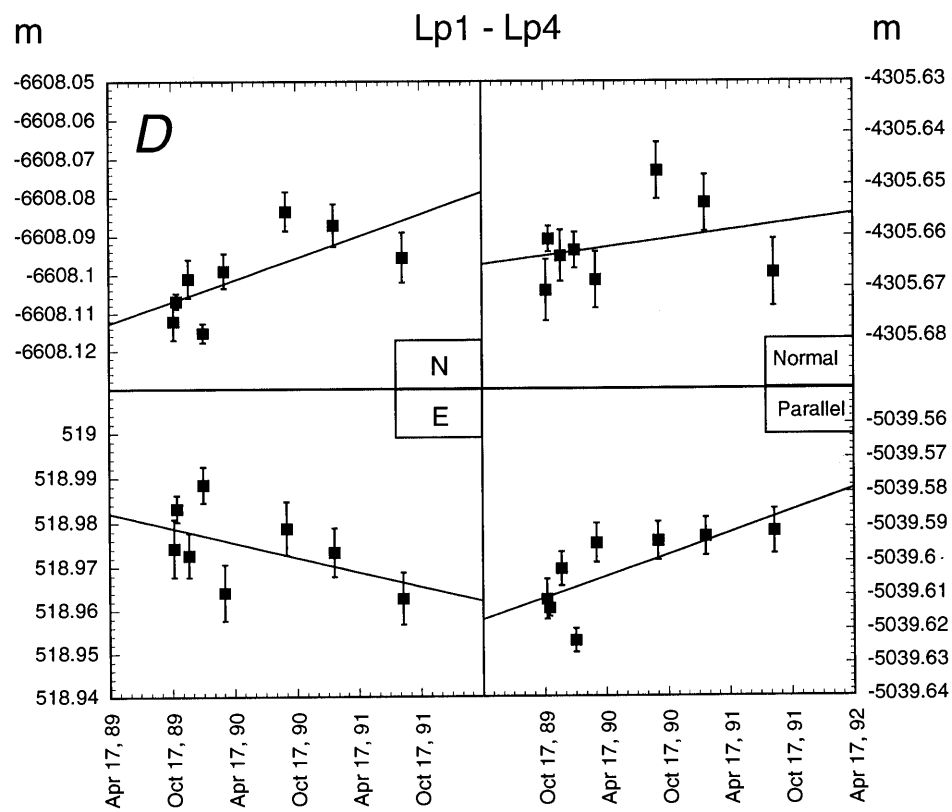

Figure 4.— Continued

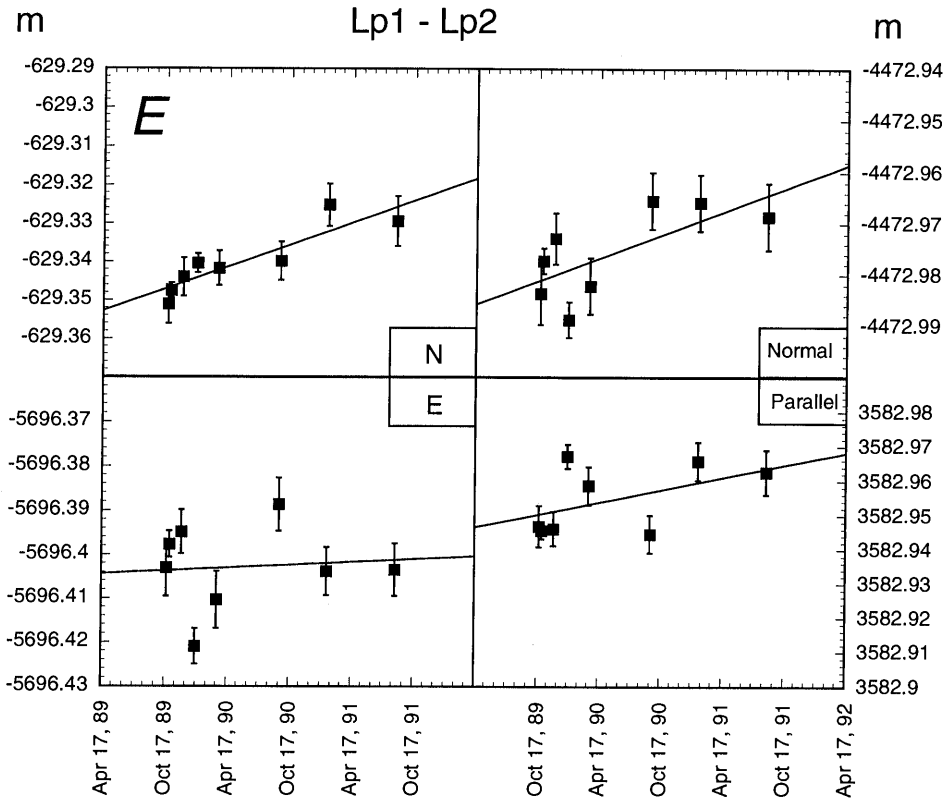

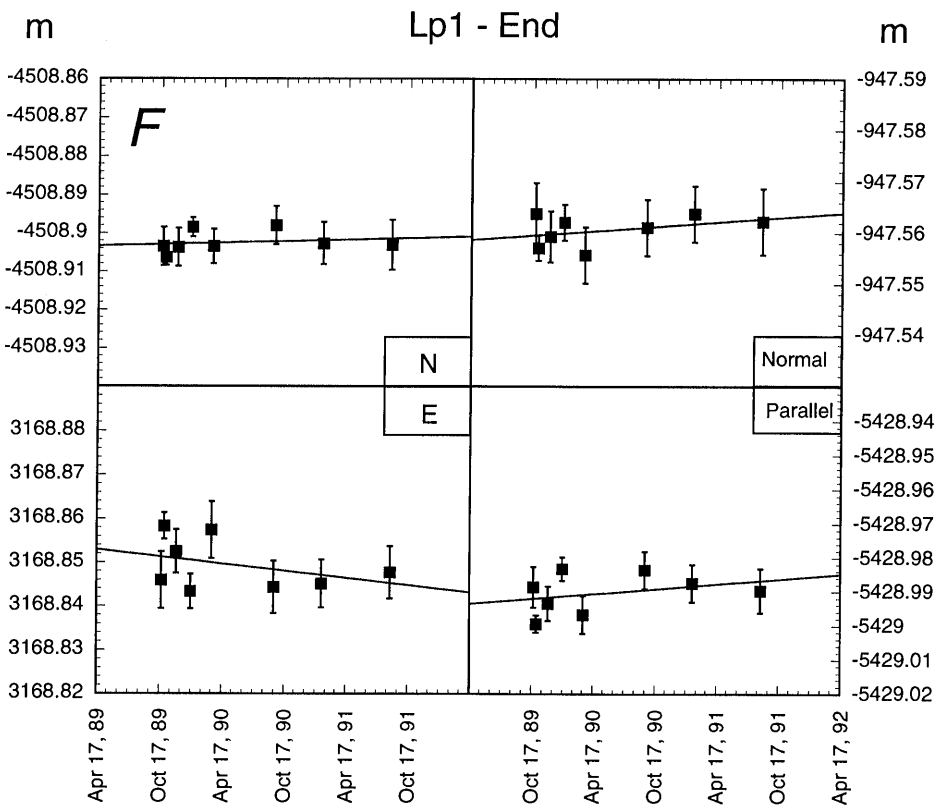

Figure 4.— Continued

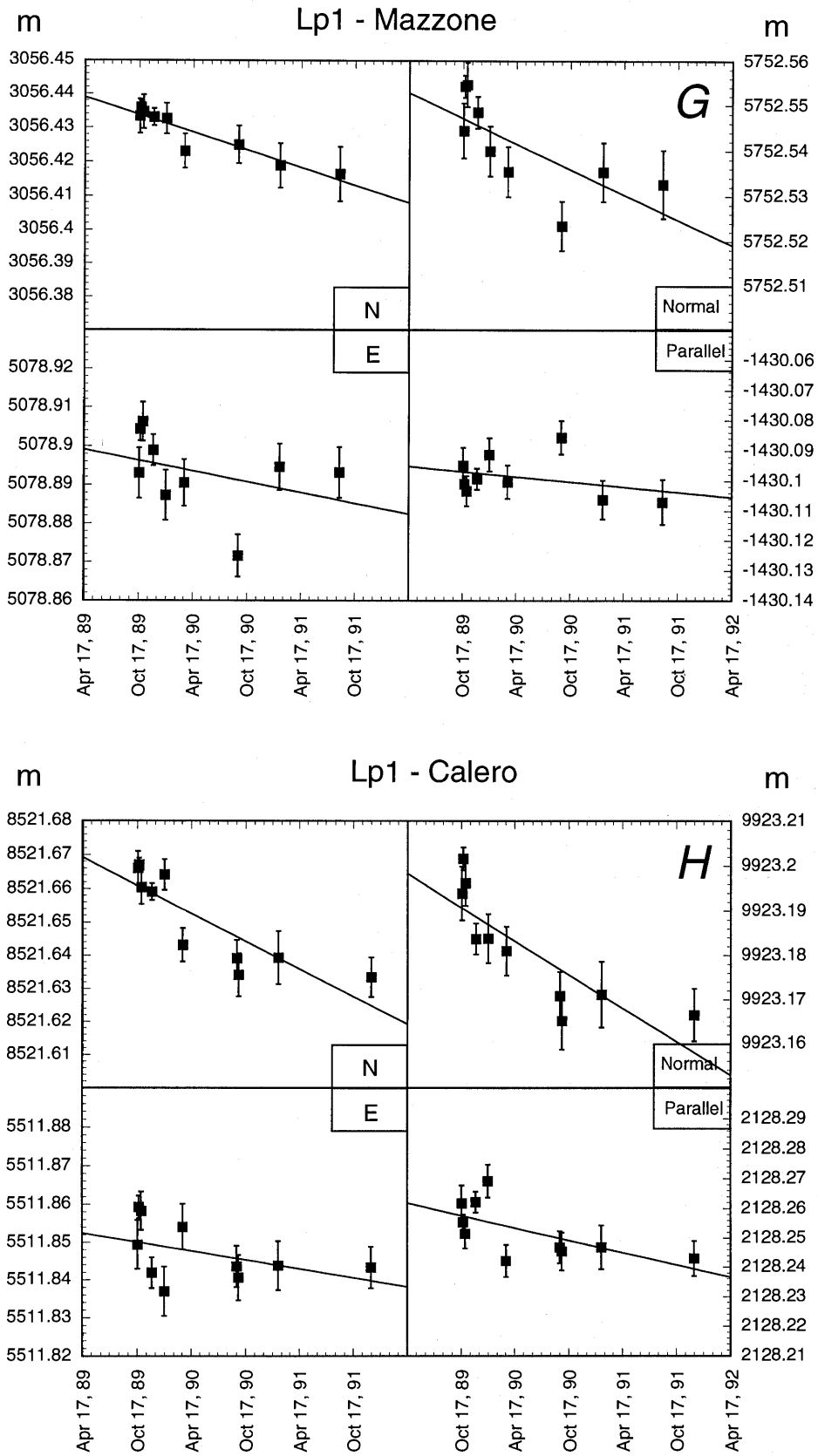

Figure 4.— Continued

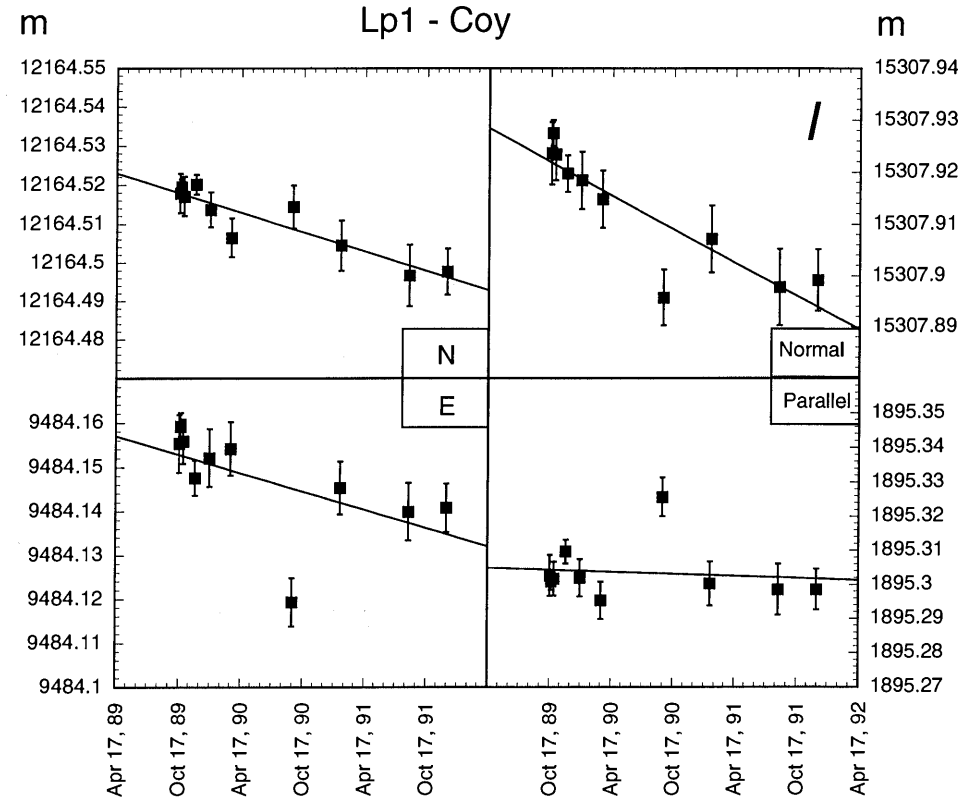

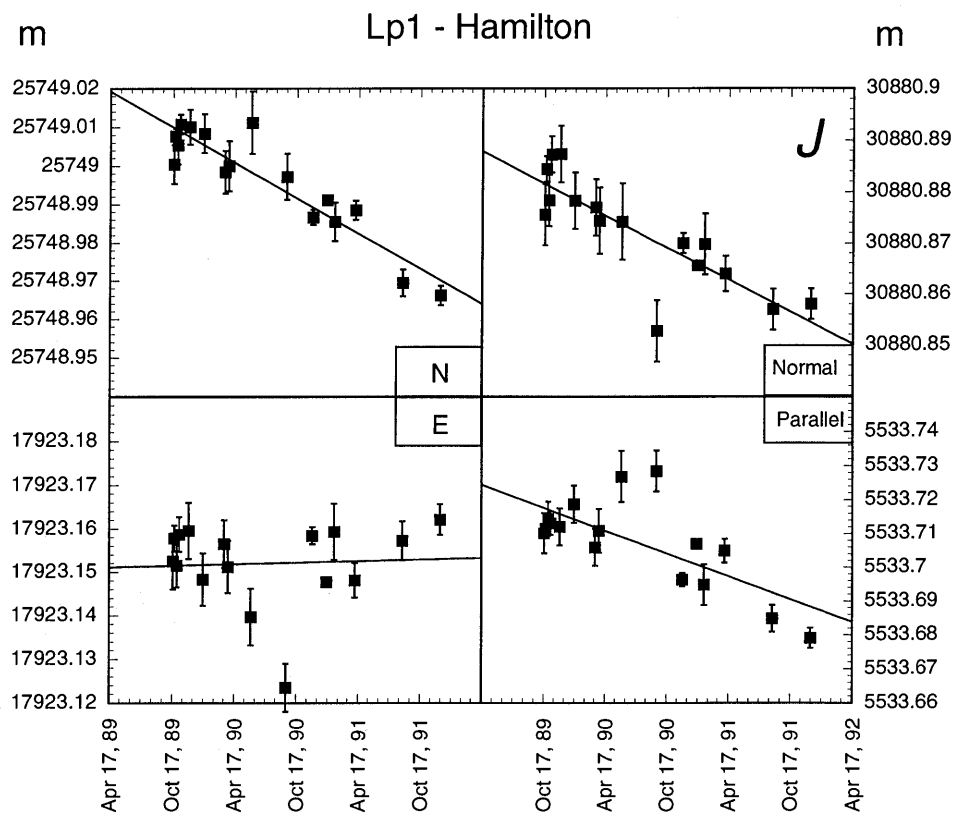

Figure 4.— Continued

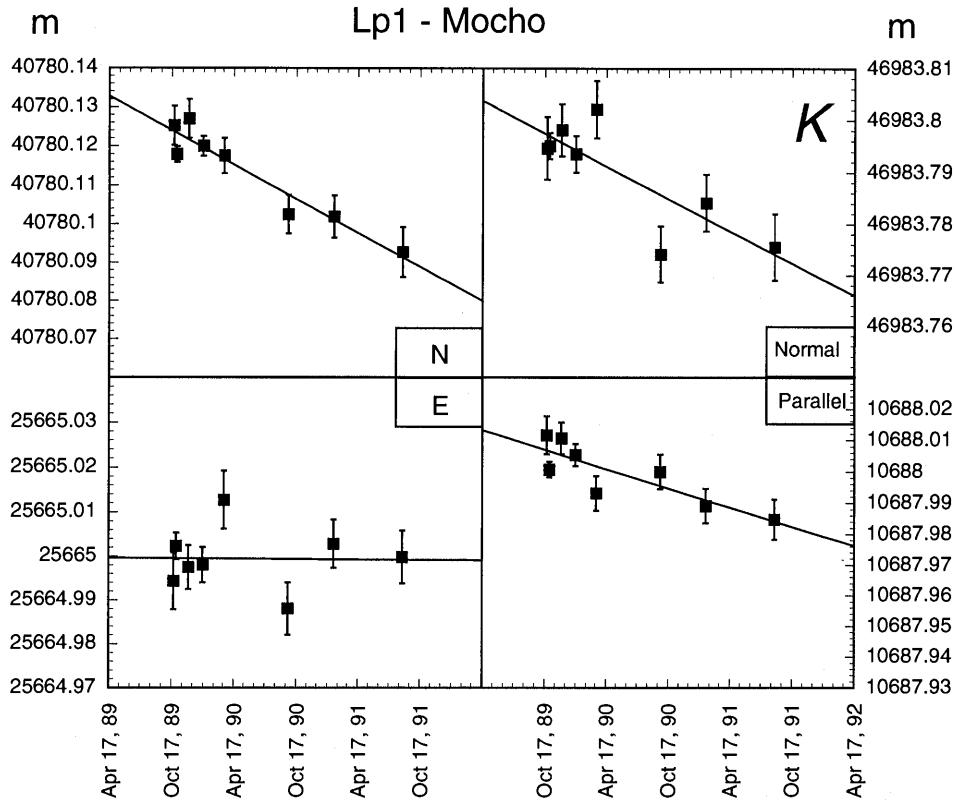

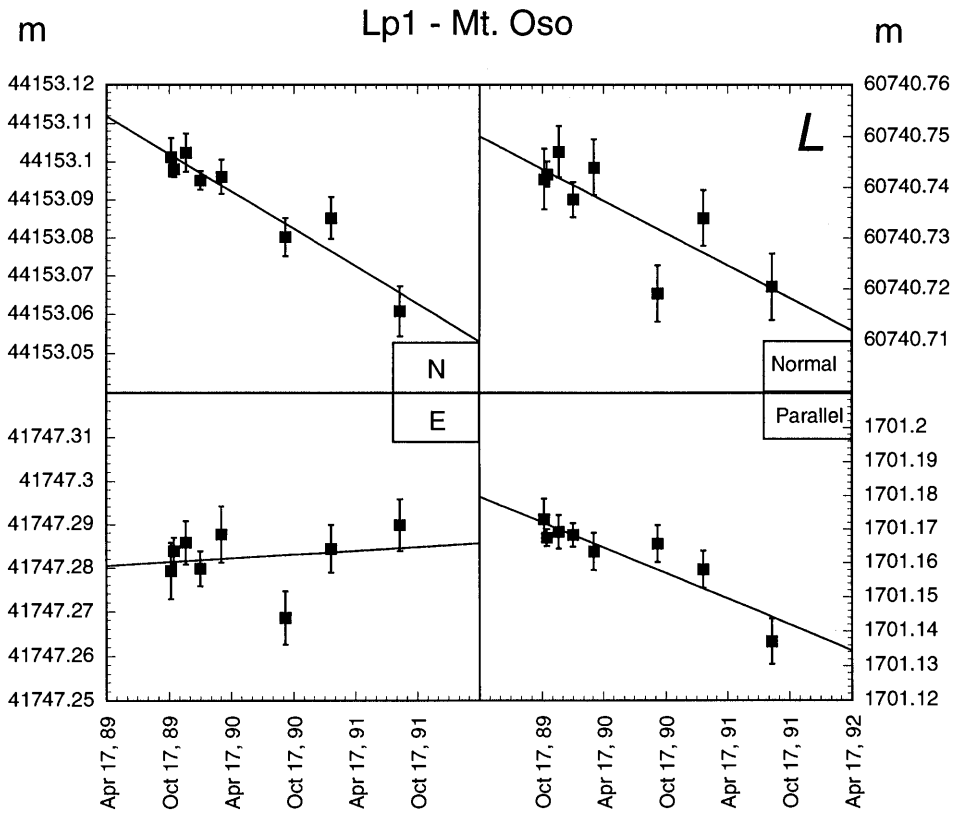

Figure 4.— Continued

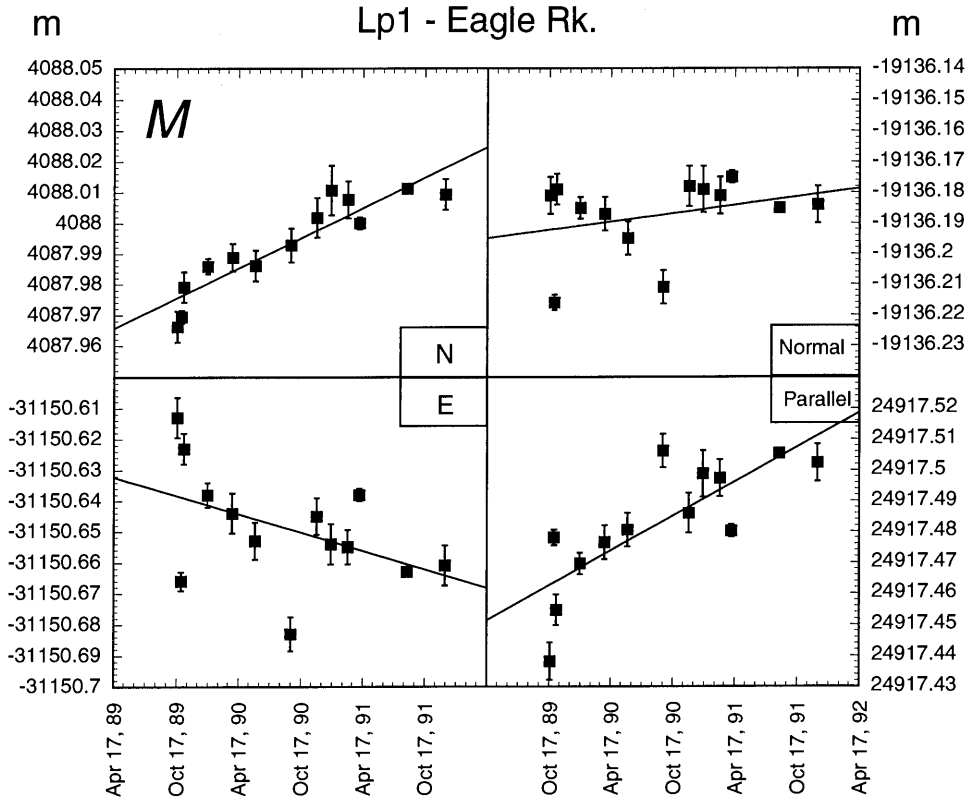

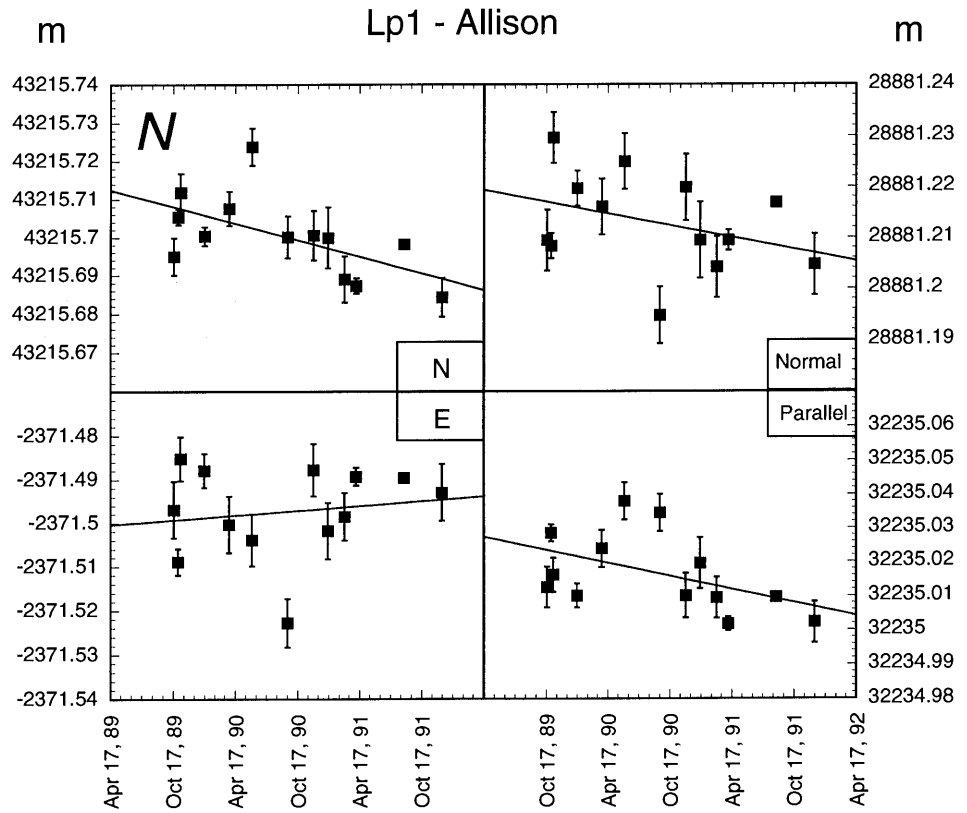

Figure 4.— Continued

measurements were reduced to integer values in the local data. Final coordinate estimates of the local stations were determined by processing the combined local and fiducial data using the ionosphere-free linear combination of the L1 and L2 phases and the resolved integer biases. We simultaneously estimated atmospheric propagation delay parameters (solving for a constant zenith delay parameter for each station for 8-hour periods), satellite orbit parameters, and clock synchronization errors (Davis and others, 1989).

DATA PRECISION AND ACCURACY

The short-term precision of GPS measurements depends on error sources related to satellite and receiver clocks, propagation delays, satellite orbit and constellation characteristics, length and time of observation, the geographic location of a network, receiver types, post-processing software, and set-up procedures (for example, Larson and Agnew, 1991). By using optical plummets and a careful centering routine with several redundant height measurements, we estimate the absolute antenna set-up errors to be less than 1 to 2 mm in all coordinate components. Four receiver station days were left out in the final computations because operators noted significant shifts in antenna positions caused by bovine impact or tripod instability during the surveys (occupations of Halmaur in May 1992 and January 1993, Antelynx in May 1992, and Bayshore in January 1993). Benchmark occupations usually lasted about 6 hours, except in the May 1992 survey when occupation times of up to 14 hours were used.

Station Bayshore was disturbed by vehicle impact in the fall of 1990. Following this, a tie between the old Bayshore benchmark and a new reference mark (Bayshore RM 1) was measured in December 1990. In May and June 1991 the original Bayshore benchmark was re-surveyed. Figure 3*I* shows the relative displacement before and after the benchmark disturbance determined by subtracting the tie from the later measurements of Bayshore RM 1. Because the tie was measured after the disturbance, we do not know the true offset. The station appears to have been offset to the north in the disturbance (fig. 3*I*). Therefore, we estimated the displacement rate of Bayshore using only data collected after the incident, from February 1991 to January 1993 (fig. 3*I*), which results in a larger error associated with the velocity vector at this site.

During the June 1991 and May 1992 campaigns, most of the baselines were measured two to four times to estimate the precision of the survey results. Furthermore, the

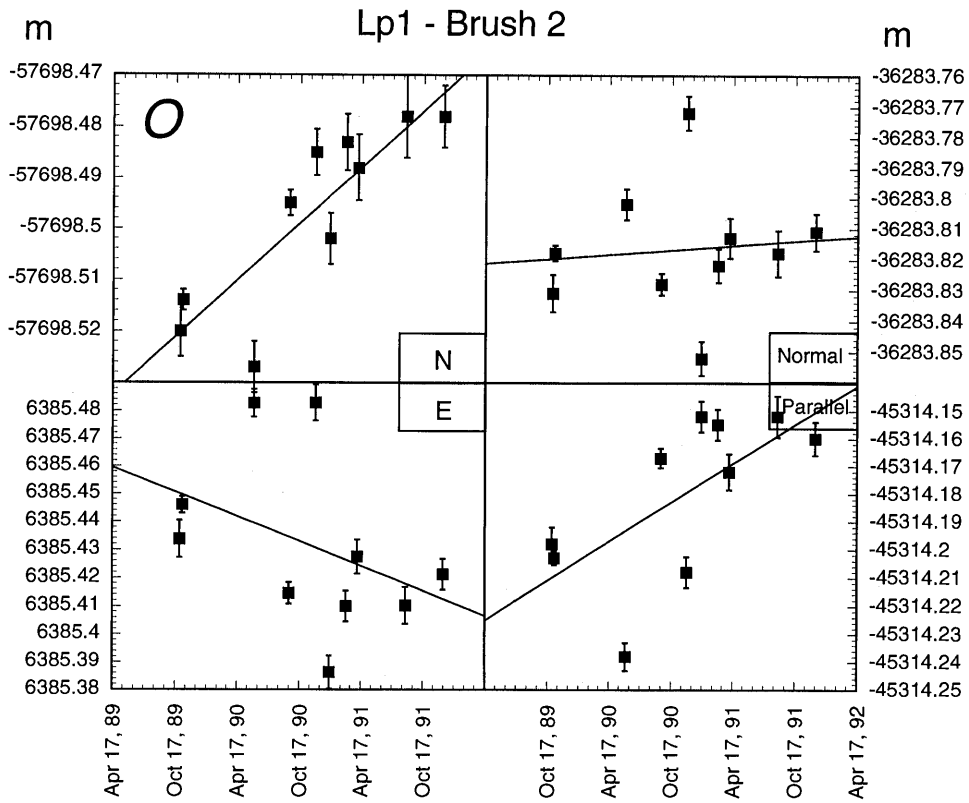

Figure 4.— Continued

Table 1.—*Coordinates and names of benchmarks surveyed following the 1989 Loma Prieta earthquake*

Station	Stamping	Latitude			Longitude		
		°	'	"	°	'	"
Black Mountain profile							
Pigeon Point	PROP. COR. 1973	37	10	58.9	-122	23	40.3
Halmaur	HALMAUR	37	13	42.2	-122	21	34.1
Haul	HAUL 1989	37	16	25.4	-122	17	2.9
True	TRUE 1990	37	18	44.2	-122	12	58.8
BM10	BMT10 RM1 1977	37	17	24.6	-122	9	12.2
PAWT	PAWT ERC BM1	37	19	28.2	-122	10	1.8
Foothill	FOOTHILL 1989	37	21	45.7	-122	7	23.8
Bend	BEND SURVEY PT 1987	37	25	34.8	-122	2	5.5
Bayshore	BAYSHORE 1989	37	28	48.5	-121	56	55.1
Bayshore RM 1	RM 1	37	28	48.5	-121	56	55.1
Antelynx	ANTELYNX 1989	37	30	24.2	-121	55	7.9
Bay Area monitor network							
Eagle Rock		37	8	49.0	-122	11	42.1
Allison	ALLISON V A 2659	37	29	56.1	-121	52	16.7
Hamilton	"unstamped"	37	20	30.2	-121	38	34.9
LP1	LOMA PRIETA 1	37	6	34.5	-121	50	40.7
Brush 2	BRUSH 2 1978	36	35	23.2	-121	46	22.1
Loma Prieta profile							
Cliff	CLIFF 1931	36	56	59.1	-122	3	5.7
Gregor	GREGOR 1989	36	58	56.2	-121	55	25.1
Fire	FIRE 1989	37	2	49.0	-121	56	15.9
LP2	SKYLAND 2	37	6	14.2	-121	54	31.4
LP4	BUZZARD	37	6	0.2	-121	50	20.0
End	END 1989 / nd*	37	4	8.3	-121	48	32.4
LP1	LOMA PRIETA 1	37	6	34.5	-121	50	40.7
Mazzone	MAZZONE 1989	37	8	13.0	-121	47	14.3
Calero	CALERO 1989 / ca*	37	11	11.0	-121	46	57.5
Coy	COY 1989	37	13	9.2	-121	44	16.6
Hamilton	"unstamped"	37	20	30.2	-121	38	34.9
Mocho	MOCHO 1875 1969	37	28	38.4	-121	33	21.4
Mt. Oso	MT OSO NO. 1 1931	37	30	29.9	-121	22	30.1

* Calero and End benchmarks were damaged and replaced in 1991

profile was measured within the same week with TI 4100 and Trimble receivers in January, April, and September of 1990 (table 2). The average, unweighted repeatabilities of the measured baselines in the June 1991 survey are 5.3 mm in the north, 5.8 mm in the east, and 20.1 mm in the vertical component. The repeatabilities of baselines formed to Foothill, which was a commonly occupied site prior to June 1991, are about twice that of the other baselines in the June 1991 campaign. We believe these high repeatabilities are due to the poor location of Foothill near a fence and high vegetation. The average precision of repeated station estimates in the May 1992 campaign is 2.4 mm in the north, 5.5 mm in the east, and 15.8 mm in the vertical components. Occupations of up to 14 hours clearly improved the precision of these measurements; however, other factors, such as satellite coverage and operator errors may have affected the reported precision. The TI 4100 and Trimble results in April of 1990, which were reduced with good tracking data, agree at the 3.9-mm, 3.3-mm, and 13-mm level in the north, east, and vertical components, respectively. The day-to-day precision of repeated measurements is nearly independent of the length of the orbital arcs we estimate (1 to 4 days). The short-term repeatability is also about the same for

Table 2.— *Occupation schedule and receiver types used during occupations of the Black Mountain profile between January 1990 and January 1993*

[Short term repeatabilities given in the text are derived from multiple occupations in April 1990, June 1991 (each station occupied at least three times), and May 1992 (each station occupied at least twice)]

	Jan 90	Apr 90	Sep 90	Feb 91	May 91	June 91	Mar 92	May 92	Jan 93
Pigeon Point	SDT+TI	SDT+TI	SST+TI	TI	SST	SST	AS	SST	AS
Halmaur	SDT+TI	SDT	SST+TI	TI	SST	SST	AS	SST	AS
Haul	SDT+TI	SDT+TI	SST+TI	TI	SST	SST	AS	SST	AS
True	SDT+TI	SDT+TI	SST+TI	TI	SST	SST	AS	SST	AS
BM10	SDT+TI	SDT+TI	SST+TI	TI	SST	SST	AS	SST	AS
PAWT	SDT+TI	SDT+TI	SST+TI	TI	SST	SST	AS	SST	AS
Foothill	SDT+TI	SDT+TI	SST+TI	TI	SST	SST	AS	SST	AS
Bend	SDT+TI	SDT+TI	SST+TI	TI	SST	SST	AS	SST	AS
Bayshore	SDT+TI	SDT+TI	SST+TI		SST	SST			
Bayshore RM 1				TI			AS	SST	AS
Antelynx	SDT+TI	SDT+TI	SST+TI	TI	SST	SST	AS	SST	AS

SDT - Trimble 4000 SDT
SST - Trimble 4000 SST
TI - TI 4100
AS - Ashtech LM XII

broadcast and improved orbits; however, the broadcast orbit solutions may contain rotational or scale biases at the few parts in the 10^7 level.

RESULTS

PRE-LOMA PRIETA EARTHQUAKE DISPLACEMENT FIELD

Trilateration measurements have been conducted throughout the San Francisco Bay area during the last two decades (Lisowski and others, 1991a). Except for the effects of the 1979 Coyote Lake and the 1984 Morgan Hill earthquakes, the velocity field appears to have been steady during that time period. Figure 5 shows the velocity field in the region computed from: (1) 20 years of trilateration data (1970 to 1989), (2) several years of GPS data for five Bay area monitor stations (Lisowski and others, 1990b), and (3) 6 years of Very Long Baseline Interferometry (VLBI) data collected at Presidio, Fort Ord, and Fort Ord S (Clark and others, 1990; D. Caprette, written commun., 1992). The velocity field presented here differs from that of Lisowski and others (1991a) primarily in the inclusion of GPS and VLBI data. The trilateration and GPS networks are linked through common benchmarks (or ties between co-located trilateration and GPS benchmarks) at Loma Prieta, Eagle Rock, Allison, Hamilton, and Brush 2 (fig. 2). The GPS baseline velocities constrain the rigid body rotation of the trilateration network, while the VLBI data constrain the translation of the network with respect to the North American plate.

The velocities of two VLBI stations in the region (Fort Ord and Presidio, fig. 2) are shown relative to a North American reference frame defined by a fixed origin at the Westford, Massachusetts VLBI station and a fixed azimuth from Westford to the VLBI station at Richmond, Florida (Clark and others, 1990). Figure 6 shows the time-displacement histories of the VLBI data. Pre-Loma Prieta VLBI measurements at Fort Ord S, which is located near the GPS station Brush 2, did not begin until 1988. The pre-seismic velocity of Fort Ord S is therefore poorly determined. There are, however, five years of VLBI data at Fort Ord, which is located 8.9 km north of Fort Ord S and Brush 2. Within uncertainties the velocity of the two VLBI stations, Fort Ord and Fort Ord S, are indistinguishable. Thus, we compute the velocity field in figure 5 assuming that Fort Ord and Brush 2 moved at the same rates prior to the earthquake.

The velocity field in the southern San Francisco Bay area exhibits 38 ± 5 mm/yr of right-lateral shear across a 120-km-wide zone, as described by Lisowski and others (1991a). Figure 5 shows that the easternmost stations of the trilateration network are moving at about 1 cm/yr with respect to North America, indicating that most of the 4.8-cm/yr relative motion between the Pacific and North American plates (DeMets and others, 1987) is contained within the network. The velocity vectors are approximately parallel to the regional trend of the San Andreas fault system and do not appear to be influenced by the local left bend in the San Andreas fault trace through the Santa

Cruz Mountains. The displacement field broadens towards the northwest. Whereas the creeping segment of the San Andreas fault southeast of San Juan Bautista accommodates 35 mm/yr of slip, deformation becomes distributed between the San Andreas, Hayward, and Calaveras faults in the San Francisco Bay area. Deviations from the simple shear pattern are apparent along the southern Calaveras fault in the closely spaced Hollister network. Stations just east of the Calaveras fault appear to move towards the fault at an oblique angle. Even though we removed coseismic line-length changes and postseismic transients due to the 1979 Coyote Lake and the 1984 Morgan Hill earthquakes along the Calaveras fault, these deviations persist. It is possible that the complex series of creeping and locked fault segments along the Calaveras fault causes the more complicated displacement-rate vectors

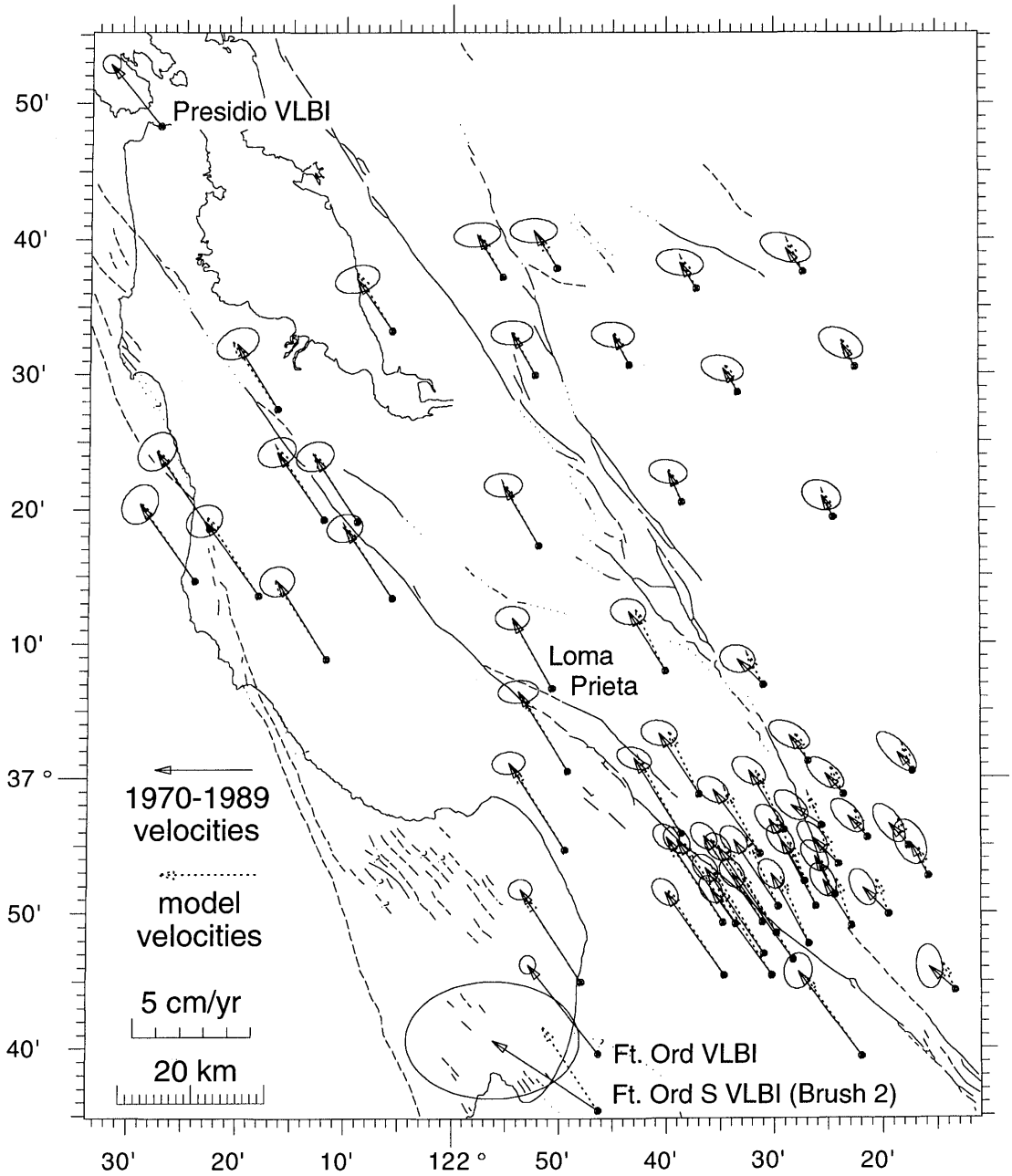

Figure 5.— Pre-Loma Prieta earthquake site velocities (solid arrows with 95-percent error ellipses) in the southern San Francisco Bay region determined from VLBI, trilateration, and GPS measurements. The GPS and trilateration station Brush 2 is assumed to move with the VLBI determined velocity of Fort Ord. All velocity vectors are shown relative to North America. Dashed arrows show vectors computed from a kinematic model of the principal San Francisco Bay area faults (fig. 7).

(Oppenheimer and others, 1990). Alternatively, the southern Calaveras or the southern Sargent faults may accommodate convergence by oblique slip (Matsu'ura and others, 1986).

Pre-Loma Prieta displacement rates are available for only a few of the stations monitored after the earthquake, so that to compare pre- and post-earthquake velocities we must interpolate the pre-seismic velocity field between stations. We utilize a kinematic model of the preseismic velocity field using three-dimensional elastic dislocations (Erickson, 1987; Okada, 1985). Uniform-slip boundary elements in an elastic, homogenous, and isotropic half space represent the Bay area faults. Interseismic shear about a locked upper crustal strike-slip fault is approximated by slip on a buried fault plane below the seismic zone at a rate comparable to the average geologic slip-rate (for example, Lisowski and others, 1991a). Surface creep on the Hayward, Calaveras, and the central San Andreas fault is modeled by shallow fault elements. Our objective here is not so much to find the correct kinematic model of San Francisco Bay area tectonics, as it is to develop a close-fitting approximation of the preseismic velocity field that can be used to compute the expected velocities at stations whose preseismic velocities are not available.

We developed a best-fitting model using a linear inversion method (Du and others, 1992) that inverts trilateration and GPS data for right-lateral strike-slip magnitudes on the individual segments of the San Francisco Bay area faults shown in figure 7. All faults are assumed to be vertical with no dip-slip component. A priori constraints on the starting model come from geologically determined slip rates (closely based on a compilation of Lienkaemper and others, 1991). Our results (fig. 7) include (1) deep (>15 km) slip on the Peninsular segment of the San Andreas fault at about 20-25 mm/yr (prior was 20±3 mm/yr), (2) deep slip (>11 km) on the Hayward fault at about 14 mm/yr (prior was 9±2 mm/yr), (3) deep slip (>10 km) on the northern Calaveras fault at about 10-12 mm/yr (prior was 6±4 mm/yr) and at up to 28 mm/yr (prior was 17±5

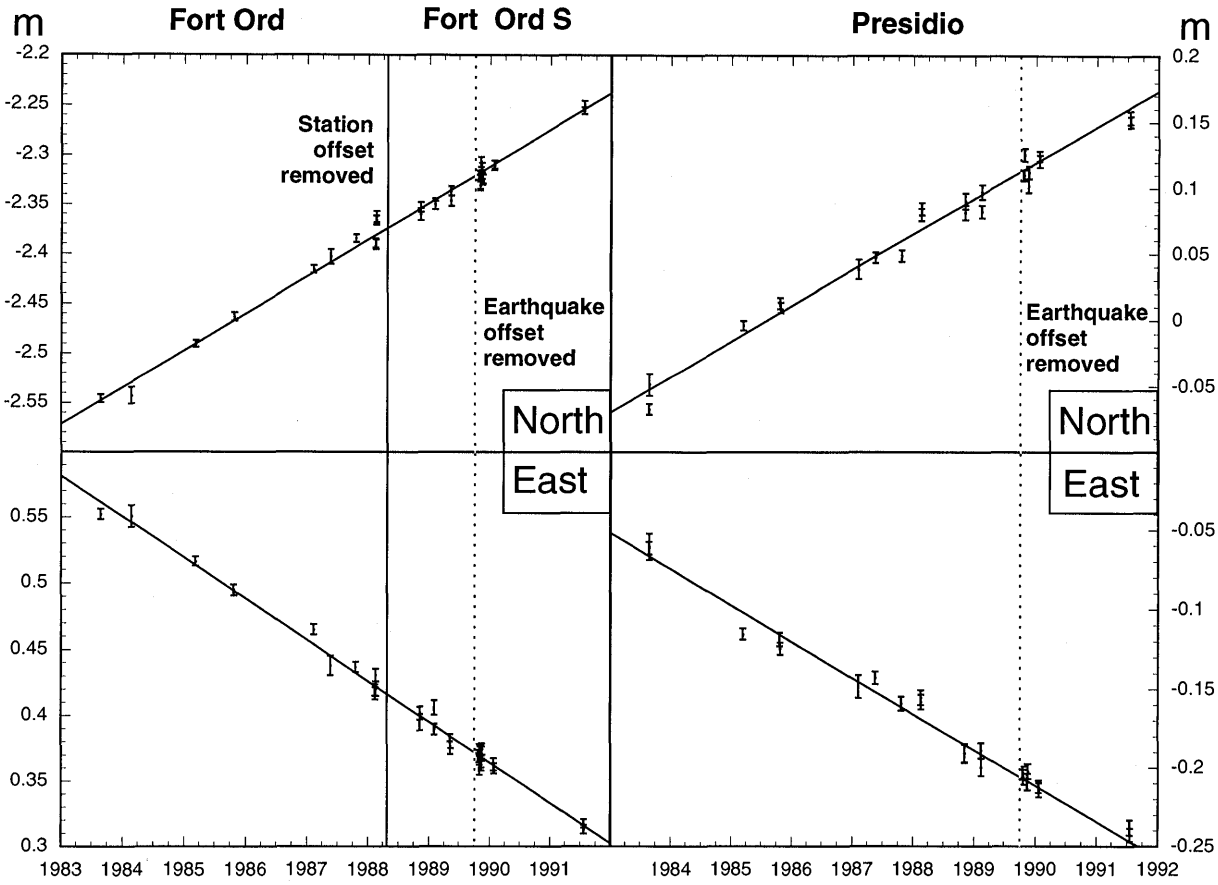

Figure 6.— Time-displacement plots of pre- and post-Loma Prieta earthquake VLBI measurements in the San Francisco Bay area (Presidio, Fort Ord, and Fort Ord S), relative to a North American reference frame. The displacements of Fort Ord and Fort Ord S located 8.9 km to the south are shown on the same plot. Loma Prieta earthquake offsets and the offset introduced in the 1988 change of stations (Fort Ord to Fort Ord S) have been removed from the data (Clark and others, 1990). The line fits are based on the pre-earthquake data at Presidio and on the Fort Ord data between 1983 and early 1988. The preseismic and postseismic displacement rates at Presidio and at Fort Ord/Fort Ord S are not significantly different.

mm/yr) on the southern Calaveras fault, and (4) shallow creep on the East Bay and southern San Andreas faults at rates comparable to the a priori values. The deep slip rate on the southern Calaveras fault appears too high and may be related to effects of the Coyote Lake and Morgan Hill earthquakes that occurred during the measurement period.

Figure 5 shows a comparison of the measured and modeled station velocities. To facilitate the comparison, the model velocities are adjusted so that Loma Prieta moves at the observed velocity. We note that most velocities are fit well within their 95-percent uncertainties except for several of the sites near the southern Calaveras fault. The model also slightly underpredicts the velocities southwest of the San Andreas fault south of Loma Prieta.

The kinematic model shown in figure 7 can be used to compute the predicted preseismic velocities of all the stations monitored after the earthquake (table 3). Figure 8 shows the measured postseismic velocities in comparison with pre-earthquake velocities, either measured at these sites or derived from the kinematic model.

POST-LOMA PRIETA EARTHQUAKE DISPLACEMENT FIELD

Figure 3 shows the changes with time of the coordinates of the stations in the Black Mountain profile relative to station Bend. The least-squares estimates of the relative station velocities are shown as solid lines. Within the measurement errors we see no evidence for changes in velocity during the surveyed 3-year period following the earthquake. The average root-mean-square (rms) residuals about the best fit line are 6.0 mm and 7.1 mm in the north and east, respectively. These residuals are slightly larger than the short-term precision estimates, presumably because of the more poorly determined broadcast orbit solutions and the fact that some error sources (for example, atmospheric and orbital) are correlated in the day-to-day comparisons (Davis and others, 1989). The estimates of the vertical displacement component do not show a trend above the data noise; the average rms residual about the mean is 3.3 cm.

A tie between the two profiles is provided by four measurements of the Bend-to-LP1 baseline (fig. 3*J*). Time-displacement plots of stations in the Loma Prieta profile relative to station LP1 are shown in figure 4. We note that several sites show a significant convergence normal to the San Andreas fault. There is some indication that fault-normal rates decayed during the 2-year period (Savage and others, 1994) at some sites (for example, figs. 4*G* and *H*). However, we assume constant postseismic velocities in our analysis. The solution for the baseline to Brush 2 shows a large scatter in the east component (fig. 4*O*), resulting in a weak tie to the VLBI reference frame.

Figure 8 shows the postseismic velocity field in the region based on (1) nine occupations of the Black Mountain profile between January 1990 and January 1993, (2) nine occupations of the Loma Prieta profile between October 1989 and December 1991 (Savage and others, 1994), (3) 12-14 occupations of the San Francisco Bay area monitor network between October 1989 and December 1991, (4) four occupations of ties between LP1 and Bend, and

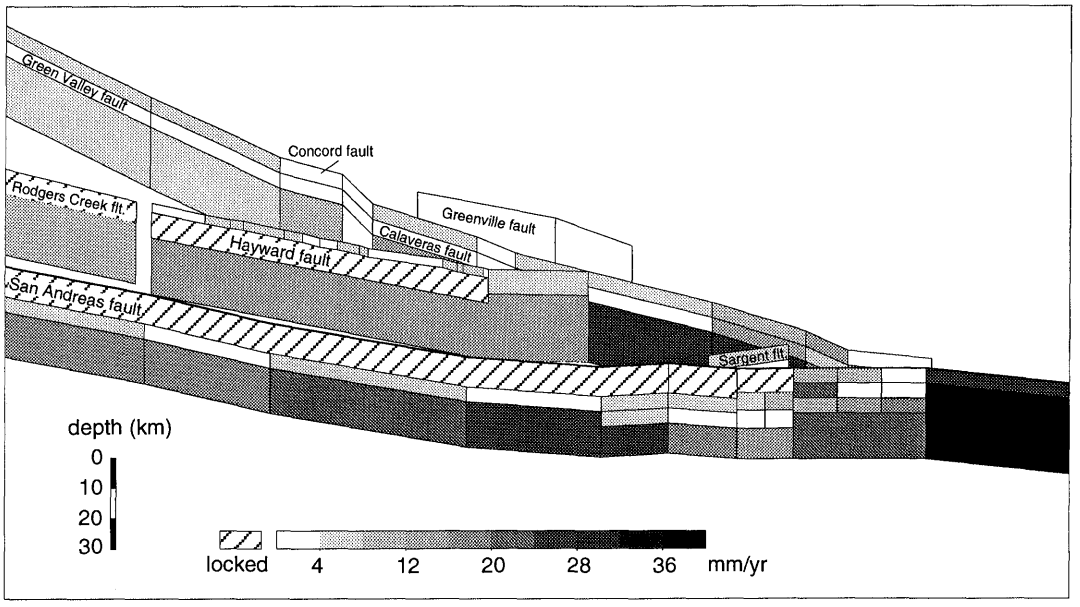

Figure 7.— Slip rates on segments of the San Francisco Bay area fault system used to model the preseismic velocity field. The fault elements that end at 30 km depth in the plot continue to 1000 km depth in the model.

Table 3.— Preseismic and postseismic relative station velocities

[The pre-earthquake horizontal velocities were computed from a kinematic model of the preseismic deformation (fig. 7). The postseismic velocities and their uncertainties (1 sigma) were determined from a least-squares fit to the GPS data and their full-position covariances]

Baseline		Preseismic (cm/yr)		Postseismic (cm/yr)					
From	To	North	East	North	+/-	East	+/-	Up	+/-
GPS									
Bend -	Pigeon Point	0.8	-0.6	0.77	0.11	-1.41	0.12	1.5	0.9
Bend -	Halmaur	0.8	-0.6	0.75	0.14	-1.69	0.14	1.3	1.0
Bend -	Haul	0.7	-0.5	0.51	0.11	-1.28	0.13	1.3	1.0
Bend -	True	0.5	-0.4	0.67	0.09	-0.93	0.09	0.1	0.7
Bend -	BM10	0.5	-0.3	0.30	0.10	-0.62	0.10	-0.2	0.8
Bend -	PAWT	0.4	-0.3	0.13	0.10	-0.76	0.10	-0.2	0.7
Bend -	Foothill	0.2	-0.1	0.69	0.09	-0.96	0.09	-0.2	0.7
Bend -	Bayshore RM 1	-0.2	0.2	-0.38	0.29	0.66	0.30	0.6	1.1
Bend -	Antelynx	-0.8	0.6	-0.43	0.08	0.38	0.08	0.2	0.6
Bend -	LP1	-0.4	0.1	-0.18	0.14	-0.04	0.14	-0.7	1.1
LP1 -	Cliff	0.5	-0.5	1.37	0.26	-2.18	0.25	0.7	1.8
LP1 -	Gregor	0.4	-0.4	1.63	0.25	-2.32	0.25	1.0	1.8
LP1 -	Fire	0.3	-0.3	0.52	0.19	-2.24	0.19	0.7	1.3
LP1 -	LP2	0.1	-0.1	-0.04	0.24	-1.69	0.24	3.6	1.7
LP1 -	LP4	0.1	-0.1	0.34	0.23	-1.56	0.23	0.6	1.6
LP1 -	End	0.0	0.0	0.23	0.25	-0.61	0.23	-1.8	1.7
LP1 -	Mazzone	-0.2	0.2	0.31	0.21	0.89	0.21	2.2	1.7
LP1 -	Calero	-0.3	0.3	0.46	0.15	1.51	0.15	0.5	1.2
LP1 -	Coy	-0.4	0.4	0.79	0.14	0.86	0.14	2.6	1.1
LP1 -	Hamilton	-1.7	1.1	-0.13	0.14	1.77	0.13	1.4	1.0
LP1 -	Mocho	-2.0	1.1	-0.12	0.24	1.41	0.23	0.7	1.6
LP1 -	Mt. Oso	-2.0	1.1	-0.32	0.27	1.48	0.25	1.4	1.7
LP1 -	Eagle Rock	0.3	-0.4	1.51	0.21	-1.86	0.17	-0.9	1.2
LP1 -	Allison	-1.2	0.7	0.10	0.20	0.94	0.16	-0.5	1.1
LP1 -	Brush 2	0.8	-1.3	1.08	0.51	-1.84	0.21	2.8	1.4
VLBI									
Westford	Presidio	2.6	-2.1	2.09	0.3	-1.97	0.16	-1.42	0.48
Westford	Fort Ord	3.8	-3.0						
Westford	Fort Ord S	3.0	-4.5	4.08	0.25	-3.16	0.18	1	1.36

(5) Very Long Baseline Interferometry (VLBI) data collected at Fort Ord S and at Presidio between October 1989 and July 1991 (fig. 6, D. Caprette, written commun., 1992). The GPS station velocities were determined using a least squares algorithm that computes station velocities and covariances relative to a local reference station from the station coordinates and the associated covariance matrices of the individual campaigns (M. Murray, written commun., 1991). Formal errors from the Bernese GPS solutions were scaled by a factor of five, as they appear to underestimate the observed scatter of the residuals about the solution by about that factor (M. Murray, oral commun., 1992). Table 3 lists the computed relative GPS station velocities and their 1-sigma uncertainties.

The velocities of the VLBI stations Fort Ord S and Presidio are shown relative to fixed North American sites (fig. 8, Clark and others, 1990). Because the tie to the VLBI network through Brush 2 is noisy (fig. 4*O*), we present the velocities of the GPS sites holding the velocity vector at Mt. Oso, located about 60 km northeast of Loma Prieta, at its pre-earthquake rate (fig. 8).

Several features in the postseismic velocity field (fig. 8) are worthy of note. Stations east of the Calaveras fault as well as those in the Black Mountain profile have velocities consistent with their pre-earthquake velocities. Many of the Black Mountain profile sites have moved slightly more northeasterly since the earthquake (fig. 8). This may be caused by the weak tie between Bend and LP1, which is based on only four surveys. Over the 60-km-long Black Mountain profile, from the Pacific coast (Pigeon Pt.) to just east of the Hayward fault (Antelynx), right-lateral shear at 22±5 mm/yr occurred since the earth-

quake. The postseismic displacement rates do not differ significantly from the pre-earthquake rate of 20±4 mm over approximately the same region.

In contrast, some stations in the Loma Prieta profile show dramatic changes in velocity after the earthquake (Lisowski and others, 1991b; Savage and others, 1994). Stations near Santa Cruz and at Eagle Rock moved obliquely towards the fault at an accelerated rate. The most significant difference between the pre- and post-earthquake velocity fields is the fault-normal contraction centered northeast of Loma Prieta mountain. Stations Fire to Coyote show significant fault-normal motion (see also fig. 4) that would not have been anticipated from the pre-earthquake data.

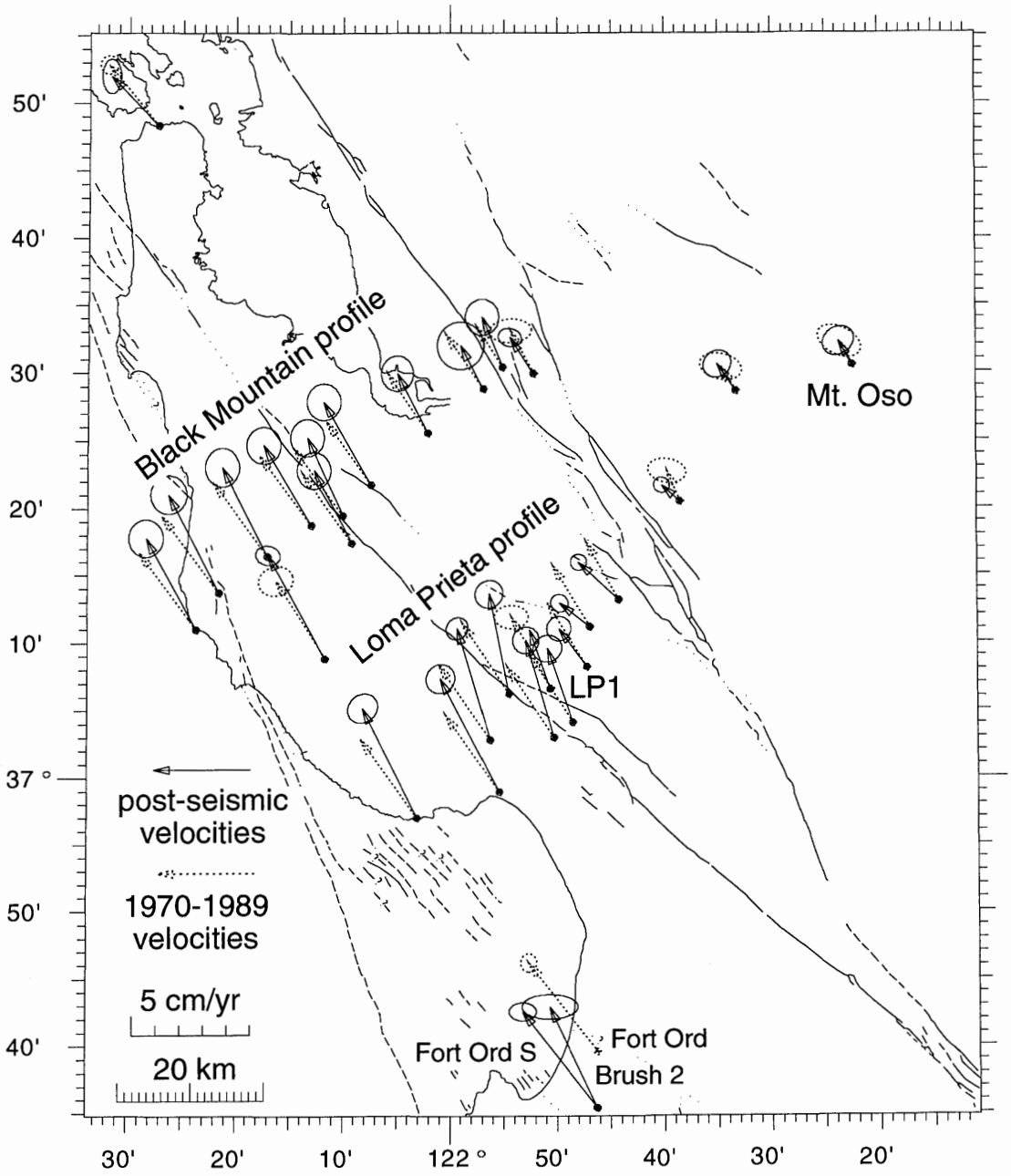

Figure 8.— Postseismic velocity field determined from GPS measurements. The velocities (solid arrows) and associated errors were computed relative to LP1. A rigid body translation is then added so that Mt. Oso displaces at its pre-Loma Prieta velocity. Postseismic velocities relative to stable North America are shown for the two VLBI stations in the area. The discrepancy between the GPS-derived vector at Brush 2 and the VLBI vector at Fort Ord S, which is not significant at 95-percent confidence, is likely due to the poor results in the Brush 2 - LP1 baseline (fig. 4O). Dashed arrows show the preseismic velocities, either measured with error ellipses or computed from the kinematic model (fig. 7), without error ellipses.

There is a large difference between the postseismic velocity vectors at the GPS station Brush 2 and the VLBI station at Fort Ord S, less than 100 m away. The discrepancy, which is not significant at the 95-percent confidence level, is almost certainly associated with errors in the GPS baseline determinations of LP1 to Brush 2. The large scatter in the east component of Brush 2 in the time-displacement plots (fig. 4*O*) may be caused by incorrectly resolved integer phase ambiguities.

Whereas only minor changes have been observed in the Black Mountain profile 44 km northwest of the 1989 epicenter, measurements along the Loma Prieta profile show significant changes in displacement rates from pre-earthquake values. The difference between the post- and pre-earthquake velocities (fig. 9) represents the component of the measured signal that exceeds the secular deformation field. The displacement rates predicted by the preseismic model (fig. 7) were subtracted from the postseismic rates, assuming that the motion of Mt. Oso did not change after the Loma Prieta earthquake. The error ellipses were determined under the assumption that the errors in the pre- and post-earthquake velocities are equal.

DATA INTERPRETATION AND MODEL

We model the residual site velocities with rectangular uniform-slip displacement discontinuities embedded in a homogeneous elastic half-space (Okada, 1985). Using a forward-modeling approach, we conclude that two distinct fault planes are required to fit the data. A single fault plane, at any depth, does not produce the observed fault-

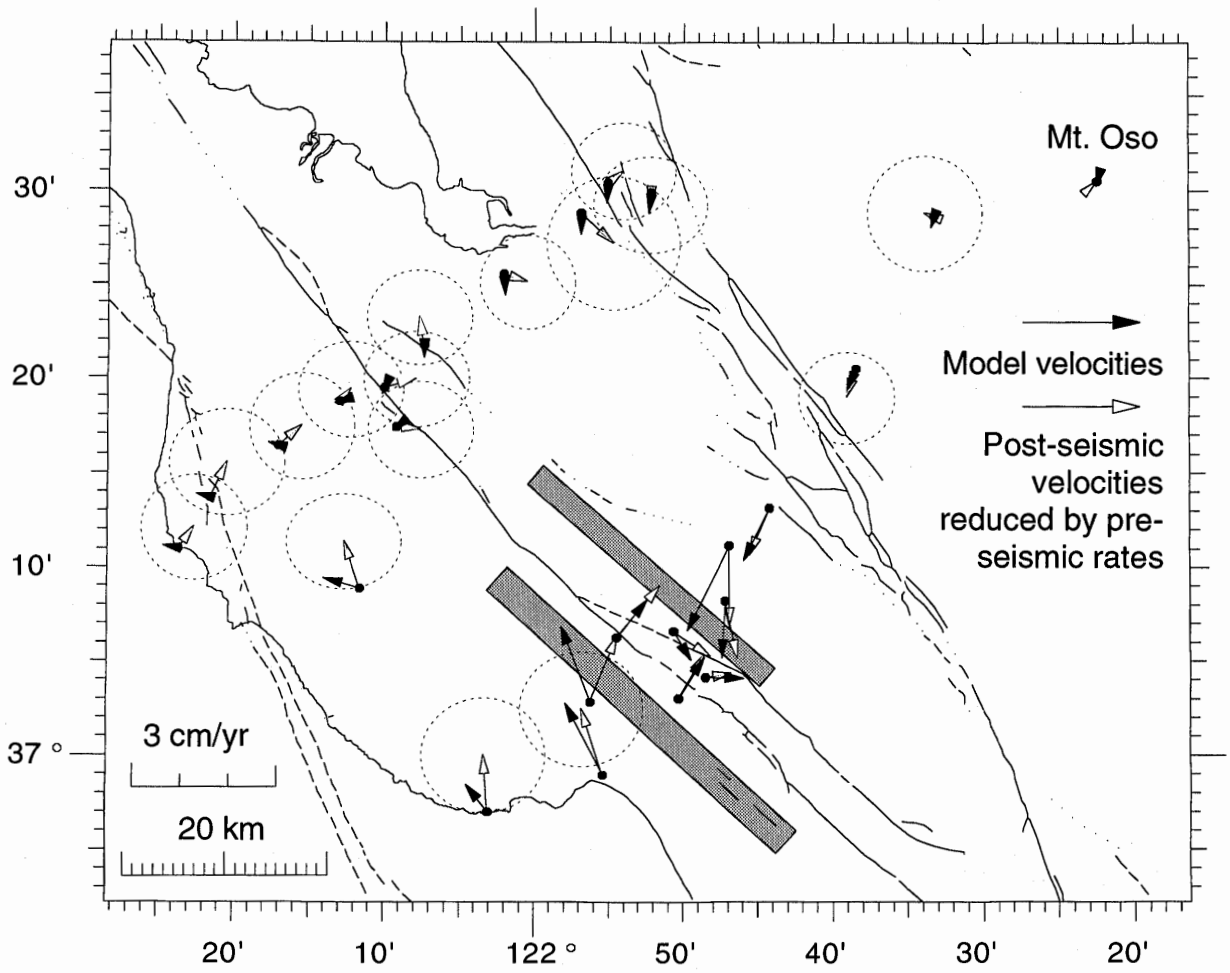

Figure 9.— Excess postseismic station velocities (secular displacement rates subtracted from postseismic rates) assuming the velocity of Mt. Oso was unaffected by the earthquake. Error ellipses for the sites near Loma Prieta are not shown for clarity. They are the same order of magnitude as the error ellipses at other sites. Also shown are the velocities (filled arrows) computed from a dislocation model involving slip on two faults; strike slip on the Loma Prieta fault and thrusting on a reverse fault in the Foothills thrust system. The two shaded rectangles show the projections of the faults used to compute the modeled station displacements. The first fault lies in the Loma Prieta aftershock zone, from 6 to 17 km depth, dipping 70° SW, with a strike-slip displacement rate of 0.10 m/yr. The second fault slips 0.12 m/yr on a reverse fault dipping 47° SW, striking subparallel to the San Andreas fault, from 1.4 to 5.8 km depth.

normal and fault-parallel displacements at the surface. As an example, we show the predicted displacement fields from uniform slip on a 5-km-wide, down-dip extension of the Loma Prieta rupture. Figure 10 compares the measured and predicted excess velocities computed from models involving strike slip, dip slip, and oblique slip. The magnitude of the slip is adjusted to provide the best fit (in a least-squares sense) to the residual displacement rates. The models involving a deep source do not fit the data along the Loma Prieta profile well and predict a significant acceleration along the Black Mountain profile that is not observed in the data. Table 4 lists the model parameters and misfits to these models.

We use a quasi-Newton algorithm (Arnadottir, 1993; Arnadottir and Segall, 1994) to estimate the geometry and position of the dislocation that best fits the data. The algorithm allows upper and lower bounds on all of the dislocation parameters. The best-fitting one-fault model with the strike and dip of the Loma Prieta rupture is located at a depth of 13 to 15 km (table 4). This suggests that transient slip may have occurred within rather than below the rupture plane. However, the misfit, ($\sqrt{\mathrm{RSS/df}}$, table 4), is 2.3, which suggests that the model is inadequate. More importantly, the spatial distribution of residuals demonstrates that even the best-fitting one-fault model does not provide an adequate fit to the data.

We used the quasi-Newton method to investigate the possibility that the data could be satisfactorily fit with multiple faults. In this calculation, one dislocation is constrained to have the strike and dip of the Loma Prieta rupture, while the other dislocation is not constrained. We found a better fit to the data with two slipping faults (table 4). One dislocation is roughly coincident with the Loma Prieta coseismic rupture, the second is located northeast of the San Andreas fault near the Foothills thrust belt. The surface projections of the two model slip planes and the predicted velocity vectors are shown in figure 9. The best-fit model, ($\sqrt{\mathrm{RSS/df}}$ =1.8), includes a combination of strike-slip at a rate of 0.10 m/yr, from 6 to 17 km depth on the Loma Prieta fault and reverse slip at a rate of 0.12 m/yr on a 47° southwest-dipping thrust plane at shallow depth (1.4 to 5.8 km) northeast of the San Andreas. The velocities predicted by the model are shown in figure 9. While the model by no means provides a perfect fit, it does explain both the accelerated fault-parallel motion and the fault-normal convergence.

The depth of postseismic slip on the Loma Prieta fault is primarily constrained by the narrowness of the zone of accelerated deformation and the absence of increased displacement rates on the Black Mountain profile. There is some trade-off between the down-dip fault width and the amount of slip on the faults. For example, models with somewhat wider faults and lower slip rates would produce similar surface displacements. It is possible that limited aseismic slip or ductile flow occurred below the 1989 rupture zone, but that this was masked by shallower deformation sources. Our inversion results indicate pure strike-slip motion on the Loma Prieta rupture plane since the earthquake. We believe that significant dip slip has not occurred on the Loma Prieta fault as any reverse component would cause the sites southwest of the San Andreas to move oceanward (fig. 10*B* and *C*), opposite to the observed trend. Finally, the location, strike, and dip-parallel rake of the thrust fault is constrained by the nearly San Andreas fault-perpendicular contraction northeast of the fault.

DISCUSSION

ALTERNATIVE MODELS

The postseismic displacement pattern following the Loma Prieta earthquake has also been interpreted by Linker and Rice (1991, and this chapter) and by Lisowski and others (1991b). Linker and Rice (this chapter) model the displacement field resulting from the interaction of the earthquake rupture with a linear viscoelastic zone that represents the deep aseismic portion of the fault. They also developed a non-linear model that assumes rate- and state-dependent friction on the down-dip aseismic region of the fault zone. Their models, involving a relatively deep deformation source below the coseismic rupture, predict the fault-parallel velocities of the Loma Prieta profile well, but do not predict the observed fault-normal contraction and appear to overpredict the rates in the Black Mountain profile. Figure 10D shows the displacements predicted by model 1 of Linker and Rice (this chapter, figure 6A) for comparison. As with the deep-fault oblique-slip model in figure 10C, their relaxation model is not capable of producing fault-trace normal contraction. Both deep models also overpredict displacement rates in the Black Mountain profile. On the other hand, some of the increased fault-parallel shear observed in the Loma Prieta profile may be explained by the transfer of stress to a ductile region below the fault zone, as proposed by Linker and Rice (this chapter).

The model proposed by Lisowski and others (1991b) involves strike-slip shear on the Loma Prieta rupture plane (0.83 m/yr at 4 to 11 km depth), as well as fault-normal compaction of the fault zone at a rate of 0.11 m/yr (3 to 7 km depth). The compaction is required to explain the fault-normal site-velocity vectors. This model successfully predicts the horizontal displacement measurements. Lisowski and others (1991b), however, offer no satisfactory physical model of the proposed fault-zone collapse at decimeter rates.

Our model involves contemporaneous pure strike-slip and thrust faulting at high rates on two faults with similar strikes. The inferred slip on the Loma Prieta fault may

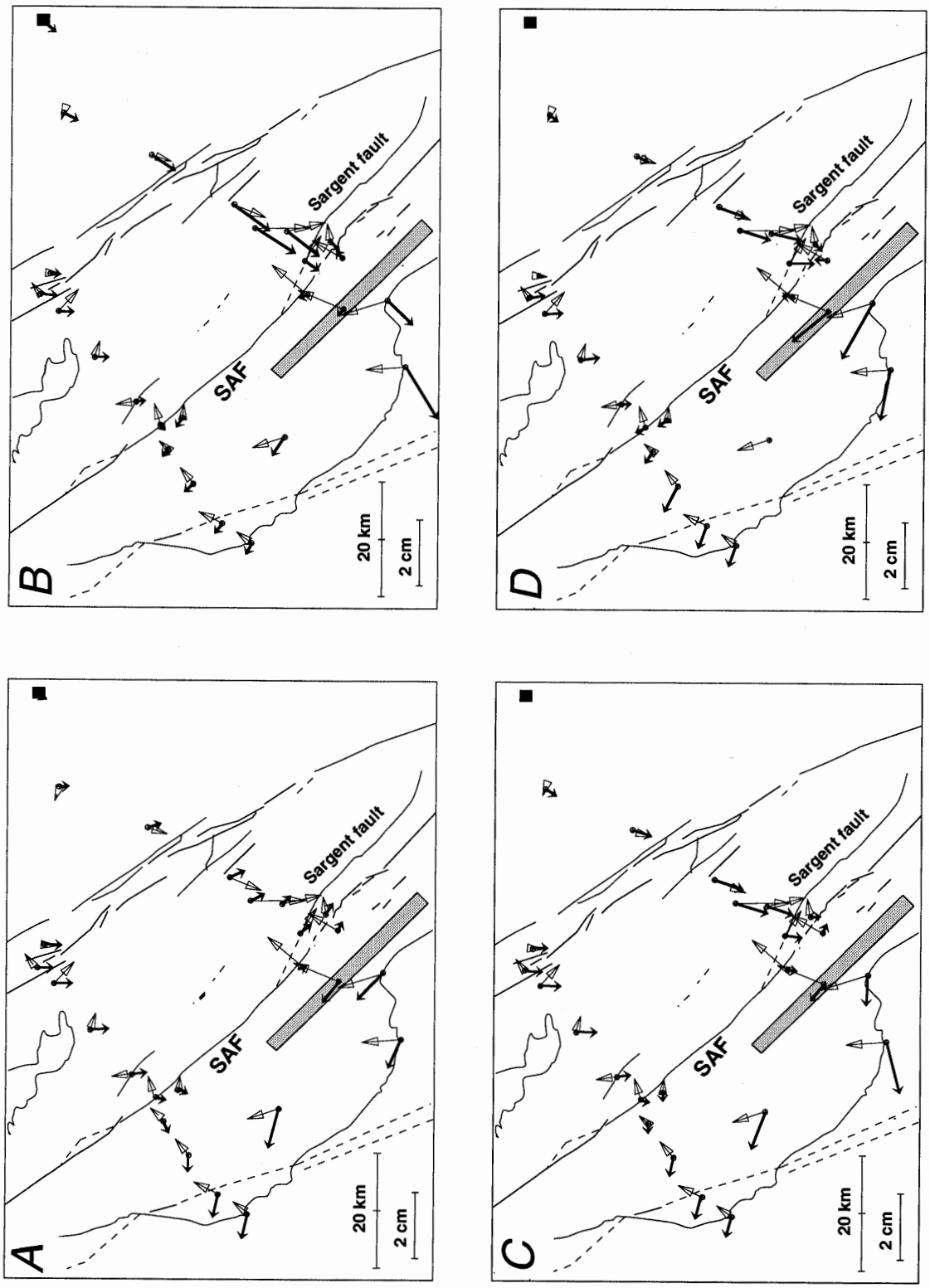

Figure 10.— Velocity field predicted by slip on a buried fault plane below the Loma Prieta rupture representing postseismic slip or flow in the lower crust: strike slip only (A), reverse slip only (B), oblique reverse slip (C), and displacement rates (D) predicted by a viscoelastic relaxation model of Linker and Rice (this volume). The model parameters for A–C are listed in table 4.

Table 4.— *Fault parameters for models of postseismic accelerated fault creep*

[Locations of the center of the faults are given relative to the Loma Prieta main shock hypocenter. A misfit of $\sqrt{RSS/df} = 1$ would indicate that the kinematic model fully represents the physical situation and that the error estimates are correct. Here RSS is the weighted sum of the squared residuals and df is the number of degrees of freedom (number of data minus the number of model parameters). The model involving two faults (Loma Prieta fault and a thrust fault northeast of the San Andreas fault) results in a better fit than models assuming one slipping fault on or below the Loma Prieta earthquake rupture. The bold-faced values indicate constrained parameters]

Model		Length along strike (km)	Depth to center (km)	Width along dip (km)	Dip (° SW)	Azimuth (°)	Location East (km)	Location North (km)	Dip-slip (m/yr)	Strike-slip (m/yr)	RSS	$\sqrt{RSS/df}$
Down-dip of Loma Prieta fault		32	***18.0***	***5.0***	***-70***	***132***	-2.0	-3.0	***0.00***	0.69	308	2.59
strike slip only												
Down-dip of Loma Prieta fault		30	***18.0***	***5.0***	***-70***	***132***	-0.7	-3.0	-0.87	***0.00***	294	2.53
dip slip only												
Down-dip of Loma Prieta fault		23	***18.0***	***5.0***	***-70***	***132***	-0.8	-3.0	-0.74	0.56	242	2.32
oblique slip												
Loma Prieta fault		39	13.8	2.2	***-70***	***132***	1.3	-3.0	-0.69	0.75	219	2.26
2-fault model	Loma Prieta fault	38	11.2	12.0	***-70***	***132***	0.0	0.0	0.00	0.10	114	1.83
	Foothills thrust	30	3.6	6.1	-47	130	1.0	11.5	-0.12	0.00		

represent creep around high-slip asperities that released most of the earthquake moment (Beroza, 1991; Hartzell and others, 1991; Steidl and others, 1991; Wald and others, 1991; Arnadottir and Segall, 1994). We do not have a unique explanation for the dominance of the strike-slip component on the Loma Prieta fault. One possibility is that postseismic fault creep may be concentrated around the southern half of the rupture that underwent mostly strike slip during the earthquake (Beroza, 1991; Arnadottir and Segall, 1994). A large postseismic strain anomaly, measured with a borehole tensor strain meter near the San Andreas fault about 30 km southeast of the Loma Prieta epicenter, may be further evidence of continued aseismic slip in this region (Gwyther and others, 1992).

THRUSTING NORTHEAST OF THE SAN ANDREAS FAULT

Northeast of the San Andreas fault lie several sub-parallel southwest-dipping faults of the Foothills thrust belt (fig. 1, and Aydin and Page, 1984), with a dominant component of thrust motion (McLaughlin, 1990). Some of these faults appear to have been active in the Quaternary, as evidenced by offset young alluvial deposits and soil horizons (Haugerud and Ellen, 1990; McLaughlin, 1990). Broad zones of contractional surface deformation during the Loma Prieta earthquake follow the trend of these fault zones intermittently over a total distance of about 20 km (Haugerud and Ellen, 1990). Our model thrust fault appears to coincide with the Foothills thrust system.

A cross section perpendicular to the San Andreas fault shows the mapped faults, the post-earthquake seismicity, and the model faults found from the inversion of the excess postseismic velocities (fig. 11). The modeled reverse fault lies close to the Berrocal fault zone and has a comparable dip (McLaughlin, 1990). This zone has experienced strongly increased earthquake activity since the Loma Prieta event (Reasenberg and Simpson, 1992). Focal mechanisms of all aftershocks greater than M=2.0 along the Foothills thrust belt indicate that these events occurred predominantly on reverse faults (fig. 11*B*). The seismicity near the Loma Prieta rupture, on the other hand, is complex and includes all types of fault plane solutions (Oppenheimer, 1990). Note that the fault slip we model exceeds by several orders of magnitude the estimated slip accumulated in aftershocks and must be dominantly aseismic.

Stress redistribution accompanying the Loma Prieta main shock increased the loading on thrust faults northeast and updip of the rupture (Reasenberg and Simpson, 1992). Figure 12 shows a cross section perpendicular to the San Andreas fault, with the contoured coseismic stress changes resolved on planes striking N60°W and dipping 45° SW overlaid on a plot of the aftershocks. Shear and normal

stress changes both affect the tendency for slip through a Coulomb Failure Function (Reasenberg and Simpson, 1992)

$$CFF = \tau_s + \mu\sigma_n,$$

where τ_s is the shear traction in the slip direction, σ_n the fault-normal traction, and μ is the coefficient of friction. A coefficient of friction of 0.6 has been chosen for the calculation in figure 12. The slip distribution during the earthquake is important in determining the induced stress field in the near field of the earthquake rupture. In this calculation we used the heterogeneous fault slip distribution of Beroza (1991). We found that co-seismically induced static stress changes of 1 to 2 MPa that enhance thrust loading occurred northeast of the San Andreas fault. The stress changes on fault planes of somewhat different strikes and dips are comparable to those shown in figure 12. We conclude that the increased micro-seismicity and the aseismic thrusting inferred from geodetic data reflect deformation in response to coseismic stress changes. Aftershock seismicity near the Foothills thrust belt is restricted to an approximately 15-km-wide zone along the northern half of the Loma Prieta rupture. This may be related to the observation that most of the thrust component of the earthquake slip is concentrated northwest of the Loma Prieta epicenter (Beroza, 1991; Steidl and others, 1991; Marshall and others, 1991; Arnadottir and Segall, 1993).

IMPLICATIONS FOR SEISMIC HAZARD IN THE SAN FRANCISCO BAY REGION

Continued slip at decimeter rates on faults in the San Francisco Bay region will change the loading of nearby segments of the San Andreas fault and the Hayward fault. We modeled the change in loading on northwest-striking fault planes due to the Loma Prieta earthquake and modeled postseismic fault slip with the method outlined above, assuming that fault-parallel shear stress as well as fault-normal stresses determine the fault response through a Coulomb failure criterion. A detailed analysis of coseismic static stress changes on San Francisco Bay area faults shows that micro-seismicity rates increased or decreased in accordance with the computed stress changes (Reasenberg and Simpson, 1992). Reduced creep rates, observed along the southern Hayward fault following the earthquake, are evidence of induced left-lateral shear stress across that segment of the fault (Lienkaemper and others, 1992).

Figure 13 shows the contoured changes in frictional failure conditions for right-lateral strike-slip shear on northwest-striking fault planes at a depth of 10 km due to the coseismic rupture (fig. 13*A*), and from the predicted yearly postseismic fault slip (fig. 13*B*). Secular tectonic loading is not included, and the modeled postseismic stresses indicate a relaxation or enhancement of fault loading above the background. The results are only directly applicable to N45°W-striking fault planes. However, deviations of fault strike by up to 10° do not change the pattern significantly. We find that the postseismic fault slip further increases the load on the San Andreas fault immediately northwest of the Loma Prieta rupture, while the combined coseismic and postseismic effects have a retarding effect on the Hayward fault zone and on most of the Calaveras and San Gregorio-Hosgri fault zones. The yearly postseismic stress changes are about an order of magnitude less than those induced coseismically. If the Loma Prieta earthquake stress changes advanced the occurrence of the next earthquake north of the rupture by 2-25 years (Reasenberg and Simpson, 1992), then the postseismic changes enhance this effect by about 10 percent per year.

Similar postseismic adjustments occurred following the 1979 Coyote Lake and the 1984 Morgan Hill earthquakes along the Calaveras fault (Oppenheimer and others, 1990). While the coseismic stress perturbations on neighboring fault segments induced by these moderate earthquakes were small (Du and Aydin, 1990), postseismic fault creep adjacent to the coseismic ruptures may have caused the observed south-to-north propagation of earthquakes along the Calaveras fault (Oppenheimer and others, 1990).

The stress changes caused by coseismic and postseismic fault slip only add to stresses accumulated by background tectonic loading of the San Francisco Bay area faults and to stress changes produced by previous earthquakes (for example, the 1906 San Francisco earthquake). If a fault segment is near instability, the stress release associated with the Loma Prieta earthquake may only slightly retard the imminent failure. The January 15, 1993, Gilroy earthquake that occurred in a region of induced left-lateral shear east of the southern termination of the Loma Prieta rupture is a timely reminder of this. The Peninsular segment of the San Andreas fault, the updip extension of the Loma Prieta rupture (from about 8 km to the surface), and several thrust faults that parallel the San Andreas fault through most of the San Francisco Bay region appear to represent significant seismic hazards in the wake of the Loma Prieta earthquake. Continued reverse faulting may also relieve normal traction along the southern Hayward fault and increase the likelihood of faulting there, despite a decrease in right-lateral stress.

Rapid fault slip along a fault of the Foothills thrust belt since the Loma Prieta earthquake emphasizes the potential earthquake hazards associated with these faults. While records of historic seismicity in the area reach only as far back as the early 19th century, they show that the last 80 years have been marked by unusual seismic quiescence. In 1865, a M=6.5 earthquake may have ruptured a thrust

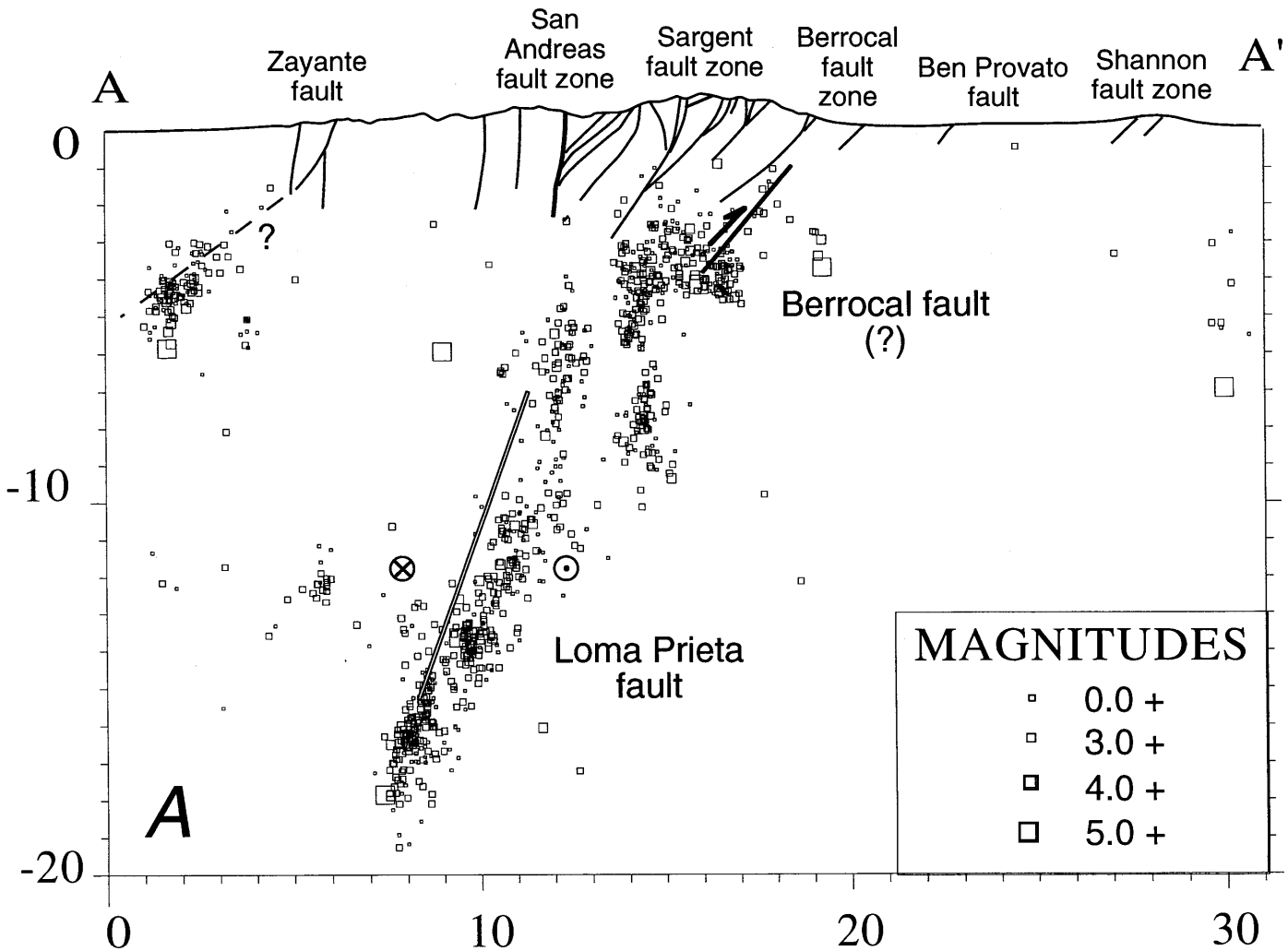

Figure 11.— A, Southwest-to-northeast cross section (Gregor to Coy in figure 2) of the geology (modified from McLaughlin, 1990) and Loma Prieta aftershocks. Also shown are the two model faults. Note the strike slip on the Loma Prieta fault and the dip slip on the Berrocal fault. The plotted earthquakes are from a 15-km-wide zone centered on the line of section (box in B) and include all well-located events from one month after the Loma Prieta earthquake until December 1992. B, Map view of post-earthquake microseismicity and focal plane solutions of earthquakes greater than M = 2 northeast of the San Andreas.

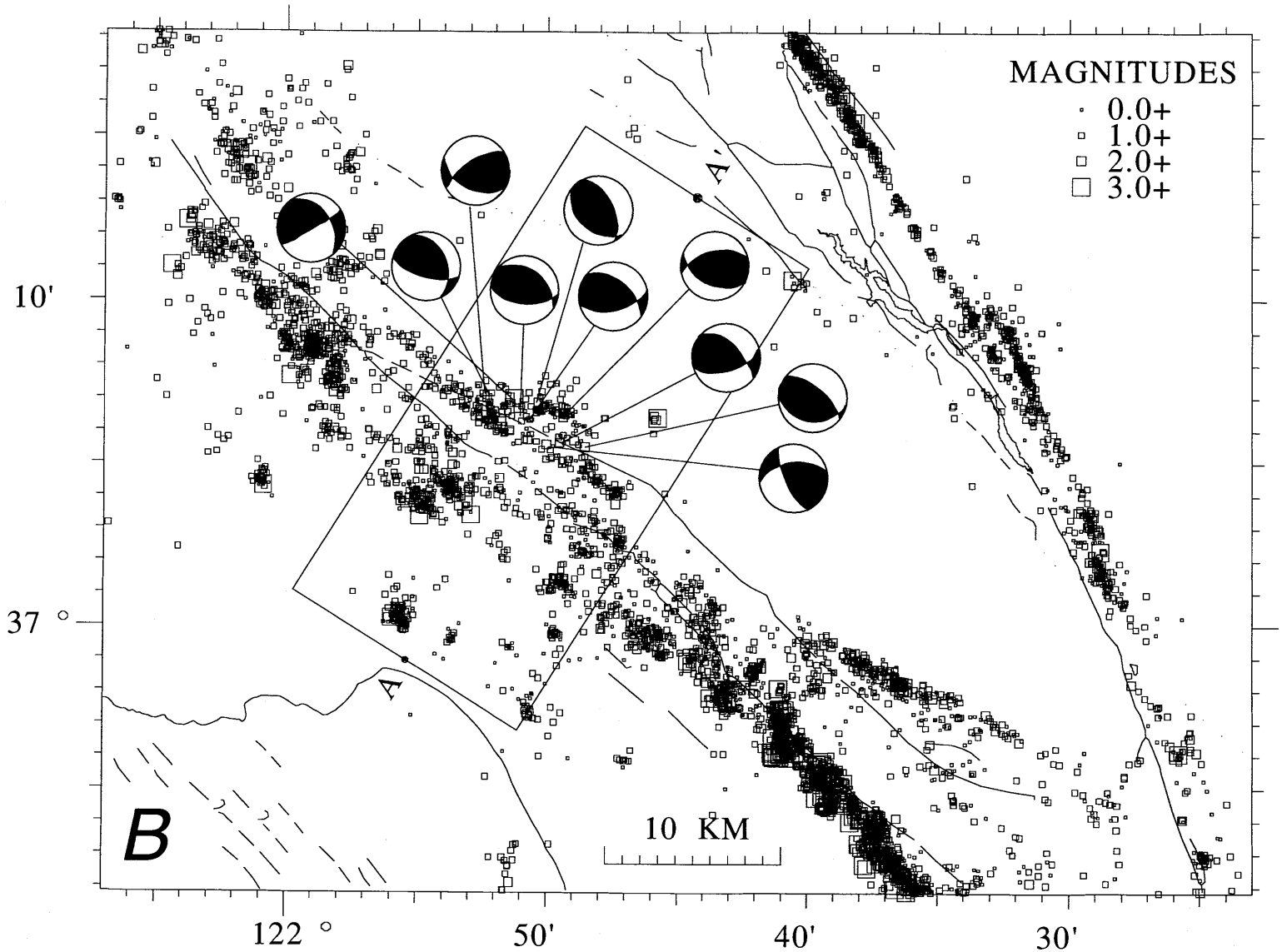

Figure 11.— Continued

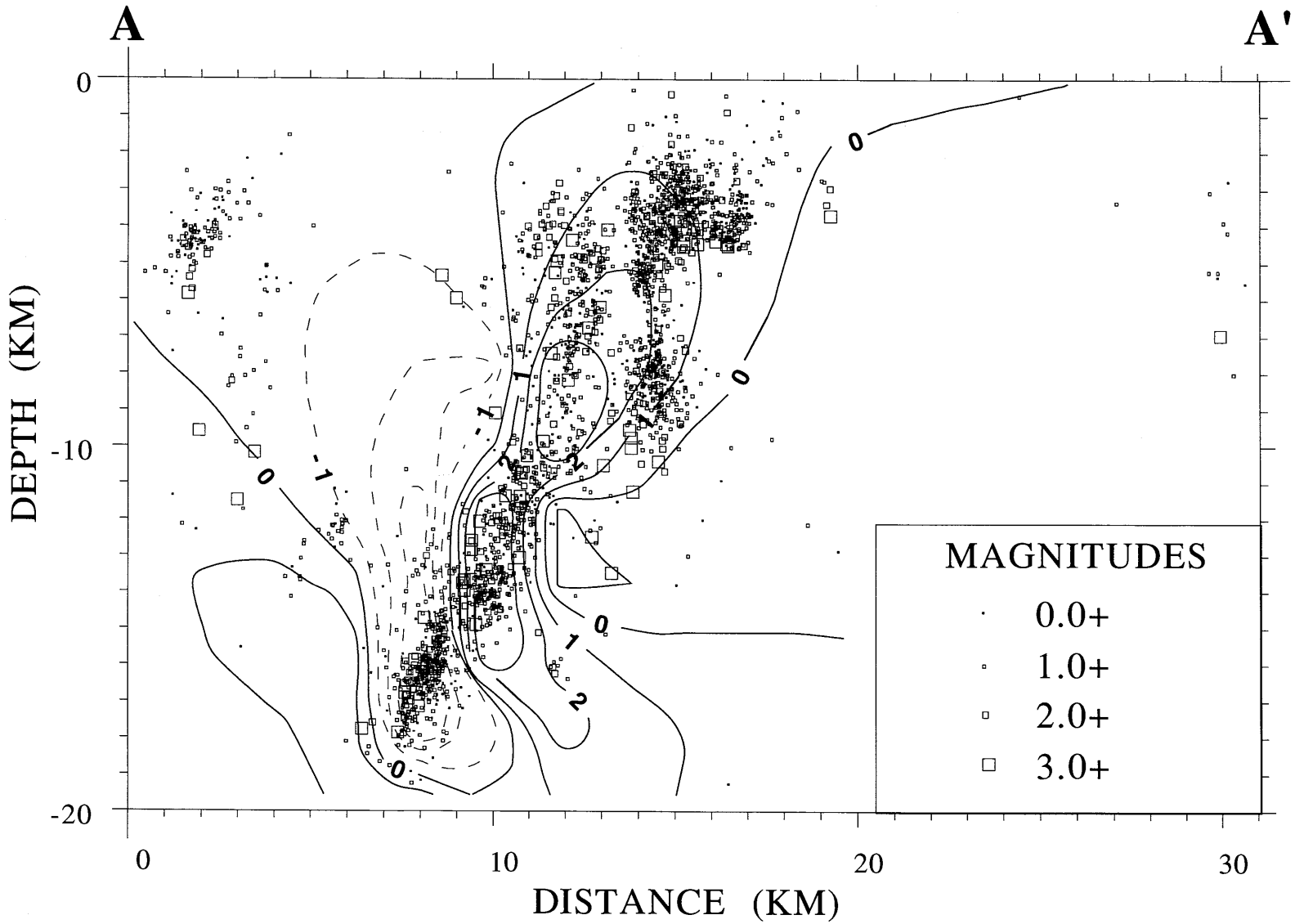

Figure 12.— Contoured stress changes (in MPa) induced by the Loma Prieta earthquake on 45° SW dipping fault planes. Dashed contours indicate decreases in CFF, solid contours increases. The coseismic displacement distribution determined by Beroza (1991) was discretized into 272 uniform slip fault elements in an elastic, isotropic, and homogeneous halfspace. Both fault-normal stresses and dip-parallel shear stresses effect the loading of the fault through a Coulomb failure criterion assuming a coefficient of friction $\mu = 0.6$.

fault northeast of the San Andreas fault with two M=5 foreshocks in the preceding year (Tuttle and Sykes, 1992). This earthquake was preceded by a M=7 break in 1838 that involved the Peninsular San Andreas fault segment and maybe the Loma Prieta fault segment and followed in 1868 by a large earthquake on the southern Hayward fault (for example, Tuttle and Sykes, 1992). An earthquake comparable to the 1865 event in the southern Santa Cruz Mountains constitutes a significant hazard to the south San Francisco Bay region.

ACKNOWLEDGMENTS

We thank Dave Oppenheimer and Greg Beroza for aftershock data and Doug Caprette for providing the VLBI data. Thora Arnadottir, Yijun Du, Jeff Freymueller, and Mark Murray wrote very useful programs used in our analyses. A large number of Stanford students and faculty helped with the GPS surveys of the Black Mountain profile. We benefited from discussions with Mark Linker. Ruth Harris and Mark Murray provided very helpful reviews. We acknowledge support from NSF grants EAR-9003575, EAR-9002164, and EAR-9116117, and from the U.S. Geological Survey.

REFERENCES CITED

Anderson, D.L., 1975, Accelerated plate tectonics: Science, v. 187, p. 1077-1079.

Arnadottir, T., 1993, Earthquake dislocation models derived from inversion of geodetic data: Stanford, CA, Stanford University, Ph.D. dissertation, 127 p.

Arnadottir, T., and Segall, P., 1994, The 1989 Loma Prieta earthquake imaged from inversion of geodetic data: Journal of Geophysical Research, v. 99, p. 21,835-21,855.

Aydin, A., and Page, B.M., 1984, Diverse Pliocene-Quaternary tectonics in a transform environment, San Francisco Bay region, California: Geological Society of America Bulletin, v. 95, p. 1303-1317.

Behr, J., Bilham, R., Bodin, P., Burford, R.O., and Bürgmann, R., 1990, Aseismic slip on the San Andreas fault south of Loma Prieta: Geophysical Research Letters, v. 17, p. 1445-1448.

Beroza, G.C., 1991, Near-source modeling of the Loma Prieta earthquake: Evidence for heterogeneous slip and implications for earthquake hazard: Bulletin of the Seismological Society of America, v. 81, p. 1603-1621.

Beutler, G., Bauersima, I., Gurtner, W., Rothacher, M., Schildknecht, T., Mader, G.L., and Abell, M.D., 1987, Evaluation of the 1984 Alaska Global Positioning System campaign with the Bernese GPS software: Journal of Geophysical Research, v. 92, p. 1295-1303.

Blewitt, G., 1989, Carrier phase ambiguity resolution for the Global Positioning System applied to geodetic baselines up to 2000 km: Journal of Geophysical Research, v. 94, p. 10187-10203.

Bott, N.H.P., and Dean, D.S., 1973, Stress diffusion from plate boundaries: Nature, v. 243, p. 339-341.

Budianski, B., and Amazigo, C., 1976, Interaction of fault slip and lithosphere creep: Journal of Geophysical Research, v. 81, p. 4897-4900.

Clark, T.A., Ma, C., Sauber, J.M., Ryan, J.W., Gordon, D., Shaffer, D.B., Caprette, D.S., and Vandenberg, N.R., 1990, Geodetic measurements of deformation in the Loma Prieta, California earthquake with Very Long Baseline Interferometry: Geophysical Research Letters, v. 17, p. 1215-1218.

Cohen, S.C., 1979, Postseismic surface deformations due to lithospheric and asthenospheric viscoelasticity: Geophysical Research Letters, v. 6, p. 129-131.

Davis, J.L., Prescott, W.H., Svarc, J.L., and Wendt, K.J., 1989, Assesment of Global Positioning System measurements for studies of crustal deformation: Journal of Geophysical Research, v. 94, p. 13635-13650.

DeMets, C., Gordon, R.G., Stein, S., and Argus, D.F., 1987, A revised estimate of Pacific-North America motion and implications for western North America plate boundary zone tectonics: Geophysical Research Letters, v. 14, p. 911-914.

Du, Y., and Aydin, A., 1990, Stress transfer during three sequential moderate earthquakes along the central Calaveras fault: EOS Transactions American Geophysical Union, v. 71, p. 1652.

Du, Y., Aydin, A., and Segall, P., 1992, Comparison of various inversion techniques as applied to the determination of a geophysical deformation model for the 1983 Borah Peak earthquake: Bulletin of the Seismological Society of America, v. 82, p. 1840-1866.

Ellsworth, W.L., 1990, Earthquake history, 1769-1989: U.S. Geological Survey Professional Paper 1515, p. 153-181.

Erickson, L.L., 1987, User's Manual for DIS3D: A three dimensional dislocation program with applications to faulting in the earth: Stanford, CA, Stanford University, M.S. thesis, 167 p.

Gwyther, R.L., Gladwin, M.T., and Hart, R.H.G., 1992, A shear strain anomaly following the Loma Prieta earthquake: Nature, v. 356, p. 142-144.

Hager, B.H., King, R.W., and Murray, M.H., 1991, Measurements of crustal deformation using the Global Positioning System: Annual Review of Earth and Planetary Sciences, v. 19, p. 351-382.

Hartzell, S.H., Stewart, G.S., and Mendoza, C., 1991, Comparison of L_1 and L_2 norms in a teleseismic waveform inversion for the slip history of the Loma Prieta, California, earthquake: Bulletin of the Seismological Society of America, v. 81, p. 1518-1539.

Haugerud, R.A., and Ellen, S.D., 1990, Coseismic ground deformation along the northeast margin of the Santa Cruz Mountains: U.S. Geological Survey Open File Report 90-274, p. 32-37.

Kasahara, K., 1981, Earthquake mechanics: Cambridge, Cambridge University Press, 248 p.

King, G.C.P., Lindh, A.G., and Oppenheimer, D.H., 1990, Seismic slip, segmentation, and the Loma Prieta earthquake: Geophysical Research Letters, v. 17, p. 1449-1452.

Kovach, R.L., and Beroza, G.C., 1993, Seismic potential from reverse faulting on the San Francisco Peninsula: Bulletin of the Seismological Society of America, v. 83, p. 597-602.

Langbein, J.O., 1990, Postseismic slip on the San Andreas fault at the northwestern end of the 1989 Loma Prieta earthquake rupture zone: Geophysical Research Letters, v. 17, p. 1223-1226.

Larson, K.M., and Agnew, D.C., 1991, Application of the Global Postioning System to crustal deformation measurements 1. Precision and accuracy: Journal of Geophysical Research, v. 96, p. 16547-16565.

Larson, K.M., Webb, F.H., and Agnew, D.C., 1991, Application of the Global Postioning System to crustal deformation measurements 2. The influence of errors in orbit determination networks: Journal of Geophysical Research, v. 96, p. 16567-16584.

Lawson, J.J., 1908, The California earthquake of April 18, 1906: Report of the State Earthquake Investigation Commission, Carnegie Institution of Washington, Washington, D.C.

Lehner, F.K., Li, V.C., and Rice, J.R., 1981, Stress diffusion along rupturing plate boundaries: Journal of Geophysical Research, v. 86, p. 6155-6169.

Li, V.C., and Rice, J.R., 1987, Crustal deformation in great California earthquake cycles: Journal of Geophysical Research, v. 92, p. 11533-11551.

Lienkaemper, J.J., Borchardt, G., and Lisowski, M., 1991, Historic creeprate and potential for seismic slip along the Hayward Fault, California: Journal of Geophysical Research, v. 96, p. 18261-18283.

Lienkaemper, J.J., Galehouse, J.S., and Simpson, R.W., 1992, Hayward fault, California: Longterm creep rates versus slower creep since 1989 Loma Prieta earthquake: Eos (American Geophysical Union Transactions), v. 73, p. 119.

Linker, M.F., and Rice, J.R., 1991, The effective viscosity of the San Andreas fault beneath the seismogenic zone: Constraints from the response to the 1989 Loma Prieta earthquake: Eos (American Geophysical Union Transactions), v. 72, p. 310-311.

Lisowski, M., Prescott, W.H., Savage, J.C., and Johnston, M.J., 1990a, Geodetic estimate of coseismic slip during the 1989 Loma Prieta, California earthquake: Geophysical Research Letters, v. 17, p. 1437-1440.

Lisowski, M., Prescott, W.H., Savage, J.C., and Svarc, J.L., 1990b, A possible geodetic anomaly observed prior to the Loma Prieta, California, earthquake: Geophysical Research Letters, v. 17, p. 1211-1214.

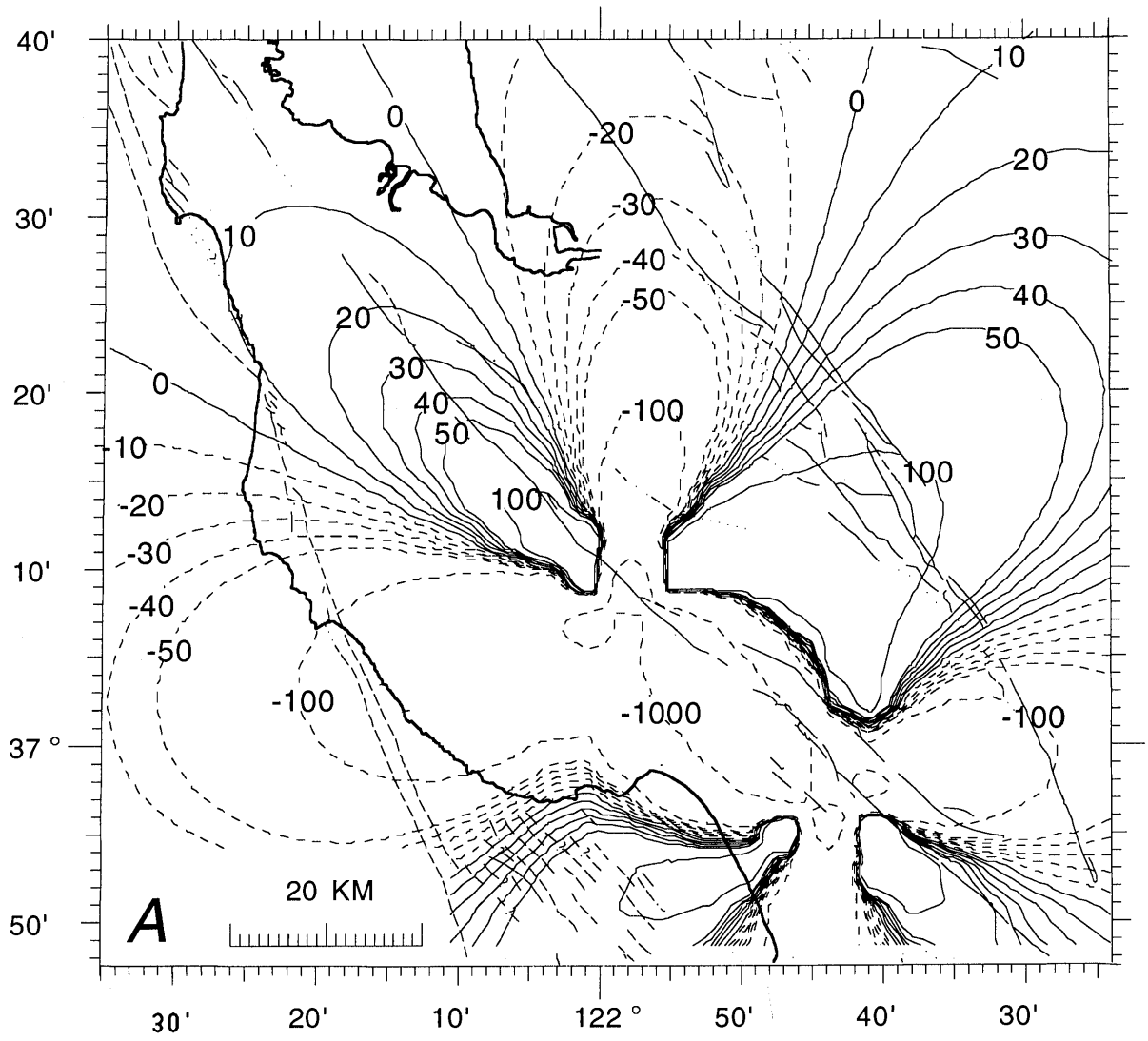

Figure 13.— *A*, Horizontal stress changes (in kPa) at 10 km depth on N45°W-striking strike-slip faults caused by the Loma Prieta earthquake. Both fault-normal stresses and strike-parallel shear stresses effect the loading of the faults through a Coulomb failure criterion assuming a coefficient of friction $\mu = 0.6$. The peninsular segment of the San Andreas fault, the northernmost segment of the creeping section of the San Andreas fault, and the central Calaveras fault experienced increased right-lateral stress (positive), whereas the San Gregorio-Hosgri and the southern Hayward fault show a stress decrease. *B*, Stress changes (in kPa) induced by postseismic slip inferred from geodetic data. The pattern of postseismic stress changes is similar, but of lower magnitude, to the coseismically induced static stress changes.

Lisowski, M., Savage, J.C., and Prescott, W.H., 1991a, The velocity field along the San Andreas fault in central and southern California: Journal of Geophysical Research, v. 96, p. 8369-8389.

———1991b, Surface deformation after the Loma Prieta, California, earthquake: Eos (American Geophysical Union Transactions), v. 72, p. 119.

Marshall, G.A., Stein, R.S., and Thatcher, W., 1991, Faulting geometry and slip from co-seismic elevation changes: The October 17, 1989 Loma Prieta, California, earthquake: Bulletin of the Seismological Society of America, v. 81, p. 1660-1693.

Matsu'ura, M., Jackson, D.D., and Cheng, A., 1986, Dislocation model for aseismic crustal deformation at Hollister, California: Journal of Geophysical Research, v. 91, p. 12661-12674.

McLaughlin, R., 1990, Sargent fault zone at Loma Prieta: U.S. Geological Survey Open File Report 90-274, p. 19-22.

Nur, A., and Mavko, G., 1974, Postseismic viscoelastic rebound: Science, v. 183, p. 204-206.

Okada, Y., 1985, Surface deformation due to shear and tensile faults in a half-space: Bulletin of the Seismological Society of America, v. 75, p. 1135-1154.

Oppenheimer, D.H., 1990, Aftershock slip behavior of the 1989 Loma Prieta, California earthquake: Geophysical Research Letters, v. 17, p. 1199-1202.

Oppenheimer, D.H., Bakun, W.H., and Lindh, A.G., 1990, Slip partitioning of the Calaveras fault, California, and prospects for future

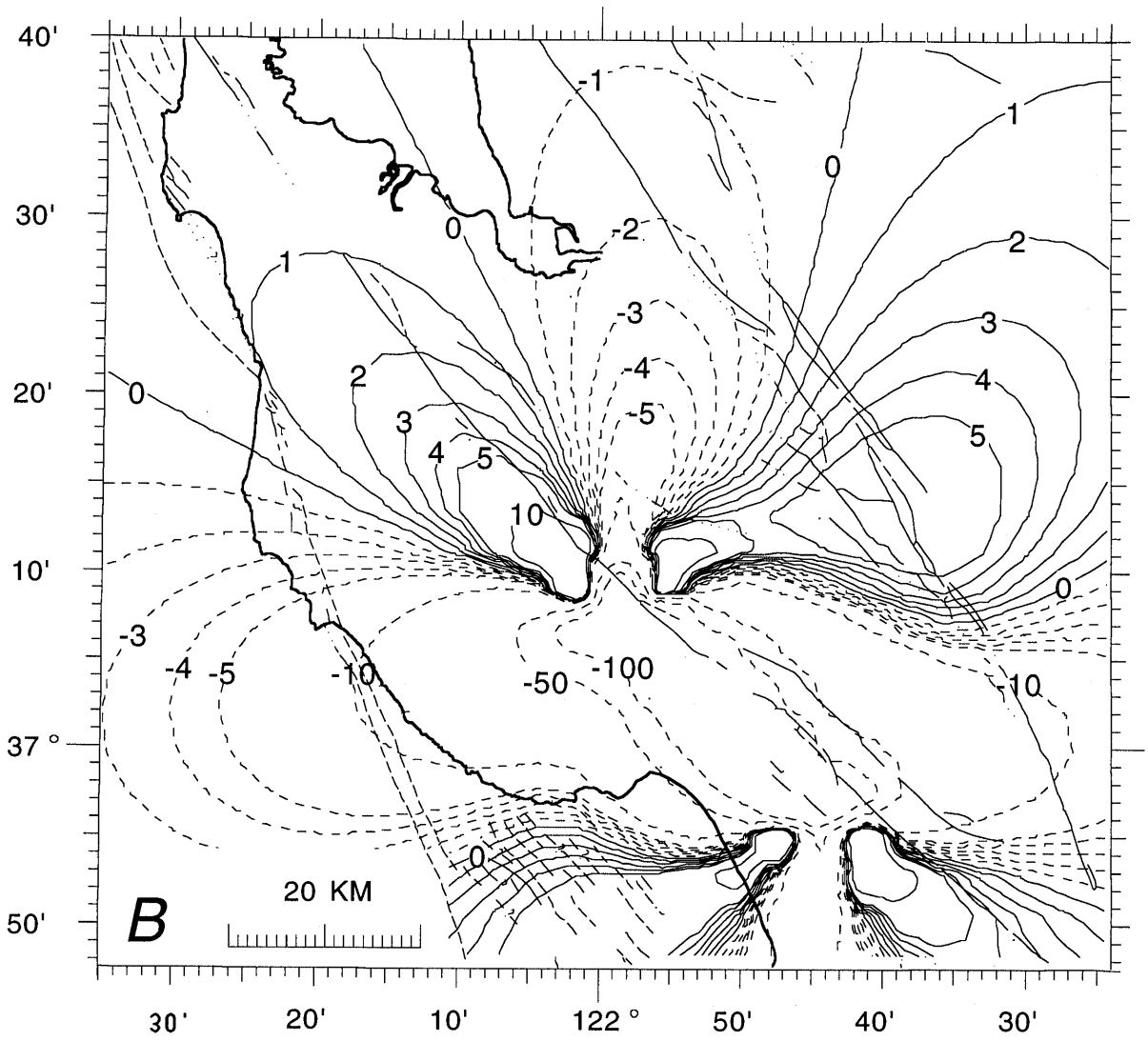

Figure 13.— Continued

earthquakes: Journal of Geophysical Research, v. 95, p. 8483-8498.

Reasenberg, P.A., and Simpson, R.W., 1992, Response of regional seismicity to the static stress change produced by the Loma Prieta earthquake: Science, v. 255, p. 1687-1690.

Rothacher, M., Beutler, G., Gurtner, W., Schildknecht, T., and Wild, U., 1990, Documentation for Bernese GPS Software Version 3.2: Bern, University of Bern.

Rundle, J.B., and Jackson, D.D., 1977, A three-dimensional viscoelastic model of a strike-slip fault: Geophysical Journal of the Royal Astronomical Society, v. 49, p. 575-591.

Rymer, M.J., 1990, Near-fault measurement of postseismic slip associated with the 1989 Loma Prieta, California, earthquake: Geophysical Research Letters, v. 17, p. 1789-1792.

Savage, J.C., 1971, A theory of creep waves propagating along a transform fault: Journal of Geophysical Research, v. 76, p. 1954-1966.

Savage, J.C., and Prescott, W.H., 1978, Asthenosphere readjustment and the earthquake cycle: Journal of Geophysical Research, v. 83, p. 3369-3376.

Savage, J. C., Lisowski, M., and Svarc, J. L., 1994, Postseismic deformation following the 1989 (M = 7.1) Loma Prieta, California, earthquake: Journal of Geophysical Research, v. 99, p. 13757-13765.

Scholz, C.H., 1977, A physical interpretation of the Haicheng earthquake prediction: Nature, v. 267, p. 121-124.

Steidl, J.H., Archuleta, R.J., and Hartzell, S.H., 1991, Rupture history of the 1989 Loma Prieta, California, earthquake: Bulletin of the Seismological Society of America, v. 81, p. 1573-1602.

Thatcher, W., 1974, Strain release mechanism of the 1906 San Francisco earthquake: Science, v. 184, p. 1283-1285.

———1983, Nonlinear strain buildup and the earthquake cycle on the San Andreas fault: Journal of Geophysical Reseach, v. 88, p. 5893-5902.

———1986, Cyclic deformation related to great earthquakes at plate boundaries: Royal Society of New Zealand Bulletin, v. 24, p. 245-272.

Toksöz, M.N., Shakal, A.F., and Michael, A.J., 1979, Space-time migration of earthquakes along the North Anatolian fault zone and seismic gaps: Pure and Applied Geophysics, v. 117, p. 1258-1270.

Tuttle, M.P., and Sykes, L.R., 1992, Re-evaluation of several large historic earthquakes in the vicinity of the Loma Prieta and Peninsular segments of the San Andreas fault, California: Bulletin of the Seismological Society of America, v. 82, p. 1802-1820.

Wald, D.J., Helmberger, D.V., and Heaton, T.H., 1991, Rupture model of the 1989 Loma Prieta earthquake from the inversion of strong-motion and broadband teleseismic data: Bulletin of the Seismological Society of America, v. 81, p. 1540-1572.

Williams, C.R., Arnadottir, T., and Segall, P., 1993, Coseismic deformation and dislocation models of the 1989 Loma Prieta earthquake derived from Global Positioning System measurements: Journal of Geophysical Research, v. 98, p. 4567-4578.

Wood, M.D., and Allen, S.S., 1973, Recurrence of seismic migrations along the central California segment of the San Andreas fault system: Nature, v. 244, p. 213-215.

AFTERSHOCKS AND POSTSEISMIC EFFECTS

SHALLOW, POSTSEISMIC SLIP ON THE SAN ANDREAS FAULT AT THE NORTHWESTERN END OF THE LOMA PRIETA EARTHQUAKE RUPTURE ZONE

By John Langbein,
U.S. Geological Survey

CONTENTS

ABSTRACT

A small, 10 km by 10 km geodetic network spanning the San Andreas fault was measured 7, 77, 157, 194, 422, 547, and 756 days following the Loma Prieta earthquake. This network is located at the northwestern end of the rupture plane defined by the locations of numerous aftershocks. In the initial 70-day interval, the measured line-length changes revealed that 4.7±0.6 of right-lateral slip occurred within the network. However, during the later 2-year interval only 2.1±0.5 mm/yr of right-lateral slip could be detected. Thus, it appears that the measured slip is a typical response of a fault following a major shock in that the rate of slip decreases rapidly with time. However, the magnitude of the postseismic slip is less than 0.5 percent of the inferred co-seismic slip at depth. In addition, we estimate that secular strain is accumulating at 0.19±0.05 ppm/yr of fault-parallel strain, –0.37±0.06 ppm/yr of fault-normal strain, and 0.20±0.05 ppm/yr of fault-tensor-shear strain which appears to be caused by postseismic, dextral slip on the rupture plane of the Loma Prieta earthquake.

INTRODUCTION

Immediately following the Loma Prieta earthquake, U.S. Geological Survey personnel installed and measured a small geodetic network on the northwestern end of a zone defined by the epicenters of aftershocks that occurred within 2 days of the main shock (fig. 1). The intent of these observations is to detect possible fault slip following the main shock and to monitor the deformation rate for anomalous changes that might precede a large and potentially damaging earthquake on the San Francisco peninsula segment of the San Andreas fault northwest of the Loma Prieta shock. The network was set up to the northwest rather than to the southeast for several reasons. With only a short segment between the southern end of the rupture zone and the creeping section of the San Andreas fault south of San Juan Bautista (Burford and Harsh, 1980), the potential for an earthquake larger than M=6 is low. Furthermore, there already were several geodimeter baselines (Lisowski and Prescott, 1981; King and others, 1981; Savage and others, 1979) and volumetric strain meters (Johnston and others, 1986; Johnston and others, 1987) for detecting deformation on the segment to the southeast. Within the zone defined by the aftershocks, there was already geodetic coverage because several baselines are monitored using a central point at Loma Prieta (Savage and others, 1987). However, geodetic coverage just to the northwest of the aftershock zone has been poor because of dense tree growth and steep topography. Nonetheless, we were able to install a few monuments that could be measured with a two-color geodimeter. The advantage of this instrument over a global positioning system (GPS) (Prescott and others, 1989a) and the more traditional terrestrial distance measuring instrument (Savage and Prescott, 1973) is its higher precision of 0.10 to 0.15 part per million for lengths between 2 and 10 km (Langbein, 1989), which makes it possible to detect small displacements and possible changes in rates. The data to be discussed here indicate displacements of 4 mm in the 2.5-month period following the main shock, and these displacements can be interpreted as 5 to 6 mm of shallow, cumulative fault slip on this segment of the San Andreas fault between Black Mountain and Loma Prieta. However, the measurements during the next 2 years detected a similar amount of displacements, indicating a substantial reduction in rate. Although other geodetic measurements

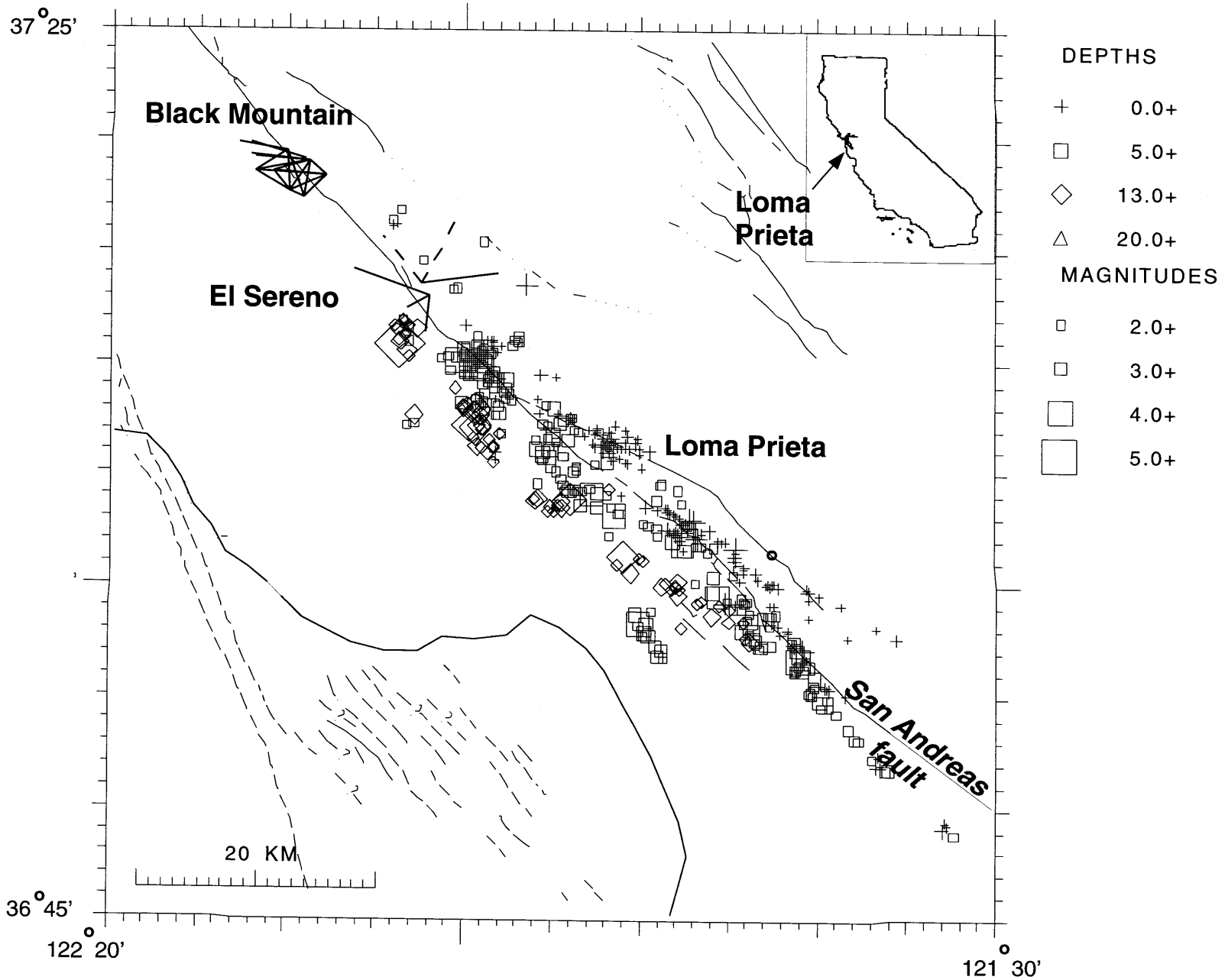

Figure 1.—Map showing the location of the two-color network centered on El Sereno Ridge with respect to the Loma Prieta earthquake aftershock zone, mapped faults, and some of the additional geodetic coverage on the San Francisco peninsula. The approximate location of this map within California is shown in the inset. The aftershocks are those M=2 or larger and occurring within the first 7 days after the main shock. The precise locations are a result of relocating the events with an improved velocity model using well recorded waveforms (Dietz and Ellsworth, this chapter). The geodetic network north of El Sereno is the Black Mountain network measured since 1970 by Prescott and others (1989b) using a single-color geodimeter.

have detected significant deformation following the main shock (Lisowski and others, 1991; Burgmann, and others, 1994), these measurements have not been able to unambiguously detect any decrease in rate that is usually characteristic of postseismic slip because of the lower precision of these techniques (Savage and Prescott, 1973; Prescott and others, 1989b). It also is possible that these large, 100-km networks are more sensitive to slip at depth caused by visco-elastic relaxation of the lower crust (Savage and Prescott, 1978), which may have a time scale of years rather than days, as is often found with shallow slip.

THE DATA

Within one week following the Loma Prieta earthquake, we installed and measured the lengths of the four baselines shown in figures 1 and 2. During the first week of Janu-

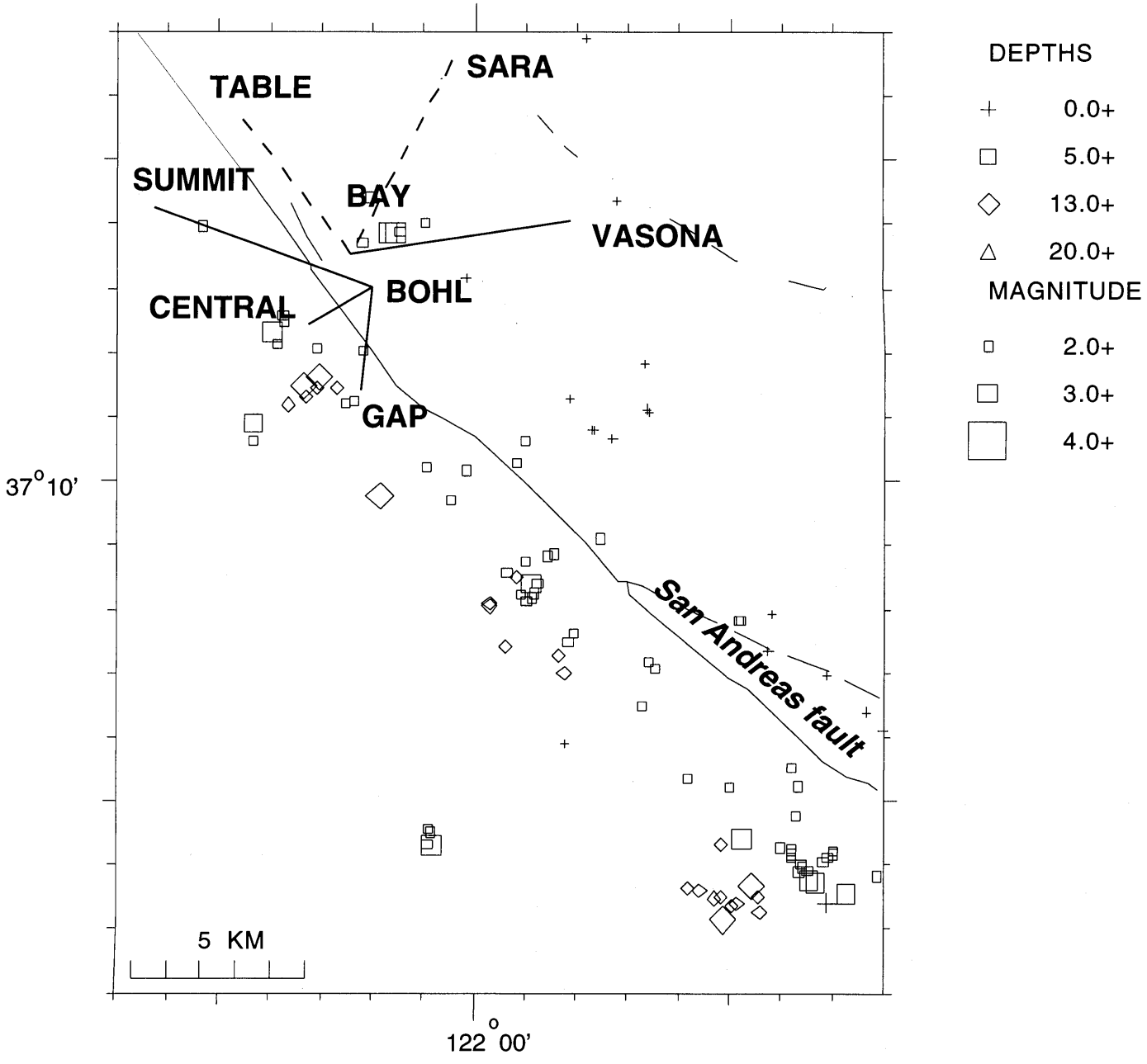

Figure 2.—Detailed map showing the locations of the six baselines of the El Sereno network. The four baselines shown with solid lines were measured starting 7 days after the Loma Prieta earthquake. The other two baselines, shown with dashed lines, have measurements starting 7 days after the main shock. Also plotted are the locations of the aftershocks (Dietz and Ellsworth, this chapter) near and within the network for the period spanning the surveys of the network. Most of the shocks occurred within a month of the main shock. Again, only earthquakes with magnitudes greater than 2 are shown.

ary 1990, these baselines were surveyed again, and two additional baselines were measured for the first time. In mid-March 1990, three out of the original four baselines were measured for the third time. Finally, in late April 1990, all six baselines were measured again. The three most recent surveys included measurements on all six baselines with the exception of the December 1990 survey, when the monument at GAP was not recovered. Because of difficult line-of-sight conditions, we needed to use two central monuments, BOHL and BAY, on El Sereno Ridge so that we could have a 360° view of the surroundings. Two of the six baselines cross the surface trace of the San Andreas fault at about 45° angles, and their length changes are sensitive to fault slip. A third baseline, from BAY to VASONA, does not cross the San Andreas fault but is oriented at 45° to the fault strike and provides a sensitive measure of off-fault shear strain. A fourth baseline crosses the San Andreas fault at a steep angle and is useful for detecting displacements perpendicular to the fault. The last two baselines, from BAY to SARA and TABLE, are useful for detecting off-fault deformation.

The instrument used to measure the baseline lengths is a portable, two-color geodimeter (Slater and Huggett, 1976), with a nominal precision between 0.4 mm and 0.9 mm for lengths between 2 and 7 km (Langbein, 1989). For distances of less than 10 km, this instrument has at least a factor of three better precision than any other geodetic techniques (Savage and Prescott, 1973; Prescott and others, 1989a). Because the instrument ranges on two wavelengths, it is able to detect differences in travel time due to dispersion in the atmosphere. Whereas the use of two optical wavelengths gives the instrument its high precision, it also limits the maximum range to that obtained with its long wavelength, blue. The scatter of the blue light during hazy conditions limits the use of the instrument to clear nights. The March 1990 survey was incomplete due to foggy conditions.

The results of measuring the six baselines are shown in figure 3 and clearly show that two of the fault-crossing baselines changed length by 4 mm between the first two surveys and show some changes in length during the next 2 years. The sense of the initial set of displacements is consistent with approximately 5 to 6 mm of right-lateral slip on the San Andreas fault, or localized displacement of the monument at BOHL to the southeast by the same amount. While the baselines to SUMMIT and GAP showed significant displacements during the initial 2.5 months, the other two baselines did not show any length changes within their one standard deviation error bars. With any instrument that measures distance, one needs to be careful about possible drift in the instrumentation which could manifest itself as a length change. Typically, the drift would cause a change in the length scale, thus causing all of the baselines to either extend or contract in length. However, since the lengths of two baselines remain unchanged and the other two baselines show displacements of equal magnitude but in the opposite sense, a change of the length scale in the instrumentation is unlikely.

The 2- to 4-mm amplitude of displacement on the baseline BOHL-CENTRAL has a suspicious seasonal periodicity that has been seen elsewhere in central California (Langbein and others, 1990). The monument at CENTRAL is placed at the edge of a steep embankment next to a highway. Any soil dilation corresponding to the seasonal rainfall would contaminate the data from this baseline. Accordingly, the data from this baseline will be ignored in the following discussion.

DISCUSSION

Although a localized displacement vector to the southeast of the monument BOHL is consistent with the observations, the simplest tectonic model is 4.7±0.6 mm of shallow, right-lateral slip on the segment of the San Andreas fault located within the network during the 2.5 months following the main shock (fig. 4). Because the network is limited spatially, we cannot place any definitive bounds on the extent of the slip plane. Accordingly, we use the simplest model of a throughgoing fault plane that splits the crust into two rigid blocks. The results of estimating right-lateral slip as a function of time on the basis of this simple model are shown in figure 4. However, in a few tests of varying the top and bottom edges of the dislocation surface, we could reject with a 99 percent confidence level those models that specify zero slip between the surface and 3 km depth. All other models with slip on the San Andreas fault provide an adequate fit to the observations, and it seems likely that slip did occur at shallow depths.

The inferred value of slip for late 1990 appears anomalous. However, confidence for that particular value of slip is low because only one out of the two fault-crossing baselines was measured during that survey. The baseline to GAP was not measured. Accordingly, in the following discussion, the slip value from late 1990 is ignored.

The observed 4.7 mm of fault slip should be interpreted as postseismic slip, which often occurs after large earthquakes (Smith and Wyss, 1968; Langbein and others, 1983). As shown in figure 2, there are a number of aftershocks located within the El Sereno network. Just to the north of the network, the number of aftershocks decreases significantly. The cumulative moment of these tiny aftershocks would translate into slip much smaller than the inferred 4.7 mm. The presence of seismicity is evidence for deformation, but most of the deformation could be happening aseismically.

While estimating the slip as a function of time, the three components of tensor strain rate are fit simultaneously to the data using the method discussed by Langbein (1989).

The results of this simultaneous adjustment for both slip and strain rate indicate 0.19±0.05 ppm/yr of fault-parallel strain, -0.37±0.06 ppm/yr of fault-normal strain, and 0.20±0.05 ppm/yr of tensor shear. The local strike of the fault is taken to be N54°W. Recall, however, that data from the five baselines are used to estimate four parameters, so these estimates are statistically co-dependent.

There are three sets of geodetic measurements that have detected postseismic deformation. Two sets of these measurements use GPS to re-occupy a profile of monuments oriented perpendicular to the San Andreas fault and spanning a 50- to 80-km-wide zone. The profile of Lisowski and others (1991) spans the epicentral area of the Loma Prieta earthquake and the second profile of Burgmann and Segall (1991) is located approximately 10 km northwest of the two-color network. Lisowski and others' (1991) measurements show 8 mm/yr near surface slip, an additional fault-parallel 20-mm/yr displacement distributed over a 20-km-wide zone centered on the San Andreas fault, and 18 mm/yr contraction over 15-km-wide zone for which the San Andreas forms the southwestern boundary. These displacement rates translate into a 0.5 ppm/yr shear strain and 1.2 ppm/yr fault-normal contraction. By comparison, the two-color network has detected lower rates by a factor of two to three than the GPS observations spanning the epicentral area. However, to the northwest of the two-color network the data from the GPS network of Burgmann and Segall (1991) show rates that can be explained by secular strain accumulation. Thus, the strain rates derived from the two-color data fit between the high rate within the epicentral area and the low rate to the northwest.

Burgmann and others (this volume) have modeled the GPS data measurements from both the epicentral area and

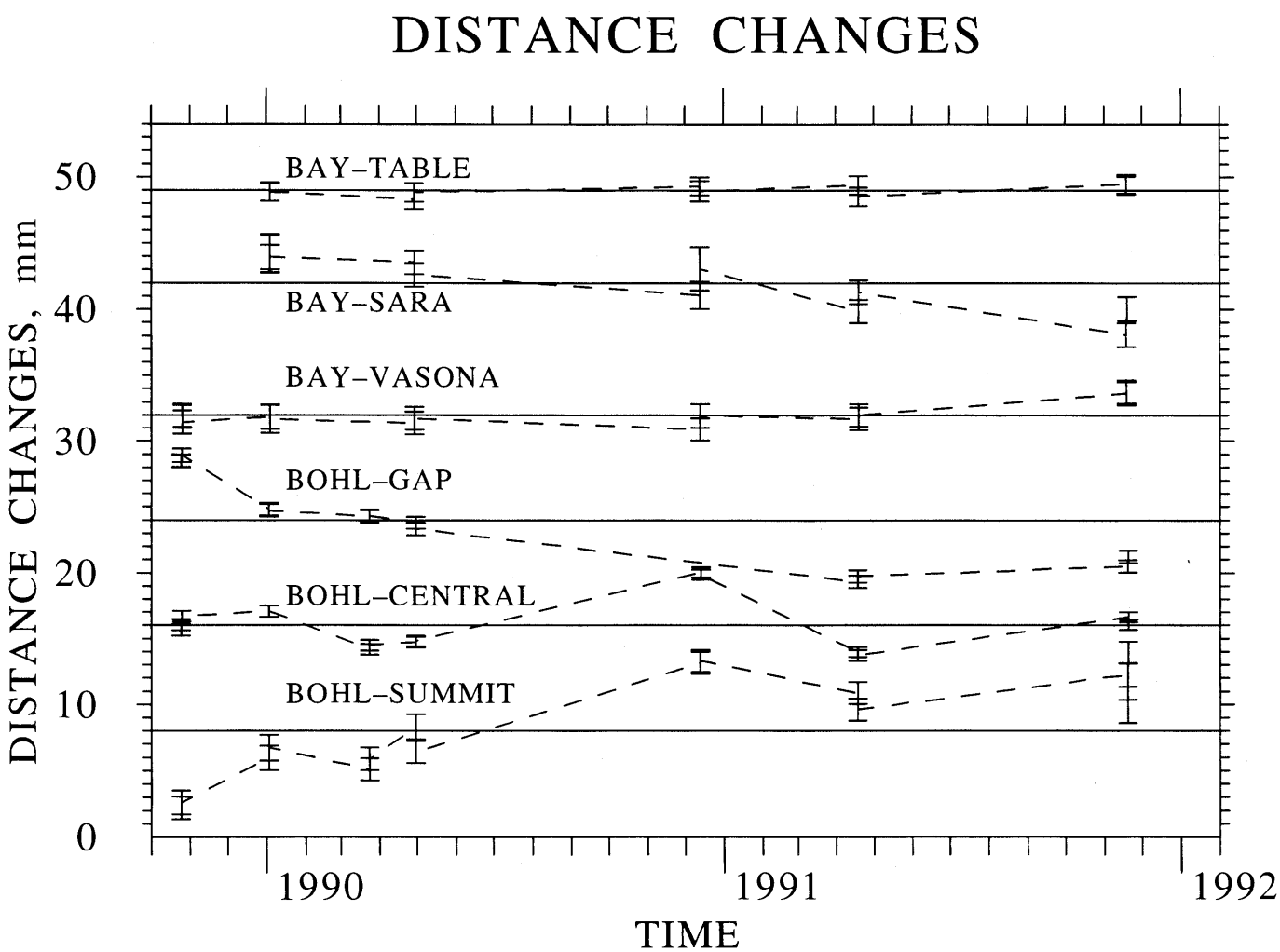

Figure 3.—Line-length changes observed on the six baselines of the El Sereno network using a two-color geodimeter. The error bars represent the one standard deviation level derived by Langbein (1989). Typically, each baseline is measured twice during a single evening using different reflectors. Hence, the observations of length from a single evening are plotted with overlapping error bars. The data for the baseline BOHL-CENTRAL were not used in the modeling that is discussed in the text.

the Black Mountain profile in terms of deep, dextral slip on the Loma Prieta rupture plane and thrust slip on a fault plane northeast and paralleling the San Andreas fault. Although the lateral extent of the thrust fault is poorly constrained from the GPS data, Burgmann and others model this fault as extending beneath the baseline from BAY to VASONA. Given Burgmann and others' slip rate of 120 mm/yr of thrust on this foothills fault, it would predict approximately 3.6 mm/yr of extension on this baseline, which is clearly not the case. Instead, if thrust is indeed occurring, then it must be located southeast of the two-color network.

However, the 100 mm/yr of dextral slip on the plane representing rupture of the Loma Prieta fault determined by Burgmann and others is broadly consistent with the two-color measurements. In fact, if we use the model of time-dependent slip on the San Andreas fault shown in figure 4, and slip on the two planes discussed in Burgmann and others, a satisfactory fit to the two-color data is obtained. The inferred value of postseismic slip on the Loma Prieta plane using the two-color data is 157±23 mm/yr, which is within 50 percent of the value estimated by Burgmann and others of 100 mm/yr. However, the model derived from the two-color data implies −14±6 mm/yr of thrust on the foothills fault, which is not consistent with the estimate of Burgmann and others of 120 mm/yr.

Finally, the third set of postseismic measurements, which have been described by Rymer (1990), are a series of taped distance measurements on small-aperture (0.5 to 7.7 m) quadrilaterals. One quadrilateral is located 3.4 km southeast of the station GAP straddling a subparallel trace of the San Andreas fault. At this site during the 6 months following the main shock, Rymer (1990) recorded a cumulative of 5±2 mm of right-lateral slip consistent with the observations described here.

The unique feature of the two-color data is that we can infer a decrease in slip rate over the 2 years following the

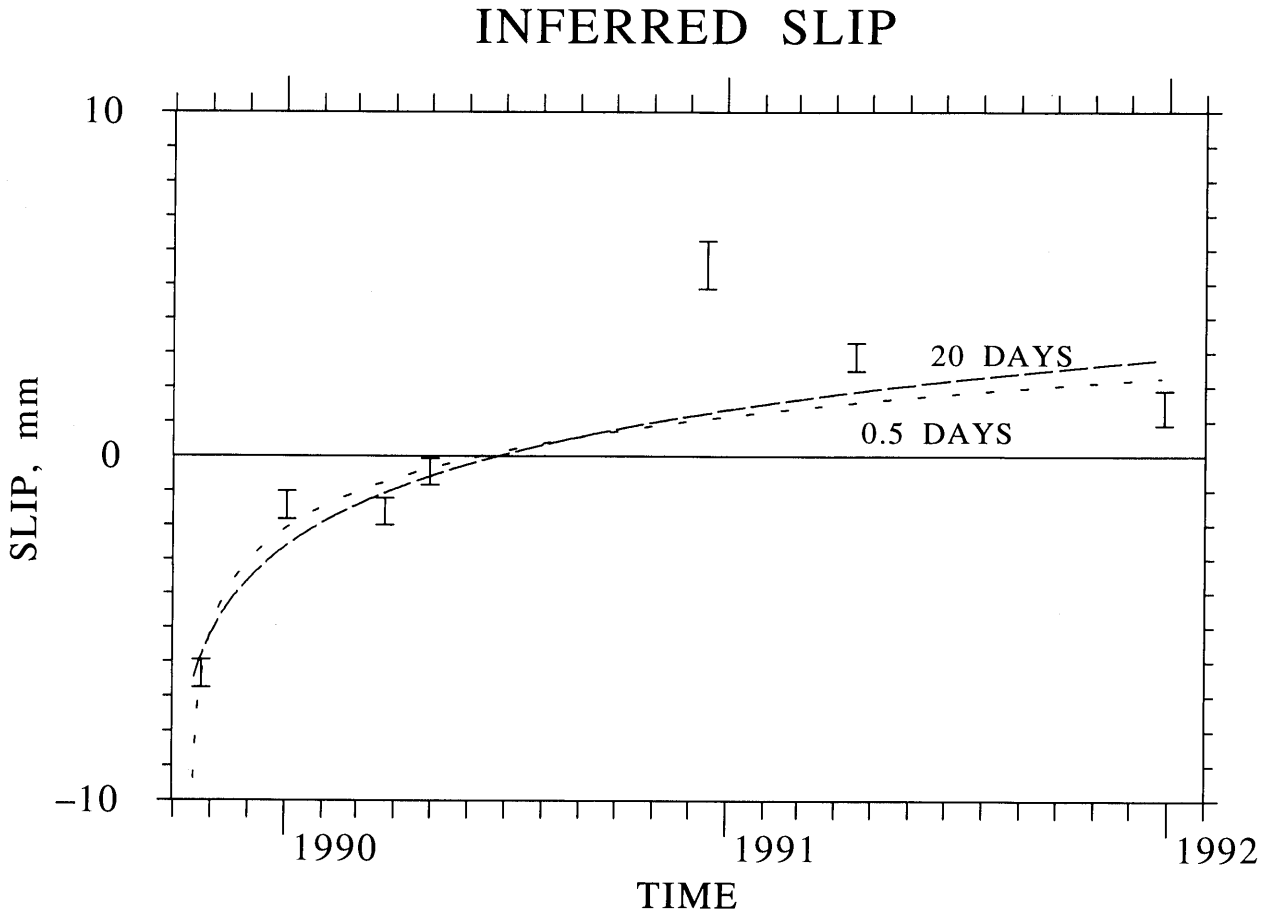

Figure 4.—Values of inferred slip as a function of time following the Loma Prieta main shock. The error bars represent one standard deviation. Since the total amount of slip following the earthquake is unknown, only the relative slip is plotted. The two curves show the predicted slip as a function of the logarithm of time for two differing decay times, 0.5 and 20 days. The value of slip for December 1990 was not used in estimating the parameters of the logarithmic curves.

main shock. To demonstrate that slip has been occurring during the interval between January 1990 and November 1991, a different function of slip with time is fit to the observed line-length changes. For the interval between October 1989 and the January 1990 surveys, slip is assumed to occur as a single event at an unspecified time. However, for the observations from early January through November 1991, slip is assumed to occur at a constant rate. Estimates of these two parameters yield 4.7±0.6 mm of slip between early October 1989 and early January 1990, and a significant slip rate of 2.1±0.5 mm/yr for the period following January 1990. This rate appears to be marginally faster by 1.7 standard deviations than the apparent background rate of mm/yr 1.2±0.2 mm/yr estimated for the Black Mountain network (fig. 1) by Prescott and others (1989b).

Although the slip rate recorded within days after the main shock is significant, the rate of postseismic slip appears to be decreasing inversely with time. Along with the estimated slip, figure 4 shows two curves representing postseismic slip as $U_o\log(t/\tau+1)+B$, where t is the time of observation since the time of the main shock (Langbein and others, 1983). Here we have specified two differing values for the decay time τ as 0.5 days and 20 days and estimated corresponding values for U_o and B by least-squares fitting. With the exception of the inferred slip in late 1990, the comparison in figure 4 shows reasonable agreement between the inferred values of slip as a function of time and the postseismic slip predicted from the logarithmic functions. However, those functions having decay times of less than a month fit the observed slip data better than those functions with decay periods in excess of several months. Thus the short decay time (τ) found here is consistent with that found in other cases of shallow, postseismic slip following the 1966 Parkfield and 1979 Imperial Valley earthquakes (Smith and Wyss, 1968; Langbein and others, 1983).

Breckenridge and Simpson (this volume) show data for changes in the rates of fault slip on other fault segments in response to the Loma Prieta earthquake, which they suggest is caused by the Loma Prieta earthquake perturbing the regional stress field. They demonstrate that the spatial pattern of stress changes predicted from their stress model was consistent with the changes in slip that they observed from creepmeters along the Hayward, San Andreas, and Calaveras fault system. Furthermore, their model predicts an increase in rate of slip on the section of the San Andreas fault that bisects the two-color network immediately following the Loma Prieta earthquake. The results presented here support their model. However, their creep data show that the time constant is about a year for the postseismic slip rate to return to its secular rate. This observation is inconsistent with the time-constant for postseismic slip determined from the measurements discussed here. It could be that the time-constant of deformation detected by the creep data and the GPS observations is due to a deep-seated process with a long time constant, but that there is a short time constant associated with near-surface fault-slip.

REFERENCES

Burford, R.O., and Harsh, P.W., 1980, Slip on the San Andreas fault in central California form alinement array surveys: Bulletin of the Seismological Society of America, v. 70, p. 1233-1261.

Burgmann, R., and Segall P., 1991, Postseismic GPS monitoring NW of the 1989 Loma Prieta rupture zone: Eos, v. 72, no. 44, p. 119.

Johnston, M.J.S., Linde A.T., Gladwin M.T., and Borcherdt, R.D., 1987, Fault failure with moderate earthquakes: Tectonophysics, v. 144, p. 189-206.

Johnston, M.J.S., Borcherdt R.D., and Linde A.T., 1986, Short period strain ($0.1\text{-}10^{-5}$ s): Near source strain field for an earthquake (M_L 3.2) near San Juan Bautista, California: Journal of Geophysical Research, v. 91, p. 11497-11502.

King, N.E., Savage, J.C., Lisowski, M., and Prescott, W.H., 1981, Preseismic and co-seismic deformation associated with the Coyote Lake, California earthquake: Journal of Geophysical Research, v. 86, p. 892-898.

Langbein, J., McGarr, A., Johnston, M.J.S, and Harsh, P.W., 1983, Geodetic measurements of postseismic crustal deformation following the 1979 Imperial Valley earthquake, California: Bulletin of the Seismological Society America, v. 73, p. 1203-1224.

Langbein, J., 1989, The deformation of the Long Valley caldera, eastern California, from mid-1983 to mid-1988; measurements using a two-color geodimeter: Journal of Geophysical Research, v. 94, p. 3833-3850.

Langbein, J., Burford, R.O., and Slater, L.E., 1990, Variations in fault slip and strain accumulation at Parkfield, California: Initial results using two-color geodimeter measurements, 1984-1988: Journal of Geophysical Research, v. 95, p. 2533-2552.

Lisowski, M., and Prescott, W.H., 1981, Short-range distance measurements along the San Andreas fault system in Central California, 1975-1979: Bulletin of the Seismological Society America v. 71, p. 1607-1624.

Lisowski, M., Prescott, W.H., Savage, J.C., and Johnston, M.J.S., 1990, Geodetic estimate of co-seismic slip during the 1989 Loma Prieta, California, earthquake: Geophysical Research Letters, v. 17.

Lisowski, M., Savage, J.C. and Prescott, W.H, 1991, Surface deformation after the Loma Prieta, California Earthquake: Eos, v. 72, no. 44, p. 119.

Prescott, W.H., Davis, J.L, and Svarc, J.L, 1989a, Global positioning system measurements for crustal deformation: Precision and accuracy: Science, v. 244, p. 1337-1340.

Prescott, W.H., Savage, J.C. and Lisowski, M., 1989b, Crustal strain, *in* National Earthquake Reduction Program, Summaries of Technical Reports (v. 29): U.S. Geological Survey Open-File Report 90-54.

Rymer, M.J., 1990, Near-fault measurement of postseismic slip associated with the 1989 Loma Prieta, California, Earthquake: Geophysical Research Letters, v. 17, p. 1789-1792.

Savage, J.C., and Prescott, W.H., 1973, Precision of geodolite distance measurements for determining fault movements: Journal of Geophysical Research, v. 78, p. 6001-6008.

Savage, J.C., and Prescott, W.H., 1978, Asthenosphere readjustment

and the earthquake cycle: Journal of Geophysical Research, v. 83, p. 3369-3376.

Savage, J.C, Prescott, W.H., Lisowski, M., and King, M, 1979, Geodolite measurements of deformation near Hollister, California, 1971-1978:, Journal of Geophysical Research, v. 84, p. 7599-7615.

Savage, J.C, Prescott, W.H, and Lisowski, M., 1987, Deformation along the San Andreas fault 1982-1986 as indicated by frequent Geodolite measurements: Journal of Geophysical Research, v. 92, p. 4785-4797.

Slater, L.E., and Huggett, G.R, 1976, A multi-wavelength distance-measuring instrument for geophysical experiments: Journal of Geophysical Research, v. 81, p. 6299-6306.

Smith, S.W., and Wyss, M., 1968, Displacement on the San Andreas fault initiated by the 1966 Parkfield earthquake: Bulletin of the Seismological Society of America, v. 68, p. 1955-1974.

THE LOMA PRIETA, CALIFORNIA, EARTHQUAKE OF OCTOBER 17, 1989:
EARTHQUAKE OCCURRENCE

AFTERSHOCKS AND POSTSEISMIC EFFECTS

MODELS OF POSTSEISMIC DEFORMATION AND STRESS TRANSFER ASSOCIATED WITH THE LOMA PRIETA EARTHQUAKE

By M.F. Linker,
Harvard University and U.S. Geological Survey;
and J.R. Rice, Harvard University

CONTENTS

ABSTRACT

Recent geodetic observations indicate that the velocity field at the Earth's surface has been perturbed by the Loma Prieta earthquake. We interpret this change in terms of models in which transient postseismic slip occurs beneath the locked seismogenic portion of the San Andreas fault zone. In our three-dimensional finite element calculations, the deep aseismic region of the fault zone is either treated as linear Maxwell viscoelastic or is made to follow a steady-state version of the laboratory-derived rate- and state-dependent friction law, in which slip rate depends exponentially on the ratio of shear stress to effective normal stress. We refer to this second rheology as our "hot-friction" model. Comparison of model predictions to observed postseismic displacements provides a constraint on the ratio of Maxwell relaxation time, t_r, for material in the deep aseismic region of the fault zone to fault-zone thickness, h. Neither quantity can be constrained independently. Best fit to the initial 1.3 years of data is obtained with $t_r/h \approx 0.3$ yr/km thickness. If we assume that postseismic slip has occurred in a fault zone of thickness $h \leq 1$ km, then using a shear modulus of 30 GPa we obtain an estimate of the effective viscosity of material in the deep aseismic region of the fault zone, $\eta_{eff} \leq 3 \times 10^{17}$ Pa-s. Previous estimates made for the material of the lower crust, based on laboratory measurements of steady-state dislocation or diffusion creep, exceed this value by at least an order of magnitude. The laboratory-derived hot-friction model can yield postseismic deformation of magnitude comparable to that observed, but only if $d\tau/d(\ln V)$ is of the order 0.5 MPa, where τ is the resistance to sliding and V is the slip rate. Laboratory measurements indicate that $d\tau/d(\ln V)$ can be written approximately as $c\sigma$, where σ is the effective normal stress equal to total normal stress minus pore pressure and c is on the order of 0.015 for mid-crustal conditions. To be consistent with our models, the effective normal stress in the deep aseismic portion of the fault zone must, therefore, be extremely low, perhaps on the order of 30 MPa. In the context of the laboratory-derived hot-friction model, the occurrence of postseismic deformation may be evidence that pore pressure in the aseismic portions of the fault zone and perhaps the lower crust is near lithostatic.

INTRODUCTION

The occurrence of the Loma Prieta earthquake brought immediate concern that another large and damaging earthquake might occur in the San Francisco Bay region in the near future (Working Group, 1990). This concern rose from numerous examples of earthquake triggering and migration (see, for example, Richter, 1958; Mogi, 1968; Allen 1969; Yonekura, 1975; Scholz, 1977; Sykes and others, 1981; Doser, 1986; Stein and Ekström, 1992) in-

cluding two earthquake pairs in the San Francisco Bay region (Toppazada and others, 1981). In 1836 an M=7 event occurred on the northern half of the Hayward fault and 2 years later an M=7 event occurred on the San Francisco peninsula. Similarly, in 1865 an M=6.5 event occurred in the vicinity of Loma Prieta and 3 years later an M=7 event occurred on the southern segment of the Hayward fault. More recently, on the Calaveras fault three moderate events have occurred in spatial sequence, migrating towards the north (Oppenheimer and others, 1990).

Previous workers have suggested that earthquake migration and triggering might be the result of stress transfer between earthquake source regions. Numerous attempts to relate static coseismic stress changes to the occurrence of future events (Stein and Lisowski, 1983; Mavko and others, 1985; Oppenheimer and others, 1988; Poley and others, 1987; Hudnut and others, 1989; Du and Aydin, 1990; Seeber and Armbruster, 1990; Michael and others, 1990; Michael, 1991; Reasenberg and Simpson, 1992) demonstrate that the magnitude of the static coseismic stress change is likely to be small, except perhaps in the region immediately adjacent to the main rupture. Though postseismic relaxation associated with inelastic deformation processes could act to increase the magnitude of the stress transfer relative to the static coseismic stress change, the total stress change in the far-field is still likely to be modest compared to typical earthquake stress drop (Rice and Gu, 1983). Furthermore, the rate of stress transfer resulting from postseismic relaxation may be small compared to the background loading rate, and so its contribution to the far-field stress state is likely to be negligible, unless postseismic relaxation occurs at a sufficiently high rate (Lehner and others, 1981). Nevertheless, the observations of earthquake triggering and migration are numerous, and so we have undertaken a study of the stress transfer associated with the Loma Prieta earthquake.

In the first 50 years following the great 1906 San Francisco earthquake, the shear strain rate near the San Andreas fault decreased by about a factor of three (fig. 1) (Thatcher, 1983), and so we might expect similar transient postseismic deformation to follow the Loma Prieta earthquake. Indeed, geodetic data indicate that postseismic deformation has taken place at rates that exceed the pre-earthquake rate (Bürgmann and others, 1991, this chapter; Lisowski and others, 1991a, 1991b; Bürgmann and others, 1992; Savage and others, 1994). Therefore, the Loma Prieta earthquake provides us an opportunity not only to study the stress transfer that could potentially lead to a future major earthquake, but more generally, to obtain constraints on the rheological properties of the crust, fault zone, and upper mantle.

We use the finite element method to examine three dimensional models of postseismic deformation and stress transfer associated with the Loma Prieta earthquake. We use preseismic (Lisowski and others, 1991b) and preliminary postseismic measurements made during the initial 1.3 years following the earthquake (Bürgmann and Segall, 1991; Lisowski and others, 1991a; Bürgmann and others, 1992) to constrain parameters that control the relaxation process. Our models are additionally constrained by consideration of heat flow data, laboratory-based rheologies and constitutive parameters, seismic observations of pre-

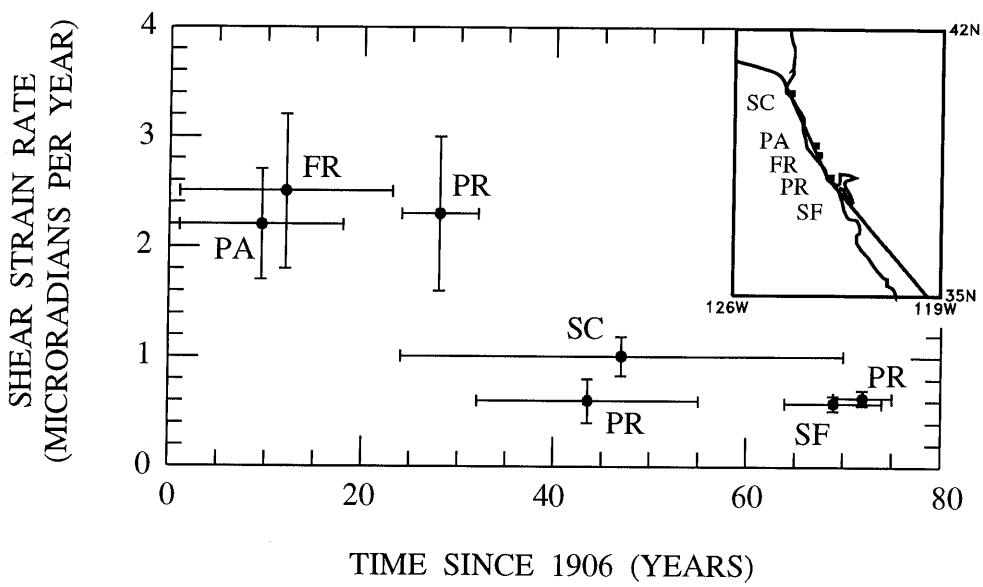

Figure 1.—Geodetically measured right-lateral shear strain rate near the San Andreas fault in northern California following the great 1906 San Francisco earthquake (from Thatcher, 1983). Inset map indicates the location of the networks.

earthquake microseismicity, and seismological studies of the main shock.

Our paper is organized as follows. First, we study the magnitude of stress transfer by examining models of the static coseismic stress field and long-time limits of postseismic relaxation. We then examine time-dependent models and compare predicted displacements to geodetic data in attempts to constrain the parameters that control the relaxation time-scale. Our first set of time-dependent models incorporate linear Maxwell viscoelasticity in the inelastically deforming regions of the model. Our second set of time-dependent models employ a steady-state version of the laboratory-derived rate- and state-dependent friction model in which aseismic slip rate depends exponentially on the ratio of shear stress to effective normal stress (Blanpied and others, 1991), where the effective normal stress is the total normal stress minus the pore pressure. We refer to the nonlinear model as our "hot-friction" model.

Our principle conclusions are as follows. (1) The largest stress changes associated with the earthquake occur adjacent to the main rupture, for example, along the San Francisco Peninsula segment of the San Andreas fault. (2) In that region, postseismic relaxation processes could lead to an increase in shear stress by an amount that exceeds the static coseismic stress increase. (3) Northeast to north of Loma Prieta, both coseismic slip and postseismic relaxation reduce the right-lateral shear stress and the compressive stress along the Hayward and Calaveras faults. (4) Models in which deep aseismic fault slip occurs beneath the seismogenic zone are capable of producing strike-slip displacements consistent with the initial 1.3 years of postseismic deformation observed along the profile of GPS stations that crosses through the epicenter (Lisowski and others, 1991a). These deep-slip models, however, appear to be incapable of producing fault-trace normal contraction compatible with the observations there and an additional source of deformation may be required. (5) Northwest of Loma Prieta, the postseismic displacements predicted by our deep-slip models may exceed the observations, though a careful treatment of all of the pre-earthquake and post-earthquake geodetic data is required to better establish a measure of the change in the velocity field associated with the earthquake. (6) The time-scale for postseismic relaxation appears to be sufficiently long so that the average background tectonic stress rate is likely to exceed the stress rate resulting from relaxation, except perhaps within about 20 km of the edge of the coseismic rupture. (7) In linear viscoelastic models that incorporate postseismic fault slip, the parameter controlling the relaxation time is the ratio of fault-zone material relaxation time to the thickness of the fault zone, t_r/h. This parameter appears to have a value of approximately 0.3 years/km thickness. If relaxation takes place in a shear zone that is less than 1 km thick and if the shear modulus is 30 GPa, then the effective viscosity in the deforming region must be less than about 3×10^{17} Pa-s. This value is at least one order of magnitude lower than any obvious interpretation of laboratory measurements of the steady-state creep of solid crustal rocks controlled by dislocation or diffusion creep. Transient creep response to a sudden change in stress has not been as well characterized in the laboratory and so probably cannot be ruled out as a possible mechanism. (8) The laboratory-derived hot-friction model can yield postseismic deformation of magnitude comparable to that observed, but only if $d\tau/d(\ln V)$ is of the order 0.5 MPa, where τ is the resistance to sliding and V is the slip rate. Laboratory measurements indicate that $d\tau/d(\ln V)$ can be written approximately as $c\sigma$ (Stesky, 1975, 1978; Dieterich, 1981; Ruina, 1983), where σ is the effective normal stress and c is of order 0.015 for mid-crustal conditions (Blanpied and others, 1991). Therefore, to be consistent with our models, the effective normal stress must be extremely low, perhaps of order 30 MPa. (9) In the context of the laboratory-derived hot-friction model, the occurrence of postseismic deformation may be evidence that pore pressure in the aseismic portions of the fault zone and perhaps the nearby lower crust is near lithostatic.

PHYSICAL MODELS OF POSTSEISMIC DEFORMATION

Models of postseismic deformation have been motivated primarily by observations of deformation that followed large earthquakes in subduction zones and along the San Andreas fault. In these models deformation occurs as the result of fault slip on a down-dip projection of the seismic rupture or as distributed shear in a broad zone beneath the brittle seismic layer (Savage and Prescott, 1978; Savage, 1983; Thatcher, 1983; Thatcher and Rundle, 1984; Li and Rice, 1987; Lyzenga and others, 1991). Unfortunately, the displacement field at the earth's surface is rather insensitive to the location of the deformation source, and so generally it is not possible to reject either of these models on the grounds that they do not fit the deformation data (Savage and Prescott, 1978; Savage, 1990; Segall, 1991). Therefore, physical models of postseismic deformation must be defended as well as motivated on broad geophysical and geological grounds. England and Molnar (1991), for example, propose that the upper continental crust is weak relative to the lower parts of the lithosphere and that crustal blocks passively follow the deformation of the substrate. Within this context, postseismic deformation could be caused by transient interaction between the individual crustal blocks as well as between the blocks and the substrate. This concept has been adopted either explicitly or implicitly in much of the modeling mentioned above.

We examine three models of the geometrical distribution of inelastic material that shears postseismically (fig. 2). In Model 1, postseismic fault slip is allowed to occur down-dip from the seismogenic zone but is confined to the crust. In Model 2, slip is allowed to extend from the base of the seismogenic zone downward through the crust and into the upper mantle. In Model 3, slip is allowed to extend from the base of the seismogenic zone downward through the crust to where it terminates at its intersection with a horizontal detachment zone in the lower crust.

In the Earth, immediately after the earthquake, stress changes and presumably slip rates are highest near the edge of the coseismic rupture. Therefore, Model 1 can be thought of as a short-time version of either Model 2 or Model 3.

In Model 2, crustal blocks are thought of as effectively welded to the substrate, at least on the time-scale of the repeat-time for large crustal earthquakes. Postseismic motion is interpreted as the result of transient motion between the crustal blocks whose boundaries extend into the upper mantle. We refer to Model 2 as our throughgoing fault model.

Model 3 is based on previous studies of postseismic deformation (for example, Li and Rice, 1987) that were motivated by the recognition that elevated temperatures in the lower crust may give rise to inelastic flow in response to the stress changes associated with earthquakes (Brace and Kohlstedt, 1980; Meissner and Strehlau, 1982; Sibson, 1982; Chen and Molnar, 1983). This class of models can be further motivated by compilations of seismic, geological, and geophysical data in central California (see, for example, Saleeby, 1986; Fuis and Mooney, 1990) and by electrical conductivity measurements, which indicate that horizontal seismic reflectors in the lower crust frequently coincide with horizontal layers of high conductivity and, by inference, with regions of elevated fluid content (Hyndman and Shearer, 1989) and fluid pressure (Rice, 1992). All of these observations are in accord with the commonly held view that large-scale horizontal shearing or fault-slip occurs in the middle to lower crust. In Model 3, motion of the shallow portion of the crust is coupled through this horizontal shear zone to the motion of the substrate that drives the system. We refer to Model 3 as our detachment model.

Tse and Rice (1986) studied models based on rate- and state-dependent friction (Dieterich, 1981; Ruina, 1983), in which the fault-zone rocks at depth are hot enough to be in the "velocity strengthening" range of frictional response. In this case, time-varying stress occurs naturally in the aseismic portion of the fault zone. In contrast, Li and Rice (1987), Fares and Rice (1988), and Ben-Zion and others (1993) treated the aseismic portion of the fault zone within the crust as freely slipping, so that only the shear stress in the basal shear zone varies with time. Their free-slip condition is consistent with an assumption that the relaxation time for postseismic crustal fault slip is considerably shorter than for basal shear.

In this paper, we include the effects of time-varying stress in the aseismic portion of the fault zone as well as in the basal shear zone. We treat the region outside the fault zone and basal shear zone as purely elastic, with the thought that stress changes associated with earthquakes are too small to cause any appreciable inelastic deformation there. We additionally include the effects of finite rupture length and so our models are three dimensional.

THREE-DIMENSIONAL FINITE ELEMENT MODELS

We use the finite element method to model stress changes and deformation associated with the earthquake. Our modeling strategy is as follows. Coseismic slip is imposed on a segment of the fault zone that represents the coseismic rupture surface. This imposed slip produces a stress field throughout the body that represents the static coseismic stress change in the earth. We then use two approaches to model the postseismic deformation and stress transfer resulting from that coseismic stress field. First we examine coseismic and long-time fully-relaxed postseismic stress states. Then we examine time-dependent models in which stress and displacement are calculated while the system relaxes toward the fully-relaxed state. By comparing the computed time-dependent displacements to deformation data, we attempt to constrain the parameters that control the time-scale for relaxation.

The solutions we present employ fixed-displacement boundary conditions along the outer surfaces of the model where it has been cut away from the surroundings. The remote boundaries of our model are located sufficiently far from the coseismic rupture so that fixed-displacement and stress-free boundary conditions give nearly the same solution in the regions of interest.

We ignore the effects of the shallow creeping zone along the San Andreas fault that begins southeast of Loma Prieta near San Juan Bautista and only consider models that are geometrically symmetric along strike about the epicenter. We additionally ignore any deformation associated with slip on the Hayward and Calaveras faults. We assume a crustal thickness of 25 km, which is representative of the region near the San Andreas fault (Oppenheimer and Eaton, 1984), and represent the horizontal shear zone in the lower crust with a 5-km-thick layer of elements that extends from 20 to 25 km in depth.

Our finite element mesh represents a volume with dimensions 217 km along strike by 265 km perpendicular to strike by 62.5 km in depth (fig. 2*A*). Minimum element-dimensions correspond to $3.5 \times 2.5 \times 1.0$ km^3. Approximately 10,000 nodes, or 30,000 degrees of freedom, comprise the

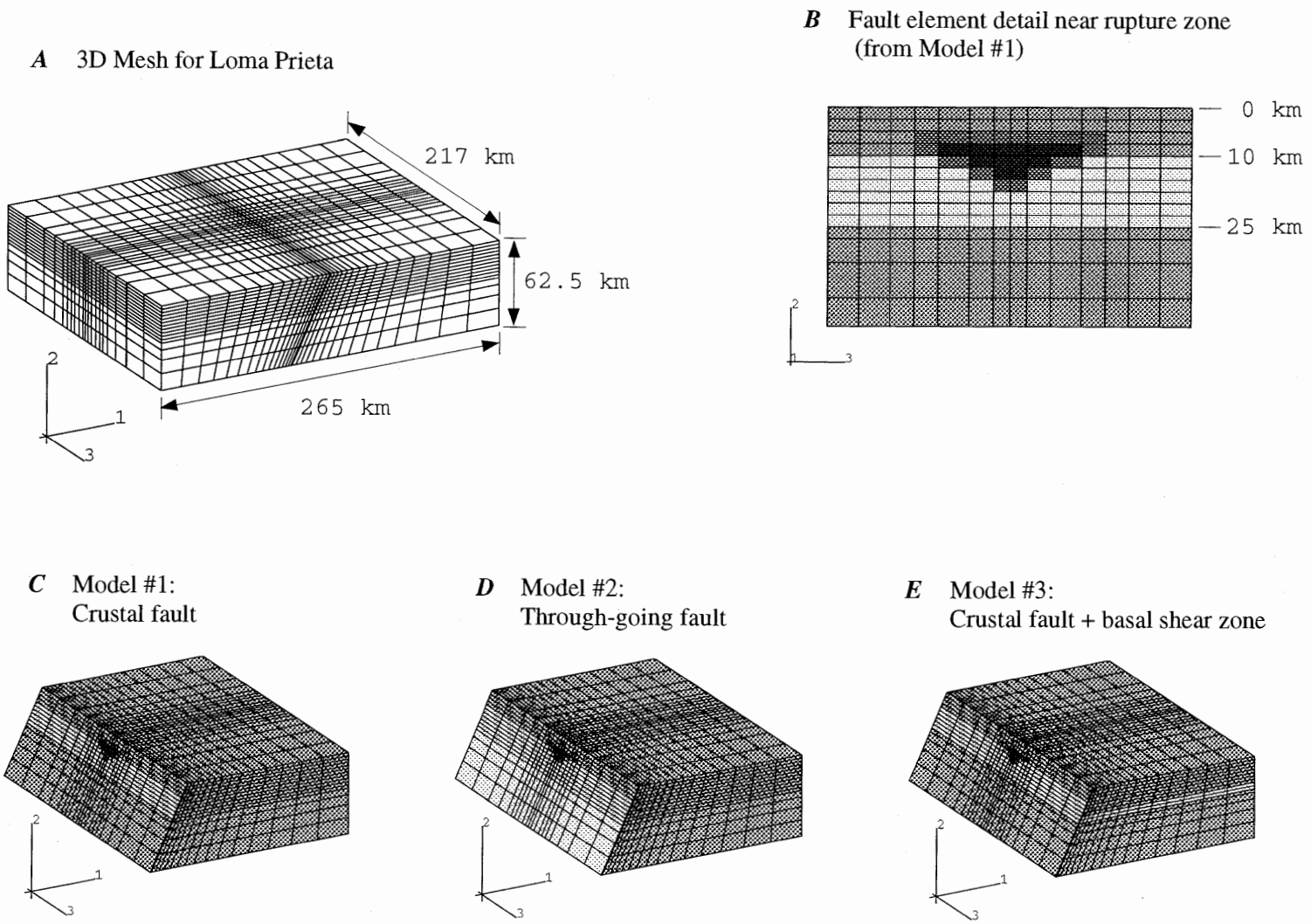

Figure 2.—Finite element (FE) models used to represent three distributions of regions undergoing viscoelastic relaxation. *A*, Three-dimensional FE mesh used to model the crust and upper mantle near Loma Prieta. *B*, Close-up view of fault-zone elements in and around the coseismic rupture zone for a particular model of postseismic relaxation, Model 1. Black region denotes core of coseismic rupture where the imposed coseismic slip is uniform. In the surrounding dark-gray region the imposed coseismic slip tapers to zero away from the core of the rupture. Lightest gray region slips aseismically in response to the stress changes induced by coseismic slip. Gray regions above and below the aseismically slipping zone are locked. *C*, View of Model 1 in which the southwest side of model has been cut away to reveal the dipping fault zone. The aseismically slipping portion of the fault is confined to lie between the shallow seismogenic zone and the base of the crust. *D*, View of Model 2 in which the aseismically slipping portion of the fault zone extends through the Moho and into the upper mantle. *E*, View of Model 3 in which the aseismically slipping portion of the fault zone is confined to the crust but intersects a horizontal shear zone, or detachment zone, that lies in the lower crust.

mesh of eight-noded isoparametric-brick elements. We use the finite element code ABAQUS (Hibbitt and others, 1991). Elastic three-dimensional and viscoelastic two-dimensional models were run on a SUN 4 workstation and require several hours of CPU time and 10 to 20 Mbytes of disk space for output. All computations for three-dimensional time-dependent models were performed on Cray 2 and Cray YMP supercomputers at the National Center for Supercomputing Applications (Urbana, Illinois). The linear viscoelastic solutions typically require about 3 hours of Cray CPU time for 65 time increments using an explicit time-integration method to reach about 5 years of model time. The nonlinear hot-friction models use appreciably more CPU time, since the creep rate varies dramatically during the relaxation process. Typical run times for three dimensional nonlinear models range from 4 to 10 hours on the Cray 2 to reach 2 years of model time. It is likely that some computation time could be saved if an implicit integration procedure was used, but we did not take that approach.

In our models, the fault zone is represented by a thin layer of finite elements (fig. 2). The seismic portion of the fault zone is treated as elastic, and coseismic slip is imposed via a shear transformation strain, γ^T, which changes the stress-free shape of the material in the rupture zone (Aki and Richards, 1980; Rice, 1980). The equivalent seismic slip is $h\gamma^T$, where h is the thickness of the layer of fault elements. At distances greater than order h from the edge of the rupture, this technique produces results equivalent to those obtained by imposing slip on a surface.

Any estimate of the stress field close to the edge of the coseismic rupture will be extremely sensitive to one's estimate of the slip distribution. One might incorporate estimates of the slip distribution determined from seismic records (Beroza, 1991; Hartzell and others, 1991; Steidl and others, 1991; Wald and others, 1991) or measurements of the static displacement field (Marshall and others, 1991), but we have not taken this approach. Future work on this problem may be warranted since the largest stress changes occur in this near-rupture region. Farther from the edge of the rupture, the stress field is less sensitive to the slip distribution and can therefore be estimated with greater confidence.

In this spirit, we assume that the transformation strain and hence coseismic slip are uniform except in the outermost elements of the rupture zone (fig. 2*B*). In these perimeter elements, we specify that the shear modulus is only 1 percent of the nominal shear modulus, and Poisson's ratio is chosen so that the bulk modulus remains uniform. In addition, the transformation strain tapers to zero here. This procedure roughly simulates a freely slipping zone and has the effect of suppressing large local stresses that are poorly modeled without extensive mesh refinement and that have magnitudes which depend critically on the slip distribution near the edge of the rupture.

The characteristics of our coseismic rupture were chosen to correspond to estimates obtained by other workers. Specifically, we used scalar moment = 3×10^{19} Nm, dip=64°, and rake=145°. The rupture extends from 5 km to 17.5 km in depth (fig. 2*B*). The shape of the rupture perimeter was chosen to mimic the distribution of preseismic microseismicity (Olson, 1990) and initial aftershock distribution (Dietz and Ellsworth, 1990). The chosen moment and rake is that from Lisowski and others' (1990) preferred model, in which they specify uniform slip on a rectangular dislocation in a homogeneous elastic half space to model horizontal geodetic data. Seismic and other geodetic estimates of the moment generally range from 1 to 4×10^{19} Nm, dips range from 55° to 80°, and rakes range from 115° to 155° (see summary by Marshall and others, 1991, table 7).

MAGNITUDE OF COSEISMIC AND LONG-TIME POSTSEISMIC STRESS TRANSFER

ANALYTICAL MODELS

Before presenting results for the Loma Prieta earthquake, we review simple analytical models to obtain an understanding of how stress fields associated with generic models of stress transfer vary in space. Our analysis follows the work of Rice and Gu (1983).

We consider two limiting states: (1) immediate coseismic and (2) fully-relaxed downward continuation of the crustal fault zone and underlying horizontal substrate. The latter corresponds to Model 3 (fig. 2*E*) at times sufficiently large that relaxation has gone to completion. We compare the far-field solution for a finite, vertical, strike-slip dislocation in an elastic half-space to the corresponding solution in an elastic plate (fig. 3).

The static coseismic change in right-lateral shear stress on the still locked segment of the fault zone as a function of distance, r, from the center of the rupture is

$$\tau_{o+}(r) \approx (1/4)(D^2L/r^3)\Delta\tau,$$

and the long-time state when the deep aseismic portion of the fault zone and the horizontal detachment are fully-relaxed is

$$\tau_{\infty}(r) \approx (5/16)(HL/r^2)\Delta\tau,$$

where D is rupture depth, L is rupture length, H is the thickness of the elastic portion of the crust, and $\Delta\tau = 2\mu\Delta u/\pi D$ is the coseismic stress drop associated, via a

crack model, with a long surface-breaking strike-slip rupture over depth D, with average slip Δu, in a half-space with shear modulus μ. These solutions are valid at distances from the center of the rupture that are large compared to rupture half-length. The ratio of long-time to short-time stress is $\tau_\infty/\tau_{0+} \approx (5/4)(H/D)(r/D)$. At distances from the rupture $r >> D$ relaxation of the horizontal substrate yields postseismic stress changes that greatly exceed the coseismic change.

For example, given an earthquake with average stress drop Δt, rupture length equal to twice the elastic plate thickness, $L=2H$, and rupture depth $D=H/2$, then at a distance from the center of the rupture equal to $2H$ the static coseismic stress change is approximately $0.016\Delta\tau$ while the stress change after complete relaxation of basal shear stress is approximately $0.16\Delta\tau$. In this example, postseismic relaxation increases the far-field stress by an order of magnitude relative to the static coseismic stress

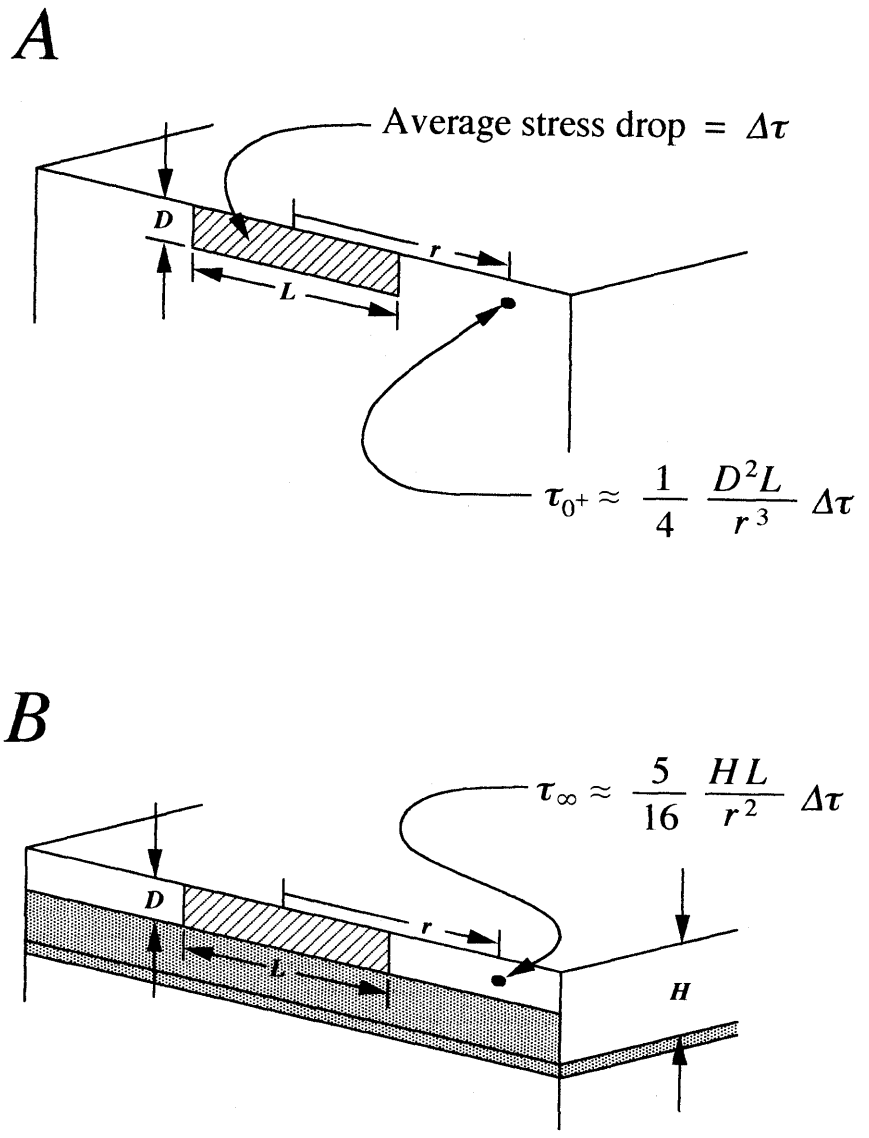

Figure 3.—Dislocation models comparing (*A*) short-time coseismic static shear stress change, τ_{0+}, to (*B*) long-time limit, τ_∞, of Model 3 (fig. 2*E*) in response to coseismic stress drop, $\Delta\tau$, on the main rupture surface of depth D and length L. In the first case stress is carried by the elastic half space, while in the latter case stress is carried by an elastic plate, with thickness H, floating on a traction-free substrate meant to represent a fully-relaxed horizontal shear zone in the lower crust. The solutions are valid at distances from the center of the rupture that are large compared to rupture half-length. The transition from short-time to long-time stress state corresponds to a change from $1/r^3$ to $1/r^2$ decay of stress with distance, r, from the center of the rupture.

change. Note, however, that the total magnitude of the stress change in the far-field is still only about 16 percent of the earthquake stress drop.

COSEISMIC AND LONG-TIME FULL-RELAXED POSTSEISMIC STRESS STATES

We estimate the coseismic and long-time fully-relaxed postseismic static stress changes associated with our three geometrical models of the Loma Prieta region (fig. 2). Note that in inhomogeneous viscoelastic systems, the fully-relaxed-limit solution does not necessarily provide an upper bound on changes of stress during the relaxation process.

The models are now purely elastic and postseismic relaxation is represented by introducing freely slipping regions that, in the earth, might deform in a time-dependent manner. This approach saves dramatically on computation time since only one "time-step" is need to achieve "relaxation." The states obtained with these elastic models should be interpreted as representing the long-time fully-relaxed limits of the corresponding viscoelastic models that are presented in later sections of this paper.

The calculations are done using the finite element method as discussed previously. The "free-slip" regions are incorporated by specifying that the shear modulus of the "relaxed" material is reduced relative to the surroundings. To simulate free-slip with this procedure, one needs μ_{fault}/h to be small compared to $\mu_{surroundings}/H$, where h is the thickness of the layer of fault elements and H is a scale-length for the surrounding region. We use a reduced shear modulus that is 1 percent of the nominal shear modulus, 30 GPa, and choose Poisson's ratio so that the bulk modulus is uniform. In the finite element mesh, the thickness of the fault zone and basal shear zone are 1 km and 5 km, respectively. Further reduction of the low shear modulus does not affect the stress distribution appreciably. The mantle is made stiffer than the crust by a factor of two.

Profiles of the changes in stress along profiles corresponding approximately with the San Francisco peninsula segment of the San Andreas fault and to the Hayward and Calaveras faults (fig. 4) are plotted in figure 5 as components of the traction vector resolved onto vertical planes. The values plotted in figure 5 are in general agreement with those obtained by Simpson and Reasenberg (this chapter), who used shear traction-free rectangular dislocations to represent relaxed, deep fault zones and horizontal detachment faults.

In the San Andreas profiles (figs. 5*A* and 5*B*), the values of stress represent averages over the bottom one-quarter of the locked seismogenic zone, which extends from 0 to 10 km in depth in our models (fig. 2). Very close to the end of the rupture, computed stress changes are sensitive to the assumed spatial distribution of slip. We have not attempted to incorporate detailed estimates of the coseismic slip distribution in our models and have only plotted those stress changes that we consider to be relatively reliable in this context.

Along the San Andreas profile, the coseismic change in static shear stress is largest close to the end of the rupture, as expected (fig. 5*A*). Here, relaxation can double or even quadruple the change in shear stress. Farther from the end of the rupture, at distances that are large compared to the 17.5 km rupture depth, the ratio of postseismic to coseismic shear stress reaches values exceeding 10:1, but the total change in shear stress is quite small. These three observations are qualitatively consistent with the results obtained above with simple analytical models. Both coseismic slip and subsequent postseismic relaxation result in fault-normal compression relative to the pre-seismic state (fig. 5*B*).

The enhancement of shear and normal stress on the San Andreas fault that results from postseismic relaxation can be rationalized if one considers the stress concentration in the vicinity of a shear crack in an elastic body. In our fully-relaxed models, the tip of this shear crack lies along the base of the seismogenic zone, adjacent to the points sampled in figures 5*A* and 5*B*. Here, the stress field will be dominated by near-field terms so that the state of stress along the up-dip projection of the aseismically slipped zone will be approximately pure shear. Recall that coseismic slip was oblique, reverse plus right-lateral, on a steeply SW-dipping fault segment so that postseismic slip on the aseismic portion of the fault zone will likewise be oblique, reverse plus right-lateral. By Mohr-circle analysis it is simple to demonstrate that the resolved shear and normal stress on a vertical plane extending upward from the tip of the aseismically slipped zone will therefore be right-lateral and compressive, in agreement with figures 5*A* and 5*B*, respectively.

Stress changes along the Hayward/Calaveras trend (fig. 4) are plotted in figures 5*C* and 5*D*. There we plot the change in traction that occurs on a vertical plane trending 21° clockwise from the strike of the modeled coseismic rupture plane versus position along strike measured from a point lying adjacent to the Loma Prieta epicenter and coinciding, approximately, with the southeast end of the M=6.2, 1984 Morgan Hill rupture (Bakun and others, 1984).

Coseismic slip and postseismic relaxation lead to decreases in both right-lateral shear stress and in compressive stress along the Hayward/Calaveras trend. At positions 0 to 7 km the coseismic decrease in right-lateral shear stress is exceeded by the decrease in compressive stress. The ratio of the two is about 0.10/0.23 = 0.4 (figs. 5*C* and 5*D*). Therefore, this portion of the fault would be moved toward failure if the effective coefficient of friction is

greater than about 0.4 (see extensive discussion by Reasenberg and Simpson (1992) and by Simpson and Reasenberg (this chapter)).

Postseismic relaxation appears to have only a moderate effect on the overall state of stress along the Hayward/Calaveras trend. In the far-field, postseismic relaxation of the lower crust can result in changes in shear stress that are large relative to the static coseismic change (fig. 5*C*, Model 3) but, as noted previously, the total magnitude of the stress change is rather small.

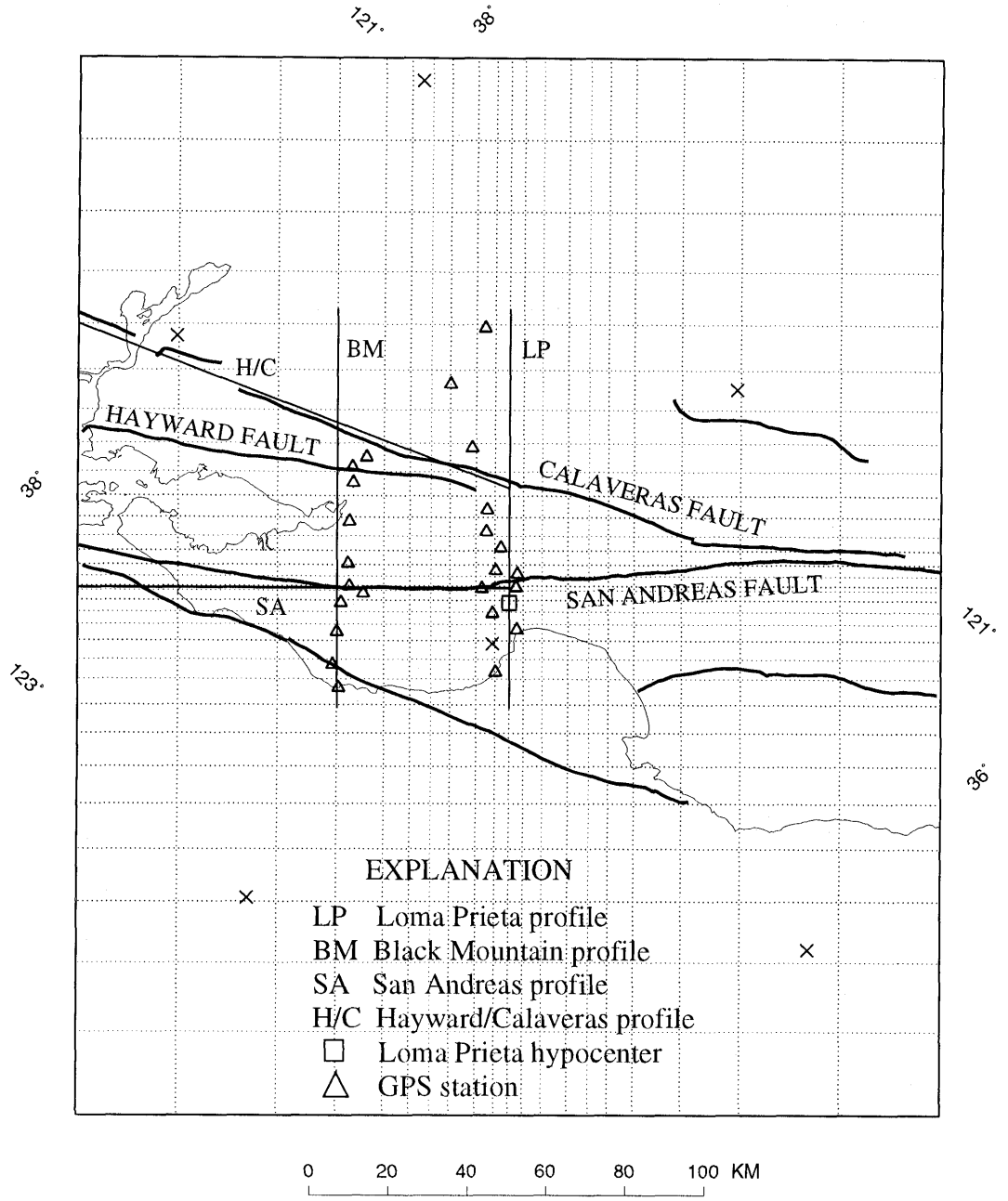

Figure 4.—Overlay of finite element mesh onto a map of the San Francisco Bay region. The shoreline and major faults are indicated by light and heavy sinuous lines, respectively. The Loma Prieta epicenter (U.S. Geological Survey Staff, 1990) is plotted as a square and geodetic stations occupied by the GPS are plotted as triangles. The perimeter of the finite element mesh is indicated by the dark bounding box and the profiles along which computed stresses and displacements are plotted in subsequent figures are indicated by solid lines. The relative position of the finite element mesh is chosen so that the strike of the model San Andreas fault is N44°W. The model center-line, normal to the fault trace, passes though the main shock epicenter and the model San Andreas fault overlies the mapped fault trace NW of Loma Prieta.

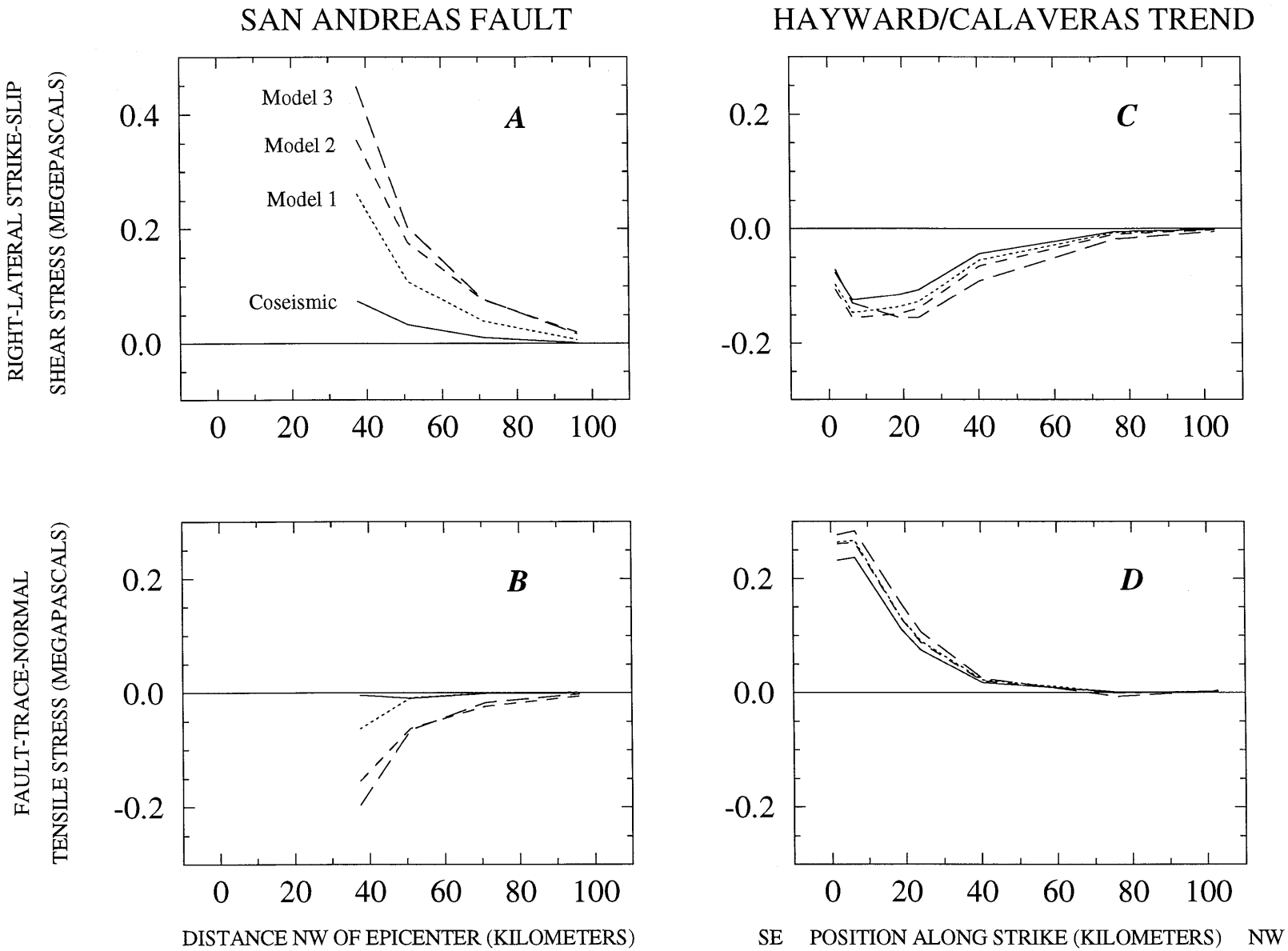

Figure 5.—Profiles of the changes in horizontal right-lateral shear traction and fault-trace-normal traction on vertical planes lying along trends indicated in figure 4, tension reckoned positive. Solid curves correspond to static coseismic state. Dotted, short-dashed, and long-dashed curves correspond, respectively, to long-time fully-relaxed versions of Models 1, 2, and 3 (fig. 2). *A*, Shear traction along the San Francisco Peninsula segment of the San Andreas fault in the bottom 1/4 of the locked seismogenic zone, 7.5 to 10 km depth. *B*, Tensile stress along same profile as in *A*. *C*, Shear traction along a trend corresponding approximately with the Hayward and Calaveras faults, averaged over the depth interval 5.0 to 7.5 km. Position along strike is measured from a point near the southeast end of the Hayward fault (see fig. 4). *D*, Tensile stress along same profile as in *C*.

A RELATIVE TIME-SCALE FOR POSTSEISMIC RELAXATION

In later sections of this paper we analyze time-dependent viscoelastic models to constrain the absolute time-scale for the relaxation process. Here, we construct a relative time-scale by estimating the amount of time that background tectonic loading requires to contribute a change in shear stress equal to that resulting from long-time postseismic relaxation. This relative time-scale can later be compared to estimates of the system relaxation time.

If, for example, the average tectonic contribution to the rate of shear-stress accumulation is the ratio of a typical earthquake stress drop to an earthquake cycle time, then this tectonic loading rate is likely to be about 5 MPa/200 yr = 0.025 MPa/yr. Along the Peninsula segment of the San Andreas fault, 80 km from the epicenter, the increase in shear stress resulting from complete relaxation of the lower crust is about 0.05 MPa (fig. 5*A*, Model 3). This increase is then equivalent to about 2 years of tectonic loading. Postseismic relaxation is, therefore, unlikely to contribute significantly to the stress rate at distances beyond 80 km, unless the time-scale for relaxation of the lower crust is less than a few years. In contrast, 40 km from the epicenter the corresponding increase in shear stress is about 0.4 MPa (fig. 5*A*, Model 3) and consequently represents about 16 years at the tectonic loading rate. Therefore, relaxation of the lower crust will contribute significantly to the stress rate in the region near the end of the Loma Prieta rupture, provided that the time-scale for relaxation is on the order of 16 years or less.

TIME-DEPENDENT MODELS

We analyze our three geometrical models of postseismic relaxation (fig. 2) while employing two different Maxwell viscoelastic rheologies. First, we use linear viscoelasticity to model the presumably nonlinear behavior of materials in the inelastically shearing portions of the fault zone and lower crust. With this approach, any estimate of relaxation time, obtained by fitting our models to data, must be interpreted as an effective relaxation time that physically reflects the response of a nonlinear creep process to stress changes resulting from the earthquake. Our second set of time-dependent models employ a nonlinear rheology that represents a steady-state creep version of the laboratory-derived rate- and state-dependent friction law (Stesky, 1975, 1978; Dieterich 1981; Ruina, 1983; Blanpied and others, 1991). With this law the aseismic slip rate depends exponentially on the ratio of shear stress to effective normal stress.

Using either viscoelastic rheology, we treat the static coseismic stress change and resulting deformation as changes to the state that would have existed in absence of the earthquake. It can be shown that the postseismic problem can be treated exactly in this manner if one assumes that a preexisting steady-state of inelastic shearing existed in all aseismic regions of the model prior to the earthquake.

The more traditional approach to this problem is to precondition the model by imposing a cycle of repeated characteristic earthquakes until the system responds in a periodic manner (Savage, 1983; Thatcher and Rundle, 1984; Li and Rice, 1987; Dmowska and others, 1988; Fares and Rice, 1988; Lyzenga and others, 1991; Ben-Zion and others, 1993; Reches and others, 1994). In our situation, this strategy may be difficult to apply with any confidence since there is some question as to how the Loma Prieta earthquake relates to characteristic events for the region (Anderson, 1990; Segall and Lisowski, 1990).

We represent the aseismically shearing regions (fig. 2) with Maxwellian viscoelasticity as

$$\varepsilon_{ij} = \varepsilon_{ij}^{el} + \varepsilon_{ij}^{cr},$$

where ε_{ij}^{el} is the elastic strain, ε_{ij}^{cr} is the inelastic creep strain, and ε_{ij} is the total strain. We adopt the standard assumptions of elementary plasticity theory—that the inelastic creep strain is not affected by hydrostatic pressure and that the volumetric creep strain is zero (see, for example, Malvern, 1969). The creep law can then be written in terms of deviatoric stress, $S_{ij} \equiv \sigma_{ij} - (1/3)\sigma_{kk}\delta_{ij}$, where σ_{ij} is the stress tensor and we sum on repeated indices. In the creeping portion of the model

$$\sigma_{ij} = \left(K - \frac{2}{3}\mu\right)\varepsilon_{kk}\delta_{ij} + 2\mu\left(\varepsilon_{ij} - \varepsilon_{ij}^{cr}\right),$$

where K and μ are the elastic bulk and shear moduli, respectively. We adopt the von Mises formulation and write the flow law in terms of the second invariant of the deviatoric stress, $J_2 = S_{ij}S_{ij}/2$. The Mises equivalent tensile stress, q, is defined so that, in a state of uniaxial tension, q is equal to the tensile stress:

$$q \equiv \sqrt{\tfrac{3}{2} S_{ij}S_{ij}}$$

The creep law is then written as

$$\dot{\varepsilon}_{ij}^{cr} = \frac{3}{2}\frac{S_{ij}}{q}\dot{\varepsilon}_{cr}(q),$$

where $\dot{\varepsilon}_{cr}(q)$ is the scalar Mises equivalent tensile creep rate, defined so that $\dot{\varepsilon}_{cr}(q) = \dot{\varepsilon}_{11}^{cr}$ in response to a uniaxial load $\sigma_{11} = q$.

LINEAR VISCOELASTIC MODELS

In the case of linear viscoelasticity $\dot{\varepsilon}^{cr}(q) = q/A$, where A is a constant. In fluid mechanics, it is conventional to define a shear viscosity, η, such that in a state of pure shear $\tau = \eta\dot{\gamma}$, where τ is the shear stress and $\dot{\gamma}$ is the engineering-shear-strain rate. We adopt this convention so that $A=3\eta$ and

$$\dot{\varepsilon}_{cr}(q) = \frac{q}{3\eta}.$$

The linear creep law as employed in our finite element calculations is, therefore,

$$\dot{\varepsilon}_{ij}^{cr} = \frac{S_{ij}}{2\eta}.$$

The viscous resistance to shear across a thin layer depends on the ratio of viscosity to layer thickness, η/h. Dimensional analysis, therefore, tells us that the time-scale for relaxation of the system will be proportional to

$$\frac{H}{h}\frac{\eta}{\mu} = \frac{H}{h}t_r,$$

where H is the effective length-scale of the elastic surroundings and t_r is the relaxation time of the viscoelastic material. In Models 1 and 2, H corresponds to the down-dip dimension of the coseismic rupture while in Model 3, H corresponds to the thickness of the elastic portion of the crust. In our finite element calculations we treat H as a known quantity. By comparing model predictions to data we can, therefore, hope to constrain the ratio t_r/h but neither t_r or h independently. We include a 1-km-thick fault zone in our finite element models, and in Model 3 additionally include a 5-km-thick basal shear zone. We then make t_r/h uniform throughout the model by specifying that the viscosity of the material in the basal shear zone is five times that of the material in the aseismic portion of the fault zone. By this procedure, time is measured in units of t_r km/h and t_r and h are the unknown material relaxation time and shear-zone thickness in the earth.

By comparing computed displacements to those observed geodetically we can hope to equate model-time αt_r km/h with time t and by doing so constrain t_r/h. Rewriting this expression, we obtain

$$\eta = \mu\frac{t}{\alpha}\frac{h}{km},$$

which demonstrates how the parameters used to constrain viscosity will trade off. Note that if $(t/\alpha)(h/\text{km})$ is of order one year and $\mu=30$ GPa, then $\eta \approx 10^{18}$ Pa-s. In what follows we examine solutions at $\alpha=5$ and $\alpha=20$ and geodetic observations at $t=1.3$ years.

In figure 6 we plot calculated and observed postseismic displacements measured relative to extrapolation of the pre-earthquake velocity field. The displacements are plotted along two profiles that lie perpendicular to the strike of the model fault zone (fig. 4). The first profile crosses through the center of the rupture and is referred to as the Loma Prieta profile. The second lies 44 km to the northwest and is referred to as the Black Mountain profile. These two profiles correspond approximately with two profiles of GPS stations measured frequently since the earthquake (Bürgmann and others, 1991, and this chapter; Lisowski and others, 1991a; Bürgmann and others, 1992; Savage and others, 1994). We plot three components of displacement from Models 1, 2, and 3 (fig. 2) at two model times, $t=5t_r$ km/h in figure 6*A* and $t=20t_r$ km/h in figure 6*B*.

At $t=5t_r$ km/h the computed displacements are nearly equal for the three models (fig. 6*A*). This indicates that at short-time all three models are dominated by aseismic fault slip in the down-dip portion of the fault zone confined above the Moho. At $t=20t_r$ km/h the computed displacements for the three models differ to a larger degree (fig. 6*B*). Therefore, if one of these models is correct for Loma Prieta at long-time, there is some hope of resolving which one it is.

Also plotted in figure 6 are measures of the observed postseismic displacement field 1.3 years after the earthquake, made relative to extrapolation of the pre-earthquake velocity field. The bulk of the pre-earthquake geodetic data are from ground-based laser ranging measurements (EDM) and so do not constrain the rigid body component of the pre-earthquake velocity field. In contrast, all of the post-earthquake data are from GPS measurements in which the rigid body motion is constrained by making simultaneous observations to remote stations. As of this writing, though there are some pre-earthquake GPS observations, there is no self-consistent estimate of the change in the velocity field—post-earthquake minus pre-earthquake—based on all of the geodetic data, and so we have plotted the data as we describe in the following paragraphs.

The data plotted along the Loma Prieta profile represent the difference between estimates of post- and pre-earthquake velocity obtained by assuming that the velocity field far to the northeast of the San Andreas fault did not change (Lisowski and others, 1991a, 1991b). This measure of the change in velocity is then multiplied by 1.3 years to obtain an estimate of the postseismic displacement measured relative to extrapolation of the pre-earthquake velocity. The error bars assume no error in the estimate of the pre-earthquake velocity field and thus underestimate the actual uncertainty.

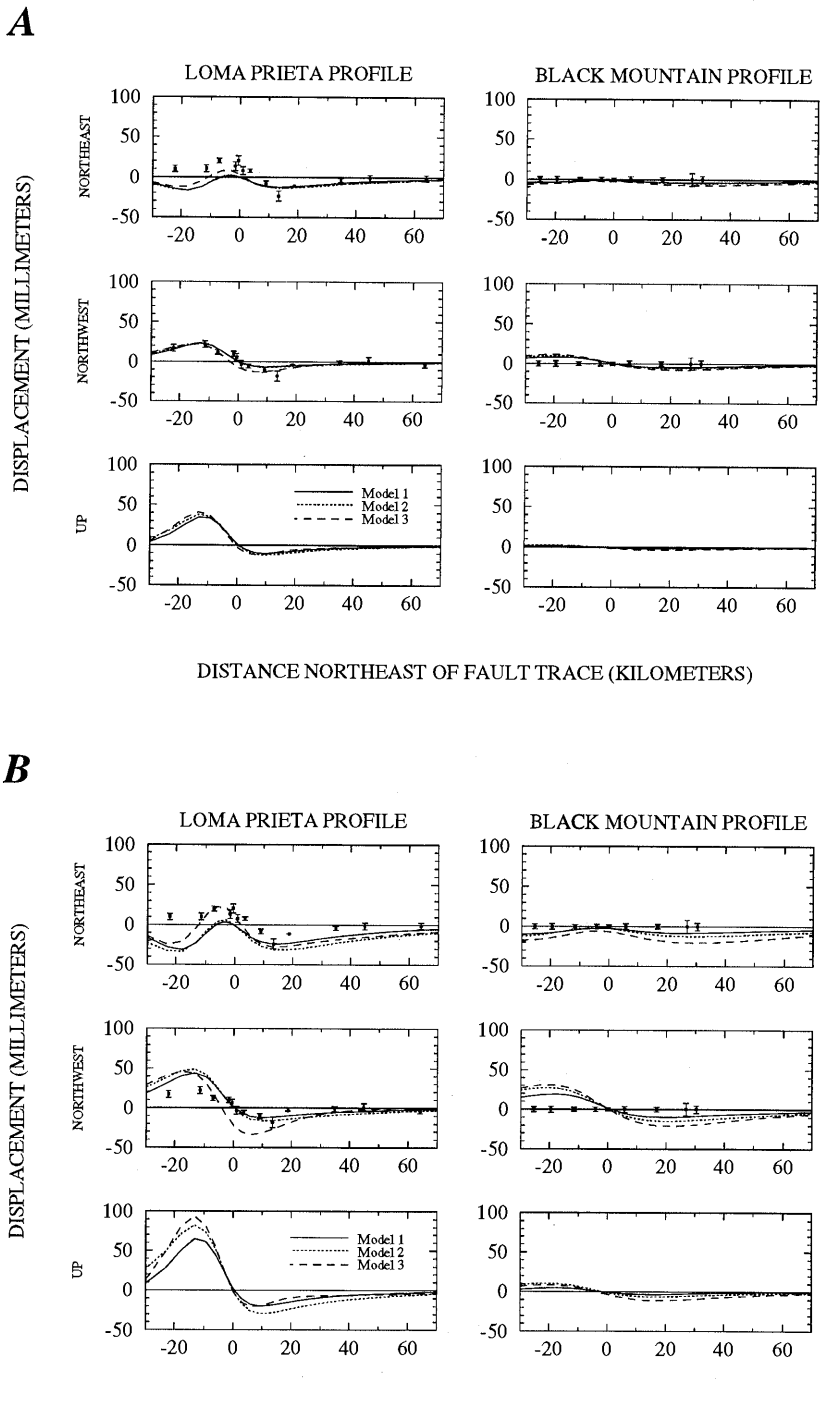

Figure 6.—Profiles of observed and calculated postseismic displacements measured relative to extrapolation of the pre-earthquake velocity field. The Loma Prieta and Black Mountain profiles lie perpendicular to the strike of the San Andreas fault. The former passes through the center of the model rupture and also through the Loma Prieta epicenter, while the latter lies 44 km to the northwest along strike (see fig. 4). Observed displacements are based on geodetic measurements and correspond to 1.3 years after the earthquake (Lisowski and others, 1991a, 1991b; Bürgmann and others, 1992). Calculated displacements represent versions of Models 1, 2, and 3 (solid, dotted, and dashed curves, respectively) in which the relaxing portions of the models are made linear Maxwell viscoelastic (see fig. 2). Figures *A* and *B* correspond to model times of $5t_r$ km/*h* and $20t_r$ km/*h* respectively, where t_r is the Maxwell relaxation time of the viscoelastic material, and *h* is the thickness of the viscously deforming region.

Analysis of the Black Mountain data indicates that the change in velocity there—post- minus pre-earthquake—may not be measurably different from zero (Bürgmann and others, 1992). Lacking a better estimate of the relative postseismic deformation, we plot zero displacement along the Black Mountain profile to indicate that the relative postseismic displacement is likely to be small. Along with the null data, we also plot an estimate of the uncertainty in the displacement accumulated during the first 1.3 years after the earthquake. We estimate this uncertainty by taking the uncertainty in the velocity measured during the post-earthquake interval January 1990 to May 1992 (Bürgmann and Segall, written commun., 1993) and multiplying by 1.3 years. The resulting error bars place a lower bound on the detection threshold of postseismic deformation relative to the pre-earthquake rate. Relative postseismic deformation smaller than these error bars would go unnoticed in 1.3 years.

At $t=5t_r$ km/h the predicted fault-trace-normal components of displacement are inconsistent with the data along the Loma Prieta profile, but along the Black Mountain profile they may be small enough to satisfy the data. If we were to add about 0.3 ppm or 0.2 ppm/yr of regional fault-normal compression to our model, then we could probably match the data along the Loma Prieta profile but then probably violate the Black Mountain data. The predicted strike-slip components of displacement appear to be remarkably consistent with the data along the Loma Prieta profile but may not be consistent with the observations along the Black Mountain profile, where the computed displacements appear to exceed the observations. The predicted vertical displacements along the Loma Prieta profile may be sufficiently large to be detected by GPS measurements, whose precision in the vertical is about 20 to 30 mm (Davis and others, 1989; Bürgmann and others, this chapter). The predicted vertical displacements along the Black Mountain profile are extremely small. The predicted tilts along the Loma Prieta profile exceed 1 μradian and so could potentially be detected by leveling measurements.

At $t=20t_r$ km/h, the predicted displacements far exceed all of the observations, and so we can say with confidence that $20t_r$ km/h > 1.3 yr or t_r/h > 0.07 yr/km.

If we accept the agreement at $t=5t_r$ km/h between predicted and observed strike-slip displacements along the Loma Prieta profile while overlooking the disagreement with fault-trace-normal motion there as well as possible disagreement with strike-slip motion along the Black Mountain profile, then we can conclude that $5t_r$ km/$h \approx$ 1.3 yr or $t_r/h \approx$ 0.3 yr/km.

If we assume that postseismic slip is occurring within a fault zone with $h \leq 1$ km and take μ=30 GPa, we then obtain an estimate of the effective viscosity of the deep aseismic portion of the fault zone; $\eta_{eff} \leq 3\times10^{17}$ Pa-s. This value is lower than any obvious interpretation of laboratory measurements (Carter and Tsenn, 1987; Kirby and Kronenberg, 1987a, 1987b) of solid-state creep of crustal rocks at mid-crustal conditions (Lachenbruch and Sass, 1973).

Li and Rice (1987) and Fares and Rice (1988) studied two-dimensional earthquake cycle models by comparing model calculations to the observed decay in strain rate that followed the 1906 San Francisco earthquake (fig. 1). Their physical model is equivalent to our Model 3 except that they assumed that the aseismic down-dip portion of the fault zone is freely slipping. As discussed previously, this assumption is equivalent to assuming that t_r/h in the aseismic portion of the fault zone is much much less than in the lower crust, that is $(t_r/h)_{fz} << (t_r/h)_{lc}$. It is likely that this assumption only affects their solutions at short-time following the earthquake and does not strongly affect their estimate of $(t_r/h)_{lc}$. They obtained values in the range 0.2 yr/km $\leq (t_r/h)_{lc} \leq$ 1.7 yr/km. The contemporary velocity field in the northern San Francisco Bay region (Prescott and Yu, 1986) requires values at the low end of this range (Fares and Rice, 1988).

We, therefore, conclude that t_r/h may be approximately uniform in the deep aseismic portion of the fault zone and in the lower crust and appears to take on a value of about 0.3 yr/km thickness. The apparent spatial uniformity of t_r/h indicates that the proposed deep postseismic slip that occurred in the 1.3 yr following the Loma Prieta earthquake and the basal shear that followed the 1906 earthquake might be controlled by the same physical process.

We interpret the apparently consistent values of $(t_r/h)_{fz}$ and $(t_r/h)_{lc}$ and the corresponding low value of the effective viscosity of the material in the deep aseismic portion of the fault zone as indications that postseismic relaxation may result from frictional sliding assisted by elevated pore pressure. This process may be taking place both in the deep portion of the fault zone and in horizontal shear zones in the lower crust. In the next section of this paper we evaluate this proposition by examining models of postseismic deformation that incorporate a constitutive law for frictional sliding.

NON-LINEAR VISCOELASTIC MODELS: HOT-FRICTION

We now represent the aseismically shearing regions with a nonlinear creep law derived from a steady-state version of the laboratory-derived rate- and state-dependent friction law (Stesky, 1975, 1978; Dieterich, 1981; Ruina, 1983; Blanpied and others, 1991). At steady-state the resistance to sliding is described approximately by

$$\tau = \tau_o + c\sigma \ln V/V_o ,$$

where V is the slip rate, c is a constant, σ is the effective normal stress, and τ_o is the shear stress when $V=V_o$. We

interpret τ_o as the pre-earthquake shear stress across the aseismic portion of the fault and, in the case of Model 3, across the basal shear zone in the lower crust, σ as the effective normal stress equal to total normal stress minus pore pressure, V as the slip rate across the shear zone, and V_o as the pre-earthquake slip rate. In using a steady-state form of the friction law, we implicitly assume that postseismic slip greatly exceeds the slip weakening distance and so the state variable remains always at its steady-state value, appropriate to the current slip rate. The factor c is more commonly denoted as $a - b$ (see, for example Blanpied and others (1991)). While we use the friction law to describe hot frictional slip occurring deep within the crust, the same law has been used in studies of shallow aseismic creep on near-surface portions of a fault zone (Wesson, 1988; Marone and others, 1991).

We make our calculations relative to the pre-earthquake state and define new parameters in that context. The friction law becomes

$$\hat{\tau} = c\sigma \ln \frac{V_o + \hat{V}}{V_o},$$

where $\hat{\tau}$ and $\hat{V}$ are the shear stress and slip speed measured relative to the pre-earthquake state, $\hat{\tau} = \tau - \tau_o$, and $\hat{V} = V - V_o$. In a narrow shear zone, a state of pure shear will dominate the deviatoric stress tensor (Rice, 1992). Therefore, from the previous section, $q = \sqrt{3}\hat{\tau}$ and $\dot{\varepsilon}_{cr} = \dot{\gamma}/\sqrt{3} = \hat{V}/\sqrt{3}h$, where q and $\dot{\varepsilon}_{cr}$ are now the Mises equivalent tensile stress and strain rate measured relative to the pre-earthquake state, and h is, as before, the thickness of the shear zone. Inverting the friction law we thus obtain

$$\dot{\varepsilon}_{cr}(q) = \frac{V_o}{\sqrt{3}h}\left(e^{q/\sqrt{3}c\sigma} - 1\right),$$

so that the nonlinear creep law employed in our finite element calculations is

$$\dot{\varepsilon}_{ij}^{cr} = \frac{\sqrt{3}}{2}\frac{V_o}{h}\frac{S_{ij}}{q}\left(e^{q/\sqrt{3}c\sigma} - 1\right).$$

We refer to the above formulation as our "hot-friction" model.

Dimensional analysis tells us that the general form of the post-seismic slip rate across the aseismically slipping regions, measured relative to the pre-earthquake rate, will have the form

$$\hat{V} = V_o f\left(\frac{\mu V_o t}{c\sigma H}, \frac{\Delta\tau}{c\sigma}, \frac{x}{H}\right),$$

where t is the time since the earthquake, $\Delta\tau$ is a representative coseismic static-stress change in the creep zone, V_o is a representative pre-earthquake slip rate, and x is position. The time-scale for postseismic relaxation is now governed by the quantities $c\sigma H/\mu V_o$, $\Delta\tau/c\sigma$, and x/H.

In our finite element calculations we assume values of H, such as rupture depth in the case of Models 1 and 2, and thickness of the elastic portion of the crust in the case of Model 3, just as with the previous linear models. We additionally assume that $\mu = 30$ GPa, as in all previous analyses. To constrain V_o we have studied two-dimensional earthquake cycle models in the manner of Li and Rice (1987) and Fares and Rice (1988) but using the steady-state friction law. Preliminary analyses in which we compare the decay in strain rate to that observed after the 1906 earthquake (fig. 1) indicate that $0.1 \le V_o/V_{plate} \le 1.0$ in the deep aseismic portion of the fault zone within the crust, where V_{plate} is the average plate velocity. This range is consistent with values obtained by Tse and Rice (1986) and by Rice (1993), in which they incorporate the full rate- and state-dependent constitutive law throughout the crustal fault zone and thereby model both stable and unstable fault slip throughout the earthquake cycle. We use $V_o = V_{plate} = 20$ mm/yr, which is representative of estimates of the average slip rate along this segment of the San Andreas fault (Working Group, 1990). In our calculations, smaller values of V_o would yield smaller values of postseismic slip rate since there is a direct trade-off between V_o and our measure of time. Finally, laboratory measurements indicate that at mid-crustal conditions of elevated temperature with pore fluids present, $0.010 \le c \le 0.020$ (Blanpied and others, 1991). These constraints on H, μ, V_o, and c, together with comparisons of model predictions and geodetic data, provide us a means of constraining the effective normal stress, σ.

We analyze Models 1, 2, and 3 (fig. 2) while incorporating the hot-friction constitutive law in the deep aseismic portion of the fault zone and lower crust. In figure 7 we plot profiles of postseismic displacement analogous to those in figure 6. The solution plotted is for Model 1 with $c\sigma = 0.5$ MPa. Larger values of $c\sigma$ yield greatly reduced postseismic slip rate and so also reduced displacement at the free surface. This observation is consistent with inspection of the creep law and with our dimensional analysis. The former indicates that the initial postseismic slip rate will scale exponentially with the ratio $\Delta\tau/c\sigma$. Models 2 and 3 yield displacement profiles nearly identical to those in figure 7 at times less than or equal to 2 years. Only at greater times do the surface displacements from the three models differ substantially.

Perhaps the greatest difference between the response of the nonlinear hot-friction model and the linear viscoelastic model is their time dependence. In figure 8 we plot the strike-slip components of displacement, from nonlinear

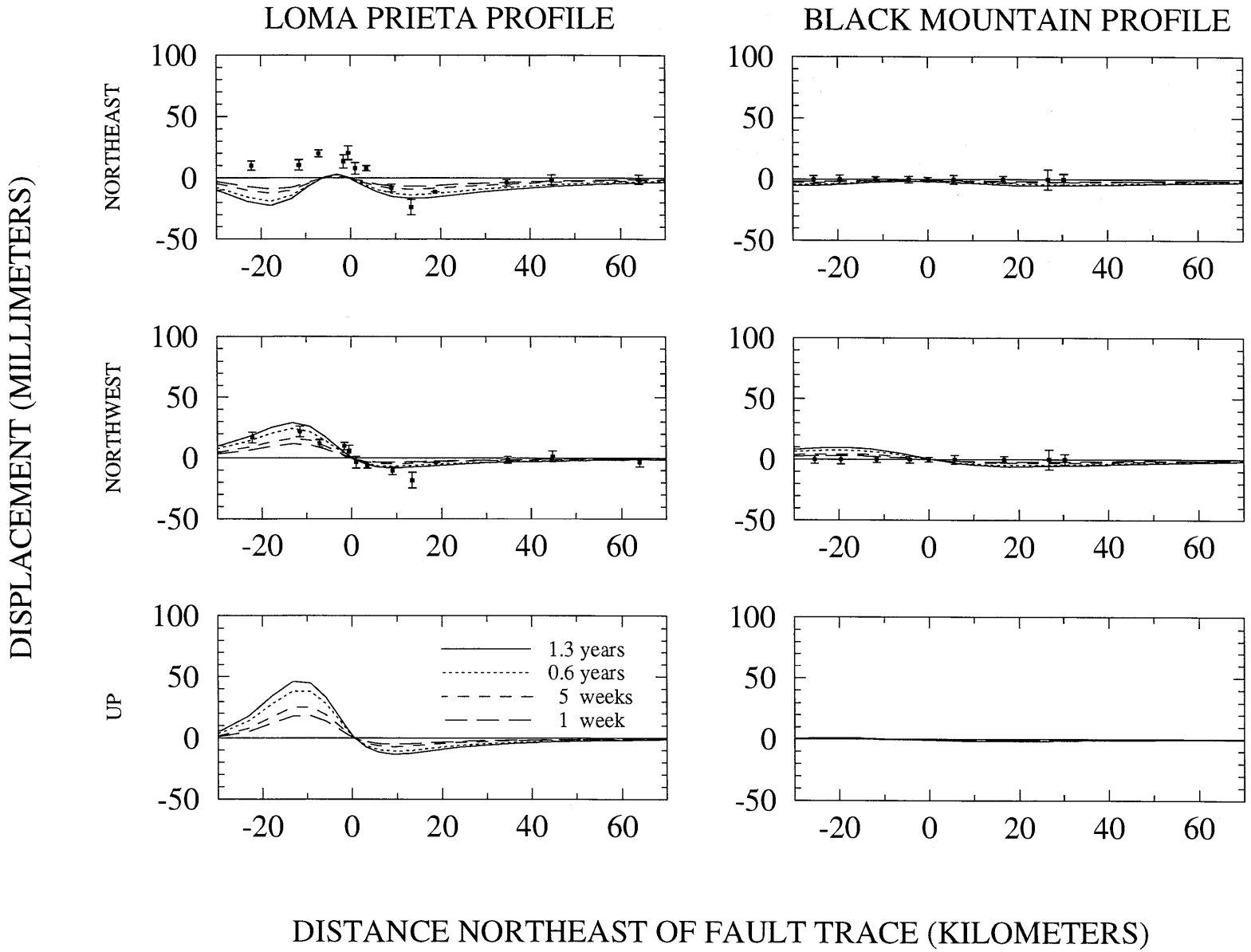

Figure 7.—Profiles of postseismic displacement analogous to those in figure 6, but for a version of Model 1 (fig. 2*C*) in which the viscoelastic material in the deep aseismic region of the fault zone obeys the nonlinear hot-friction law. The solution plotted is for $c\sigma$=0.5 MPa, where σ is the effective normal stress, equal to the total normal stress minus the pore pressure. In laboratory measurements made at mid-crustal conditions, c is in the range 0.010 to 0.020 (Blanpied and others, 1991). As in figure 6, the observed displacements correspond to 1.3 years after the earthquake. The relative agreement between the model predictions and the data indicates that the effective normal stress in the deep aseismic portion of the fault zone is on the order of 0.5 MPa/0.015 ≈ 30 MPa.

and linear versions of Model 1, of a point lying on the Loma Prieta profile 13 km southwest of the model fault trace (see figs. 2*C*, 4, 6, and 7). We again use $c\sigma$=0.5 MPa in the nonlinear model, as in figure 7, and then choose the time-scale for the linear model so that the displacement at 2 years equals that of the nonlinear model. The nonlinear hot-friction model yields very rapid postseismic motion immediately after the earthquake in comparison to the linear model. This very rapid short-term motion results principally from rapid postseismic slip that occurs near the edge of the coseismic rupture, where $\Delta\tau$ is large compared to $c\sigma$. Given time, this highly stressed region of the model relaxes to the degree that $\hat{\tau} < c\sigma$. After that point, the nonlinear creep law behaves more or less linearly, since the exponential dependence on shear stress becomes approximately linear when $\hat{\tau} \ll c\sigma$.

The measured postseismic velocity field appears to be time independent during the initial two post-earthquake years (Bürgmann and Segall, 1991; Lisowski and others, 1991a; Bürgmann and others, 1992), but the uncertainty in the data is sufficiently large that rejection of the nonlinear model on the basis of its strong time-dependence may not be possible. Future examination of the data is required to establish the degree to which time-dependence is allowed. Note that in figure 8, the initial 9 mm of predicted postseismic displacement occurs within 2 days of the earthquake.

In figure 9 we plot contours of Mises stress in the deep aseismic portion of the fault zone. Again, we examine Model 1 with $c\sigma$=0.5 MPa as in figures 7 and 8. Figure 9*A* shows the static coseismic state, and figure 9*B* shows the state after 2 years of relaxation. The static coseismic Mises stress is less than 1 MPa beyond a distance of about 7 km from the edge of the rupture. Therefore, it is only within a narrow region close to the edge of the rupture that the creep law behaves strongly nonlinearly, since it is only here that $\hat{\tau}$ is ever greater than $c\sigma$=0.5 MPa. Note the tendency for development of a relaxation front that propagates from the edge of the rupture into the creep zone as relaxation proceeds.

If the friction law that we have examined applies to the earth, then immediately following an earthquake very rapid postseismic slip at depth occurs wherever $\Delta\tau > c\sigma$. As a result, estimates of coseismic deformation based on geodetic data may be contaminated by postseismic deformation whenever the first post-earthquake survey lags too far behind the time of the earthquake. In figures 7 and 8, for example, over half of the displacement that accumulates in 1.3 years occurs during the first month following the earthquake. Note, however, that the displacements at issue here are small compared to the coseismic displacement.

Returning again to figure 7, we compare the model predictions to the geodetic data. Along the Loma Prieta

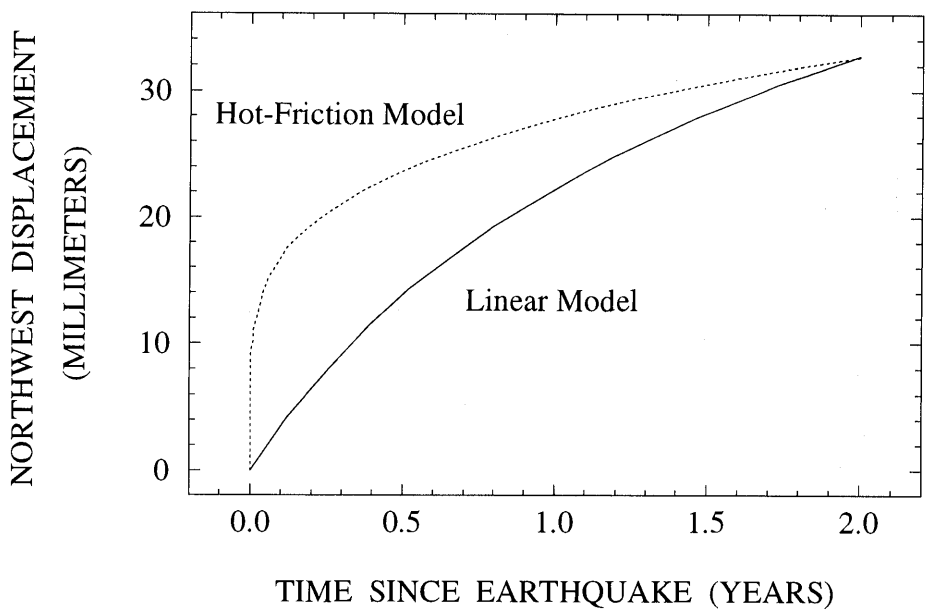

Figure 8.—Time histories of displacement of the free surface for nonlinear versus linear versions of Model 1 (fig. 2*C*). The nonlinear hot-friction model used $c\sigma$=0.5 MPa, as in figure 7. The time-scale for the linear model was chosen so that the displacement at two years equals that of the nonlinear model. The point for which displacement is plotted lies along the Loma Prieta profile 13 km to the southwest of the fault trace. Note that with the nonlinear hot-friction model, the displacement at 1 month after the earthquake is nearly one-half of the total that accumulates by the end of 2 years.

profile, the hot-friction model does reasonably well in comparison to the observed strike-slip component of displacement but does not generate displacements compatible with the observed fault-trace-normal displacements. The addition of a uniform fault-trace-normal component of compression would bring the predictions toward agreement with the data along the Loma Prieta profile. Along the Black Mountain profile, the computed strike-slip displacements appear to exceed the observed values, but, as discussed previously, the error bars do not include the uncertainty in the pre-earthquake velocity field, nor do they address the unconstrained rigid body motion associated with the pre-earthquake EDM data. All of these comparisons are much like those made with the linear models (fig. 6*A*).

We can conclude that the effective normal stress in the deep aseismic portion of the fault zone is extremely low, provided that we accept the agreement between the predicted and observed strike-slip displacements along the Loma Prieta profile while overlooking the disagreements both with fault-trace-normal motion there as well as with strike-slip motion along the Black Mountain profile. If we accept that $c\sigma$=0.5 MPa and take c=0.015 from the laboratory measurements (Blanpied and others, 1991), we then obtain an estimate of the effective normal stress in the deep aseismic portion of the fault zone; σ=33 MPa. This

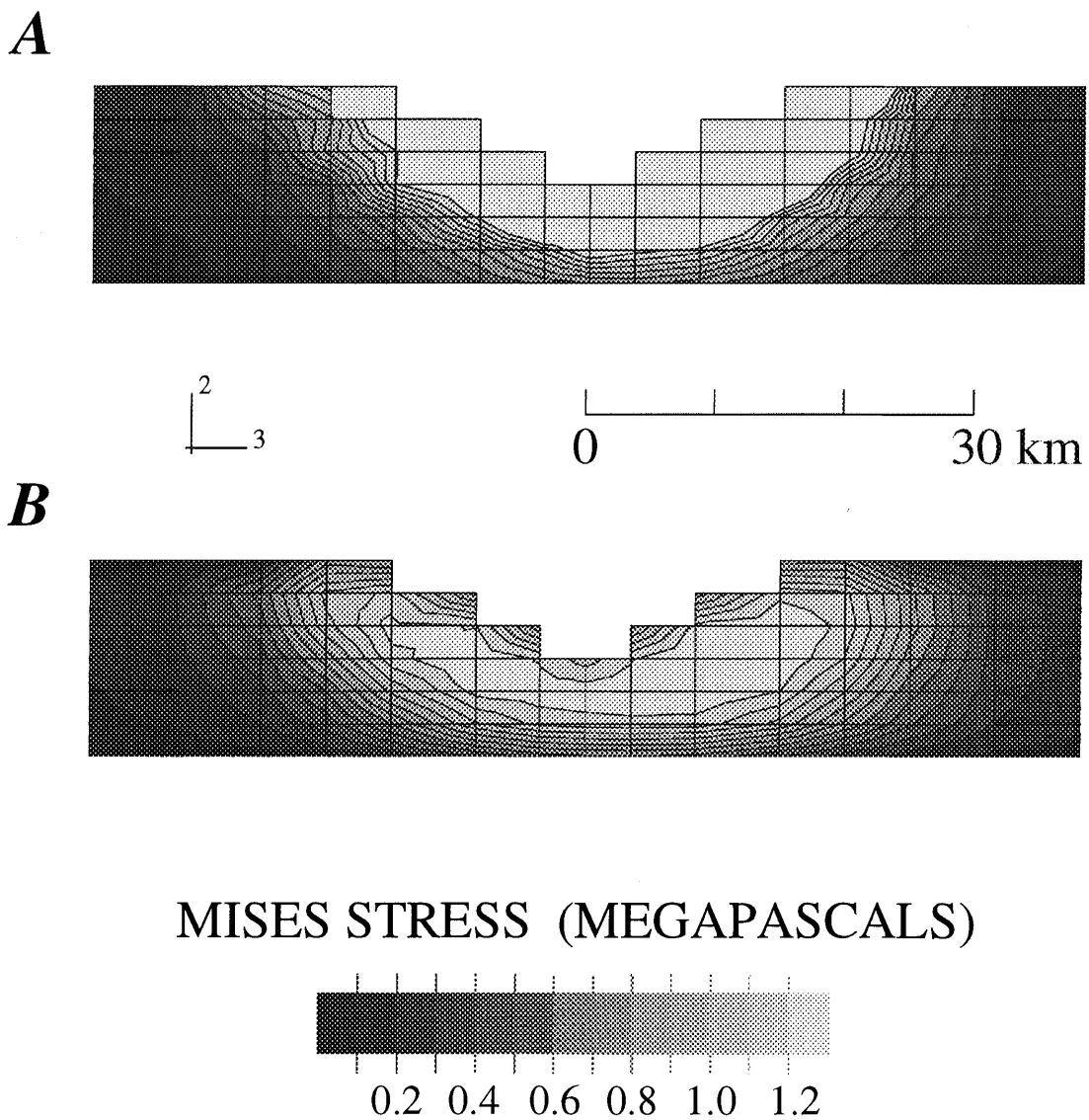

Figure 9.—Contours of Mises stress in the deep aseismic portion of the fault zone for the nonlinear hot-friction version of Model 1 (fig. 2*C*) using $c\sigma$=0.5 MPa. The contour interval is 0.1 MPa and the maximum contour level is 1.2 MPa. *A*, Static coseismic stress state. *B*, Stress state after 2 years of relaxation. Note the development of a relaxation front that propagates from the edge of the rupture into the creep zone as relaxation proceeds.

value is a factor of 10 smaller than the effective overburden stress that would exist at 18 km depth if pore-pressure was hydrostatic. Therefore, if deep aseismic slip is the cause of the observed postseismic strike-slip deformation near Loma Prieta and if hot-frictional shearing is the mechanism by which this process takes place, then pore pressure in the deep aseismic portion of the fault zone must be substantially elevated above the hydrostatic level.

DISCUSSION AND CONCLUSIONS

ALTERNATIVE GEOMETRIC MODELS

We have demonstrated that models of postseismic deformation that include deep sources of viscous relaxation can generate displacement fields that agree with some, but not all, of the geodetic data.

Our models appear to be capable of producing strike-slip displacements that are compatible with the observations along the Loma Prieta profile but may exceed those made along the Black Mountain profile. We have examined one model of postseismic deformation in which coseismic slip is non-uniform. The goal was to establish the degree to which postseismic strike-slip displacement along the Black Mountain profile could be suppressed by moving the centroid of coseismic strike slip away from Black Mountain. The non-uniform slip model is motivated by analysis of leveling data (Marshall and others, 1991) and by seismological estimates of the distribution of coseismic slip (Beroza, 1991; Hartzell and others, 1991; Steidl and others, 1991; Wald and others, 1991). We have examined an extreme model in which all of the strike slip is in the southeast half of the rupture and all of the reverse slip is in the northwest half of the rupture. The moment and average rake are as in the uniform slip models. The non-uniform slip model employs the linear viscoelastic rheology in the deep aseismic portion of the fault zone and so falls into the category of Model 1 (fig. 2*C*).

As expected, the non-uniform model does suppress postseismic strike-slip displacement along the Black Mountain profile in comparison to the corresponding uniform-slip model. At $t=5t_r$ km/*h* the strike-slip displacement along the Black Mountain profile is about 70 percent of that obtained with the uniform slip model and plotted in figure 6*A*. However, this reduction is more than compensated for by an accompanying reduction in strike-slip displacement along the Loma Prieta profile. To match the data there we must now choose 1.3 yr = $t \approx 20t_r$ km/*h*, which corresponds to larger strike-slip displacements along the Black Mountain profile than those obtained with the uniform slip model at $t=5t_r$ km/*h*. Thus, the non-uniform coseismic slip model does not help to suppress postseismic strike-slip displacements along the Black Mountain profile relative to along the Loma Prieta profile.

Our models also appear to be incompatible with the fault-trace-normal contraction observed along the Loma Prieta profile. This discrepancy could be suppressed by adding a uniform fault-trace-normal compressive strain to our models of magnitude about 0.3 ppm, or 0.2 ppm/yr. This strain would be interpreted as a regional postseismic change in fault-trace-normal strain rate, though we are not aware of any independent data that reveals such a feature. The addition of this regional fault-trace-normal compression would, furthermore, make our models less consistent with the data from the Black Mountain profile, if the change in velocity along the Black Mountain profile is indeed not measurably different from zero (Bürgmann and others, 1992).

We conclude that alternative models of postseismic deformation should be examined in future work. Two overlapping viewpoints should be considered. First, our deep-slip models do a remarkably good job of matching the strike-slip component of postseismic displacement along the Loma Prieta profile, but they do not appear to be capable of generating the observed fault-trace-normal contraction there. Therefore, future models should include similar deep-slip sources, while additionally incorporating sources that contribute a greater degree of fault-trace-normal contraction. Second, our deep-slip models may generate strike-slip displacements along the Black Mountain profile that exceed the observed displacements. Therefore, future work should also examine models that incorporate sources of deformation that are shallower than our deep-slip sources. By moving the deformation sources toward the free surface the width of the postseismic displacement field will be narrowed relative to those generated with our deep sources. This narrowing of the displacement field will make it easier to satisfy the data from the Black Mountain profile, if indeed the current lack of postseismic signal holds up to further data analysis. A planned re-leveling across the Loma Prieta profile (W.H. Prescott, written commun., 1993) may also help to resolve the depth of the postseismic deformation source.

Bürgmann and others (1992) have performed trial-and-error searches to determine the location of the rectangular dislocation with uniform slip that best fits the geodetic data. They conclude that the postseismic source probably lies at depths above the 18-km-deep Loma Prieta hypocenter. They further conclude that postseismic slip occurred not only in the Loma Prieta aftershock zone but also on a shallow thrust fault lying north of Loma Prieta. If their model is correct, then perhaps postseismic slip in the aftershock zone represents stress relaxation between patches that slipped seismically in the earthquake. This interpretation is similar to our deep-source models, but now creeping patches lie within the seismogenic zone and presumably represent aseismic "non-asperity" regions. This view is in accord with the interpretation that aftershocks concentrate in regions that have relatively small coseismic

slip (Oppenheimer and others, 1990) and are therefore most severely stressed by the earthquake. Analyses like ours could be performed by including shallow creeping patches within the seismogenic zone, whose location is constrained by seismologic estimates of the slip distribution in the earthquake. The shallow thrust fault proposed by Bürgmann and co-workers may be confined to rather shallow depths and consequently may represent stable fault creep (Tse and Rice, 1986; Scholz, 1990) of the sort examined by Marone and others (1991). Such a model could be examined within the framework of our finite element analyses or through use of the boundary element method.

COMPARISON TO STRAIN-METER OBSERVATIONS AT SAN JUAN BAUTISTA

The strain rate within a few kilometers of the surface trace of the San Andreas fault near San Juan Bautista (SJB) has been monitored by a Gladwin borehole tensor strain meter since 1983. The observations surrounding the time of the Loma Prieta earthquake are summarized here (Gwyther and others, 1992). Approximately one year prior to the Loma Prieta earthquake, the right-lateral strain rate increased to about 1 μradian/yr. Immediately following the earthquake, a 2-month transient occurred in which the right-lateral strain rate actually became negative and about 0.5 μradian of left-lateral strain accumulated. Following that short transient, the strain rate increased to about 2 μradian/yr, right-lateral, and has remained at that level for about 2 years. These changes in strain rate presumably reflect variations in slip rate on the fault that may be associated with the earthquake.

While our models do not attempt to include the effects of the shallow San Andreas creep zone that extends 150 km to the southeast from SJB, it is still interesting to compare our model predictions to the data. In the case of our nonlinear hot-friction models, the right-lateral strain rate near SJB is very high immediately following the earthquake but rapidly decays to about 0.4 μradian/yr above the pre-earthquake rate when averaged over the interval 0.5 to 2.0 postseismic years. This temporal behavior is qualitatively consistent with the time history of displacement plotted in figure 8. None of our models predict an immediate postseismic transient in which left-lateral strain accumulates in the vicinity of SJB. Furthermore, the predicted rate of postseismic strain measured relative to the pre-earthquake rate is only 40 percent of the observed value. The former is about 0.4 μradian/yr, while the latter is about 1 μradian/yr. We conclude that models that attempt to include the effects of the shallow San Andreas creep zone are required to obtain better agreement with the data from SJB.

ALTERNATIVE PHYSICAL PROCESS

We have proposed that postseismic deformation may result from frictional sliding assisted by elevated pore pressure. Alternatively, postseismic transient deformation may result from transient creep (Carter and Kirby, 1978; B. Evans, oral commun.). The displacement across our deep aseismic fault zone, required to match the observed strike-slip displacement along the Loma Prieta profile at 1.3 years, is about 0.5 m at a distance of 2.5 km from the edge of the coseismic rupture. If this deformation occurs within a shear zone with thickness $h \leq 1$ km, then the corresponding transient strain is $\gamma_{tr} \geq 0.5 \times 10^{-3}$ and its average rate is $\dot{\gamma}_{tr} \geq 2 \times 10^{-11}$/s.

SUMMARY

We have demonstrated that postseismic relaxation can increase the stress change at intermediate distances from the edge of the coseismic rupture by an amount well in excess of the coseismic change. Postseismic relaxation can have this same effect in the far-field, but the magnitude of the total stress change there is very small compared to typical earthquake stress drops. Along the Hayward and Calaveras fault trends, northeast to north of Loma Prieta, both coseismic slip and postseismic relaxation reduce the right-lateral shear stress and the compressive stress.

Our models of deep aseismic fault slip occurring beneath the seismogenic zone are capable of producing strike-slip displacements consistent with the initial 1.3 years of observed postseismic deformation along the profile of GPS stations that crosses through the epicenter (Lisowski and others, 1991a). However, these models appear to be incapable of producing fault-trace normal contraction compatible with the observations there, and an additional source of deformation may be required. For example, Bürgmann and others (1992, and this chapter) investigate models that include postseismic fault slip on shallow thrust faults north of Loma Prieta, while Savage and others (1994) consider models that include postseismic collapse of the coseismic rupture zone in the direction perpendicular to the plane of the rupture. Linker (1993) has shown that the magnitude and time-scale of Savage and co-workers' proposed fault-trace-normal collapse may be consistent with a relaxation time-scale controlled by postseismic flow of pressurized fluid out of the fault zone and into the country rock.

Along the Black Mountain GPS profile, northwest of Loma Prieta, postseismic displacements predicted by these same deep-slip models may exceed the observations, though a careful treatment of all of the pre-earthquake and post-earthquake geodetic data is required to better

establish a measure of the change in the velocity field associated with the earthquake (see Bürgmann and others, this chapter).

The time-scale for postseismic relaxation appears to be sufficiently long that the average background tectonic stress rate is likely to exceed the stress rate resulting from relaxation, except perhaps close to the edge of the coseismic rupture. If the time-scale for relaxation of the lower crustal detachment zone turns out to be on the order of 16 years or less, then its contribution to the stress rate within about 20 km of the end of the Loma Prieta rupture will be at least comparable to the average background stress rate.

In our linear viscoelastic models, the parameter controlling the relaxation time is the ratio of material relaxation time to the thickness of the deforming region, t_r/h. This parameter appears to have a value of approximately 0.3 yr/km thickness, at least in the deep aseismic portion of the fault zone. If relaxation takes place in a shear zone that is less than 1 km thick and if the shear modulus is 30 GPa, then the effective viscosity in the deforming region must be less than about 3×10^{17} Pa-s. This value is at least one order of magnitude lower than any obvious interpretation of laboratory measurements of the steady-state creep of solid crustal rocks at mid-crustal conditions.

The laboratory-derived hot-friction model can yield postseismic deformation of magnitude comparable to that observed, but only if $d\tau/d(\ln V)$ is on the order of 0.5 MPa, where τ is the resistance to sliding and V is the slip speed. Laboratory measurements indicate that $d\tau/d(\ln V)$ can be written approximately as $c\sigma$ (Stesky, 1975, 1978; Dieterich, 1981; Ruina, 1983), where σ is the effective normal stress equal to total normal stress minus pore pressure and c is on the order of 0.015 for mid-crustal conditions (Blanpied and others, 1991). Therefore, to be consistent with our models, the effective normal stress in the deep aseismic portion of the fault zone must be extremely low, perhaps on the order of 30 MPa.

In the context of the laboratory-derived hot-friction model, the occurrence of postseismic deformation may be evidence that pore pressure in the aseismic portions of the fault zone and perhaps the lower crust is near lithostatic.

ACKNOWLEDGMENTS

We wish to thank R. Bürgmann, M. Lisowski, J.C. Savage, and P. Segall for early access to the GPS data and for helpful discussions. We additionally thank B. Evans and R.W. Simpson for helpful discussions. P. Segall and R.W. Simpson provided careful reviews that led to correction of a sign error. This work was supported by the United States Geological Survey, National Earthquake Hazards Reduction Program, under grants G1844 and G1788 to Harvard University. Supercomputer services were provided by grants to Harvard University from the NSF National Center for Supercomputing Applications, Urbana Illinois. Some of the study was done through access to a network of workstations supported primarily by J. Bloxham, A.M. Dziewonski, G.A. Ekström, and R.J. O'Connell at Harvard. Hibbitt, Karlsson, and Sorensen, Inc. of Pawtucket, Rhode Island, provided ABAQUS through an academic license agreement.

REFERENCES CITED

Aki, K., and Richards, P.G., 1980, Quantitative seismology: New York, Freeman, 932 p.

Allen, C.R., 1969, Active faulting in northern Turkey: California Institute of Technology, Division of Geological Sciences Contribution 1577, 32 p.

Anderson, R.S., 1990, Evolution of the northern Santa Cruz mountains by advection of crust past a San Andreas fault bend: Science, v. 249, p. 397-401.

Bakun, W.H., Clark, M.M., Cockerham, R.S., Ellsworth, W.L., Lindh, A.G., Prescott, W.H., Shakal, A.F., and Spudich, P., 1984, The 1984 Morgan Hill, California, earthquake: Science, v. 225, p. 288-291.

Ben-Zion, Y., Rice, J.R., and Dmowska, R., 1993, Interaction of the San Andreas fault creeping segment with adjacent great rupture zones, and earthquake recurrence at Parkfield: Journal of Geophysical Research, v. 98, p. 2135-2144.

Beroza, G.C., 1991, Near source modeling of the Loma Prieta earthquake: Evidence for heterogeneous slip and implications for earthquake hazard: Bulletin of the Seismological Society of America, v. 81, p. 1603-1621.

Blanpied, M.L., Lockner, D.A., and Byerlee, J.D., 1991, Fault stability inferred from granite sliding experiments at hydrothermal conditions: Geophysical Research Letters, v. 18, p. 609-612.

Brace, W.F., and Kohlsted, D.L., 1980, Limits on lithospheric stress imposed by laboratory experiments: Journal of Geophysical Research, v. 85, p. 6248-6252.

Bürgmann, R., and Segall, P., 1991, Postseismic GPS monitoring NW of the Loma Prieta rupture zone: Eos, Transactions of the American Geophysical Union, v. 72, p. 119.

Bürgmann, R., Segall, P., Lisowski, M., and Svarc, J.P., 1992, Rapid aseismic slip on the Berrocal fault zone following the Loma Prieta earthquake: Eos, Transactions of the American Geophysical Union, v. 73, p. 119.

Carter, N.L., and Kirby, S.H., 1978, Transient creep and semibrittle behavior of crystalline rocks: Pure and Applied Geophysics, v. 116, p. 807-839.

Carter, N.L., and Tsenn, M.C., 1987, Flow properties of continental lithosphere: Tectonophysics, v. 136, p. 27-63.

Chen, W., and Molnar, P., 1983, Focal depths of intracontinental and intraplate earthquakes and their implications for the thermal and mechanical properties of the lithosphere: Journal of Geophysical Research, v. 88, p. 4183-4214.

Davis, J.L., Prescott, W.H., Svarc, J.L., and Wendt, K.J., 1989, Assessment of global positioning system measurements for studies of crustal deformation: Journal of Geophysical Research, v. 94, p. 13,635-13,650.

Dieterich, J.H., 1981, Constitutive properties of faults with simulated gouge, *in* Carter, N.L., Friedman, M., Logan, J.M., and Stearns, D.W., eds., Mechanical Behavior of Crustal Rocks: Washington,

D.C., American Geophysical Union, Geophysical Monograph Series v. 24, p. 103-120.

Dietz, L.D., and Ellsworth, W.D., 1990, The October 17, 1989 Loma Prieta earthquake and its aftershocks: geometry of the sequence from high-resolution locations: Geophysical Research Letters, v. 17, p. 1417-1420.

Doser, D.I., 1986, Earthquake processes in the Rainbow Mountain-Fairview Peak-Dixie Valley, Nevada, region 1954-1959: Journal of Geophysical Research, v. 91, p. 12,572-12,586.

Du, Y., and Aydin, A., 1990, Stress transfer during three consecutive moderate earthquakes along the Central Calaveras Fault: Eos, Transactions of the American Geophysical Union, v. 71, p. 1652.

England, P., and Molnar, P., 1991, Inferences of the deviatoric stress in actively deforming belts from simple physical models: Philosophical Transactions of the Royal Society of London, v. 337, p. 151-164.

Fares, N., and Rice, J.R., 1988, Crustal deformation modeling for San Andreas fault earthquake cycles, abstract T32B-07: AGU Fall Meeting Program, p. 149.

Fuis, G.S., and Mooney, W.D., 1990, Lithospheric structure and tectonics from seismic-refraction and other data: U.S. Geological Survey Professional Paper 1515, p. 207-236.

Gwyther, R.L., Gladwin, M.T., and Hart, R.H.G., 1992, A shear-strain anomaly following the Loma Prieta earthquake: Nature, v. 356, p. 142-144.

Hartzell, S.H., Stuart, G.S., and Mendoza, C., 1991, Comparison of L1 and L2 norms in a teleseismic waveform inversion for the slip history of the Loma Prieta, California, earthquake: Bulletin of the Seismological Society of America, v. 81, p. 1518-1539.

Hibbitt, Karlsson, and Sorensen, Inc., 1991, ABAQUS, Vers. 4.8 and 4.9: Pawtucket, RI.

Hudnut, K.W., Seeber, L., and Pacheco, J., 1989, Cross-fault triggering in the November 1987 Superstition Hills earthquake sequence, Southern California: Geophysical Research Letters, v. 16, p. 199-202.

Hyndman, R.D., and Shearer, P.M., 1989, Water in the lower continental crust: modeling magnetotelluric and seismic reflection results: Geophysical Journal International, v. 98, p. 343-365.

Kirby, S.H., and Kronenberg, A.K., 1987a, Correction to "Rheology of the lithosphere: selected topics" by S. H. Kirby and A. K. Kronenberg: Reviews of Geophysics, v. 25, p. 1680-1681.

———1987b, Rheology of the lithosphere: selected topics: Reviews of Geophysics, v. 25, p. 1219-1244.

Lachenbruch, A., and Sass, J., 1973, Thermo-mechanical aspects of the San Andreas fault system, *in* Kovach, R., and Nur, A., eds., Proceedings of the conference on tectonic problems of the San Andreas fault system: Stanford, Calif., Stanford University Publications in the Geological Sciences, v. 13, p. 192-205.

Lehner, F.K., Li, V.C., and Rice, J.R., 1981, Stress diffusion along rupturing plate boundaries: Journal of Geophysical Research, v. 86, p. 6155-6169.

Li, V.C., and Rice, J.R., 1987, Crustal deformation in great earthquake cycles: Journal of Geophysical Research, v. 92, p. 11,533-11,551.

Linker, M.F., 1993, In-situ permeability constrained by observations of postseismic deformation associated with the Loma Prieta earthquake: Eos, Transactions of the American Geophysical Union, v. 74, p. 564-565.

Lisowski, M., Prescott, W.H., Johnston, M.J., and Savage, J.C., 1990, Geodetic estimate of coseismic slip during the 1989 Loma Prieta, California, earthquake: Geophysical Research Letters, v. 17, p. 1437-1440.

Lisowski, M., Savage, J.C., and Prescott, W.H., 1991a, Surface deformation after the Loma Prieta, California, earthquake: Eos, Transactions of the American Geophysical Union, v. 72, p. 119.

———1991b, The velocity field along the San Andreas fault in central and southern California: Journal of Geophysical Research, v. 96, p. 8369-8389.

Lyzenga, G.A., Raefsky, A., and Mulligan, S.G., 1991, Models of recurrent strike-slip earthquake cycles and the state of crustal stress: Journal of Geophysical Research, v. 96, p. 21,623-21,640.

Malvern, L.E., 1969, Introduction to the mechanics of a continuous media: Englewood Cliffs, N. J., Prentice-Hall, 713 p.

Marone, C.J., Scholz, C.H., and Bilham, R., 1991, On the mechanics of earthquake afterslip: Journal of Geophysical Research, v. 96, p. 8441-8452.

Marshall, G.A., Stein, R.S., and Thatcher, W., 1991, Faulting geometry and slip from co-seismic elevation changes: The 18 October 1989, Loma Prieta, California, earthquake: Bulletin of the Seismological Society of America, v. 81, p. 1660-1693.

Mavko, G.M., Schultz, S., and Brown, B.D., 1985, Effects of the 1983 Coalinga, California earthquake on creep along the San Andreas fault: Bulletin of the Seismological Society of America, v. 75, p. 475-489.

Meissner, R., and Strehlau, J., 1982, Limits of stress in continental crusts and their relation to the depth-frequency distribution of shallow earthquakes: Tectonics, v. 1, p. 73-89.

Michael, A.J., 1991, Spatial variations in stress within the 1987 Whittier Narrows, California, aftershock sequence: New techniques and results: Journal of Geophysical Research, v. 96, p. 6303-6319.

Michael, A.J., Ellsworth, W.L., and Oppenheimer, D.H., 1990, Coseismic stress changes induced by the 1989 Loma Prieta, California earthquake: Geophysical Research Letters, v. 17, p. 1441-1444.

Mogi, K., 1968, Migration of Seismic Activity: Bulletin of the Earthquake Research Institute, University of Tokyo, v. 46, p. 53-74.

Olson, J., 1990, Seismicity in the twenty years preceding the 1989 Loma Prieta, California earthquake: Geophysical Research Letters, v. 17, p. 1429-1432.

Oppenheimer, D.H., Bakun, W.H., and Lindh, A.G., 1990, Slip partitioning of the Calaveras fault, California, and prospects for future earthquakes: Journal of Geophysical Research, v. 95, p. 8483-8498.

Oppenheimer, D.H., and Eaton, J.P., 1984, Moho orientation beneath central California from regional earthquake traveltimes: Journal of Geophysical Research, v. 89, p. 10,267-10,282.

Oppenheimer, D.H., Reasenberg, P.A., and Simpson, R.W., 1988, Fault plane solutions for the 1984 Morgan Hill, California, earthquake sequence: Evidence for the state of stress on the Calaveras fault: Journal of Geophysical Research, v. 93, p. 9007-9026.

Poley, C.M., Lindh, A.G., Bakun, W.H., and Schulz, S.S., 1987, Temporal changes in microseismicity and creep near Parkfield, California: Nature, v. 327, p. 134-137.

Prescott, W.H., and Yu, S.B., 1986, Geodetic measurements of horizontal deformation in the northern San Francisco Bay region, California: Journal of Geophysical Research, v. 91, p. 7475-7484.

Reasenberg, P.A., and Simpson, R.W., 1992, Response of regional seismicity to the static stress change produced by the Loma Prieta earthquake: Science, v. 255, p. 1687-1690.

Reches, Z., Schubert, G., and Anderson, C., 1994, Modelling of periodic great earthquakes on the San Andreas fault: Effects of nonlinear rheology: Journal of Geophysical Research, v. 99, p. 21,983-22,000.

Rice, J.R., 1980, The mechanics of earthquake rupture, *in* Dziewonski, A.M., and Boschi, E., eds., Physics of the Earth's Interior (Proceedings of the International School of Physics "Enrico Fermi", Course 78, 1979): Italian Physical Society, North-Holland Publ. Co., p. 555-649.

———1992, Fault stress states, pore pressure distributions, and the weakness of the San Andreas fault, *in* Evans, B., and Wong, T.f.,

eds., Fault Mechanics and Transport Properties of Rocks: Orlando, Florida, Academic Press, p. 475-503.

———1993, Spatio-temporal complexity of slip on a fault: Journal of Geophysical Research, v. 98, p. 9885-9907.

Rice, J.R., and Gu, J., 1983, Earthquake aftereffects and triggered seismic phenomena: Pure and Applied Geophysics, v. 121, p. 187-219.

Richter, C.F., 1958, Elementary seismology: San Francisco, W.H. Freeman, p. 768.

Ruina, A.L., 1983, Slip instability and state variable friction laws: Journal of Geophysical Research, v. 88, p. 10,359-10,370.

Saleeby, J.B., 1986, C-2: Central California offshore to Colorado Plateau: Geological Society of America Centennial Continent/Ocean Transect 10, scale 1:500,000, 2 sheets.

Savage, J.C., 1983, A dislocation model of strain accumulation and release at a subduction zone: Journal of Geophysical Research, v. 88, p. 4984-4996.

———1990, Equivalent strike-slip earthquake cycles in half-space and lithosphere-asthenosphere earth models: Journal of Geophysical Research, v. 95, p. 4873-4879.

Savage, J.C., and Prescott, W.H., 1978, Asthenosphere readjustment and the earthquake cycle: Journal of Geophysical Research, v. 83, p. 3369-3376.

Savage, J.C., Lisowski, M., and Svarc, J.L., 1994, Postseismic deformation following the 1989 (M=7.1) Loma Prieta, California, earthquake: Journal of Geophysical Research, v. 99, p. 13,757-13,765.

Scholz, C.H., 1977, A physical interpretation of the Haicheng earthquake prediction: Nature, v. 267, p. 121-124.

———1990, The mechanics of earthquakes and faulting: Cambridge, U.K., Cambridge University Press, 439 p.

Seeber, L., and Armbruster, J.G., 1990, Fault kinematics in the 1989 Loma Prieta rupture area during the 20 years before that event: Geophysical Research Letters, v. 17, p. 1425-1428.

Segall, P., 1991, Fault mechanics: Reviews of Geophysics Supplement, U.S. National Report to International Union of Geodesy and Geophysics 1987-1990, p. 864-876.

Segall, P., and Lisowski, M., 1990, Comparison of surface displacements in the 1906 San Francisco and 1989 Loma Prieta earthquakes: Science, v. 250, p. 1241-1244.

Sibson, R.H., 1982, Fault zone models, heat flow, and the depth distribution of earthquakes in the continental crust of the United States: Bulletin of the Seismological Society of America, v. 72, p. 151-163.

Steidl, J.H., Archuleta, R.J., and Hartzell, S.H., 1991, Rupture history of the 1989 Loma Prieta, California, earthquake: Bulletin of the Seismological Society of America, v. 81, p. 1573-1602.

Stein, R.S., and Ekström, G., 1992, Seismicity and geometry of a 110-km-long blind thrust fault 2. Synthesis of the 1982-1985 California Earthquake Sequence: Journal of Geophysical Research, v. 97, p. 4865-4883.

Stein, R.S., and Lisowski, M., 1983, The 1979 Homestead Valley earthquake sequence, California: Control of aftershocks and postseismic deformation: Journal of Geophysical Research, v. 88, p. 6477-6490.

Stesky, R.M., 1975, The mechanical behavior of faulted rock at high temperature and pressure: Cambridge, Massachusetts Institute of Technology, Ph.D. thesis.

———1978, Mechanisms of high temperature frictional sliding in Westerly granite: Canadian Journal of Earth Science, v. 15, p. 361-375.

Sykes, L.R., Kisslinger, J., House, L., Davies, J., and Jacob, K.H., 1981, Rupture zones and repeat times of great earthquakes along the Alaska-Aleutian arc, *in* Simpson, D., and Richards, P., eds., Earthquake Prediction, an International Review: Washington, D.C., American Geophysical Union, Maurice Ewing v. 4, p. 217-274.

Thatcher, W., 1983, Nonlinear strain buildup and the earthquake cycle on the San Andreas fault: Journal of Geophysical Research, v. 88, p. 5893-5902.

Thatcher, W., and Rundle, J.R., 1984, A viscoelastic coupling model for the cyclic deformation due to periodically repeated earthquakes at subduction zones: Journal of Geophysical Research, v. 89, p. 7631-7640.

Toppazada, T.R., Reel, C.R., and Park, D.L., 1981, Preparation of isoseismal maps and summaries of reported effects for pre-1990 California earthquakes: California Division of Mines and Geology Open-File Report 81-11, 182 p.

Tse, S.T., and Rice, J.R., 1986, Crustal earthquake instability in relationship to the depth variation of frictional slip properties: Journal of Geophysical Research, v. 91, p. 9452-9472.

U.S. Geological Survey Staff, 1990, The Loma Prieta, California, earthquake: An anticipated event: Science, v. 247, p. 286-293.

Wald, D.J., Helmberger, D.V., and Heaton, T.H., 1991, Rupture models of the 1989 Loma Prieta earthquake from the inversion of strong-motion and broadband teleseismic data: Bulletin of the Seismological Society of America, v. 81, p. 1540-1572.

Wesson, R.L., 1988, Dynamics of fault creep: Journal of Geophysical Research, v. 93, p. 8929-8951.

Working Group On California Earthquake Probabilities, 1990, Probabilities of large earthquakes in the San Francisco Bay region, California: U.S. Geological Survey Circular 1053, 51 p.

Yonekura, N., 1975, Quaternary tectonic movements in the outer arc of southwest Japan with special reference to seismic crustal deformation: Bulletin of the Department of Geography, University of Tokyo, v. 7, p. 19-71.

THE LOMA PRIETA, CALIFORNIA, EARTHQUAKE OF OCTOBER 17, 1989:
EARTHQUAKE OCCURRENCE

AFTERSHOCKS AND POSTSEISMIC EFFECTS

A SHEAR STRAIN ANOMALY FOLLOWING THE LOMA PRIETA EARTHQUAKE

By M.T. Gladwin, R.L. Gwyther, and R.H.G. Hart,
University of Queensland, Australia

CONTENTS

ABSTRACT

Borehole tensor strain instruments deployed along the San Andreas fault for the past 10 years have provided sufficient resolution and stability to sample regional tectonic processes. Data obtained from an instrument at San Juan Bautista in the near field region of the Loma Prieta earthquake provide the first high-resolution continuous shear strain observations associated with a large earthquake. A change in fault-parallel shear-strain rate of approximately 1 με per year occurred about a year prior to the earthquake and persisted to the time of the event. The strain rate decreased immediately after the earthquake, but following the Chittenden sequence of earthquakes in April 1989, a new and higher rate of fault-parallel shear accumulation (0.84 με per year relative to the 1989 rate) was established. This strain rate has continued through 1993. Associated creep-rate changes are apparent at a number of sites on the surface trace of the fault within 30 km, indicating that the measured change of strain rate at the time of the earthquake has regional significance. We propose that the observed strain accumulation results from increased slip around a nearby locked section of the fault arising from loading by the failed Loma Prieta source region to the north. This model is consistent with suggestions of an increased probability of a moderate earthquake near San Juan Bautista and with evidence that interactions between fault regions are important in earthquake processes.

INTRODUCTION

A Gladwin borehole tensor strainmeter (Gladwin, 1984) installed near the San Andreas fault at San Juan Bautista in late 1983 has provided continuous areal and shear strain data with sub-nanostrain resolution and long-term stability better than 100 $n\varepsilon$ per year (Gladwin and others, 1987). Raw data from the instrument consist of diameter changes in three directions at 120° to each other in the horizontal plane. These are reduced to areal strain ε_a, and engineering shear strains γ_1 and γ_2 (approximately parallel to and at 45° to the fault respectively), which are defined in terms of strain tensor components (ε_{xx}, ε_{yy} , and ε_{xy} by

$$e_a=\varepsilon_{xx}+\varepsilon_{yy}$$

$$\gamma_1=\varepsilon_{xx}-\varepsilon_{yy}$$

$$\gamma_2=2\varepsilon_{xy}$$

where, as subscripts to ε, the x direction is east and y is north. The strainmeter is grouted into the surrounding rock, and this instrument inclusion is softer to shear than to compression. Observed strain components are thus scaled by hole-coupling parameters (Gladwin and Hart, 1985) determined by tidal calibration.

Data from borehole inclusions are initially dominated by grout compression of the instrument, by thermally controlled decay as the instrument site re-establishes equilibrium with its surroundings, and by an exponential recovery of the virgin stress field relieved at the borehole during the drilling process (Berry and Fairhurst, 1966; Berry, 1967). The exponential signals are characteristic of viscoelastic rheology as typified by Burghers solids (Jaeger and Cook, 1976). They have no relevance to the monitoring of regional strain changes and were removed by an exponential least-squares fitting procedure over the interval January 1984 to February 1988 (Gladwin and others, 1991).

Raw data from the three instrument gauges commencing in 1984 (3 months after installation) are shown in figure 1*A*. In determination of the exponentials to be removed from the raw gauge data streams, all data known to be contaminated were eliminated from the fit (Gladwin and others, 1991; Gwyther and others, 1992). The same intervals of data are used for determination of exponentials for all three gauges, and no linear trend has been removed. The resulting exponentials, determined from data during early 1984, and from May 1986 to April 1988, are shown also in figure 1*A* (offset for clarity). The data following the Morgan Hill earthquake in April 1984 and anomalous data associated with field experiments at the site in 1986 were excluded. The instrument was off line for 6 months during 1987. All data after April 1988 were also excluded and provide no constraint on the least-squares fitting. Figure 1*B* gives the residuals from the determined exponentials. The residuals indicate stable gauge behavior from mid-1986, an emerging anomaly on all components beginning in late 1988, the strain offsets for the Loma Prieta earthquake in October 1989 and significantly differing behavior on all gauges since that time. The postseismic data indicate immediate postseismic recovery for about 3 months, and following the Chittenden earthquakes in April 1990 the establishment of new, relatively linear trends.

These residuals were then reduced to the strains ε_a, γ_1, and γ_2 shown in figure 2*A*. The data differ slightly from those presented in Gladwin and others (1991), owing to a refinement of the selection of data windows since that time. The dominant signals present are the coseismic strain offsets of the Loma Prieta earthquake. These have been documented elsewhere (Gladwin and others, 1991); the present discussion is confined to the observed strain-rate changes. In figure 2*B* the coseismic offsets have been removed from the data to make long term trends more apparent.

It is important to investigate how choices made in estimating and removing the exponential borehole response can influence interpretation of the strain data determined from the gauge residuals. These effects are examined in figure 3. The representative strain data shown are produced from residuals obtained for three different data windows marked a, b and c used in the fitting procedure. We are documenting an apparent change of strain rate at the time of the Loma Prieta earthquake. The critical issue is whether the choice of data interval significantly affects determination of the strain-rate change. It is evident from figure 2 that any reasonable choice of fitted window demonstrates that a gradient change occurred in the raw datasets. For the extremes of fitting intervals shown, the effect on the observed change of strain rate before and after the Loma Prieta earthquake are shown in table 1.

Interval c is inappropriate because it extends into the data which is to be used to determine the pre-earthquake gradient. In the following discussion, interval b has been used because it gave the best variance over the available 1987 dataset.

RESULTS

An anomalous change in γ_1 is apparent by late 1988, showing a remarkably linear strain accumulation of 1 $\mu\varepsilon$ per year relative to the pre-1988 rate (Gladwin and others, 1991). The azimuth of maximum shear for the accumulating shear strain is approximately parallel to the local San Andreas fault strike. The long-term stability of the measurements is particularly evident in the areal strain data. Areal strain is estimated from the sum of the three components and is seen to be constant (with the exception of the coseismic offset at the Loma Prieta event) at better than 1 microstrain over the whole 10-year period.

Immediately after the earthquake the fault-parallel shear-strain rate decreased for about 2 months and then gradually returned to the pre-anomaly value. These data are shown in figure 4. In May 1990, following the Chittenden aftershock sequence (four magnitude 4 to 5 earthquakes on April 18, 1990, centered on an area approximately 15 km north west of SJT), the present linear γ_1 shear accumulation rate of approximately 2 $\mu\varepsilon$ per year with the original sense had been established.

The absolute strain rates may of course differ from those indicated on these figures (approximately 1 $\mu\varepsilon$ per year from late 1988 to the Loma Prieta event, and approximately 2 $\mu\varepsilon$ per year relative to the pre-1988 rate from May 1990 through December 1993) because the data have been effectively detrended by the exponential removal procedure. The point at issue is that there are significant changes of strain rate documented in the data, one preceding the Loma Prieta earthquake and another following it. Both appear to be linear with time, and their relative magnitudes are not an artifact of the exponential removal procedure.

An alternative and useful means for determining the physical significance of these data is to plot γ_1 against γ_2 (see fig. 5). The shear state at a particular time is represented by a point in this shear space, its history is represented by the locus of these points, and the shear required to move from one shear state to another is the vector

Figure 1.—*A*, Raw gauge data for the SJT site beginning 3 months after installation. Fitted exponential curves are shown offset for clarity. The recording system was nonoperational for 5 months during 1987. *B*, Residual gauge data produced by removal of the fitted exponentials. Units are nominal microstrain only.

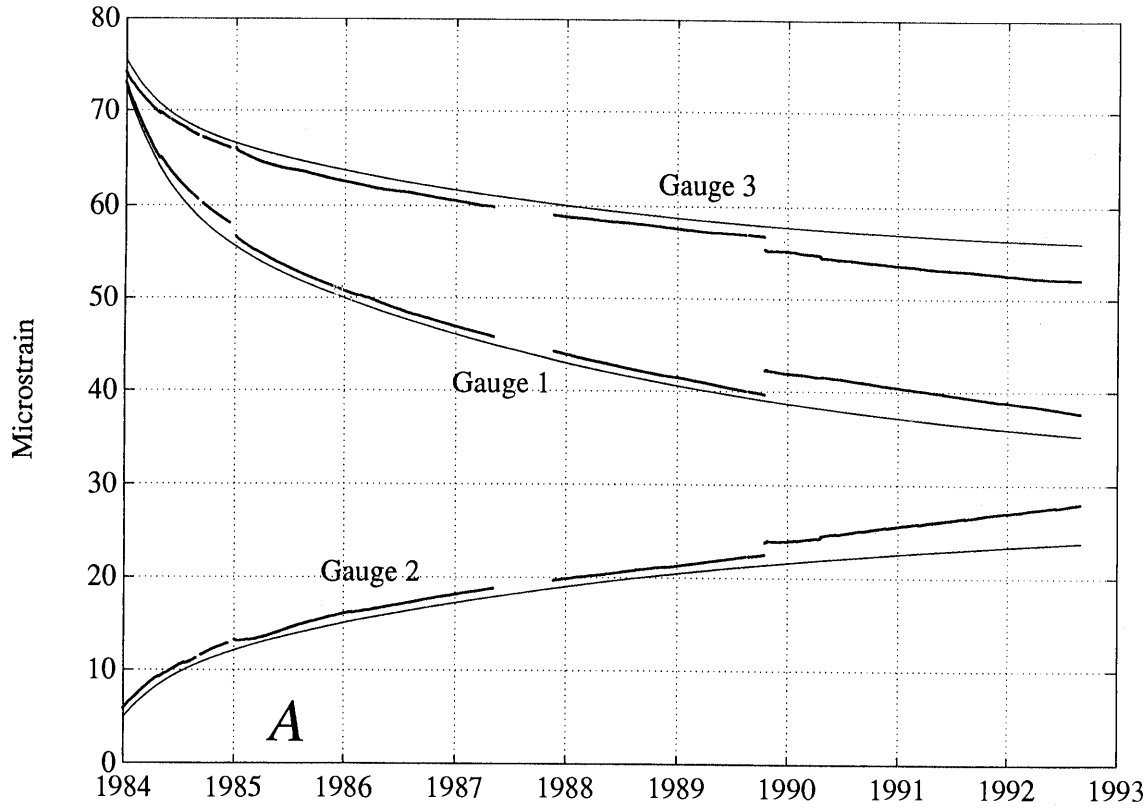
Microstrain
80
70
60
50
40
30
20
10
0
1984
1985
1986
1987
1988
1989
1990
1991
1992
1993
Gauge 3
Gauge 1
Gauge 2
A

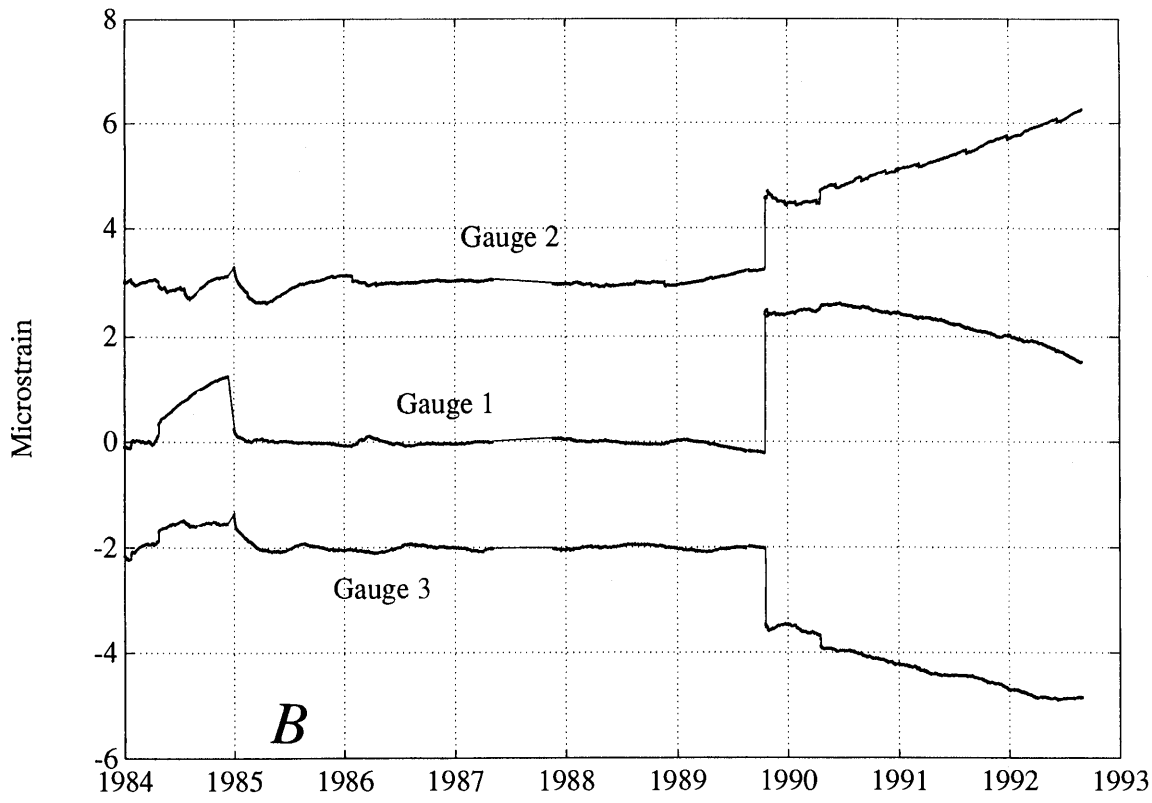
Microstrain
8
6
4
2
0
-2
-4
-6
1984
1985
1986
1987
1988
1989
1990
1991
1992
1993
Gauge 2
Gauge 1
Gauge 3
B

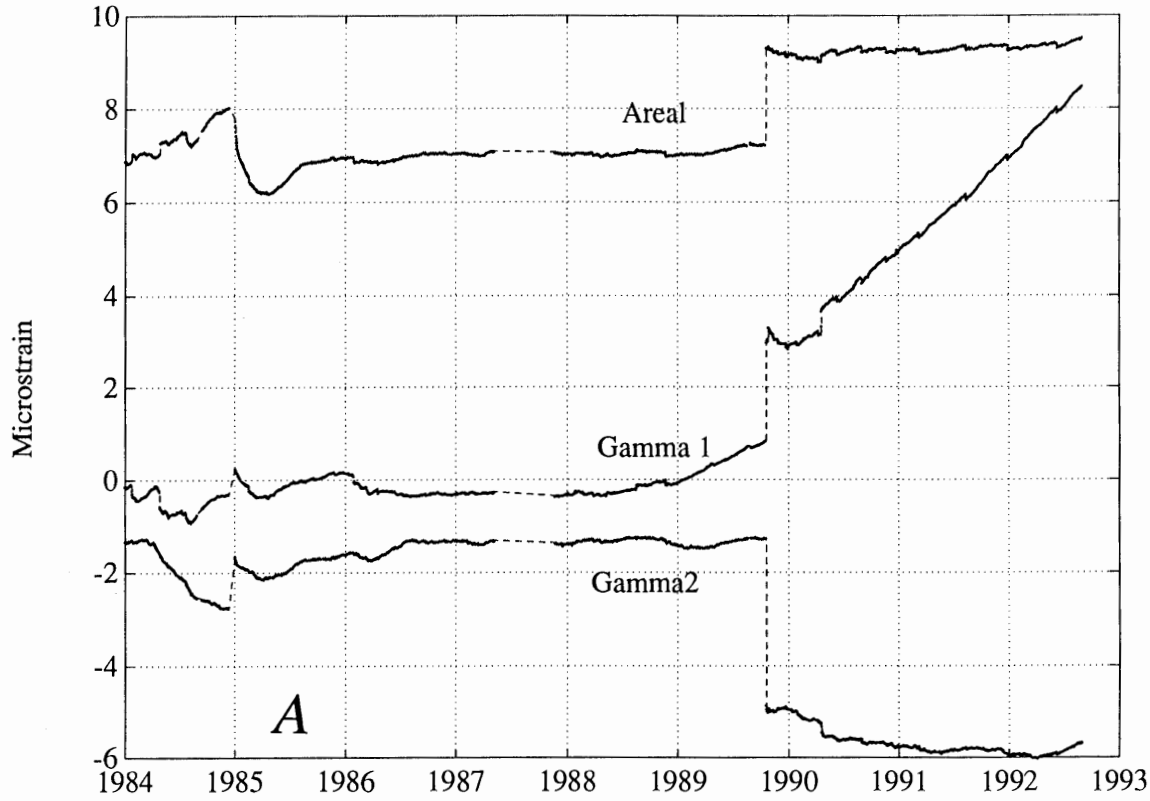
Microstrain
10
8
6
4
2
0
-2
-4
-6
Areal
Gamma 1
Gamma2
A
1984
1985
1986
1987
1988
1989
1990
1991
1992
1993

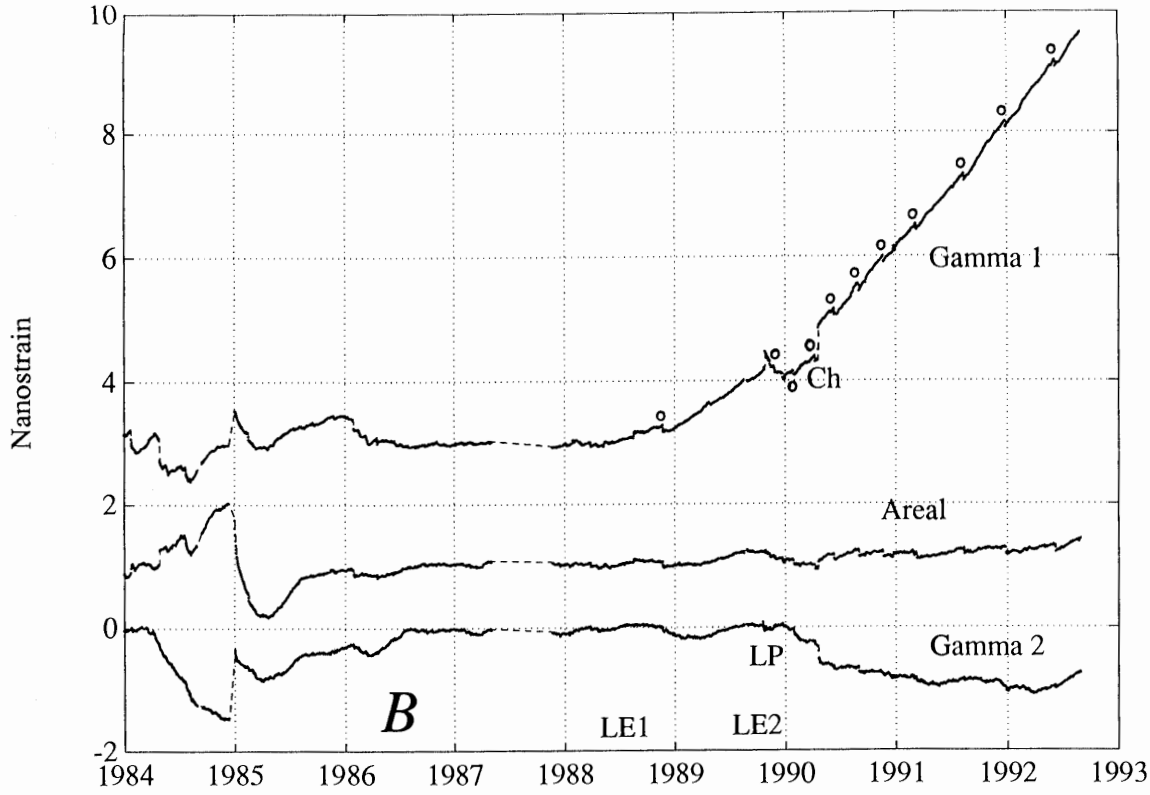
Nanostrain
10
8
6
4
2
0
-2
Gamma 1
Ch
Areal
LP
Gamma 2
B
LE1
LE2
1984
1985
1986
1987
1988
1989
1990
1991
1992
1993

connecting these points. With the local trace of the San Andreas approximately at N48°W, the γ_1 axis also represents approximately fault-parallel shear, and the γ_2 axis approximate extension normal to the fault. Time is marked at 3-month intervals, and direction of the coseismic offset of the Loma Prieta event is indicated in the upper and lower parts of the figure by the arrow. The Chittenden aftershock sequence is marked as CH on the lower part of the figure.

The shear-strain step C-C′, coseismic with the Loma Prieta event, is seen to increase both right-lateral shear across the fault (arising mainly from the γ_1 component, +1840 $n\varepsilon$) and normal compression (arising mainly from the γ_2 component, -3790 $n\varepsilon$). This fault-normal compression from shear alone must be combined with the contribution due to the areal strain step (+2140 $n\varepsilon$) to find the effective change in fault normal strain in the vicinity of the instrument of approximately 1600 $n\varepsilon$. Apart from a 5-month period immediately prior to the Loma Prieta event (see B-C in the figure) during which the maximum shear accumulation was oriented at N56°W, the predominant trend of both anomalies (see sections A-B and D-E in the figure) is a shear vector at angle E6°S corresponding to a maximum shear accumulation at N42°W, close to the local San Andreas fault strike of N48°W.

To verify instrument and coupling stability, response to earth strain tides was examined using the dominant, thermally uncontaminated tidal components O_1 and M_2. Sixty-day data windows of 90-minute data were used to provide normalised tidal component amplitude every 30 days. The strain step of the Loma Prieta event and other easily identifiable strain steps associated with earthquakes or creep events were removed from the record before the tidal analysis. Results are shown in figure 6 for the ε_a and γ_1 data sets. Error bars indicate the precision of determination for each point, assuming equal partition of noise over all tidal components. It is clear that there have been no significant or systematic changes of tidal admittance on this instrument over the whole period under discussion. This result has been confirmed elsewhere (Linde and others, 1991).

DISCUSSION

Apart from coseismic steps, the strain data show several readily identifiable steps which correlate closely with the main creep events on the closest creepmeter XSJ, 2 km to the east of our instrument. Events from late 1988 to 1992 are tabulated in table 2, and the detailed correspondence of the events with the main creep events gives further confidence that the data represent regional tectonic activity. Further, the events show (Gladwin and others, 1993) remarkable similarity suggestive of a small source (less than 0.5 kilometers in depth and at most a few kilometers in extent) directly under San Juan Bautista. The shear strain resulting from such a source cannot account for the size of the post Loma Prieta strain anomaly. Other explanations for this anomaly need to be examined.

A non-tectonic source from the instrument or its immediate vicinity is unlikely because of the stability of the tidal response, consistency of our internal instrument checks, the long-term stability of the areal strain record (better than 1 $\mu\varepsilon$ over 10 years), and the detailed correspondence in time of all observed strain steps with either earthquakes or creep events on nearby creep meters.

Though the strain signals could arise from small-scale processes in a nearby section of the fault, observations of anomalous creep events at three sites up to 30 km away indicate a more extended source. Figure 7 shows long-term creepmeter data for 5 sites covering 40 km of the fault south of San Juan Bautista with long-term trends (Burford, 1988). A distinct increase in creep rate following the Loma Prieta earthquake is evident on sites XSJ, XHR and CWC, spanning 16 km of the fault. The XFL site (29 km from XSJ) shows only a marginal increase, and the more remote site XMR (40 km) shows no effect.

The creep anomalies in figure 6 are unusual, especially for CWC and XHR, and begin at the time of the Loma Prieta earthquake. The creep anomaly at the nearby XSJ begins about the time of the establishment of the new shear strain anomaly at SJT, which, given the causal time correspondence, suggests that these signals are not just the consequence of normal interactions between fault sections in this creeping section, but are linked to the earthquake. We conclude that the failure of the Loma Prieta source region transferred load to the San Juan Bautista region just to its south, resulting in increased creep rate. The simplest explanation of an increased creep rate is frictional response to the increased fault-parallel shear loading indicated by the coseismic γ_1 step at San Juan Bautista.

◄ Figure 2.—*A*, Areal strain and shear strains from the SJT borehole tensor strainmeter at San Juan Bautista near the San Andreas fault in northern California. Exponential trends have been removed from this data. A dominant feature is the coseismic strain step from the Loma Prieta earthquake in October 1989. *B*, Removal of this step reveals the details of the strain records, in particular the striking anomaly in the γ_1 component, the relative constancy of the other two strain components, and trend reversal on γ_1 for 3 months following the Loma Prieta event. All steps in the data can be associated with seismic events or nearby creep events. For example, the times of the two Lake Elsman earthquakes are indicated (LE1, LE2), as are the times of the Loma Prieta earthquake (LP), the Chittenden earthquake sequence (Ch), and creep events also monitored on a nearby creepmeter (o) and documented in table 2.

However, slip via creep does not itself result in linearly increasing elastic strain. We suggest that our linear shear-strain anomaly is best explained by continued aseismic slip around a nearby locked section of the fault, the slip being associated with loading transferred from the Loma Prieta source region particularly after the Chittenden aftershock sequence (April 1990).

The response at the site immediately after the Loma Prieta earthquake and prior to the Chittenden events seems to indicate that this load transfer towards the SJT site was

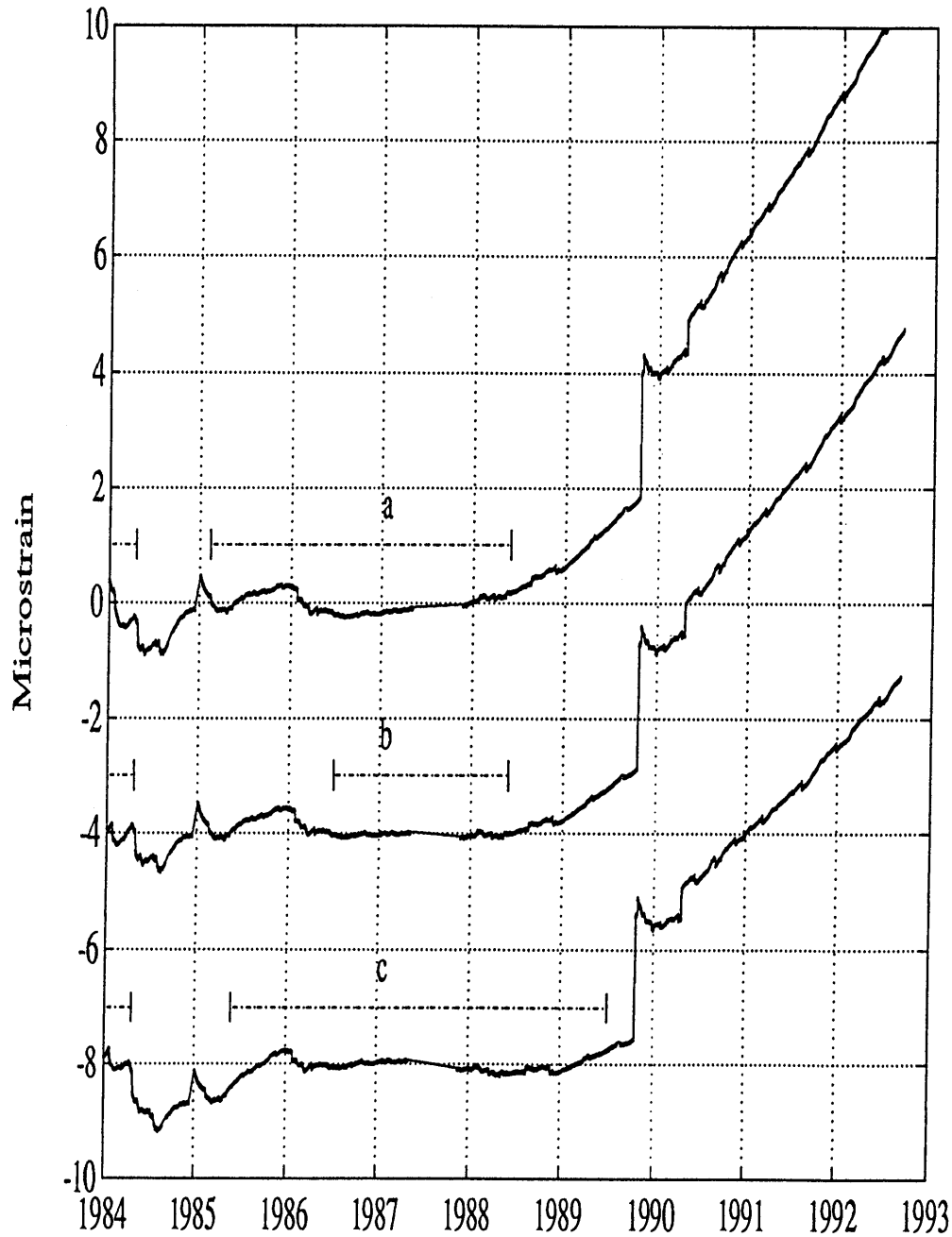

Figure 3.—Representative γ_1 shear-strain data illustrating the effect of the choice of data window used for the exponential fitting. The intervals used in three separate fit sets are marked as a, b, and c. Estimates of the change of strain rate from before to after the Loma Prieta event are only marginally affected for the three extreme choices shown. The choices have some effect on the timing of the pre-event anomaly only. Note that for choice c the change of gradient is well defined before the end of the fitting interval, indicating that the end point of the fit interval is not producing the effects discussed. The changes of gradient that determine the anomalies under discussion are clear on all residual sets.

Table 1.—*Average gradient of shear strain γ_1 determined over three periods*

[Values are residual gauge data after removal of exponential functions fitted over the three selection intervals 1985/02 to 1988/04 (a), 1986/06 to 1988/04 (b), and 1985/05 to 1989/07 (c). The lowest row of data indicates that the change in strain rate after the Loma Prieta earthquake is very similar for the three fitting intervals shown.]

	Selection Interval		
	1985/02 to 1988/04 (a)	1986/06 to 1988/04 (b)	1985/05 to 1989/07 (c)
1986-1988	0.11 ± .11	-0.03 ± .08	0.01 ± .14
1989 to L.P.	1.56 ± .08	1.16 ± .09	0.75 ± .09
Post-L.P.	2.4 ± .10	2.01 ± .11	1.54 ± .12
Difference	0.84 ± .13	0.85 ± .14	0.79 ± .15

initially prevented by the strength of an asperity region associated with the Chittenden aftershock sequence. When this region ultimately failed in 1990, the SJT site immediately began to respond to the fault parallel shear expected from the Loma Prieta event in the sense of a continued afterslip at the Loma Prieta region.

A range of simple dislocation models of slip around a locked region were considered. The model which resulted in a fault-parallel shear-strain rate most comparable to that observed was a locked region extending along the fault strike at depth of 1.5 to 5 km, with the surrounding fault surface slipping at the regional average of 14 mm per year. While this model indicated a locked region shallower than the study mentioned above, uncertainty in the absolute value of the observed γ_2 strain rate indicates that our data are broadly consistent with the presence of such a locked region at moderate depth on the fault. The data thus suggest an increased probability of a moderate earthquake in the San Juan Bautista region.

We have previously suggested (Gladwin and others, 1991) that the pre-Loma Prieta strain changes were related to a broad regional effect, based on the timing of the Lake Elsman foreshock and a marginal geodetic anomaly (Lisowski and others, 1990) near the Loma Prieta source. The effects we are reporting also appear to have some regional expression in increased creep activity since the Loma Prieta earthquake. The anomaly in γ_1 is now so large that it would be expected to be detectable by geodetic observations in the area. Unfortunately, the major geodetic network is centered well to the north of San Juan Bautista, making even inversion for the determination of the southern extent of the Loma Prieta rupture zone itself difficult (Johnston and others, 1990). Recent data from the southern end of this network is not yet available, but a change of fault-parallel shear-strain rate of $1\mu\varepsilon$ per year coincident with the Loma Prieta event should easily be identified in the observational period to date if it extended over the total geodetic network involved. These data are critical in providing constraints on the scaling of the anomaly in the northerly direction. Some data has been taken in a small HP3808 network extending from San Juan Bautista north to Pajaro Gap, particularly following the earthquake (Johnston, oral comm., 1993), but the results from this network are not yet published. Data from this network was not taken for many years prior to the Loma Prieta earthquake, so there is no likely contribution on the issue of whether or not a change of gradient has occurred following the event. There is no associated areal strain anomaly indicated in the data, and so no corroboration of the anomaly by reference to the dilatometer at Searle Road, approximately 5 km away, is available. The dilatometer shows no significant areal strain change.

Scaling of the anomaly cannot be determined from a single site, and the significance of these data will remain unknown until it is confirmed or denied from measurements at other nearby instrument sites. There is no evidence that the observed anomaly extends sufficiently far north to be measured in the Loma Prieta geodetic network. Our modelling suggests the presence of a source 5 km long. This source would produce minimal deformation in the geodetic network. Hence, although we are confident that the observed anomaly is not an instrumental artifact or of very localized origin, the only currently available supportive evidence that this anomaly is of regional significance is the increased creep activity in stations south of SJT.

ACKNOWLEDGMENTS

This work was performed under a grant from the U. S. Geological Survey, Department of the Interior. Contents do not represent policy of that agency, and no endorsement of the agency is to be assumed. The instruments were previously developed under awards of the Australian Research Grants Scheme and fabricated by R. Willoby and staff in-house. We thank R. Liechti for maintenance support, K. Breckenridge for data retrieval and assistance with creepmeter data, and Drs. A. Linde and M. Johnston for general support in the program.

REFERENCES CITED

Berry, D.S., 1967, Deformation of a circular hole driven through a stressed viscoelastic material: International Journal of Rock Mechanics and Mining Science, v. 4, p.181-187.

Berry, D.S., and Fairhurst, C., 1966, Influence of rock anisotropy and time-dependent deformation on the stress-relief and high-modulus inclusion techniques of in-situ stress determination: American Society for Testing Materials, STP 402, p.190-206.

Burford, R.O., 1988, Retardations in fault creep rates before local moderate earthquakes along the San Andreas fault system, central

California: Pure and Applied Geophysics, v. 126, p. 499-529.
Gladwin, M.T., 1984, High precision multi component borehole deformation monitoring: Reviews of Scientific Instruments, v. 55, p. 2011-2016.
Gladwin M.T., Breckenridge, K.S., Hart, R. and Gwyther, R.L., 1994, Measurements of the strain field associated with episodic creep events on the San Andreas Fault at San Juan Bautista, California: Journal of Geophysical Research, v. 99, no. B3, p. 4559-4565.
Gladwin, M.T., Gwyther, R.L., Hart, R. and Francis, M., 1987, Borehole tensor strain measurements in California: Journal of Geophysical Research, v. 92 , no. B8, p. 7981-7988.
Gladwin, M.T., Gwyther, R.L., Higbie, J.W. and Hart, R., 1991, A medium term precursor to the Loma Prieta earthquake?: Geophysical Research Letters, v. 18, no. 8, p. 1377-1380.
Gladwin, M.T., and Hart, R., 1985, Design parameters for borehole strain instrumentation. Pure and Applied Geophysics, v. 123, p. 59-88.
Gwyther, R.L., Gladwin, M.T., and Hart, R.H.G., 1992, A shear strain anomaly following the Loma Prieta earthquake: Nature, v. 356, p,142-144.
Jaeger, J.C. and Cook, N.G.W., 1967, Fundamentals of rock mechanics: London, Chapman and Hall.

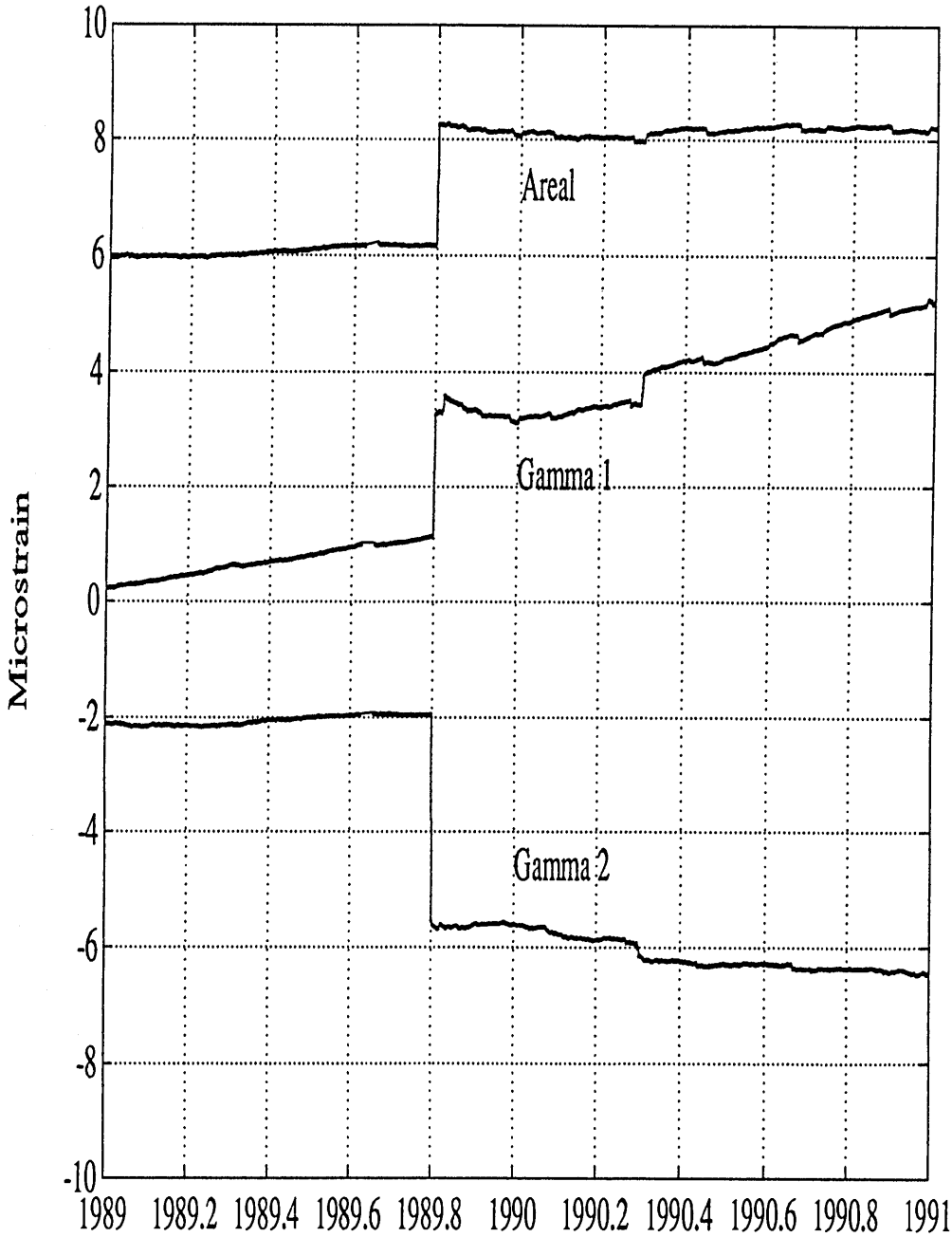

Figure 4.—Detail of the strains immediately following the Loma Prieta earthquake. The γ_1 record shows that the post-earthquake strain rate shown in figure 2 did not begin until after the Chittenden sequence in April 1990.

Johnston, M.J.S., Linde, A.T., and Gladwin, M.T., 1990, Near-field high resolution strain measurements prior to the October 18, 1989, Loma Prieta Ms 7.1 earthquake: Geophysical Research Letters, v. 17, no. 10, p. 1777 - 1780.

Linde, A.T., Gladwin, M.T., and Johnston, M.J.S., 1991, The Loma Prieta earthquake, 1989 and earth strain tidal amplitudes: an unsuccessful search for associated changes: Geophysical Research Letters , v. 19 no. 3, p 317-320.

Lisowski, M., Prescott, W.H., Savage, J.C., and Svarc, J.L., 1990, A possible geodetic anomaly observed prior to the Loma Prieta, California, earthquake: Geophysical Research Letters, v. 17, no. 8, p. 1211-1214.

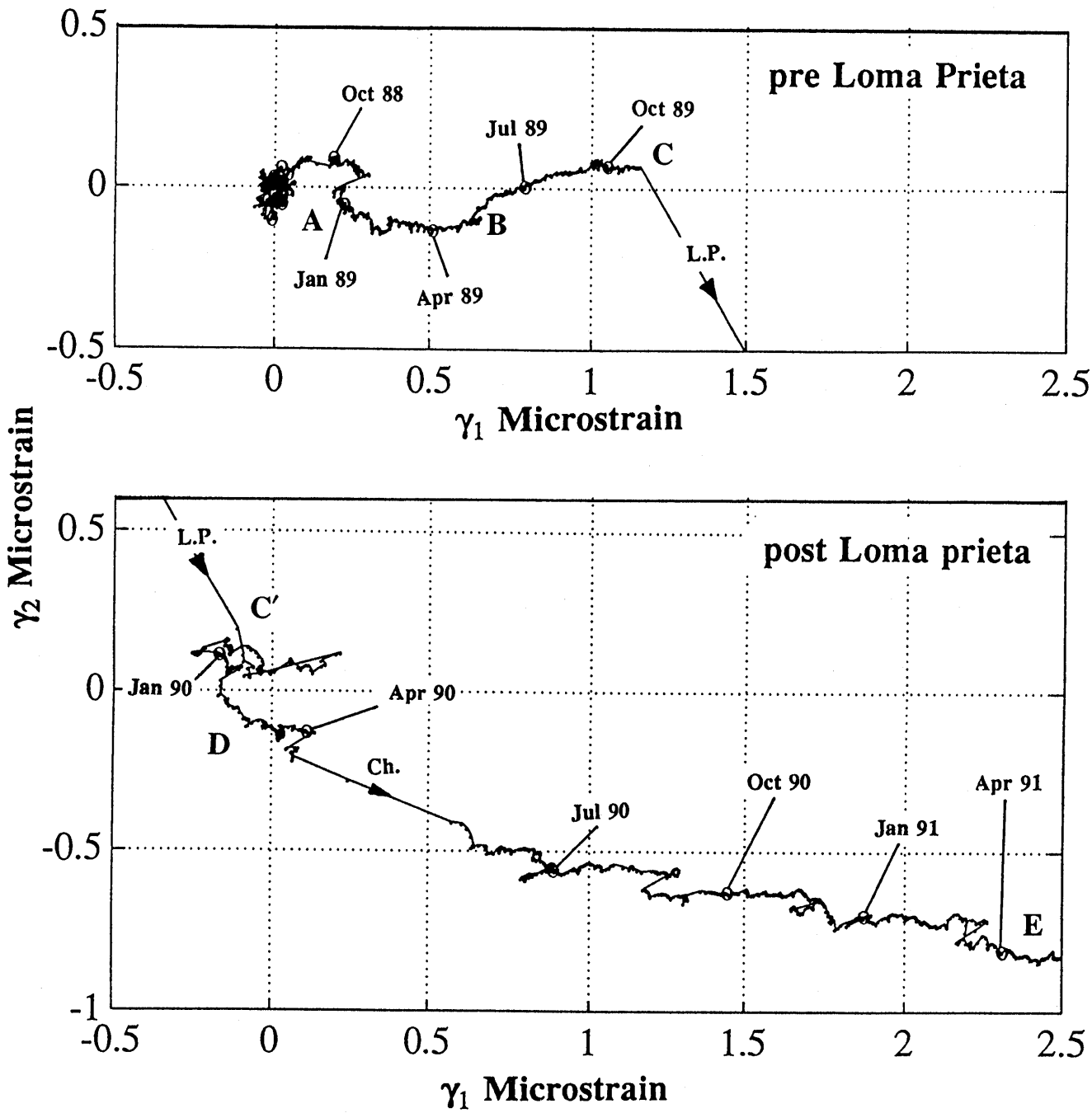

Figure 5.—Pre- and post-Loma Prieta plots of tensor strain components γ_2 against γ_1 in με for the period July 1986 to April 1991. The shear strain γ_1 is a measure of shear strain approximately parallel to the San Andreas fault at this locality, while γ_2 is a measure of shear strain in approximately a north-south or east-west direction, and thus extension normal to the fault. Three monthly intervals are indicated on the figure. The initiation and completion of the step associated with the Loma Prieta earthquake is shown by L.P. The size of this step was γ_1=+1840 $n\varepsilon$ and γ_2=-3790 $n\varepsilon$. The Chittenden aftershock sequence strain step is indicated by Ch. For any shear-strain change ($\Delta\gamma_1$, $\Delta\gamma_2$), the maximum shear strain change is $\Delta\gamma = \sqrt{\Delta\gamma_1^2 + \Delta\gamma_2^2}$ and $\Theta = 1/2\tan^{-1}[\Delta\gamma_2/\Delta\gamma_1]$ is the angle N of E for the axis of maximum extension.

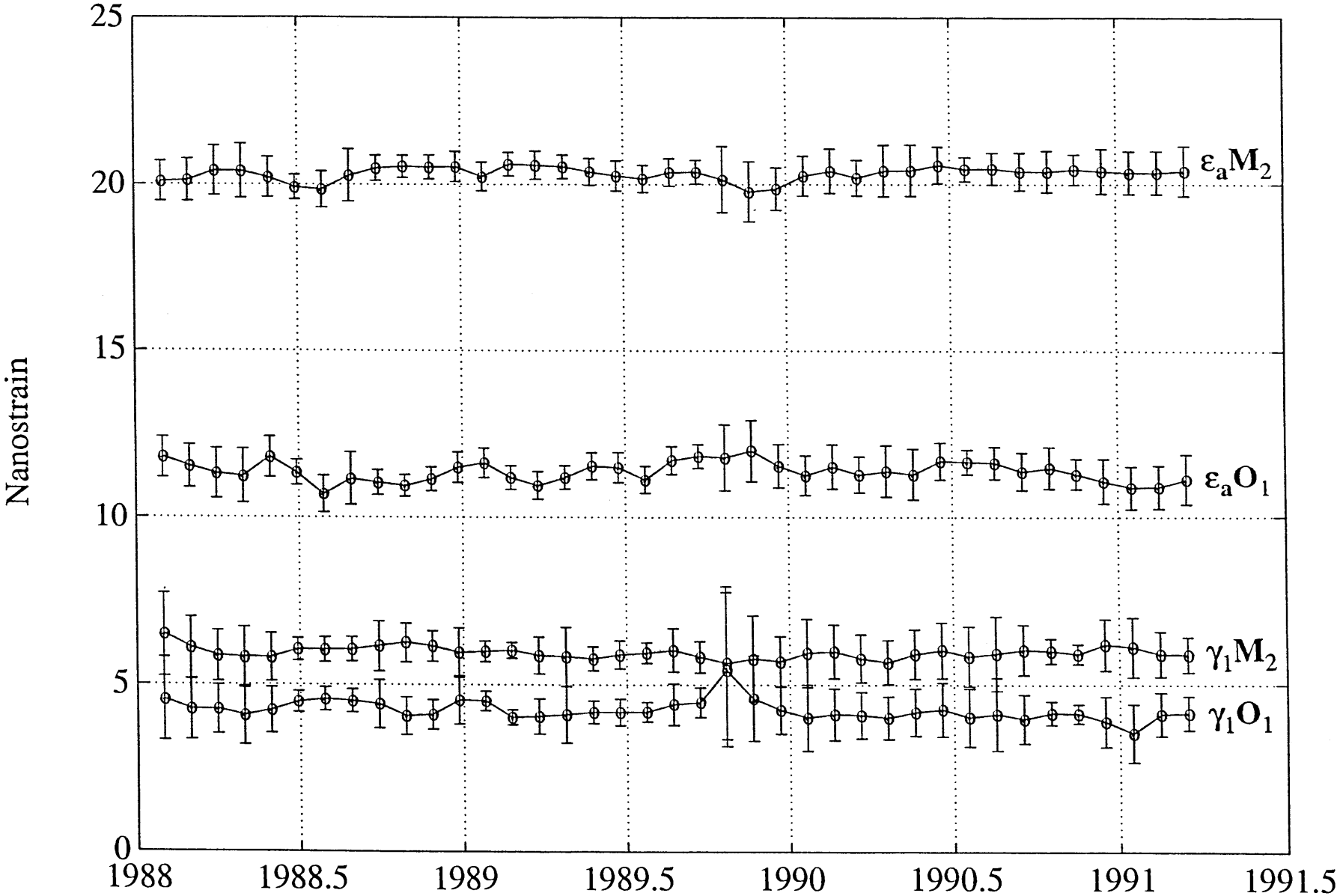

Figure 6.—Amplitude of the M_2 and O_1 tidal components of areal strain ε_a, and shear strain γ_1 for the period 1988 to mid-1991. Sixty-day windows of 90-minute data were used to provide normalised tidal component amplitude every 30 days. The strain step of the Loma Prieta event and other easily identifiable strain steps were removed from the record. Error bars indicate the precision of determination, assuming Gaussian noise. There is no significant change in instrument performance for any component.

Table 2.—*Surface creep events recorded at XSJ creepmeter at San Juan Bautista in 1988-1992 period, and corresponding strain offsets observed at SJT*

[Each strain event preceded the surface creep event by less than 1 hour]

No.	Date	Strain event			Creep event
		γ_1	γ_2	ε_a	Size
		$n\varepsilon$	$n\varepsilon$	$n\varepsilon$	mm
1	21.11.88	-100	-40	-80	1.7
2	22.12.89	-77	-38	-60	0.5
3	27.01.90	-69	-41	-53	0.6
4	07.04.90	-90	-55	-75	1.9
5	09.06.90	-100	-50	-90	3.9
6	04.07.90		None		0.3
7	30.08.90	-120	-52	-91	3.2
8	20.11.90	-50	-45	-70	2.1
9	08.03.91	-95	-50	-80	3.6
10	06.08.91	-120	-50	-90	5.0
11	27.12.91	-90	-50	-80	0.3
12	07.06.92	-110	-45	-90	5.3

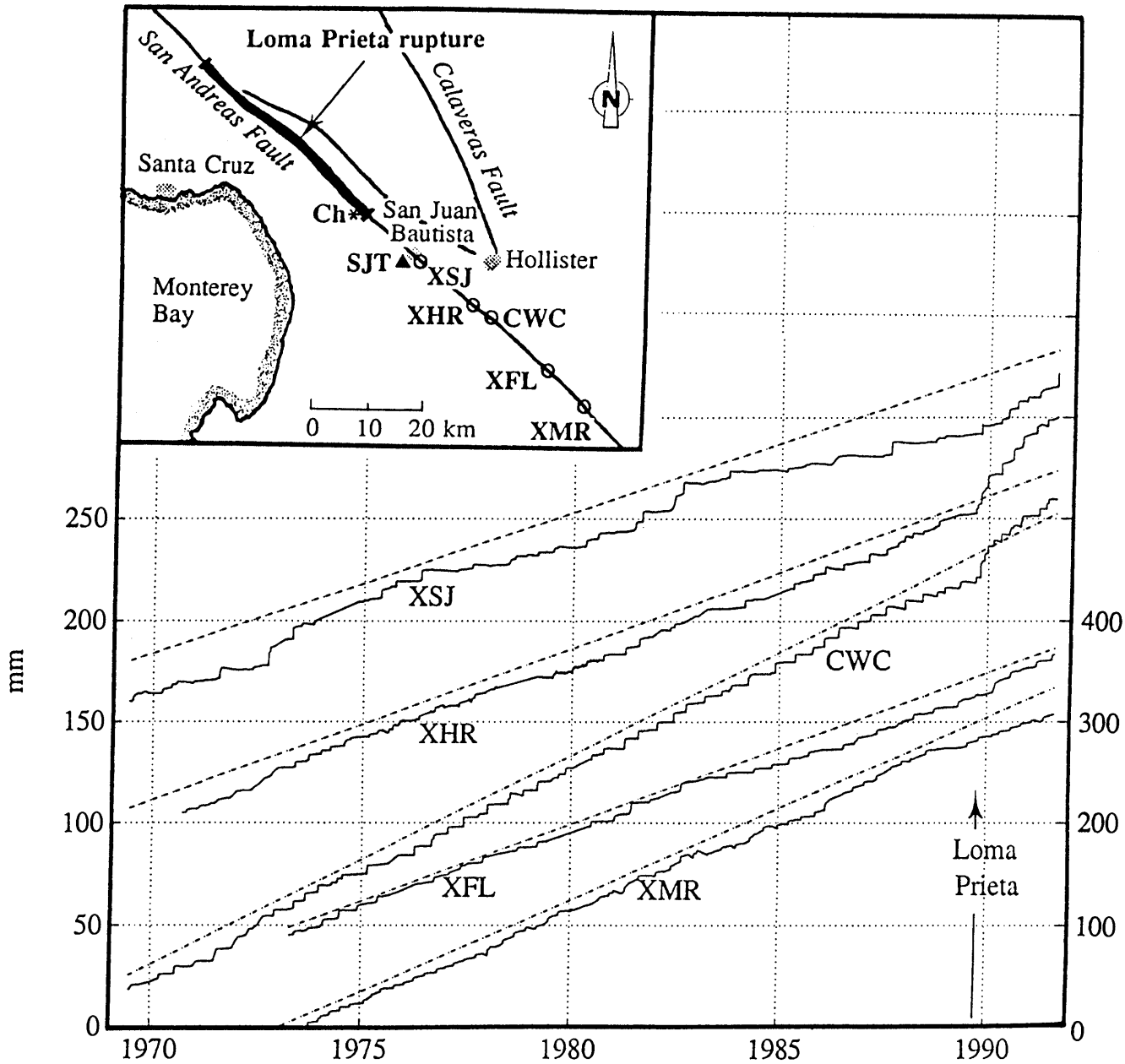

Figure 7.—Surface-creep data (provided by K. Breckenridge, USGS) from creepmeters along the fault south of San Juan Bautista, with positions of creepmeters XSJ, XHR, CWC, XFL and XMR, tensor strainmeter SJT, and Chittenden aftershock Ch indicated in the inset map. The trend lines indicated are from Burford (1988). Note that for the XMR data, the scale at the right axis should be used.

THE LOMA PRIETA, CALIFORNIA, EARTHQUAKE OF OCTOBER 17, 1989:
EARTHQUAKE OCCURRENCE

AFTERSHOCKS AND POSTSEISMIC EFFECTS

A MAGNETOTELLURIC SURVEY OF THE LOMA PRIETA EARTHQUAKE AREA: IMPLICATIONS FOR EARTHQUAKE PROCESSES AND LOWER CRUSTAL CONDUCTIVITY

By Randall L. Mackie and Theodore R. Madden, Massachusetts Institute of Technology; and
Edward A. Nichols, University of California, Berkeley

CONTENTS

ABSTRACT

We conducted a magnetotelluric survey around the Loma Prieta earthquake zone one year after the earthquake to look for possible electrical anomalies in the lower crustal part of the earthquake zone. We collected data at stations on each side of the San Andreas fault from Hollister to near Palo Alto. We used a two-dimensional transverse magnetic (TM) mode inversion algorithm to interpret the observed TM mode data since it is the TM mode that is sensitive to lower crustal resistivity variations near ocean-continent boundaries, whereas the transverse electric (TE) mode is not. Inversions of the data suggested a vertical zone of increased lower crustal conductance in the vicinity of the San Andreas fault near the region that experienced the main shock and aftershocks. The inferred zone of increased lower crustal conductance may be a permanent feature of this part of the San Andreas fault zone, or it may be a temporal feature related to the Loma Prieta earthquake. Because healing and ductile deformation processes in the lower crust should decrease its conductance with time, we speculate that this anomalous zone may be related to the Loma Prieta earthquake. With only data collected after the earthquake, we cannot confirm this speculation. However, because of the short time period between the Loma Prieta earthquake and our measurements, we think that fluids were already present there before the earthquake, but that the rupturing process of the earthquake increased the lower-crustal fluid connectivity. Regardless, the conductance values determined by our inversions correspond to lower-crustal connected fluid porosities of about 0.06 percent for a 5-km-wide leakage zone. Higher fluid porosities would be needed if the fluids were concentrated in narrower zones, but we cannot determine the exact geometry of these zones.

INTRODUCTION

More than 5,000 aftershocks occurred over a distance of 60 km along the San Andreas fault zone and up to 20 km in depth following the Loma Prieta earthquake (Oppenheimer, 1990). The main shock and aftershocks generally fell along a fault plane that dips 70° to the west and strikes approximately 130° from north. The earthquake was unusual because the epicenter was at a depth of almost 18 km (Dietz and Ellsworth, 1990), which is deeper than expected for this region of the San Andreas fault (Furlong and Langston, 1990), and because it is debatable whether or not the earthquake actually occurred on the San Andreas fault (Segall and Lisowski, 1990; Dietz and Ellsworth, 1990).

Large-scale tectonic processes, such as earthquakes, may have a dramatic influence on the electrical conductivity of the crust. This is because these processes can affect the fluid regime in the crust (Torgensen, 1990), where the primary control of electrical conductivity is connected saline fluids. The crust, in general, becomes more resistive with depth, although some regions of the world appear to have conductive zones in the middle or lower crust (for example, Jones, 1987). At shallow depths, the increased resistivity is due to the narrowing of cracks (Brace and others, 1965). Deeper in the crust, temperatures are high

enough so that rocks deform ductilely rather than brittlely (Heard, 1976), and this should eliminate much of the connected porosity (Brace and Kohlstedt, 1980). It is more likely, however, that the middle-to-lower crust actually deforms semi-brittlely (Carter and Tsenn, 1987; Evans and others, 1990), which may be partly responsible for the fact that finite resistivities are measured for the lower crust.

Because the main shock of the Loma Prieta earthquake was at a depth of 18 km, brittle deformation occurred down to at least that depth in the Loma Prieta region, and possibly deeper. Furthermore, it is possible that semi-brittle deformation, where the main deformation mechanisms are crystal plasticity and microcracking (Evans and others, 1990), would exist to even greater depths. Such deformation might have caused an increase in the fracture and microcrack connected porosity in the lower crustal part of the fault zone and hence an increase in conductivity in that zone. (An alternate scenario is that fluids were brought into this zone after the earthquake, but we believe this is less likely because of the time scales required for fluids to percolate through a fairly impermeable crust.)

Fluids at high pore pressures in the lower crustal part of a fault zone have been proposed to play an important role in the earthquake cycle (Rice, 1992). The existence of elevated pore pressures in a very narrow permeable slip zone having the usual laboratory frictional values may explain why the San Andreas fault does not show a pronounced heat flow peak and why the principal stress directions are at large angles relative to the trace of the San Andreas (Rice, 1992). Fluids at high pore pressures in the fault slip zone would give the lower crust a special role in the earthquake cycle as the pore pressure there is probably already close to the overburden pressure.

Magnetotelluric (MT) measurements, under certain geographic circumstances, can provide information about vertical zones in the lower crust that have anomalous electrical properties. This occurs when currents are forced through these zones, which is the case near ocean-continental boundaries because of the mismatch of the current systems as a function of depth. Because the San Andreas fault system is parallel and close to the coast, we can take advantage of the currrent system set up by the ocean-continent adjustments to study the electrical properties of the lower crustal part of the fault zone. Therefore, we collected MT data in the Loma Prieta earthquake region to investigate the lower crustal properties of that area. Unfortunately, since all of our MT data were collected after the earthquake, we will not be able to make any statements concerning time changes in conductivity across the fault zone that might have been due to the earthquake itself.

THE MAGNETOTELLURIC TM-MODE COAST EFFECT

Electromagnetic fields are affected by an ocean-continent boundary in two very distinct ways. One type of coast effect is due to the concentration of near-surface electrical currents running parallel to the coast in both the ocean and the oceanic upper mantle, which causes anomalies in the vertical magnetic field recorded near an ocean coast. In the work herein, we are concerned with another coast effect—one that perturbs the electric fields running perpendicular to the coast.

Because the ocean has such a high conductance, most of the induced electrical current in oceanic regimes is concentrated in the ocean itself up to periods of 500 s, whereas in a continental regime the current is mostly in the mantle. Because electrical currents are divergence-free, there is continuity in the normal component of current at the ocean-continent boundary. This results in extra current perpendicular to the coast (the transverse magnetic or TM mode) in the continental upper crust compared to what would be induced were the ocean absent. Consequently, the currents must readjust in some broad zone around the ocean-continent boundary. This readjustment takes place by leaking currents out of the upper crust, across the resistive lower crust, and into the mantle (fig. 1). In this readjustment zone, the current system is still dominated by the oceanic current system.

The width of this readjustment zone depends on the conductance of the upper crust and the resistance of the lower crust (Ranganayaki and Madden, 1980). The distance at which the current has been reduced by a factor of e by leaking into the mantle is termed the adjustment distance, and is equal to the square root of the product of the integrated upper crustal conductance and the integrated lower crustal resistance (Ranganayaki, 1978). The adjustment distance can be 100 km or more for continental regimes, and even at these distances the upper crustal current system is still contaminated by excess ocean currents. It actually takes several adjustment distances for the current system to return to normal continental values.

Vertical zones in the lower crust that have an anomalously high conductance can dramatically alter the TM response across that zone (Park and others, 1991; Mackie, 1991). This is because more current is attracted out of the ocean by this leakage zone, but less current remains in the upper crust inland of this zone. This results in a dramatic shift in the TM-mode response across the zone. The transverse electric (TE) mode response would not be sensitive to this zone. This is because the component of the electric field parallel to conductivity boundaries is continuous across those boundaries, and therefore, the TE-mode responses are not anomalously perturbed from their normal

values. By carefully following the readjustment of the TM current system perpendicular to the ocean-continent boundary, one can map out anomalous vertical features in the lower crustal resistivity structure. (However, we would not be sensitive to anomalously conductive horizontal layers in the lower crust since we can only determine the integrated vertical resistivity properties.)

Because most of the geologic features in California are oriented parallel to the ocean-continent boundary, we are in a good position to look for anomalous zones in the lower crust in the region associated with the Loma Prieta earthquake. By mapping the TM-mode response across the fault at several different locations, we can look for anomalous vertical conductivity channels in the lower crustal part of the fault zone.

GEOLOGIC FRAMEWORK

California has been subjected to many tectonic events throughout its history, including arc-related compressional orogenies, arc volcanism and plutonism, and Cenozoic transform motion (Burchfiel and Davis, 1972, 1975; Dickinson, 1981). The geology in the area of the Coast Ranges of central California, as shown in figure 2, is characterized by three main lithologic sequences (Bailey and others, 1970; Page, 1981): (1) the Salinian formation (plutonic and metamorphic rocks from a magmatic arc environment), (2) the Franciscan formation (a subduction zone complex), and (3) the Great Valley sequence (forearc basin sediments). Interspersed among the outcrops of these formations are surface deposits that are predominately Cenozoic and Mesozoic marine and non-marine sediments and alluvium.

The Salinian block, bounded on the northeast by the San Andreas fault, is composed of metasedimentary rocks that have been invaded by granitic plutons. It is believed to have been translated some 600 km northward from its original position as part of the Klamath-Sierra Nevada terrane. The resistivities of the granites of the Salinian formation are much more resistive than the sedimentary and metamorphic rocks to the east, and are typically around 500 Ω-m (Mazzella and Morrison, 1974).

The Franciscan formation is an assemblage of both oceanic and terriginous materials. It consists of graywacke, shale, mafic volcanic rock, chert, limestone, and metamorphic rocks of zeolite and blueschist facies. These components commonly occur in a pervasively sheared argillaceous matrix. Much of the Franciscan formation has undergone blueschist metamorphism at temperatures of around 200°C and pressures of around 6–8 kbar (Page, 1981). It is believed that the Franciscan formation originated in a subduction zone along the western margin of the North American plate in the late Mesozoic era and that these rocks underwent metamorphism as the oceanic plate was subducted under the continental plate. Surface

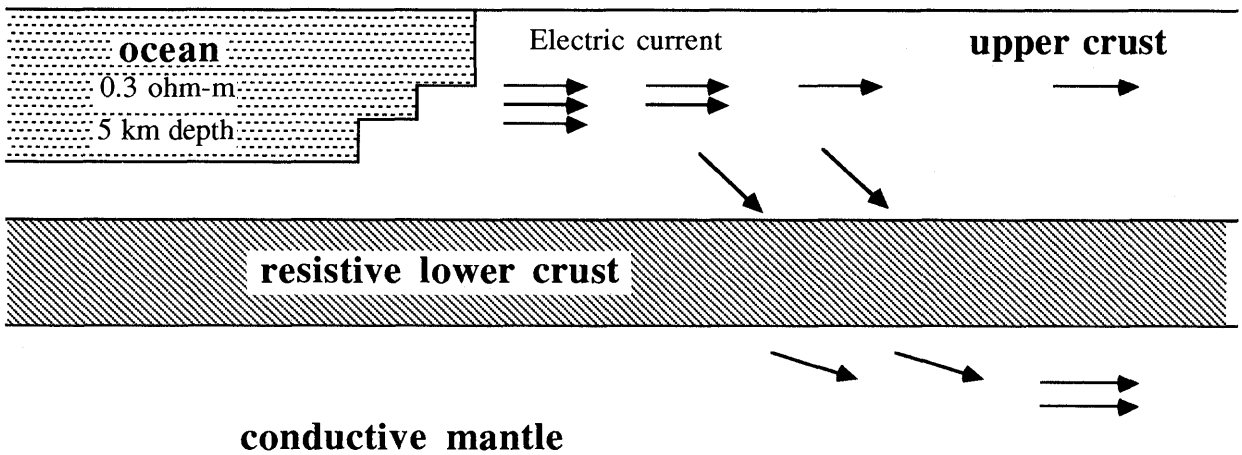

Figure 1.—Simple sketch showing the magnetotelluric TM-mode coast effect. The ocean induces extra current that gets trapped in the continental upper crust. This extra current in the continental upper crust gradually leaks off into the mantle as one moves away from the coast. This leakage effect is what makes one sensitive to the electrical properties of the lower crust.

electrical measurements show typical resistivity values of 5–50 Ω-m for the sedimentary and metamorphic rocks of the Franciscan formation (Mazzella and Morrison, 1974).

Finally, the Great Valley sequence is composed of stratified terriginous clastic sediments, primarily gray-wackes and shales, derived from the Klamath-Sierra Nevada terrane. These sediments are believed to rest on an ophiolite basement, beneath which the Franciscan formation has been thrust, and are even more conductive than the Franciscan rocks, typically being about 1–10 Ω-m.

THE MAGNETOTELLURIC DATA

A magnetotelluric survey was conducted in conjunction with Electromagnetic Instruments, Inc. (EMI) from October 20-30, 1990, one year after the Loma Prieta earthquake. EMI collected a total of ten sites in pairs of two simultaneous recordings, one on each side of the fault (except for site 10, which was on the fault because of logistical problems). Fig. 2 shows the locations of these stations. EMI collected E_x, E_y, H_x, H_y, and H_z data at each pair of stations using synchronized clock control. They recorded data in three bands, with sample frequencies of 500 Hz, 20 Hz, and 2 Hz, thus yielding coverage over a period range from approximately 0.005–1000 s. The data were processed to yield a 10 by 10 cross-power matrix per frequency (approximately 6 frequencies per decade) for each pair of stations. From this cross-power matrix, MT parameters could be computed using the horizontal magnetic fields at the second site as a remote reference.

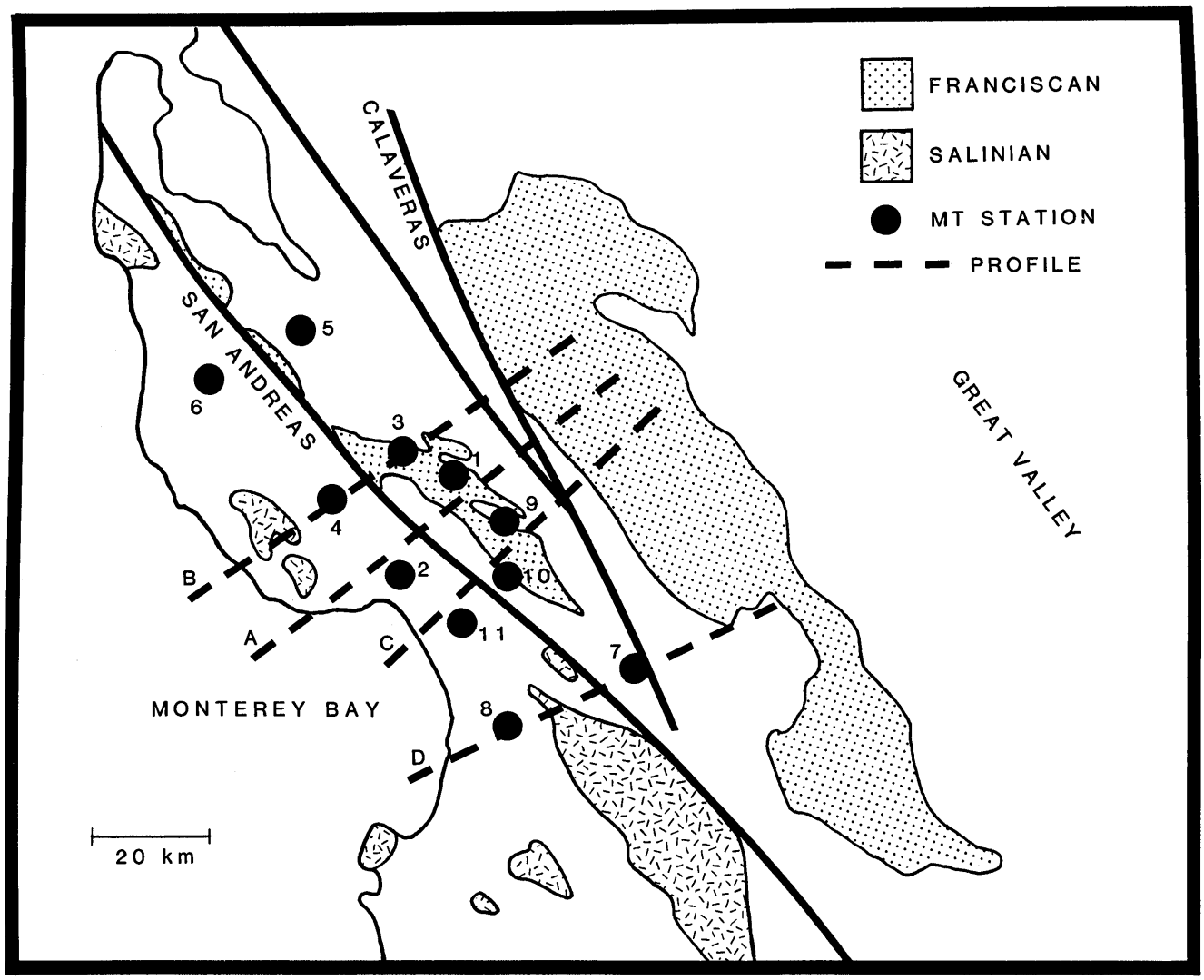

Figure 2.—Simplified geologic map (after Bailey, 1966) showing the locations of the Franciscan Formation, the Salinian Block, and major faults. In between the Franciscan and Salinian outcrops are surface deposits of marine and non-marine sedimentary rocks and alluvial deposits. Also shown are the location of the MT stations and the profiles used for the inversion analysis.

Remote referencing was fairly successful for canceling out the effects of random noise disturbances in the data at most sites, but there were additional noise problems that the remote referencing was not able to deal with. Robust processing methods also were not able to deal with those noise problems (Egbert, oral commun., 1992). In general, the data were noisier the closer they were to the industrialized San Francisco Bay area to the north. Sites 5 and 6, the furthest north, were the noisiest data of all and were basically unusable. Site 8 also was noisy, which we later discovered was because that site was located close to an electrical power sub-station.

At many of the sites (1,2,3,4,5,6) the data in the band from 1 to 100 s seemed to be contaminated by some man-made noise source. There are two lines of evidence for this. First, the magnetotelluric responses at these sites in this frequency band are characterized by slopes close to 1 in log of apparent resistivity versus log of period, and a sudden decrease of the phase to near 0°, which is characteristic of local noise sources (Qian and Pedersen, 1991). This is clearly evident in the MT data from site 1, Calero, shown in figure 3. Second, and probably more important, there is a large anomaly in the tipper magnitude from 1 to 100 s at these same sites. (Figure 4 shows an example of the anomaly from site 1, Calero.) The tipper is a measure of the ratio of the vertical magnetic field to the horizontal magnetic field. Local industrial noise sources, which act like vertical magnetic dipoles and horizontal electric dipoles, can create large tipper magnitudes which are clearly non-MT. These sources generate coherent electromagnetic energy, but their impedances are different than those of natural MT signals at periods longer than 1 s. At periods greater than 100 s, however, the natural MT signals were stonger than the man-made noise. It is possible that this noise problem is due to the BART transportation system in the San Francisco Bay area, which acts like a large vertical dipole (Fraser-Smith and Coates, 1978; Ho and others, 1979), although any local industrial source could cause similar features in the data.

At the same time that EMI was collecting data, we (Madden and Mackie) collected single-site, longer-period (10–1000 s) MT data at several additional stations, mostly along the San Andreas fault zone. We attempted to gather data at the same time EMI was collecting long-period data so we could use the EMI data for remote referencing (we synchronized our clocks with EMI's clocks every couple of days). However, because of logistical problems in setting up the stations, we were only successful in coordinating this at one site (site 11, shown on the map in fig. 2). At the other stations, the daytime man-made noise problems prevented us from obtaining valid impedance estimates. The data from the EMI group were generally less contaminated with the man-made noise because they typically collected their long-period data (greater than 1 s) during the night, when such noise is at a minimum, whereas we collected all our data during the day when these noise problems were highest. Unfortunately, the natural MT signals are also usually stronger during the day than at night, which reduces the advantage of night-time recording.

TWO-DIMENSIONAL INVERSION OF THE DATA

An eigen-state analysis (LaTorraca and others, 1986) was used to decompose the impedance tensors for each site. At all stations except site 3, the major electric eigenvector direction, which corresponds to the maximum amplitude eigen value of the impedance tensor, was approximately perpendicular to the coastline, and this is the mode we identify as the transverse magnetic (TM) mode. The TM mode near ocean-continent boundaries has lower phases at longer periods as compared with the TE mode. This is due to ocean electrical current perpendicular to the coastline being trapped in the continental upper crust (Mackie, 1991). At site 3, the maximum amplitude eigen value corresponded to the TE mode, and the TM mode corresponded to the minimum eigen value. We suspect this is due to local inhomogeneities that caused a static shift in the electric field perpendicular to the ocean and probably gave us a mixed MT impedance.

Data from sites 5, 6, and 8 were unusable because they were too contaminated by man-made noise. Data from the remaining sites were mostly usable, although we edited out the data at some of the sites (1,2,3,4) from 1 to 100 s that appeared contaminated by man-made noise sources. Finally, selective editing of outliers and obviously inconsistent data was done for all stations prior to running two-dimensional inversions of the data. The remaining data were input to the two-dimensional TM-mode inversion algorithm described in Mackie and others (1988). We used only TM-mode inversions of the data for two reasons: (1) the lower crustal resistivity anomalies discussed earlier affect only the TM mode and (2) two-dimensional TM-mode interpretation is more accurate for profiles centrally located across elongate three-dimensional bodies (Wannamaker and others, 1984). We do, however, show the TE-mode data and model predictions even though the TE data were not used in the inversions.

The inversion procedure we used to interpret the data is the one we term the maximum likelihood inverse (Mackie and others, 1988; Madden, 1990). The maximum likelihood inverse gives the solution that maximizes the joint probability of fitting the observed data, subject to data covariance constraints, and adhering to an *a priori* model, subject to model covariance constraints (Tarantola, 1987). Our formulation of the inverse problem holds the block geometry of the system fixed—only resistivities are al-

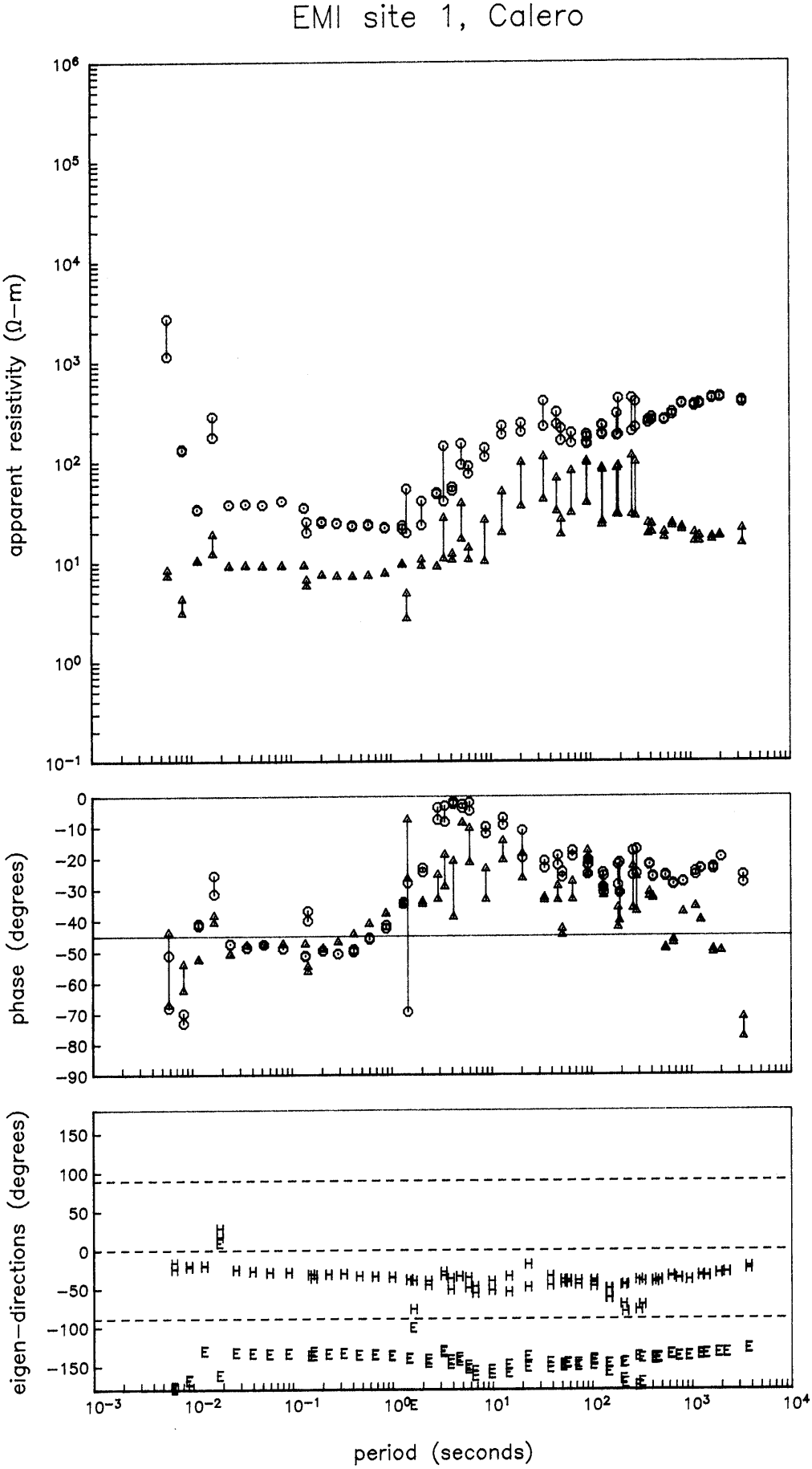
EMI site 1, Calero
apparent resistivity (Ω−m)
phase (degrees)
eigen−directions (degrees)
period (seconds)

◀ Figure 3.—Eigen-analysis results of the MT data at site 1, Calero. Shown are the maximum and minimum apparent resistivities, associated E/H phases, and the electric field and magnetic field eigen-directions. Note the steep slope in the apparent resistivities and phases near 0° in the period range from 1 to 100 s. We believe these are not natural MT responses but rather are due to Bay Area Rapid Transit noise contaminating the signals. This behavior was at most sites in our survey area.

lowed to vary during the inversion. Additionally, in all our inversions, we gave equal weight to fitting the phases and ln (amplitudes).

The profiles along which we did inversions are shown in figure 2. Each profile used data from only two or three stations. For each profile, we ran many inversions of the data using different model constraints and *a priori* models. The *a priori* models were all generally constrained using available geologic and geophysical data. First, we

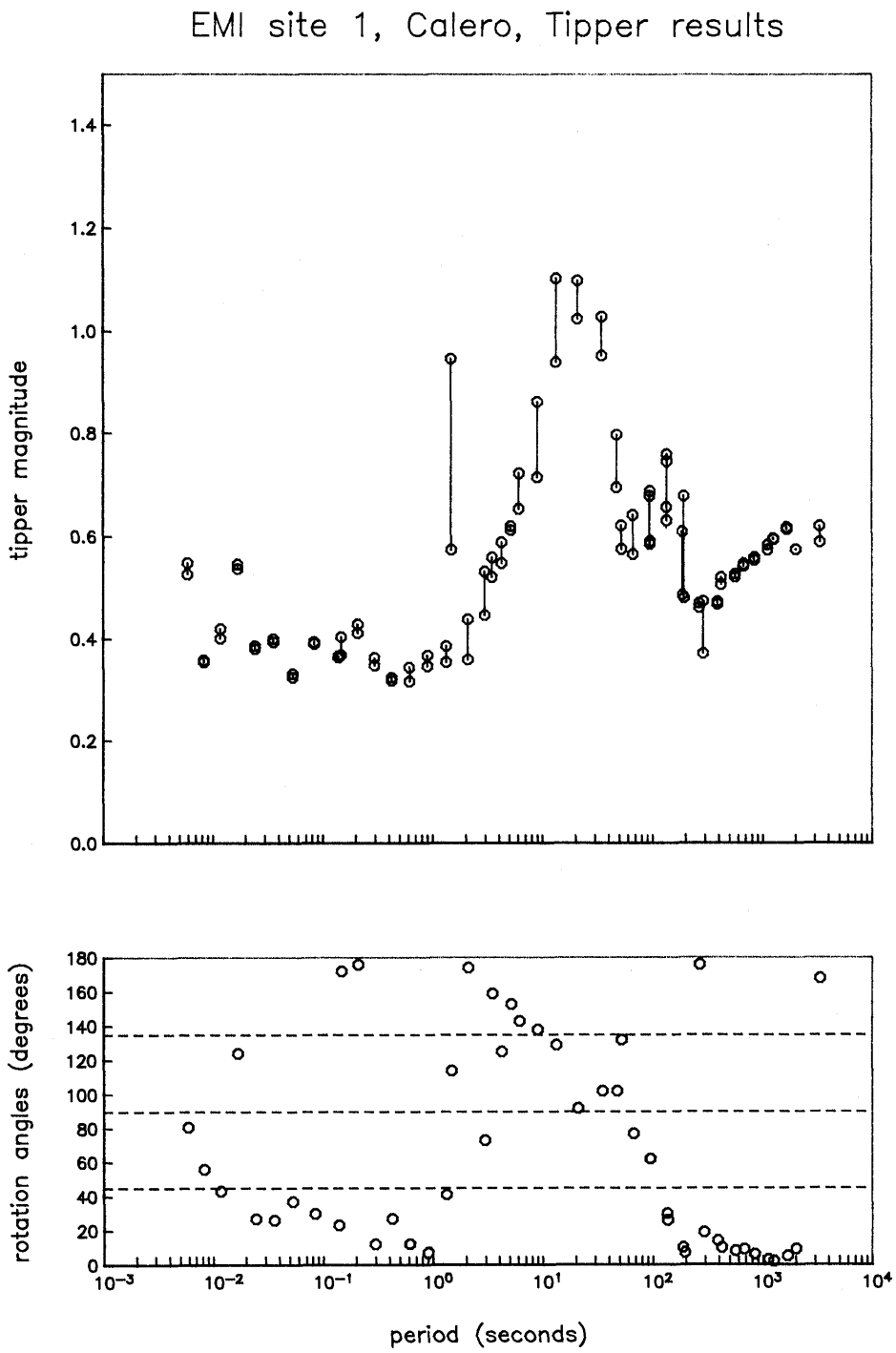

Figure 4.—Plot of the tipper amplitude at site 1, Calero. Shown are the amplitudes in the direction where H_z is most correlated with H_y. Note the large anomaly in the period range from 1 to 100 s. We believe this is evidence of Bay Area Rapid Transit interference in the natural signals. Similar anomalies were observed at most sites in our survey area.

used long-period (greater than 1 hour) MT data from the Hollister area (Bennett, 1985; Mackie and others, 1988), shorter-period (10–10,000 s) MT data from central California (Park and others, 1991), and the results of a controlled-source EM measurement on the Pacific Ocean floor (Cox and others, 1986) to constrain the lower crust and mantle *a priori* resistivity values. Second, we used the seismic tomographic inversions and MT analysis of Eberhart-Phillips and others (1990) to help constrain the *a priori* upper crustal resistivity variations. Third, we used bathymetric contour maps for approximating the ocean floor topography. Finally, we used surface geologic information (Clark and Rietman, 1973) for setting the very near surface resistivity information. We show one *a priori* model for profile A in figure 5. Other *a priori* models were tested that included putting vertical conductive zones in the lower crust and making the entire lower crust much more conductive. The *a priori* models for the other profiles are essentially the same except for minor upper crustal differences. The inversion procedure weights fitting the data much more strongly than adhering to the *a priori* model (by a factor of 10^5 in the ratio of the data to model covariances), although it never completely looses sight of the *a priori* model. The inversion procedure itself is not biased, although there certainly are biases introduced by our choice of an *a priori* model and by the *a priori* model constraints.

Profile A uses data from sites 1 and 2 and goes over the epicenter of the main earthquake shock. We feel that these data sites represent our best data, so we will focus on the results for this profile. In the following discussion, it should be understood that a lightly weighted smoothing operator and a small diagonal term were always included in the model covariance operator used in the inversion, and that an "unconstrained inversion" means no additional constraints were used beyond those, whereas a "constrained inversion" means additional constraints were used. A grayscale plot of the results of an unconstrained two-dimensional TM-mode inversion of the data from these sites is shown in figure 6. The horizontal scale of the plot is the square root of distance from the ocean-continent boundary. The vertical scale is the square root of depth, but we

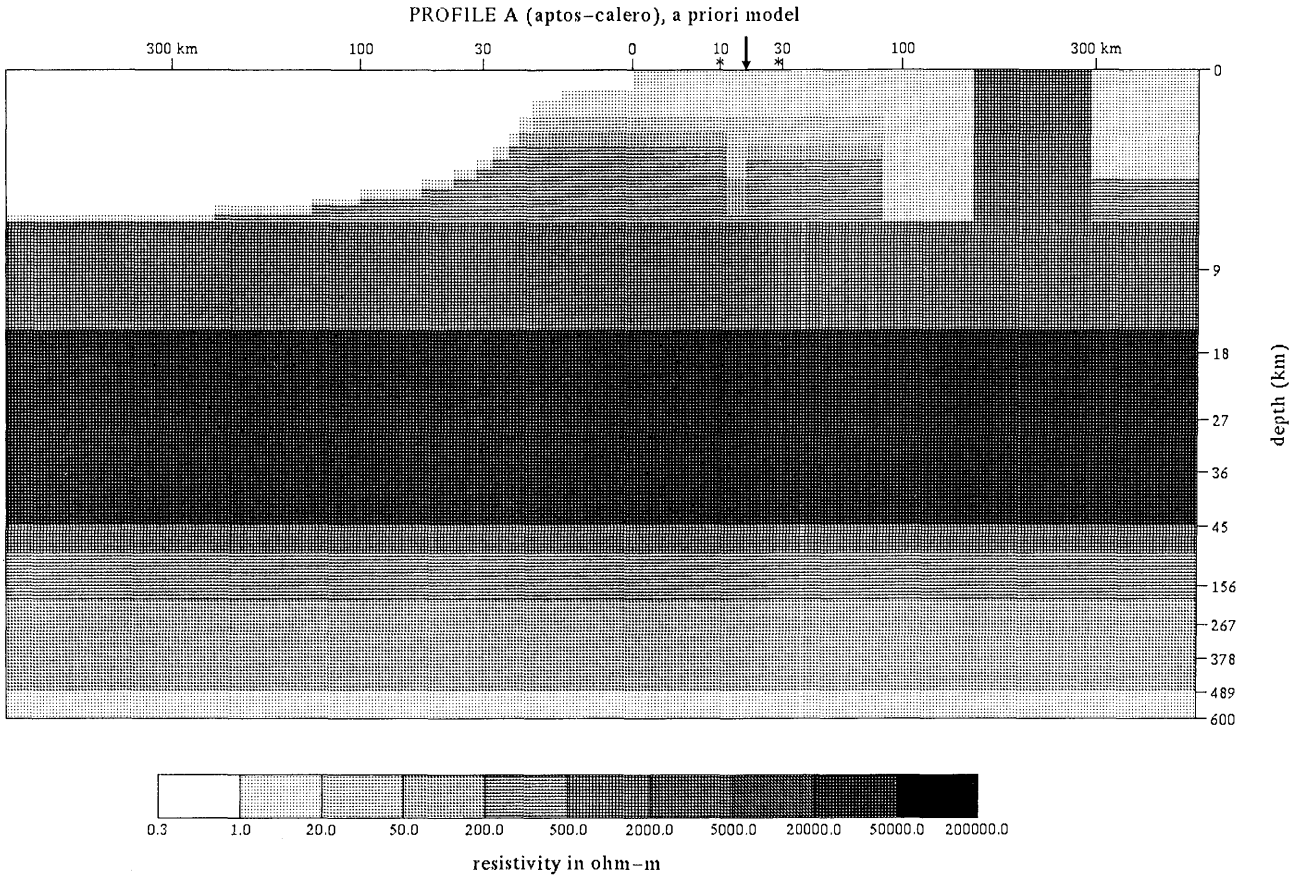

Figure 5.—Grayscale plot of the *a priori* model used for inversions along profile A (fig. 2). Resistivities are given in Ω-m. The horizontal scale goes as the square root of distance from the coastline. The vertical scale goes as the square root of distance and is broken up into two sections—one for 0–45 km and one for 45–600 km. On this and all other grayscale plots, the station locations are marked with asterisks and the San Andreas fault is marked with an arrow. See the text for a discussion of how the *a priori* values were set.

have broken it up into two different sections, the first one for 0–45 km depth and the second for 45–600 km depth. The models actually extend much further out on either side, but we show only the central portions of each one as there were only minor variations beyond the section we show. The station locations are marked with an asterisk. The inversion resulted in a wide area of increased conductance in the lower crust around the fault zone, with the largest change (10 times more conductance) concentrated in the immediate vicinity of the fault zone. Additionally, the lower crust was made more resistive away from the fault zone both under the ocean and under the continent. These changes were made by the inversion routine in order to, first, attract enough current onto the continental upper crust, and second, to lose enough of that current between the two data sites to fit the data at those sites. We show the predictions from this model in figure 7 as solid lines. (We show the predictions for all periods between 0.01 s and 2000 s even though the data from 1 to 100 s were not used in the inversion.) The TE-mode predictions are also shown, although we did not use them in the inversion analysis. (At some of the data sites there was a static shift between the observed TM- and TE-mode apparent resistivities. Therefore, in plotting out the predicted TE-mode data, we applied, where necessary, a static shift correction to the predicted TE data so that they agreed with the observed TE data at the higher frequencies.) As seen on this and following plots, the TE-mode predictions are actually quite good at most sites except site 7, Hollister, where they are the worst. This gives us increased confidence as to the validity of our two-dimensional interpretation.

We ran a second inversion of the data from profile A starting with the same *a priori* model except that we constrained the lower crust and upper mantle to remain at their *a priori* values. We show the resulting model in figure 8. For this inversion, we required all resistivity changes to be put into the upper crust. There are mostly minor changes in the upper crustal resistivity values as opposed to the results from the previous inversion, except just above the lower crust near the fault zone and under the Sierra Nevada. In both those places, the conductance

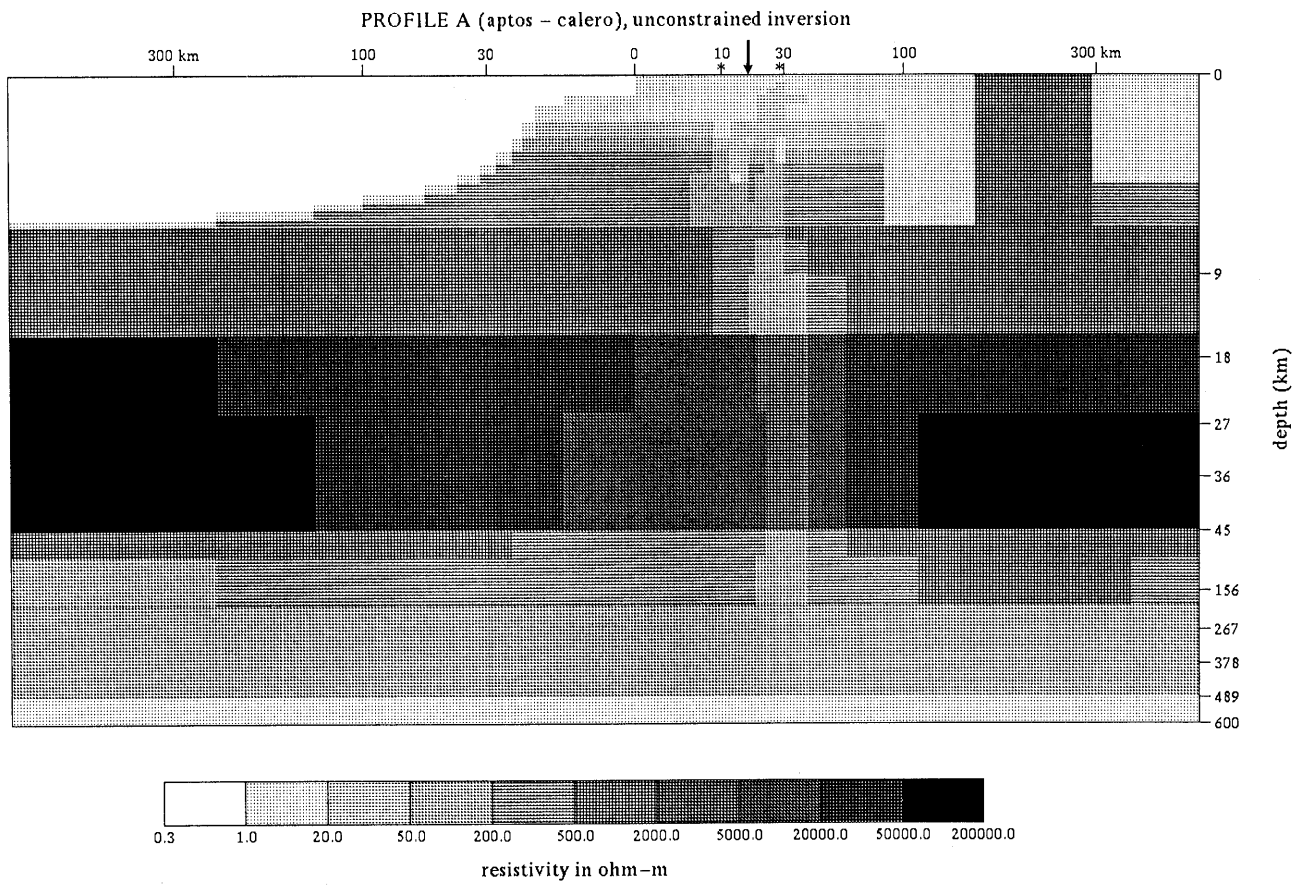

Figure 6.—Grayscale plot of the result of a smoothed but otherwise unconstrained two-dimensional TM-mode inversion of the data along profile A (fig. 2). Note the broad area of leakage put into the lower crust in the vicinity of the San Andreas fault zone. The data predicted by this model are shown in figures 7 and 9.

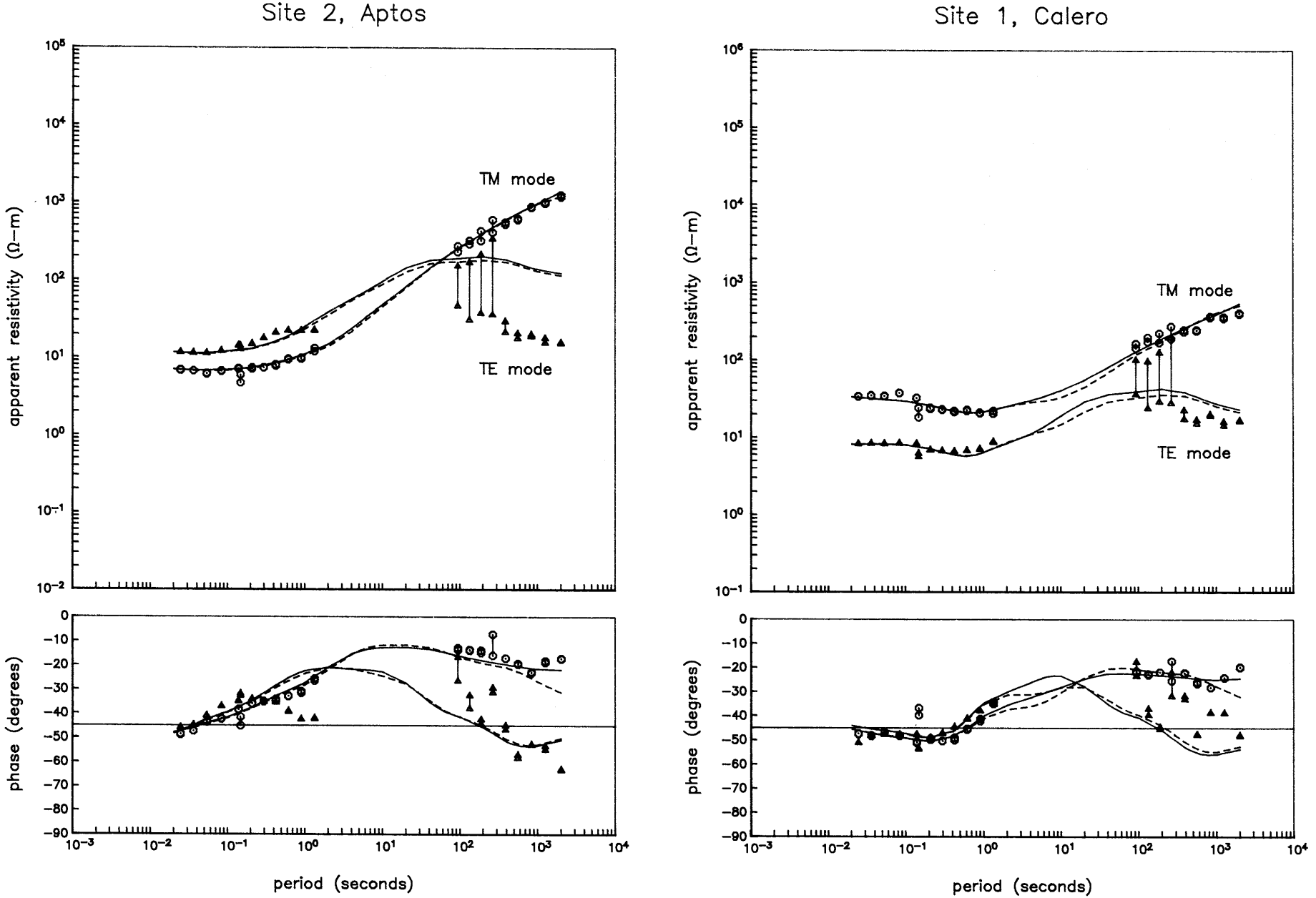

Figure 7.—Observed and predicted data at (left) site 2, Aptos (west of the San Andreas fault), and (right) site 1, Calero (east of the San Andreas fault). The solid lines are the predicted data from the model in figure 6, and the dashed lines are the predicted data from the model in figure 8. We show both the predicted TM- and TE-mode data, even though only the TM-mode data were used in the analysis. The predicted TE-mode data were static shifted so that they agreed with the observed TE-mode data at the highest frequencies.

was increased as compared to the previous inversion. This was most likely necessary to attract the additional current onto the continental upper crust and to pull it down from the surface to the bottom of the upper crust across the fault zone. However, the increased conductance under the Sierra Nevada is probably unrealistic (Park and others, 1991). We show the TM- and TE-mode predictions from this model in figure 7 as dashed lines.

Looking at figure 7, it seems as if there are not many differences in the predictions between the two models. This is because it is difficult to see subtle changes in the slopes of the apparent resistivities, but the changes in the phase are more obvious since they show integrated effects of changes in the apparent resistivity curves. In figure 9, we plot the observed and predicted TM phases for the two models just discussed. In this figure, the circles correspond to the TM phase data from site 2, Aptos (nearest the ocean), and the triangles correspond to the TM phase data from site 1, Calero. The predicted data from each site are shown with solid and dashed lines respectively. The TM-mode data show an increase of about 5-10° in the magnitude of the phase from site 2, Aptos, to site 1, Calero, and with our choice of *a priori* model, this is fit only when the inversion puts a conductive window in the lower crust.

Unfortunately, the interpretation of these data is nonunique. With the resistive lower crust we put into the *a priori* models, the observed data cannot be fit without changes in the lower crustal resistivity between the two stations. However, there are other models that can fit the observed data without any lower crustal leakage paths and using only upper crustal resistivity variations (Eberhart-Phillips and others,1990; Stanley, oral commun., 1992). These models, however, must have lower crusts with much lower resistivities than we have put into our models (1,000 Ω-m vs. 30,000 Ω-m). Although these models will fit the observed data at the shorter periods, they fail to predict the longer period data that we have previously analyzed at Hollister (Mackie and others, 1988). We have, however, used the results of that study to help constrain our interpretation in this study. This is because at the longer periods involved in the Mackie and others (1988) study, the electric fields perpendicular to the coastline at longer periods must be similar up and down along the coast since the curl of the electric field must be small at these periods and any significant changes in the

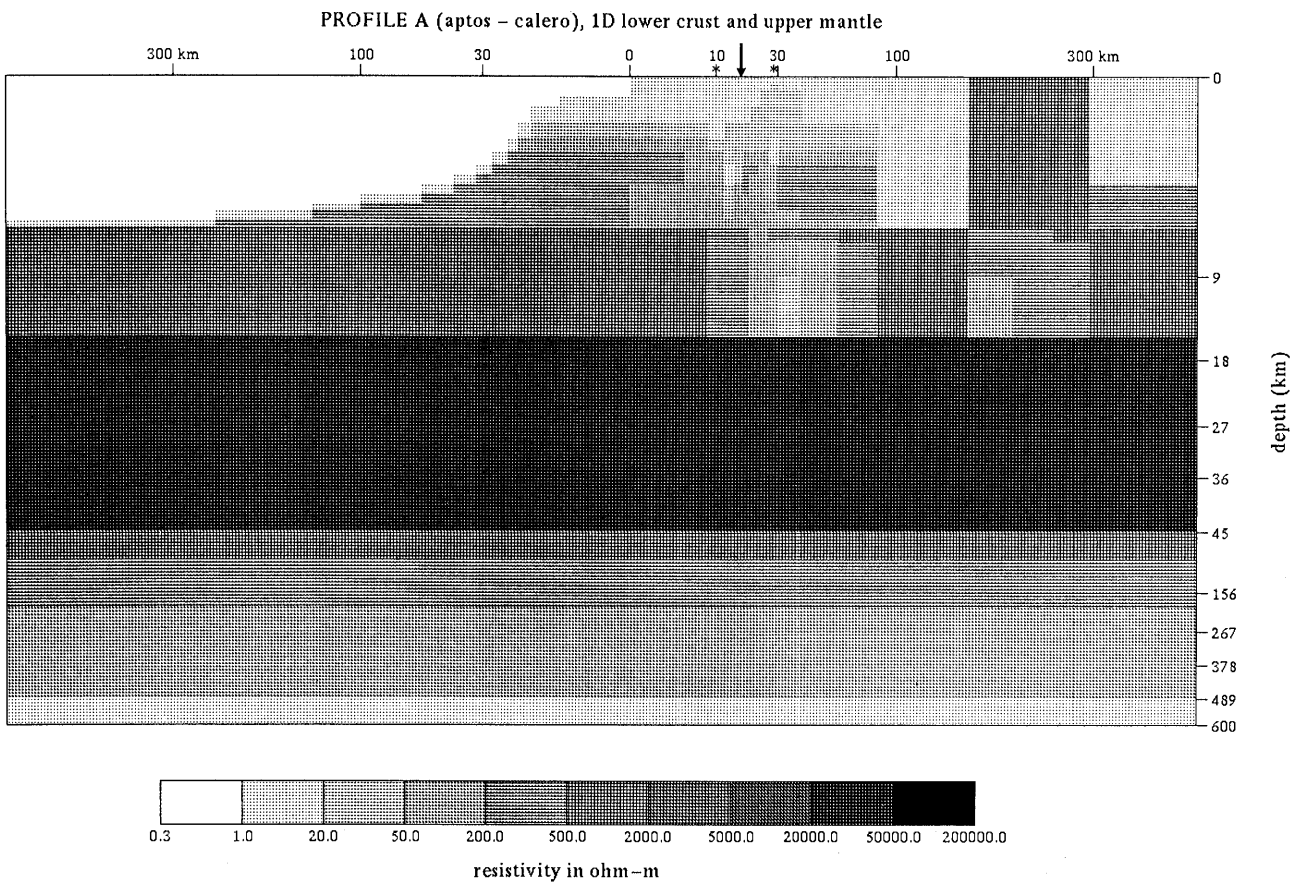

Figure 8.—Grayscale plot of the result of an inversion that kept the lower crust and upper mantle at its *a priori* values, thus forcing all changes to be put into the upper crust. The data predicted by this model are shown in figures 7 and 9.

Model 1, conductive window in lower crust

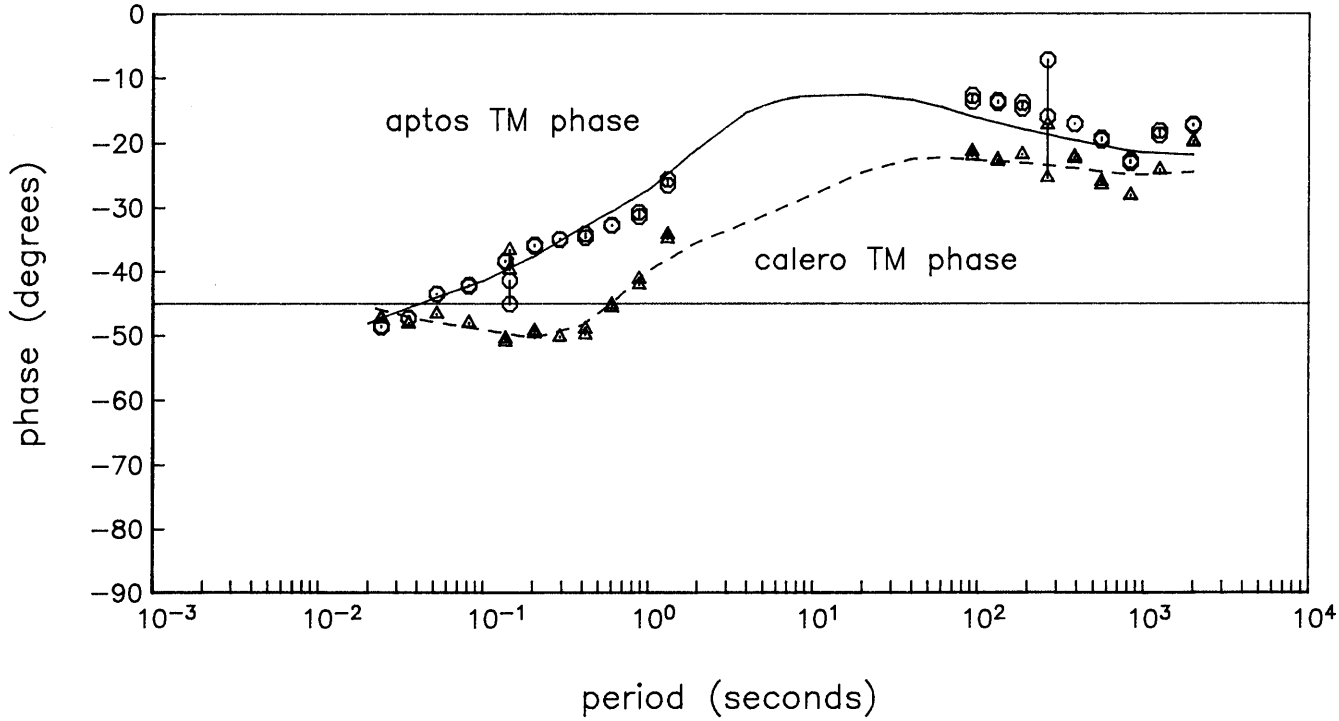

Model 2, uniform lower crust and mantle

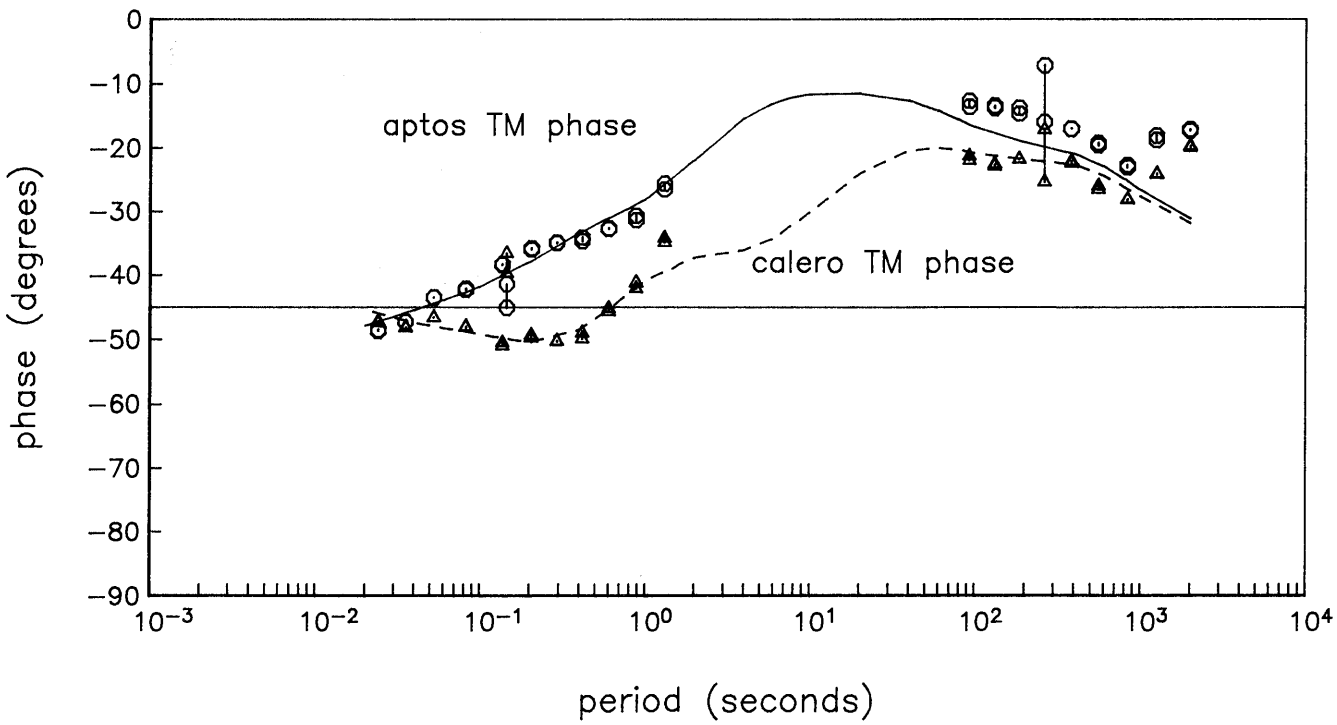

electric field would involve huge vertical magnetic fields. Therefore, any model we produce to fit the shorter period data of this study should also do a good job at predicting the longer period data of the Mackie and others (1988) study. The longer period data are especially sensitive to the lower crustal and mantle resistivity properties, and therefore, even though we did not explicitly include them in the inversion scheme, they played an important role in constraining the range of possible models that fit the data.

The unconstrained inversion increased the conductance in the lower crust over a broad zone, but the data are not sensitive to the details of the geometry of the lower crustal leakage path between the two stations. Physically, it is probably more realistic that any anomalies in the lower crustal resistivity around the Loma Prieta earthquake area would be concentrated in a narrower zone. The broad zone of lower crustal leakage shown in figure 6 has a horizontal dimension of approximately 50 km. If that lower crustal leakage zone was made 10 times narrower (5 km), then it should require 10 times more conductance to get the same amount of current leakage as the broader zone. For the model in figure 6, this corresponds to a lower crustal resistivity value somewhere between 100 and 1,000 Ω-m for a zone 5 km wide versus 1,000–10,000 Ω-m for a 50-km-wide zone.

Therefore, we assigned a narrow conductive leakage path in the lower crust for the *a priori* model and ran an inversion. This inversion reduced the resistivity in the lower crustal fault zone from its *a priori* value of 1,000 Ω-m to approximately 300 Ω-m, and slightly increased the resistivity under the western edge of the Sierra Nevada (fig. 10). This was necessary to encourage leakage through the narrow zone. The predicted and observed TM-mode phases are shown in the top panel of figure 11. This model resulted in a little more separation in the phases than the previous unconstrained model in figure 6 because the narrow zone loses more current across a short

◀ Figure 9.—Plot of the observed and predicted TM-mode phases for the model of figure 6 and the model of figure 8. Note that the data are fit only when the inversion is allowed to put some leakage into the lower crust. If the lower crust and upper mantle are uniform, then the observed data cannot be fit.

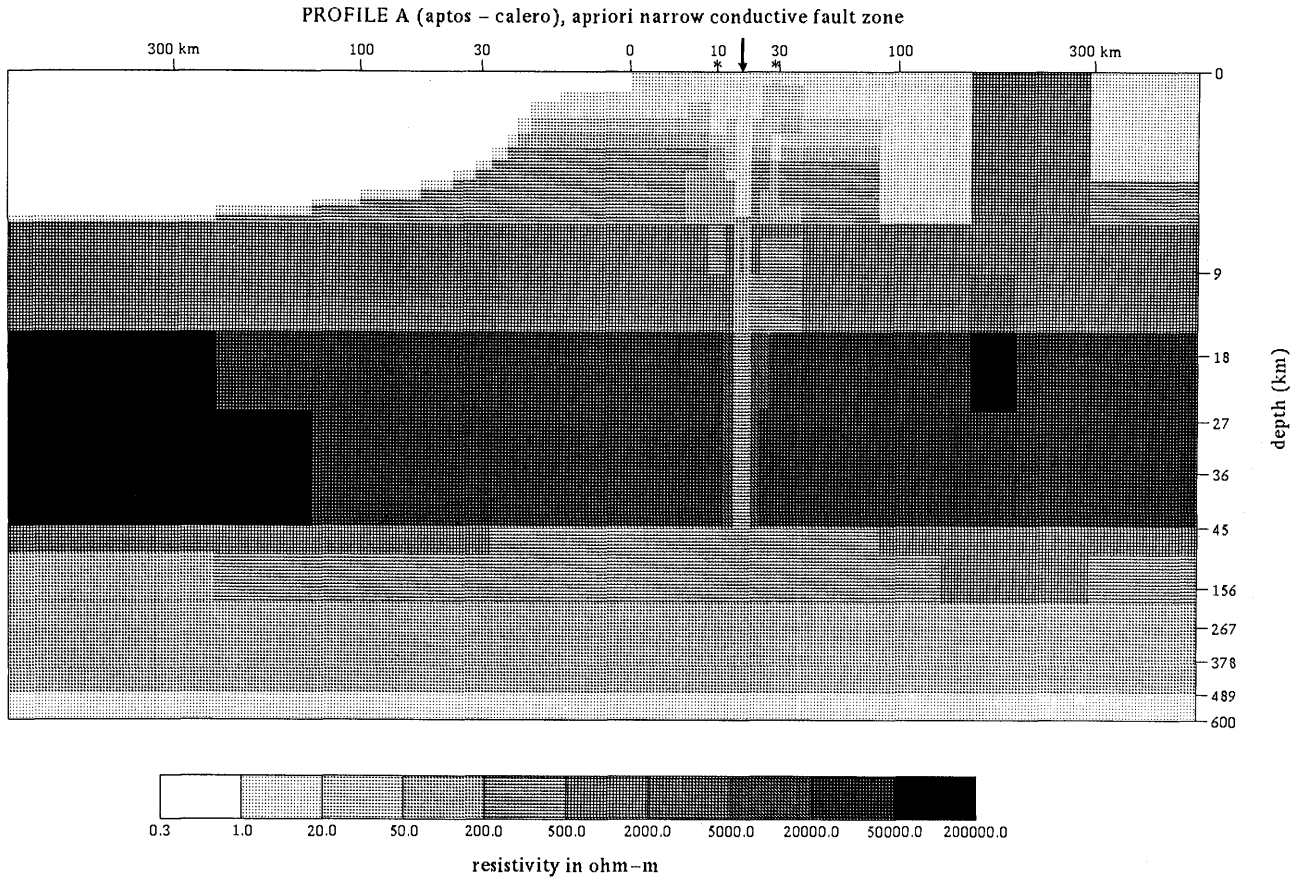

Figure 10.—Grayscale plot of the result of an unconstrained inversion of the data along profile A where the *a priori* model had a narrow conductive (1,000 Ω-m) fault zone in the approximate position of the San Andreas. The inversion made the fault zone even more conductive, forcing it down to about 300 Ω-m. The data predicted by this model are shown in the top panel of figure 11.

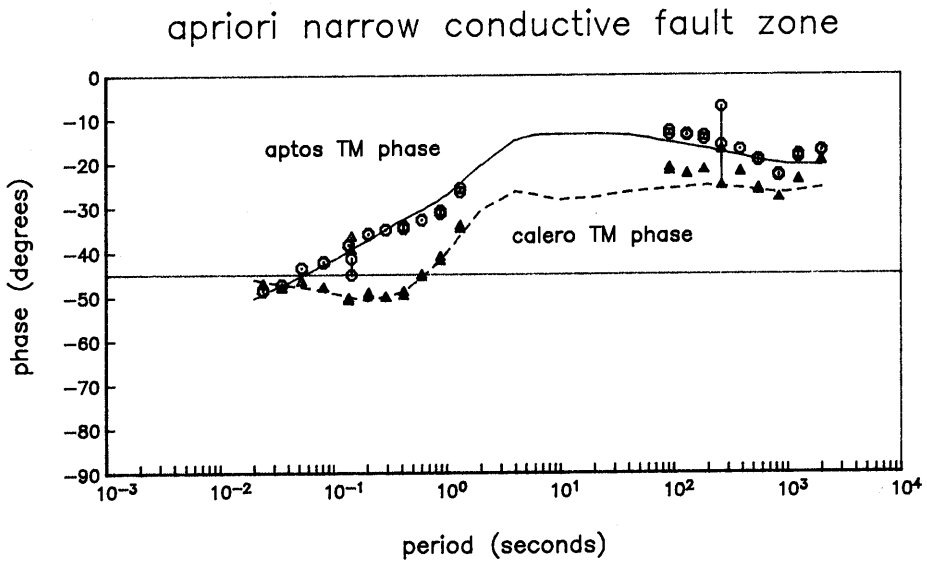

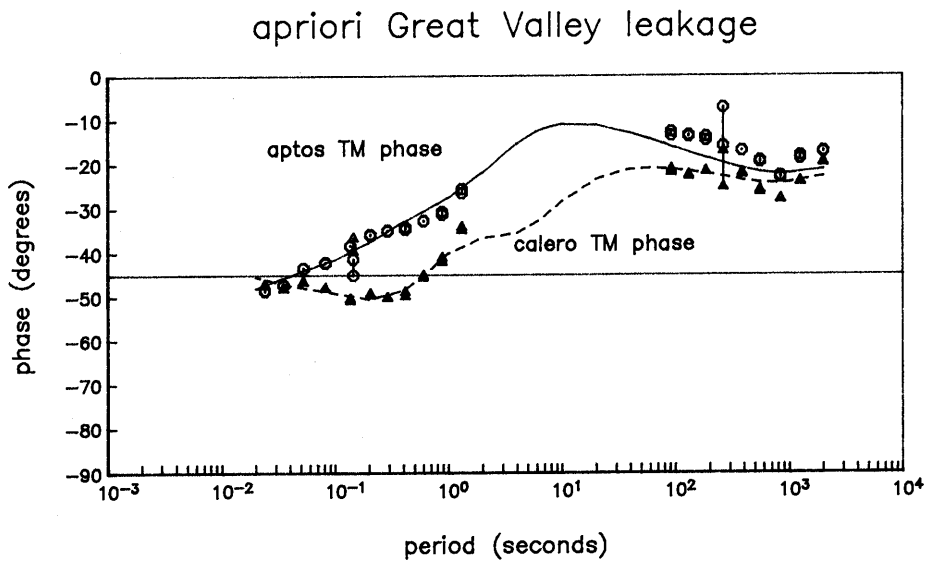

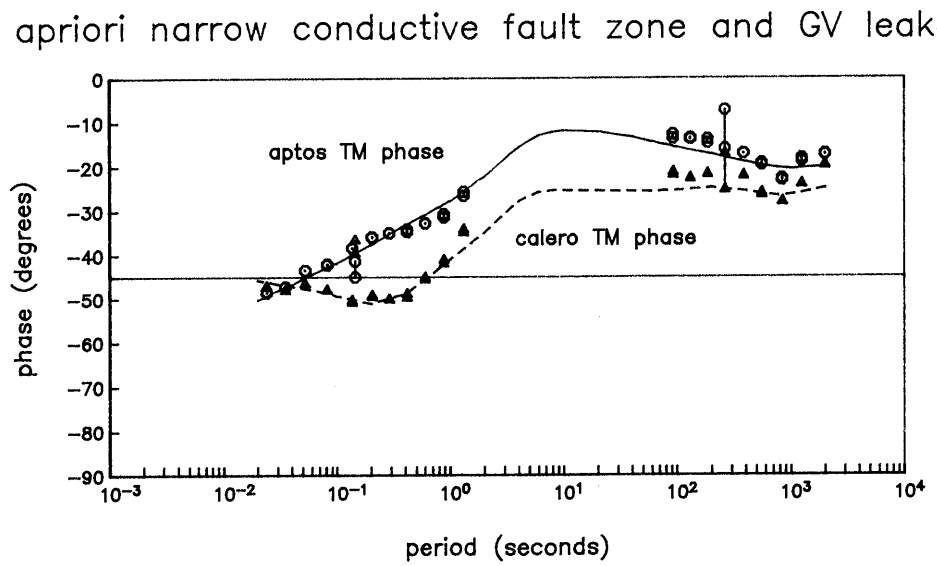

Figure 11.—Plots of the observed and predicted TM-mode phases for three different inversion results. In the top panel are the predictions for the model in figure 10. The middle panel shows the results of an inversion with *a priori* Great Valley leakage, and the bottom panel shows the results of an inversion with *a priori* Great Valley leakage and a narrow conductive fault zone.

distance as opposed to the broad zone. (It should be noted that due to the smoothing constraints of our inversion scheme, it is difficult for the inversion to put in abrupt conductivity boundaries unless they were assigned *a priori*, which is why the unconstrained inversion put in a broad zone of increased conductance.)

Although we did not have data further to the east in the Great Valley and Sierra Nevada, we felt it was important to see how the inferred leakage zones of Park and others (1991) on both sides of the southern Great Valley might affect the interpretation of our data. Park and others (1991) collected data within 100 km of our test area, but he observed longitudinal uniformity of the Great Valley resistivity structure over a distance of approximately 150 km, so it is likely that the inferred Great Valley leakage paths of Park and others (1991) would exist further to the north near our study area. Therefore, we ran an inversion where we *a priori* assigned the Great Valley leakage zones using the results of Park and others (1991) as a guide in setting the resistivities and widths of those zones. The Great Valley leakage has the effect of attracting more ocean current onto the continental upper crust. Consequently, the inversion did not need to make the oceanic lower crust as resistive as did the unconstrained inversion without Great Valley leakage (fig. 6). As before, however, it put in a broad area of increased conductance around the Loma Prieta earthquake zone, with electrical properties not much different than before. The observed and predicted TM-mode phases are shown in the middle panel of figure 11. This model does not fit the observed data as well as the previous model with an *a priori* narrow fault leakage zone. If, however, we run an inversion where we *a priori* assign the Great Valley leakage and a narrow conductive fault zone, we find that the resulting model predicts the observed data very well, and this is shown in the bottom panel of figure 11. The lower crustal resistivities of the narrow fault zone were again reduced to around 300 Ω-m from the *a priori* values of 1,000 Ω-m, but the inversion also put in increased conductivities around the narrow fault zone to account for the extra current from the Great Valley leakage.

SUMMARY OF MODELING RESULTS

Although the interpretation of our data is non-unique, we believe it is likely that there is a vertical lower crustal conductive zone in the vicinity of the San Andreas fault. In a smoothed but otherwise unconstrained inversion, a broad area of increased conductance in the lower crust was put in by the inversion. Another inversion of the data that fixed the *a priori* lower crust and upper mantle (all changes forced into the upper crust) was not able to fit the data as well and required some unrealistic resistivities under the Sierra Nevada. It is possible, however, to fit the data without any lower crustal leakage paths (Eberhart-Phillips and others, 1990; Stanley, oral commun., 1992), but these models require much more conductive lower crusts than we put into our *a priori* models, and they do not give model responses that agree with the longer period data we have analyzed at Hollister (Mackie and others, 1988). The inferred Great Valley leakage of Park and others (1991) had only a minor effect on the results of the inversions, and that was mainly in the resistance of the lower crust away from the fault zone. Although we cannot determine the exact geometry of the lower crustal leakage, we suspect a narrow conductive zone is geologically more realistic.

For the remaining profiles, we tested the various hypotheses for lower crustal leakage just described for profile A. The results for profiles B and C were similar to those obtained for profile A in that unconstrained inversions resulted in broad zones of increased conductance in the lower crust around the San Andreas fault zone. As for profile A, these data could also be fit with models that resulted from inversions with *a priori* narrow lower crustal fault zones. For the sake of brevity, however, we will only show the model predictions from the results of two different inversions of the data for each of the remaining profiles. For the first inversion, we started with an *a priori* model that had a narrow conductive fault zone and Great Valley leakage. The upper mantle and lower crusts in these models were similar to those that resulted from inversions of the data along profile A, and for this inversion we forced all changes to be made only in the upper crust and in the lower crust in the vicinity of the San Andreas fault. This is a reasonable approach since all the profiles should see approximately the same lower crust and upper mantle away from the fault zone. For the second inversion, we took out the narrow fault zone and Great Valley leakage and forced all changes to be put only into the upper crust.

The results of the inversions along profile B (figs. 12, 13) again suggest the existence of a conductive zone in the lower crust in the vicinity of the San Andreas fault zone similar to that shown in figure 10 for profile A. The statements made earlier about non-uniqueness and alternative models apply along this profile as well. There is a change of almost 20° in the observed TM-mode phase between the two sites along this profile, although they are only separated by a distance of 17 km. (The amplitude of the phases at site 4, however, seem to be somewhat too low in comparison with the slope of the apparent resistivity curve, so the true change in phase across the zone may be a little less than 20°.) The only way the inversion can even come close to fitting the data is by making the narrow fault zone very conductive (approximately 50 Ω-m over the 5 km width as compared to 300 Ω-m for profile A). The results from the inversion that constrains the lower crust and upper mantle to remain fixed at their *a priori* values show that the current levels

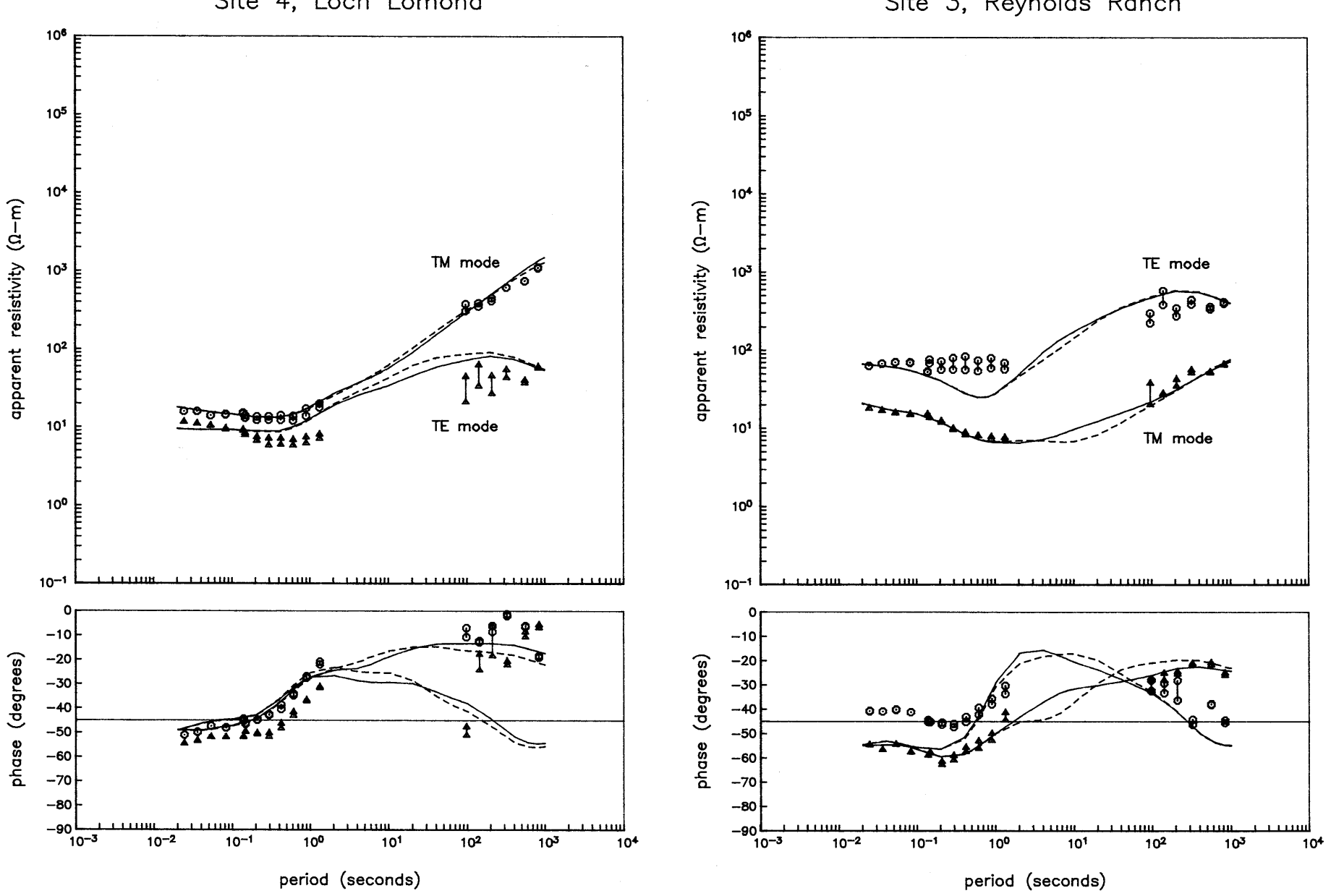

Figure 12.—Observed and predicted data at (left) site 4, Loch Lomond (west of the San Andreas fault), and (right) site 3, Reynolds Ranch (east of the San Andreas fault). The solid lines are the predicted data from an inversion with an *a priori* narrow fault zone, and the dashed lines are the predicted data from an inversion where no fault zone was put into the *a priori* model and all changes were forced into the upper crust. We show both the predicted TM- and TE-mode data, even though only the TM-mode data were used in the analysis. The predicted TE-mode data were static shifted so that they agreed with the observed TE-mode data at the highest frequencies.

and changes in those levels across the fault zone are incorrectly predicted.

On the other hand, the data from the sites along profile C show very little systematic separation in phases across the fault zone (figs. 14, 15). The data at the stations along this profile did not have anomalous tippers in the band from 1 to 100 s, but the apparent resistivities and phases were not quite consistent with each other either (the data from 0.1 to 1 s were not used because of noise). For inversions where the data from 1 to 100 s were not used, as with profiles A and B, results were obtained that indicated that some lower crustal leakage was preferred by the inversions, but not nearly as much as indicated for profiles A and B. When we included the data from 1 to 100 s in the inversion, then lower crustal leakage similar to that in profile A was preferred. The model predictions for the inversion without the conductive fault zone are not too different than those with the narrow fault zone, except that there is more separation between the curves when the fault zone is included. The results along this profile are too ambiguous to make any definitive statements about lower crustal leakage here, but the inversions clearly favored some lower crustal leakage when no constraints were placed on the inversions.

Finally, we look even further south to profile D, located near Hollister. The town of Hollister is actually in the creeping section of the Calaveras fault. The transition from creeping to locked behavior along the San Andreas fault occurs near the town of San Juan Bautista just west of Hollister. Unfortunately, the data from EMI site 8 was unusable, so we only had data from site 7 to use for the inversion. The data for this site is a combination of the original EMI data and MIT data from our second trip out to the field. The data for periods greater than 10 seconds is the MIT data (this was more coherent and less noisy than the original EMI data), and the higher frequency data is the EMI data. With just one station, we cannot say anything definitive about the resistivity structure along this profile except that the general trend of the data is in keeping with the data further to the north. These data can be fit equally well with or without a conductive zone in the lower crust (fig. 16).

Before we end this section, let us return briefly to the issue of the TE-mode data and model predictions. In all cases except site 7, Hollister, the predicted TE-mode data were actually fairly close to the observed data even though they were not used in the inversion analysis. It is well known that the TE-mode response can be dramatically altered because of finite strike lengths of bodies or other three-dimensional inhomogeneities, whereas the TM mode is much less affected (Wannamaker and others, 1984). Near the interior edge of a conductive three-dimensional body, the fields will be depressed because not enough current is induced in the body to bring the levels up to their two-dimensional values, nor is enough current gathered into the body to do likewise. This depresses the MT response there as compared to what would be observed for a two-dimensional model with infinite strike. This flattens out the TE response, which is what we observe at the Hollister site. The fact that Hollister sits in a conductive valley and thus may be seeing the effects of finite strike lengths may explain the disparity at this site between its observed and predicted TE-mode data.

GEOPHYSICAL IMPLICATIONS FOR THE SAN ANDREAS FAULT SYSTEM

In general, the electrical conductivity and distribution of fluids in the lower crust has always been somewhat of an enigma. The fact that finite resistivities are measured for the lower crust most likely implies that it has a small, connected, and fluid-filled porosity (Brace and others, 1965; Lee and others, 1983; Shankland and Ander, 1983), although graphite has also been proposed as a possible conduction mechanism in the lower crust (Duba and Shankland, 1982; Frost and others, 1989). There are many lines of evidence suggesting that free water is present to at least moderate depths within the crust. These include electromagnetic field studies (Shankland and Ander, 1983), isotopic studies of batholithic rocks (for example, Taylor, 1977), geochemical studies (for example, Kerrich and others, 1984; Kerrich, 1986), analyses of metamorphic rocks (for example, Etheridge and others, 1984), and seismic studies (for example, Nur and Simmons, 1969; Jones and Nur, 1982). At greater depths within the crust, the issue is far more controversial since granulite facies rocks and anhydrous mafic silicates (such as garnets and pyroxenes) commonly associated with the lower crust indicate that it should be fluid-free (Newton, 1990). It is argued (Yardley, 1986) that any water introduced into a granulite facies lower crust would be consumed by rehydration reactions forming lower-grade minerals. However, it is also possible that a small amount of water may be present in the lower crust in equilibrium with a hydrated mineralogy that is not present at the Earth's surface (Gough, 1986).

Even if a very small amount of free water does exist in the lower crust, it may not necessarily exist in a connected form; rather, because lower crustal rocks are believed to deform ductilely, it is conceivable that the water may exist only in isolated pockets or in absorbed hydrous phases unless the wetting angles are low enough (Watson and Brenan, 1987) or unless fluid pressures can be maintained at close to the rock pressure for geologically significant times (Walder and Nur, 1984). Another problem with maintaining water in a permeable crust is that over a period of time, the water should migrate upwards and out of the lower crust, unless it is trapped by some impermeable layer, because of buoyancy forces (Bailey, 1990).

apriori narrow conductive fault zone

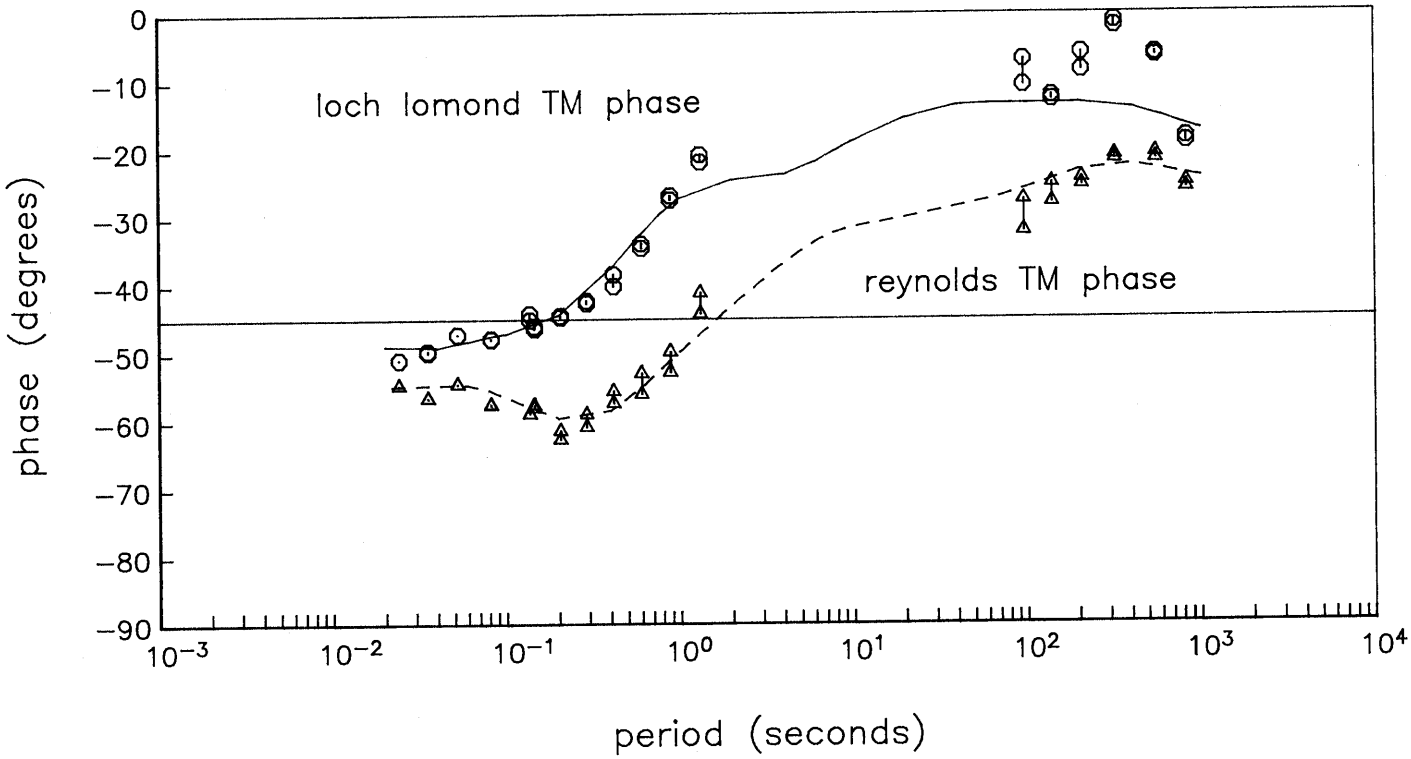

no fault zone allowed

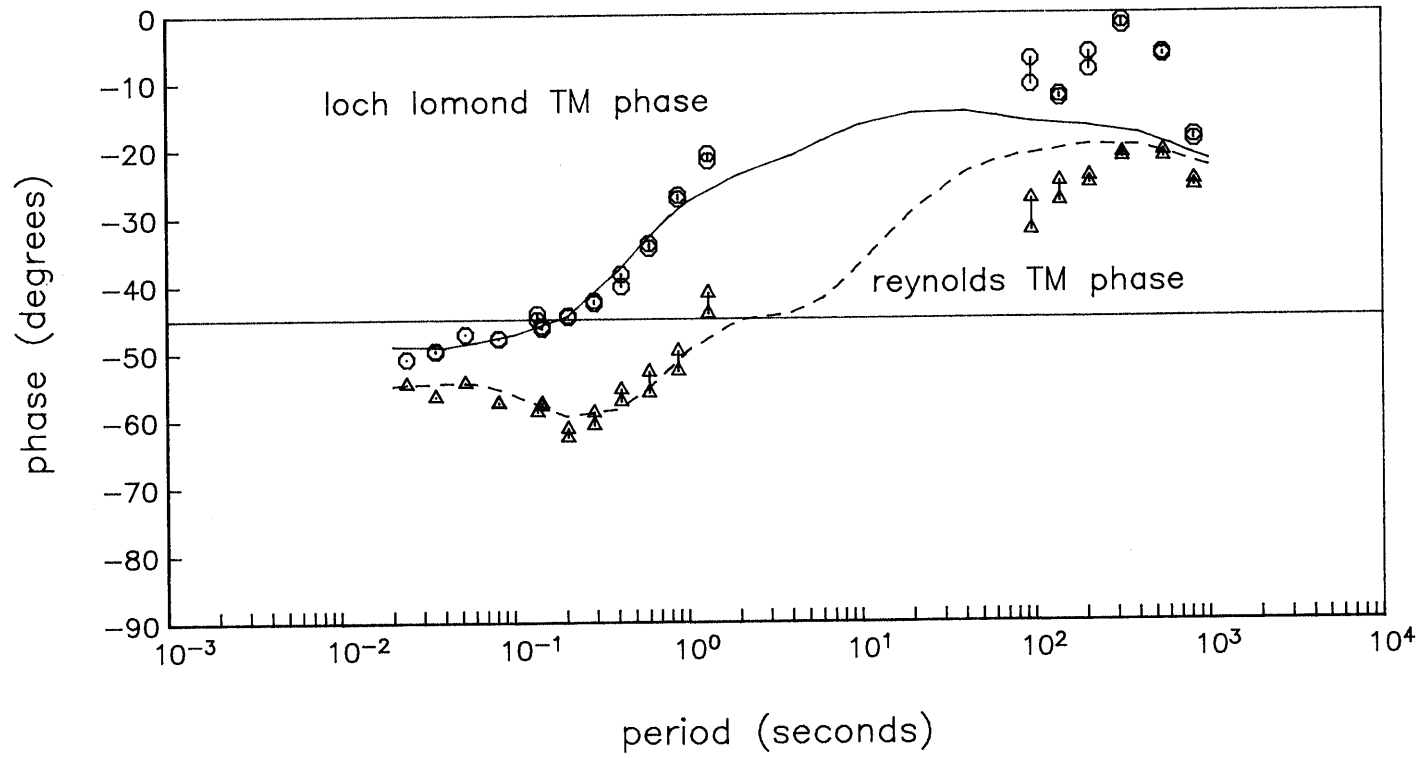

This may not be an issue if the hydraulics of the Earth's crust are time-dependent (Nur and Walder, 1990), as is quite likely.

Our inversions of the Loma Prieta magnetotelluric data suggest that there may be vertical zones of increased electrical conductance in the lower crust that broadly correlate with the San Andreas fault zone in the area that was involved with the Loma Prieta earthquake. Our findings are contrary to those of Park and others (1991) and Eberhart-Phillips and others (1990) who found no evidence for an anomalously conductive San Andreas fault zone. However, in a study of the telluric field variations around the Palmdale section of the San Andreas fault (Madden and others, 1993), systematic changes in the telluric field relationships were attributed to small increases in the lower crustal conductance in a vertical zone associated with the San Andreas fault (60 milli-Seimens over a 5-year period, which is too small to be seen by MT measurements). The strain necessary to cause this increase in lower crustal conductivity would be less than could be measured by the usual surface-strain measurements.

We believe that connected fluids in the lower crustal part of the fault zone are responsible for its high conductance relative to the lower crust away from the fault zone. The question, then, is about what amount of fluid are we talking? Typically, porosity estimates for the lower crust are derived by using Archies Law with an exponent of 2 (Brace and others, 1965) and the laboratory values for saline solution resistivities at high pressures (Quist and Marshall, 1968), which probably results in overestimates of the fluid porosities. This is because, first of all, an exponent of 1 in Archies Law is probably more appropriate for lower crustal conditions. Looking at the data in Brace and others (1965), we see that the resistivity of crystalline rocks at pressures from 0 to 10 kbar is linearly dependent upon the crack volume of the rock, thus implying that the resistivity is linearly related to the crack porosity. In lower crustal crystalline rocks, conduction is almost certainly through microcracks and along grain-edge tubules as opposed to pores in sedimentary rocks. The much more efficient connectivity of this pore geometry greatly reduces the amount of fluid needed to explain the resistivity of lower crustal rocks compared to Archies Law for sedimentary rocks. Secondly, the data from Quist and Marshall (1968) were for saline solutions only up to 0.1 molar, whereas deep crustal fluids are almost certainly much more saline (Orville, 1963; Roedder, 1972). Recent laboratory work on more concentrated saline solutions (Ucok and others, 1980) show fluid resistivities about an order of magnitude lower than the results of Quist and Marshall (1968) at lower crustal conditions.

◀ Figure 13.—Plot of the observed and predicted TM-mode phases for the inversion results with and without an *a priori* narrow conductive fault zone. Note that the data are fit only when there is lower crustal leakage around the San Andreas fault zone.

The results of our MT inversions suggest that resistivities in the lower crustal fault zone averaged over a 5-km-wide zone may be as low as 50 Ω-m. Concentrated saline solutions (20 wt percent NaCl) at temperatures of around 300°C for the lower crust have resistivities of about 0.01 Ω-m (Ucok and others, 1980). Using these values and an exponent of 1 in Archies Law yields a connected porosity of approximately 0.02 percent for a 50 Ω-m, 5-km-wide fault zone if the connections are efficient. We should really multiply this by three due to inefficiencies in tubule connection, thus yielding a porosity of 0.06 percent. (Compare this with a 0.0001 percent porosity estimate for the lower crust away from the fault zone with a resistivity of 30,000 Ω-m.) If the same amount of conductance were put into a fault zone 1 km wide, it would need to have a resistivity of 10 Ω-m to give the same leakage effect. This translates to a porosity of 0.3 percent. Similarly, a 100-m-wide fault zone zone would require a connected porosity of 3.0 percent.

If the lower crustal part of the San Andreas fault zone is as conductive as our inversions suggest, then this will have important implications for the fluid regime of the lower crustal part of fault zones. The question we cannot answer is whether the inferred high conductance of the lower crustal part of the fault zone is an inherent feature of fault systems, or whether it results from the earthquake itself. We do not believe that it is a permanent feature of the fault zone because non-elastic healing processes over time would close up much of the porosity connectivity, thus decreasing the conductivity. We believe a more likely scenario is that the hydraulics and conductivity of fault zones are time-dependent. While brittle failure occurred down to at least 18 km depth, any pore-pressure buildup before the earthquake associated with the closing of permeable pathways would increase the likelihood of semi-brittle failure down to depths below the main shock of the earthquake. This may have increased the efficiency of fluid connectivity in and around the lower crustal part of the San Andreas fault zone. This hypothesis is based on the difficulty of bringing pore fluids into the lower crustal zone in such a small time scale (one year). However, it also requires that these fluids were inefficiently connected before the earthquake, which would probably lead to high fluid pressures (lithostatic) and a weakening of the mechanical strength of the lower crustal part of the fault zone. This is a very important issue for understanding the earthquake cycle (Rice, 1992), but without having analyzed data from before the earthquake, we cannot be any more than speculative about these interpretations.

CONCLUSIONS

We conducted a wide-band MT survey around the Loma Prieta region one year after the Loma Prieta earthquake. The survey was designed to look for lower crustal electri-

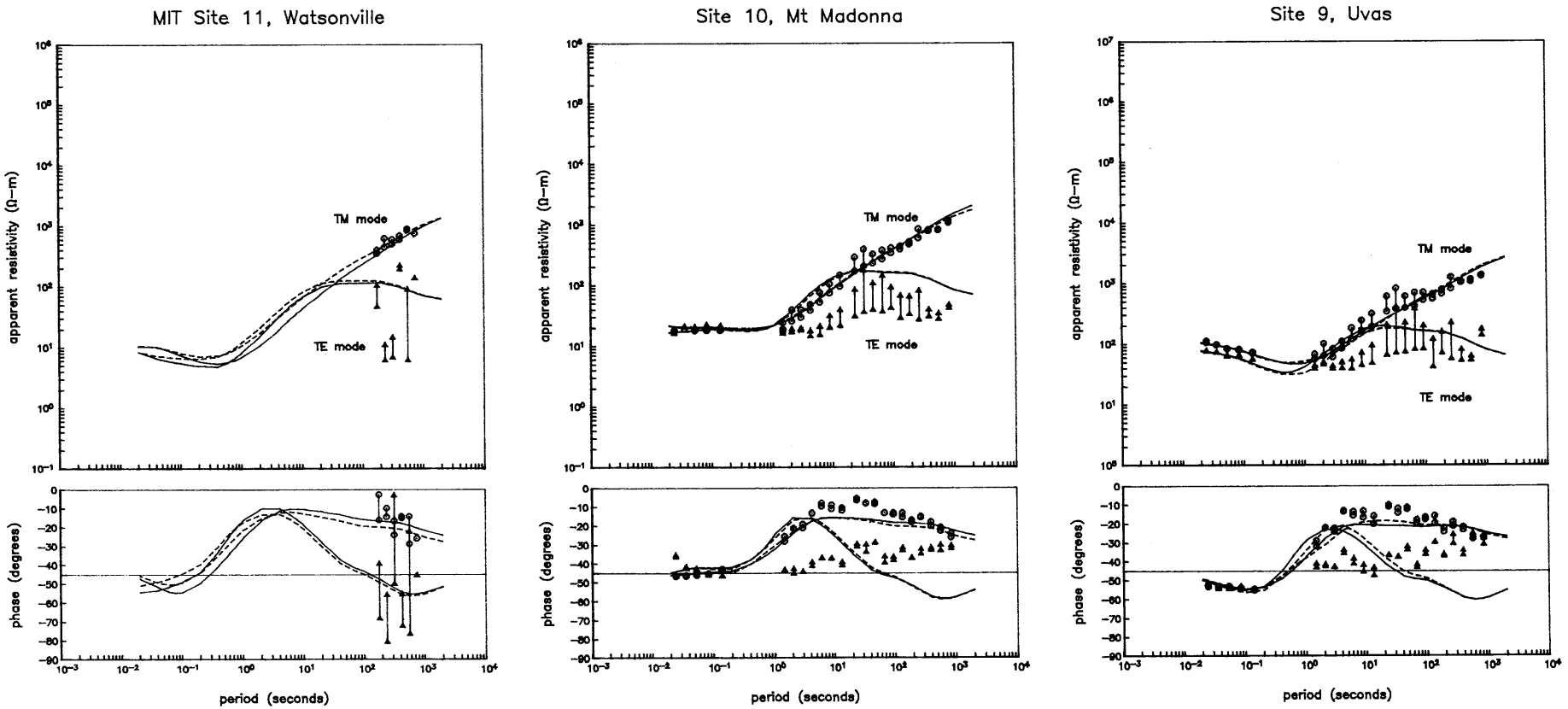

Figure 14.—Observed and predicted data at (left) site 11, Watsonville (west of the San Andreas fault), (middle) site 10, Mt. Maddona (near the fault), and (right) site 9, Uvas (east of the San Andreas fault). The solid lines are the predicted data from an inversion with an *a priori* narrow fault zone, and the dashed lines are the predicted data from an inversion where no fault zone was put into the *a priori* model and all changes were forced into the upper crust. We show both the predicted TM- and TE-mode data, even though only the TM-mode data were used in the analysis. The predicted TE-mode data were static shifted so that they agreed with the observed TE-mode data at the highest frequencies.

cal resistivity anomalies both across the fault zone and along it (from north to south). Local industrial noise seemed to contaminate the data at some sites in the band from 1 to 100 s, and at those sites, we did not use the data in that band in the analyses.

The results of our two-dimensional TM-mode inversions of the data suggested that vertical zones of enhanced lower crustal conductivity exist in the vicinity of the San Andreas fault. If we forced the changes to be put into a 5-km-wide zone, then we obtained lower crustal resistivity values as low as 50 Ω-m in that zone. To explain such dramatic conductivities relative to the lower crust away from the fault zone, we believe that fluids were present in the lower crustal part of the fault zone before the earthquake, but were inefficiently connected, and that the earthquake and its associated aftershocks increased the efficiency of fluid connectivity in that zone. An alternate interpretation is that the conductance of the fault zone is an inherent feature of that zone, but laboratory work suggests that non-elastic healing processes would eliminate much of the porosity connectivity, thus reducing the conductivity of that zone. Although our data alone cannot distinguish between the two interpretations, we believe the time-dependent interpretation is more consistent with the mechanics of the lower crust. Without having analyzed data from before the earthquake, it is impossible to test this hypothesis.

ACKNOWLEDGMENTS

We would like to thank Frank Morrison, Electromagnetic Instruments Inc., and the students from U.C. Berkeley for the tremendous job they did in collecting the MT field data and putting up with poison oak, thick brush, and long hours in the field. Useful discussions were held with Dal Stanley, Frank Morrison, Brian Evans, Gary Egbert, Steve Park, Jim Larsen, and Jim Rice. Reviews by Dal Stanley, Paul Reasenberg, and an anonymous reviewer greatly improved the manuscript. The CRAY X-MP EA/464 at the MIT supercomputer facility was used for running all the inversions. This work was supported in full by NSF grant 9011919-EAR.

REFERENCES CITED

Bailey, E.H., ed., 1966, Geology of northern California: California Division of Mines and Geology, v. 190, 508 p.

Bailey, E.H., Blake, Jr., M.C., and Jones, D.L., 1970, On-land Mesozoic oceanic crust in California Coast Ranges: U.S. Geological Survey Professional Paper 700-C, p. C70–C81.

Bailey, R.C., 1990, Trapping of aqueous fluids in the deep crust: Geophysical Research Letters, v. 17, no. 8, p. 1129–1132.

Bennett, B.R., 1985, A long-period magnetotelluric study in California: Massachusetts Institute of Technology, masters thesis, 115 p.

Brace, W.F., and Kohlstedt, D.L., 1980, Limits on lithospheric stress imposed by laboratory experiments: Journal of Geophysical Research, v. 85, no. B11, p. 6248–6252.

Brace, W.F., Orange, A.S., and Madden, T.R., 1965, The effect of pressure on the electrical resistivity of water-saturated crystalline rocks: Journal of Geophysical Research, v. 70, p. 5669–5678.

Burchfiel, B.C., and Davis, G.A., 1972, Structural framework and evolution of the southern part of the cordilleran orogen, western United States: Americal Journal of Science, v. 272, no. 2, p. 97–118.

——1975, Nature and controls of cordilleran orogenesis, western United States: extensions of an earlier synthesis: American Journal of Science, v. 275-A, p. 363–396.

Carter, N.L., and Tsenn, M.C., 1987, Flow properties of continental lithosphere: Tectonophysics, v. 136, no. 1/2, p. 27–63.

Clark, J.C., and Rietman, J.D., 1973, Oligocene stratigraphy, tectonics, and paleogeography southwest of the San Andreas fault, Santa Cruz Mountains and Gabilan Range, California Coast Ranges: U.S. Geological Survey Professional Paper 783, 18 p.

Cox, C.S., Constable, S.C., Chave, A.D., and Webb, S.C., 1986, Controlled-source electromagnetic sounding of the oceanic lithosphere: Nature, v. 320, no. 6057, p. 52–54.

Dickinson, W.R., 1981, Plate tectonics and the continental margin of California, *in* Ernst, W.G., ed., The Geotectonic Development of California: Englewood Cliffs, N.J., Prentice-Hall, p. 1–28.

Dietz, L.D., and Ellsworth, W.L., 1990, The October 17, 1989, Loma Prieta, California, earthquake and its aftershocks; geometry of the sequence from high-resolution locations: Geophysical Research Letters, v. 17, no. 9, p. 1417–1420.

Duba, A.G., and Shankland, T.J., 1982, Free carbon & electrical conductivity in the Earth's mantle: Geophysical Research Letters, v. 9, no. 11, p. 1271–1274.

Eberhart-Phillips, D., Labson, V.F., Stanley, W.D., Michael, A.J., and Rodriguez, B.D., 1990, Preliminary velocity and resistivity models of the Loma Prieta earthquake region: Geophysical Research Letters, v. 17, no. 8, p. 1235–1238.

Etheridge, M.A., Wall, V.J., Cox, S.F., and Vernon, R.H., 1984, High fluid pressures during regional metamorphism and deformation: implications for mass transport and deformation mechanisms: Journal of Geophysical Research, v. 89, no. B6, p. 4344–4358.

Evans, B.R., Fredrich, J.T., and Wong, T.W., 1990, The brittle-ductile transition in rocks: recent experimental and theoretical progress, *in* Geophysical Monograph Series 56, The Heard Volume: American Geophysical Union.

Fraser-Smith, A.C., and Coates, D.B., 1978, Large-amplitude ULF electromagnetic fields from BART: Radio Science, v. 13, no. 4, p. 661–668.

Frost, B.R., Fyfe, W.S., Tazaki, K., and Chan, T., 1989, Grain-boundary graphite in rocks and implications for high electrical conductivity in the lower crust: Nature, v. 340, p. 134–136.

Furlong, K.P., and Langston, C.A., 1990, Geodynamic aspects of the Loma Prieta earthquake: Geophysical Research Letters, v. 17, no. 9, p. 1457-1460.

Gough, D.I., 1986, Seismic reflectors, conductivity, water and stress in the continental crust: Nature, v. 323, p. 143-144.

Heard, H.C., 1976, Comparison of the flow properties of rocks at crustal conditions: Philosophical Transactions of the Royal Society of London, v. A283, p. 173–186.

Ho, A.M. -H, Fraser-Smith, A.C., and Villard, O.G., Jr., 1979, Large-amplitude ULF magnetic fields produced by a rapid transit system: close-range measurements: Radio Science, v. 14, no. 6, p. 1011–1015.

Jones, A.G., 1987, MT and reflection: an essential combination: Geophysical Journal of the Royal Astronomical Society, v. 89, no. 1, p. 7–18.

Model 1, conductive window in lower crust

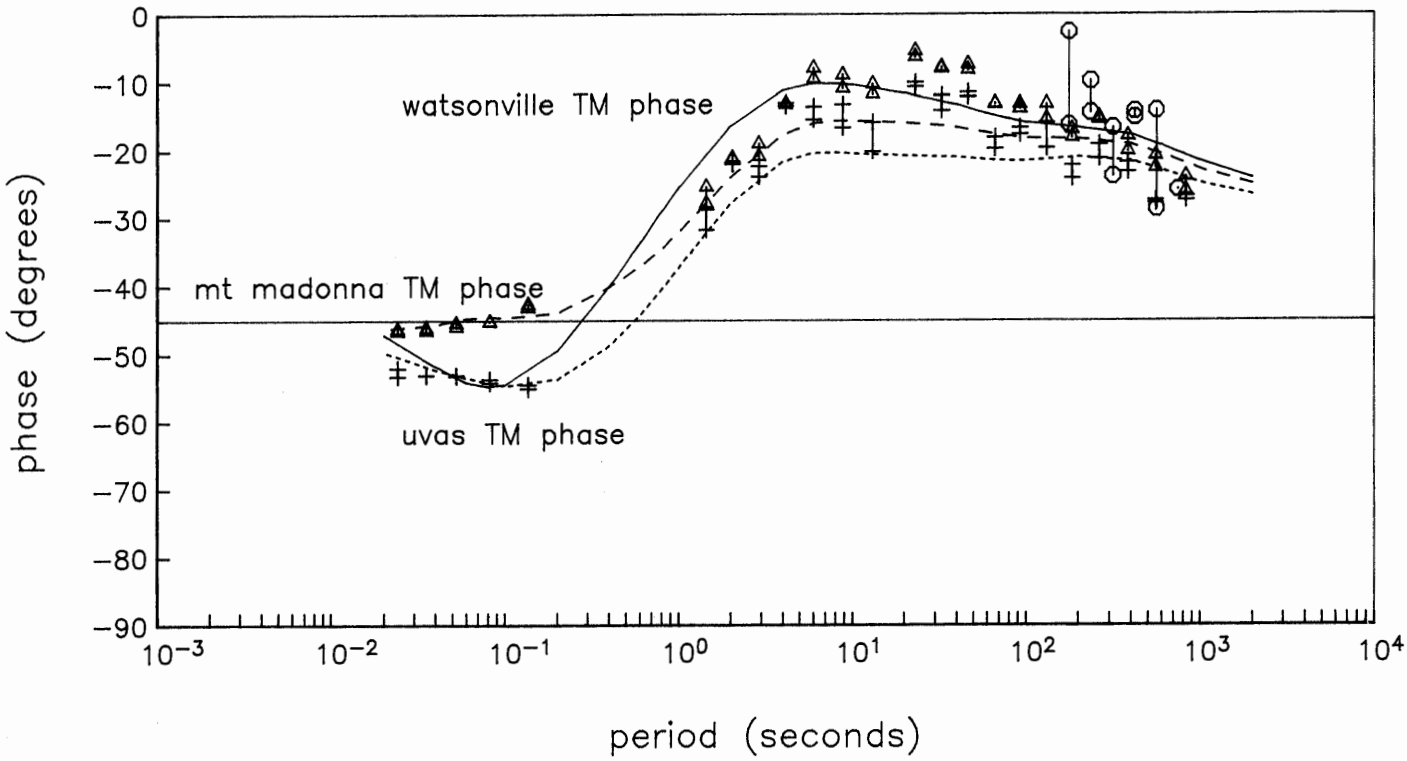

Model 2, uniform lower crust and mantle

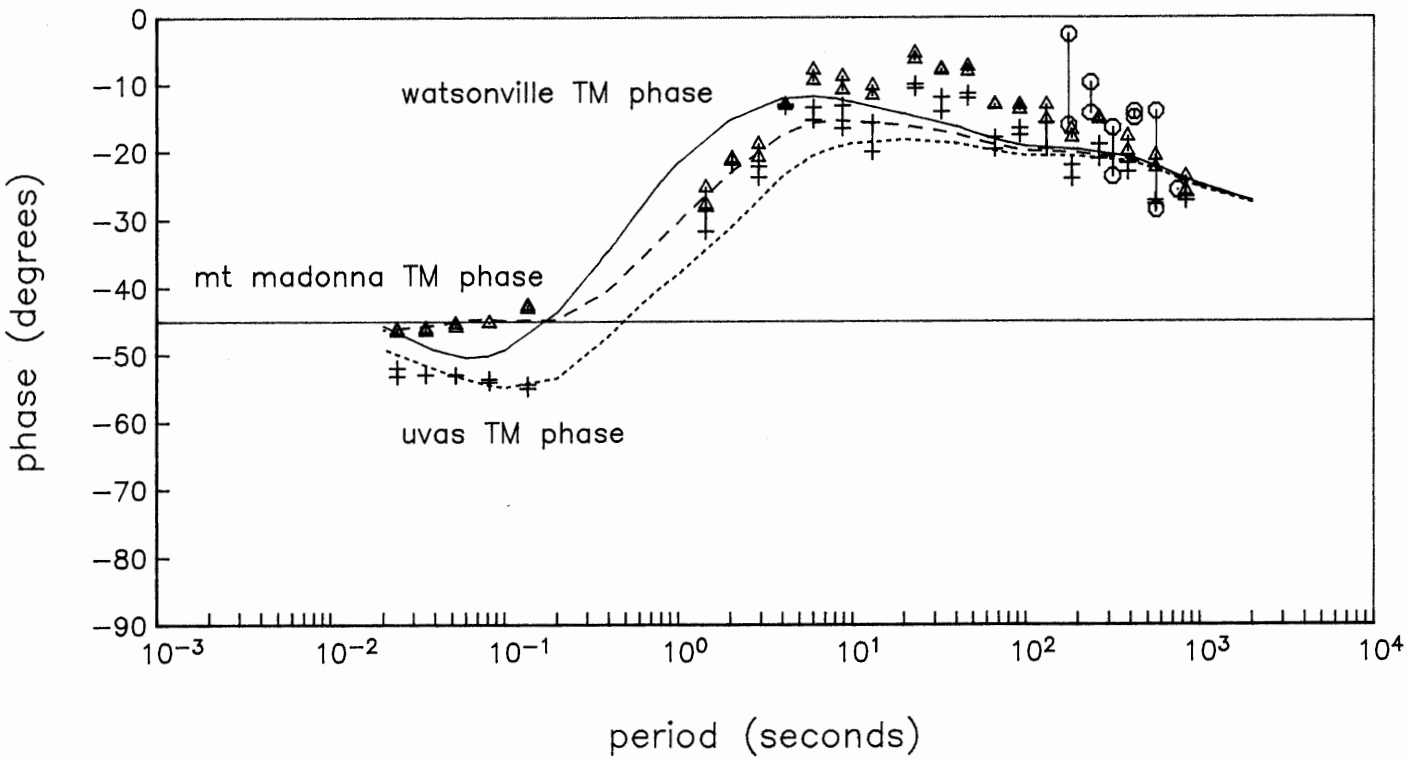

Jones, T.D., and Nur, A., 1982, Seismic velocity and anisotropy in mylonite and the reflectivity of deep crustal fault zones: Geology, v. 10, no. 5, p. 260–263.

Kerrich, R., 1986, Fluid transport in lineaments: Philosophical Transactions of the Royal Society of London, v. A317, p. 219–251.

Kerrich, R., LaTour, T.E., and Willmore, L., 1984, Fluid participation in deep fault zones: evidence from geological, geochemical, and $^{18}O/^{16}O$ relations: Journal of Geophysical Research, v. 89, no. B6, p. 4331–4343.

LaTorraca, G.A., Madden, T.R., and Korringa, J., 1986, An analysis of the magnetotelluric impedance for three-dimensional conductivity structures: Geophysics, v. 51, no. 9, p. 1819–1829.

Lee, C.D., Vine, F.J., and Ross, R.G., 1983, Electrical conductivity models for the continental crust based on laboratory measurements on high-grade metamorphic rocks: Geophysical Journal of the Royal Astronomical Society, v. 72, no. 2, p. 353–371.

Mackie, R.L., 1991, Three-dimensional magnetotelluric modeling and inversion with applications to the California Basin and Range Province: Massachusetts Institute of Technology, Ph.D. dissertation, 238 p.

Mackie, R.L., Bennett, B.R., and Madden, T.R., 1988, Long-period magnetotelluric measurements near the central California coast: a land-locked view of the conductivity structure under the Pacific Ocean: Geophysical Journal, v. 95, no. 1, p. 181–194.

Madden, T.R., 1990, Inversion of low-frequency electromagnetic data, *in* Oceanographic and Geophysical Tomography: Elsevier Science Publishers, p. 377–408.

Madden, T.R., LaTorraca, G.A., and Park, S.K., 1993, Electrical conductivity variations around the Palmdale section of the San Andreas fault zone: Journal of Geophysical Research, v. 98, no. B1, p. 795–808.

Mazzella, A., and Morrison, H. F., 1974, Electrical resistivity variations associated with earthquakes on the San Andreas fault: Science, v. 185, no. 4154, p. 855–857.

Newton, R.C., 1990, Fluids and shear zones in the deep crust: Tectonophysics, v. 182, no. 1/2, p. 21–37.

Nur, A., and Simmons, G., 1969, The effect of saturation on velocity in low porosity rocks: Earth and Planetary Science Letters, v. 7, p. 183–193.

Nur, A., and Walder, J., 1990, Time-dependent hydraulics of the Earth's crust, *in* The Role of Fluids in Crustal Processes: National Academy Press, p. 113–127.

Oppenheimer, D.H., 1990, Aftershock slip behavior of the 1989 Loma Prieta California earthquake: Geophysical Research Letters, v. 17, no. 8, p. 1199–1202.

Orville, P.M., 1963, Alkali ion exchange between vapor and feldspar phases: American Journal of Science, v. 261, no. 3, p. 201–237.

Page, B.M., 1981, The southern Coast Ranges, *in* Ernst, W.G., ed., The Geotectonic Development of California: Englewood Cliffs, N.J., Prentice-Hall, p. 329–417.

Park, S.K., Biasi, G.P., Mackie, R.L., and Madden, T.R., 1991, Magnetotelluric evidence for crustal suture zones bounding the southern Great Valley, California: Journal of Geophysical Research, v. 96, p. 353–376.

Qian, W., and Pedersen, L.B., 1991, Industrial interference magnetotellurics: an example from the Tangshan area, China: Geophysics, v. 56, no. 2, p. 265–273.

Quist, A.S., and Marshall, W.L., 1968, Electrical conductances of aqueous sodium chloride solutions from 0 to 800° and at pressures to 4000 bars: Journal of Physical Chemistry, v. 72, no. 2, p. 684–702.

Ranganayaki, R.P., 1978, Generalized thin sheet approximation for magnetotelluric modeling: Massachusetts Institute of Technology, Ph.D. dissertation, 204 p.

Ranganayaki, R.P., and Madden, T.R., 1980, Generalized thin sheet analysis in magnetotellurics, an extension of Price's analysis: Geophysical Journal of the Royal Astronomical Society, v. 60, no. 3, p. 445–457.

Rice, J.R., 1992, Fault stress states, pore pressure distributions, and the weakness of the San Andreas fault, *in* Evans and Wong, Fault Mechanics and Transport Properties in Rocks: Academic Press, p. 475–503.

Roedder, E., 1972, Composition of fluid inclusions, *in* Fleischer, M., ed., Data of Geochemistry (sixth edition): U.S. Geological Society Professional Paper 440-JJ, 164 p.

Segall, P., and Lisowski, M., 1990, Surface displacements in the 1906 San Francisco and 1989 Loma Prieta earthquakes: Science, v. 250, p. 1241–1243.

Shankland, T.J., and Ander, M.E., 1983, Electrical conductivity, temperatures, and fluids in the lower crust: Journal of Geophysical Research, v. 88, no. B11, p. 9475–9484.m

Tarantola, A., 1987, Inverse problem theory: Methods for data fitting and model parameter estimation: New York, Elsevier.

Taylor, H.P., Jr., 1977, Water/rock interaction and the origin of H_2O in granitic batholiths: Journal of the Geological Society of London, v. 133, p. 509–558.

Torgensen, T., 1990, Crustal-scale fluid transport: Eos, Transactions, American Geophysical Union, v. 71, p. 1–4.

Ucok, H., Ershaghi, I., and Olhoeft, G.R., 1980, Electrical resistivity of geothermal brines: Journal of Petroleum Technology, v. 32, p. 717–727.

Walder, J., and Nur, A., 1984, Porosity reduction and crustal pore pressure development: Journal of Geophysical Research, v. 89, no. B13, p. 11539–11548.

Wannamaker, P.E., Hohmann, G.W., and Ward, S.H., 1984, Magnetotelluric responses of three-dimensional bodies in layered earths: Geophysics, v. 49, no. 9, p. 1517–1533.

Watson, E.B., and Brenan, J.M., 1987, Fluids in the lithosphere, 1. Experimentally-determined wetting characteristics of CO_2-H_2O fluids and their implications for fluid transport, host-rock physical properties, and fluid inclusion formation: Earth and Planetary Science Letters, v. 85, no. 4, p. 497–515.

Yardley, B.W.D., 1986, Is there water in the deep continental crust?: Nature, v. 323, no. 6084, p. 111.

◀ Figure 15.—Plot of the observed and predicted TM-mode phases for the inversion results with and without an *a priori* narrow conductive fault zone. It is difficult to tell much difference between the two models within the spread of the data, but we believe that data are fit slightly better when there is a somewhat conductive fault zone.

Figure 16.—Observed and predicted data at site 7, Hollister (east of the ● San Andreas fault). The solid lines are the predicted data from an inversion with an *a priori* narrow fault zone, and the dashed lines are the predicted data from an inversion where no fault zone was put into the *a priori* model and all changes were forced into the upper crust. We show both the predicted TM- and TE-mode data, even though only the TM-mode data were used in the analysis. Both models fit the data equally well.

Site 7, Hollister

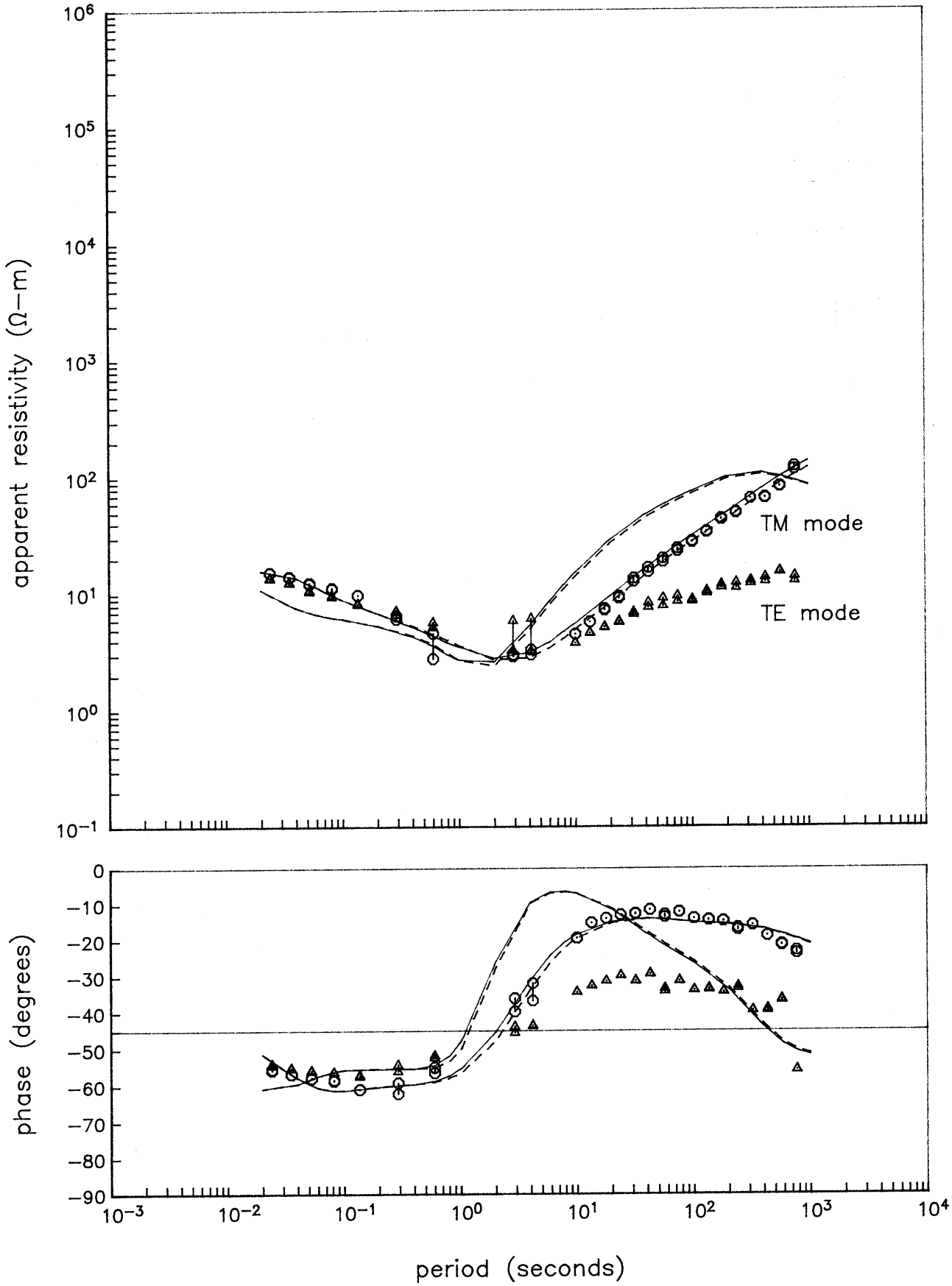

☆ U.S. GOVERNMENT PRINTING OFFICE: 1997 - 573-046 / 20077 REGION NO. 8